Axonal Membrane Trafficking Regulation and Its Failure in Cargo Delivery



A thesis submitted for the degree of

DPhil in Biochemistry (TSRI/OU)

Trinity Term 2023

Tai Chaiamarit

Lincoln College

University of Oxford

Under the supervision of:

Professor Ilan Davis

Dr. Sandra E. Encalada

Declaration

I hereby declare that this thesis is my own work. The experiments were performed by me, unless otherwise stated. The experiments were done in the Encalada lab (Scripps Research) and in the Davis lab in the Department of Biochemistry (Oxford), unless otherwise stated for the works in collaboration. This thesis has not been submitted for any other degree or professional qualification.

The following figures were published and were partly produced in collaboration with co-authors: Figures 2.1-2.2, Figures 2.4-2.5, Figures 2.7-2.15, Figures 3.1-3.7.

The following figures contain data from others: fluorescence images and FIB-SEM data in Figure 3.8 were collected by Adriaan Verhelle and Yin Wu (Encalada Lab, Scripps Research) and Jesse Aaron (Janelia Research Campus); the vector maps in Figure 4.1 were made by Francesca Robertson (Davis Lab, Oxford); the iCLIP data from Figure 4.11A were from Jeff Lee (Davis Lab, Oxford).

Tai Chaiamarit

21 April 2023

Table of Content

Abstract i

Acknowledgements ii

List of Figures iv

List of Abbreviations vii

1 Introduction 1

1.1 Introduction to the thesis 1

1.2 Background and the research problems 2

1.2.1 The specialized form and function of neurons 2

1.2.2 The microtubule (MT) cytoskeleton and the regulation of molecular motor-based transport in axons 5

1.2.3 The roles of small GTPases in axonal trafficking and transport regulation 10

1.2.4 Membrane trafficking and protein quality control mechanisms in axons 13

1.2.6 Cultured primary neurons as a model system to study axonal transport regulation, membrane trafficking, and mechanisms of neurodegeneration 17

1.2.7 Localized protein synthesis and synaptic plasticity 19

1.2.8 Post-transcriptional regulation in neurons and a departure from 'protein-centric' to 'RNA-centric' views 23

1.3 The research aims and questions 26

1.4 Significance 27

1.5 The limitations 28

1.6 The outline of the thesis 30

1.7 References 30

2 Endosomal Sorting Generates Axonal Endoggresomes 44

2.1 Introduction 46

2.2 Materials and Methods 49

2.2.1) Mouse primary neuronal cultures 49

2.2.2) Cloning, transfection, and transduction of DNA constructs 51

2.2.3) Fluorescent dyes and drug assays 57
2.2.4) Correlative fluorescence and SEM study of cultured primary neurons ... 60
2.2.5) Immunofluorescence (IF) of cultured primary neurons 63
2.2.6) Biochemical Assays in Neuro2a cells 64
2.2.7) Calcium imaging and potassium chloride (KCl)-induced depolarization 67
2.2.8) Cell death assay and imaging 68
2.2.9) Quantitation and data analysis 69
2.3 Results 75
2.3.1 PrP^{PG14} is transported in vesicles by kinesin-1 to form aggregates in axons 75
2.3.2 PrP^{PG14} aggregates are Golgi-derived and sorted through endosomal pathway 78
2.3.3 Transient access of PrP^{PG14} to the axonal cell surface contributes to endoggresome formation 82
2.3.4 An ARL8b/kinesin-1/HOPS pathway drives PrP^{PG14} endoggresome formation in axons 85
2.3.5 ARL8b is a master regulator of ARESTA and a key determinant of PrP^{PG14} axonal entry 90
2.3.6 Misfolded PrP is degraded in the soma but persists in axons due to impaired retrograde transport and diminished lysosomal degradation capacity 94
2.3.7 PrP^{PG14} neurons display ARESTA-dependent impaired calcium intake dynamics and decreased neuronal viability 99
2.4 Conclusions and discussion 102
2.5 References 107
3 Mutant Prion Protein Endoggresomes are Hubs for Local Axonal Organelle-Cytoskeletal Remodeling 116
3.1 Introduction 118
3.2 Materials and Methods 121
3.2.1 Quantitative analysis of cargo motility in whole axons 123
3.2.2 Single-particle tracking (SPT) of mitochondria 123

3.2.3 Quantitative analysis of local cargo motility disruption 123
3.2.4 Quantitation of kinesin-1 and kinesin-3 fluorescence intensity..... 124
3.2.5 Sub-pixel colocalization analysis 124
3.2.6 Fluorescence Recovery After Photobleaching (FRAP) 125
3.2.7 Super-resolution Radial Fluctuation (SRRF) Microscopy..... 125
3.2.8 STORM sample preparation and imaging..... 125
3.2.9 Membrane-extraction SEM (ME-SEM) preparation and imaging..... 126
3.2.10 TMRE Assay..... 127
3.2.11 Correlative fluorescence and FIBSEM preparation and imaging..... 128
3.2.12 Figure plotting and statistical analyses..... 131
3.3 Results 132
3.3.1 Axonal transport of neuronal cargoes is differentially impaired in axons with PrP^{PG14} endoggresomes..... 132
3.3.2 Micro-movement analysis reveals local transport jams at axonal PrP^{PG14} aggregate sites..... 137
3.3.3 Local alterations to the actin and MT cytoskeletal organization at PrP^{PG14} aggregate sites, revealed at super-resolution 139
3.3.4 Selective retention of kinesin-1 and kinesin-3 at PrP^{PG14} aggregate sites and depletion from cargoes 143
3.3.5 Retention of kinesin-1 at PrP^{PG14} aggregate sites requires its cargo-binding regulatory domain..... 147
3.3.6 Enhanced mitochondrial fission at PrP^{PG14} aggregate sites requires Rab7 GTPase activity..... 150
3.3.7 Dysfunctional mitochondria are retained at PrP^{PG14} aggregate sites..... 153
3.3.8 Correlative fluorescence and FIB-SEM of PrP^{PG14} aggregate sites revealed organelle-cytoskeletal remodeling *in situ* 154
3.4 Conclusion and discussions 157
3.5 References 163
4 Mechanism and Function of mRNA transport to the axonal pre-synapse..... 173
4.1 Introduction 175

4.2 Materials and Methods 177

4.2.1 *Drosophila* genetics 177

4.2.2 *Drosophila* larval fillet preparation and spaced chemical stimulation 190

4.2.3 *Drosophila* larval brain primary culture 193

4.2.4 Immunofluorescence (IF) 195

4.2.5 RNA single-molecule fluorescence in situ hybridization (smFISH) 197

4.2.6 Image analysis for smFISH and IF at the NMJ 200

4.2.7 Live imaging of mRNA with MS2-MCP system with denoising 203

4.2.8 RNA single-molecule hybridization chain reaction (smHCR) 204

4.2.9 High-throughput larval locomotion assay and analysis 207

4.2.10 Generation of graphs, figures, and statistical analyses 209

4.3 Results 209

4.3.1 Absolute quantitation of mRNA copy number in the *Drosophila* larval motoneurons 209

4.3.2 Oscillatory bidirectional motion of mRNA in motoneuron axons 212

4.3.3 Reduction of Kinesin-1 and Cytoplasmic Dynein motor speed impairs axonal mRNA localization and synaptic plasticity 215

4.3.4 Kinesin-1 and Imp are putative axonal transport machinery for *rab11* mRNA and are required for synaptic plasticity. 220

4.3.5 Reduction of *rab11* mRNA copy number, not protein, correlates with NMJ development 223

4.3.6 A family of RabGTPase transcripts are localized to axon terminals and glial extensions at the NMJ and are important for function 225

4.4 Conclusion and discussion 229

4.5 References 234

5 Thesis conclusions and Future Directions 244

5.1 Conclusions 244

5.2 Future Directions 248

5.2.1 Investigating the maturation and cell-to-cell spread of mutant PrP endoggresomes 248

5.2.2 Targeting the subcellular pathways for the reversal of misfolded PrP-induced pathologies.....253

5.2.3 Investigating the localized translation of *Rab* GTPases in *Drosophila* models of neurodegenerative diseases.....256

5.3 References..... 259

Appendix..... 265

A. Curriculum Vitae (CV).....265

B. Chassefeyre R*, Chaiamarit T*, Verhelle A*, Novak SW, Andrade LR, Leitao ADG, Manor U, Encalada SE. 2021. Endosomal Sorting Drives the Formation of Mutant Prion Protein Endoggresomes. *Science Advances* 7(52), https://www.science.org/doi/10.1126/sciadv.abg3693 *Co-authors 266

C. Chaiamarit T, Wu Y, Verhelle A, Encalada SE. 2023. Fluorescence Assays for Real-Time Tracking of Cell Surface Protein Internalization and Endosomal Sorting in Axons of Primary Mouse Hippocampal Neurons. *Bio-protocol*, *13*(7), e4651. https://doi.org/10.21769/BioProtoc.4651.....267

D. Chaiamarit T, Verhelle A, Chassefeyre R, Shukla N, Novak SW, Andrade LR, Manor U, Encalada SE. 2023. Mutant Prion Protein Endoggresomes are Hubs for Local Axonal Organelle-Cytoskeletal Remodeling. *bioRxiv*, 2023.03.19.533383. https://doi.org/10.1101/2023.03.19.533383.....268

E. Nieto-Torres JL, Shanahan SL, Chassefeyre R, Chaiamarit T, Zaretski S, Landeras-Bueno S, Verhelle A, Encalada SE, Hansen M. 2021. LC3 Phosphorylation Regulates FYCO1 Binding and Directional Transport of Autophagosomes. *Current Biology* S0960-9822(21)00750-8. https://doi.org/10.1016/j.cub.2021.05.052.....269

Axonal Membrane Trafficking Regulation and Its Failure in Cargo Delivery

Tai Chaiamarit, Lincoln College, OXON, DPhil in Biochemistry (TSRI/OU), Trinity term 2023

Abstract

Regulation of axonal trafficking of membrane-bound compartments is important for delivery of various neuronal cargoes towards the distal synapses and for quality control of damaged cellular components/toxic proteins. The contribution of Rab GTPase pathways in neurodegenerative pathologies and the regulatory mechanism to replenish various Rab proteins in the axonal periphery remain unclear. In the Encalada lab, we modeled familial prion disease axonopathies in primary murine hippocampal neurons, to determine (1) the biogenesis pathway that forms neurotoxic mutant prion protein (PrP^{mut}) aggregates and (2) the consequences of PrP^{mut} aggregate formation on cytoskeletal-organelle interactions within swollen axons that PrP^{mut} aggregates reside. Firstly, I, and the research team, identified that the small GTPase ARL8 recruits kinesin-1 and HOPS for axonal transport and fusion, respectively, that generates neurotoxic PrP^{mut} aggregates in non-degradative endolysosomes, called 'endoggresomes.' This axonal rapid endosomal sorting and transport-dependent aggregation (ARESTA) mechanism forms endoggresomes rapidly, and as a result impair calcium dynamics and neuronal viability. Inhibition of ARESTA reduces axonal endoggresome densities and rescues neuronal dysfunction, providing an anti-aggregation target to ameliorate prionopathies. Secondly, axonal micro-domain analysis of live organelle dynamics within endoggresome sites showed deficits to the MT-based active transport system, that result in enhanced mitochondrial-Rab7 endosomal contacts that induce mitochondrial fission via Rab7 activity and render retained mitochondria dysfunctional. In the Davis lab, I studied post-transcriptional fate of *rab* GTPase mRNA towards their axonal localization and function at the *Drosophila* larval neuromuscular junction (NMJ) pre-synapse. I found that a conserved RNA-binding protein Imp and kinesin-1 are required for *rab11* mRNA delivery to axon termini and are required for synaptic plasticity and unimpaired locomotory behavior. Furthermore, I detected transcripts of multiple important *rab* GTPases for endosome recycling at the axonal and glial periphery at the NMJ, uncovering an unorthodox regulatory mechanism of axonal membrane trafficking.

Acknowledgements

I would like to thank both of my supervisors, Dr. Sandra Encalada and Prof. Ilan Davis, for the opportunity to join your fantastic research groups. I am grateful for Sandra who has trained me in thinking about scientific methods, learning the standard practice in research conduct, writing research proposal and scientific publication, and giving effective presentation from the very first day of my PhD. Sandra has provided continuing support and frequent communication, leading to successful submission of my three first-/co-first-author publications. I thank Ilan for professional and personal supports, during my transition from Scripps to Oxford, for guiding my thesis writing process, and for pitching crazy experimental ideas.

For former and present members of the Encalada lab, I thank Romain Chassefeyre for training me on various primary neuronal culture techniques; I thank Adriaan Verhelle for great teamwork and input on my experiments; I thank George Campbell for teaching me MATLAB coding and a myriad of image analysis tricks; I thank Kayal Madhivanan, David Soriano-Castell, Adeola Adeyemo, Andre Leitao, Nandini Shukla for listening to my complains during lunchtime and for always giving valuable feedback during my lab meeting.

For former and present members of the Davis lab, I thank Jeff Lee for all the helps, from finding reagents in the lab to basically writing all useful codes to make my life easier; I thank Francesca Robertson for teaching me *Drosophila* genetics; I thank Dalia Gala and Darragh Ennis for training me on *Drosophila* larval dissection and various staining protocols; I thank Danail Stoychev for the help with image analysis; I thank Richard Parton for microscopy training; I thank Laetitia Dewavrin for being the most amazing part II MSc student I could

ever ask for; I thank Maria Kiourlappou, Julia Olivares Abril, Jana Joha, Arianna Ceccarelli for collaboration and for bringing good vibes to the lab.

All my collaborators, without whom this work would not have come this far. I thank Uri Manor and teams, especially Leo Andrade and Sammy Weiser Novak, for always blowing my mind with amazing EM images. I thank Michael Petrascheck and his lab members for sitting through my joint lab meetings and giving valuable feedbacks, and all the labs in the DNC for amazing happy hours. I thank my Scripps Research committee: Ashok Deniz, Stuart Lipton, Sergio Catz, Ian Wilson for supports and critical feedbacks on my projects. I thank my Oxford advisory committee and confirmation of status examiners: Jordan Raff, Benoît Kornmann, and Petros Ligoxygakis for valuable time and feedbacks.

I give special thanks to Ian Wilson for coordinating the Skaggs-Oxford program and keeping me in the planned timeline. Thank you for visiting me in Oxford every year, and cheers to all amazing meals we had.

I thank my friends at Scripps, my Thai friends in the San Diego community, my friends from Lincoln College and Department of Biochemistry, my friends from the Oxford Thai Society (OTS), and my comrades in the Thai Democracy Advocates (THAI-DA), UK.

I thank for the scholarship from the Development and Promotion of Science and Technology Talents Project (DPST), Royal Thai government, and the fellowship from the Skaggs-Oxford program, thank you Dawn Eastmond.

Last but not least, thank you for the love and support from my family, especially my mom and dad back in Thailand, and my partner Peechaya in Oxford. I would not have made it through PhD without so much love from you.

List of Figures

Figure 1.1 Specialized compartments of a neuron

Figure 1.2 Axonal transport regulation by MT PTMs and molecular motors

Figure 1.3 The cycle of Rab GTPases and their functions in membrane trafficking regulations and quality control mechanisms

Figure 1.4 The *Drosophila* larval neuromuscular junction (NMJ) synapse

Figure 2.1 Isolation of hippocampus from mouse neonates for primary hippocampal culture

Figure 2.2 Growth of cultured primary hippocampal neurons

Figure 2.3 Schematic of mouse PrP constructs and sequence

Figure 2.4 BFA Treatment and validation of PrP^{PG14}-mCh retention in the ER

Figure 2.5 Specific labeling of PrP^{PG14}-mCh-BBS by BTX-AF647

Figure 2.6 Correlative fluorescence and S3EM study axonal endoggresomes

Figure 2.7 Analysis and definition of PrP^{PG14} vesicles and endoggresomes

Figure 2.8 Characterization of PrP^{PG14} vesicle and aggregates in axons

Figure 2.9 The identity and ultrastructure of PrP^{PG14} endoggresomes

Figure 2.10 Endoggresome formation requires the rapid transit of PrP^{PG14} to axonal cell surface

Figure 2.11 The Axonal Rapid Endosomal Sorting and Transport-dependent Aggregation (ARESTA) drives endoggresome formation

Figure 2.12 ARL8b merges indirect and direct ARESTA and tags PrP^{PG14} vesicles for axonal entry

Figure 2.13 Misfolded PrP^{PG14} is degraded in the soma but sustained in axons due to impairments to local lysosomal degradation and retrograde transport

Figure 2.14 Impaired calcium intake dynamics and neuronal viability in PrP^{PG14} neurons are ARESTA-dependent

Figure 2.15 Opposing roles of neuronal endolysosomal pathways which clear misfolded PrP in the soma but promote endoggresome formation in axons

Figure 3.1 Axonal transport is progressively impaired in PrP^{PG14}-mCh axons

Figure 3.2 Local axonal transport disruption of mito-EGFP micro-movements within PrP^{PG14}-mCh aggregate sites

Figure 3.3 Actin accumulation and selective impairment to MT track PTMs at PrP^{PG14} aggregate sites

Figure 3.4 Kinesin-1 and kinesin-3 accumulation at PrP^{PG14} aggregate sites and depletion from mitochondria and vesicles

Figure 3.5 Retention of kinesin-1 (KIF5C) at PrP^{PG14} AGG sites requires its cargo-binding domain

Figure 3.6 Rab7-mediated mitochondrial fission at PrP^{PG14} aggregate sites

Figure 3.7 Dysfunctional mitochondria accumulates within PrP^{PG14} aggregate sites

Figure 3.8 Correlative fluorescence and FIBSEM of cultured primary neurons

Figure 3.9 Working model of the mechanism of cytoskeletal-organelle remodeling by PrP^{PG14} endoggresomes

Figure 4.1 Transgenesis of Rab11 MS2 lines for MS2-MCP imaging

Figure 4.2 Transgenesis of Rab11Δ3'UTR-2xFRT and FLP mating scheme for tissue-specific knockdown in post-developmental stages

Figure 4.3 *Drosophila* larval fillet preparation, smFISH, IF, and KStim paradigm

Figure 4.4 Growth and morphology or cultured neurons from the brain of *Drosophila* 3^{rd} instar larvae

Figure 4.5 A semi-automated and automated pipeline of 3D segmentation of fluorescence signal inside the motoneuron terminal boutons

Figure 4.6 smHCR schematic and imaging

Figure 4.7 Larval crawling assay analysis

Figure 4.8 Sensitive detection of *rab11* transcripts at the NMJ pre-synapse

Figure 4.9 Live imaging of *rab11* and *gdi* mRNAs by MS2/MCP system

Figure 4.10 *Kinesin-1* and *dynein* mutant larvae show defects in locomotion, synaptic plasticity, and mRNA localization

Figure 4.11 Imp is a putative RBP for *rab11* mRNA localization in axons and is required for synaptic plasticity

Figure 4.12 *Rab11* mRNA and protein level in *rab11* knockdown and stimulated NMJ

Figure 4.13 Functional requirements of multiple *Rab* species and the mRNA localization in the axon termini and glial extension at the NMJ

Figure 5.1 Diagram of *Rab* mRNA localization in neurons/neuronal precursors and glia of *Drosophila*

List of Abbreviations

3'UTR	3'untranslated region
3D	3 dimensions
5'UTR	5'untranslated region
Aβ	amyloid beta
AAV	adeno-associated virus
Ac	acetylation/acetylated
AD	Alzheimer's disease
AF	Alexa Fluor
AGG	aggregate
ALS	amyotrophic lateral sclerosis
Ant	anterograde
APC	adenomatous polyposis coly
ARESTA	axonal rapid endosomal sorting and transport-dependent aggregation
ARF	ADP-ribosylation factor
ARL	ADP ribosylation factor(Arf)-like
ASD	autism spectrum disorder
attB	attachment site from bacteria
attP	attachment site from bacteriophage
BBS	Bungarotoxin binding sequence
BFA	Brefeldin-A
Brp	Bruchpilot
BTX	Bungarotoxin
CaMKII	calcium/calmodulin-dependent protein kinase II
Cdc42	cell division cycle 42
cDNA	complementary DNA
CDS	coding sequence
CHM	chloroideremia
CJD	Creutzfeldt–Jakob disease

CLEM	correlative light-electron microscopy
CRIMIC	CRISPR-mediated integration cassette
CRISPR	clustered regularly interspaced short palindromic repeats
DAPI	4′,6-diamidino-2-phenylindole
DHC	dynein heavy chain
DIV	day in vitro
Dlg	Discs large
DMEM	Dulbecco's Modified Eagle Medium
DMSO	dimethylsulfoxide
DN	dominant negative
DNA	deoxyribonuclein acid
Dnase	deoxyribonuclease
EB1	End binding 1
EE	early endosome
ER	endoplasmic reticulum
ERAD	ER-associated degradation
EU	European Union
FBS	fetal bovine serum
FFI	fatal familial insomnia
FIBSEM	focused ion beam scanning electron microscopy
FISH	fluorescence in situ hybridization
FLP	flippase enzyme
fps	frame per second
FRAP	fluorescence recovery after photobleaching
FRT	flippase enzyme recognition target
GA	glutaraldehyde
GAP	GTPase activating protein
GC	guide contruct
GDF	GDI displacement factor

GDI	GDP disassociation inhibitor
GDP	guanosine diphosphase
GEF	guanine nucleotide exchange factor
GFP	green fluorescent protein
GGT	geranylgeranyl transferase
GO	gene ontology
GPI	glycosylphosphatidylinositol
gRNA	guide RNA
GSS	Gerstmann–Sträussler–Scheinker
GTP	guanosine triphosphase
GTPase	guanosine triphosphatase
HA	homology arm
HC	homology construct
HCR	hybridization chain reaction
HD	Huntington's disease
HMDS	hexamethyldisilazane
HOPS	homotypic fusion and protein sorting
HPS	Hermansky-Pudlak syndrome
HRP	horseradish peroxidase
HTT	Huntingtin
iCLIP	individual-nucleotide resolution UV crosslinking and immunoprecipitation
IF	immunofluorescence
IGF2	insulin-like growth factor 2
ILV	intra-luminal vesicle
Imp	insulin-like growth factor 2 mRNA-binding protein
INF2	inverted formin 2
IPOD	insoluble protein deposit
JF	Janelia Fluor
JUNQ	juxta nuclear quality control compartment

K-S	Kolmogorov-Smirnov
kB	kilobase
KCl	potassium chloride
KHC	kinesin heavy chain
KIF	kinesin family member
KLC	kinesin light chain-1
kV	kilovolt
LAMP1	lysosomal associated membrane protein 1
LE	late endosome
LLRK	leucine-rich repeat kinase
lncRNA	long non-coding RNA
LoG	Laplacian of Gaussian
MAP	microtubule-associated protein
MBOP	mushroom body output neuron
MCP	MS2 capping protein
ME	membrane extraction
MF	molecular function
Mfn1	Mitofusin 1
MiMIC	Minos-mediated integration cassette
miRNA	micro-RNA
Miro	mitochondrial Rho GTPase
mRNA	messenger RNA
MT	microtubule
mTOR	mammalian target of rapamycin
MVB	multivesicular body
N2a	Neuroblastoma 2a
NBA	Neurobasal-A
NMJ	neuromuscular junction
NON-AGG	non-aggregate

OrR	Oregon-R
osk	oskar
OXPHOS	oxidative phosphorylation
PBS	phosphate-buffered saline
PCR	polymerase chain reaction
PD	Parkinson's disease
PFA	paraformaldehyde
PFU	plaque-forming unit
Pi	inorganic phosphate
PK	proteinase K
PMD	protein misfolding disease
PMSF	phenylmethylsulfonyl fluoride
PNS	post-nuclear supernatant
poly(A)	polyadenylation
PrD	prion disease
PrP	prion protein
PrP^{c}	cellular PrP
PrP^{mut}	mutant PrP
PrP^{Sc}	Scrapie isoform of PrP
PSD	post-synaptic density
PSD-95	post synaptic density-95
PSF	point spread function
pTIRFM	pseudo-total internal reflection fluorescence microscopy
PTM	post-translational modification
QC	quality control
Rab	Ras-like proteins in the brain
Rac	Ras-related C3 botulinum toxin substrate
RBP	RNA-binding protein
RE	recycling endosome

REP	Rab escort protein
RESET	rapid ER stress-induced export
Ret	retrograde
Rev	reversal
RFP	red fluorescent protein
RIPA	radioimmunoprecipitation assay
RMCE	recombinase-mediated cassette exchange
RNA	ribonucleic acid
ROI	region of interest
rRNA	ribosomal RNA
S3EM	serial section scanning electron microscopy
SA	splice acceptor
SDS-PAGE	sodium dodecyl-sulfate polyacrylamide gel electrophoresis
SEM	scanning electron microscope/microscopy
SFPQ	splicing factor proline and glutamine rich
sgg	shaggy
shRNA	short hairpin RNA
SIM	structured illumination microscopy
siRNA	small interfering RNA
SMA	spinal muscular atrophy
smFISH	single-molecule FISH
smHCR	single-molecule HCR
SPT	single-particle tracking
SR	super-resolution
SRRF	super-resolution radial fluctuation
SS	signal sequence
SSR	subsynaptic reticulum
Stat	stationary
STORM	stochastic optical reconstruction microscopy

SYP	synaptophysin
SYT	synaptotagmin
TCA	trichloroacetic acid
TCS	Thrombin cleavage sequence
Tdt	terminal deoxynucleotidyl transferase
TMRE	tetramethylrhodamine, ethyl ester
tub	tubulin
TX	Triton X-100
Tyr	tyrosination/tyrosinated
UAS	upstream activation sequence
UPR	unfolded protein response
UTR	untranslated region
VNC	ventral nerve cord
WB	western blot
XLMR	X-linked non-specific mental retardation

1

Introduction

Content

1.1. Introduction to the thesis

Membrane trafficking regulation in the axon is important for the precise transport and delivery of various neuronal cargoes—e.g., pre-synaptic proteins, messenger ribonucleic acid (mRNA), signaling molecules, and membrane-bound organelles—to the distal synapses. Impaired axonal transport has a disruptive impact on axonal health, including synaptic function, and has been implicated in various neurodegenerative pathologies, including in Alzheimer's disease (AD) and prion diseases (PrDs) (Nagano and Araki, 2021; Winckler et al., 2018). How the proper localization of proteins and mRNAs of membrane trafficking regulators—namely the Ras-like proteins in the brain (Rab) family of small GTPases—contribute to axonal function/dysfunction in health and in disease remains unclear. The research work presented in this thesis provides mechanistic insights into the roles of small GTPases in the development of early- and late- PrD pathologies, specifically during the formation of toxic misfolded mutant prion protein (PrP) aggregates in mammalian axons. The consequences of the formation of these mutant PrP aggregates to mitochondrial dysfunction are also

characterized herein. Furthermore, this thesis explores the mechanism and function of the delivery of the *rab* GTPase mRNA for localized translation in the *Drosophila* neuromuscular junction (NMJ) during synaptic development and plasticity, to contribute to our understanding for the cellular basis of learning and memory.

Chapter 1 will provide an introduction to the studies presented herein, by first discussing the background and context of the research, followed by discussing the knowledge gaps and specific questions addressed in this thesis, by outlining the research aims/objectives, the significance, and finally the limitations of this study. Experimental chapters follow Chapter 1.

1.2 Background and the research problems

1.2.1 The specialized form and function of neurons

"Seeing is believing" is pertinent to the discovery of neurons by Santiago Ramón y Cajal. In the late 1880s, there were conflicting theories about whether the nervous system was made up of a continuous network, or if it was made up of distinct units that join ends to relay the information (de Castro, 2019). Cajal was the first scientist to visualize the individual functional cell of the brain under the microscope called a "**neuron**," comprised of structurally and functionally distinct compartments called **dendrites** (receiving information from another neuron), **the cell body/soma** (processing the information), and **the axon** (sending the information to another neuron via the synapse) (**Figure 1.1A**). Neurons are specialized cells that form the neural networks that perform sensory, motor, and cognitive functions (Raine, 1999). On average, the human brain is made up of 100 billion neurons with tremendous diversity in morphology and function. The

brain also contains 10- to 50-fold more glial cells than neurons, which provide various supporting roles (Herculano-Houzel, 2012). Regardless of such tremendous complexity of the neural and glial network in the brain, it is worth noting that the discovery of the complex neuronal structure by Cajal was made possible because of key experimental designs: (1) the staining method developed by Golgi, a fellow scientist, which allowed for the sparse labeling of a neuron in its entirety, and (2) the analysis of brains from young animals, where the axon undergoes continuous growth while it searches for connections with other neurons using the actively growing and motile growth cones (de Castro, 2019) (**Figure 1.1B**).

Following Cajal's legacy, neurobiology research studies nowadays rely heavily on animal models, various labeling techniques, and advanced imaging methodologies to gain insights into the cellular and molecular processes underpinning specialized function of the brain at the level of individual neurons down to individual synapses. A single neuron works by propagating electrical signals using voltage-gated ion channels—which are crucial for the generation of the resting potential and the propagation of action potentials down the axon. The transfer of electrical signals from one neuron to the next is achieved primarily at the chemical synapse following neurotransmitter release (**Figure 1.1C**). The neurotransmitters—especially neuropeptides—as well as the enzymes that locally synthesize small-molecule neurotransmitters (such as Acetylcholine), are made in the cell body and are transported in vesicles a long way to the synapse and then are recycled in the endomembrane system (Schlager and Hoogenraad, 2009) (**Figure 1.1C**). In addition, many membrane-bound organelles such as mitochondria also travel to distal axonal regions via active microtubule-based transport, to support neuronal, and specifically, synaptic function (Guedes-Dias and Holzbaur, 2019). Even though diffusion can account for the distribution of

small biomolecules (i.e., proteins with an average diameter of 3 nm), vesicles with an average diameter of 20 nm and mitochondria that can be up to 10 μm in length can take 10 to 1800 times longer, respectively, compared to a protein, to reach the destination by diffusion (Encalada and Goldstein, 2014). For example, the α motor neuron in humans has a typical cell body diameter of 50 mm that is localized in the lumbar spinal cord, but projects 1 meter long axons toward the muscles in the lower extremities (Moughamian and Holzbaur, 2012) (**Figure 1.1D**). If this neuron were to rely on diffusion to deliver a 10-μm mitochondria, it would take 34 years to reach the axon termini. The axon is vulnerable to various types of damage leading to Wallerian degeneration (Rotshenker, 2011), as well as to many age-related proteinopathies, including AD and amyotrophic lateral sclerosis (ALS). In these diseases, early signs include axonal dystrophic swellings (Delisle and Carpenter, 1984; Masliah et al., 1991). Thus, understanding the regulation of active transport and delivery of cargoes inside axons is important, as the mechanistic insights could provide the scope for development of therapeutic strategies to revert neuronal defects in disease. Some of the fundamental questions addressed in this thesis include: (1) how are axons vulnerable to protein misfolding in neurodegenerative diseases and (2) how do neurons mobilize mRNA, in addition to proteins, to the axonal termini to maintain the synaptic function?

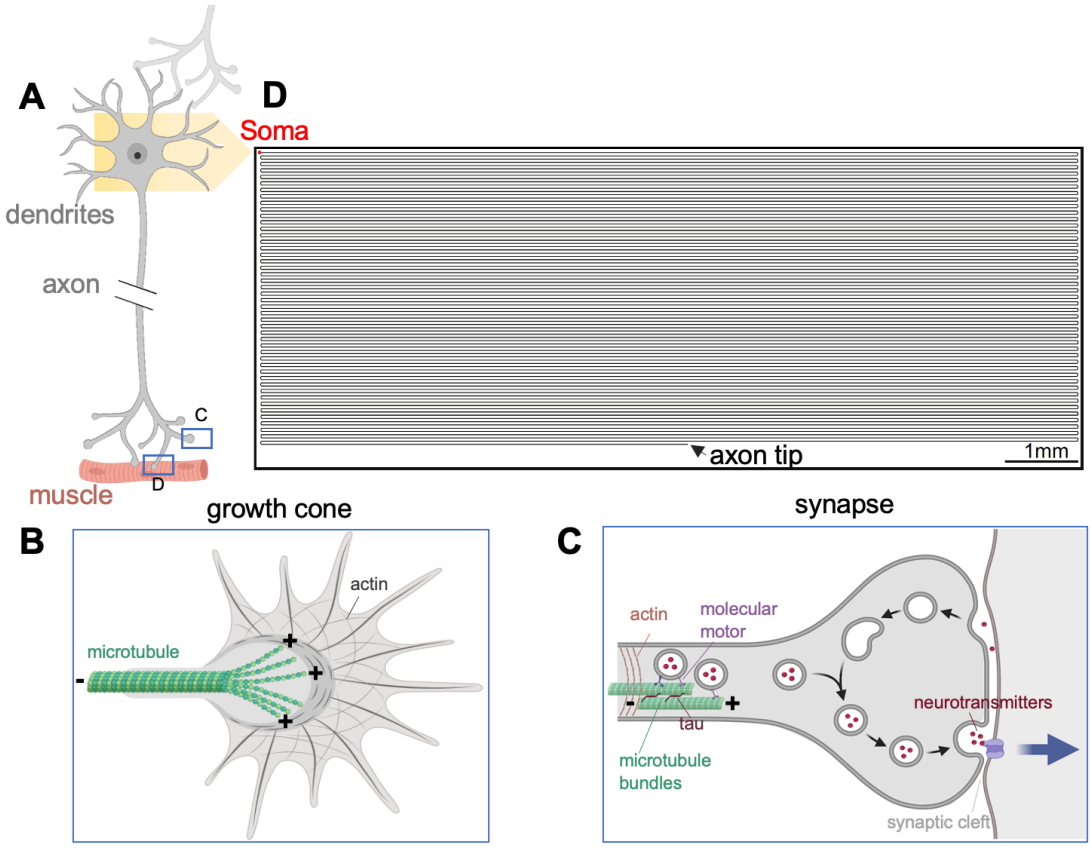


Figure 1.1 Specialized compartments of a neuron (A) A typical neuronal morphology comprises of dendrites, soma, and the axon. **(B)** The axonal growth cone, showing polarized microtubule (MT) (– and + ends) and actin organization. **(C)** The synapse, with some detail in the axon terminus of cargo transport by molecular motors on MT bundles, to facilitate neurotransmitter release and recycling by the endomembrane system. **(D)** To-scale representation a human α motor neuron (adapted with permission from a drawing by Peter Hollenbeck).

1.2.2 The microtubule (MT) cytoskeleton and the regulation of molecular motor-based transport in axons

Mature, functioning neurons are post-mitotic cells that do not undergo cell division after their identity is established shortly after birth (Raine, 1999). Neurons extend protrusions during development in part by a mechanism that includes the sliding of tubulin polymers, called microtubules (MTs), outwardly (Lu et al., 2013). Interactions between the microtubules and actin cytoskeleton and complex signaling pathways result in the specification of the axon, a single

neurite with the structure and function to communicate pre-synaptically with other neurons (Lalli, 2012). During axonal growth, MTs are bundled and uniformly arranged in the plus-end-out orientation, while the rest of neurites develop into dendrites with mixed microtubule polarity (Cg et al., 1988). This plus-end-out MT organization in the axon is conserved in invertebrates and vertebrates (Stone et al., 2008).

The extended architecture and arborization of dendrites and axons pose several challenges for the efficient delivery of cellular components to a distal location. All the 'traffic signals' encoded in the MT network are not completely understood, but our current understanding is that the polarized MT organization and tubulin post-translational modifications (PTMs) provide the physical and chemical properties for selective microtubule associated proteins (MAPs) to direct cargo sorting and transport along MT tracks (Janke and Magiera, 2020; Meiring et al., 2020). The specific PTMs on α-tubulin include acetylation on Lysine 40 (K40-Ac) and detyrosination consisting of the removal of one, two, or three amino acids at the C-terminal tail (of tyrosinated tubulin), and generation of Δ2- and Δ3- tubulins by subsequent removal of glutamate residues, respectively. β-tubulin can be phosphorylated on Serine 172 and polyaminated on Glutamine 15 (Janke and Magiera, 2020). The C-terminal tails of both α- and β-tubulins can also be polyglycylated and polyglutamylated as branches (Janke and Magiera, 2020). In addition to these PTMs, tubulin isotypes exist, such as β1-, β2-, and β3-tubulins, that arise through evolution with the potential to give rise to novel MT function (Janke and Magiera, 2020). How the tubulin isotypes assemble into MTs and how each type of tubulin PTMs occur to tubulin monomers/oligomers/polymers is not well understood yet in the field, but the

concept of 'tubulin code' is proposed to dictate the identity and function of a MT track (Janke and Magiera, 2020).

Acetylation and tyrosination of tubulins are the most well-understood PTMs to have functional consequences on axonal transport regulation (Janke and Magiera, 2020). Axonal MTs have uniform polarity (plus-end-out) and are heavily acetylated (K40-Ac) (**Figure 1.2A**), rendering these MT tracks mechanically stable (permits bending and bundling) and chemically resistant to nocodazole, a drug that disrupts MT assembly/disassembly (Xu et al., 2017). The MTs in the main branch of the axon are also detyrosinated, but the minor branches and the tips of axons still contain dynamic, tyrosinated MT tracks (Arregui et al., 1991). These are important tubulin codes for plus-end-directed molecular motors because kinesin-1 prefers to bind and translocate on acetylated, detyrosinated (stable) tracks (Tas et al., 2017), while kinesin-3 prefers to use unmodified MT tracks that still contain the tyrosine tail, via association with MAPs (Guedes-Dias et al., 2019; Tas et al., 2017). This has implications for the coordination of cargo transport by kinesin-1 and kinesin-3 along the main MT shaft, in the minor branches, near the axonal termini, or at the synapse. The cellular prion protein (PrP^C) and mitochondria are two axonal cargoes that utilize kinesin-1, also called Kinesin Heavy Chain (KHC/KIF5), to translocate along axons. PrP^C vesicles and mitochondria associate with different cargo adaptors to bind to KHC, namely the Kinesin Light Chain 1 (KLC1) and Miro/Milton, respectively (Encalada et al., 2011; Guo et al., 2005; Stowers et al., 2002) (**Figure 1.2B**). In contrast, synaptic vesicle precursors containing synaptophysin (SYP), synaptotagmin (SYT), or RAB3 are well-known kinesin-3 (KIF1A) cargoes (Okada et al., 1995) (**Figure 1.2C**). Differential association of different pre-synaptic cargoes with different KIFs could dictate the transport

dynamics and localization of these cargoes. Dynein, the primary minus-end-directed motor protein in neurons, on the other hand, is initially associated with tyrosinated MTs that are concentrated at axonal termini. However, dynein translocates processively on acetylated, detyrosinated MTs along the axon shaft—and this tubulin code facilitates the efficient retrograde transport of various cargoes inside autophagosomes for degradation in lysosomes in the soma (McKenney et al., 2016). Molecular motors that translocate in the opposite polarity such as kinesin-1 and dynein are known to simultaneously and stably associate with cargoes to coordinate their activities rather than to perform a tug-of-war (Encalada et al., 2011; Pilling et al., 2006). Coordination occurs between molecular motors of the same polarity, such as kinesin-1 and kinesin-3 (Campbell, 2018), and which associate simultaneously on the surface of SYP vesicles and other neurotrophin-carrying vesicles (Zahavi et al., 2021). Thus, it is possible that kinesin-3 can associate with many other canonical kinesin-1 cargoes and vice versa to coordinate the anterograde movement of various cargoes, as they translocate on MTs with different tubulin PTM codes. However, kinesin-1 and kinesin-3 association with cargo has not been tested systematically for many ubiquitous axonal cargoes and has not been visualized directly with quantitative microscopy. In **Chapter 3** of my thesis, I investigate the axonal transport regulation of mutant PrP vesicles and mitochondria by directly visualizing kinesin-1 and kinesin-3 association on individual cargoes and also visualizing acetylated and tyrosinated MT tracks, using super-resolution microscopy, in healthy and dystrophic axons.

MTs in dendrites have been traditionally described as having mixed polarity, yet recent studies found that acetylated MTs are uniformly bundled at the MT core, and these MTs are mostly minus-end-out, while tyrosinated MTs

arrange as the shell around the acetylated MT tracks, and these are mostly plus-end-out (Katrukha et al., 2021; Tas et al., 2017). This dendritic MT organization provides the distinct traffic lanes for kinesin-1 cargoes to move along 'the inner lanes' while kinesin-3 cargoes are hypothesized to move along 'the outer MT lanes.' Giving the importance of this MT track organization and properties imparted by the PTM tubulin code of axons and dendrites, alterations of tubulin PTM codes could have significant effects on cargo mislocalization. To what extent the tubulin codes on MTs in axons and dendrites change in the pathological condition remains largely untested.

Impairments to axonal transport and to the MT cytoskeleton have been shown to be directly associated with neurotoxicity in neurodegenerative disorders (Sferra et al., 2020; Sleigh et al., 2019). In the late 1990s, it was first proposed that cytoskeletal abnormalities rather than Amyloid beta peptide (Aβ) deposition, drive the pathogenesis of AD (Terry, 1996). Since then, accumulating evidence suggests that disruption of axonal transport is a key component of pathological lesions at early, as well as during late stages of neurodegeneration (Goldstein, 2012; Stokin et al., 2005). For example, tau is a MAP that normally decorates axonal MTs, but when tau is hyperphosphorylated due to mutations or as a result of imbalanced activity of tau kinases/phosphatases, loss-of-function toxicity ensues in the tauopathies and in AD (Gong and Iqbal, 2008). How the misfolded PrP aggregates lead to axonopathies via disruption to MT structure and axonal transport deficits is unclear, and this is a central question that will be addressed in **Chapter 3** of this thesis.

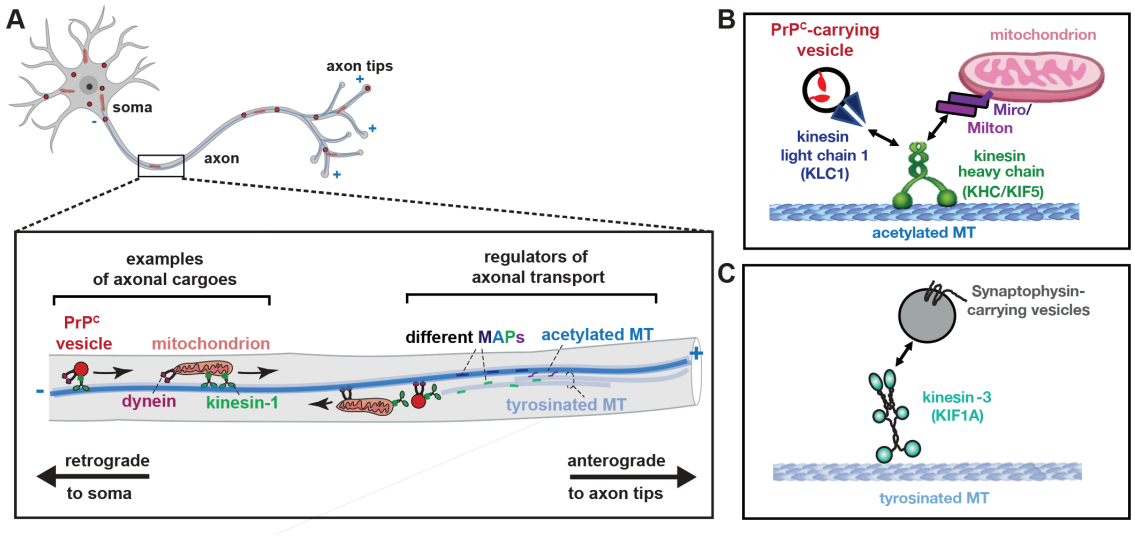


Figure 1.2 Axonal transport regulation by MT PTMs and molecular motors. (A) Polarized organization of MT in axon with the plus-end-out towards the axon tips. Examples of neuronal cargoes, PrP^C vesicles and mitochondria, that utilize kinesin-1 and dynein that stably associate with these cargoes for bidirectional axonal transport. Regulators of axonal transport include MT PTMs and different MAPs. **(B)** Kinesin-1 cargoes share KHC/KIF5 motor subunit but have different cargo adaptors, such as KLC1 for PrP^C vesicles and Miro/Milton for mitochondria. Kinesin-1 preferentially associates with acetylated MT tracks. **(C)** Kinesin-3/KIF1A associates with Synaptophysin-carrying vesicles and tyrosinated MT.

1.2.3 The roles of small GTPases in axonal trafficking and transport regulation

Ras-like proteins from rat brain (Rab), a large family of small GTPases, are found in all eukaryotic cells and, as the name implies, are highly expressed in the nervous system (Touchot et al., 1987). Rab GTPases regulate the identity, the trafficking and sorting, and the maturation process of membrane-bound endolysosomes via acting on effector proteins when Rab is bound to GTP (Stenmark, 2009). Many Rab proteins are important for neuronal activities, and defective Rab function has direct consequences on neurodegeneration (Kiral et al., 2018; Kohrs et al., 2021). How different Rab proteins coordinate membrane trafficking pathways in highly polarized neurons is an active area of research.

In *Drosophila*, 33 genes encode proteins that belong to a family of Rab GTPases (Zhang et al., 2007). The function of Rab GTPases is conserved from yeast to humans (Lipatova et al., 2015). The accepted notion is that various types of Rab GTPases exist to coordinate vesicular transport sub-steps into a pathway (Lipatova et al., 2015). The *Drosophila* neuro-muscular system has been a model system to study basic Rab function as *Drosophila* has 23 Rab proteins with orthologs to mammalian Rabs (Gillingham et al., 2014). Moreover, *Drosophila* does not have the expansion of many Rab paralogs that occurs during the evolution of mammalian Rabs, whereby humans have 66 Rabs identified to date (Gillingham et al., 2014).

Rab proteins exist in multiple forms, and they are activated within a regulated pathway (**Figure 1.3A**). Newly synthesized Rabs need to be mono- or di-prenylated at the C-terminus specifically by a Rab geranylgeranyl transferase (RabGGTse, in short GGT), a process that requires a Rab escort protein (REP) (Preising and Ayuso, 2004). Then, a mono- and di-prenylated Rab has high affinity for the GDP disassociation inhibitor (GDI), which solubilizes the C-terminal hydrophobic moieties of Rabs to keep them as a cytosolic pool (Soldati et al., 1993; Wu et al., 2007). To associate with membrane, GDI is proposed to be replaced by a GDI displacement factor (GDF), to entrap Rab to its correct membrane target, but the GDF identity and its mechanism remain elusive (Ismail, 2016). To date, only one GDF has been identified, called Yip3 in yeast or PRA1 in human, but this GDF only works to replace GDI associated with Rab5, Rab7, Rab9, and not all other Rabs (Sivars et al., 2003). Instead, the guanine nucleotide exchange factor (GEF) is proposed to be sufficient to replace GDI for correct membrane targeting (Blümer et al., 2013). In addition to recruitment function, the GEF also drives the change in membrane identity. For example, the

heterodimer Mon1-Ccz1 GEF replaces Rab5 with Rab7, a key event in the early endosome (EE) to late endosome (LE) maturation (Langemeyer et al., 2020). Membrane-bound Rab GDP is activated by the Rab-specific GEF, to replace the GDP with a highly abundant GTP, and the GTP-bound active Rab conformation is recognized by various effectors, such as tethering proteins for membrane fusion and motor proteins for MT- or actin-based transport (Langemeyer et al., 2020). A GTP-bound Rab is inactivated by a GTPase activating protein (GAP) to release inorganic phosphate (Pi), to control the lifetime of Rab's active form (Pylypenko et al., 2017). A membrane-bound Rab can be extracted and kept cytosolic with GDI to translocate and associate with other membrane identities in other sub-cellular regions (Dirac-Svejstrup et al., 1994). The Rab-GDI protein complex is assumed to float around the cell as a cytosolic pool, but to what extent -and when- *de novo* synthesis of the Rabs and GDI occur at the distal location remain unknown. In this thesis, I investigate the localized production of Rabs and GDI at the distal axonal synapses in **Chapter 4.**

Various deficits in the Rab GDP-GTP cycle are directly implicated in familial diseases of the nervous system. Mutations in REP1 cause X-linked retinal degeneration disease called chloroideremia (CHM), a genetic disease with progressive vision loss, and the mutations of GGT α-subunit cause Hermansky-Pudlak syndrome (HPS) (Pereira-Leal et al., 2001; Preising and Ayuso, 2004). Many effectors/interactors of Rabs are associated with neurodegenerative diseases, including the leucine-rich repeat kinase (LRRK1/2) in Parkinson's disease, Huntingtin (HTT) in Huntington's disease, and KIF1A-C in Spastic paraplegia (Gillingham et al., 2014). GDI is implicated in X-linked non-specific mental retardation (XLMR), and a mouse model lacking GDI showed defects in learning and short-term memory formation (Bianchi et al., 2009). This disease

relevance highlights the functional importance of regulatory steps in the Rab GDP-GTP cycle, that still require better mechanistic understanding in various neurological diseases.

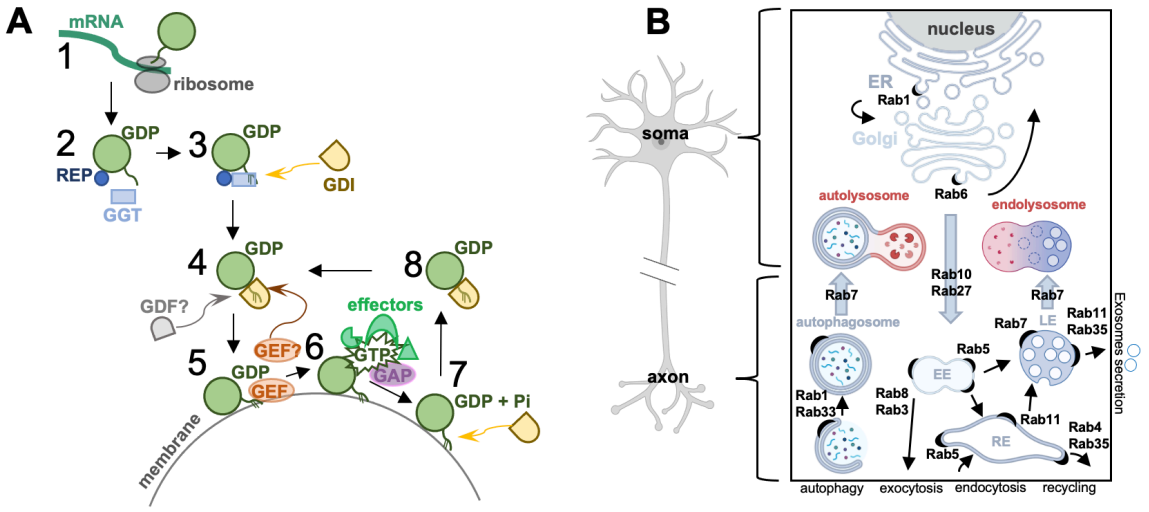


Figure 1.3 The cycle of Rab GTPases and their functions in membrane trafficking regulations and quality control mechanisms. (A) A generalized diagram of Rab synthesis (**1**); immediate association with a Rab escort protein (REP) (**2**); prenylation by a geranylgeranyl transferase (GGT) and association with a GDP disassociation inhibitor (GDI) (**3**); GDI replacement by a GDI displacement factor (GDF) (**4**) to allow Rab association with membrane (**5**); Rab activation by a guanine nucleotide exchange factor (GEF) (**6**), by which the GTP-bound active Rab conformation is recognized by various effectors; Rab inactivation by GTPase activating protein (GAP) to release inorganic phosphate (Pi) (**7**); Membrane-bound Rab can be recycled and kept as cytosolic pool by GDI association (**8**). **(B)** Membrane trafficking regulation in neurons. A secretory pathway follows ER-Golgi trafficking and Rab6-mediated Golgi exit, towards Rab3- and Rab8-mediated exocytosis. The endolysosomal pathway follows Rab5 early endosome (EE) that mature into late endosome (LE)/Multivesicular body (MVB) for lysosomal degradation via Rab7 near the soma or exosome secretion via Rab11 and Rab35. The recycling endosome involves Rab11, Rab4, and Rab35 for cargo recycling or converging to the endolysosomal pathway. Autophagy is regulated by Rab1 and Rab33 at early autophagosome formation and Rab7-mediated degradation in autolysosome.

1.2.4 Membrane trafficking and protein quality control mechanisms in axons

Rab GTPases are central to membrane trafficking regulation in neurons, from the secretory to endolysosomal systems, and in protein quality control (QC)

mechanisms (**Figure 1.3B**). Neurotrophic factors—such as the Trk receptors, a family of receptor tyrosine kinases important for neuronal function—require the Golgi-derived vesicle association with Rab6 and multiple kinesins to enter the axon and traffic along MTs to the synaptic cell surface (Zahavi et al., 2021) (**Figure 1.3B**). In contrast, a disease-associated mutant PrP is also trafficked to the cell surface via the secretory pathway, where it was proposed to become cytotoxic (Hegde et al., 1999; Weidemann et al., 1989). PrP is a glycosylphosphatidylinositol (GPI)-anchor protein that is synthesized in the ER and modified post-translationally in the Golgi, and the properly folded, GPI-anchor PrP^{C} is packed in the luminal side of Golgi-derived vesicles for exocytosis to the neuronal cell surface (Harris, 2003). PrP^{C} is proposed to be neuroprotective with unclear mechanisms (Llorens and del Río, 2012), yet PrP^{C} is required in PrDs (Brandner et al., 1996), as mice lacking PrP^{C} ($Prnp^{o/o}$) are resistant to prion infection. The level of PrP expression strongly correlates with PrD progression, and the reduction of PrP level after the onset of PrD can reverse PrD pathologies (Mallucci et al., 2003). Thus, understanding the factors that control PrP synthesis and delivery via the secretory pathway is a crucial step towards unraveling a therapeutic strategy for PrDs.

PrP misfolding in the ER can be enhanced by point mutations—such as G113V and A116V—and by insertional mutations in the octapeptide repeat regions (e.g. PG14), which cause PrDs in animals and humans (Bernardi and Bruni, 2019; Biasini et al., 2008). The ER has the protective QC mechanism called the unfolded protein response (UPR) to maintain proteostasis (Ma and Hendershot, 2001). Upon protein overexpression or overload by protein misfolding, the ER utilizes the ER-associated degradation (ERAD) pathway to kick out defective proteins from the ER into the cytosol for degradation by

proteosomes (Qi et al., 2017). However, misfolded mutant PrP as well as other misfolded GPI-anchor proteins are found to be poor ERAD substrates (Ashok and Hegde, 2008). Instead mutant PrP is targeted towards the cell surface via the rapid ER stress-induced export (RESET) clearance mechanism, for fast endocytosis and degradation in lysosomes (Satpute-Krishnan et al., 2014). All misfolded mutant PrP molecules are targeted to RESET effectively in non-neuronal cells by ER chaperones (Zavodszky and Hegde, 2019); however, it had remain unclear whether RESET could effectively clear misfolded mutant PrP in neurons. Additional mechanisms could be responsible for the escape of misfolded mutant PrP from QC *en route* to become cytotoxic, and it is likely that a trafficking pathway that involves small GTPases exists to discriminate PrP trafficking and aggregation. The pathway responsible for the formation of toxic mutant PrP aggregates in neurons had remained uncovered, and this is the central objective of the **Chapter 2**.

The extended axonal projections require additional QC mechanisms to target misfolded protein clearance from the periphery. Neurons keep acidic, degradative lysosomes near the soma (Kulkarni and Maday, 2018). So, misfolded membrane proteins at the synapse are endocytosed to become Rab5-EE and sort into Rab7-LE, which recruit dynein for retrograde transport towards lysosomal degradation near the soma (Ciechanover and Kwon, 2015). For cytosolic contents, macroautophagy is responsible for engulfing cytosolic content to form autophagosomes which undergo retrograde transport toward the soma, where fusion with degradative lysosomes results in their clearance (Ciechanover and Kwon, 2015) (**Figure 1.3B**). Lysosomal enzymes are synthesized in the ER, and follow the secretory pathway transported in Golgi-derived vesicles anterogradely to fuse with misfolded proteins in LE and autophagosomes that travel

retrogradely (Farfel-Becker et al., 2020; Lie et al., 2021). Thus, the functioning lysosomes in proximal axons acquire their identity and degradative capacity from the post-Golgi compartments (Lie et al., 2021), and it is unclear whether defects in lysosomal maturation and/or in the transport of endolysosomal system contributes to axonopathies in PrD. Endolysosomal QC is carefully investigated in **Chapter 2** of this thesis, regarding the itinerary of misfolded mutant PrP degradation and aggregation in axons.

Endosomes can undergo alternative trafficking itinerary at the distal axon. Different sets of GTPases, such as Rab11 and Rab35, can divert the Rab7-LE that contains intra-luminal vesicles (ILVs), called the multivesicular body (MVB), to the cell surface and release these ILVs as exosomes (Xu et al., 2022). Normally, exosome secretion is an important means for delivering signaling molecules to the synaptic cleft or to neighboring cells (Qin and Xu, 2014). However, in mutant PrP-expressing cells, the recycling endosome (RE) Rab11 protein and GDI were found to be misregulated (Massignan et al., 2010), and endosomal recycling towards the exosome secretion pathway might be the crucial route of cell-to-cell spread of infectious PrP (Liu et al., 2017). In conclusion, Rab GTPases are central to membrane trafficking regulation along the axonal length and provide QC pathways towards degradation of misfolded proteins. When these pathways fail, trafficking and sorting of endolysosomes is impaired, affecting axonal health.

1.2.6 Cultured primary neurons as a model system to study axonal transport regulation, membrane trafficking, and mechanisms of neurodegeneration

The primary neuronal cultures from mouse brains usually contain neurons and glial cells that survive for several days in appropriate conditions in petri dishes. Hippocampal neurons derived from rat embryos or from newborn mouse neonates are a common model in neuronal cell biology research because these neurons are relatively homogeneous, can be grown on poly-lysine-treated coverslips, develop polarized dendrites and axons, form synaptic connections, and exhibit synchronous activity (Kaech and Banker, 2006; Misonou and Trimmer, 2005; Seibenhener and Wooten, 2012). This system is particularly helpful to study localization and trafficking of cellular components like fluorescently tagged proteins and organelles in different parts of neurons, using fluorescence microscopy approaches, or standard biochemical methods. Within the single axon, which is easily distinguishable by morphology, MTs are uniformly polarized with the plus-ends-out, and thus it is possible to dissect molecular mechanism of axonal transport regulation with this system (Encalada et al., 2011; Kaech and Banker, 2006).

Cultured primary hippocampal neuron has several advantages over other neuronal cell lines and the *in vivo* model for several reasons. Primary neurons in culture are consistently in a post-mitotic phase and have the same genetic background as their source animals. This allows parallel investigations whereby the electrophysiology or behavior of mutants or transgenic animals (rats/mice) can be monitored in live animals, while their mutational effects on the real-time organelle movement and disease progression in a single axon can be investigated in culture. Secondly, *bona fide* axons and synapses form in primary culture, while

commonly used neuronal cell lines, such as Neuro2a/N2a, develop lamellipodial protrusions that resemble neurites to an extent (Lin et al., 2011). Thus, I prefer to use the primary neuronal culture to study axonopathies. Thirdly, the density of primary neurons in culture is easily controllable, with known numbers of surviving neurons and glia, with the possibility of adjusting the ratio of neurons: glia for co-culture (Ioannou et al., 2019).

In addition, primary neurons have previously provided valuable insights to neurodegenerative mechanisms. For example, in a Parkinson's disease model, primary neurons recapitulate α-synuclein aggregation and Lewy body formation, and primary neurons facilitate the biochemical and high-resolution/ ultrastructural studies of their formation and toxicity mechanism at the sub-cellular level (Mahul-Mellier et al., 2020). In another example, the study on early defects to axonal transport in model of AD was done *live* in primary culture from kinesin-1 mutant mice (Stokin et al., 2005). It is thus important to establish *in cellulo* disease models, test them well, and use them to study the subcellular mechanisms of neurodegeneration at the single axon level, by high-resolution microscopy or complementary methods, in parallel to the *in vivo* characterization of axonopathies.

In **Chapter 2,** a murine primary hippocampal cell culture system is used to generate a model for the expression of mutant PrP aggregates inside axons to identify and characterize novel endolysosomal trafficking pathways responsible for the formation of mutant PrP aggregates. In **Chapter 3,** this model system is used to investigate the consequences of PrP aggregate formation on the integrity of axonal transport and cytoskeletal and organelle-organelle interactions.

1.2.7 Localized protein synthesis and synaptic plasticity

The regulatory processes of protein trafficking discussed in the previous sections are extremely important for up- or down-regulation of the receptors and other membrane proteins at the synapse, which contribute to the changes in the signaling properties of neurons, termed synaptic plasticity (Buckley et al., 2000). Synaptic plasticity refers broadly to the neuronal activity-dependent changes that result in modified synaptic transmission, and these modifications can be enhanced or repressed and can occur in short- or long-term (from milliseconds to days) (Citri and Malenka, 2008). Synaptic plasticity can also refer to changes in morphology/structures of the synapse in addition to changes in the physiology, and this type of plasticity includes alteration of branching, volume, and contacts between pre- and post-synaptic sites (Bai and Suzuki, 2020). Activity-dependent synaptic plasticity is necessary and sufficient for encoding memory at the network level (Takeuchi et al., 2014). The molecular mechanisms underlying different kinds of plasticity seem to be diverse, depending on the types of synapses and the scale of such changes.

Local protein synthesis from the localized mRNA at individual synapses is crucial for synaptic development, plasticity, and in encoding memory (Kang and Schuman, 1996). For example, local production of calcium/calmodulin-dependent protein kinase II (CaMKII) in dendrites is important for synaptic stabilization and memory consolidation in rodents (Miller et al., 2002). In *Drosophila*, aversive olfactory learning (association of odors with punishment), a dopamine-driven plasticity in the brain circuit, leads to increased *CaMKII* mRNA number in the dendrites of Mushroom Body Output Neurons (MBOPs) (Mitchell et al., 2021). However, the local protein synthesis in the axonal growth cone and the pre-

synaptic site is thought to occur at a low level compared to dendrites and the soma, and the mechanism and function of axonal mRNAs are less understood (Sasaki, 2020). The translation of *β-actin* mRNA, an abundant axonal transcript, was shown to be important during axonal regeneration post-injury, and a reduction in *β-actin* mRNA localization and translation is implicated in the spinal muscular atrophy (SMA) disease model (Sasaki, 2020). In addition, disruptions to local translation of active zone pre-synaptic proteins are thought to be involved in many neurodevelopmental disease pathophysiology, including in autism spectrum disorder (ASD) and fragile X syndrome (Sasaki, 2020). The advanced use of -omics and *in situ* RNA detection technologies led to the discovery of myriad of pre- and post-synaptic transcriptomes, many of which have little to no mechanistic understanding for their function and roles in synaptic plasticity (Hafner et al., 2019). Excitatory and inhibitory pre-synaptic boutons have different sets of localized transcripts and translational signature that could contribute to differential post-synaptic potentiation or depression during learning and memory (Hafner et al., 2019). Because membrane recycling, fusion, and the endolysosomal quality control system are very active at the pre-synapse, it remains unknown whether localized translation of membrane trafficking regulators, especially of Rab GTPases, happens in axons at the pre-synapse, and whether this is required for the alteration of synaptic properties. This central question will be addressed in the **Chapter 4** of my thesis.

The neuromuscular junction (NMJ) of *Drosophila* larvae is a well-studied, well-established model to study activity-dependent synaptic development and plasticity since the 1990s (Bai and Suzuki, 2020). *Drosophila* NMJ synapses use glutamate predominantly as the neurotransmitter, in contrast to vertebrate NMJ that uses acetylcholine (Menon et al., 2013). Nonetheless, the post-synaptic

glutamate receptors and the post-synaptic scaffolds of *Drosophila* NMJ are homologous to the AMPA ionotropic glutamate receptors and the post-synaptic densities (PSD) in the mammalian brain, respectively (Menon et al., 2013). The molecular mechanisms underlying synaptic development in the fly larval NMJ are also reused during new synapse formation, a process called synaptogenesis, which is an important aspect to the learning and memory processes happening in adult neurons (Shen and Cowan, 2010).

The larval NMJ is easily accessible for electrophysiology recording and imaging experiments upon micro-dissection. The NMJ synapses between the body wall muscles 6 and 7 of the larval abdominal segments develop in a stereotypical repeated pattern (**Figure 1.4A-B**) (Shen and Cowan, 2010). The motor neurons are specified and extend their axonal growth cones to innervate the body wall musculature during stages 13 – 15 of embryonic development and form the oval-shaped boutons that host various pre-synaptic cargoes and translation machineries during the larval stages (Shen and Cowan, 2010). By the third-instar larval stage, each NMJ of the muscle group 6+7 usually contains 50–100 type I glutamatergic boutons, and each bouton contains approximately 10 active zones (Shen and Cowan, 2010) (**Figure 1.4C**). The mature larval NMJ synapse can be visualized by staining against the abundant synaptic proteins—such as Discs large (Dlg), a *Drosophila* ortholog of the mammalian post-synaptic density-95 (PSD-95) scaffolding protein and Bruchpilot (Brp), a protein essential for glutamate release in the synaptic active zone (Paul et al., 2015) (**Figure 1.4C**). Many of these stereotypical, quantifiable parameters are called the 'NMJ morphometry' and are convenient tools to screen the effects of mutations or experimental conditions on NMJ development (Nijhof et al., 2016). In addition, the larval NMJs also contain immature boutons that contain synaptic vesicles

but lack the post-synaptic densities, and these are referred to as 'ghost boutons' (Ataman et al., 2008). The ghost boutons form naturally, but several acute neuronal stimulation paradigms can induce ghost bouton formation extensively, and this method is commonly used as a proxy for the degree of synaptic plasticity at the NMJ (Ataman et al., 2008; Piccioli and Littleton, 2014). In **Chapter 4** of my thesis, I use the *Drosophila* larval NMJ synapse as a model to investigate sub-cellular processes, including RNA localization and localized translation, in synaptic development and plasticity.

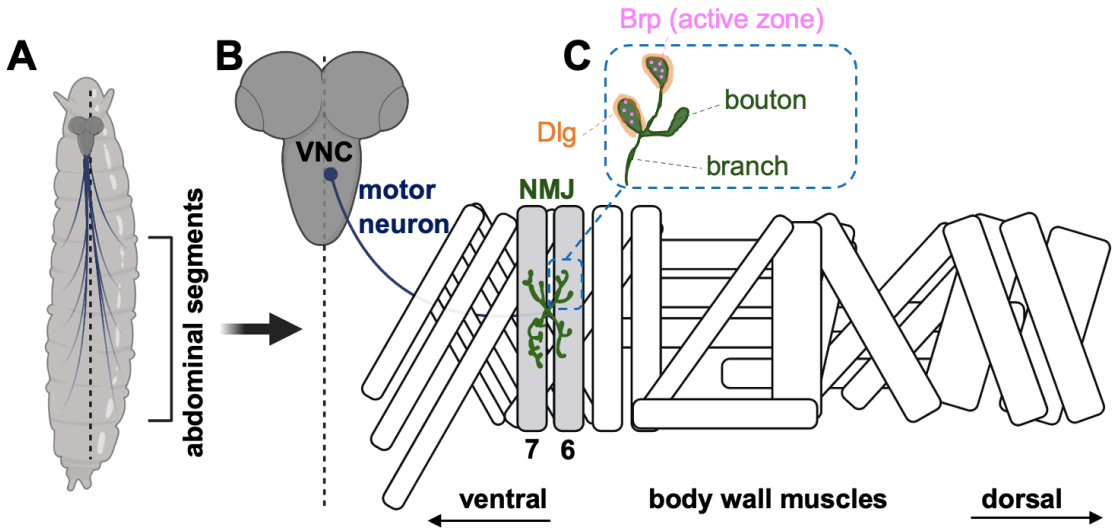


Figure 1.4 The *Drosophila* larval neuromuscular junction (NMJ) synapse. (A) Schematic of the third-instar larva with the brain and motor nerves that innervate the body wall muscles in the abdominal segments. **(B)** A motor neuron cell body is in the ventral nerve cord (VNC) and the axon terminus is located at the NMJ. The organization of the abdominal body wall muscles (from the right hemi-segment) from the larval fillet preparation. **(C)** The inset shows the Type 1b glutamatergic boutons at muscles 6 and 7. The mature synapse contains the subsynaptic reticulum (SSR) stained by Discs large (Dlg) antibody (orange) and the active zones stained by the Bruchpilot (Brp) antibody (pink), while the immature synapse lacks Dlg and Brp.

1.2.8 Post-transcriptional regulation in neurons and a departure from 'protein-centric' to 'RNA-centric' views

The central dogma of molecular biology states that deoxyribonucleic acid (DNA) is transcribed into mRNA that exits the nucleus, finds the ribosome, and gets translated into a protein that performs a function (Crick, 1958). This concept follows a common interpretation that proteins perform most if not all the cellular function, and mRNA is only an intermediate state, or a 'messenger' for DNA. The 'protein-centric' assumption was later challenged by the discovery of the prevalence of RNA regulatory mechanisms post-transcription, including the functional roles of other regulatory RNA species, such as long non-coding RNAs (lncRNAs) and microRNAs (miRNAs), during development, in synaptic plasticity, and in neurological diseases (Kosik, 2006; Statello et al., 2021).

Asymmetrical distribution pattern of mRNA was first observed during embryonic development (Jeffery *et al*, 1983). This phenomenon was later realized to be common in other cells, and it was proposed that localized expression of proteins stems from corresponding localization of their transcripts (Lawrence and Singer, 1986). RNA localization bias to one region of a cell could be a result of the RNA population at that particular site being protected from degradation, or that there are RNA-anchoring factors at that region, or that RNA is being actively transported according to the tubulin code and MT organization (Engel et al., 2020). In polarized cells, such as epithelial cells and neurons, active transport of RNA along MT is common, and the signal that send RNAs to the axon is sufficient to direct the same RNAs towards the bottom pole of epithelial cells, due to the similarity in the plus-end-out MT orientation (Goering et al., 2023). This strongly suggests that the RNA traffic rules are shared among different cell

types. Despite the prevalence of RNA localization in all kingdoms of life from bacteria to inside highly complex human brains (Tian et al., 2020), the mechanism and function of RNA localization is not yet well understood in the axon.

Post-transcriptional regulation operates on mRNA after its production in the nucleus, towards its intracellular localization, stabilization and protection from degradation, and translational control mostly via the activity of RNA-binding proteins (RBPs) (Corbett, 2018). There is an estimate report that one mRNA can be translated into 6,000 copies of a protein molecule on average (Schwanhäusser et al., 2011). Thus, localizing and stabilizing the mRNA pool at a distant location for local protein production is an energy-efficient means to supply and replenish proteins with high copy number (Rajgor et al., 2021). It is conceivable that mislocalization of even one molecule of mRNA could have drastic consequences on the development and function of neurons.

The 'zipcode' signals within the newly synthesized transcripts to recruit RBPs to direct its delivery to a proper location could be anywhere in the protein coding and non-coding regions of the mRNA, but many studies agree that the regulatory hubs cluster within the 3'end of the untranslated region (3'UTR) (Chaudhuri et al., 2020; Patel et al., 2012). For example, the U-rich motifs in the 3'UTR and its association with poly(U)-binding proteins are associated with increased transcript stability (Vejnar et al., 2019). On the other hand, G-rich motifs in the 3'UTR can bind the adenomatous polyposis coly (APC)—a MAP (Barth et al., 2008) that links axonally-enriched *β-actin* and *β-tubulin* transcripts to kinesin-1 (KIF5A), kinesin-2 (KIF3AB-KAP3), and End binding 1 (EB1), a plus-end tracking protein—for axonal entry, bidirectional transport, and delivery

of mRNA to dendritic and axonal periphery (Baumann et al., 2020, 2022). Many other RBPs such as Splicing Factor Proline and Glutamine Rich (SFPQ) and Staufen are known to interact with kinesin-1 and dynein for bidirectional transport of mRNAs, but there is little to no direct evidence for their simultaneous association with RNA cargoes (Rodrigues et al., 2021). It is likely that diverse RBPs that link different motor proteins and transcripts form a complex to efficiently sort specific RNA cargoes to its common destination. The *cis*- and *trans*-acting signal in many axon-localized transcripts that links mRNA transport to its stabilized residence in the periphery remains to be further investigated. The post-transcriptional regulatory mechanisms that direct transcripts of Rab GTPases along MT tracks to the distal axons is unknown, despite their vital roles and the requirements to have multiple protein copies at the synapse.

Multiple mRNA copies of the same gene or of different genes can compete for a limited amount of their RBP targets (Cosker et al., 2016). While some RBPs are expressed in response to stimuli to bind and direct mRNA into the axon, many RBPs are constitutively expressed, and the activity-dependent transcription of the transcript targets produces enough mRNA copies to occupy available RBPs for axonal localization (Gomes et al., 2014). Studying RBP function requires sophisticated tools to quantitatively measure and detect its activity and function in a spatial and temporal-specific manner. For instance, a conserved RBP called the insulin-like growth factor 2 (IGF2) mRNA-binding protein (Imp) displayed dynamic up- and down-regulation expression patterns during development in vertebrates and invertebrates to perform a variety of post-transcriptional regulatory functions (Degrauwe et al., 2016). In the embryos, Imp is not required for localization of *oskar (osk)* mRNA but is important for its

translational activation (Munro et al., 2006). At a later stage, Imp becomes important for a timely differentiation of neuroblasts into different neuronal subtypes in *Drosophila*, by working antagonistically with a conserved RBP called Syncrip via the regulation of RNA stability (Munro et al., 2006; Samuels et al., 2020). During the fly larval NMJ development, Imp is required pre-synaptically in motor neurons for bouton growth and neuromuscular activity (Boylan et al., 2008). The transport dynamics of Imp along MT of the mature axon is bidirectional with frequent reversals, while Imp movement along MT in the egg chamber is rather unidirectional, suggesting that the transport of Imp is also differentially regulated in different developmental stages (Boylan et al., 2008). Imp targets include a variety of transcripts, including the regulators of actin dynamics, as well as small GTPases—such as Rac1, Cdc42, Arf79f, various Rab GTPases, as well as GDI (Hansen et al., 2015). In **Chapter 4** of my thesis, I aim to dissect the role of the Imp as the putative *trans*-factor for distal mRNA localization to the larval NMJ pre-synapse, with *Drosophila* genetic tools to disrupt Imp in a tissue- and time-specific manner.

1.3 The research aims and questions

This thesis contains three experimental chapters, **Chapter 2**, **Chapter 3**, and **Chapter 4**. The aims/objectives of the studies are the following:

In **Chapter 2**, I aim to characterize (1) the identity of neurotoxic misfolded aggregates of mutant prion protein (PrP^{mut}) and (2) the pathways that form PrP^{mut} aggregates in axons, via endolysosomal Rab GTPases.

In **Chapter 3**, I aim to investigate the consequences of PrP^{mut} aggregate buildups on (1) microtubule and actin cytoskeleton organization locally, (2)

transport of vesicles and mitochondria through the aggregate sites and their association the molecular motors that carry these cargoes, and (3) mitochondrial-endosomal interactions locally at these aggregate sites, via Rab7 activity.

In **Chapter 4**, I aim to determine (1) the axonal transport mechanisms and machinery of mRNAs that encode Rab GTPase proteins at distal axonal sites that form neuromuscular synapses and (2) the function of localized *Rab* mRNAs in synaptic development and plasticity.

1.4 Significance

Neurological disorders are increasingly becoming the major issues in medical and public health, and the severity of the health burden of brain diseases are third only after cardiovascular disease and cancer in the EU population (Deuschl et al., 2020). Ageing is the primary risk factor for most neurological diseases (Hou et al., 2019), which is alarming for the years ahead when many countries are becoming 'ageing societies.' Thus far, there are few to no effective ways to treat or reverse neurodegeneration upon diagnosis (Hou et al., 2019). The basic and translational research studies need to address the causes and common pathways of proteinopathies that primarily affect the brain in order to come up with effective therapeutic strategies for these diseases in the near future.

The experiments in this thesis are systematically planned, conducted, and analyzed up to the highest standard practice of the field. Successful completion of the aims in **Chapter 2** reveals the identity and the biogenesis pathway of neurotoxic PrP aggregates that are anti-aggregation targets amendable in the prionpathies, and potentially in other proteinopathies that share similar trafficking itinerary as the PrP. The novel insights upon completion of the aims

in **Chapter 3** identify sub-cellular pathways that lead to cytoskeletal and transport disruptions at the early stages of prionopathies, and merit further experimental tests for reversing these commonly identified pathological features.

In **Chapter 4**, I aim to uncover the mechanistic basis of cellular trafficking regulation with the 'RNA-centric' approach. Localized protein translation of long-lived distally located mRNAs, apart from its role in learning and memory, when mis-regulated is implicated in many neurodevelopmental and neurodegenerative diseases (Gamarra et al., 2021). The research focus and approaches presented in Chapter 4 could shed light on the roles of many RNA species at the synapse to be further tested for their disease relevance.

Finally, throughout my PhD, I engage in the philosophy of open-access science and transparent research methodologies—e.g., the use of automated analysis pipeline to speed up the research process and to reduce human bias, the careful validation of methodologies and tools, and the use of open-access platforms and open-access peer-reviewed publications to share detailed code, protocols, and new findings. The optimized methodologies and pipelines presented in this thesis could be beneficial for many research communities that share similar models and interests in solving scientific problems in neurons.

1.5 The limitations

The works presented in this thesis primarily focus on the roles of small GTPases as the central players in neuronal trafficking regulation and pathophysiology of familial PrDs. The processes that control the fate of a neuronal cargo, both to send it to function distally or to subject it to a QC mechanism, are a lot more complex with regards to the upstream and

downstream regulators. The working models presented in this thesis are simplified based on the working hypotheses and new findings, and thus should not be taken as a complete understanding of the trafficking processes in neurodegeneration.

The limitations of the studies also stem from the choice of the model systems. Primary neurons grown in culture often lack the 3D supporting environment compared to those neurons *in vivo*, and thus such primary culture is often considered non-physiological. The findings, such as the biogenesis pathway of PrP^{mut} aggregates and pathological lesions observed inside cultured primary neuron axons, should be confirmed in the mouse brain and in specific cell types primarily affected by familial prionopathies.

Drosophila is an animal model of choice for studies of gene function in the nervous system, but *Drosophila* lacks the mammalian counterparts of many synaptic proteins and their structural complexity. The lack of redundancy might facilitate the functional knockout/knockdown studies to study gene function, but events that occur in mammalian neurons in human diseases might be more complex, or different, and thus require a complementary mammalian model system. In this study, I use the larval NMJ as a model to study the localized translation of small GTPases and its role in the structural plasticity of the pre-synapse. While the traditional view of synaptic plasticity is studying the modification to the strength or efficacy of synaptic transmission, here I do not perform electrophysiology studies of the NMJ. The assumption that structural and physiological processes are tightly coupled at the larval NMJ should be considered carefully, as the morphological and physiological plasticity processes can be independent in other systems (Bai and Suzuki, 2020). These limitations

are acknowledged here; however, these limitations should not affect the conclusions of the research findings in this thesis in any way.

1.6 The outline of the thesis

This thesis contains five main chapters. **Chapter 1** Introduction has provided the background and context of the studies, the objectives, the significance, and the limitations of the work done in this thesis. Following Chapter 1 are **three experimental chapters (Chapter 2-4)**, each of which contains a specific introduction, methods, results, discussion, and references. Finally, **Chapter 5** summarizes the concepts and novelty from the experimental chapters, followed by future directions.

1.7 References

Arregui, C., Busciglio, J., Caceres, A., Barra, H.S., 1991. Tyrosinated and detyrosinated microtubules in axonal processes of cerebellar macroneurons grown in culture. J Neurosci Res 28, 171–181. https://doi.org/10.1002/jnr.490280204

Ashok, A., Hegde, R.S., 2008. Retrotranslocation of prion proteins from the endoplasmic reticulum by preventing GPI signal transamidation. Mol Biol Cell 19, 3463–76. https://doi.org/10.1091/mbc.e08-01-0087

Ataman, B., Ashley, J., Gorczyca, M., Ramachandran, P., Fouquet, W., Sigrist, S.J., Budnik, V., 2008. Rapid Activity-Dependent Modifications in Synaptic Structure and Function Require Bidirectional Wnt Signaling. Neuron 57, 705–718. https://doi.org/10.1016/j.neuron.2008.01.026

Bai, Y., Suzuki, T., 2020. Activity-Dependent Synaptic Plasticity in *Drosophila melanogaster*. Frontiers in Physiology 11. https://doi.org/10.3389/fphys.2020.00161

Barth, A.I.M., Caro-Gonzalez, H.Y., Nelson, W.J., 2008. Role of Adenomatous Polyposis Coli (APC) and Microtubules in Directional Cell Migration and Neuronal Polarization. Semin Cell Dev Biol 19, 245–251. https://doi.org/10.1016/j.semcdb.2008.02.003

Baumann, S., Komissarov, A., Gili, M., Ruprecht, V., Wieser, S., Maurer, S.P., 2020. A reconstituted mammalian APC-kinesin complex selectively transports defined packages of axonal mRNAs. Sci Adv 6, eaaz1588. https://doi.org/10.1126/sciadv.aaz1588

Baumann, S.J., Grawenhoff, J., Rodrigues, E.C., Speroni, S., Gili, M., Komissarov, A., Maurer, S.P., 2022. APC couples neuronal mRNAs to multiple kinesins, EB1, and shrinking microtubule ends for bidirectional mRNA motility. Proceedings of the National Academy of Sciences 119, e2211536119. https://doi.org/10.1073/pnas.2211536119

Bernardi, L., Bruni, A.C., 2019. Mutations in Prion Protein Gene: Pathogenic Mechanisms in C-Terminal vs. N-Terminal Domain, a Review. Int J Mol Sci 20, 3606. https://doi.org/10.3390/ijms20143606

Bianchi, V., Farisello, P., Baldelli, P., Meskenaite, V., Milanese, M., Vecellio, M., Mühlemann, S., Lipp, H.P., Bonanno, G., Benfenati, F., Toniolo, D., D'Adamo, P., 2009. Cognitive impairment in Gdi1-deficient mice is associated with altered synaptic vesicle pools and short-term synaptic plasticity, and can be corrected by appropriate learning training. Hum Mol Genet 18, 105–117. https://doi.org/10.1093/hmg/ddn321

Biasini, E., Medrano, A.Z., Thellung, S., Chiesa, R., Harris, D.A., 2008. Multiple biochemical similarities between infectious and non-infectious aggregates of a prion protein carrying an octapeptide insertion. Journal of Neurochemistry 104, 1293–1308. https://doi.org/10.1111/j.1471-4159.2007.05082.x

Blümer, J., Rey, J., Dehmelt, L., Mazel, T., Wu, Y.-W., Bastiaens, P., Goody, R.S., Itzen, A., 2013. RabGEFs are a major determinant for specific Rab membrane targeting. Journal of Cell Biology 200, 287–300. https://doi.org/10.1083/jcb.201209113

Boylan, K.L.M., Mische, S., Li, M., Marqués, G., Morin, X., Chia, W., Hays, T.S., 2008. Motility Screen Identifies Drosophila IGF-II mRNA-Binding Protein—Zipcode-Binding Protein Acting in Oogenesis and Synaptogenesis. PLOS Genetics 4, e36. https://doi.org/10.1371/journal.pgen.0040036

Brandner, S., Raeber, A., Sailer, A., Blättler, T., Fischer, M., Weissmann, C., Aguzzi, A., 1996. Normal host prion protein (PrPC) is required for scrapie spread within the central nervous system. Proceedings of the National

Academy of Sciences 93, 13148–13151. https://doi.org/10.1073/pnas.93.23.13148

Buckley, K.M., Melikian, H.E., Provoda, C.J., Waring, M.T., 2000. Regulation of neuronal function by protein trafficking: a role for the endosomal pathway. J Physiol 525, 11–19. https://doi.org/10.1111/j.1469-7793.2000.t01-2-00011.x

Campbell, G.E., 2018. Kinesin-1 and Kinesin-3 Coordinate: The Transcript of Synaptic Vesicle Precursors in Mammalian Axons. Scripps Research Institute.

Cg, D., Ca, S., Ga, B., 1988. The establishment of polarity by hippocampal neurons in culture. The Journal of neuroscience : the official journal of the Society for Neuroscience 8. https://doi.org/10.1523/JNEUROSCI.08-04-01454.1988

Chaudhuri, A., Das, S., Das, B., 2020. Localization elements and zip codes in the intracellular transport and localization of messenger RNAs in Saccharomyces cerevisiae. Wiley Interdiscip Rev RNA 11, e1591. https://doi.org/10.1002/wrna.1591

Ciechanover, A., Kwon, Y.T., 2015. Degradation of misfolded proteins in neurodegenerative diseases: therapeutic targets and strategies. Exp Mol Med 47, e147–e147. https://doi.org/10.1038/emm.2014.117

Citri, A., Malenka, R.C., 2008. Synaptic Plasticity: Multiple Forms, Functions, and Mechanisms. Neuropsychopharmacol 33, 18–41. https://doi.org/10.1038/sj.npp.1301559

Corbett, A.H., 2018. Post-transcriptional Regulation of Gene Expression and Human Disease. Curr Opin Cell Biol 52, 96–104. https://doi.org/10.1016/j.ceb.2018.02.011

Cosker, K.E., Fenstermacher, S.J., Pazyra-Murphy, M.F., Elliott, H.L., Segal, R.A., 2016. The RNA-binding protein SFPQ orchestrates an RNA regulon to promote axon viability. Nat Neurosci 19, 690–696. https://doi.org/10.1038/nn.4280

Crick, F.H., 1958. On protein synthesis. Symp Soc Exp Biol 12, 138–163.

de Castro, F., 2019. Cajal and the Spanish Neurological School: Neuroscience Would Have Been a Different Story Without Them. Front. Cell. Neurosci. 13, 187. https://doi.org/10.3389/fncel.2019.00187

Degrauwe, N., Suvà, M.-L., Janiszewska, M., Riggi, N., Stamenkovic, I., 2016. IMPs: an RNA-binding protein family that provides a link between stem cell maintenance in normal development and cancer. Genes Dev 30, 2459–2474. https://doi.org/10.1101/gad.287540.116

Delisle, M.B., Carpenter, S., 1984. Neurofibrillary axonal swellings and amyotrophic lateral sclerosis. J Neurol Sci 63, 241–250. https://doi.org/10.1016/0022-510x(84)90199-0

Deuschl, G., Beghi, E., Fazekas, F., Varga, T., Christoforidi, K.A., Sipido, E., Bassetti, C.L., Vos, T., Feigin, V.L., 2020. The burden of neurological diseases in Europe: an analysis for the Global Burden of Disease Study 2017. The Lancet Public Health 5, e551–e567. https://doi.org/10.1016/S2468-2667(20)30190-0

Dirac-Svejstrup, A.B., Soldati, T., Shapiro, A.D., Pfeffer, S.R., 1994. Rab-GDI presents functional Rab9 to the intracellular transport machinery and contributes selectivity to Rab9 membrane recruitment. Journal of Biological Chemistry 269, 15427–15430. https://doi.org/10.1016/S0021-9258(17)40696-X

Encalada, S.E., Goldstein, L.S.B., 2014. Biophysical Challenges to Axonal Transport: Motor-Cargo Deficiencies and Neurodegeneration. Annual Review of Biophysics 43, 141–169. https://doi.org/10.1146/annurev-biophys-051013-022746

Encalada, S.E., Szpankowski, L., Xia, C.H., Goldstein, L.S., 2011. Stable kinesin and dynein assemblies drive the axonal transport of mammalian prion protein vesicles. Cell 144, 551–65. https://doi.org/10.1016/j.cell.2011.01.021

Engel, K.L., Arora, A., Goering, R., Lo, H.-Y.G., Taliaferro, J.M., 2020. Mechanisms and consequences of subcellular RNA localization across diverse cell types. Traffic 21, 404–418. https://doi.org/10.1111/tra.12730

Farfel-Becker, T., Roney, J.C., Cheng, X.T., Li, S., Cuddy, S.R., Sheng, Z.H., 2020. The secret life of degradative lysosomes in axons: delivery from the soma, enzymatic activity, and local autophagic clearance. Autophagy 16, 167–168. https://doi.org/10.1080/15548627.2019.1669869

Gamarra, M., de la Cruz, A., Blanco-Urrejola, M., Baleriola, J., 2021. Local Translation in Nervous System Pathologies. Frontiers in Integrative Neuroscience 15, 689208. https://doi.org/10.3389/fnint.2021.689208

Gillingham, A.K., Sinka, R., Torres, I.L., Lilley, K.S., Munro, S., 2014. Toward a Comprehensive Map of the Effectors of Rab GTPases. Developmental Cell 31, 358–373. https://doi.org/10.1016/j.devcel.2014.10.007

Goldstein, L.S., 2012. Axonal transport and neurodegenerative disease: can we see the elephant? Prog Neurobiol 99, 186–90. https://doi.org/10.1016/j.pneurobio.2012.03.006

Gomes, C., Merianda, T.T., Lee, S.J., Yoo, S., Twiss, J.L., 2014. Molecular determinants of the axonal mRNA transcriptome. Developmental Neurobiology 74, 218–232. https://doi.org/10.1002/dneu.22123

Gong, C.-X., Iqbal, K., 2008. Hyperphosphorylation of Microtubule-Associated Protein Tau: A Promising Therapeutic Target for Alzheimer Disease. Curr Med Chem 15, 2321–2328. https://doi.org/10.2174/092986708785909111

Guedes-Dias, P., Holzbaur, E.L.F., 2019. Axonal transport: Driving synaptic function. Science 366, eaaw9997. https://doi.org/10.1126/science.aaw9997

Guedes-Dias, P., Nirschl, J.J., Abreu, N., Tokito, M.K., Janke, C., Magiera, M.M., Holzbaur, E.L.F., 2019. Kinesin-3 Responds to Local Microtubule Dynamics to Target Synaptic Cargo Delivery to the Presynapse. Curr Biol 29, 268-282 e8. https://doi.org/10.1016/j.cub.2018.11.065

Guo, X., Macleod, G.T., Wellington, A., Hu, F., Panchumarthi, S., Schoenfield, M., Marin, L., Charlton, M.P., Atwood, H.L., Zinsmaier, K.E., 2005. The GTPase dMiro is required for axonal transport of mitochondria to Drosophila synapses. Neuron 47, 379–393. https://doi.org/10.1016/j.neuron.2005.06.027

Hafner, A.-S., Donlin-Asp, P.G., Leitch, B., Herzog, E., Schuman, E.M., 2019. Local protein synthesis is a ubiquitous feature of neuronal pre- and postsynaptic compartments. Science 364, eaau3644. https://doi.org/10.1126/science.aau3644

Hansen, H.T., Rasmussen, S.H., Adolph, S.K., Plass, M., Krogh, A., Sanford, J., Nielsen, F.C., Christiansen, J., 2015. Drosophila Imp iCLIP identifies an RNA assemblage coordinating F-actin formation. Genome Biology 16, 123. https://doi.org/10.1186/s13059-015-0687-0

Harris, D.A., 2003. Trafficking, turnover and membrane topology of PrP: Protein function in prion disease. British Medical Bulletin 66, 71–85. https://doi.org/10.1093/bmb/66.1.71

Hegde, R.S., Tremblay, P., Groth, D., DeArmond, S.J., Prusiner, S.B., Lingappa, V.R., 1999. Transmissible and genetic prion diseases share a common pathway of neurodegeneration. Nature 402, 822–826. https://doi.org/10.1038/45574

Herculano-Houzel, S., 2012. The remarkable, yet not extraordinary, human brain as a scaled-up primate brain and its associated cost. Proceedings of the National Academy of Sciences 109, 10661–10668. https://doi.org/10.1073/pnas.1201895109

Hou, Y., Dan, X., Babbar, M., Wei, Y., Hasselbalch, S.G., Croteau, D.L., Bohr, V.A., 2019. Ageing as a risk factor for neurodegenerative disease. Nat Rev Neurol 15, 565–581. https://doi.org/10.1038/s41582-019-0244-7

Ioannou, M.S., Liu, Z., Lippincott-Schwartz, J., 2019. A Neuron-Glia Co-culture System for Studying Intercellular Lipid Transport. Current Protocols in Cell Biology 84, e95. https://doi.org/10.1002/cpcb.95

Ismail, S., 2016. A GDI/GDF-like system for sorting and shuttling ciliary proteins. Small GTPases 8, 208–211. https://doi.org/10.1080/21541248.2016.1213782

Janke, C., Magiera, M.M., 2020. The tubulin code and its role in controlling microtubule properties and functions. Nat Rev Mol Cell Biol 21, 307–326. https://doi.org/10.1038/s41580-020-0214-3

Kaech, S., Banker, G., 2006. Culturing hippocampal neurons. Nat Protoc 1, 2406–2415. https://doi.org/10.1038/nprot.2006.356

Kang, H., Schuman, E.M., 1996. A requirement for local protein synthesis in neurotrophin-induced hippocampal synaptic plasticity. Science 273, 1402–1406. https://doi.org/10.1126/science.273.5280.1402

Katrukha, E.A., Jurriens, D., Salas Pastene, D.M., Kapitein, L.C., 2021. Quantitative mapping of dense microtubule arrays in mammalian neurons. eLife 10, e67925. https://doi.org/10.7554/eLife.67925

Kiral, F.R., Kohrs, F.E., Jin, E.J., Hiesinger, P.R., 2018. Rab GTPases and Membrane Trafficking in Neurodegeneration. Curr Biol 28, R471–R486. https://doi.org/10.1016/j.cub.2018.02.010

Kohrs, F.E., Daumann, I.-M., Pavlovic, B., Jin, E.J., Kiral, F.R., Lin, S.-C., Port, F., Wolfenberg, H., Mathejczyk, T.F., Linneweber, G.A., Chan, C.-C., Boutros, M., Hiesinger, P.R., 2021. Systematic functional analysis of

rab GTPases reveals limits of neuronal robustness to environmental challenges in flies. eLife 10, e59594. https://doi.org/10.7554/eLife.59594

Kosik, K.S., 2006. The neuronal microRNA system. Nat Rev Neurosci 7, 911–920. https://doi.org/10.1038/nrn2037

Kulkarni, V.V., Maday, S., 2018. Neuronal endosomes to lysosomes: A journey to the soma. J Cell Biol 217, 2977–2979. https://doi.org/10.1083/jcb.201806139

Lalli, G., 2012. Crucial polarity regulators in axon specification. Essays Biochem 53, 55–68. https://doi.org/10.1042/bse0530055

Langemeyer, L., Borchers, A.-C., Herrmann, E., Füllbrunn, N., Han, Y., Perz, A., Auffarth, K., Kümmel, D., Ungermann, C., 2020. A conserved and regulated mechanism drives endosomal Rab transition. eLife 9, e56090. https://doi.org/10.7554/eLife.56090

Lawrence, J.B., Singer, R.H., 1986. Intracellular localization of messenger RNAs for cytoskeletal proteins. Cell 45, 407–415. https://doi.org/10.1016/0092-8674(86)90326-0

Lie, P.P.Y., Yang, D.S., Stavrides, P., Goulbourne, C.N., Zheng, P., Mohan, P.S., Cataldo, A.M., Nixon, R.A., 2021. Post-Golgi carriers, not lysosomes, confer lysosomal properties to pre-degradative organelles in normal and dystrophic axons. Cell Rep 35, 109034. https://doi.org/10.1016/j.celrep.2021.109034

Lin, C.-H., Hsieh, M., Fan, S.-S., 2011. The promotion of neurite formation in Neuro2A cells by mouse Mob2 protein. FEBS Letters 585, 523–530. https://doi.org/10.1016/j.febslet.2011.01.003

Lipatova, Z., Hain, A.U., Nazarko, V.Y., Segev, N., 2015. Ypt/Rab GTPases: principles learned from yeast. Crit Rev Biochem Mol Biol 50, 203–211. https://doi.org/10.3109/10409238.2015.1014023

Liu, S., Hossinger, A., Göbbels, S., Vorberg, I.M., 2017. Prions on the run: How extracellular vesicles serve as delivery vehicles for self-templating protein aggregates. Prion 11, 98–112. https://doi.org/10.1080/19336896.2017.1306162

Llorens, F., del Río, J.A., 2012. Unraveling the neuroprotective mechanisms of PrPC in excitotoxicity. Prion 6, 245–251. https://doi.org/10.4161/pri.19639

Lu, W., Fox, P., Lakonishok, M., Davidson, M.W., Gelfand, V.I., 2013. Initial Neurite Outgrowth in Drosophila Neurons Is Driven by Kinesin-Powered Microtubule Sliding. Current Biology 23, 1018–1023. https://doi.org/10.1016/j.cub.2013.04.050

Ma, Y., Hendershot, L.M., 2001. The Unfolding Tale of the Unfolded Protein Response. Cell 107, 827–830. https://doi.org/10.1016/S0092-8674(01)00623-7

Mahul-Mellier, A.-L., Burtscher, J., Maharjan, N., Weerens, L., Croisier, M., Kuttler, F., Leleu, M., Knott, G.W., Lashuel, H.A., 2020. The process of Lewy body formation, rather than simply α-synuclein fibrillization, is one of the major drivers of neurodegeneration. Proceedings of the National Academy of Sciences 117, 4971–4982. https://doi.org/10.1073/pnas.1913904117

Mallucci, G., Dickinson, A., Linehan, J., Klöhn, P.-C., Brandner, S., Collinge, J., 2003. Depleting neuronal PrP in prion infection prevents disease and reverses spongiosis. Science 302, 871–874. https://doi.org/10.1126/science.1090187

Masliah, E., Hansen, L., Albright, T., Mallory, M., Terry, R.D., 1991. Immunoelectron microscopic study of synaptic pathology in Alzheimer's disease. Acta Neuropathol 81, 428–433. https://doi.org/10.1007/BF00293464

Massignan, T., Biasini, E., Lauranzano, E., Veglianese, P., Pignataro, M., Fioriti, L., Harris, D.A., Salmona, M., Chiesa, R., Bonetto, V., 2010. Mutant prion protein expression is associated with an alteration of the Rab GDP dissociation inhibitor alpha (GDI)/Rab11 pathway. Mol Cell Proteomics 9, 611–22. https://doi.org/10.1074/mcp.M900271-MCP200

McKenney, R.J., Huynh, W., Vale, R.D., Sirajuddin, M., 2016. Tyrosination of α-tubulin controls the initiation of processive dynein-dynactin motility. EMBO J 35, 1175–1185. https://doi.org/10.15252/embj.201593071

Meiring, J.C.M., Shneyer, B.I., Akhmanova, A., 2020. Generation and regulation of microtubule network asymmetry to drive cell polarity. Current Opinion in Cell Biology, Cell Architecture 62, 86–95. https://doi.org/10.1016/j.ceb.2019.10.004

Menon, K.P., Carrillo, R.A., Zinn, K., 2013. Development and plasticity of the Drosophila larval neuromuscular junction. Wiley Interdiscip Rev Dev Biol 2, 647–670. https://doi.org/10.1002/wdev.108

Miller, S., Yasuda, M., Coats, J.K., Jones, Y., Martone, M.E., Mayford, M., 2002. Disruption of Dendritic Translation of CaMKIIα Impairs Stabilization of Synaptic Plasticity and Memory Consolidation. Neuron 36, 507–519. https://doi.org/10.1016/S0896-6273(02)00978-9

Misonou, H., Trimmer, J.S., 2005. A primary culture system for biochemical analyses of neuronal proteins. Journal of Neuroscience Methods 144, 165–173. https://doi.org/10.1016/j.jneumeth.2004.11.007

Mitchell, J., Smith, C.S., Titlow, J., Otto, N., van Velde, P., Booth, M., Davis, I., Waddell, S., 2021. Selective dendritic localization of mRNA in Drosophila mushroom body output neurons. eLife 10, e62770. https://doi.org/10.7554/eLife.62770

Moughamian, A.J., Holzbaur, E.L.F., 2012. Cytoplasmic Dynein Dysfunction and Neurodegenerative Disease, in: Dyneins. Elsevier, pp. 584–601. https://doi.org/10.1016/B978-0-12-382004-4.10023-8

Munro, T.P., Kwon, S., Schnapp, B.J., St Johnston, D., 2006. A repeated IMP-binding motif controls oskar mRNA translation and anchoring independently of *Drosophila melanogaster* IMP. J Cell Biol 172, 577–588. https://doi.org/10.1083/jcb.200510044

Nagano, S., Araki, T., 2021. Axonal Transport and Local Translation of mRNA in Neurodegenerative Diseases. Frontiers in Molecular Neuroscience 14, 697973. https://doi.org/10.3389/fnmol.2021.697973

Nijhof, B., Castells-Nobau, A., Wolf, L., Gooyert, J.M.S., Monedero, I., Torroja, L., Coromina, L., Laak, J.A.W.M. van der, Schenck, A., 2016. A New Fiji-Based Algorithm That Systematically Quantifies Nine Synaptic Parameters Provides Insights into Drosophila NMJ Morphometry. PLOS Computational Biology 12, e1004823. https://doi.org/10.1371/journal.pcbi.1004823

Okada, Y., Yamazaki, H., Sekine-Aizawa, Y., Hirokawa, N., 1995. The neuron-specific kinesin superfamily protein KIF1A is a unique monomeric motor for anterograde axonal transport of synaptic vesicle precursors. Cell 81, 769–780. https://doi.org/10.1016/0092-8674(95)90538-3

Patel, V.L., Mitra, S., Harris, R., Buxbaum, A.R., Lionnet, T., Brenowitz, M., Girvin, M., Levy, M., Almo, S.C., Singer, R.H., Chao, J.A., 2012. Spatial arrangement of an RNA zipcode identifies mRNAs under post-transcriptional control. Genes Dev. 26, 43–53. https://doi.org/10.1101/gad.177428.111

Paul, M.M., Pauli, M., Ehmann, N., Hallermann, S., Sauer, M., Kittel, R.J., Heckmann, M., 2015. Bruchpilot and Synaptotagmin collaborate to drive rapid glutamate release and active zone differentiation. Frontiers in Cellular Neuroscience 9, 29. https://doi.org/10.3389/fncel.2015.00029

Pereira-Leal, J.B., Hume, A.N., Seabra, M.C., 2001. Prenylation of Rab GTPases: molecular mechanisms and involvement in genetic disease. FEBS Lett 498, 197–200. https://doi.org/10.1016/s0014-5793(01)02483-8

Piccioli, Z.D., Littleton, J.T., 2014. Retrograde BMP Signaling Modulates Rapid Activity-Dependent Synaptic Growth via Presynaptic LIM Kinase Regulation of Cofilin. J. Neurosci. 34, 4371–4381. https://doi.org/10.1523/JNEUROSCI.4943-13.2014

Pilling, A.D., Horiuchi, D., Lively, C.M., Saxton, W.M., 2006. Kinesin-1 and Dynein are the primary motors for fast transport of mitochondria in Drosophila motor axons. Mol Biol Cell 17, 2057–68. https://doi.org/10.1091/mbc.e05-06-0526

Preising, M., Ayuso, C., 2004. Rab escort protein 1 (REP1) in intracellular traffic: a functional and pathophysiological overview. Ophthalmic Genet 25, 101–110. https://doi.org/10.1080/13816810490514333

Pylypenko, O., Hammich, H., Yu, I.-M., Houdusse, A., 2017. Rab GTPases and their interacting protein partners: Structural insights into Rab functional diversity. Small GTPases 9, 22–48. https://doi.org/10.1080/21541248.2017.1336191

Qi, L., Tsai, B., Arvan, P., 2017. New insights into the physiological role of ERAD. Trends Cell Biol 27, 430–440. https://doi.org/10.1016/j.tcb.2016.12.002

Qin, J., Xu, Q., 2014. Functions and application of exosomes. Acta Pol Pharm 71, 537–543.

Raine, C.S., 1999. Characteristics of the Neuron. Basic Neurochemistry: Molecular, Cellular and Medical Aspects. 6th edition.

Rajgor, D., Welle, T.M., Smith, K.R., 2021. The Coordination of Local Translation, Membranous Organelle Trafficking, and Synaptic Plasticity in Neurons. Front Cell Dev Biol 9, 711446. https://doi.org/10.3389/fcell.2021.711446

Rodrigues, E.C., Grawenhoff, J., Baumann, S.J., Lorenzon, N., Maurer, S.P., 2021. Mammalian Neuronal mRNA Transport Complexes: The Few

Knowns and the Many Unknowns. Front Integr Neurosci 15, 692948. https://doi.org/10.3389/fnint.2021.692948

Rotshenker, S., 2011. Wallerian degeneration: the innate-immune response to traumatic nerve injury. Journal of Neuroinflammation 8, 109. https://doi.org/10.1186/1742-2094-8-109

Samuels, T.J., Järvelin, A.I., Ish-Horowicz, D., Davis, I., 2020. Imp/IGF2BP levels modulate individual neural stem cell growth and division through myc mRNA stability. eLife 9, e51529. https://doi.org/10.7554/eLife.51529

Sasaki, Y., 2020. Local Translation in Growth Cones and Presynapses, Two Axonal Compartments for Local Neuronal Functions. Biomolecules 10, 668. https://doi.org/10.3390/biom10050668

Satpute-Krishnan, P., Ajinkya, M., Bhat, S., Itakura, E., Hegde, R.S., Lippincott-Schwartz, J., 2014. ER stress-induced clearance of misfolded GPI-anchored proteins via the secretory pathway. Cell 158, 522–33.

Schlager, M.A., Hoogenraad, C.C., 2009. Basic mechanisms for recognition and transport of synaptic cargos. Molecular Brain 2, 25. https://doi.org/10.1186/1756-6606-2-25

Schwanhäusser, B., Busse, D., Li, N., Dittmar, G., Schuchhardt, J., Wolf, J., Chen, W., Selbach, M., 2011. Global quantification of mammalian gene expression control. Nature 473, 337–342. https://doi.org/10.1038/nature10098

Seibenhener, M.L., Wooten, M.W., 2012. Isolation and Culture of Hippocampal Neurons from Prenatal Mice. J Vis Exp 3634. https://doi.org/10.3791/3634

Sferra, A., Nicita, F., Bertini, E., 2020. Microtubule Dysfunction: A Common Feature of Neurodegenerative Diseases. Int J Mol Sci 21, 7354. https://doi.org/10.3390/ijms21197354

Shen, K., Cowan, C.W., 2010. Guidance molecules in synapse formation and plasticity. Cold Spring Harb Perspect Biol 2, a001842. https://doi.org/10.1101/cshperspect.a001842

Sivars, U., Aivazian, D., Pfeffer, S.R., 2003. Yip3 catalyses the dissociation of endosomal Rab–GDI complexes. Nature 425, 856–859. https://doi.org/10.1038/nature02057

Sleigh, J.N., Rossor, A.M., Fellows, A.D., Tosolini, A.P., Schiavo, G., 2019. Axonal transport and neurological disease. Nat Rev Neurol 15, 691–703.

Soldati, T., Riederer, M.A., Pfeffer, S.R., 1993. Rab GDI: a solubilizing and recycling factor for rab9 protein. Mol Biol Cell 4, 425–434. https://doi.org/10.1091/mbc.4.4.425

Statello, L., Guo, C.-J., Chen, L.-L., Huarte, M., 2021. Gene regulation by long non-coding RNAs and its biological functions. Nat Rev Mol Cell Biol 22, 96–118. https://doi.org/10.1038/s41580-020-00315-9

Stenmark, H., 2009. Rab GTPases as coordinators of vesicle traffic. Nat Rev Mol Cell Biol 10, 513–525. https://doi.org/10.1038/nrm2728

Stokin, G.B., Lillo, C., Falzone, T.L., Brusch, R.G., Rockenstein, E., Mount, S.L., Raman, R., Davies, P., Masliah, E., Williams, D.S., Goldstein, L.S., 2005. Axonopathy and transport deficits early in the pathogenesis of Alzheimer's disease. Science 307, 1282–8. https://doi.org/10.1126/science.1105681

Stone, M.C., Roegiers, F., Rolls, M.M., 2008. Microtubules Have Opposite Orientation in Axons and Dendrites of Drosophila Neurons. Mol Biol Cell 19, 4122–4129. https://doi.org/10.1091/mbc.E07-10-1079

Stowers, R.S., Megeath, L.J., Górska-Andrzejak, J., Meinertzhagen, I.A., Schwarz, T.L., 2002. Axonal transport of mitochondria to synapses depends on milton, a novel Drosophila protein. Neuron 36, 1063–1077. https://doi.org/10.1016/s0896-6273(02)01094-2

Takeuchi, T., Duszkiewicz, A.J., Morris, R.G.M., 2014. The synaptic plasticity and memory hypothesis: encoding, storage and persistence. Philos Trans R Soc Lond B Biol Sci 369, 20130288. https://doi.org/10.1098/rstb.2013.0288

Tas, R.P., Chazeau, A., Cloin, B.M.C., Lambers, M.L.A., Hoogenraad, C.C., Kapitein, L.C., 2017. Differentiation between Oppositely Oriented Microtubules Controls Polarized Neuronal Transport. Neuron 96, 1264-1271 e5. https://doi.org/10.1016/j.neuron.2017.11.018

Terry, R.D., 1996. The pathogenesis of Alzheimer disease: an alternative to the amyloid hypothesis. J Neuropathol Exp Neurol 55, 1023–5.

Tian, L., Chou, H.-L., Fukuda, M., Kumamaru, T., Okita, T.W., 2020. mRNA Localization in Plant Cells1[OPEN]. Plant Physiol 182, 97–109. https://doi.org/10.1104/pp.19.00972

Touchot, N., Chardin, P., Tavitian, A., 1987. Four additional members of the ras gene superfamily isolated by an oligonucleotide strategy: molecular cloning of YPT-related cDNAs from a rat brain library. Proceedings of the

National Academy of Sciences 84, 8210–8214. https://doi.org/10.1073/pnas.84.23.8210

Tremblay, R.G., Sikorska, M., Sandhu, J.K., Lanthier, P., Ribecco-Lutkiewicz, M., Bani-Yaghoub, M., 2010. Differentiation of mouse Neuro 2A cells into dopamine neurons. J Neurosci Methods 186, 60–67. https://doi.org/10.1016/j.jneumeth.2009.11.004

Vejnar, C.E., Messih, M.A., Takacs, C.M., Yartseva, V., Oikonomou, P., Christiano, R., Stoeckius, M., Lau, S., Lee, M.T., Beaudoin, J.-D., Musaev, D., Darwich-Codore, H., Walther, T.C., Tavazoie, S., Cifuentes, D., Giraldez, A.J., 2019. Genome wide analysis of 3′ UTR sequence elements and proteins regulating mRNA stability during maternal-to-zygotic transition in zebrafish. Genome Res. 29, 1100–1114. https://doi.org/10.1101/gr.245159.118

Weidemann, A., König, G., Bunke, D., Fischer, P., Salbaum, J.M., Masters, C.L., Beyreuther, K., 1989. Identification, biogenesis, and localization of precursors of Alzheimer's disease A4 amyloid protein. Cell 57, 115–126. https://doi.org/10.1016/0092-8674(89)90177-3

Winckler, B., Faundez, V., Maday, S., Cai, Q., Almeida, C.G., Zhang, H., 2018. The Endolysosomal System and Proteostasis: From Development to Degeneration. J. Neurosci. 38, 9364–9374. https://doi.org/10.1523/JNEUROSCI.1665-18.2018

Wu, Y.-W., Tan, K.-T., Waldmann, H., Goody, R.S., Alexandrov, K., 2007. Interaction analysis of prenylated Rab GTPase with Rab escort protein and GDP dissociation inhibitor explains the need for both regulators. Proc Natl Acad Sci U S A 104, 12294–12299. https://doi.org/10.1073/pnas.0701817104

Xu, M., Ji, J., Jin, D., Wu, Y., Wu, T., Lin, R., Zhu, S., Jiang, F., Ji, Y., Bao, B., Li, M., Xu, W., Xiao, M., 2022. The biogenesis and secretion of exosomes and multivesicular bodies (MVBs): Intercellular shuttles and implications in human diseases. Genes & Diseases. https://doi.org/10.1016/j.gendis.2022.03.021

Xu, Z., Schaedel, L., Portran, D., Aguilar, A., Gaillard, J., Marinkovich, M.P., Théry, M., Nachury, M.V., 2017. Microtubules acquire resistance from mechanical breakage through intralumenal acetylation. Science 356, 328–332. https://doi.org/10.1126/science.aai8764

Zahavi, E.E., Hummel, J.J.A., Han, Y., Bar, C., Stucchi, R., Altelaar, M., Hoogenraad, C.C., 2021. Combined kinesin-1 and kinesin-3 activity drives axonal trafficking of TrkB receptors in Rab6 carriers. Developmental Cell 56, 494-508.e7. https://doi.org/10.1016/j.devcel.2021.01.010

Zavodszky, E., Hegde, R.S., 2019. Misfolded GPI-anchored proteins are escorted through the secretory pathway by ER-derived factors. eLife 8, e46740. https://doi.org/10.7554/eLife.46740

Zhang, J., Schulze, K.L., Hiesinger, P.R., Suyama, K., Wang, S., Fish, M., Acar, M., Hoskins, R.A., Bellen, H.J., Scott, M.P., 2007. Thirty-one flavors of Drosophila rab proteins. Genetics 176, 1307–1322. https://doi.org/10.1534/genetics.106.066761

2

Endosomal Sorting Generates Axonal Endoggresomes

Content

2.1 Introduction 46

2.2 Materials and Methods 49

2.2.1) Mouse primary neuronal cultures 49

A. Mouse lines and husbandry 49

B. Hippocampal Neuron Plating Preparation 49

2.2.2) Cloning, transfection, and transduction of DNA constructs 51

A. Cloning of DNA constructs 51

B. Transfection of DNA constructs 55

C. Transduction of Adenovirus and Adeno-Associated Virus (AAV) 55

D. Knock-down using shRNAs & siRNAs 56

2.2.3) Fluorescent dyes and drug assays 57

A. Brefeldin A (BFA) treatment 57

B. BTX-AF647 labeling of PrP^{WT}/PrP^{PG14}-mCh-BBS at the cell surface 57

C. Thrombin treatment to cleave off PrP at the cell surface 59

D. LysoTracker Assay to probe acidic endolysosomes 59

E. Magic Red Cathepsin B Assay to probe the activity of Cathepsin B enzyme in degradative lysosomes 59

2.2.4) Correlative Fluorescence and SEM study of cultured primary neurons 60

A. Correlative Fluorescence and SEM 60

B. Correlative Fluorescence and Serial-Section SEM (S3EM) 60

2.2.5) Immunofluorescence (IF) of cultured primary neurons 63

2.2.6) Biochemical Assays in Neuro2a cells 64
A. Proteinase-K-resistance assay 64
B. Detergent insolubility assay 65
C. SDS-PAGE and immunoblotting 66
D. Sucrose gradient vesicle flotations 66
2.2.7) Calcium imaging and potassium chloride (KCl)-induced depolarization 67
2.2.8) Cell death assay and imaging 68
2.2.9 Quantitation and data analysis 69
A. Neuronal soma image analysis 69
B. Analysis of axonal transport dynamics from time-lapse movies 69
C. Colocalization and cotransport quantifications 69
D. Definition of PrP^{PG14} vesicles versus aggregates/endoggresomes 70
E. Calculation of densities of Lysotracker-positive particles 72
F. ERSE-mCh and Vps41 fluorescence quantification 72
G. Calcium imaging analysis 73
H. Cell death quantitation 73
I. Generation of graphs and figures 74
J. Statistical analyses 74
2.3 Results 75
2.3.1 PrP^{PG14} is transported in vesicles by kinesin-1 to form aggregates in axons 75
2.3.2 PrP^{PG14} aggregates are Golgi-derived and sorted through endosomal pathway 78
2.3.3 Transient access of PrP^{PG14} to the axonal cell surface contributes to endoggresome formation 82
2.3.4 An ARL8b/kinesin-1/HOPS pathway drives PrP^{PG14} endoggresome formation in axons 85
2.3.5 ARL8b is a master regulator of ARESTA and a key determinant of PrP^{PG14} axonal entry 90
2.3.6 Misfolded PrP is degraded in the soma but persists in axons due to impaired retrograde transport and diminished lysosomal degradation capacity 94
2.3.7 PrP^{PG14} neurons display ARESTA-dependent impaired calcium intake dynamics and decreased neuronal viability 99
2.4 Conclusions and discussion 102
2.5 References 107

Declaration. This thesis chapter is modified from Chassefeyre R, Chaiamarit T, Verhelle A, Novak SW, Andrade LR, Leitao ADG, Manor U, Encalada SE. 2021. Endosomal Sorting Drives the Formation of Mutant Prion Protein Endoggresomes. *Science Advances* 7(52) (**Appendix B**) and Chaiamarit T, Wu Y, Verhelle A, Encalada SE. 2023. Fluorescence Assays for Real-Time Tracking of Cell Surface Protein Internalization and Endosomal Sorting in Axons of Primary Mouse Hippocampal Neurons. *Bio-protocol*, 13(7), e4651 (**Appendix C**).

2.1 Introduction

Misfolded protein aggregation is a common pathological feature in neurodegenerative diseases (Lee et al., 2011; Lim and Yue, 2015). The axon is especially vulnerable to aggregation and intracellular transport jams, whereby axonal swellings are formed (Kasher et al., 2009). Misfolded proteins that are cytotoxic could be transported to the synapse and spread to neighboring cells (Stokin et al., 2005; Vaquer-Alicea and Diamond, 2019). Nevertheless, the molecular mechanisms that drive the formation of misfolded protein aggregates in axons remain unknown.

Sporadic, infectious, and familial prion diseases (PrDs) are progressive and fatal neurodegenerative disorders commonly associated with neuronal loss, spongiform change, and astrogliosis (Scheckel & Aguzzi, 2018). Brain lesions occur following conversion of the glycosylphosphatidylinositol (GPI)–anchored cellular or wild-type prion protein (PrP^{C} or PrP^{WT}) into an aggregate-prone misfolded PrP conformation (called PrP^{Sc} or scrapie) (Prusiner, 1998; Soto & Satani, 2011; Zanusso et al., 2007). In familial human PrDs caused by mutations in the single *PRNP* gene (Prusiner, 2013; Wadsworth et al., 2003)—i.e.,

Creutzfeldt–Jakob disease (CJD), Gerstmann–Sträussler–Scheinker (GSS) disease, and fatal familial insomnia (FFI)—misfolded PrP aggregates are found in several brain regions, including within swollen/dystrophic axons (Gu et al., 2007; Medrano et al., 2008; Nixon et al., 2000). Previously, infectious or familial PrP mutants have been observed to accumulate in the cytosol as aggresomes (Kovacs et al., 2012; Kristiansen et al., 2005; Ma and Lindquist, 2001), or accumulate inside endocytic compartments in cultured cells and in neurons from the brains of human patients diagnosed with PrDs (Borchelt et al., 1992; Kovacs et al., 2012; Marijanovic et al., 2009; Yim et al., 2015), suggesting that misfolded PrP can form aggregates and accumulate within endolysosomal pathways. Yet, the connection between endolysosomal trafficking in PrP aggregation remains unclear as pathways have not been defined. Both PrP^{WT} and PrP mutants (PrP^{mut}) transit to the cell surface from the ER via the Golgi in the luminal side of vesicular compartments, from where they are endocytosed back for sorting in endosomes and to lysosomes for degradation (Borchelt et al., 1992; Caughey et al., 1991; Hegde and Rane, 2003; Mironov et al., 2003; Satpute-Krishnan et al., 2014; Zavodszky and Hegde, 2019). PrP is also found in multivesicular bodies (MVBs), which is proposed to be a site where PrP^{Sc} converts PrP^{C} to misfolded conformations (Marijanovic et al., 2009; Yim et al., 2015) and gets released into exosomes for cell-to-cell spread (Fehlinger et al., 2017; Goold et al., 2011). How mutant PrP gets sorted in endolysosomal compartments in axons *en route* to become neurotoxic aggregates remains unclear. Identification of the subcellular itinerary where mutant PrP aggregates form, transit, and become neurotoxic in axons is critical for understanding the axonal etiology of prion and other neurodegenerative disorders.

In this chapter, I present a full report based on published peer-reviewed article (Chassefeyre et al., 2021) where I took part in the identification of endosomal sorting mechanisms that generate large membrane-bound aggregate structures called 'endoggresomes.' Endoggresomes (Endosomal aggresomes) are membrane-bound neurotoxic aggregates formed along the length of axons and distend axons into swellings. For endoggresome biogenesis in axons, ADP ribosylation factor-like GTPase 8b (ARL8b) recruits the kinesin-1 and the Homotypic Fusion and Protein Sorting (HOPS) complex, onto mutant PrP vesicles and shuttle them into the axon and to fuse vesicles into enlarged endoggresomes, respectively. The formation of axonal endoggresomes impairs neuronal calcium dynamics and leads to neuronal death. Reducing the function of ARL8b, kinesin-1, or HOPS components inhibits endoggresome formation in axons and circumvents neuronal toxicity. In addition, we found alternative routes of endoggresome formation via access to axonal cell surface that converged onto ARL8b for homotypic fusion. Dysfunctions of endolysosomal quality control and of retrograde transport in axons explain misfolded PrP endoggresome accumulation instead of clearance overtime. Our findings hence pinpoint the endolysosomal trafficking system as a key player in the discriminating journey of misfolded mutant PrP within neurons towards degradation versus aggregation and point to the ARL8b/kinesin-1/HOPS pathway as an anti-aggregation target that can modulate neuronal dysfunction in the prionopathies.

2.2 Materials and Methods

2.2.1) Mouse primary neuronal cultures

A. Mouse lines and husbandry

The mouse protocols were reviewed and approved by Institutional Animal Care and Use Committee (IACUC) at Scripps Research, and all colonies were maintained following the guidelines recommended by the Department of Animal Resources (DAR). Wild-type (WT) mice were of C57BL/6 background (Charles River Laboratories). The generation of Kinesin-1C null (*Kif5c*$^{-/-}$) and KLC1 null (*Klc1*$^{-/-}$) mice were described previously (Encalada et al., 2011). *Kif5c*$^{-/-}$ mice were maintained as homozygotes and were backcrossed in the C57BL/6 background for at least 6 generations before the experiments. *Klc1*$^{-/-}$ mice were bred as heterozygotes to generate homozygous pups. The conditional homozygous kinesin-1B floxed mouse (*Kif5b*$^{pflox/pflox}$) was generated as described previously (Cui et al., 2011). I collected newborn to 2-day-old mouse neonates for primary hippocampal culture in this study.

B. Hippocampal Neuron Plating Preparation

The brains of newborn to 2-day-old mouse neonates were collected as described in a detailed published peer-review protocol written by me (Chaiamarit et al., 2023). Briefly, I washed the decapitated pup heads in sterile, cold Hank's buffer solution (HBSS) supplemented with 0.08% D-glucose, 0.17% HEPES, and 1% Pen-Strep (**Figure 2.1A**). I removed the skin and the soft skull using two forceps, and I transferred the brains to a new plate containing fresh HBSS (**Figure 2.1B**). Extracted hippocampi from both hemispheres (**Figure 2.1C**) were washed twice with cold HBSS without Pen-Strep in a biosafety hood. Then, I incubated the

hippocampi in 37°C water bath for 20 minutes in a sterile solution of 45 U papain, 0.01% DNase, 1 mg DL-cysteine, 1 mg BSA, and 25 mg D-Glucose in PBS. After the tissue digestion, I washed hippocampi twice with Dulbecco's Modified Eagle Medium (DMEM) supplemented with 10% fetal bovine serum (FBS), pre-heated to 37°C, and I performed ten to twelve cycles of aspiration by pipetting. I transferred the dissociated neurons in DMEM + 10% FBS onto 24-well plates containing 12-mm glass coverslips pretreated with 50 µg/ml poly-L-lysine in Borate buffer and incubated for 1 hour for cell attachment. Lastly, I replaced the DMEM with Neurobasal-A (NBA) medium, supplemented with 2% B-27 and 0.25% GlutaMAX. Primary neurons were maintained in a clean primary neuron only incubator at 37°C, 5% CO_2 atmosphere for up to 15 days.

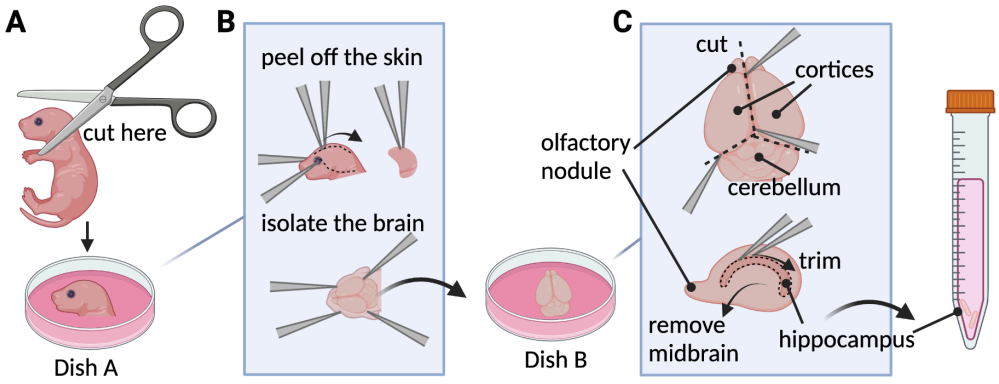


Figure 2.1 Isolation of hippocampus from mouse neonates for primary hippocampal culture. (A) Decapitation, **(B)** isolation of the brain, **(C)** dissection and harvest of the hippocampus (dotted lines). From Chaiamarit et al., 2023.

I monitored and inspected the primary culture under the microscope for density, growth, and health every 1-3 days (**Figure 2.2**). At Day *In Vitro* 2 (DIV 2), healthy neurons grow extensive neurites with identifiable growth cones (**Figure 2.2A**). At DIV 4-5, axons and dendrites are distinguishable by morphology, as described previously (Encalada et al., 2011) (**Figure 2.2B**). From

this stage forward, neurons are ready for transfection and imaging. By DIV 9-10, axons and dendrites continue to grow and fasciculate extensively (**Figure 2.2C**). DIV 10-12 neurons were used for physiological assays, such as calcium imaging.

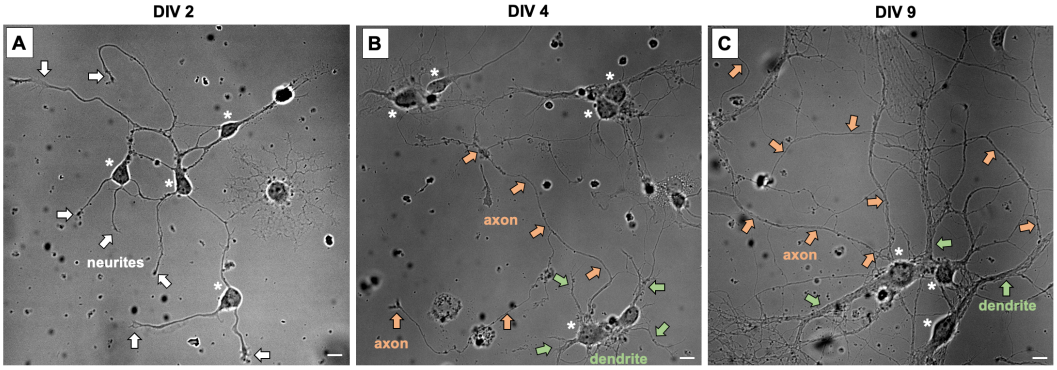


Figure 2.2 Growth of cultured primary hippocampal neurons (A) at 2 DIV, (B) at 4 DIV, (C) at 9 DIV. Neurons plated onto 12-mm coverslips inside 12 wells in a 24-well plate. One brain plated onto 12 coverslips yielded 75,000-100,000 cells/coverslip. Images were taken with Nikon Plan Fluor 40X/1.3NA oil Objectives using Differential Interference Contrast (DIC) optics. Scale bar = 10 μm. From Chaiamarit et al., 2023. Images collected by Yin Wu.

2.2.2) Cloning, transfection, and transduction of DNA constructs

A. Cloning of DNA constructs

1. PrP constructs

All mouse PrP (MoPrP/PrP) constructs were derived from the MoPrP.Xho PrP^{WT}-EGFP and MoPrP.Xho PrP^{PG14}-EGFP constructs (a gift from David Harris, Boston University) (Barmada et al., 2004; Medrano et al., 2008). All PrP constructs in this study contain a signal sequence (SS) for secretion, octapeptide P(Q/H)GG(T/S)WGQ repeats (five times for WT or fourteen times for PG14 mutant), 3F4 epitope MKHM, glycosylation sites, a fluorescent protein (or none), and GPI anchor, unless stated otherwise (**Figure 2.3A-B**). The In-Fusion® HD Cloning Plus Kit (Clontech) was used for cloning and modifying PrP in pcDNA3.1 plasmid before putting modified fragments into the recipient

MoPrP.Xho vector for transfection. All PCR amplifications were performed using the Phusion® High-Fidelity DNA Polymerase (NEB). The following constructs were made by Romain Chassefeyre, a postdoc in the Encalada lab. For the MoPrP.Xho PrP^{WT}-mCherry (mCh) and MoPrP.Xho PrP^{PG14}-mCh constructs (**Figure 2.3A**), EGFP was replaced with mCh using assembly PCR strategy. Briefly, three individual PCRs were performed to amplify the (1) N-terminus of PrP^{WT} or PrP^{PG14}, (2) C-terminus of PrP, (3) mCh including 20- and 22-bp overlaps to the 3' of (1) and 5' of (2), respectively. PCR products (1-3) were gel purified and subsequently stitched together (1 ng each), using a PCR reaction performed without primers. After 20 cycles, PCR was interrupted, 0.5 µM of end-piece primers were added to amplify the complete product. The reaction was supplemented with 100 µM dNTP and 0.5 mM $MgCl_2$ and ran for 30 more cycles. The same strategy was used to generate MoPrP.Xho PrP^{WT}-mTagBFP2 and MoPrP.Xho PrP^{PG14}-mTagBFP2 (by replacing mCh with mTagBFP2) and to generate untagged MoPrP.Xho PrP^{WT} and MoPrP.Xho PrP^{PG14}. To generate the photoactivatable (PA) constructs—Mo.PrP.XhoPrP^{WT}-PAmCh and MoPrP.Xho PrP^{PG14}-PAmCh—PAmCh1-C1 plasmid was a gift from Vladislav Verkhusha, Albert Einstein College of Medicine, New York (Subach et al., 2009). To generate Bungarotoxin binding sequence (BBS)-tagged constructs, MoPrP.Xho PrP^{WT}-mCh-BBS and MoPrP.Xho PrP^{PG14}-mCh-BBS, a 13 amino-acid BBS tag (WRYYESSLEPYPD) was inserted at the BspEI site in the linker between mCh and C-terminal PrP sequence downstream of mCh (**Figure 2.3C**). To generate the Thrombin cleavage sequence (TCS) tagged constructs MoPrP.Xho PrP^{WT}-mCh-TCS and MoPrP.Xho PrP^{PG14}-mCh-TCS (**Figure 2.3D**), 6 amino-acid TCS tag (LVPRGS) was amplified and inserted at the BspEI site downstream of mCh.

Adriaan Verhelle, a postdoc in the Encalada lab, generated the plasmid for AAV transduction. PrP^{WT}-mCh and PrP^{PG14}-mCh were cloned into the pAAV-hSyn-MCS backbone between the BamHI and EcoRI sites (gift from T. Golde, U. of Florida).

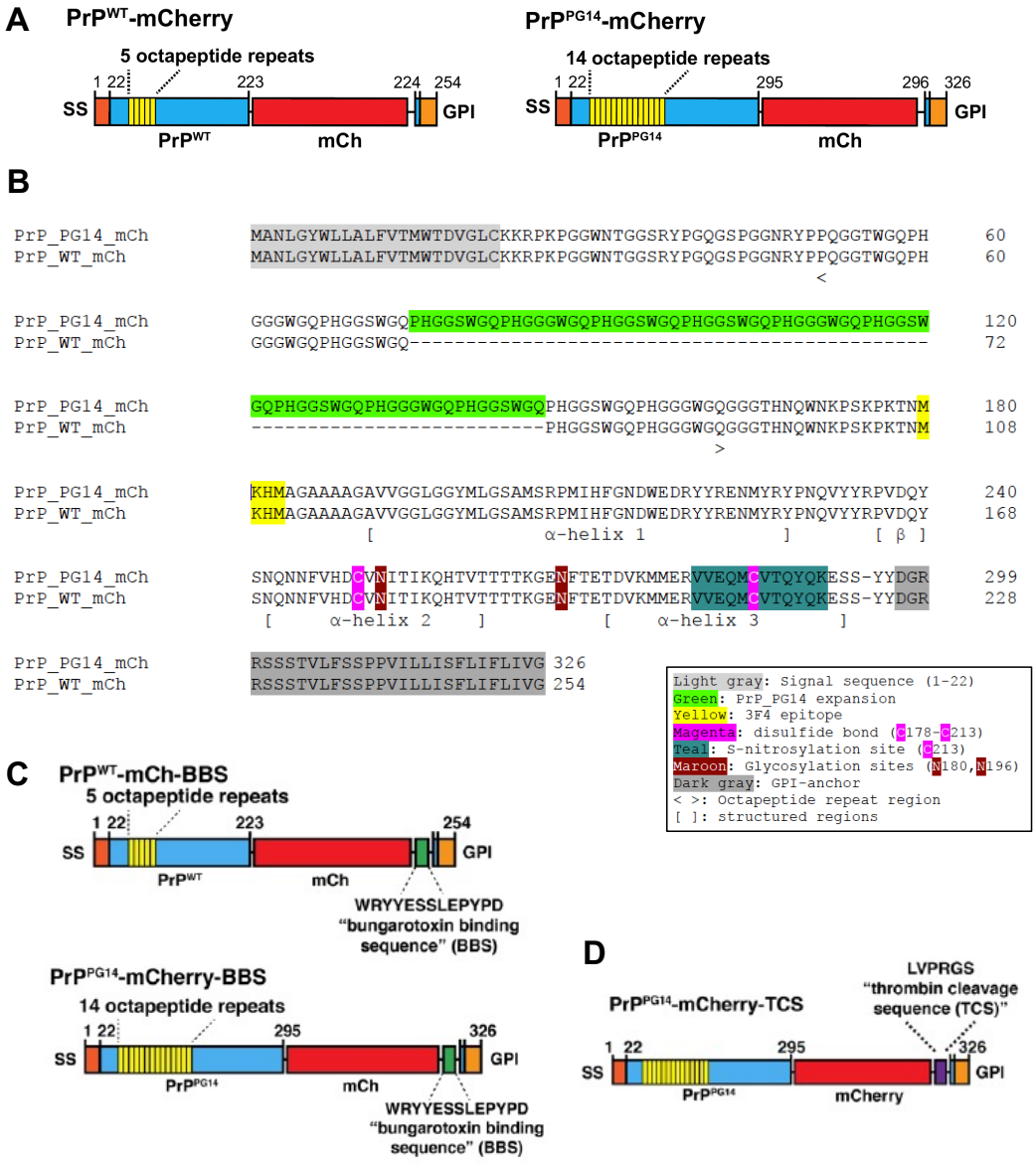


Figure 2.3 Schematic of mouse PrP constructs and sequence. (A) PrP^{WT}-mCh and PrP^{PG14}-mCh, (B) Full amino acid sequence and annotation, (C) PrP^{WT}-mCh-BBS and PrP^{PG14}-mCh-BBS, (D) PrP^{PG14}-mCh-TCS. SS = Signal sequence, GPI = GPI anchor.

2. Organelle marker constructs

The following constructs were made by Romain Chassefeyre. RFP in LAMP1-RFP plasmid (a gift from Erika Holzbaur, University of Pennsylvania) (Maday and Holzbaur, 2016) was replaced with EGFP to generate LAMP1-EGFP. To generate the signal sequence SS-EGFP label of Golgi-derived vesicles, SS derived from Neuropeptide Y (NPY) were amplified from mouse brain cDNA and cloned between BglII and BamHI sites in pEGFP-N3 vector. To make EGFP-Rab5, EGFP-Rab7 and EGFP-Rab11, the sequences were amplified from mouse brain cDNA and cloned between XhoI and BamHI sites in the pEGFP-C1 vector (a gift from Hilal Lashuel, Swiss Federal Institute of Technology) (Nakagawa et al., 2004).

3. ARL8b constructs

The following constructs were made by Romain Chassefeyre. T34N and Q75L mutations were introduced in pDEST47-ARL8b^{WT}-GFP plasmid (Addgene #67404), using the QuikChange II XL Site-Directed Mutagenesis kit (Agilent). To generate untagged ARL8b constructs, the ARL8b coding sequence was cloned in the pBI-CMV3 bidirectional promoter vector.

4. KIF5C, KLC, and SKIP constructs

The KLC1-TAP plasmid was a gift from Larry S. B. Goldstein (U. California San Diego). George Campbell, a PhD student in the Encalada lab, made the following constructs. 2xmCh-KIF5C was designed by subcloning 2xmCh from KIF5C(1-560)-2xmChEF(C) (Addgene #61664) in pCDNA3.1. Then, full-length KIF5C sequence was amplified from pGFP-KIF5C (a gift from Michelle Peckham, University of Leeds) (Dunn et al., 2008), and cloned downstream of 2xmCh. To

generate the SKIP 1-186 construct, the sequence of the first 186 amino acids was cloned in pcDNA3.1 at the HindIII and BamHI site, and this was done by Romain Chassefeyre.

B. Transfection of DNA constructs

Hippocampal neurons were transfected using Lipofectamine 2000 (Thermo Fisher), following the manufacturers' instructions. DNA and Lipofectamine were diluted in Neurobasal-A medium. For most experiments, neurons grown on 12 mm coverslips in 24-well plates were transfected using 2 µL of Lipofectamine and 0.4 or 0.8 µg of DNA per well. Medium was changed 1 hour after transfection to avoid toxicity.

C. Transduction of Adenovirus and Adeno-Associated Virus (AAV)

Cre-recombinase adenovirus transduction (University of Iowa, Ad5CMVCre) was performed as described previously (Encalada et al., 2011). Briefly, hippocampal neurons isolated from Kinesin-1B conditional knockout mice ($KifB^{pflox/pflox}$) were treated at 6 DIV with 0, 100, or 400 MOI of adenovirus, corresponding to 0, $5x10^6$, or $2x10^7$ plaque-forming units (PFU), respectively. Neurons were incubated for 2 hours with the virus and then washed twice with Neurobasal-A medium (Gibco) containing 2% B-27 (Gibco), and 0.25% GlutaMAX (Gibco).

AAV virus was made using the AAV-DJ Helper Free Packaging System (Cell Biolabs) using published protocols (McClure et al., 2011) by Adriaan Verhelle. Hippocampal neurons growing in 24-well plates were treated overnight with 4 µL of the viral stock at DIV7 and imaged at DIV12.

D. Knock-down using shRNAs & siRNAs

To knockdown ARL8b from neurons, the following previously validated 21-mer shRNA inserts were cloned separately by Romain Chassefeyre in the pLKO.3G vector (Addgene plasmid #14748): scrambled shRNA (CCTAAGGTTAAGTCGCCCTCG), ARL8b shRNA #1 (CCTCTCGAAATGAACTGCATA), ARL8b shRNA #3 (CGAGGAGTCAATGCAATTGTT). Validation of shRNA constructs for reduction of ARL8b was done by transfecting Neuro2a (N2a) cells at 40% confluency with pLKO3.G-ARL8b shRNA #1 and #2 either separately or together using Lipofectamine 2000. Dynein was knocked down by transfection of neurons with a previously validated DHC1 shRNA lentiviral construct (GTGATGCCATACGAGAGAA), and a scrambled shRNA construct was used as control (GCACACGTATCGACGTATC) (Encalada et al., 2011). Transfection rates were $>$ 80% and were ascertained by counting GFP-positive cells. ShRNAs were expressed for 48 or 72 hours prior to harvesting, lysed in radioimmunoprecipitation assay (RIPA) buffer, and evaluated by Western blots using rabbit anti-ARL8b (Proteintech) and anti-alpha-tubulin as a loading control (Sigma Aldrich). N2a cells were harvested at the same time points for reverse-transcriptase PCR generation using iScript cDNA Synthesis kit (Bio-Rad), and quantitative PCR (qPCR) was performed using the FastStart Universal SYBR Green Mastermix (Roche) to test for reduced ARL8b mRNA levels. To knockdown VPS41 from neurons, the ON-TARGET plus SMART pool siRNA from Dharmacon was used.

2.2.3) Fluorescent dyes and drug assays

A. Brefeldin A (BFA) treatment

To retain PrP^{PG14} in the ER, I applied 5 µg/mL Brefeldin-A (BFA) (BioLegend) at the same time as PrP^{WT}-mCh or PrP^{PG14}-mCh transfections and incubated for 2-6 hours (**Figure 2.4A**). During this timeframe, the majority of PrP^{PG14}-mCh was retained in the ER (**Figure 2.4B-C**). The growth media was used to wash off BFA to release PrP^{PG14}-mCh from the ER at a desirable timepoint prior to fixation and imaging.

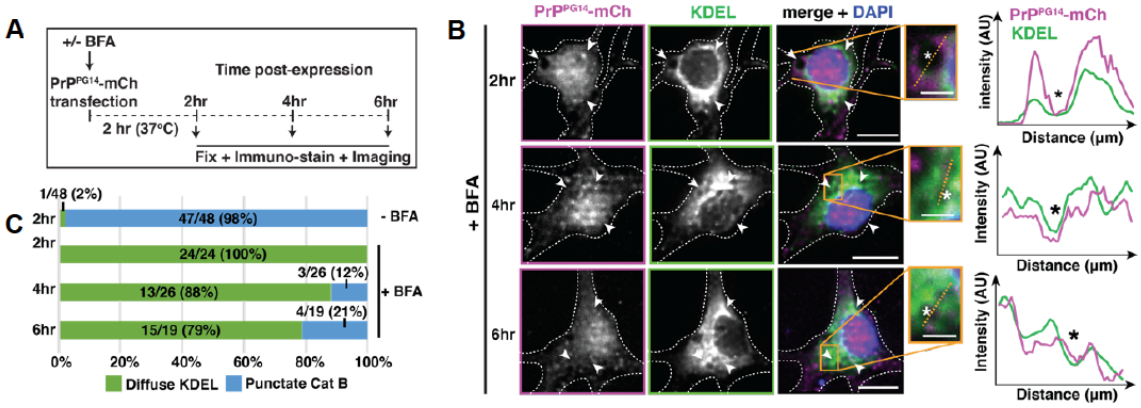


Figure 2.4 BFA Treatment and validation of PrP^{PG14}-mCh retention in the ER. (A) Timeline for transfection with/without BFA treatment. **(B)** Representative images of neuronal cell bodies showing PrP^{PG14}-mCh colocalization with antibody against ER (KDEL) and with DAPI nuclear marker at 2-, 4-, and 6-hours post-transfection and BFA treatment. Arrowheads and asterisks in insets and linescan intensity profiles (from orange dotted lines) point to colocalization and non-colocalization events, respectively. Scale bars = 10 µm, Scale bars of insets = 250 nm. **(C)** Quantitation of PrP^{PG14}-mCh colocalization with either KDEL or cathepsin B antibodies, showing a certain percent leakage of PrP^{PG14} population from the ER during BFA treatment overtime.

B. BTX-AF647 labeling of PrP^{WT}/PrP^{PG14}-mCh-BBS at the cell surface

For characterization of PrP^{PG14} exocytosis and endocytosis in the soma or axons, neurons were transfected with PrP^{PG14}-mCh-BBS (or PrP^{WT}-mCh-BBS control) constructs (**Figure 2.3C**). Neurons were treated with AlexaFluor647-labeled-α-Bungarotoxin (BTX-AF647/BTX-a647) by applying it to the media and as

described previously (Sekine-Aizawa and Huganir, 2004). Briefly, I pre-treated neurons with 100 µM tubocurarine hydrochloride (Sigma) for 1 hour to eliminate non-specific binding to other receptors (Sekine-Aizawa and Huganir, 2004). Then, I incubated neurons with 7 µg/mL BTX-AF647 in the media, during indicated times and at indicated temperatures. Endocytosed population of PrP^{PG14} was studied by observing colocalization or co-transport of PrP^{PG14}-mCh-BBS, BTX-AF647, and endolysosomal marker (such as LAMP1-EGFP) (**Figure 2.5A**). This BTX-AF647 labeling was specific, as neurons that were transfected with PrP^{PG14} without BBS sequence (PrP^{PG14}-mTagBFP2) did not have BTX-AF647 signal, while neurons that were transfected with PrP^{PG14}-mCh-BBS showed strong colocalized pattern with BTX-AF647 (**Figure 2.5B**).

To inhibit clathrin mediated-endocytosis, I added 80 µM Dynasore (Sigma) 30 minutes prior to BTX-AF647 treatment, and I kept 80 µM Dynasore during the BTX-AF647 labeling. DMSO was used as a control. Internalized PrP^{PG14} particles were defined as PrP^{PG14}-mCh-BBS particles that were both positively for BTX-AF647 and were actively transporting within axons.

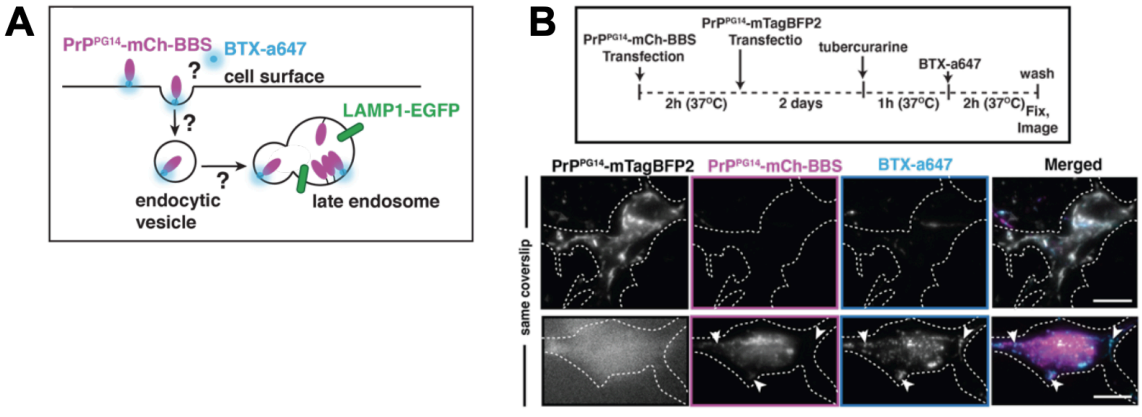


Figure 2.5 Specific labeling of PrP^{PG14}-mCh-BBS by BTX-AF647. (A) Outline of the internalization assay, (B) Timeline and representative images. Top panels show a neuron

transfected with PrP^{PG14}-mTagBFP2 lacking BBS and lacking BTX-AF647 signal, and bottom panels show a neuron transfected with PrP^{PG14}-mCh-BBS with BTX-AF647, from the same coverslip. Scale bar = 10 µm.

C. Thrombin treatment to cleave off PrP at the cell surface

Romain Chassefeyre performed the following experiments. Hippocampal neurons were transfected with PrP^{PG14}-mCh-TCS or PrP^{PG14}-mCh (no TCS control) (**Figure 2.3D**). At 2 hours post-transfection, neurons were treated with 5 units/ml of Thrombin protease (Sigma) and was maintained for 48 hours. Neurons were washed in growth media 2-3 times before imaging.

D. LysoTracker Assay to probe acidic endolysosomes

I incubated neurons in 50 nM of LysoTrackerGreen or other LysoTracker colors (Molecular Probes) in growth media for 2 hours at 37°C. Then, I washed neurons 2-3 times in growth media and waited 30 minutes prior to live imaging for stable fluorescence signal. I imaged LysoTrackerGreen signal with 488-nm laser.

E. Magic Red Cathepsin B Assay to probe the activity of Cathepsin B enzyme in degradative lysosomes

First, I diluted 250X DMSO stock of Magic Red Cathepsin B Assay in sterile H_2O. I applied Magic Red Cathepsin B solution into neurons in each well and incubated for 2 hours at 37°C. Then, I washed away the Magic Red 2 to 3 times with growth media. I waited 30 minutes prior to live imaging for stable fluorescence signal. I imaged Magic Red signal with the excitation wavelength of 561 nm laser and used emission filter of >610 nm.

2.2.4) Correlative Fluorescence and SEM study of cultured primary neurons

A. Correlative Fluorescence and SEM

The following protocol was performed by Romain Chassefeyre and Malcom Wood. Briefly, hippocampal neurons were plated in microfluidic chambers and co-transfected at 8 DIV with PrP^{PG14}-mCh and soluble EGFP. Two days after transfection, the positions of transfected neurons inside the microfluidic chamber were mapped using live-fluorescence microscopy with a Nikon S Plan Fluor ELWD 20X/0.45 [infinity]/0-2 Objective. Neurons were fixed in ice-cold 2.5% glutaraldehyde in 0.1 M Na cacodylate buffer (pH 7.3), and 1% trehalose was added prior to removal of chamber to expose cells for washing with buffer. Neurons were fixed in 1% osmium tetroxide, washed thoroughly with distilled water and dehydrated in a graded ethanol series. Samples were immersed in 100% hexamethyldisilazane (HMDS) for 3 minutes and allowed to dry prior to mounting on a stub with carbon tape. Samples were sputter coated with iridium at 10 μA to a thickness of approximately 5 nm (EMS model 150T S). The coverslips were then examined on a Hitachi S4300 SEM (Hitachi High Technologies America Inc., Pleasanton CA) at 5kV with settings adjusted according to needs.

B. Correlative Fluorescence and Serial-Section SEM (S3EM)

Hippocampal neurons were plated on 35-mm gridded #1.5 glass bottom dish (Cellvis) pretreated with 50 μg/mL poly-L-lysine in Borate buffer and transfected at 8 DIV with PrP^{PG14}-mCh using Lipofectamine 2000 (Thermo Fisher). Two days after transfection, neurons were first imaged using live-fluorescence and phase-contrast microscopy with a Nikon S Plan Fluor ELWD 20X/0.45

[infinity]/0-2 Objective, to map the location of transfected neurons on the grid (**Figure 2.6A**). PrP^{PG14}-mCh endoggresome sites were imaged using super-resolution radial fluctuation (SRRF) microscopy settings (Gustafsson et al., 2016) (20 frames/second, 100 frames) with a pseudo-total internal reflection fluorescence microscopy (pTIRFM) setup, with an Andor iXon + DU897 EM Camera, and a 100X/1.49 NA oil objective (**Figure 2.6B**). Samples were fixed on the gridded culture dish while live imaging by carefully mixing an equal volume of 2X EM-fixative (5% glutaraldehyde, 4% paraformaldehyde in 0.1 M cacodylate buffer with 3mM $CaCl_2$) warmed to 37°C with 2 mL of Neurobasal-A medium, containing 2% B-27 and 0.25% GlutaMAX. Samples were immediately removed from the microscope, fixative-media solution was discarded, and cells were left in fresh ice-cold fixative for 90 minutes and rinsed three times with ice cold 0.1 M cacodylate buffer with 3 mM $CaCl_2$. Samples were transferred to the Salk Institute and the following protocol was performed by Sammy Weiser Novak. Coverslips were post-fixed and stained with 1.5% reduced osmium for 35 minutes, rinsed five times with MilliQ water, and stained again with 1% aqueous uranyl acetate for 1 hour at RT, before serial dehydration with graded solutions of ice-cold ethanol in water. Samples were then fully dehydrated in two 10-minute rinses of anhydrous ethanol at RT before infiltration with Durcupan resin. After 3:1, 1:1, 1:3 ethanol-resin two-hour infiltration steps, samples were infiltrated with pure resin for two hours before another change of fresh pure resin and left overnight at RT. A final change of fresh resin was performed, and infiltrated samples were polymerized for 48 hours at 65°C. Coverslips were dissolved by immersion in concentrated hydrofluoric acid. Correlative light-electron microscopy (CLEM) was achieved using laser branded fiducials in a thinly embedded sample, as previously described (Burel et al., 2018). Briefly, regions of

interest (ROIs) that included SRRF-imaged PrP^{PG14}-mCh axon segments were identified by their grid positions and dark osmium staining. ROIs were marked using the cutting laser of a Zeiss PALM laser cutting microscope to provide orientation and fiducial guides for further trimming and ultramicrotomy. ROIs were carefully identified under a dissecting microscope and excised from the coverslip using a jeweler saw and a scalpel, with careful thought given to the future blockface orientation. The 1×2×2 mm sample block was glued to a blank resin block such that the ROIs were orthogonal to the cutting plane and approximately 100 µm from the cutting surface. Laser marks on the block face helped to identify the location of the ROI using the ultramicrotome optics. The block was carefully trimmed using a 90° diamond trimming knife (Diatome). About 200 serial sections were collected in total over four chips (**Figure 2.6C-D**).

The chips were mounted on aluminum stubs using double-sided carbon sticky tape and loaded into a Zeiss Sigma VP SEM. Chip mapping and the imaging of serial sections was facilitated by SmartSEM (Zeiss) and Atlas 5 (FIBICS) software packages. Maps of all serial sections on the silicon chips were collected at 500 nm/pixel. Laser marks could be identified in the resin boundary at low magnification, demarcating the ROI in each section. The ROI of the axon segment containing the PrP^{PG14}-mCh endoggresomes was identified and captured across 40 serial section scanning electron micrographs. ROIs were imaged at 2 nm/pixel using an electron backscatter detector (Gatan). In high-vacuum mode, a 3 keV beam in high-current mode with a 30 µm aperture at a working distance of 9 mm was found to produce signal from which we could resolve membrane and organelle (e.g., microtubule) ultrastructure (**Figure 2.6E**). Sections were aligned using Adobe Photoshop and elastic alignment functions (Saalfeld et al., 2012)

embedded in Fiji. The orthogonal projection (e.g., x-z) of the S3EM data was created in Fiji and used to correlate the SRRF-processed data and to produce overlay in Adobe Illustrator. Sections were sampled from throughout the aggregate and non-aggregate sites with reference to the correlated volume.

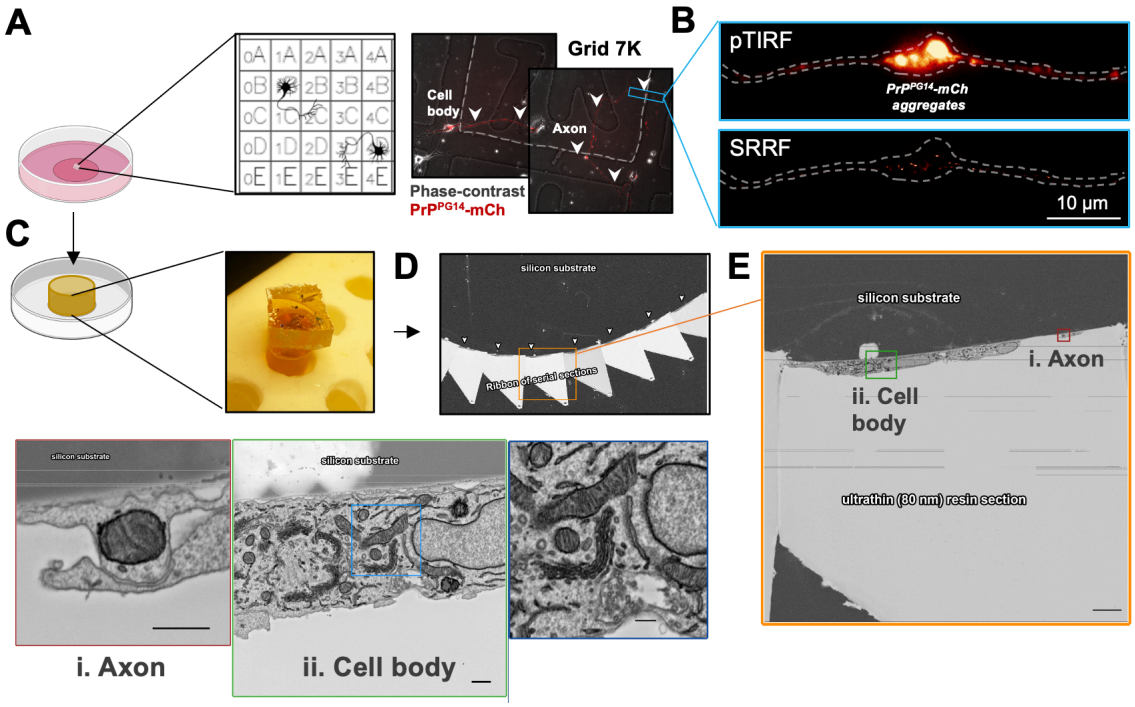


Figure 2.6 Correlative fluorescence and S3EM study axonal endoggresomes. **(A)** Transfected neurons on a Gridded glass bottom dish are identifiable by phase-contrast mode and fluorescence of PrP^{PG14}-mCh. **(B)** Identification of PrP^{PG14}-mCh aggregate site and super-resolution radial fluctuation (SRRF) processing to generate super-resolved map of PrP^{PG14}-mCh endoggresomes. **(C)** Resin embedding of neurons. **(D)** Layering of ultrathin (80 nm) resin sections on silicon substrate. **(E)** Identification of cross section of cell body and axon of a neuron, showing well-preserved ultrastructure. Scale bars (E, i) = 500 nm, (ii) = 50 nm. Procedures (C-E) were performed by Sammy Weiser Novak.

2.2.5) Immunofluorescence (IF) of cultured primary neurons

I performed most of IF in cultured primary neurons. Neurons were fixed with 4% paraformaldehyde (PFA) containing 4% sucrose for 30 minutes at 37°C. I washed neurons once in 50 mM Glycine in PBS and 3 more times in PBS. I permeabilized neurons by incubating the coverslips in 0.1% Triton X-100 in PBS

for 8-10 minutes followed by 3 washes with PBS. I incubated the coverslips in blocking solution (10% IgG-Free BSA, 5% donkey serum or goat serum in PBS) for 30 minutes at room temperature, followed by incubation with primary antibodies in blocking solution for 1 hour at RT or overnight at 4°C. After 3 washes in PBS, neurons were incubated with secondary antibodies in blocking solution for 1 hour at RT or overnight at 4°C. If applicable, neurons were counterstained with 300 nM DAPI (Thermo Fisher) for 5 minutes. After 3 washes in PBS, coverslips were washed once in H_2O and mounted in ProLong Diamond antifade reagent (Thermo Fisher).

The following antibodies were used for immunofluorescence (IF): mouse anti-KDEL (1:100, Santa Cruz Biotechnology); rabbit anti-GM130 (1:100, Abcam); goat anti-mouse Cathepsin B (1:40, R and D systems); rabbit polyclonal IgG anti-mCh (1:100 Gentex), recombinant Fab anti-PrP (1:200 clone HuM-D13) (*91*), rabbit anti-ARL8b (1:200, ProteinTech), and mouse anti-Vps41 (1:100 clone D-12, Santa Cruz Biotechnology).

2.2.6) Biochemical Assays in Neuro2a cells

Neuro2a (N2a) cells (ATCC) were grown in DMEM, supplemented with 10% FBS and 1% Pen-Strep in an incubator at 37°C and in a 5% CO_2 atmosphere. Cells were passaged twice a week to low confluency using 0.05% Trypsin-EDTA. The following protocols were performed by Romain Chassefeyre, Adriaan Verhelle, and André Leitão.

A. Proteinase-K-resistance assay

N2a cells were transfected with PrP^{WT}-mCh or PrP^{PG14}-mCh (in pcDNA3.1 vector) and lysed 48 hours after transfection in PBS containing 0.5% Nonidet P-

40, 0.5% sodium deoxycholate, 0.2% Sarkosyl, and 0.5% Triton X-100. Proteins in 500 µg of lysate were digested using 0, 0.05, 0.1, 0.5, 1 or 5 µg/mL of Proteinase K (PK) (Thermo Fisher), during 30 minutes at 37°C. The reaction was blocked by adding 0.8 mg/ml of freshly prepared phenylmethylsulfonyl fluoride (PMSF). The equivalent of 20 µg of each sample was analyzed by immunoblotting using an anti-PrP specific antibody (D13) (gift of D. Burton, Scripps Research). Samples corresponding to 1 and 5 µg/ml of PK were also precipitated using trichloroacetic acid (TCA) to concentrate the proteins. The equivalent of 120 µg of each sample was analyzed by immunoblotting.

The PK assay of sucrose gradient floated fraction was done on 20 µg of an 8/35% sucrose floated vesicle fraction that was digested using 0, 0.5, 1, 2 or 5 µg/mL of PK for 30 minutes at 37°C. The digestion reaction was blocked by addition of 0.8 mg/ml of freshly prepared PMSF. The sample was analyzed by immunoblotting with Fab anti-PrP (1:200 clone Hum-D13).

B. Detergent insolubility assay

A detergent insolubility assay was used following previously established protocols (Daude et al., 1997). Briefly, N2a cells were transfected with PrP^{WT}-mCh or PrP^{PG14}-mCh constructs using Lipofectamine 2000. At two days post-transfection, membrane-bound vesicles were isolated in a sucrose gradient vesicle floatation assay. Vesicles in the 8/35% sucrose fraction were lysed in a buffer containing 150 mM NaCl, 50 mM Tris-HCl (pH 7.5), 0.5% Triton X-100, and 0.5% sodium deoxycholate, supplemented with protease inhibitors (1 mg/mL pepstatin + leupeptin, 0.5 mM phenylmethylsulfonyl fluoride, 2 mM EDTA). Lysates were centrifuged for 5 minutes at 16,000 g to remove cellular debris, followed by ultracentrifugation at 265,000 g for 40 minutes to pellet detergent-

insoluble protein. 15 µg of both pellet and supernatant fraction were analyzed by immunoblotting using Fab anti-PrP (1:200 clone Hum-D13).

C. SDS-PAGE and immunoblotting

Cell lysates were resuspended in Laemmli buffer and resolved by SDS-PAGE in 8–12% polyacrylamide gels. Proteins were electrotransferred onto PVDF membranes. Membranes were blocked for 30 minutes at RT in TBS containing 0.1% Tween 20 and 5% dry milk and were incubated overnight at 4°C with primary antibodies diluted in TBS-Tween-milk. After six washes in TBS-Tween, the membranes were further incubated for 1 hour at RT with fluorescent conjugate secondary antibodies (Li-Cor) diluted in TBS-Tween-milk. After 6 more washes in TBS-Tween, the membranes were imaged using Li-Cor Odyssey imaging system.

D. Sucrose gradient vesicle flotations

N2a cells grown in 150 × 20 mm dishes were transfected with PrP^{WT}-mCh or PrP^{PG14}-mCh constructs using Lipofectamine 2000. Cells were washed twice with PBS and harvested from each 150 mm dish using 10 mL 1×PBS. Cells were harvested and resuspended in 0.5 mL of a solution comprised of 8% sucrose in distilled water, 3 mM Imidazole, and 1× cOmplete™ Protease Inhibitor (Millipore-Sigma). Resuspended cells were homogenized using a 25-gauge syringe needle attached to a 1 mL syringe, and samples were homogenized by 20 passages. A 100 µL fraction of the resulting homogenate was collected (fraction 1) and the remainder was centrifuged at 3,000 g using a Sorvall RT7 Plus benchtop centrifuge. The supernatant was collected, and the pellet was again resuspended in minimal volume of 8% sucrose solution and centrifuged as above. The two

rounds of supernatant fractions were pooled to constitute the post-nuclear supernatant (PNS) (fraction 2). The PNS in 8% w/v sucrose was mixed with a solution of 70% sucrose in distilled water, 3 mM Imidazole and 1× cOmplete™ Protease Inhibitor to constitute a ~40% sucrose solution containing the PNS.

The PNS was bottom-loaded on a sucrose step gradient consisting of 35%, and 8% sucrose. After centrifugation at 41,500 rpm for 2 hours at 4°C on an Optima LE-90K SW50.1 rotor (Beckman Coulter), fractions were collected, including the 8/35% (8/35) sucrose fraction containing membrane-bound floated vesicles. Protein concentration of fractions were measured using a Pierce™ BCA Protein Assay Kit (ThermoFisher), run on SDS-PAGE, and analyzed by Western blot using Fab anti-PrP (1:200 clone Hum-D13), anti-mCh polyclonal antibody raised in rabbit, 1:1000 (Genetex), or anti-Rab7 monoclonal antibody raised in rabbit (1:1000 clone D95F2 XP®; Cell Signaling Technology).

2.2.7) Calcium imaging and potassium chloride (KCl)-induced depolarization

I performed the following procedure. Hippocampal cultures from WT (C57BL6) or *Kif5c*$^{-/-}$ mice were plated directly on #1.5 glass-bottom dishes (MatTek), at the density of 8-15 neurons per 420 µm^2 field of view. Cultures were loaded with 2 µM Fluo-4 AM (Thermo Fisher) in Neurobasal-A media supplemented with B-27 without phenol red for 30 minutes at 37°C, as recommended by Invitrogen protocol. Cultures were washed 3 times and incubated for another 30 minutes in the B-27 supplemented Neurobasal-A without phenol red prior to imaging to allow complete de-esterification of intracellular AM esters. Prior and during imaging, calcium imaging buffer (140 mM NaCl, 5 mM KCl, 2 mM $CaCl_2$, 0.8 mM $MgCl_2$, 10 mM glucose, 10 mM HEPES, pH 7.4) was applied. Neurons were imaged using a Nikon S Plan Fluor ELWD 20X/0.45 [infinity]/0-2 Objective in a

temperature-controlled enclosure set to 37°C. Epifluorescence excitation was provided by a metal-halide-doped mercury arc lamp (Nikon Intensilight). High temporal-resolution images (5 frames/second) were taken for 1 minute with EM-CCD camera (Andor iXon3 897). Fluo-4 AM fluorescence were collected using Chroma filters (ET-GFP [ET470/40x T495lpxr, ET525/50m]. Depolarization was induced by applying KCl to a final concentration of 30 mM at the 30-second time point during acquisition. Still images of PrP^{WT}-mCh or PrP^{PG14}-mCh of the same region were collected using ET-DsRed [ET545/30x, T570lp, ET620/60m] Chroma filter.

2.2.8) Cell death assay and imaging

I performed the following procedure. ReadyProbes® Cell Viability Imaging Kit (Blue/Green) (Thermo Fisher) was used to quantify cell death. Briefly, two drops of NucBlue® Live reagent (Hoechst 33342) and two drops of NucGreen® Dead reagent were added onto 10-14 DIV hippocampal neurons grown on the coverslips containing 1 mL of Neurobasal-A medium (NBA) (Gibco), supplemented with 2% B-27 (Gibco) and 0.25% GlutaMAX (Gibco). Neurons were incubated at 37°C for 30 minutes prior to fixation with 4% PFA (Electron Microscopy Services) containing 4% sucrose (Sigma) for 30 min at 37°C. Cells were washed once in 50 mM Glycine in PBS and 3 more times in PBS before mounted in ProLong Diamond antifade reagent (Thermo Fisher). Fixed neurons were imaged using a Nikon S Plan Fluor ELWD 20X/0.45 [infinity]/0-2 Objective. Epifluorescence excitation was provided by a metal-halide-doped mercury arc lamp (Nikon Intensilight). Blue and Green nuclei staining were collected using UV-2E/C [AT350/50x, T400lp, ET460/50m] and ET-GFP [ET470/40x, T495lpxr,

ET525/50m] Chroma filters respectively. PrP^{WT}-mCh or PrP^{PG14}-mCh fluorescence were collected using ET-DsRed [ET545/30x, T570lp, ET620/60m] Chroma filter.

2.2.9 Quantitation and data analysis

A. Neuronal soma image analysis

I processed all images of neuronal soma in Fiji/ImageJ (National Institutes of Health). Rolling-ball background fluorescence correction was applied to all images. 3D Deconvolution was applied using synthetic Gaussian point spread function (PSF) and Richardson-Lucy (RL) algorithms in DeconvolutionLab2 (Sage et al., 2017). All images and line scan fluorescence intensity graphs were displayed as maximum intensity projection.

B. Analysis of axonal transport dynamics from time-lapse movies

Axonal transport analysis was performed using the custom-made and previously validated *KymoAnalyzer* ImageJ package of macros (Neumann et al., 2017). *KymoAnalyzer* is freely available for download from http://www.encalada.scripps.edu/kymoanalyzer, and a detailed description of the software as well as of the definition of all parameters calculated, are available in the website and in the publication (Neumann et al., 2017). Briefly, kymographs were generated from time-lapse movies. Particle trajectories were manually assigned from the kymograph images. Track and segment-related parameters were automatically calculated by *KymoAnalyzer*.

C. Colocalization and cotransport quantifications

Colocalization was roughly determined by merging line scan intensity profiles of different channels in the same graph and quantifying the average number of

peaks that overlapped between different channels. For cotransport analyses, individual and merged color kymographs were generated and quantification of the average number of tracks that overlapped between each pair of vesicular cargoes was analyzed. Vesicle tracks were sorted in anterograde, retrograde and stationary populations, or as indicated for individually analyzed parameters. Endoggresome tracks were sorted in mobile and stationary populations, or as indicated for individually analyzed parameters.

D. Definition of PrP^{PG14} vesicles versus aggregates/endoggresomes

The definition of PrP^{PG14} endoggresomes/aggregates was based on (1) their biochemical profile, a definition that we used in biochemical assays, or by (2) their fluorescence intensity profile in imaging assays, when PrP^{PG14} was tagged with a fluorescence protein (PrP^{PG14}-mCh or -EGFP), or untagged, as recognized with antibodies against PrP, a definition that we used for axonal transport and axonal density analyses. First, biochemically, PrP^{PG14} endoggresomes were defined as previously (Chiesa et al., 2003; Ivanova et al., 2001; Medrano et al., 2008), as PrP^{PG14} protein that is recognized on an SDS-PAGE gel compared to PrP^{WT} by their (1) detergent insolubility and (2) limited proteinase K (PK) digestion at PK concentrations below 1-2 μg/mL compared to PrP^{WT} (Biasini et al., 2008; Chiesa et al., 2003, 2000, 1998; Ivanova et al., 2001; Nazor et al., 2005). Second, in fluorescence imaging assays for axonal transport analyses, fluorescently tagged (mCh or EGFP) PrP^{PG14} endoggresomes/aggregates were recognized as those PrP^{PG14} particles whose transport was slow (< 0.5 μm/second), in movies taken at 1 Hz for 5 minutes. At this temporal resolution, PrP^{PG14}-mCh or -EGFP vesicles were too faint and moved too fast (0.5-3.0 μm/second) to be tracked

accurately. Instead, PrP^{PG14}-mCh or -EGFP-tagged vesicles were identified as those PrP^{PG14} particles actively moving at speeds that resembled those of PrP^{WT}-mCh or -EGFP vesicles (between 0.5-3.0 μm/second), when imaged at 10 Hz (imaged for 15 seconds). To quantify densities of PrP^{PG14} endoggresomes/ aggregates in fixed axons, still images were taken of axons or neurons transfected with fluorescently labeled PrP^{PG14} constructs (mCh or EGFP) or transfected with untagged PrP^{PG14} and stained by antibodies against PrP. Quantification of the maximal gray intensities of five small PrP^{PG14} vesicle puncta was done for each image analyzed, after subtracting the fluorescence background using the Brightness and Contrast tool of ImageJ. PrP^{PG14} endoggresome/aggregates were defined as particles that displayed maximal gray fluorescence intensities at least 5 times above that of the average maximal gray fluorescence intensities of five PrP^{PG14} vesicles in the same axon (Chaiamarit et al., 2023). The particles still present in the image after thresholding were considered as endoggresomes. Axon length was measured using the polyline tool of ImageJ. Endoggresome density was expressed as the average number of aggregates per 100 μm of axon length.

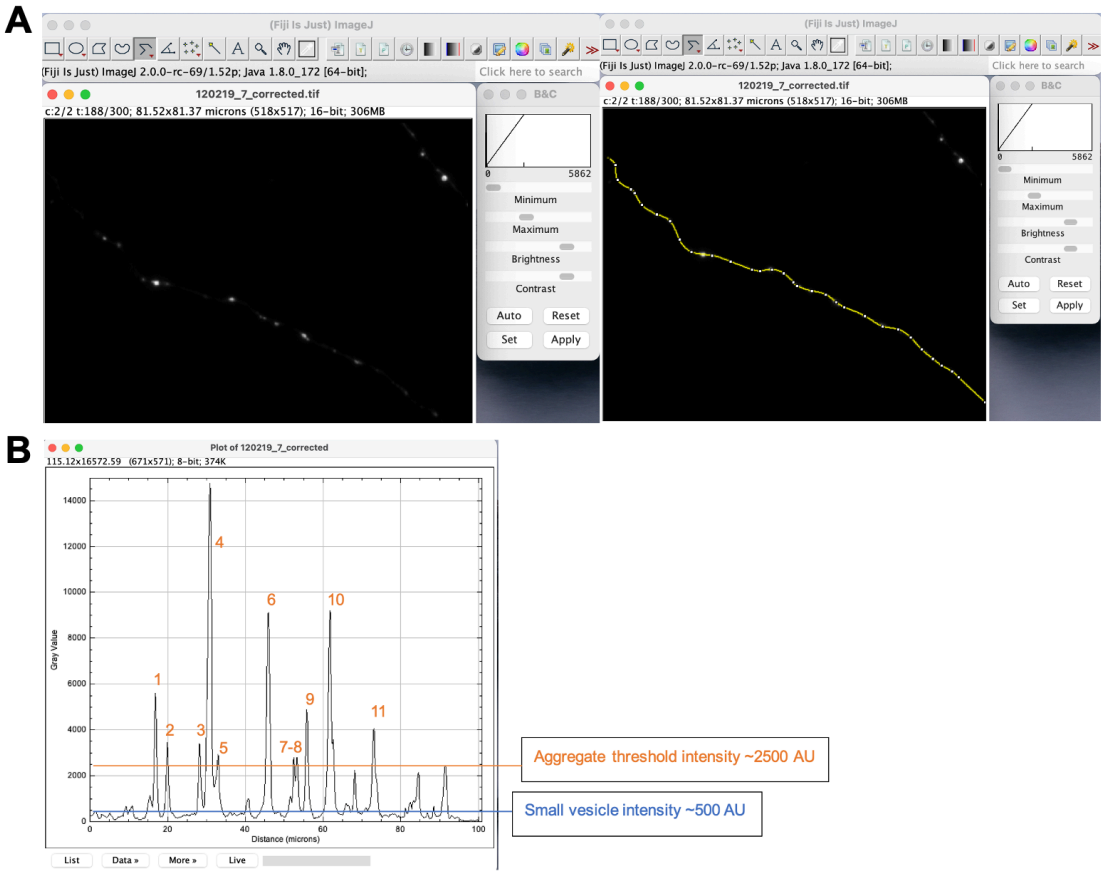


Figure 2.7 Analysis and definition of PrP^{PG14} vesicles and endoggresomes. (A) An axon image (left) and overlay of a linescan (right) drawn using segmented line tool, (B) the plot profile of fluorescence intensity/gray value in arbitrary unit (AU). (From Chaiamarit et al., 2023)

E. Calculation of densities of Lysotracker-positive particles

For Lysotracker-positive vesicle densities, I measured the axon length using the polyline tool of ImageJ and quantified all the particles labelled by Lysotracker-Green along this line. Densities were plotted per 100 µm of axon length.

F. ERSE-mCh and Vps41 fluorescence quantification

Neurons were co-transfected with the pEGFP-C1, MoPrP.Xho PrP^{WT}-EGFP or MoPrP.Xho PrP^{PG14}-EGFP and the transcriptional ER stress reporter ERSE-mCh (a gift from Lars Plate, Vanderbilt University) (Plate et al., 2016).

Increases in the activity of ER stress pathways activate ERSE and soluble mCh is synthesized. Total fluorescence intensities (gray values, arbitrary unit, a.u.) of ERSE-mCh and Vps41 were quantified using ImageJ, using circular ROIs of 30 µm in diameter centered around the soma. The polyline tool was used to draw ROIs spanning the entire axonal length.

G. Calcium imaging analysis

Regions of interest (ROIs) were marked around soma of neurons expressing PrP^{WT}-mCh or PrP^{PG14}-mCh, and we measured average fluorescence for each ROI at a given timepoint. The average Fluo-4 AM fluorescence overtime was collected using an ImageJ Plugin Time Series Analyzer V3 and normalized to $\Delta F/F$ by subtracting fluorescence intensity of each time point (F) to an average fluorescence prior to addition of KCl (F_0) and divided by F. Rolling-ball background fluorescence correction was applied to all images prior to fluorescence intensity analysis.

H. Cell death quantitation

All image processing was done in ImageJ. The total number of NucBlue Live positive nuclei (blue channel) were determined as follows: background fluorescence was corrected on each image, by applying a Gaussian blur filter with a radius of 12 to a duplicate of each image and subtracting this filtered image from the original. An automatic threshold was applied to the resulting images using the Li algorithm followed by a watershed filter, both in ImageJ. Total nuclei were counted using a minimum size threshold of 15 and circularity of 0.10. The total amount of NucGreen Dead positive nuclei (green channel) were determined using the same method, now using a Gaussian blur filter with a

radius of 10, thresholding using the Yen algorithm available in ImageJ, and nuclei determination using a minimum size threshold of 15 and circularity of 0.10.

I. Generation of graphs and figures

Graphs of average values were generated using Microsoft Excel. Cumulative frequency graphs were generated using the CDF function in MATLAB (Mathworks). Box plots were generated using BoxPlotR from RStudio. Figures were originally drawn in Adobe Illustrator and rearranged in Microsoft PowerPoint for this thesis.

J. Statistical analyses

All the transport parameters measured in this study were first tested for normality using the MATLAB Lilliefors test. For parameters following a normal distribution, we performed a Student's t-test. For non-normal parameters, we performed a permutation t-test (rndttest function in MATLAB). For all parameters, differences in medians were also checked using the Wilcoxon rank-sum test (rnk function in MATLAB). The non-parametric Kolmogorov-Smirnov test was used to evaluate the equality of two sample distributions (in cumulative distribution functions). Most of the parameters are presented as mean ± SEM. Multiple comparison corrections were used where appropriate. Details about each parameter, including definition of center, value and definition of n, statistical test used and p values, can be found in specific figures and/or in figure legends.

2.3 Results

2.3.1 PrP^{PG14} is transported in vesicles by kinesin-1 to form aggregates in axons

Transfection of PrP^{WT}-mCh or PrP^{PG14}-mCh in cultured hippocampal neurons followed by fluorescence live imaging in axons showed that PrP^{PG14}-mCh forms large inclusions that accumulate from day one to day five post-transfection, while PrP^{WT}-mCh remains as small vesicles in axons (**Figure 2.8A**). These observations are consistent with a previous report of a PrP^{PG14}-EGFP transgenic mouse model that produces intra-axonal aggregates in multiple brain regions (Medrano et al., 2008). Correlation of PrP^{PG14}-mCh and intact SEM of transfected axons revealed that axons become swollen at the inclusion sites (**Figure 2.8B**). To test whether PrP^{PG14} inclusions are misfolded aggregates, PrP^{PG14}-EGFP was transfected and imaged in differentiated N2a cells where PrP^{PG14}-EGFP forms inclusions in the cell extensions (**Figure 2.8E**). Western Blot showed that PrP^{PG14} from N2a cells exhibited partial PK resistance (**Figure 2.8F**), in agreement with a previous report (Chiesa et al., 2000) and confirming that PrP^{PG14} is partly and constitutively misfolded upon transient expression. Thus, from this point forward, the word aggregates and inclusions of PrP^{PG14} are used interchangeably. Next, to investigate whether other familial prion disease mutant PrP forms inclusions in our model, a point mutation D178N/M129 in humans (D177N/M128 in mouse) that causes prion fatal familial insomnia (FFI) (Medori et al., 1992) was transfected and the density of inclusions was analyzed at 2 days post-transfection. PrP^{D177N}-mCh forms axonal inclusions with the density similar to PrP^{PG14} (**Figure 2.8D**). In summary, misfolded aggregates of mutant PrP progressively accumulate in axons where dystrophic swellings are formed.

In addition to large PrP^{PG14}-mCh inclusions, high-resolution live imaging revealed small PrP^{PG14}-mCh vesicles that move bidirectionally 20-50 times faster (1-4 µm/second) than PrP^{PG14}-mCh inclusions which remain mostly stationary (0.05-0.1 µm/second) (**Figure 2.8G**). Both PrP^{WT}-mCh and PrP^{PG14}-mCh vesicles in axons showed an anterograde transport bias towards the axon termini (**Figure 2.8G-I)**. We hypothesized that kinesin-1C (KIF5C), an anterograde motor that was previously identified to carry PrP^{C} vesicles in axons (Encalada et al., 2011), was loaded on PrP^{PG14} vesicles and contributed to the appearance of PrP^{PG14} inclusions. Cultured hippocampal neurons from *Kif5c*$^{-/-}$ mice showed a significant impairment of anterograde movement of PrP^{PG14}-mCh vesicles, such as reduced flux of anterograde-moving vesicles, reduced time in anterograde motion, increased time paused, and increased number of stalled vesicles (**Figure 2.8H-I**). These observations indicate that misfolded PrP^{PG14} is actively transported in vesicles by kinesin-1 in axons.

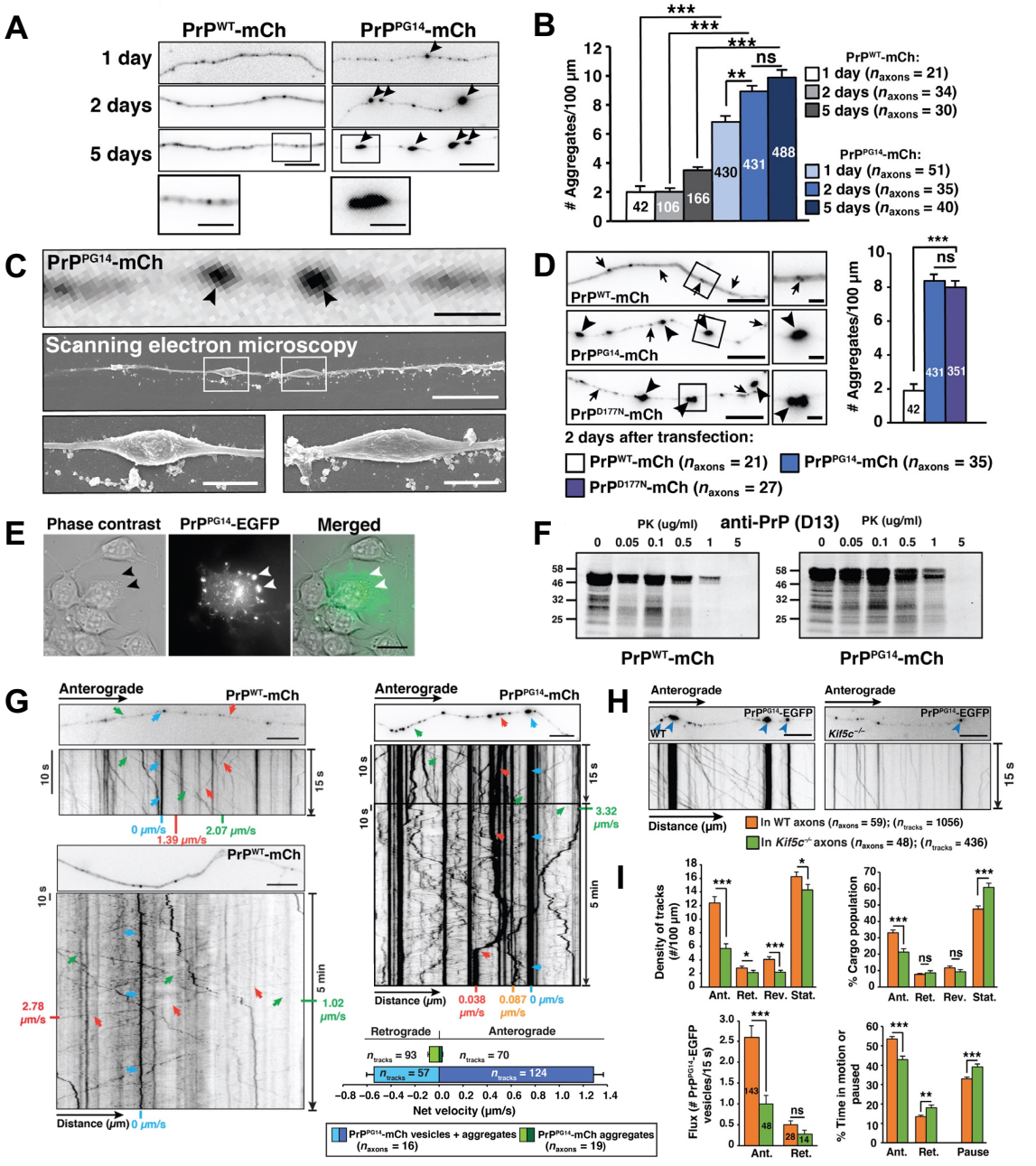


Figure 2.8 Characterization of PrP^{PG14} vesicle and aggregates in axons (**A**) Representative images of axons expressing PrP^{WT}-mCh and PrP^{PG14}-mCh (left). Arrowheads point to aggregates. Scale bars = 10 µm. Insets show enlargements. Scale bars = 5 µm. (**B**) Quantitation of aggregate densities. Bars represent means ± SEM. Numbers of aggregates shown inside bars. **p<0.01, ***p<0.001, ns = not significant, Student's t-test, Šidák correction. (**C**) Correlative fluorescence and SEM images of aggregate swellings 2 days post-transfection of PrP^{PG14}-mCh. Arrowheads point to aggregates. Scale bars = 10 µm. Insets show enlargements. Scale bars = 2 µm. (**D**) Representative images of axons expressing PrP^{WT}-mCh, PrP^{PG14}-mCh, or PrP^{D177N}-mCh 2 days post-transfection (left). Arrows point to vesicles. Arrowheads point to aggregates. Scale bars = 10 µm. Insets show enlargements. Scale bars = 2 µm. Quantitation of aggregate densities (right)

Bars represent means ± SEM. Numbers of aggregates shown inside bars. ***p<0.001, ns = not significant, Student's t-test, Šidák correction. **(E)** Phase contrast and fluorescence images of a differentiated N2a cell expressing PrP^{PG14}-EGFP. Scale bar = 20 µm. **(F)** Representative Western Blots showing partial proteinase K resistance of PrP^{PG14}-EGFP aggregates from cell lysates, performed in 3 biological replicates. Bars represent means ± SEM. **(G)** First frame (top panels of each set) and kymographs from time-lapse movies of axons expressing PrP^{WT}-mCh or PrP^{PG14}-mCh at two time-scales (15 sec, 10Hz and 5 min, 1Hz). Arrows point to vesicles moving in the anterograde (green), or retrograde (red) directions, or those are stationary (blue). The graphs showed average net velocities of different PrP^{PG14}-mCh vesicles and aggregates population. (**H**) Representative first frames and kymographs of PrP^{PG14}-EGFP vesicle and aggregate transport in WT and *Kif5c*$^{-/-}$ hippocampal axons. Scale bars = 10 mm. (**I**) Densities of PrP^{PG14}-EGFP vesicles in WT and *Kif5c*$^{-/-}$ axons; PrP^{PG14}-EGFP vesicles population breakdown in WT and *Kif5c*$^{-/-}$ axons; PrP^{PG14}-EGFP vesicle flux in WT and *Kif5c*$^{-/-}$ axons. Numbers of vesicles are shown inside bars; Percent time PrP^{PG14}-EGFP vesicles spent in motion or paused in WT and *Kif5c*$^{-/-}$ axons. Bars represent means ± SEM. *p<0.05, **p < 0.01, ***p<0.001, ns = not significant, Student's t-test, Ant. = anterograde, Ret. = retrograde, Rev. = reversals, Stat. = stationary. These data were collected by Romain Chassefeyre.

2.3.2 PrP^{PG14} aggregates are Golgi-derived and sorted through endosomal pathway

To investigate the origin and identity of PrP^{PG14} inclusions in axons, PrP^{PG14}-mCh was co-transfected and imaged live with various EGFP-labelled organelle markers. First, PrP^{PG14}-mCh co-transported with the signal sequence of Neuropeptide Y (SS-EGFP) in axons, a marker for Golgi-derived vesicles (**Figure 2.9B**). Photoactivation of PrP^{PG14}-PAmCh in the soma showed the rapid transition of PrP^{PG14}-PAmCh vesicles from soma into axons and showed large PrP^{PG14}-PAmCh aggregates that colocalized with a late endosome (LE) marker EGFP-Rab7 in axons after 1 hour (**Figure 2.9A**). These observations suggest a direct soma-to-axon entry of PrP^{PG14} vesicles following secretory pathway from Golgi in the cell body into axons that end up in the endosomal pathway. At 2 days post-transfection, PrP^{PG14}-mCh vesicles and large aggregates colocalized and co-transported with EGFP-tagged Rab5, Rab7, Rab11, and LAMP1—markers for

early endosomes (EE), recycling endosomes (RE), late endosomes (LE), and endo-lysosomes respectively (**Figure 2.9B-C**). To confirm that these observations are not due to organelle marker overexpression, antibody staining of endosomal markers and PrP^{PG14}-mCh in axons showed similar colocalization patterns (**Figure 2.9D**), suggesting that PrP^{PG14} vesicles/aggregates are sorted through endosomal pathway. To further confirm whether misfolded PrP^{PG14} aggregates resided inside endosomes, PrP^{PG14} was co-fractionated biochemically with Rab7 from detergent-free sucrose floated membrane fractions (**Figure 2.9E**). PrP was detected in floated vesicle fractions of N2a cells transfected with either PrP^{WT}-mCh or PrP^{PG14}-mCh, and the floated vesicle fractions were also positive for Rab7, confirming the biochemical isolation of LEs (**Figure 2.9E-F**). Furthermore, the floated vesicle fractions were partially resistant to PK digestion and more detergent insoluble compared to PrP^{WT}-mCh (**Figure 2.9G-H**), indicating that endosomal PrP^{PG14} are misfolded aggregates.

To visualize the ultrastructure of PrP^{PG14} aggregates in axons, we performed a series of cross sections along axons in aggregate versus non-aggregate regions and subjected axonal ultra-thin sections to SEM (**Figure 2.6**). Cross-sections were mapped back to PrP^{PG14}-mCh fluorescence where large electron-dense structures were found resided within endosomes (**Figure 2.9I**). We named this structure 'endoggresomes'. The presence of endoggresomes suggest mechanisms that either promote mutant PrP aggregate formation in axons or impair their clearance.

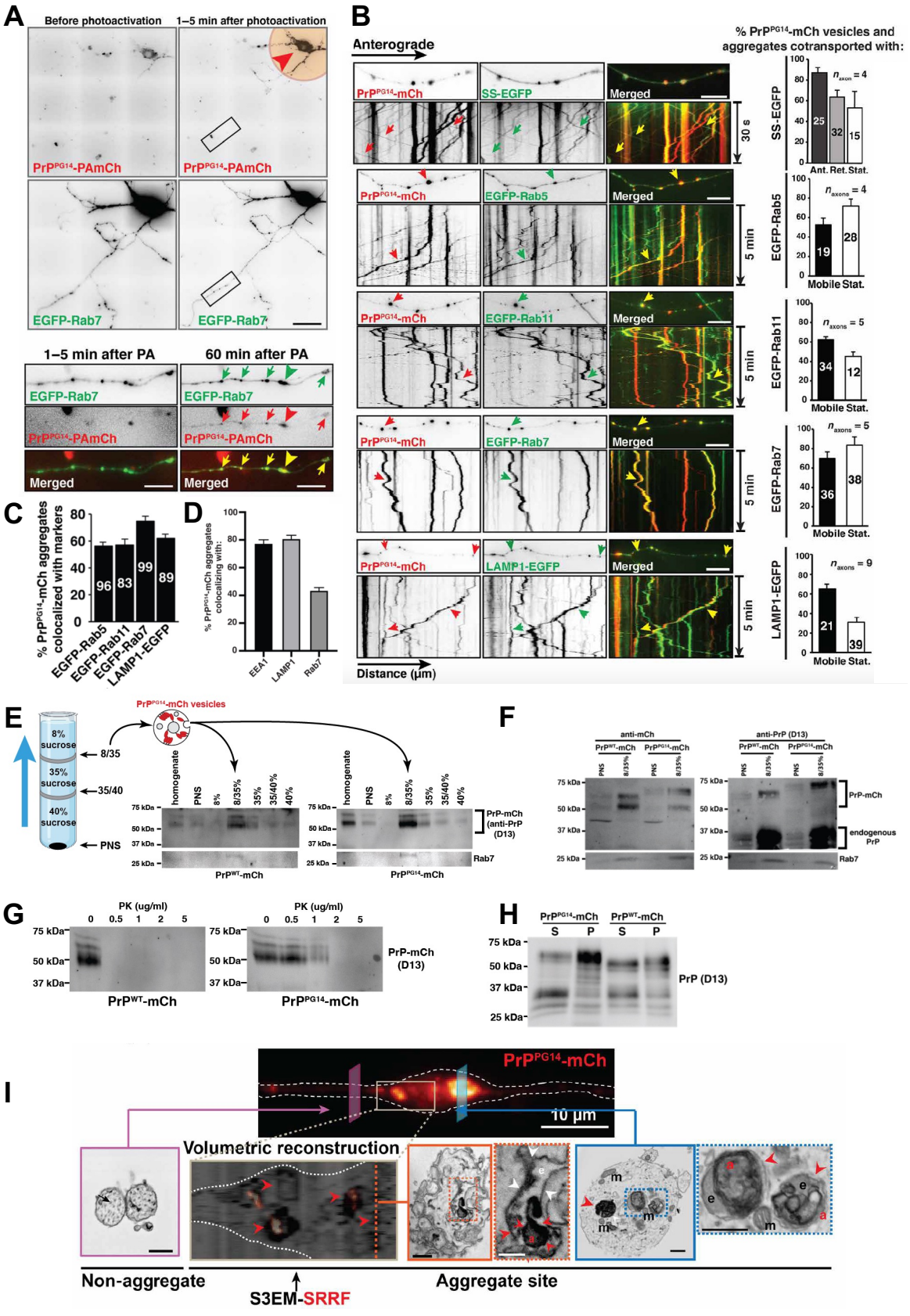

A
Before photoactivation
1–5 min after photoactivation
PrP^PG14-PAmCh
EGFP-Rab7
1–5 min after PA
60 min after PA
Merged
B
Anterograde
% PrP^PG14-mCh vesicles and aggregates cotransported with:
PrP^PG14-mCh
SS-EGFP
EGFP-Rab5
EGFP-Rab11
EGFP-Rab7
LAMP1-EGFP
Merged
30 s
5 min
Distance (µm)
Ant. Ret. Stat.
Mobile Stat.
C
% PrP^PG14-mCh aggregates colocalized with markers
96
83
99
89
EGFP-Rab5
EGFP-Rab11
EGFP-Rab7
LAMP1-EGFP
D
% PrP^PG14-mCh aggregates colocalizing with
EEA1
LAMP1
Rab7
E
PrP^PG14-mCh vesicles
8% sucrose
35% sucrose
40% sucrose
8/35
35/40
PNS
homogenate
8%
8/35%
35%
35/40%
40%
PrP-mCh (anti-PrP (D13))
Rab7
PrP^WT-mCh
PrP^PG14-mCh
F
anti-mCh
anti-PrP (D13)
PrP-mCh
endogenous PrP
G
PK (ug/ml)
0 0.5 1 2 5
PrP-mCh (D13)
H
S P S P
PrP (D13)
I
PrP^PG14-mCh
10 µm
Volumetric reconstruction
Non-aggregate
S3EM-SRRF
Aggregate site

Figure 2.9 The identity and ultrastructure of PrP^{PG14} endoggresomes. **(A)** Representative images of a hippocampal neuron co-transfected with PrP^{PG14}-PAmCh and EGFP-Rab7 before and after photoactivation (pink circle, arrowhead) of the cell body with a 405 nm laser (middle panels; scale bar = 50 µm). Enlargements of inset to bottom panels, scale bar = 10 µm. Arrows indicate colocalization. Arrowheads points to endoggresomes. Number of neurons = 3. **(B)** First-frame images and kymographs of representative time-lapse movies of axons co-expressing PrP^{PG14}-mCh and various compartment markers (left): SS-EGFP (SS = Signal Sequence of NPY, Golgi-derived), EGFP-Rab5 (EE), EGFP-Rab11 (RE), EGFP-Rab7 (LE), or LAMP1-EGFP (endolysosomes). Arrows point to cotransport events. Quantitation of cotransport (right). Bars represent means ± SEM. Vesicle or aggregate numbers are shown inside bars. Ant. = anterograde, Ret. = retrograde, Stat. = stationary. Scale bars = 10 µm. **(C)** Quantitation of percent of PrP^{PG14}-mCh aggregates that colocalize with EGFP-Rab5, EGFP-Rab11, EGFP-Rab7, or LAMP1-EGFP. Numbers of aggregates are shown inside bars. Bars represent means ± SEM. **(D)** Quantitation of percent of PrP^{PG14}-mCh aggregates that colocalize with antibodies against EEA1, LAMP1, and Rab7. Bars represent means ± SEM. **(E)** Schematic diagram of a membrane floatation experiment (left) showing the 8/35 fraction ran on the WB (right) and in (F) and used as starting material for the PK and detergent insolubility assays in (G) and (H) respectively. Representative WB probed with an antibody against PrP(D13) show PrP^{PG14}-mCh signal and endogenous PrP, and against Rab7. The experiments were performed in 3 biological replicates. **(F)** Representative WB showing PNS and 8/35 fractions from floatations of N2a cells transfected with PrP^{WT}- or PrP^{PG14}-mCh and probed with indicated antibodies, performed in 6 biological replicates. **(G)** Representative WB of PK-treated 8/35 membrane fractions of PrP^{WT}- or PrP^{PG14}-mCh from N2a cells, performed in 3 biological replicates. **(H)** Representative WB of 8/35 membrane detergent soluble (S) versus insoluble (P) fractions of PrP^{WT}- or PrP^{PG14}-mCh from N2a cells, performed in 2 biological replicates. **(I)** Correlative fluorescence (top) and S3EM representative cross sections (bottom). Volumetric 3D reconstruction through axonal PrP^{PG14}-mCh aggregate site is shown with SRRF fluorescence overlay. Red arrowheads point to PrP^{PG14}-mCh-positive aggregates. White arrowheads point to endosomes. m = mitochondria. Scale bar of top panel of correlative image = 10 µm. All other scale bars = 500 nm. Data from (A)-(D) were collected by Romain Chassefeyre. Data from (E)-(H) were collected by Adriaan Verhelle and Andre Leitao. Data from (I) were collected by me and Sammy Weiser Novak.

2.3.3 Transient access of PrP^{PG14} to the axonal cell surface contributes to endoggresome formation

PrP^{C} is a secreted protein that transits to the neuronal cell surface (Hegde and Rane, 2003). To determine whether PrP^{PG14} expressed in cultured neurons accessed the plasma membrane along the axon *en route* to aggregation, neurons were transfected with PrP^{PG14}- or PrP^{WT}-mCh fusion constructs containing a Bungarotoxin Binding Sequence (BBS) and treated in the media with AlexaFluor 647-labeled bungarotoxin (BTX)/BTX-AF647/BTX-a647 (Sekine-Aizawa and Huganir, 2004). BTX-AF647 labeling was specific as AF647 signal was not observed in neurons expressing PrP^{WT}-mCh or PrP^{PG14}-mCh without the BBS sequence (**Figure 2.10A**). Addition of the BBS sequence did not alter endoggresome densities in axons (**Figure 2.10B**).

First, to take a snapshot of PrP trafficking at the axonal cell surface, neurons were treated with BTX-AF647 for 10 minutes at 4°C to inhibit active endocytosis and then fixed without permeabilization prior to imaging (**Figure 2.10C**). BTX-AF647 signal colocalized with a subset of PrP^{PG14}-mCh-BBS-positive puncta along axons (**Figure 2.10C**), suggesting that rapid endocytosis of PrP^{PG14}-mCh-BBS occurred throughout axons. To determine if PrP^{PG14} was sorted into endo-lysosomes following internalization, neurons co-expressing PrP^{PG14}-mCh-BBS and LAMP1-EGFP were treated with BTX-AF647 for 2 hours at 37°C prior to imaging (**Figure 2.10D**). We observed extensive cotransport between PrP^{PG14}-mCh-BBS, LAMP1-EGFP, and BTX-AF647 in axons (**Figure 2.10D**), indicating PrP^{PG14}-mCh-BBS sorted into LEs post-endocytosis. Inhibition of endocytosis with Dynasore, a dynamin GTPase

inhibitor (Macia et al., 2006) resulted in a significant, albeit partial decrease in internalization of BTX-AF647-labeled PrP^{PG14}-mCh particles (**Figure 2.10H**), suggesting that PrP^{PG14}-mCh is internalized partly by clathrin-dependent pathway.

To determine whether targeting of PrP^{PG14}-mCh to the cell surface was required to form endoggresomes, neurons were transfected with PrP^{PG14}-mCh tagged with a Thrombin Cleavage Sequence (PrP^{PG14}-mCh-TCS) and treated with 5 units/mL of thrombin protease in the media for 48 hours. Thrombin treatment resulted in significantly reduced densities of PrP^{PG14}-mCh-TCS endoggresomes compared to untagged PrP^{PG14}-mCh (**Figure 2.10E-F**), indicating that PrP^{PG14} access to the plasma membrane contributes substantially to the formation of PrP^{PG14} endoggresomes in axons. We further tested this cell surface requirement by transfecting an anchorless PrP^{PG14} mutant ($PrP^{PG14/S232X}$-EGFP) that is unable to associate with membranes (Satpute-Krishnan et al., 2014). While $PrP^{PG14/S232X}$-EGFP-containing vesicles were still actively transported inside axons, the density of $PrP^{PG14/S232X}$-EGFP inclusions was significantly reduced compared to those of GPI-anchored PrP^{PG14}-EGFP (**Figure 2.10G**), suggesting that anchorless PrP^{PG14} is released upon secretion and thus bypass aggregation. These data altogether show export of PrP^{PG14} to the cell surface and subsequent rapid endocytosis along the length of axons contributes to the sorting of Golgi-derived PrP^{PG14} into endosomes to form endoggresomes in LEs.

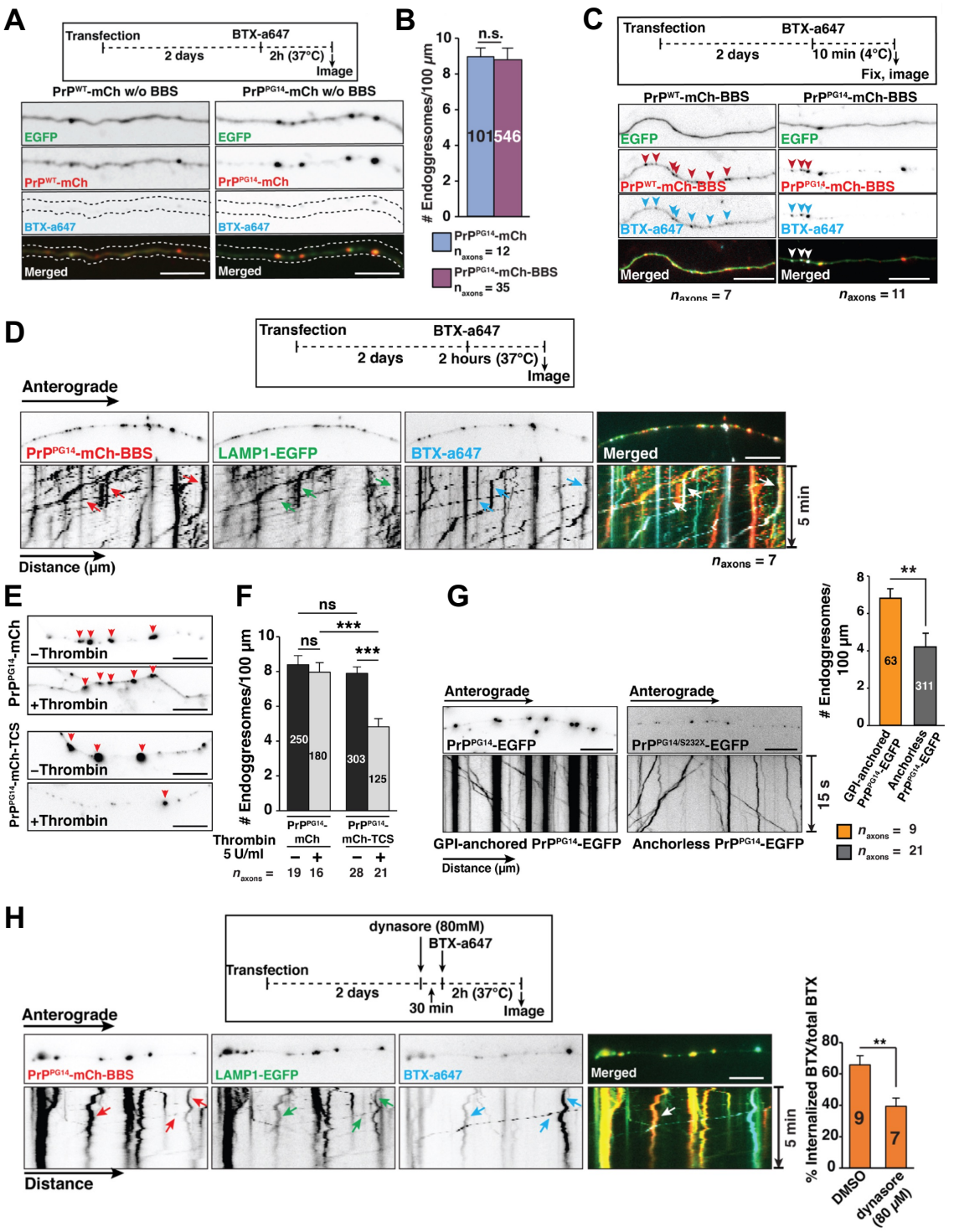


Figure 2.10 Endoggresome formation requires the rapid transit of PrP^{PG14} to axonal cell surface. **(A)** Timeline (top) and representative images of neurons expressing PrP^{WT}- or PrP^{PG14}-mCh without BBS sequence, after BTX-AF647 treatment (bottom). Scale bars = 10 µm. **(B)**

Quantitation of endoggresome densities from PrP^{PG14}-mCh and PrP^{PG14}-mCh-BBS axons. Endoggresome numbers are shown inside bars. Bars represent means ± SEM; n.s. = not significant. **(C)** Timeline of 10-min labeling assay (top) and representative images of axons expressing EGFP, PrP^{WT}-mCh-BBS or PrP^{PG14}-mCh-BBS, and labeled with BTX-AF647 (bottom). Arrowheads point to colocalization. Scale bars = 10 µm. **(D)** Timeline of 2-hr labeling assay (top) and presentative first frames of time-lapse movies and kymographs of axons expressing PrP^{PG14}-mCh-BBS and LAMP1-EGFP, labeled with BTX-AF647. Arrows point to cotransport. Scale bars = 10 µm. **(E)** Representative images of axons expressing PrP^{PG14}-mCh or PrP^{PG14}-mCh-TCS, with or without thrombin treatment. Scale bars = 10 µm. **(F)** Quantitation of endoggresome densities from (E). Number of endoggresomes are shown inside the bars. Bars represent means ± SEM; ***$p<0.001$, n.s. = not significant; Student's t-test, Tukey's correction. **(G)** Representative images and kymographs of axons expressing PrP^{PG14}-EGFP or $PrP^{PG14/S232X}$-EGFP (left). Scale bars = 10 µm. Quantitation of endoggresome densities (right). Number of endoggresomes are shown inside the bars. Bars show means ± SEM; **$p<0.01$; Student's t-test. Data in this figure were collected by Romain Chaasefeyre.

2.3.4 An ARL8b/kinesin-1/HOPS pathway drives PrP^{PG14} endoggresome formation in axons

Endosomal fusion via a small GTPase ARL8b is hypothesized to contribute to endoggresome formation. To test whether functional ARL8b is involved in PrP^{PG14} endosomal trafficking and aggregation, live imaging showed PrP^{PG14}-mCh vesicles co-transported with $ARL8b^{WT}$-GFP or with active GTP-bound $ARL8b^{Q75L}$-GFP, and LAMP1-mTagBFP2 particles, but not with soluble dominant negative (DN) GDP-bound $ARL8b^{T34N}$-GFP (**Figure 2.11A, C**). Two days after co-transfection, $ARL8b^{WT}$-mCh and PrP^{PG14}-mTagBFP2 vesicle colocalized in the soma (**Figure 2.11B**) and co-transported with SS-NPY-EGFP into the axon (**Figure 2.11D**), suggesting that ARL8b loaded onto Golgi-derived PrP^{PG14} vesicles and entered the axon as a complex. PrP^{PG14} aggregate densities were significantly decreased in axons of neurons treated with ARL8b shRNAs and in those expressing GDP-bound inactive $ARL8b^{T34N}$, while overexpression of untagged $ARL8b^{WT}$ or GTP-active $ARL8b^{Q75L}$ increased endoggresome densities in axons (**Figure 2.11E-F**).

To test the mechanism of ARL8b-mediated endoggresome formation, transport is hypothesized to be mediated by kinesin-1 via SKIP and fusion must have involved HOPS complex. Live imaging showed extensive co-transport between PrP^{PG14} vesicles, ARL8b, SKIP, KIF5C, and Vps41 subunit of HOPS (**Figure 2.11G-I**). To test whether these ARL8b effectors are required in trafficking and aggregation of PrP^{PG14} in axons, the function of Vps41 was reduced using siRNAs, and the function of SKIP was inhibited using a peptide comprising region aa 1-186 (SKIP 1-186) previously shown to bridge interactions between ARL8b and kinesin-1 (Ishida et al., 2015). We observed a significant decrease in aggregate densities following reduction and inhibition of Vps41 and SKIP (**Figure 2.11E, J, K**). Furthermore, reducing Vps41 resulted in smaller and less stationary PrP^{PG14}-mCh vesicles in the soma and axons (**Figure 2.11J-L**), suggesting that decreased PrP^{PG14} vesicle fusion correlates with restored PrP^{PG14} vesicular motility. To test whether ARL8b directly recruits kinesin-1 to PrP^{PG14} vesicles, overexpression of $ARL8b^{WT}$-GFP significantly increased the percentage of PrP^{PG14}-mTagBFP2 vesicles that cotransported with 2xmCh-KIF5C, compared to a control where there is little association between overexpressed GFP-KIF5C and PrP^{PG14}-mCh (**Figure 2.11S**).

Finally, to determine the role of kinesin-1 isoforms in endoggresome formation, we quantitated endoggresome densities in axons of kinesin-1C KO (*Kif5c*$^{-/-}$) mice, in those of kinesin light chain 1 (KLC1) KO (*Klc1*$^{-/-}$) mice, and conditional kinesin-1B KO (*Kif5b*$^{pflox/pflox}$) mice (Cui et al., 2011). Endoggresome densities were significantly decreased 2 days after PrP^{PG14}-mCh transfection, in axons from *Kif5c*$^{-/-}$, *Klc1*$^{-/-}$ and in *Kif5b*$^{pflox/pflox}$ neurons in a cre-adenovirus MOI dose-dependent manner, compared to WT hippocampal axons (**Figure 2.11M-O**).

Decreased endoggresome densities were sustained for at least 10 days in *Kif5c*$^{-/-}$ axons (**Figure 2.11P**). Overexpression of EGFP-KIF5C in *Kif5c*$^{-/-}$ neurons transfected with PrP^{PG14}-mCh restored higher axonal endoggresome densities (**Figure 2.11Q**), demonstrating that decreased densities were due to the specific removal of KIF5C. Endoggresome densities in axons of *Kif5c*$^{-/-}$ neurons expressing PrP$^{D177N(M128)}$-mCh were also significantly lower (**Figure 2.11R**), indicating a generalized requirement of kinesin-1 for generating endoggresomes of PrP mutants. Surprisingly, reducing the function of the main neuronal retrograde motor cytoplasmic dynein heavy chain 1 (DHC1) using previously validated shRNAs (Encalada et al., 2011) impaired PrP^{PG14}-mCh vesicle transport but did not alter PrP^{PG14}-EGFP endoggresome densities (**Figure 2.11M**), indicating that endoggresome formation pathway is selectively kinesin-dependent.

Altogether, these data indicate that GTP-bound active ARL8b loads onto Golgi-derived PrP^{PG14} vesicles, recruits SKIP, kinesin-1 heavy chain and light chain subunits, and Vps41 subunit of HOPS complex, whereby ARL8b acts as a key driver of the anterograde movement and fusion of PrP^{PG14} vesicles in the axon, promoting endoggresome formation. I termed this process **A**xonal **R**apid **E**ndosomal **S**orting and **T**ransport-dependent **A**ggregation (**ARESTA**).

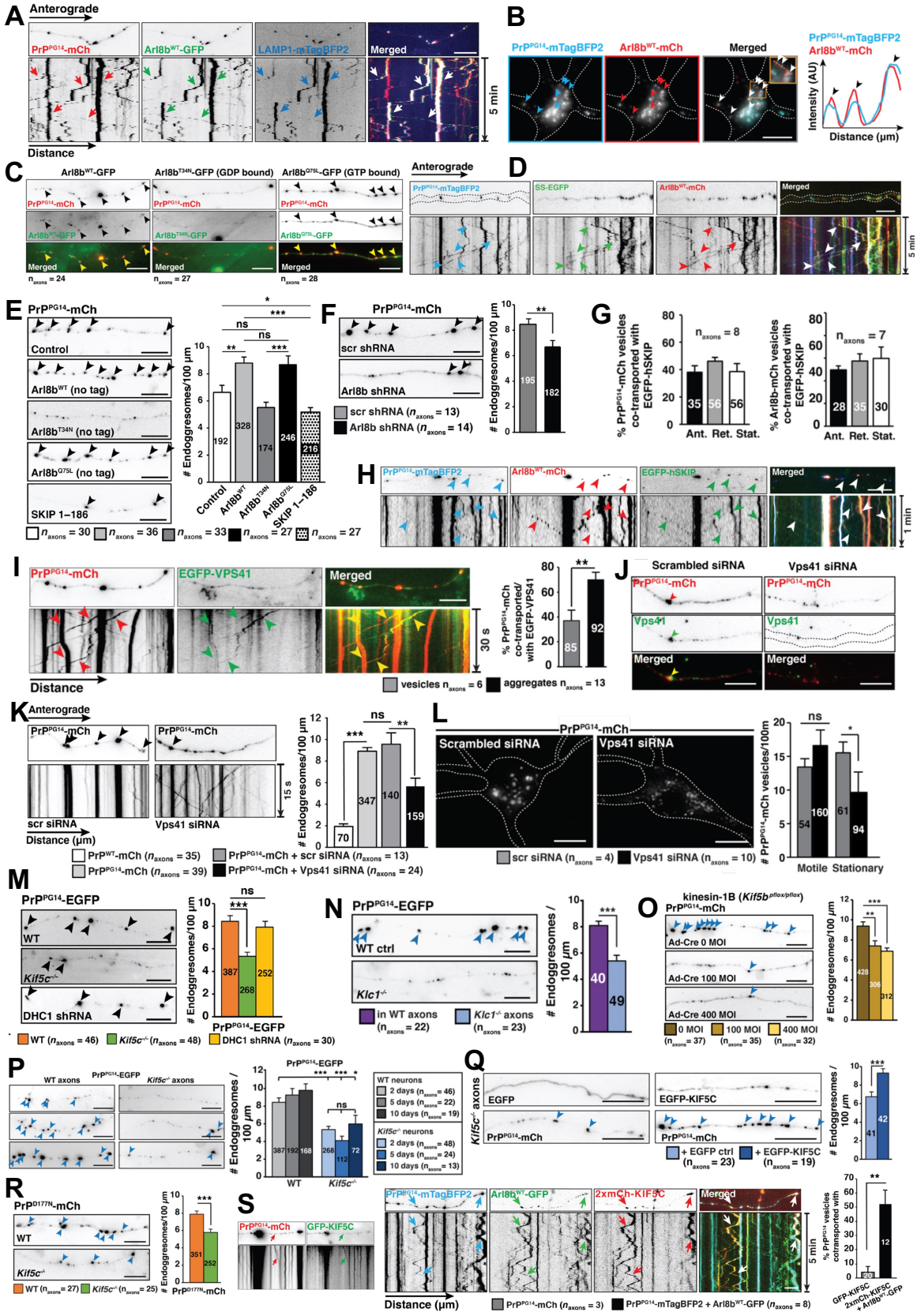

A
Anterograde
PrP^PG14-mCh
Arl8b^WT-GFP
LAMP1-mTagBFP2
Merged
5 min
Distance
B
PrP^PG14-mTagBFP2
Arl8b^WT-mCh
Merged
Intensity (AU)
Distance (μm)
C
Arl8b^WT-GFP
Arl8b^T34N-GFP (GDP bound)
Arl8b^Q75L-GFP (GTP bound)
n_axons = 24
n_axons = 27
n_axons = 28
D
Anterograde
SS-EGFP
E
Control
Arl8b^WT (no tag)
Arl8b^T34N (no tag)
Arl8b^Q75L (no tag)
SKIP 1–186
Endoggresomes/100 μm
F
scr shRNA
Arl8b shRNA
scr shRNA (n_axons = 13)
Arl8b shRNA (n_axons = 14)
G
% PrP^PG14-mCh vesicles co-transported with EGFP-hSKIP
% Arl8b-mCh vesicles co-transported with EGFP-hSKIP
Ant. Ret. Stat.
H
EGFP-hSKIP
1 min
I
EGFP-VPS41
30 s
% PrP^PG14-mCh co-transported with EGFP-VPS41
vesicles n_axons = 6
aggregates n_axons = 13
J
Scrambled siRNA
Vps41 siRNA
Vps41
K
scr siRNA
Vps41 siRNA
15 s
Distance (μm)
PrP^WT-mCh (n_axons = 35)
PrP^PG14-mCh (n_axons = 39)
PrP^PG14-mCh + scr siRNA (n_axons = 13)
PrP^PG14-mCh + Vps41 siRNA (n_axons = 24)
L
scr siRNA (n_axons = 4)
Vps41 siRNA (n_axons = 10)
PrP^PG14-mCh vesicles/100 μm
Motile Stationary
M
PrP^PG14-EGFP
WT
Kif5c^-/-
DHC1 shRNA
WT (n_axons = 46)
Kif5c^-/- (n_axons = 48)
DHC1 shRNA (n_axons = 30)
N
WT ctrl
Klc1^-/-
in WT axons (n_axons = 22)
Klc1^-/- axons (n_axons = 23)
O
kinesin-1B (Kif5b^pflox/pflox)
Ad-Cre 0 MOI
Ad-Cre 100 MOI
Ad-Cre 400 MOI
0 MOI
100 MOI
400 MOI
P
WT axons
Kif5c^-/- axons
WT neurons
2 days (n_axons = 46)
5 days (n_axons = 22)
10 days (n_axons = 19)
Kif5c^-/- neurons
2 days (n_axons = 48)
5 days (n_axons = 24)
10 days (n_axons = 13)
Q
EGFP
EGFP-KIF5C
Kif5c^-/- axons
+ EGFP ctrl (n_axons = 23)
+ EGFP-KIF5C (n_axons = 19)
R
PrP^D177N-mCh
WT (n_axons = 27)
Kif5c^-/- (n_axons = 25)
S
GFP-KIF5C
2xmCh-KIF5C
Distance (μm)
PrP^PG14-mCh (n_axons = 3)
PrP^PG14-mTagBFP2 + Arl8b^WT-GFP (n_axons = 8)
% PrP^PG14 vesicles cotransported with
GFP-KIF5C
2xmCh-KIF5C + Arl8b^WT-GFP

Figure 2.11 The Axonal Rapid Endosomal Sorting and Transport-dependent Aggregation (ARESTA) drives endoggresome formation. (A) First frames of time-lapse movies and kymographs of axons expressing PrP^{PG14}-mCh, $ARL8b^{WT}$-GFP, and LAMP1-mTagBFP2. Arrows indicate cotransport. Scale bars = 10 µm. **(B)** Representative images of hippocampal soma co-expressing PrP^{PG14}-mTagBFP2 and $ARL8b^{WT}$-mCh. Linescan intensity profiles from the soma region indicated by orange dotted line inside the inset. Arrowheads point to colocalization. **(C)** Representative images of neurons co-expressing PrP^{PG14}-mCh and $ARL8b^{WT}$-GFP, $ARL8b^{T34N}$-GFP, or $ARL8b^{Q75L}$-GFP. Arrowheads point to colocalization. Scale bars = 10 µm. **(D)** Representative first frame from time-lapse movies and corresponding kymographs of axons expressing PrP^{PG14}-mTagBFP2, SS-EGFP, and $ARL8b^{WT}$-mCh. Arrowheads point to cotransport. Scale bars = 10 µm. **(E)** Representative images of PrP^{PG14}-mCh axons overexpressing empty vector (Control), $ARL8b^{WT}$, dominant-negative (DN) GDP-bound $ARL8b^{T34N}$, or GTP-bound $ARL8b^{Q75L}$, or a SKIP 1-186 inhibitory peptide. Arrowheads point to endoggresomes. Scale bars = 10 µm. Quantitation of endoggresome densities (right). Numbers of endoggresomes are shown inside bars. Bars represent means ± SEM. *$p<0.05$, **$p < 0.01$, ***$p<0.001$, ns = not significant, Student's t-test, Šidák correction. **(F)** Representative images of axons from neurons expressing PrP^{PG14}-mCh treated with scrambled or ARL8b shRNAs (left). Arrowheads point to endoggresomes. Scale bars = 10 µm. Quantitation of endoggresome densities (right). Numbers of endoggresomes are shown inside bars. Bars represent means ± SEM. **$p < 0.01$, Student's t-test. **(G)** Quantitation of cotransport between PrP^{PG14}-mCh vesicles and EGFP-hSKIP, ARL8b-mCh and EGFP-hSKIP. Bars represent means ± SEM. Numbers of vesicles are shown inside bars. Ant. = anterograde, Ret. = retrograde, Stat. = stationary. **(H)** Representative first frame from time-lapse movies and corresponding kymographs of axons expressing PrP^{PG14}-mTagBFP2, EGFP-hSKIP, and $ARL8b^{WT}$-mCh. Arrowheads point to cotransport. Scale bars = 10 µm. **(I)** Representative first frame from time-lapse movies and corresponding kymographs of axons expressing PrP^{PG14}-mCh and EGFP-VPS41 (left). Arrowheads point to cotransport. Scale bars = 10 µm. Quantitation of % PrP^{PG14}-mCh vesicles or aggregates that cotransport with EGFP-VPS41. Numbers of vesicles/aggregates are shown inside bars. Bars represent means ± SEM. **$p < 0.01$, Student's t-test. **(J)** Representative axons from neurons co-transfected with PrP^{PG14}-mCh and Vps41 siRNA, stained with antibodies against Vps41. Scale bars = 10 µm. **(K)** Representative first frames of time-lapse movies, and kymographs of axons co-expressing PrP^{PG14}-mCh and scrambled or Vps41 siRNAs (left). Arrowheads point to endoggresomes. Scale bar = 10 µm. Quantitation of endoggresome densities (right). Numbers of endoggresomes are shown inside bars. Bars represent means ± SEM. **$p < 0.01$, ***$p<0.001$, ns = not significant, Student's t-test, Šidák correction. **(L)** Representative images of soma of neurons co-transfected with PrP^{PG14}-mCh and shRNA scrambled or Vps41 siRNA (left). Scale bar = 10 µm. Quantitation of motile and stationary axonal PrP^{PG14}-mCh vesicle densities. Numbers of vesicles are shown inside the bars. *$p < 0.01$, ns = not significant, Student's t-test. **(M)** Representative images of PrP^{PG14}-EGFP endoggresomes in WT, *Kif5c*$^{-/-}$, and DHC1 shRNA axons (left). Arrowheads point to endoggresomes. Scale bar = 10 µm. Quantitation of PrP^{PG14}-EGFP endoggresome densities (right). Numbers of endoggresomes are shown inside bars. Bars represent means ± SEM. ***$p<0.001$, ns = not significant, Student's t-test. **(N)** Images of WT and *Klc*$^{-/-}$ axons expressing PrP^{PG14}-EGFP (left). Arrowheads point to endoggresomes. PrP^{PG14}-EGFP endoggresome densities (right). Numbers of endoggresomes are shown inside bars. Bars represent means ± SEM. ***$p<0.001$, Student's t-test. **(O)** Images of *Kif5B* conditional KO axons expressing PrP^{PG14}-mCh and treated with indicated AAV-cre units (left). Arrowheads point to endoggresomes.

PrP^{PG14}mCh endoggresome densities (right). Numbers of endoggresomes are shown inside bars. Bars represent means ± SEM. ***p<0.001, **p<0.01, Student's t-test. **(P)** Images of axons from WT and *Kif5C*$^{-/-}$ neurons expressing PrP^{PG14}-EGFP at various timepoints post-transfection (left). Scale bar = 10 µm. Quantitation of PrP^{PG14}-EGFP endoggresome densities (right). Numbers of endoggresomes are shown inside bars. Bars represent means ± SEM. ***p<0.001, *p<0.05, ns = not significant, Student's t-test and Kruskal-Wallis test. **(Q)** Images of *Kif5C*$^{-/-}$ axons co-expressing soluble EGFP or EGFP-KIF5C and PrP^{PG14}-mCh (left). Scale bar = 10 µm. Quantitation of PrP^{PG14}-mCh endoggresome densities (right). Numbers of endoggresomes are shown inside bars. Bars represent means ± SEM. ***p<0.001, Student's t-test. **(R)** Representative images of PrP^{D177N}-mCh aggregates in WT and *Kif5C*$^{-/-}$ axons (left). Arrowheads point to endoggresomes. Quantitation of endoggresome densities (right). Numbers of endoggresomes are shown inside bars. Bars represent means ± SEM. ***p<0.001, Student's t-test. (S) Representative first frames of time-lapse movies, and kymographs of axons expressing PrP^{PG14}-mCh and GFP-KIF5C (left), and PrP^{PG14}-mTagBFP2, $ARL8b^{WT}$-GFP, and 2xmCh-KIF5C (middle). Arrows point to cotransport. Scale bars = 10 µm. Quantitation of cotransport (right). Numbers of vesicles shown inside bars. Bars represent means ± SEM. **p < 0.01, Student's t-test. Data in this figure were collected by Romain Chassefeyre, Adriaan Verhelle, and me.

2.3.5 ARL8b is a master regulator of ARESTA and a key determinant of PrP^{PG14} axonal entry

Endoggresome formation occurs both by accessing the axonal cell surface (**Figure 2.10**), and by direct transport and fusion (**Figure 2.11**). To test whether these pathways act independently or in concert via ARL8b, live imaging of neurons expressing PrP^{PG14}-mCh-TCS and simultaneously transfected with $ARL8b^{WT}$-GFP revealed the same endoggresome densities in axons treated or not with thrombin (**Figure 2.12A**), suggesting that $ARL8b^{WT}$ overexpression alone was sufficient to promote endoggresome formation, bypassing the contribution of internalized PrP^{PG14}. We propose that PrP^{PG14} aggregation via direct PrP^{PG14} vesicular fusion and via PrP^{PG14} internalization act in parallel.

Next, to evaluate whether ARL8b is associated with PrP^{PG14} vesicles endocytosed from the cell surface to drive endoggresome formation, live imaging of axons expressing PrP^{PG14}-mCh-BBS, $ARL8b^{WT}$-GFP, and treated in the media

with BTX-AF647 showed significant cotransport (**Figure 2.12B**), meaning that ARL8b loads onto PrP^{PG14} vesicles that are endocytosed from the cell surface along the axon, as well as to post-Golgi vesicles (**Figure 2.11B, D**). Altogether, these "indirect" and "direct" ARESTA pathways act in parallel and converge on ARL8b, a master regulator of mutant PrP endoggresome formation.

To finally determine whether ARL8b targets PrP^{PG14} in the soma for axonal entry, we followed the ER-to-LE itinerary of PrP^{PG14} and ARL8b in the soma and proximal axons of neurons treated or not with Brefeldin-A (BFA), an inhibitor of the secretory pathway (Klausner et al., 1992). Live imaging showed that while PrP^{PG14}-mTagBFP2 (or -mCh) transits from the ER to the Golgi, and to LAMP1-positive endolysosomes immediately post-BFA wash, colocalization between PrP^{PG14}-mTagBFP2 (or -mCh) and ARL8b puncta was not observed during the ER-to-LE itinerary, at 2 hours post-transfection (**Figure 2.12C**). This timeframe was after PrP^{PG14} transits to lysosomes in the soma (**Figure 2.4C**). To determine if ARL8b associated with PrP^{PG14} vesicles as they internalized to LEs from the somatic cell surface, neurons were co-transfected with PrP^{PG14}-mCh-BBS and LAMP1-mTagBFP2, treated in the media with BTX-AF647, and fixed and stained with an antibody against ARL8b. Imaging of the soma revealed PrP^{PG14}-mCh-BBS colocalized with LAMP1-mTagBFP2 vesicles and were positive for BTX-AF647 signal but were negative for ARL8b (**Figure 2.12D**). Instead, colocalization of ARL8b with PrP^{PG14}-mCh-BBS, BTX-AF647 signal, and LAMP1-mTagBFP2 vesicles occurred in the proximal axon (**Figure 2.12E**), consistent with our earlier observations in distal axonal regions, indicating that ARL8b does not load onto PrP^{PG14} vesicles that are internalized from the somatic cell surface destined for lysosomal degradation. Thus, ARL8b uniquely loads onto

post-Golgi PrP^{PG14} vesicles that enter the axon, putting ARL8b as a key regulator of PrP^{PG14} axonal entry and axonal aggregation.

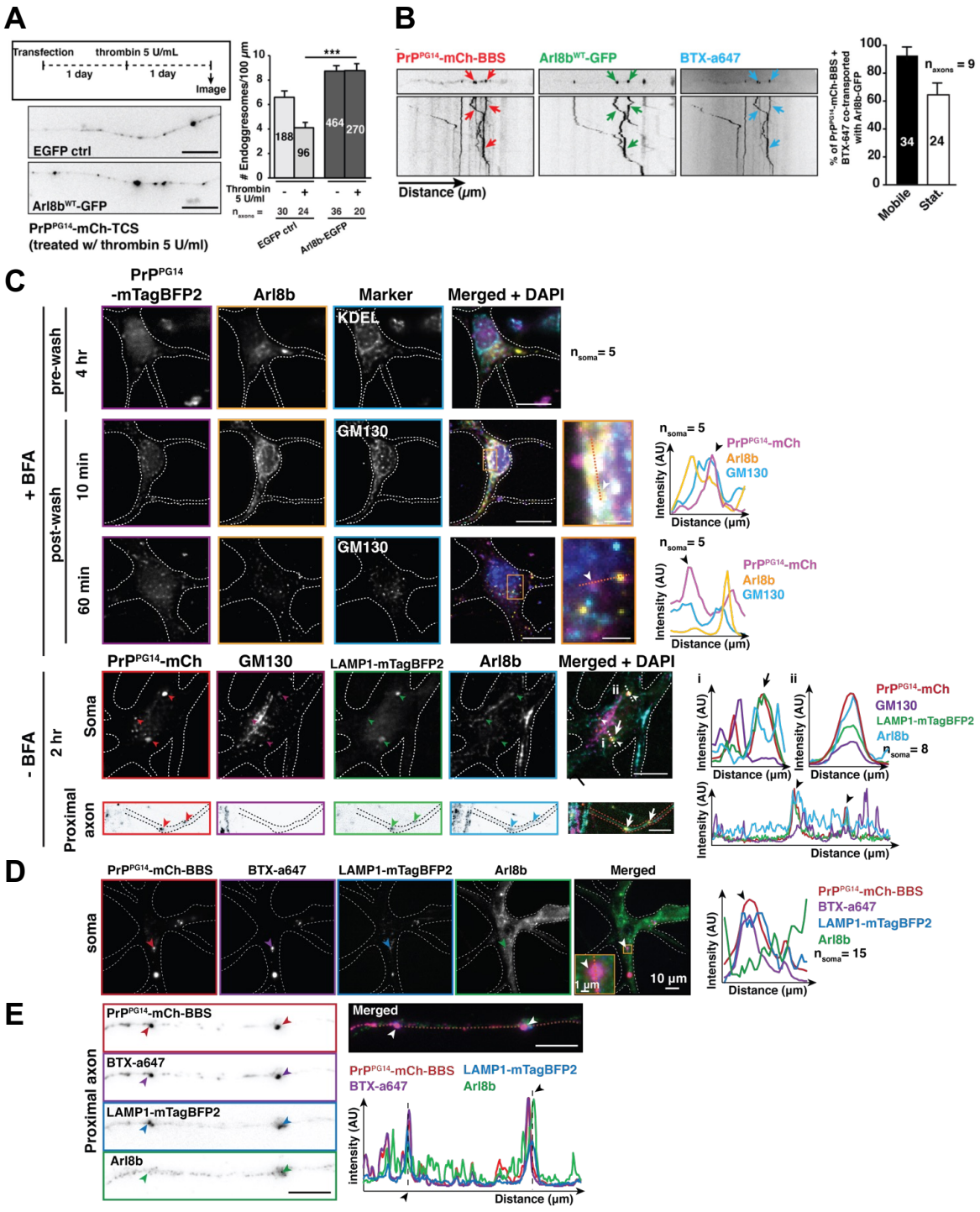


Figure 2.12 ARL8b merges indirect and direct ARESTA and tags PrP^{PG14} vesicles for axonal entry. (A) Outline of thrombin assay (top left) and representative images of axons of neurons co-expressing PrP^{PG14}-mCh-TCS and soluble EGFP or ARL8b^{WT}-GFP (bottom left). Scale bars = 10 µm. Quantitation of endoggresome densities (right). Number of endoggresomes are inside bars. Bars represent means ± SEM. ***$p < 0.01$, Kruskal-Wallis test. **(B)** Representative first frames of time-lapse movie and kymographs of axons expressing PrP^{PG14}-mCh-BBS, ARL8b^{WT}-GFP, and

labeled with BTX-AF647 (left). Arrows point to cotransport. Scale bars = 10 μm. Quantitation of cotransport (right). Number of vesicles are inside bars. Bars represent means ± SEM. **(C)** Representative images of soma and proximal axons of different neurons expressing PrP^{PG14}-mTagBFP2 or PrP^{PG14}-mCh, LAMP1-mTagBFP2 and stained with antibodies against ARL8b, ER (KDEL), Golgi (GM130), or with DAPI nuclear marker at indicated time points and conditions, with or without BFA treatment (bottom panels). Graphs to the right are of line scans of dotted lines inside insets. Arrowheads point to colocalization events, also shown in enlarged insets and in line scan intensity profiles. Scale bars in main panels = 10 μm. Scale bars in insets = 500 nm. **(D)** Representative images of PrP^{PG14}-mCh-BBS internalization in the soma (left panels) of neurons co-transfected with PrPPG14-mCh-BBS and LAMP1-mTagBFP2, labeled with BTX-AF647, and stained with an antibody against ARL8b. Arrowheads point to colocalization events, also shown in enlarged insets and in line scan intensity profile (right). Scale bars in main panel = 10 μm. Scale bars in inset = 1 μm. **(E)** Representative images of PrP^{PG14}-mCh-BBS internalization in axons (left and top right panels) of neurons co-transfected with PrP^{PG14}-mCh-BBS and LAMP1-mTagBFP2, labeled with BTX-AF647, and stained with an antibody against ARL8b. Arrowheads point to colocalizing endoggresomes. Line scan intensity profile (right). Scale bar = 10 μm. Data from (A)-(B) were collected by Adriaan Verhelle. Data from (C)-(E) were collected by me.

2.3.6 Misfolded PrP is degraded in the soma but persists in axons due to impaired retrograde transport and diminished lysosomal degradation capacity

Axonal cargoes rely heavily on retrograde transport for lysosomal degradation because distal axon has limited local degradation capacity (Lie et al., 2021; Overly et al., 1995; Overly and Hollenbeck, 1996). We hypothesized that PrP^{PG14} endoggresomes persist in axons due to a diminished local axonal degradation capacity and/or failure of PrP^{PG14} retrograde transport. Several observations suggested lysosomal clearance defects in PrP^{PG14} axons, such as increased endoggresome densities overtime compared to PrP^{WT} axons (**Figure 2.8A**). To further test the first hypothesis, we treated PrP^{PG14}-mCh neurons with BafA1, an inhibitor of a lysosomal vacuolar-type ATPase proton pump that acidifies vesicles (Pamarthy et al., 2018), and found that BafA1 treatment did not increase endoggresome densities compared to DMSO-treated controls (**Figure 2.13A**), while a positive control PrP^{WT}-mCh neurons treated with BafA1 showed a

significant increase in endoggresome densities compared to DMSO controls, indicating the lack of acidification and local degradation in PrP^{PG14} axons (**Figure 2.13A**). Finally, BTX-AF647 treatment and wash-off of neurons expressing PrP^{WT}-mCh-BBS resulted in BTX-AF647-positive particles in axons with reduced fluorescence intensity after 24 hours, compared to the steady fluorescence levels of BTX-AF647-positive PrP^{PG14}-mCh-BBS particles (**Figure 2.13C**), suggesting that a day after treatment, endocytosed PrP^{PG14}-mCh-BBS molecules were not degraded compared to PrP^{WT}-mCh-BBS internalized particles.

Next, to determine whether retrograde transport was impaired in PrP^{PG14}-mCh neurons, LAMP1-EGFP movement was analyzed. In PrP^{PG14}-mCh axons, the proportion of stationary LAMP1-EGFP vesicles was significantly increased, and less moved in the retrograde direction (**Figure 2.13D**). LAMP1-EGFP vesicles also spent more time paused and less time moving toward the soma in PrP^{PG14}-mCh versus PrP^{WT}-mCh axons (**Figure 2.13E**). Thus, PrP^{PG14} vesicles and endoggresomes, as well as LAMP1-positive LEs are not properly transported toward the soma, nor are they actively degraded in axonal lysosomes, contributing to their sustained presence in axons.

As lysosomes are enriched in the soma (Cai et al., 2010), we evaluated whether PrP^{PG14}-mCh was actively degraded in the soma by systematically analyzing the trafficking itinerary of misfolded PrP^{PG14} immediately upon neuronal expression. Live imaging of neurons expressing PrP^{PG14}-mCh and treated with BFA showed ER retention of PrP^{PG14}-mCh for at least 6 hours (**Figure 2.4B**). Untreated or post-BFA-wash neurons showed rapid, efficient, and successive translocation within minutes, and by 2 hours of expression, of PrP^{PG14}-

mCh from the ER to the Golgi, and to compartments positive for Cathepsin B (CatB), an acidic hydrolase required for lysosomal substrate degradation (**Figure 2.13F**). Neurons expressing PrP^{PG14}-mCh-BBS and treated with BTX-AF647 in the media showed colocalization of these vesicles with LAMP1-EGFP (**Figure 2.13G**), indicating internalization into LEs. Furthermore, PrP^{PG14}-mTagBFP2 vesicles colocalized with LysoTracker and Magic Red in the soma (**Figure 2.13G**), a fluorogenic substrate that activates upon cleavage by active Cat B. Live imaging showed the active disappearance of PrP^{PG14}-mCh puncta that colocalized with LAMP1-EGFP, suggesting active degradation in the soma via the cell surface (**Figure 2.13H**). To further test whether PrP^{PG14} underwent lysosomal degradation in the soma, neurons expressing PrP^{WT}-mCh or PrP^{PG14} -mCh and exposed to LysoTracker Green, were treated with either BafA1 or DMSO. Quantitative imaging showed a significant increase in fluorescence intensity of PrP^{WT}-mCh- and PrP^{PG14}-mCh-expressing neurons treated with BafA1 compared to those treated with DMSO (**Figure 2.13I**), indicating that PrP undergoes lysosomal-based degradation in the soma. Because this clearance pathway resembles a previously characterized rapid ER stress-induced export (RESET) pathway in non-neuronal cells (Satpute-Krishnan et al., 2014), we evaluated whether PrP^{PG14} expression turned on ER stress in neurons. Co-expression of PrP^{PG14}-EGFP and an ER stress transcriptional reporter (ERSE-mCh) (Plate et al., 2016) resulted in significantly increased signal compared to that observed in neurons expressing either soluble EGFP or PrP^{WT}-EGFP (**Figure 2.13J**), indicating constitutive ER stress activation. Thus, while secreted misfolded PrP is actively cleared in somatic lysosomes by a RESET pathway, PrP^{PG14} vesicles and endoggresomes are neither effectively transported toward the soma, nor are

they actively degraded in the axon, contributing to their sustained axonal presence.

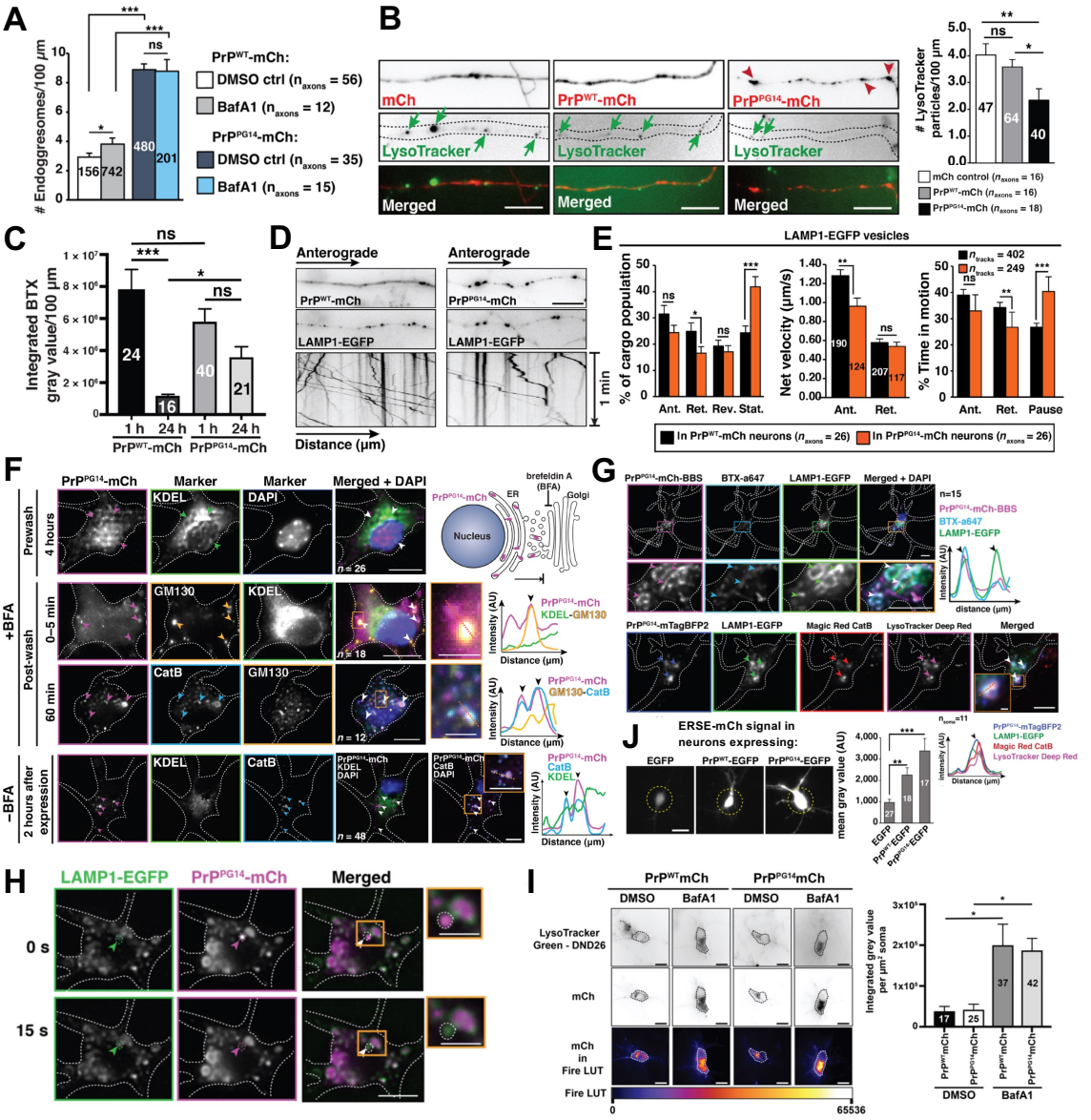


Figure 2.13 Misfolded PrP^{PG14} is degraded in the soma but sustained in axons due to impairments to local lysosomal degradation and retrograde transport. (A) Quantitation of axonal endoggresome densities in neurons treated with BafA1 or DMSO control (ctrl). Numbers of endoggresomes are shown inside bars. Bars represent means ± SEM. ***p < 0.01, *p<0.05, ns = not significant, Kruskal-Wallis test. **(B)** Representative images of Lysotracker-positive vesicles in soluble mCh, PrP^{WT}-mCh, or PrP^{PG14}-mCh-expressing axons (left). Arrows point to vesicles, arrowheads point to endoggresomes. Scale bar = 10 µm. Quantitation of LysoTracker vesicle densities (right). Numbers of vesicles are shown inside bars. Bars represent means ± SEM. *p<0.05, **p < 0.01, ns = not significant, Student's t-test, Tukey's correction. **(C)** Quantitation of BTX signal intensity per 100 µm of axon length. Numbers of axons are shown inside bars. Bars represent means ± SEM. *p<0.05, ***p<0.001, ns = not significant, Student's t-test, Tukey's correction. **(D)** Representative images of PrP^{WT}-mCh or PrP^{PG14}-mCh axons (top), and LAMP1-

EGFP first frames of time-lapse movie (middle), and kymographs (bottom). Scale bar = 10 μm. **(E)** Population breakdown of LAMP1-EGFP vesicles in PrP^{WT}-mCh or PrP^{PG14}-mCh axons (left). Average net velocities of LAMP1-EGFP vesicles in PrP^{WT}-mCh or PrP^{PG14}-mCh axons (middle). Numbers of tracks are shown inside bars. Percent time LAMP1-EGFP vesicles spent in motion or paused in PrP^{WT}-mCh or PrP^{PG14}-mCh axons (right). Bars represent means ± SEM. *p<0.05, **p < 0.01, ***p<0.001, ns = not significant, Student's t-test, Šidák correction. **(F)** Representative images of soma of neurons expressing PrP^{PG14}-mCh and stained with antibodies against ER (KDEL), Golgi (GM130), lysosomes (CatB) along with DAPI nuclear marker at indicated time points and conditions (left). Arrowheads point to colocalization. Schematic of BFA assay (top right). Line scan intensity profiles of region indicated by dotted orange line inside inset (right). Scale bars of main panels = 10 μm. Scale bars of insets = 250 nm. **(G) (top)** Representative images of neuronal soma co-transfected with PrP^{PG14}-mCh-BBS, LAMP1-EGFP, and labeled with BTX-AF647 (top left panels), and enlargement of insets (bottom left panels). Scale bars= 10 μm. Line scan intensity profiles of dotted lines (right). **(bottom)** Representative images of the soma of a neuron co-transfected with PrP^{PG14}-mTagBFP2 and LAMP1-EGFP, and treated with Magic Red and LysoTracker Deep Red. Arrowheads point to colocalization events. Scale bars of main panels and insets = 10 μm and 1 μm, respectively. Line scan intensity profiles of dotted lines from the inset (bottom right). **(H)** Representative images from a movie of a neuron co-expressing LAMP1-EGFP and PrP^{PG14}-mCh at two timepoints. Scale bars = 10 μm. Arrowheads point to PrP^{PG14}-mCh disappearing (enlarged in inset). Scale bars of insets = 5 μm. **(I) (left)** Representative inverted fluorescence images of the soma of DMSO- or BafA1-treated neurons with LysoTracker Green staining. Fire LUT shown on the bottom panels. Scale bars = 20 μm. **(right)** Quantitation of integrated gray values of LysoTracker Green in the soma, based on mCh signal. Number of neurons analyzed are indicated inside bars. Bars represent means ± SEM. *p<0.05, Student's t-test. **(J)** Representative images (left panels) and quantitation of ERSE-mCh intensity (right) in neurons co-transfected with ERSE-mCh and soluble EGFP, PrP^{WT}-EGFP, or PrP^{PG14}-EGFP. Dotted lines indicate 30 μm diameter circles ROI to measure total gray intensity values. Scale bars = 20 μm. Bars represent means ± SEM. **p<0.01, ***p<0.001, Student's t-test. Number of neurons are shown inside bars. Data from (A)-(E), (H), (J) were collected by Romain Chassefeyre. Data from (F)-(G) were collected by me. Data from (I) were collected by Adriaan Verhelle.

2.3.7 PrP^{PG14} neurons display ARESTA-dependent impaired calcium intake dynamics and decreased neuronal viability

To probe whether axonal PrP^{PG14} endoggresomes lead to neuronal dysfunction, we tested whether the intrinsic capacity of cultured hippocampal neurons expressing PrP^{PG14}-mCh to intake calcium upon KCl-induced depolarization was compromised, as shown previously for cerebellar cultured neurons (Senatore et al., 2012). Neurons transduced with PrP^{WT}-mCh or PrP^{PG14}-mCh adeno-associated virus (AAV-DJ), displayed high transduction efficiencies and

endoggresome densities were comparable to those observed in transfected axons (**Figure 2.14E**). Single-cell calcium imaging of AAV-DJ-PrP^{PG14}-mCh-transduced neurons pre-loaded with the calcium sensitive dye Fluo-4 AM resulted in a defective calcium influx in response to KCl-induced depolarization compared to AAV-DJ-PrP^{WT}-mCh-transduced neurons (**Figure 2.14A-B**). Reducing endoggresome formation via depletion of ARESTA component kinesin-1 (**Figure 2.11**), in neurons transduced with AAV-DJ-PrP^{PG14}-mCh, resulted in calcium influx dynamics comparable to those of neurons transduced with AAV-DJ-PrP^{WT}-mCh (**Figure 2.14A-B**). Importantly, calcium intake was not altered in control *Kif5c*$^{-/-}$ neurons transduced with AAV-DJ-PrP^{WT}-mCh (**Figure 2.14C-D**).

To further determine the toxicity of PrP^{PG14} endoggresomes, the neuronal viability of WT versus *Kif5c*$^{-/-}$ neurons, or versus neurons with reduced Vps41 and ARL8b function expressing PrP^{PG14}- versus PrP^{WT}-mCh was quantified. At 10 days post-PrP^{PG14}-mCh transfection, expression of PrP^{PG14}-mCh resulted in a 4.5-fold increase in neuronal death compared to non-transfected neurons or those expressing PrP^{WT}-mCh (**Figure 2.14F-G**). Notably, neuronal death at 10 days post-transfection was not significantly different in *Kif5c*$^{-/-}$ neurons expressing PrP^{PG14}-mCh compared to those expressing PrP^{WT}-mCh or untransfected (**Figure 2.14F-G**), suggesting that reduced endoggresome formation in KIF5C-depleted axons prevented neuronal death. Moreover, neuronal death was decreased when neurons were treated with shRNA against ARL8b and with siRNAs against Vps41 (**Figure 2.14H**). These data indicate that endoggresomes are neurotoxic and inhibiting their formation by reducing the function of ARESTA pathway components abrogates neurotoxicity.

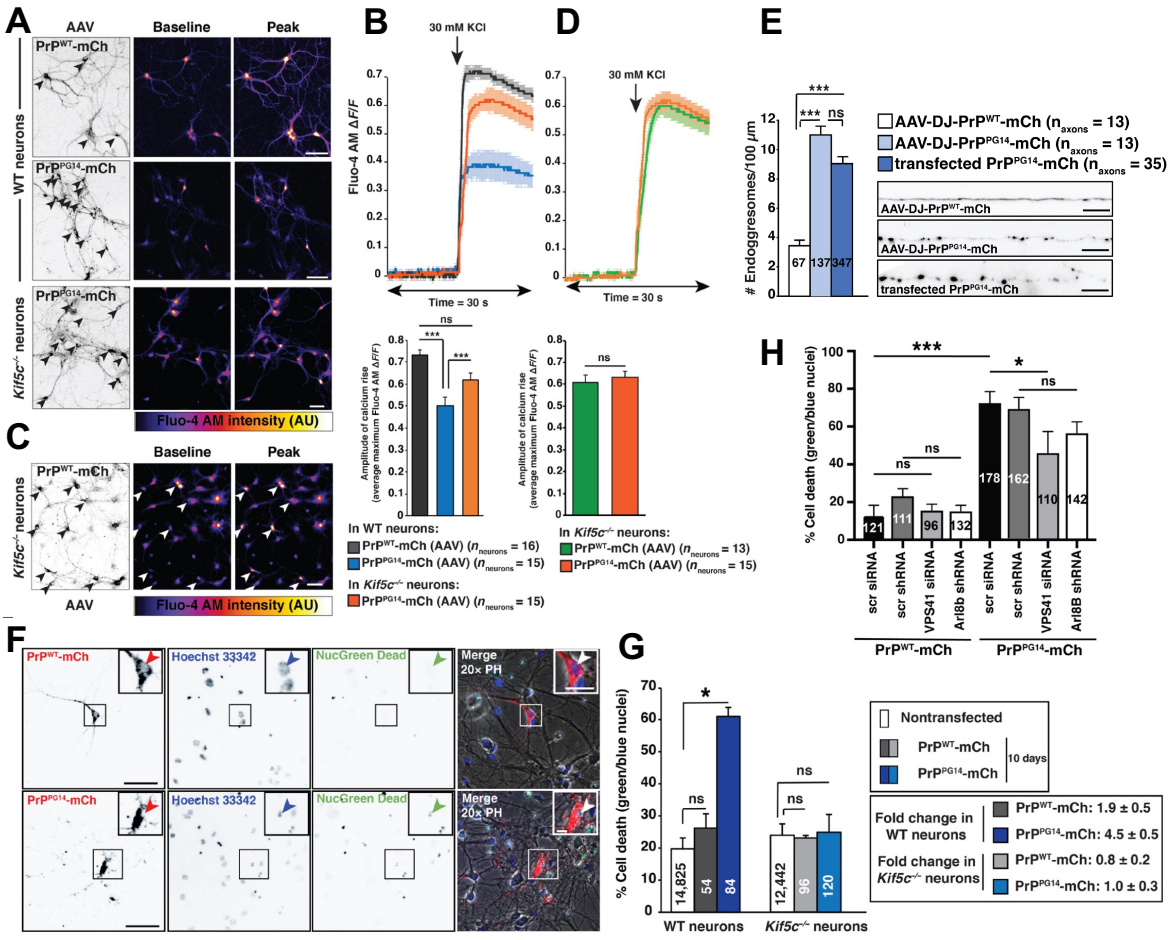


Figure 2.14 Impaired calcium intake dynamics and neuronal viability in PrP^{PG14} neurons are ARESTA-dependent. (A) Representative images of PrP^{WT}-mCh or PrP^{PG14}-mCh AAV-transduced WT or *Kif5c*$^{-/-}$ neurons (left). Arrowheads point to soma. Baseline and peak Fluo-4 AM intensities pre- (middle) and post-KCl treatment (right). Scale bars = 50 µm. **(B)** KCl-induced depolarization response curve from normalized Fluo-4 AM intensities from (A) (top). Arrow points to KCl treatment time. Average maximum amplitude of calcium rise (bottom). Bars represent means ± SEM. ***p<0.001, ns = not significant, Student's t-test, Tukey's correction. **(C)** Representative images of PrP^{WT}-mCh AAV-transduced *Kif5c*$^{-/-}$ neurons (top). Arrowheads point to soma. Baseline and peak Fluo-4 AM intensities pre- (middle) and post-KCl treatment (right). Scale bars50 mm. **(D)** KCl-induced depolarization response curve from normalized Fluo-4 AM intensities from (A and C). Arrow points to KCl treatment time. Average maximum amplitude of calcium rise (bottom). **(E)** Quantitation of endoggresome densities (left) and representative images (right) of axons from neurons transduced with AAV-DJ-PrP^{WT}-mCh, AAV-DJ-PrP^{PG14}-mCh, or transfected with MoPrP.Xho PrP^{PG14}-mCh. Number of endoggresomes are shown inside bars. Scale bar = 10 µm. **(F)** Representative images of hippocampal neurons expressing PrP^{WT}- or PrP^{PG14}-mCh and stained with Hoechst 33342 and NucGreen Dead (top panels). Arrowheads point to nuclei. Insets are enlarged in the respective top right corners of each panel. Scale bars on main figures = 100 µm. Scale bars on insets = 20 µm. Quantitation of percentage cell death (bottom left). Numbers of cells are shown inside bars. Fold changes between

indicated conditions are indicated on boxed panel (bottom right). Bars represent means ± SEM. *p<0.05, ns = non-significant, Kruskal-Wallis test. **(G)** Quantitation of percentage cell death of neurons transduced with AAV8-PrP^{WT}- or AAV8-PrP^{PG14}-mCh. Imaging was done 4 days post-siRNA/shRNA treatment and AAV8 transduction. N = 21-26 individual wells (96 well plate) were analyzed per condition from 3 independent replicates. Numbers of cells are shown inside bars. Bars represent means ± SEM. *p<0.05, ***p<0.001, ns = non-significant, Kruskal-Wallis test. Data from (A)-(D) were collected by me. Data from (E)-(H) were collected by Adriaan Verhelle.

2.4 Conclusions and discussion

In conclusion, ARL8b marks Golgi-derived PrP^{PG14} vesicles for axonal entry and orchestrates indirect and direct ARESTA pathways to generate endoggresomes in mammalian axons. ARESTA-dependent endoggresome formation negatively impacts neuronal function and viability, and modulation of ARESTA decreases endoggresome densities and rescue neuronal defects. These findings are summarized as a working model in **Figure 2.15**.

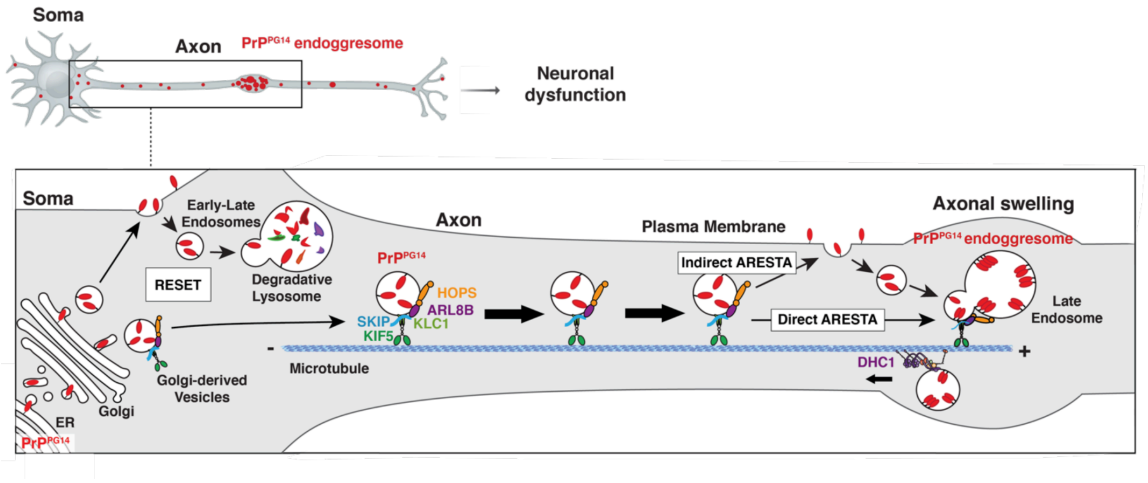


Figure 2.15 Opposing roles of neuronal endolysosomal pathways that clear misfolded PrP in the soma but promote endoggresome formation in axons. A model shows that Rapid ER Stress-induced Export (RESET) acts in the soma to degrade PrP^{PG14} via secretory-endolysosomal pathways. Alternatively, kinesin-1 (KIF5 and KLC1), SKIP, and HOPS are recruited by ARL8b that earmarks PrP^{PG14} vesicles for axonal entry towards ARESTA-dependent aggregation and biogenesis of endoggresomes. Endoggresome formation occurs following indirect targeting of PrP^{PG14} to late endosome via the axonal cell surface, via its direct homotypic fusion, or both.

Dynein-mediated retrograde transport and axonal degradative capacity are impaired in axons, thus promoting the maintenance of endoggresomes in axons. This model figure was drawn by Sandra Encalada and me.

The accumulation of misfolded proteins inside axons has been observed previously by immunohistochemistry and EM of the brains from patients who were diagnosed with neurodegenerative diseases, including in PrDs (Arnold et al., 1995; Godsave et al., 2008; Kovacs et al., 2012; Liberski et al., 2018; Sikorska et al., 2004; Veith et al., 2009). By modeling the formation of mutant PrP aggregates involved in human prion diseases (Owen et al., 1992) in mammalian neurons, the unexpected discovery is that Golgi-derived mutant PrP vesicles are sorted into two divergent itineraries: one for immediate lysosomal degradation in the soma and the other toward the axon by an ARL8b/kinesin-1/HOPS axis that ensures their axonal entry, fusion, and aggregation (**Figure 2.15**). The opposing nature of clearance versus aggregation pathways appears to stem largely from the highly polarized neuronal architecture, with an established lysosomal degradation-efficient somatic compartment where mutant PrP is actively degraded, versus an axonal compartment where ARESTA actively drives endoggresome formation, and where limited lysosomal degradation sustains them. We posit this soma versus axon compartmentalization explains the differential susceptibility of neurons versus non-neuronal cells to the formation of aggregates and to aggregate-driven toxicity that is characteristic of many neurodegenerative disorders. These distinct itineraries account for the enhanced vulnerability of axons versus the soma in generating aggregates and merit further investigation of other neurotoxic aggregate-driven mechanisms in *bona fide* neuronal systems.

In non-neuronal cells, misfolded PrP particles were shown to degrade via RESET (Zavodszky and Hegde, 2019). In neurons, the precise ratio of misfolded

PrP particles undergoing immediate somatic degradation versus ARESTA-dependent aggregation is unknown. How the population of Golgi-derived mutant PrP vesicles is selected for immediate degradation in the neuronal soma is unclear, but one hypothesis is that an ER chaperone TMED10/Tmp21 might provide a critical tag for this itinerary toward degradation, as shown in an earlier study (Zavodszky and Hegde, 2019). Our data show that a second population of Golgi-derived mutant PrP vesicles skips somatic degradation and is transported into the axon for aggregation by ARESTA. Regulated sorting and transport of mutant PrP vesicles into the axon occurs by ARL8b recruitment of kinesin-1 and HOPS. ARL8b is virtually absent from degradation-bound PrP^{PG14} vesicles in the soma, suggesting that this ARL8b complex could provide a specific axonal localization signal. Vps41 is known to be involved in direct Golgi-to-LE sorting (Pols et al., 2013), so this role appears conserved during interactions with mutant PrP vesicles in axons. How ARL8b recognizes mutant PrP vesicles at the Golgi is unclear, but the mechanism could involve known ARL8b endosomal sorting regulators, such as BLOC-One-Related Complex (BORC) (Farias et al., 2017; Pu et al., 2015). Once formed in axons, endoggresomes persist due to ineffective axonal clearance and impaired retrograde transport toward the soma to send it for the lysosomal degradation route. Consistent with our observations, defects in lysosomal maturation and degradation, as well as in retrograde axonal transport have been documented in neuronal cell lines persistently infected with prions (Shim et al., 2016), as well as in prion infected mouse models of disease (Ermolayev et al., 2009). In this study, we also found multiple conserved endosomal Rab GTPases, such as Rab5, Rab7, and Rab11, also colocalized with endoggresomes. These Rabs were known to be associated with prion disease

pathologies. For examples, genetic modulation of Rab11 results in the accumulation of mutant $PrP^{D177N/M128}$ associated with FFI in the secretory pathway (Massignan et al., 2010). Also, overexpression of Rab9 inhibits PrP^{Sc} accumulation in neuronal cell lines, pointing to a role of LEs in prion conversion (Gilch et al., 2009). Moreover, inhibition of MVB maturation via reduction of Rab7 activity resulted in significant reduction of PrP^{Sc} levels, suggesting that MVBs could be the site of PrP^{Sc}-mediated pathologies (Yim et al., 2015). Whether modulation of Rab5, Rab7, Rab9, and Rab11 could regulate aggregation, prion conversion, and cell-to-cell spread, or could tip the balance towards lysosomal degradation merits further investigation (See **Chapter 5**: Future directions)

Misfolded mutant PrP has been reported to form aggresomes in the cytosol of neurons, where they were targeted for clearance by ER-Associated Degradation (ERAD) (Ma and Lindquist, 2001), but whether these represent toxic structures is debated (Fioriti et al., 2005). Nevertheless, extensive characterization of the trafficking and turnover of many misfolded GPI-anchored PrP mutants showed that they are normally poor ERAD substrates and are not dependent on proteasomal degradation (Ashok and Hegde, 2009). Thus, RESET-like degradation in the soma and endoggresome formation in axons are favored itineraries by misfolded PrP as primary pathways. However, a shift towards aggresome formation may occur when and if RESET is overwhelmed or compromised following extensive and sustained ER stress or it may happen to those cytosolic, membraneless aggregates of PrP (See **Chapter 5**: Future directions). Further studies are needed to find mechanistic links between RESET, ARESTA, ERAD, and aggresomes.

The generality of endoggresomes and ARESTA to other neurodegenerative pathologies is a tantalizing possibility, given the reliance of tau, APP/Aβ, α-synuclein, and huntingtin on endosomal pathways for their processing and spread (van Weering and Scheper, 2019; Velier et al., 1998; Vidyadhara et al., 2019). Notably, enlarged endosomes represent a common phenotype in Alzheimer's disease (AD) pathologies, and are considered amongst the earliest neuronal lesions identified thus far (Cataldo et al., 2004, 2000; Knupp et al., 2020; Small and Petsko, 2020). Indeed, genome wide association studies (GWAS), whole exome and genome sequencing data, and multiple human genetics analyses have identified endolysosomal genes as risk hubs associated with early pathophysiological changes in AD (Giri et al., 2016; Karch and Goate, 2015). It will be key to determine whether the ubiquitous enlarged endosomes observed in early-stage neurodegenerative pathologies and associated with cellular toxicity could be regulated by the ARESTA pathway.

2.5 References

Arnold, J.E., Tipler, C., Laszlo, L., Hope, J., Landon, M., Mayer, R.J., 1995. The abnormal isoform of the prion protein accumulates in late-endosome-like organelles in scrapie-infected mouse brain. J Pathol 176, 403–11.

Ashok, A., Hegde, R.S., 2009. Selective processing and metabolism of disease-causing mutant prion proteins. PLoS Pathog 5, e1000479.

Barmada, S., Piccardo, P., Yamaguchi, K., Ghetti, B., Harris, D.A., 2004. GFP-tagged prion protein is correctly localized and functionally active in the brains of transgenic mice. Neurobiol Dis 16, 527–37.

Biasini, E., Medrano, A.Z., Thellung, S., Chiesa, R., Harris, D.A., 2008. Multiple biochemical similarities between infectious and non-infectious aggregates of a prion protein carrying an octapeptide insertion. Journal of Neurochemistry 104, 1293-308.

Borchelt, D.R., Taraboulos, A., Prusiner, S.B., 1992. Evidence for synthesis of scrapie prion proteins in the endocytic pathway. J Biol Chem 267, 16188–99.

Burel, A., Lavault, M.T., Chevalier, C., Gnaegi, H., Prigent, S., Mucciolo, A., Dutertre, S., Humbel, B.M., Guillaudeux, T., Kolotuev, I., 2018. A targeted 3D EM and correlative microscopy method using SEM array tomography. Development 145, dev160879.

Cai, Q., Lu, L., Tian, J.H., Zhu, Y.B., Qiao, H., Sheng, Z.H., 2010. Snapin-regulated late endosomal transport is critical for efficient autophagy-lysosomal function in neurons. Neuron 68, 73–86.

Cataldo, A.M., Petanceska, S., Terio, N.B., Peterhoff, C.M., Durham, R., Mercken, M., Mehta, P.D., Buxbaum, J., Haroutunian, V., Nixon, R.A., 2004. Abeta localization in abnormal endosomes: association with earliest Abeta elevations in AD and Down syndrome. Neurobiol Aging 25, 1263–72.

Cataldo, A.M., Peterhoff, C.M., Troncoso, J.C., Gomez-Isla, T., Hyman, B.T., Nixon, R.A., 2000. Endocytic pathway abnormalities precede amyloid beta deposition in sporadic Alzheimer's disease and Down syndrome: differential effects of APOE genotype and presenilin mutations. Am J Pathol 157, 277–86.

Caughey, B., Raymond, G.J., Ernst, D., Race, R.E., 1991. N-terminal truncation of the scrapie-associated form of PrP by lysosomal protease(s): implications regarding the site of conversion of PrP to the protease-resistant state. J Virol 65, 6597–603.

Chaiamarit, T., Wu, Y., Verhelle, A., Encalada, S., 2023. Fluorescence Assays for Real-Time Tracking of Cell Surface Protein Internalization and Endosomal Sorting in Axons of Primary Mouse Hippocampal Neurons. BIO-PROTOCOL 13, e4651. https://doi.org/10.21769/BioProtoc.4651

Chassefeyre, R., Chaiamarit, T., Verhelle, A., Novak, S.W., Andrade, L.R., Leitao, A.D.G., Manor, U., Encalada, S.E., 2021. Endosomal sorting drives the formation of axonal prion protein endoggresomes. Sci Adv 7, eabg3693.

Chiesa, R., Drisaldi, B., Quaglio, E., Migheli, A., Piccardo, P., Ghetti, B., Harris, D.A., 2000. Accumulation of protease-resistant prion protein (PrP) and apoptosis of cerebellar granule cells in transgenic mice expressing a PrP insertional mutation. Proc Natl Acad Sci U S A 97, 5574–9.

Chiesa, R., Piccardo, P., Ghetti, B., Harris, D.A., 1998. Neurological illness in transgenic mice expressing a prion protein with an insertional mutation. Neuron 21, 1339–51.

Chiesa, R., Piccardo, P., Quaglio, E., Drisaldi, B., Si-Hoe, S.L., Takao, M., Ghetti, B., Harris, D.A., 2003. Molecular distinction between pathogenic and infectious properties of the prion protein. J Virol 77, 7611–22.

Cui, J., Wang, Z., Cheng, Q., Lin, R., Zhang, X.M., Leung, P.S., Copeland, N.G., Jenkins, N.A., Yao, K.M., Huang, J.D., 2011. Targeted inactivation of kinesin-1 in pancreatic beta-cells in vivo leads to insulin secretory deficiency. Diabetes 60, 320–30.

Daude, N., Lehmann, S., Harris, D.A., 1997. Identification of intermediate steps in the conversion of a mutant prion protein to a scrapie-like form in cultured cells. J Biol Chem 272, 11604–12.

Dunn, S., Morrison, E.E., Liverpool, T.B., Molina-Paris, C., Cross, R.A., Alonso, M.C., Peckham, M., 2008. Differential trafficking of Kif5c on tyrosinated and detyrosinated microtubules in live cells. J Cell Sci 121, 1085–95.

Encalada, S.E., Szpankowski, L., Xia, C.H., Goldstein, L.S., 2011. Stable kinesin and dynein assemblies drive the axonal transport of mammalian prion protein vesicles. Cell 144, 551–65.

Ermolayev, V., Cathomen, T., Merk, J., Friedrich, M., Hartig, W., Harms, G.S., Klein, M.A., Flechsig, E., 2009. Impaired axonal transport in motor neurons correlates with clinical prion disease. PLoS Path 5, e1000558.

Farias, G.G., Guardia, C.M., De Pace, R., Britt, D.J., Bonifacino, J.S., 2017. BORC/kinesin-1 ensemble drives polarized transport of lysosomes into the axon. Proc Natl Acad Sci U S A 114, E2955–E2964.

Fehlinger, A., Wolf, H., Hossinger, A., Duernberger, Y., Pleschka, C., Riemschoss, K., Liu, S., Bester, R., Paulsen, L., Priola, S.A., Groschup, M.H., Schatzl, H.M., Vorberg, I.M., 2017. Prion strains depend on different endocytic routes for productive infection. Sci Rep 7, 6923.

Fioriti, L., Dossena, S., Stewart, L.R., Stewart, R.S., Harris, D.A., Forloni, G., Chiesa, R., 2005. Cytosolic prion protein (PrP) is not toxic in N2a cells and primary neurons expressing pathogenic PrP mutations. J Biol Chem 280, 11320–8.

Gilch, S., Bach, C., Lutzny, G., Vorberg, I., Schatzl, H.M., 2009. Inhibition of cholesterol recycling impairs cellular PrP(Sc) propagation. Cell Mol Life Sci 66, 3979–91.

Giri, M., Zhang, M., Lu, Y., 2016. Genes associated with Alzheimer's disease: an overview and current status. Clin Interv Aging 11, 665–81.

Godsave, S.F., Wille, H., Kujala, P., Latawiec, D., DeArmond, S.J., Serban, A., Prusiner, S.B., Peters, P.J., 2008. Cryo-immunogold electron microscopy for prions: toward identification of a conversion site. J Neurosci 28, 12489–99.

Goold, R., Rabbanian, S., Sutton, L., Andre, R., Arora, P., Moonga, J., Clarke, A.R., Schiavo, G., Jat, P., Collinge, J., Tabrizi, S.J., 2011. Rapid cell-surface prion protein conversion revealed using a novel cell system. Nature Commun 2, 281.

Gu, Y., Verghese, S., Bose, S., Mohan, M., Singh, N., 2007. Mutant prion protein D202N associated with familial prion disease is retained in the endoplasmic reticulum and forms "curly" intracellular aggregates. J Mol Neurosci 32, 90–6.

Gustafsson, N., Culley, S., Ashdown, G., Owen, D.M., Pereira, P.M., Henriques, R., 2016. Fast live-cell conventional fluorophore nanoscopy with ImageJ through super-resolution radial fluctuations. Nat Commun 7, 12471.

Hegde, R.S., Rane, N.S., 2003. Prion protein trafficking and the development of neurodegeneration. Trends Neurosci 26, 337–9.

Ishida, M., Ohbayashi, N., Fukuda, M., 2015. Rab1A regulates anterograde melanosome transport by recruiting kinesin-1 to melanosomes through interaction with SKIP. Sci Rep 5, 8238.

Ivanova, L., Barmada, S., Kummer, T., Harris, D.A., 2001. Mutant prion proteins are partially retained in the endoplasmic reticulum. J Biol Chem 276, 42409–21.

Karch, C.M., Goate, A.M., 2015. Alzheimer's disease risk genes and mechanisms of disease pathogenesis. Biol Psychiatry 77, 43–51.

Kasher, P.R., De Vos, K.J., Wharton, S.B., Manser, C., Bennett, E.J., Bingley, M., Wood, J.D., Milner, R., McDermott, C.J., Miller, C.C., Shaw, P.J., Grierson, A.J., 2009. Direct evidence for axonal transport defects in a novel mouse model of mutant spastin-induced hereditary spastic paraplegia (HSP) and human HSP patients. J Neurochem 110, 34–44.

Klausner, R.D., Donaldson, J.G., Lippincott-Schwartz, J., 1992. Brefeldin A: insights into the control of membrane traffic and organelle structure. J Cell Biol 116, 1071–80.

Knupp, A., Mishra, S., Martinez, R., Braggin, J.E., Szabo, M., Kinoshita, C., Hailey, D.W., Small, S.A., Jayadev, S., Young, J.E., 2020. Depletion of the AD Risk Gene SORL1 Selectively Impairs Neuronal Endosomal Traffic Independent of Amyloidogenic APP Processing. Cell Rep 31, 107719.

Kovacs, G.G., Molnar, K., Keller, E., Botond, G., Budka, H., Laszlo, L., 2012. Intraneuronal immunoreactivity for the prion protein distinguishes a subset of E200K genetic from sporadic Creutzfeldt-Jakob Disease. J Neuropathol Exp Neurol 71, 223–32.

Kristiansen, M., Messenger, M.J., Klohn, P.C., Brandner, S., Wadsworth, J.D., Collinge, J., Tabrizi, S.J., 2005. Disease-related prion protein forms aggresomes in neuronal cells leading to caspase activation and apoptosis. J Biol Chem 280, 38851–61.

Lee, S.J., Lim, H.S., Masliah, E., Lee, H.J., 2011. Protein aggregate spreading in neurodegenerative diseases: problems and perspectives. Neurosci Res 70, 339–48.

Liberski, P.P., Gajos, A., Sikorska, B., 2018. Dystrophic neurites accumulating autophagic vacuoles show early stages of neuritic destruction. Folia Neuropathol 56, 175–178.

Lie, P.P.Y., Yang, D.S., Stavrides, P., Goulbourne, C.N., Zheng, P., Mohan, P.S., Cataldo, A.M., Nixon, R.A., 2021. Post-Golgi carriers, not lysosomes, confer lysosomal properties to pre-degradative organelles in normal and dystrophic axons. Cell Rep 35, 109034.

Lim, J., Yue, Z., 2015. Neuronal aggregates: formation, clearance, and spreading. Dev Cell 32, 491–501.

Ma, J., Lindquist, S., 2001. Wild-type PrP and a mutant associated with prion disease are subject to retrograde transport and proteasome degradation. Proc Natl Acad Sci U S A 98, 14955–60.

Macia, E., Ehrlich, M., Massol, R., Boucrot, E., Brunner, C., Kirchhausen, T., 2006. Dynasore, a cell-permeable inhibitor of dynamin. Dev Cell 10, 839–50.

Maday, S., Holzbaur, E.L., 2016. Compartment-Specific Regulation of Autophagy in Primary Neurons. J Neurosci 36, 5933–45.

Marijanovic, Z., Caputo, A., Campana, V., Zurzolo, C., 2009. Identification of an intracellular site of prion conversion. PLoS Pathog 5, e1000426.

Massignan, T., Biasini, E., Lauranzano, E., Veglianese, P., Pignataro, M., Fioriti, L., Harris, D.A., Salmona, M., Chiesa, R., Bonetto, V., 2010. Mutant prion protein expression is associated with an alteration of the Rab GDP dissociation inhibitor alpha (GDI)/Rab11 pathway. Mol Cell Proteomics 9, 611–22.

McClure, C., Cole, K.L., Wulff, P., Klugmann, M., Murray, A.J., 2011. Production and titering of recombinant adeno-associated viral vectors. J Vis Exp e3348.

Medori, R., Tritschler, H.J., LeBlanc, A., Villare, F., Manetto, V., Chen, H.Y., Xue, R., Leal, S., Montagna, P., Cortelli, P., 1992. Fatal familial insomnia, a prion disease with a mutation at codon 178 of the prion protein gene. The New England Journal of Medicine 326, 444–9.

Medrano, A.Z., Barmada, S.J., Biasini, E., Harris, D.A., 2008. GFP-tagged mutant prion protein forms intra-axonal aggregates in transgenic mice. Neurobiol Dis 31, 20–32.

Mironov, A., Latawiec, D., Wille, H., Bouzamondo-Bernstein, E., Legname, G., Williamson, R.A., Burton, D., DeArmond, S.J., Prusiner, S.B., Peters, P.J., 2003. Cytosolic prion protein in neurons. J Neurosci 23, 7183–93.

Nakagawa, T., Futai, K., Lashuel, H.A., Lo, I., Okamoto, K., Walz, T., Hayashi, Y., Sheng, M., 2004. Quaternary structure, protein dynamics, and synaptic function of SAP97 controlled by L27 domain interactions. Neuron 44, 453–67.

Nazor, K.E., Kuhn, F., Seward, T., Green, M., Zwald, D., Purro, M., Schmid, J., Biffiger, K., Power, A.M., Oesch, B., Raeber, A.J., Telling, G.C., 2005. Immunodetection of disease-associated mutant PrP, which accelerates disease in GSS transgenic mice. EMBO J 24, 2472–80.

Neumann, S., Chassefeyre, R., Campbell, G.E., Encalada, S.E., 2017. KymoAnalyzer: a software tool for the quantitative analysis of intracellular transport in neurons. Traffic 18, 71–88.

Nixon, R., Camicioli, R., Jamison, K., Cervenakova, L., Mastrianni, J.A., 2000. The PRNP-V180I mutation is associated with abnormally glycosylated PrPCJD and Intracellular PrP accumulations. Presented at XIVth International Congress of Neuropathology Scientific Programme. Brain Pathol. 10, 670.

Overly, C.C., Hollenbeck, P.J., 1996. Dynamic organization of endocytic pathways in axons of cultured sympathetic neurons. J Neurosci 16, 6056–64.

Overly, C.C., Lee, K.D., Berthiaume, E., Hollenbeck, P.J., 1995. Quantitative measurement of intraorganelle pH in the endosomal-lysosomal pathway in neurons by using ratiometric imaging with pyranine. Proc Natl Acad Sci U S A 92, 3156–60.

Owen, F., Poulter, M., Collinge, J., Leach, M., Lofthouse, R., Crow, T.J., Harding, A.E., 1992. A dementing illness associated with a novel insertion in the prion protein gene. Brain Res Mol Brain Res 13, 155–7.

Pamarthy, S., Kulshrestha, A., Katara, G.K., Beaman, K.D., 2018. The curious case of vacuolar ATPase: regulation of signaling pathways. Mol Cancer 17, 41.

Plate, L., Cooley, C.B., Chen, J.J., Paxman, R.J., Gallagher, C.M., Madoux, F., Genereux, J.C., Dobbs, W., Garza, D., Spicer, T.P., Scampavia, L.,

Brown, S.J., Rosen, H., Powers, E.T., Walter, P., Hodder, P., Wiseman, R.L., Kelly, J.W., 2016. Small molecule proteostasis regulators that reprogram the ER to reduce extracellular protein aggregation. eLife 5, e15550.

Pols, M.S., van Meel, E., Oorschot, V., ten Brink, C., Fukuda, M., Swetha, M.G., Mayor, S., Klumperman, J., 2013. hVps41 and VAMP7 function in direct TGN to late endosome transport of lysosomal membrane proteins. Nat Commun 4, 1361.

Prusiner, S.B., 2013. Biology and genetics of prions causing neurodegeneration. Annu Rev Genet 47, 601–23.

Pu, J., Schindler, C., Jia, R., Jarnik, M., Backlund, P., Bonifacino, J.S., 2015. BORC, a multisubunit complex that regulates lysosome positioning. Dev Cell 33, 176-88.

Saalfeld, S., Fetter, R., Cardona, A., Tomancak, P., 2012. Elastic volume reconstruction from series of ultra-thin microscopy sections. Nat Methods 9, 717–20.

Sage, D., Donati, L., Soulez, F., Fortun, D., Schmit, G., Seitz, A., Guiet, R., Vonesch, C., Unser, M., 2017. DeconvolutionLab2: An open-source software for deconvolution microscopy. Methods 115, 28–41.

Satpute-Krishnan, P., Ajinkya, M., Bhat, S., Itakura, E., Hegde, R.S., Lippincott-Schwartz, J., 2014. ER stress-induced clearance of misfolded GPI-anchored proteins via the secretory pathway. Cell 158, 522–33.

Sekine-Aizawa, Y., Huganir, R.L., 2004. Imaging of receptor trafficking by using alpha-bungarotoxin-binding-site-tagged receptors. Proc Natl Acad Sci U S A 101, 17114–9.

Senatore, A., Colleoni, S., Verderio, C., Restelli, E., Morini, R., Condliffe, S.B., Bertani, I., Mantovani, S., Canovi, M., Micotti, E., Forloni, G., Dolphin, A.C., Matteoli, M., Gobbi, M., Chiesa, R., 2012. Mutant PrP suppresses glutamatergic neurotransmission in cerebellar granule neurons by impairing membrane delivery of VGCC alpha(2)delta-1 Subunit. Neuron 74, 300–13.

Shim, S.Y., Karri, S., Law, S., Schatzl, H.M., Gilch, S., 2016. Prion infection impairs lysosomal degradation capacity by interfering with rab7 membrane attachment in neuronal cells. Sci Rep 6, 21658.

Sikorska, B., Liberski, P.P., Giraud, P., Kopp, N., Brown, P., 2004. Autophagy is a part of ultrastructural synaptic pathology in Creutzfeldt-Jakob disease: a brain biopsy study. Int J Biochem Cell Biol 36, 2563–73.

Small, S.A., Petsko, G.A., 2020. Endosomal recycling reconciles the Alzheimer's disease paradox. Sci Transl Med 12, eabb1717.

Stokin, G.B., Lillo, C., Falzone, T.L., Brusch, R.G., Rockenstein, E., Mount, S.L., Raman, R., Davies, P., Masliah, E., Williams, D.S., Goldstein, L.S., 2005. Axonopathy and transport deficits early in the pathogenesis of Alzheimer's disease. Science 307, 1282–8.

Subach, F.V., Patterson, G.H., Manley, S., Gillette, J.M., Lippincott-Schwartz, J., Verkhusha, V.V., 2009. Photoactivatable mCherry for high-resolution two-color fluorescence microscopy. Nat Methods 6, 153–9.

Takalo, M., Salminen, A., Soininen, H., Hiltunen, M., Haapasalo, A., 2013. Protein aggregation and degradation mechanisms in neurodegenerative diseases. Am J Neurodegener Dis 2, 1–14.

van Weering, J.R.T., Scheper, W., 2019. Endolysosome and Autolysosome Dysfunction in Alzheimer's Disease: Where Intracellular and Extracellular Meet. CNS Drugs 33, 639–648.

Vaquer-Alicea, J., Diamond, M.I., 2019. Propagation of Protein Aggregation in Neurodegenerative Diseases. Annu Rev Biochem 88, 785–810.

Veith, N.M., Plattner, H., Stuermer, C.A., Schulz-Schaeffer, W.J., Burkle, A., 2009. Immunolocalisation of PrPSc in scrapie-infected N2a mouse neuroblastoma cells by light and electron microscopy. Eur J Cell Biol 88, 45–63.

Velier, J., Kim, M., Schwarz, C., Kim, T.W., Sapp, E., Chase, K., Aronin, N., DiFiglia, M., 1998. Wild-type and mutant huntingtins function in vesicle trafficking in the secretory and endocytic pathways. Exp Neurol 152, 34–40.

Vidyadhara, D.J., Lee, J.E., Chandra, S.S., 2019. Role of the endolysosomal system in Parkinson's disease. J Neurochem 150, 487–506.

Wadsworth, J.D., Hill, A.F., Beck, J.A., Collinge, J., 2003. Molecular and clinical classification of human prion disease. Br Med Bull 66, 241–54.

Yim, Y.I., Park, B.C., Yadavalli, R., Zhao, X., Eisenberg, E., Greene, L.E., 2015. The multivesicular body is the major internal site of prion conversion. J Cell Sci 128, 1434–43.

Zavodszky, E., Hegde, R.S., 2019. Misfolded GPI-anchored proteins are escorted through the secretory pathway by ER-derived factors. eLife 8, e46740.

3

Mutant Prion Protein Endoggresomes are Hubs for Local Axonal Organelle-Cytoskeletal Remodeling

Content

3.1 Introduction **118**

3.2 Materials and Methods **121**

3.2.1 Quantitative analysis of cargo motility in whole axons 123

3.2.2 Single-particle tracking (SPT) of mitochondria 123

3.2.3 Quantitative analysis of local cargo motility disruption 123

3.2.4 Quantitation of kinesin-1 and kinesin-3 fluorescence intensity 124

3.2.5 Sub-pixel colocalization analysis 124

3.2.6 Fluorescence Recovery After Photobleaching (FRAP) 125

3.2.7 Super-resolution Radial Fluctuation (SRRF) Microscopy 125

3.2.8 STORM sample preparation and imaging 125

3.2.9 Membrane-extraction SEM (ME-SEM) preparation and imaging 126

3.2.10 TMRE Assay 127

3.2.11 Correlative fluorescence and FIBSEM preparation and imaging 128

3.2.12 Figure plotting and statistical analyses 131

3.3 Results **132**

3.3.1 Axonal transport of neuronal cargoes is differentially impaired in axons with PrP^{PG14} endoggresomes 132

3.3.2 Micro-movement analysis reveals local transport jams at axonal PrP^{PG14} aggregate sites 137

3.3.3 Local alterations to the actin and MT cytoskeletal organization at PrP^{PG14} aggregate sites, revealed at super-resolution 139

3.3.4 Selective retention of kinesin-1 and kinesin-3 at PrP^{PG14} aggregate sites and depletion from cargoes 143

3.3.5 Retention of kinesin-1 at PrP^{PG14} aggregate sites requires its cargo-binding regulatory domain 147

3.3.6 Enhanced mitochondrial fission at PrP^{PG14} aggregate sites requires Rab7 GTPase activity 150

3.3.7 Dysfunctional mitochondria are retained at PrP^{PG14} aggregate sites 153

3.3.8 Correlative fluorescence and FIB-SEM of PrP^{PG14} aggregate sites revealed organelle-cytoskeletal remodeling in situ 154

3.4 Conclusion and discussions 157

3.5 References 163

3.1 Introduction

Many neurodegenerative diseases—including Alzheimer's disease (AD), Huntington's disease (HD), Parkinson's disease (PD), amyotrophic lateral sclerosis (ALS), and prion diseases (PrDs)—show axonal pathologies at the early stages (Burgess and Crish, 2018, Lim and Yue, 2015, Stokin et al., 2005, Li et al., 2001). Specifically, misfolded proteins implicated in these diseases are observed at axonal swelling sites and are proposed to disrupt axonal function via poisoning of axonal transport (Gunawardena et al., 2003, Lee et al., 2004), by trapping of organelles and cytoskeletal proteins, or by causing damage to mitochondria (Alexiou et al., 2018, Abramov et al., 2017, Choi et al., 2014). Axonal defects are thought to be an early pathological event in neurodegeneration that precede clinical manifestations (Stokin et al., 2005, Deckwerth and Johnson, 1994, Adalbert and Coleman, 2013). Yet, the mechanisms leading to axonal demise in many neurodegenerative diseases are largely undefined.

In **Chapter 2**, I described the biogenesis pathway of neurotoxic aggregates within enlarged endolysosomes called endoggresomes (Chassefeyre et al., 2021). In addition to endolysosome accumulation, axonal swellings of cultured primary neurons that express mutant prion protein (PrP^{PG14}) (Owen et al., 1992) also contain multiple mitochondria. The buildup of multiple membrane-bound organelles in axons could be a sign of the axonal cytoskeletal and trafficking systems breakdown. Whether these features of axonopathies are initiated by misfolded aggregates of PrP^{PG14} at localized regions, remains unexplored.

Axonal transport mechanism allows the distribution of proteins and organelles over long distances to distal synaptic sites (Chassefeyre et al., 2021,

Kuijpers et al., 2021). The coordinated activities of kinesin-1 and dynein drive the anterograde and retrograde movement of cargoes along microtubule (MT) tracks that are uniformly polarized as plus-end-out in the axon (Maday and Holzbaur, 2014). Axonal transport regulation is achieved partly by post-translational modifications (PTMs) of tubulin, including acetylation and detyrosination, that impart MT track stability and provide signals for the specific recruitment of MT associated proteins (MAPs) and molecular motors (Song and Brady, 2015, Janke and Magiera, 2020, Maday et al., 2014). An intact axonal transport system is critical for the delivery of mitochondria to distal axons to keep up with the demand for energy production and calcium buffering near the synapses (Schwarz, 2013). Mitochondria also undergo fusion/fission dynamics, to ensure the maintenance of functional pool of mitochondria in axons in response to stress signals (Youle and van der Bliek, 2012). Imbalance of mitochondrial fission dynamics is implicated in the PrD pathophysiology (Zhu et al., 2018, Shields et al., 2021). Still, it is unclear if and how PrP^{PG14} endoggresomes directly drive mitochondrial dysfunction in axons.

In this Chapter, I dissect the subcellular events that occur within local axonal swelling sites that contain enlarged PrP^{PG14} endoggresomes in primary hippocampal neurons in culture. I found that axonal swelling sites that contain enlarged endoggresomes are hubs of MT breakdown and organelle accumulation. A cascade of disruption to molecular motor-dependent movement of mitochondria, synaptic vesicle precursors, and endosomes ensues uniquely affecting their transport toward the axon termini. Axonal swellings sites trap molecular motors in addition to their cargoes Rab7-containing late endosomes (LEs) and mitochondria that are retained, resulting in elevated mitochondrial fission and dysfunction, dependent on Rab7 GTP hydrolysis activity. These

observations position axonal swelling sites containing PrP endoggresomes as axonotoxicity hubs that unleash cascades of selective cytoskeletal and motor destabilization, trigger disruptions in axonal transport of important organelles that move towards the synapse, and these sites are magnets for LE-mitochondrial contacts that promote mitochondrial fission and quality control dysfunction. Importantly, pathological features observed within the local axonal domains occur early following the initial expression of mutant PrP. Thus, the localized eddies of impairments that occur within axonal swelling sites in axons could be initiating sites that trigger axonal demise. The follow-up from this study could aim to test if the cytoskeletal and organelle-contact dysfunction pathways are potential targets of early intervention for the therapeutic development aimed at reversing local axonal deficits in the prionopathies.

3.2 Materials and Methods

Mouse primary neuronal culture was described in **Chapter 2** (Materials and Methods 2.2.1). The transfection and transduction of DNA constructs were described in **Chapter 2** (Materials and Methods 2.2.2). The following constructs were used in **Chapter 3**: PrP^{WT}-EGFP and PrP^{PG14}-EGFP in the MoPrP.Xho vector (Borchelt et al., 1996) were a gift from David A. Harris (Medrano et al., 2008). PrP^{WT}-mCh, PrP^{PG14}-mCh, PrP^{WT} -mTagBFP2, PrP^{PG14}-mTagBFP2 fusions were cloned by assembly PCR to replace EGFP as described previously (Chassefeyre et al., 2021). Synaptophysin-YFP (SYP-YFP) in cEGFP vector was a gift from Ann Marie Craig (Harms et al., 2005). Mito-EGFP in pcDNA3 vector was a gift from Christine Vande Velde (Vande Velde et al., 2011). Mito-mTagBFP2 was cloned by replacing EGFP in mito-EGFP with mTagBFP2 sequence in pcDNA3.1 from mTagBFP2-Lysosome-20 (Addgene #55308). KIF5C(1-560)-2xmCh-EF(C) (Addgene #61664) and KIF5C(1-560)-mCit (Addgene #61676) were a gift from Kristen Verhey (Norris et al., 2014). 2xmCh-KIF5C in pcDNA3.1 was cloned by inserting in-frame KIF5C full length from EGFP-KIF5C (a gift from Anthony Brown) 2xmCh sequence from KIF5C(1-560)-2xmCh-EF(C) into pcDNA3.1 using InFusion Cloning kit (Takara). EGFP-Rab7A (Addgene #28047) and EGFP-Rab7A Q67L (Addgene #28049) were a gift from Qing Zhong. SNAP-Rab7A and SNAP-Rab7A Q67L were made by cloning Rab7A sequence from EGFP-Rab7A and EGFP-Rab7A Q67L plasmids into pSNAP-tag (m) Vector (Addgene #101135). Soluble BFP (mTagBFP2) in pcDNA3.1 was derived from mTagBFP2-Lysosome-20 (Addgene #55308). Soluble EGFP (pEGFP-C1 plasmid) was a gift from Hilal Lashuel. Soluble mCherry (pmCherry-N3 plasmid) was cloned from pmCherry-mito-7 (Addgene #55102). *Kif1a* and *scrambled* shRNAs were part of a kinesin lentiviral mini-

library, in a pLL3.7 GW lentiviral vector with Gateway entry modifications and a mCherry co-expression marker (unpublished data). The knockdown efficacy of *Kif1a* shRNA was evaluated by Western blot and qPCR from lysates of cultured hippocampal neurons transduced with lentivirus containing *Kif1a* shRNA-expressing plasmids (Campbell, 2018).

Immunofluorescence (IF) of cultured primary neurons was described in **Chapter 2** (Materials and Methods 2.2.5). The following primary antibodies were used for immunofluorescence (IF) in this Chapter: mouse anti-KHC (clone H2; MAB1614; recognizes primarily KIF5C (Encalada et al., 2011)) (1:100, EMD Millipore); goat anti-KLC1 (V-17) (1:100, Santa Cruz Biotechnology); mouse anti-KIF1A (16/KIF1A) (1:100; BD Transduction Laboratory); mouse anti-alpha-tubulin (DM1A) (1:2000; Sigma-Aldrich); mouse anti-Acetylated tubulin (1:400; Sigma-Aldrich); rat anti-Tyrosinated tubulin [YL1/2] (1:1000; Abcam). The concentration of Goat anti-KLC1 (V-17) was validated previously for sub-pixel colocalization analysis (Encalada et al., 2011). The concentration of mouse anti-KHC and mouse anti-KIF1A were also validated for sub-pixel colocalization analysis (Campbell, 2018). All tubulin antibodies were validated previously to be suitable for IF for super-resolution imaging (Tas et al., 2017). The following secondary antibodies were used for IF: Donkey anti-goat IgG (H+L) Alexa Fluor 488 (1:200; ThermoFisher; A-11055); Goat anti-mouse Atto647N (1:200 Sigma); Goat anti-rat Atto594 (1:200; Rockland Immuno); Alexa Fluor 647 Phalloidin in methanol (1:40; Invitrogen)

3.2.1 Quantitative analysis of cargo motility in whole axons

I analyzed single-particle motility of cargoes using *KymoAnalyzer* as described in **Chapter 2** and published work (Neumann et al., 2017). Briefly, I generated kymographs from time-lapse movies. I assigned particle trajectories manually from the kymograph images. The software automatically calculated the track and segment-related parameters.

3.2.2 Single-particle tracking (SPT) of mitochondria

I performed SPT of mito-EGFP using *TrackMate*, a Fiji (ImageJ) plugin (Tinevez et al., 2017). The Laplacian of Gaussian (LoG) filter, median filter, and sub-pixel localization were used to detect the blobs with diameter between 1-3 µm, determined empirically, and the auto-threshold was applied on the detected feature quality. In **Figure 3.2**, I used the hyperstack displays of tracks analyzed by LAP Tracker algorithm (Jaqaman et al., 2008) with pseudo color coding based on median velocity or local displacement. For this, the frame-to-frame linking maximum distance was set to 15 µm. Gap closing, segment splitting and merging were disabled.

3.2.3 Quantitative analysis of local cargo motility disruption

In addition to SPT, I analyzed the local transport disruption of cargoes manually. I defined the AGG sites as a 10-µm window in axonal sites that contain fluorescence intensities above the average grey value of five individual PrP^{PG14} particles. NON-AGG sites are defined by a 10-µm window along axonal length that do not contain particles that had fluorescence intensities above the average grey value of five fluorescently labelled PrP^{PG14} particles. I categorized the particle trajectories into 3 groups: (1) 'pass tracks' on kymographs are defined as diagonal tracks that cross AGG/NON-AGG sites without any change in slope.

(2) Pause/Slowdown tracks are defined as diagonal tracks that cross AGG/NON-AGG sites with any change in slope. (3) Stall tracks are defined as stationary tracks with slope equal to 0 at AGG/NON-AGG sites.

3.2.4 Quantitation of kinesin-1 and kinesin-3 fluorescence intensity

KHC was detected with a validated antibody (Encalada et al., 2011), and analyzed in Fiji software. The normalized fluorescence intensity was calculated from averaged gray values of antibody staining in AGG, NON-AGG, or WT sites, subtracted by background fluorescence per image. I selected the analysis regions with an unbiased method, by making ROIs from the PrP channel to analyze the gray values from the antibody channels automatically in batch.

3.2.5 Sub-pixel colocalization analysis

Single-pixel detection and colocalization analysis were done as described previously (Encalada et al., 2011, Szpankowski et al., 2012). All primary and secondary antibodies used in this Chapter were validated for specificity and determined the working concentration by plotting a saturation curve. The 0.1μm Tetraspeck beads (Invitrogen) were used to perform registration, to check and correct for chromatic aberrations between channels. Secondary antibody-only controls were performed in all experiments. In brief, fluorescence images were processed in MATLAB for kinesin-1 and kinesin-3 composition on PrP^{WT} and PrP^{PG14} vesicles. To determine kinesin-1 and kinesin-3 composition on mitochondrial surface, the ROIs were drawn around mito-EGFP signal and transferred to the image output from MATLAB, open in Fiji. I counted the number of motor clusters on mitochondria manually.

3.2.6 Fluorescence Recovery After Photobleaching (FRAP)

I performed the FRAP of KIF5C(1-560)-mCit at the axon termini of DIV5 neurons. Briefly, I collimated a 405-nm laser and focused on an ROI. I determined the laser power and exposure time of FRAP empirically to ensure complete bleaching but avoid phototoxicity to axonal growth cones. For the acquisition, 5 images were taken prior photobleaching (1 frame/sec), followed by a photobleaching period of 3-5 seconds, and then 300 images were collected after photobleaching (1 frame/sec) for FRAP analysis. Before and after images were combined in the Nikon Elements software, and fluorescence intensity plots over time were made and analyzed in Fiji. Half-life ($t_{1/2}$) of FRAP was calculated by fitting one-component exponential curve in FRAP profiler ImageJ plugin (http://worms.zoology.wisc.edu/ImageJ/FRAP_Profiler_v2.java).

3.2.7 Super-resolution Radial Fluctuation (SRRF) Microscopy

I performed SRRF processing using NanoJ-SRRF ImageJ plugin (https://github.com/HenriquesLab/NanoJ-SRRF) as described previously (Culley et al., 2018). Briefly, I collected 100 images at 50 frames/sec to be reconstructed into a single SRRF image. SRRF parameters were set as default (ring radius = 0.5; radiality magnification = 5; axes in ring = 6), and the drift correction was applied.

3.2.8 STORM sample preparation and imaging

For direct STORM imaging experiments on hippocampal neurons, I acid pre-washed the glass bottom dishes (MatTek) to minimize background. Neurons were transfected with PrP^{PG14}-mCh at DIV7 and fixed at DIV9 with 3% PFA, 0.1% Glutaraldehyde (GA), 10% sucrose in PBS. Neurons were briefly permeabilized in 0.1% Tx-100 for 8 minutes, washed in PBS several times, and were incubated in

0.5 µM of Phalloidin-AF647 in PBS overnight at 4°C. Neurons were washed again in the next day and kept in PBS at 4°C until imaging.

The STORM buffer (50 mM TRIS, 10 mM NaCl, 0.5 mg/mL glucose oxidase, 40 µg/mL catalase, 10% glucose, 100 mM β-mercaptoethanol) was prepared according to N-STORM Protocol (Nikon, 2013). The freshly-made STORM buffer was applied on the fixed sample in MatTek dish, sealed tightly, and imaged on the Nikon inverted system equipped with 640-nm laser and the 100X/1.49NA TIRF Objective. At least 10,000 raw images were taken with sufficient blinking using the Nikon N-STORM acquisition settings, and these images were reconstructed into a STORM image using ThunderSTORM ImageJ plugin (Ovesny et al., 2014). The chosen display mode was based on an average shifted histogram approach that provides similar results as conventional Gaussian rendering in the Nikon software.

3.2.9 Membrane-extraction SEM (ME-SEM) preparation and imaging

Neurons were plated on sterile gridded glass bottom MatTek dishes. Neurons were transfected with PrP^{PG14}-mCh at DIV7 following previously described protocol, and the membrane extraction was performed directly on live cells at DIV9 (2 days post-transfection).

Initially, to test this protocol, I imaged live neurons with 20X/0.45NA objectives in the phase contrast mode, and I used 561-nm laser to find a transfected neuron and its grid coordinates. I started time-lapse imaging, and the growth media in the sample mounted on the microscope was replaced immediately with a membrane extraction solution (1% Triton X-100, 100 mM PIPES (pH 7.2), 4% sucrose, 1 mM $MgCl_2$, 10 µM taxol and 10 µM phalloidin) as

previously (Fernandes et al., 2011a). I stopped the acquisition to make sure that the primary neurons remained attached to the glass bottom dish, while all the membranes were gone. After 20 minutes, I washed the neurons three times with PBS gently to remove membrane debris from the sample. Neurons were fixed immediately afterward with 2% glutaraldehyde, 4% paraformaldehyde, 140 mM NaCl, 2 mM $CaCl_2$, 1 mM $MgCl_2$, 0.1 M HEPES (pH 7.2) for 30 minutes. I transferred the samples at this stage to further process at the Salk Institute by Leonardo R. Andrade. Neurons were post-fixed with 1% OsO_4 for 1 hour, and 1% tannic acid for 1 hour, then neurons were dehydrated with ethanol and critical point-dried from CO_2 (CPD 020 Balzers-Tec). The coverslips were then coated with a 8-nm thin carbon layer (BAF 300, Balzers) (Fernandes et al., 2011a) for imaging on Zeiss SIGMA Variable Pressure Field Emission Gun Scanning Electron Microscope (SEM). The 20x fluorescence images with the grid position and SEM micrographs were aligned manually on Adobe Illustrator.

3.2.10 TMRE Assay

I performed an assay using tetramethylrhodamine, ethyl ester (TMRE) dye kit to test mitochondrial function in culture. Neurons were grown on the coverslip and transfected at DIV7 as described previously. At 2 days post-transfection (DIV9), I treated neurons with 25 nM TMRE in the growth media for 20 minutes at 37°C, following a previously published protocol (Lin et al., 2017). Neurons were washed briefly 1 time in pre-warm PBS and replaced with the growth media to perform live imaging. Live imaging was done with 3-color simultaneous acquisition at 0.5 frame/sec on the OptoSplit III on the Nikon inverted system.

3.2.11 Correlative fluorescence and FIBSEM preparation and imaging

Hippocampi were dissected from P0 to P2 mouse neonates in cold Hanks' balanced salt solution (HBSS) (Gibco) supplemented with 0.08% d-glucose (Sigma-Aldrich), 0.17% HEPES, and 1% penicillin-streptomycin (Pen-Strep) (Gibco) (filter-sterilized and adjusted to pH 7.3). Dissected hippocampi were washed twice with cold HBSS (Gibco) and individually incubated at 37°C for 20 min in a sterile solution of 45 U of papain (Worthington), 0.01% deoxyribonuclease (DNase) (Sigma-Aldrich), 1 mg of dl-cysteine (Sigma-Aldrich), 1 mg of bovine serum albumin (BSA) (Sigma-Aldrich), and 25 mg of d-glucose (Sigma-Aldrich) in phosphate-buffered saline (PBS) (Gibco). Hippocampi were washed twice with Dulbecco's modified Eagle's medium (DMEM) (Gibco) supplemented with 10% fetal bovine serum (FBS) (Gibco) (preheated to 37°C) and disrupted by 10 to 12 cycles of aspiration through a micropipette tip. Dissociated neurons were then resuspended in warm DMEM (Gibco) supplemented with 10% FBS (Gibco) and plated on 3-mm sapphire coverslips in 35-mm MatTek dish with 20-mm glass diameter pretreated with poly-L-lysine (200 μg/ml) (Sigma-Aldrich) in borate buffer [1.24 g of boric acid (Thermo Fisher Scientific) and 1.90 g of borax (Sigma-Aldrich) in 500 ml of cell culture-grade water, adjusted to pH 8.5, and filter-sterilized]. After 1 hour, the medium was replaced with Neurobasal-A medium (Gibco), supplemented with 2% B-27 (Gibco) and 0.25% GlutaMAX (Gibco). Primary neurons were maintained in an incubator at 37°C and in a 5.5% CO_2 atmosphere.

At Day *In Vitro* (DIV) 7, hippocampal neurons were transiently transfected using Lipofectamine 3000 (Thermo Fisher Scientific), following the

manufacturer's instructions. DNA and Lipofectamine were diluted in Neurobasal-A medium (Gibco). Neurons grown on 3-mm sapphire coverslips in 35-mm MatTek dish with 20-mm glass diameter were transfected using 5 μl of Lipofectamine 3000, 5 μl of P3000, 2.5 μg PrP(WT)-mEmerald or PrP(PG14)-mEmerald, 1.25 μg Rab7-SNAP or Rab7(Q67L)-SNAP, and 0.6 μg Mito-DsRed per MatTek dish.

At DIV9, neurons were stained with JF646-SNAP (0.8 μM) in Neurobasal-A medium (Gibco), supplemented with 2% B-27 (Gibco) for 1 hour at 37°C, and then washed three times with the above medium for 5 min, followed by one more wash for 30 min. Then, neurons were fixed with 0.8% paraformaldehyde (PFA; Electron Microscopy Services) and 0.2% glutaraldehyde (Electron Microscopy Services) in 0.1 M phosphate buffer (pH 7.2) for 30 min at RT. Cells were washed once in 25 mM glycine in water for 15 min. Fixed neurons were then stored in PBS at 4°C until fluorescence imaging.

Fixed neurons were imaged with ZEISS LSM 980 with Airyscan 2, using a C-Apochromat, 40X/1.2 NA Water Korr FCS Objective. Solid-state 488-, 561-, and 647-nm lasers were used for detecting mEmerald, DsRed, and JF646-SNAP, respectively. The zoom factor was 1.7, and pixel sizes were 49.6 nm in xy and 190 nm in z. Airyscan processing was done using "3D Processing" and "Auto Filter", with "Standard" strength.

After fluorescence imaging, neurons were further fixed with 4% PFA (Electron Microscopy Services) and 2.5% glutaraldehyde (Electron Microscopy Services) in 0.1 M sodium cacodylate buffer (pH 7.4) for 30 min at RT. Fixed neurons were then stored in 0.1% glutaraldehyde in 0.1 M sodium cacodylate buffer (pH 7.4) at 4°C.

Then, the samples were prepared as described previously (Hoffman et al., 2020). Samples embedded in Eponate resin were prepared for FIB-SEM by first removing the sapphire disk from the bottom side of the resin block by repeated alternating immersion in warm water and LN2. The newly exposed Epon surface containing cells was then re-embedded in Durcupan resin and allowed to polymerize at 65°C for 48 hours.

Samples were then imaged using a micro–X-ray CT system (XRadia 510, Carl Zeiss X-ray Microscopy, Inc.) to identify the positions of the cells of interest. Fluorescence images taken previously were overlayed onto X-ray images to ensure proper ROI location. Specimens were re-mounted on a copper stud and trimmed using an ultramicrotome (EM UC7, Leica Microsystems), with supplementary X-ray CT imaging to guide the trimming process, until the region to be imaged in EM was contained in a resin "tab" with typical dimensions of ca. 100×100×65 microns. Finally, samples were sputter-coated with 10 nm gold and 100 nm carbon (PECS 682, Gatan) to maintain sample conductivity for EM.

Samples were loaded onto a custom FIB-SEM described previously (Xu et al., 2017a), consisting of a Zeiss Gemini 450 Field Emission SEM and a Zeiss Capella FIB column oriented at 90 degrees to the SEM beam. Samples were subjected to repeated FIB milling and SEM imaging to acquire 3D EM datasets. Images taken at 8×8×8nm pixel resolution were imaged at 500 kHz readout rate, with 1.2kV landing energy at 2.0 nA electron dose. Milling was performed using a 15 nA gallium ion beam source at 30kV. FIB-SEM images were laterally registered with respect to each other using a Python implementation of the SIFT-

alignment algorithm, with constrained full affine transformation (https://github.com/gleb-shtengel/FIB-SEM).

FIBSEM aligned data were visualized in Fiji Plugin BigDataViewer > Open XML/HDF5. The representative slices were preliminary taken to label on Adobe Illustrator.

3.2.12 Figure plotting and statistical analyses

Histograms were plotted in MATLAB (MathWorks), and Gaussian mode mixtures were generated using the Interactive Peak Fitter (ipf.m). Optimal fits were selected empirically based on optimal R^2 values. Box plots were plotted using the web-tool BoxPlotR (http://shiny.chemgrid.org/boxplotr/). Cumulative frequency distribution graphs were plotted using GraphPad Prism. Statistical analyses were performed using Microsoft Excel, GraphPad Prism, and MATLAB. Briefly, we first checked if the parameters were following a normal distribution using the Lilliefors test. For the parameters following a normal distribution (distribution of cargo populations, densities, etc.), we performed a Student's t-test or Tukey's multiple comparisons. Most of the other parameters that did not follow a normal distribution (velocities, run lengths, fluorescence intensity, etc.) were subjected to appropriate non-parametric tests. Differences between two medians were compared using the Wilcoxon rank-sum test, while pair-wise differences between three groups were compared with Kruskal-Wallis test. Differences between two population distribution were compared using Kolmogorov-Smirnov (K-S) test.

3.3 Results

3.3.1 Axonal transport of neuronal cargoes is differentially impaired in axons with PrP^{PG14} endoggresomes

The transient expression of fluorescently-tagged (and untagged) PrP^{PG14} in cultured mouse hippocampal neurons resulted in the accumulation of misfolded PrP^{PG14} aggregates inside endolysosomes—called endoggresomes—at localized axonal swelling sites (Chassefeyre et al., 2021) (**Chapter 2**). PrP^{PG14}-EGFP endoggresome accumulation became significantly different from PrP^{WT}-EGFP vesicles in axons at 12 hours post-transfection, and the densities increased over two days of expression (Chaiamarit et al., 2023). The densities of PrP^{PG14}-EGFP and PrP^{PG14}-mCh endoggresomes were comparable at two days post-expression, and these two constructs were used interchangeably (Chassefeyre et al., 2021). To investigate the impairments to axonal transport function in endoggresome-rich axons, I characterized the axonal transport parameters of three neuronal cargoes—mitochondria, pre-synaptic vesicles, and PrP vesicles—that actively mobilize and that are required to be delivered to the periphery for proper synaptic functions (Tarsa and Goda, 2002, Sheng and Cai, 2012, Encalada et al., 2011). Single-particle transport analyses of these cargoes were performed at high spatial and temporal resolution in axons of neurons co-transfected with PrP^{PG14}-mCh or (PrP^{WT}-mCh control) and either the mitochondrial targeting sequence of Cytochrome c Oxidase subunit VIII fused to EGFP (in short, mito-EGFP) or Synaptophysin fused to YFP (SYP-YFP). Time-lapse live videos were analyzed using a single particle tracking analysis software to analyze transport trajectory, as described previously (Neumann et al., 2017). At two days after co-expression,

the densities of motile mito-EGFP particles were significantly decreased in PrP^{PG14}-mCh axons, compared to PrP^{WT}-mCh control axons (**Figure 3.1A,B**), suggesting defective mitochondrial translocation into the axon. To further test whether the mitochondrial movement dynamics was affected in the presence of endoggresomes, segmental trajectories of mito-EGFP were analyzed at 2 days post-expression and showed that mito-EGFP spent less time moving in the anterograde direction in PrP^{PG14}-mCh endoggresome-rich axons compared to those in PrP^{WT}-mCh control axons (**Figure 3.1C**). These mito-EGFP particles also undertook shorter run lengths (**Figure 3.1D**) and had reduced instantaneous velocities (**Figure 3.1E**) significantly in the anterograde direction towards the synapse. Surprisingly, retrograde transport dynamics of mito-EGFP particles remained unchanged in PrP^{PG14}-mCh endoggresome-rich axons, compared to PrP^{WT}-mCh endoggresome-free axons (**Figure 3.1C-E**). These data show differential deficits in mitochondrial movement uniquely towards the axon termini. Notably, despite gradual accumulation of PrP^{PG14}-mCh endoggresomes from 12 hours post-PrP^{PG14}-mCh expression, mito-EGFP transport was largely comparable to that in PrP^{WT}-mCh control axons (**Figure 3.1A-C**), with an exception in the run lengths (**Figure 3.1D**). These data indicate that mitochondrial transport impairment lags behind but progresses with time alongside PrP^{PG14} aggregation.

Mitochondria utilize kinesin-1 (KIF5/KHC) to translocate anterogradely in axons towards the MT plus-ends at the axon termini (Schwarz, 2013). In addition to kinesin-1 requirement for mitochondrial transport, Nandini Shukla, a postdoc in the Encalada lab, found that a reduction of a neuronally enriched KIF1A (a kinesin-3 family protein) using a validated shRNA resulted in significant impairments to mitochondrial transport, including reduced run lengths

and velocities, compared to those in D11 scrambled shRNA controls (Chaiamarit et al., 2023). This dataset showed that KIF1A is an important driver of mitochondria anterograde movement in axons of hippocampal neurons. As the overall anterograde transport of mito-EGFP was defective upon expression of PrP^{PG14}-mCh, this raises the possibility that both kinesin-1- and kinesin-3-driven transport processes are impaired in endoggresome-containing axons.

We next analyzed the movement of a canonical KIFA cargo, a pre-synaptic vesicles carrying SYP-YFP, an integral membrane protein that is processively trafficked by kinesin-3 motor towards the MT plus-ends and is important for vesicle fusion, synaptic vesicle endocytosis, and recycling at the pre-synapse (Kwon and Chapman, 2011, Okada et al., 1995). Transport trajectories of SYP-YFP vesicles at 2 days after co-transfection with PrP constructs were analyzed using time-lapse fluorescence live imaging at high spatial and temporal resolution (**Figure 3.1F**). In comparison to control axons expression PrP^{WT}-mCh, the percent time that SYP-YFP vesicles spent in anterograde motion in PrP^{PG14}-mCh endoggresome-rich axons was significantly dropped, with increased paused time (**Figure 3.1G**). In addition, SYP-YFP vesicles undertook significantly shorter run lengths in PrP^{PG14}-mCh axons, compared to PrP^{WT}-mCh control axons (**Figure 3.1H**). Similar to mitochondrial transport dynamics, retrograde movement of SYP-YFP vesicles was also unchanged in the endoggresome-rich PrP^{PG14}-mCh axons (**Figure 3.1G-H**). A significantly higher proportion of SYP-YFP vesicles remain stationary in PrP^{PG14}-mCh axons, compared to PrP^{WT}-mCh axons (**Figure 3.1I**), suggesting the overall retention of SYP-YFP transport towards the distal axonal sites.

In addition to the accumulating PrP^{PG14} endoggresomes, axons of neurons expressing PrP^{PG14}-mCh contain motile Golgi-derived PrP^{PG14}-mCh vesicles that are actively transported toward the synapse (**Figure 3.1J**; **Chapter 2**). Transport trajectory analysis showed that two days post-expression with cytosolic marker, the percent anterograde-moving Golgi-derived PrP^{PG14}-mCh vesicles in axons significantly decreased, while the percent of retrograde and stationary populations increased (**Figure 3.1J,K**). These differences were amplified at five days post-expression, especially the time that PrP^{PG14}-mCh vesicles spent in motion in the anterograde direction was significantly decreased, while PrP^{PG14}-mCh vesicles spent more time moving back in the retrograde direction or paused (**Figure 3.1L,M**). Altogether, these data indicated that since the significant accumulation of PrP^{PG14}-mCh endoggresomes 12 hours post-transfection, the gradual progression in transport deficits of PrP^{PG14}-mCh vesicles were seen, while mito-EGFP and SYP-YFP transport became significantly impaired later, at two-day timepoint (**Figure 3.1A-H**). These observations indicate that early transport defects exhibited by PrP^{PG14}-mCh vesicles concur with PrP^{PG14}-mCh endoggresome accumulation in axons, suggesting that the movement of PrP^{PG14}-mCh vesicles that are being removed from the motile vesicle pool in axons might be the substrate of enlarged endoggresome formation (Chassefeyre et al., 2021). Moreover, the differential impairments uniquely to the anterograde movement of mitochondria and pre-synaptic vesicles suggest that anterograde transport is more susceptible to PrP^{PG14} endoggresome accumulation in axons, and these observations raise the possibility of differential impairments to the anterograde transport machinery.

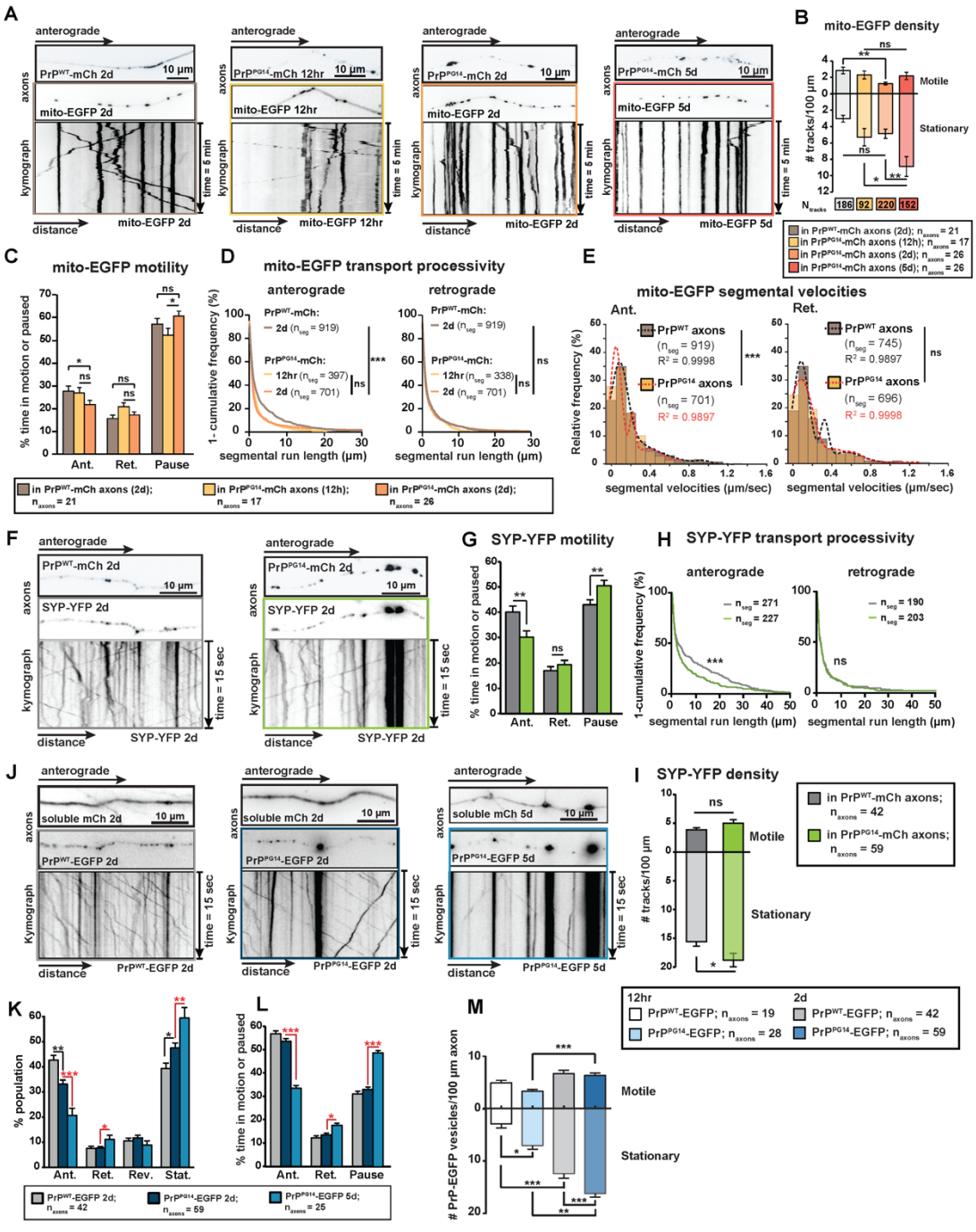


Figure 3.1 Axonal transport is progressively impaired in PrPPG14-mCh axons. **(A)** First-frame images of axons co-transfected with mito-EGFP and PrP^{WT}-mCh or PrP^{PG14}-mCh for 12 hours or 2 days (top two panels) and corresponding kymographs (bottom panel) generated from time-lapse movies (5 minutes, 300 frames, 1 frame/sec). **(B)** Densities of motile (top y-axis) or stationary (bottom y-axis) mito-EGFP. **(C)** Percent time mito-EGFP spends in anterograde (Ant.) or retrograde (Ret.) motion or paused. **(D)** Segmental run lengths of mito-EGFP plotted as 1-

cumulative frequency (%). **(E)** Segmental velocities of mito-EGFP plotted as relative frequency histogram (%) and fitted with multi-peaks Gaussian functions. R2 values indicate the degree of Gaussian fits. **(F)** First-frame images of axons co-transfected with SYP-YFP and PrPWT-mCh or PrPPG14-mCh for 2 days (top two panels) and corresponding kymographs (bottom panel) generated from time-lapse movies (15 seconds, 150 frames, 10 frame/sec). **(G)** Percent time SYP-YFP spends in anterograde (Ant.), or retrograde (Ret.) motion, or paused. **(H)** Segmental run lengths of SYP-YFP plotted as 1-cumulative frequency (%). **(I)** Densities of motile (top y-axis) or stationary (bottom y-axis) SYP-YFP. **(J)** First-frame images of axons co-transfected with soluble mCh and PrP^{WT}-EGFP or PrP^{PG14}-EGFP for 2 or 5 days (top two panels) and corresponding kymographs (bottom panel) generated from time-lapse movies (15 seconds, 150 frames, 10 frame/sec). **(K)** Percent population with anterograde (Ant.), retrograde (Ret.), reversal (Rev.), or stationary (Stat.) tracks. **(L)** Percent time PrP^{WT}-EGFP or PrP^{PG14}-EGFP spend in anterograde (Ant.), or retrograde (Ret.) motion, or paused. **(M)** PrP^{WT}-EGFP or PrP^{PG14}-EGFP densities of motile (top y-axis) or stationary (bottom y-axis) vesicles. All bar graphs are shown as mean ± SEM. ***$p<0.001$, **$p<0.01$, *$p<0.05$, ns = not significant. b, c, k, l, m Student's t-test with Tukey's multiple comparison tests; g, i Student's t-test; d, e, and h Kolmogorov-Smirnov (K-S) test.

3.3.2 Micro-movement analysis reveals local transport jams at axonal PrP^{PG14} aggregate sites

The overall movement of mitochondria in endoggresome-rich axons was impaired resulting in increased densities of stalled mitochondria (**Figure 3.1A-C**), suggesting that PrP^{PG14} endoggresomes directly hindered the movement of mitochondria and retained them within local axonal swelling sites. To test this hypothesis, I used single-particle tracking to quantitate the behavior of individual mitochondria within axonal micro-domain regions at PrP^{PG14} endoggresome-rich aggregates sites (herein referred as 'PrP^{PG14} aggregate sites or AGG) vs non-aggregate regions (NON-AGG) (**Figure 3.2A**). AGG and NON-AGG regions within the same axon were defined as 10-µm wide analysis windows (**Figure 3.2A, D**). At each window, I came up with criteria to quantify percentages of mito-EGFP that (1) passed through AGG sites, (2) paused/slowed down at the AGG sites, and (3) stalled at the AGG sites, compared to those mitochondria in control NON-AGG sites of PrP^{PG14}-mCh-expressing axons, and analyze anterograde versus retrograde movement events (**Figure 3.2A-C**). The results

indicate that about half of the mito-EGFP population stalled along PrP^{PG14}-mCh-expressing axons, with no significant differences between AGG and NON-AGG sites (**Figure 3.2C**). From the population that retained motility, a significantly lesser proportion was able to move through AGG sites without interruption, compared to movement around NON-AGG sites (**Figure 3.2B**). Moreover, a significantly greater proportion of anterograde moving mitochondria paused at- or slowed down as they encounter and mobilize through AGG, compared to NON-AGG sites (**Figure 3.2B**). These data indicate that mitochondria in endoggresome-rich axons experienced local 'traffic jams' at the AGG sites, and the slowdown of motile mitochondria is specific to the anterograde direction. To show the degree of mitochondrial arrest at the AGG sites, mitochondrial micro-movement dynamics were quantified within the AGG or NON-AGG sites and surrounding area of the analysis windows (**Figure 3.2D**). I measured the mean displacement of individual mito-EGFP from their centroid position by the automated single-particle tracking (SPT) algorithm over 5 minutes (**Figure 3.2D**). Compared to NON-AGG regions, SPT analysis revealed that mito-EGFP displacement was largely confined within the 10 µm window, meaning that mitochondria did not move away as far in the endoggresome-rich areas (**Figure 3.2E**). Further analysis of segmental velocities from the same datasets revealed that mito-EGFP at AGG sites moved significantly slower (<0.1 µm/s), compared to those mito-EGFP at NON-AGG sites (**Figure 3.2F**). Altogether, these data imply that the global deficits in axonal transport of mitochondrial along axons originate from endoggresome-rich AGG micro-domains, and that PrP^{PG14} endoggresomes act directly on disrupting cargo transport.

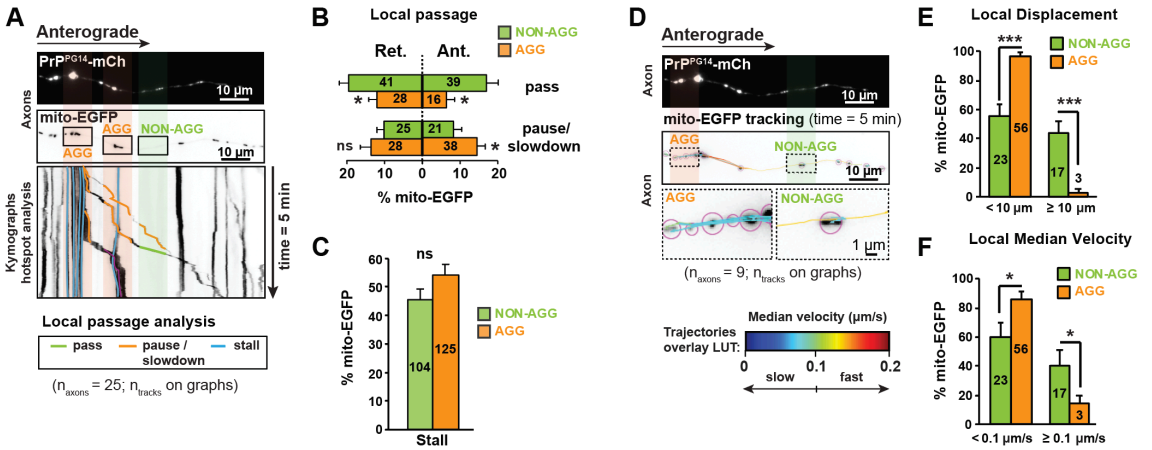


Figure 3.2 Local axonal transport disruption of mito-EGFP micro-movements within PrP^{PG14}-mCh aggregate sites. (A) First-frame images of an axon co-transfected with PrP^{PG14}-mCh (top) and mito-EGFP (middle) and corresponding kymograph from a time-lapse movie (5 minutes, 300 frames, 1 frame/sec) of mito-EGFP transport with color-coded track assignment overlay (green = pass, orange = pause/slowdown, or blue = stall) at AGG and NON-AGG sites. **(B)** Percent number of mito-EGFP that pass or pause/slowdown in anterograde (Ant.; right x-axis) vs retrograde (Ret.; left x-axis) directions at AGG vs NON-AGG sites. **(C)** Percent number of mito-EGFP that are stalled at AGG vs NON-AGG sites. **(D)** First-frame images of an axon co-transfected with PrPPG14-mCh (top) and mito-EGFP (bottom) from time-lapse movies (5 minutes, 300 frames, 1 frame/sec). Dotted rectangles outline 10 µm-wide PrPPG14 aggregate sites (AGG) or non-aggregate control sites (NON-AGG). Rainbow LUT pseudo color-coded overlays indicate median velocities ranges of tracks at AGG and NON-AGG regions (insets). **(E)** Percent number of mito-EGFP trajectories at AGG vs NON-AGG sites with track displacements of < 10 µm or ≥ 10 µm during a 5-minute acquisition period. **(F)** Percent number of mito-EGFP at AGG vs NON-AGG sites with median velocity of < 0.1 µm/s or ≥ 0.1 µm/s during the 5-minute acquisition. All bar graphs are shown as mean ± SEM. ***p<0.001, **p<0.01, *p<0.05, ns = not significant. **(B), (C), (E), (F)** Student's t-test. Number of tracks are shown inside bar graphs. All analyses were done on axons after 2 days of PrP^{PG14}-mCh transfection.

3.3.3 Local alterations to the actin and MT cytoskeletal organization at PrP^{PG14} aggregate sites, revealed at super-resolution

The cylindrical shape of the axon is supported by a regularly spaced actin-spectrin lattice below the plasma membrane, and by MT bundles that line up along the length of the axon (Zhong et al., 2014, Yogev et al., 2016). An intact actin and MT cytoskeletal organization is key to healthy, regulated axonal transport dynamics (Yogev et al., 2016, Kevenaar and Hoogenraad, 2015). To

investigate the mechanisms of transport impairments at AGG sites (**Figure 3.1**), I tested the hypothesis that the actin and MT cytoskeletal integrity is impaired at the endoggresome-rich axonal swellings. The ultrastructure of actin and MT tracks inside axons was visualized using high-resolution fluorescence and scanning electron microscopy (SEM) of cultured neurons grown on gridded coverslips, to facilitate the correlative image analysis of the same axonal regions. These neurons were transfected with PrP^{PG14}-mCh for two days, and then subjected to a membrane-extraction (ME) protocol to remove lipid membrane, while retaining MT and actin with stabilizing drugs (Fernandes et al., 2011b), and then imaged with SEM. I mapped the position of individual PrP^{PG14}-mCh endoggresomes within axons (**Figure 3.3A**) and investigated SEM micrographs of these sites. ME-SEM showed accumulation of unidentified ring-like structures that could be either actin or PrP^{PG14}-mCh aggregates or both that survived the sample preparation (**Figure 3.3A**). Similar ring-like structures of actin signal were observed using direct stochastic optical reconstruction microscopy (dSTORM) imaging of Phalloidin-AF647 at the endoggresome-rich axonal swellings (**Figure 3.3B**). These results suggest that the recruitment of actin to PrP^{PG14} endoggresomes could take part directly or indirectly in the endoggresome formation and local organelle transport jams.

ME-SEM at axonal swellings also revealed deformed MT bundles that followed the contour of the swellings, as well as broken MTs that curled up and broke at AGG sites, while NON-AGG neighboring axonal regions had straight MT bundles (**Figure 3.3A**). These observations were confirmed using 3D super-resolution (SR)-Airyscan imaging of α-tubulin antibody that showed frequent curved MT tracks around at AGG sites in contrast to straight MT tracks

observed at NON-AGG sites (**Figure 3.3A,C**). MT stability is imparted by post-translational modifications (PTMs) to tubulin (Atherton et al., 2013). Acetylation of α-tubulin is a common PTM in neuronal axonal MTs that confers MT stability and protects MTs from breakage under mechanical stress (Xu et al., 2017b). Acetylated MT tracks are preferred by kinesin-1 motor for motility (Cai et al., 2009, Konishi and Setou, 2009, Reed et al., 2006). In contrast, tyrosinated (unmodified) MT tracks, often associated with kinesin-3, are less stable than the acetylated counterparts, and these tracks might be prone to breakage upon stress or by large PrP endoggresomes (Guardia et al., 2016, Tas et al., 2017, Guedes-Dias et al., 2019). The observations of bending and breaking MTs prompted me to follow up and test whether differentially impaired MT tracks at the AGG sites are decorated with different PTMs. To this end, PrP^{PG14}-mCh-expressing axons were immunostained with previously validated tubulin PTM antibodies that recognize acetylated vs tyrosinated residues. 3D SR-Airyscan and super-resolution radial fluctuation (SRRF) imaging (Culley et al., 2018) revealed that the majority of acetylated MT tracks bent or remained undisrupted while tyrosinated MT tracks broke at AGG sites, compared to NON-AGG sites (**Figure 3.3D-G**). Overall, these results suggest the remodeling of actin and MTs at the axonal swelling sites containing PrP^{PG14} endoggresomes. Furthermore, MT tracks with PTMs that confer properties for kinesin-1 and kinesin-3-mediated transport are differential disrupted locally at AGG sites.

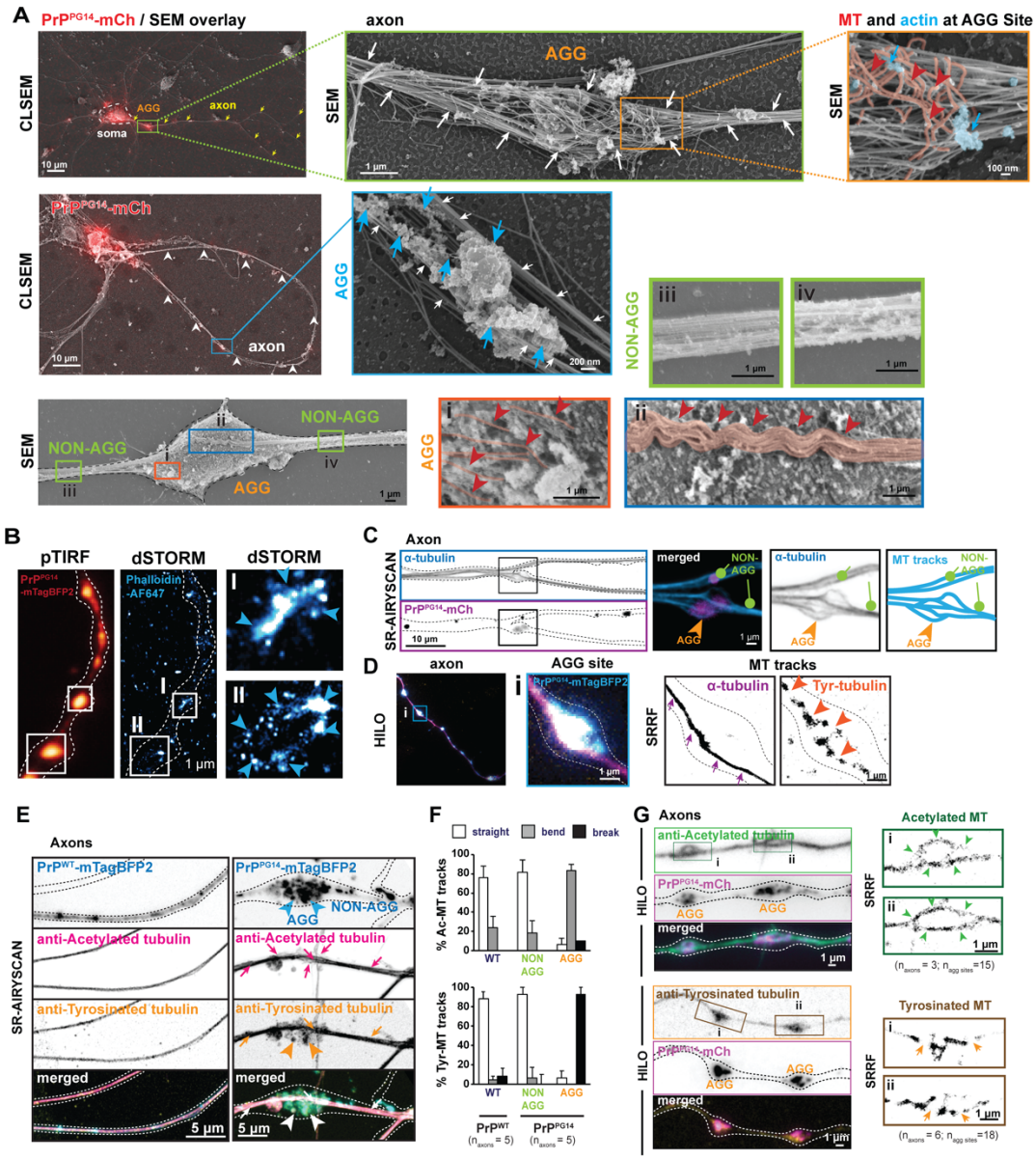


Figure 3.3 Actin accumulation and selective impairment to MT track PTMs at PrP^{PG14} aggregate sites. (A) Membrane-extracted (ME) correlative light and scanning electron microscopy (CLSEM) image of a neuron transfected with PrP^{PG14}-mCh (red). First neuron (top row): Arrowheads indicate axons. Green Inset shown on middle panel. White arrows point to MT tracks. Orange inset shown on right panel. Blue arrows point to actin. Red arrowheads point to disrupted MT tracks. Second neuron (middle row): White arrowheads indicate axons. Blue inset (right) shows an AGG site. White arrows point to MT tracks. Blue arrows point to actin. Third neuron (bottom row): Membrane-extracted SEM image of a neuron transfected with PrP^{PG14}-mCh. Insets (i-ii) show AGG sites. Red arrowheads and pseudo color highlights show MT tracks. Insets (iii-iv) show NON-AGG sites. **(B)** Images of an axon from a neuron transfected with PrP^{PG14}-mTagBFP2 (red) imaged using highly-inclined and laminated optical sheet (HILO) microscopy,

stained with Phalloidin-AF647 and imaged with direct STORM (dSTORM). Insets I-II of axonal swellings shown on the right. Arrowheads point to actin accumulation around the axonal swellings. **(C)** Super-resolution (SR) Airyscan confocal microscopy maximum projection images of PrP^{PG14}-mCh, immunostained with alpha tubulin antibody. Round Arrows indicate MT tracks at NON-AGG sites; Arrowheads indicate MT at AGG site. **(D)** HILO image of an axon from a neuron co-transfected with PrP^{PG14}-mTagBFP2 and mito-EGFP, co-immunostained with alpha tubulin and Tyrosinated (Tyr) tubulin antibodies. Inset i shows AGG site and SRRF processed images of alpha tubulin and Tyr-tubulin channels. **(E)** SR-Airyscan images of PrP^{WT}- or PrP^{PG14}-mTagBFP2 axons, co-immunostained with acetylated (Ac) and tyrosinated (Tyr) tubulin antibodies. Arrows indicate intact/straight tracks; Arrowheads indicate broken MT. **(F)** Percent Ac- or Tyr-MT track architecture (straight, bend, or break) at WT (in PrP^{WT}-mTagBFP2 axons) and NON-AGG or AGG sites (in PrP^{PG14}-mTagBFP2 axons). **(G)** HILO microscopy images of PrP^{PG14}-mCh axons immunostained against either acetylated and tyrosinated tubulin, and corresponding Super-resolution radial fluctuation (SRRF)-processed images at the AGG sites (i-ii; insets). Insets: Arrowheads point to MT tracks bending; Arrows point to MT tracks breaking. Data in (A) were collected by Leonardo Andrade.

3.3.4 Selective retention of kinesin-1 and kinesin-3 at PrP^{PG14} aggregate sites and depletion from cargoes

The local and selective disruption of mitochondrial and vesicular cargo transport (**Figure 3.2**), along with the impaired MT tracks within PrP^{PG14} endoggresome-rich AGG sites (**Figure 3.3**), suggest defective interactions between molecular motors and cargoes at those sites. To test whether molecular motors are retained at endoggresome-rich axonal micro-domains, in addition to the organelles, I quantitated the amount of kinesin-1 motor domain (KHC/KIF5) and its associated adaptor subunit kinesin light chain 1 (KLC1), and kinesin-3 (KIF1A) in AGG compared to NON-AGG sites, by immunofluorescence against validated antibodies in axons. I plotted the fluorescence intensity distributions of endogenous KHC, KLC1, and KIF1A level at the AGG sites, compared to control NON-AGG sites and PrP^{WT} aggregate-free axons ('WT sites') (**Figure 3.4A**). KHC, KLC1, and KIF1A staining signal in axons expressing PrP^{WT}-mCh was punctate (Encalada et al., 2011, Hummel and Hoogenraad, 2021), indicating that these proteins were properly localized to vesicles (**Figure 3.4A**). In contrast,

intensities of KHC, KLC1, and KIF1A motors were higher at AGG sites, indicating the accumulation of motors within axonal AGG sites containing PrP^{PG14}-mCh endoggresomes (**Figure 3.4A**). The comparison of fluorescence intensity distribution graphs between AGG and NON-AGG sites revealed significantly wider and right-skewed distributions toward higher intensities for KHC, KLC1, and KIF1A at AGG sites compared to WT control sites (**Figure 3.4B**). Notably, the KLC1 intensity distribution at NON-AGG sites was significantly lower compared to those at WT sites, suggesting that KLC1 was depleted from axonal cargo in NON-AGG areas.

Next, to test whether motor-cargo association was disrupted in addition to the motor protein accumulation at the AGG sites, I analyzed kinesin-1 and kinesin-3 composition on mitochondria that mobilized through AGG sites towards the synapse and compared to the motors on mitochondria in PrP^{WT} control axons. I used an automated single-particle localization algorithm, previously used to detect the same motor antibodies (Encalada et al., 2011, Szpankowski et al., 2012) here to compare the degree of colocalization between KHC and KIF1A subunits on mitochondria labeled with mito-EGFP (**Figure 3.4C**). The diffraction-limited detected puncta were called 'motor clusters' and could contain one or more kinesin molecules. With this analysis, I found that a higher proportion of mito-EGFP that had moved through AGG site in the proximal axon towards the analysis regions mid-axon contained no KIF1A motor on the surface, and a lesser proportion of these mito-EGFP contained two clusters of KHC motor on the surface, compared to mito-EGFP in PrP^{WT} control axons (**Figure 3.4D**). Next, I tested kinesin-1 and kinesin-3 composition on individual PrP-carrying vesicles that mobilized through AGG sites and compared

this to the composition of motors associated with PrP^{WT} vesicles in control axons. In this analysis, I used a sub-pixel colocalization analysis as previously to estimate relative copy number of motor subunits by Gaussian fittings on fluorescence intensity distribution graphs (Encalada et al., 2011, Szpankowski et al., 2012). I found that significantly more PrP vesicles contain KLC subunit alone, without the KHC motor, in PrP^{PG14} endoggresome-rich axons compared to PrP^{WT} aggregate-free axons (**Figure 3.4E**). Furthermore, those PrP-carrying vesicles in PrP^{PG14} axons with KLC-KHC colocalization had less KHC copy number, while KLC copy number remained unchanged (**Figure 3.4F**). The composition of KLC and KIF1A on PrP vesicles in PrP^{PG14} aggregate-rich axons and PrP^{WT} aggregate-free axons were similar (**Figure 3.4G**), suggesting selective detachment of KHC subunit from KLC1 subunit of kinesin-1 on individual vesicles in PrP^{PG14} endoggresome-rich axons (**Figure 3.4H**). As mitochondria and vesicles analyzed here had moved through at least one AGG site, these observations suggest that kinesin-1 and kinesin-3 are depleted away from mitochondria and vesicles as they passage through PrP^{PG14} axonal swellings, resulting in kinesin-1 and kinesin-3 accumulation at these sites.

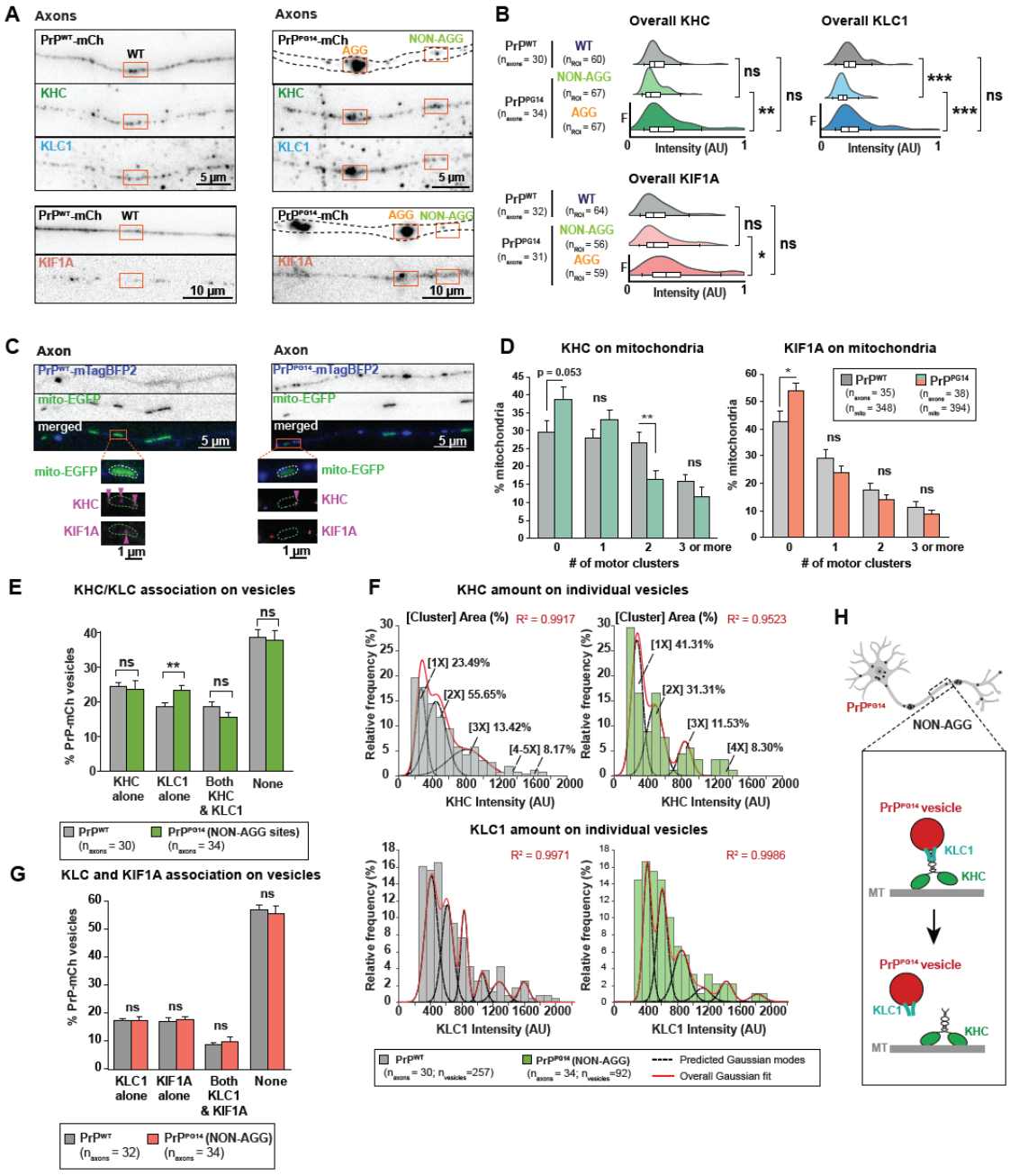


Figure 3.4 Kinesin-1 and kinesin-3 accumulation at PrP^{PG14} aggregate sites and depletion from mitochondria and vesicles. (A) Images of axons expressing PrP^{WT}-mCh or PrP^{PG14}-mCh, immunostained with KHC and KLC1 or with KIF1A antibodies. Orange boxes show AGG, NON-AGG, and WT ROIs. **(B)** Normalized intensity distribution frequencies [F] of KHC, KLC1, and KIF1A signal at AGG, NON-AGG, and WT sites plotted as box plots with kernel density estimates from histogram. **(C)** Representative inverted images of axons expressing PrP^{WT}-mTagBFP2 or PrP^{PG14}-mTagBFP2 and mito-EGFP, and immunostained with KHC and KIF1A antibodies. Insets (below) shown as overlay of sub-pixel localization detection (magenta spots;

arrowheads). **(D)** Quantitation of percent mitochondria (mean ± SEM) colocalizing with 0, 1, 2, and ≥ 3 KHC or KIF1A motor clusters. **(E)** Quantitation of percent PrP-mCh vesicles (mean ± SEM) colocalizing or not with KHC and/or KLC1 motor clusters. **(F)** Relative frequency histogram of all KHC and KLC1 Gaussian-fitted spot intensities (AU) with predicted Gaussian modes and overall multi-Gaussian fit (R^2). [1X], [2X], [3X], and [4X] are estimates of the protein copy number, and the predicted percentages of vesicles associated with [1X], [2X], [3X], and [4X] are shown. **(G)** Quantitation of percent PrP-mCh vesicles (mean ± SEM) colocalizing or not with KLC1 and/or KIF1A motor clusters. **(H)** A model of motor detachment from PrP^{PG14}-mCh vesicles in endoggresome-rich axons. ***p<0.001, **p<0.01, *p<0.05, ns = not significant; **(B)** Kruskal-Wallis test, **(D), (E), (G)** Student's t-test.

3.3.5 Retention of kinesin-1 at PrP^{PG14} aggregate sites requires its cargo-binding regulatory domain

To determine the mechanistic basis of motor sequestration at PrP^{PG14} AGG sites, I used a well characterized constitutively active truncated form of kinesin-1, called KIF5C(1-560), consisting of the motor, the neck linker and coiled coil, and the first stalk domains, but lacking the cargo binding, auto-inhibitory domain and thus cannot associate with cargoes (Jacobson et al., 2006), and tested whether KIF5C(1-560) was retained at the endoggresome-rich sites. Neurons were co-transfected with mTagBFP version of PrP^{PG14} and full-length (FL) KIF5C-2xmCh plus its adaptor subunit KLC1-TAP, or with a KIF5C(1-560)-2xmCh plus KLC1-TAP (**Figure 3.5A-B**) to recruit overexpressed motor domain to cargoes. I found that KLC1-TAP overexpression was sufficient to recruit the FL KIF5C-2xmCh to PrP^{PG14} endoggresomes (**Figure 3.5A**). These data were consistent with immunofluorescence analysis of endogenous KIF5 (KHC) and KLC1 accumulation at PrP^{PG14} AGG sites (**Figure 3.4A,B**). On the contrary, KIF5C(1-560)-2xmCh did not accumulate at the AGG sites anywhere throughout axons, despite KLC1-TAP overexpression (**Figure 3.5B**). Instead, KIF5C(1-560)-2xmCh efficiently moved passed all AGG sites to accumulate at axonal termini **(Figure 3.5B**) similar to the observation in healthy cultured neurons (Jacobson et

al., 2006). Uninterrupted movement of KIF5C(1-560) is consistent with the concept that kinesin-1 prefers acetylated MTs, and these tracks remained mostly intact albeit curved at the AGG sites (**Figure 3.3D-F**), thus providing the tracks for KIF5C(1-560) motility toward the axon termini. To rule out the possibility that KIF5C(1-560)-2xmCh accumulated at the axon terminus prior to endoggresome accumulation along axons, I performed sequential transfection of KIF5C(1-560)-2xmCh two days after the initial expression of PrP^{PG14}-mTagBFP2. In this paradigm, I found a co-transfected neuron with endoggresomes near the axon terminus that still completely lack KIF5C(1-560)-2xmCh signal at the AGG sites and found KIF5C(1-560)-2xmCh accumulated at the axon terminus (**Figure 3.5C)**. Although the delivery of KIF5C(1-560) to the MT plus-ends was not blocked, I next tested whether motility dynamics of KIF5C(1-560) were impaired as it moved through the AGG sites before reaching the axon termini. I performed the fluorescence recovery after photobleaching (FRAP) analysis of KIF5C(1-560)-mCitrine (mCit) at the tips of axons of neurons transduced with PrP^{PG14}-mCh versus PrP^{WT}-mCh control, using adeno associated viruses (AAVs) for five days, a time point previously shown to have prominent endoggresome accumulation (Chassefeyre et al., 2021). The FRAP analysis showed no significant difference in the fluorescence recovery of KIF5C(1-560)-mCit at the axon termini of PrP^{PG14} endoggresome-rich axons compared to control PrP^{WT} axons devoid of endoggresomes (**Figure 3.5D-G**), suggesting that the presence of PrP^{PG14} endoggresomes do not block the motility of KIF5C(1-560) near the axonal termini. These data altogether show that the cargo-binding domain of kinesin-1 is sufficient and is required for retention of cargo-motor complexes at PrP^{PG14} AGG swelling sites in axons. These observations suggest

that there is selectivity in motor protein retention, as motors without the cargo-binding/autoinhibition domains (and cannot bind cargo) are not retained within the AGG sites, and that only the intact cargo-motor complexes are sequestered by endoggresomes.

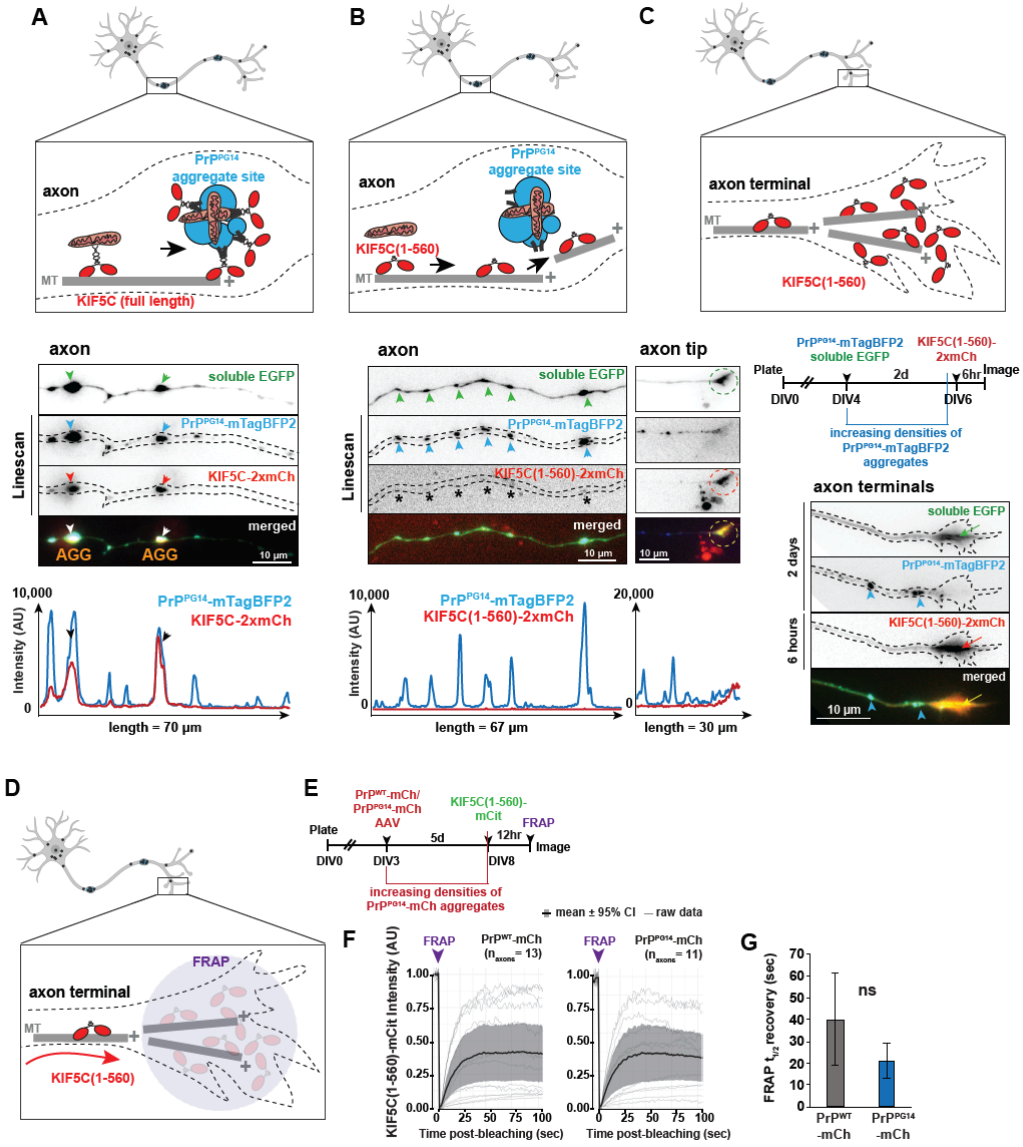


Figure 3.5 Retention of kinesin-1 (KIF5C) at PrP^{PG14} AGG sites requires its cargo-binding domain. (A) Schematic (top) and representative inverted images of axons (middle) of neurons expressing soluble EGFP, PrP^{PG14}-mTagBFP2, and KIF5C-2xmCh for 2 days, and corresponding line scan intensity profiles (bottom) ($n_{axons} = 9$). **(B)** Schematic (top) and representative inverted images of axons or axon termini (middle) from neurons expressing soluble EGFP, PrP^{PG14}-mTagBFP2, and KIF5C(1-560)-2xmCh for 2 days, and corresponding line scan intensity profiles

(bottom) (n_{axons} = 13). **(C)** Schematic (top), timeline of sequential transfection of EGFP and PrP^{PG14}-mTagBFP2 for 2 days and KIF5C(1-560)-2xmCh for 6 hours (middle), and images at the axon terminus (bottom). Arrowheads point to endoggresomes. Arrows point to EGFP and KIF5C(1-560)-2xmCh accumulation at the axonal growth cone. **(D)** Schematic of FRAP assay to study KIF5C(1-560) fluorescence recovery from axonal transport. **(E)** Timeline of FRAP assay (top) of axon terminals induced with PrP^{WT}- or PrP^{PG14}-mCh AAV for 5 days, sequentially transfected with KIF5C(1-560)-mCit for 12 hours prior to live imaging. **(F)** FRAP profile of KIF5C(1-560)-mCit in PrP^{WT}-mCh or PrP^{PG14}-mCh-transduced axons. **(G)** FRAP half-time ($t_{1/2}$) recovery (mean ± SEM) from axons in (F). ns = not significant; Student's t-test.

3.3.6 Enhanced mitochondrial fission at PrP^{PG14} aggregate sites requires Rab7 GTPase activity

In addition to mitochondrial accumulation (**Figure 3.1-3.2**), time-lapse live imaging using high-resolution microscopy revealed enhanced mitochondrial fission at PrP^{PG14} AGG sites (**Figure 3.6A**). To check imbalance of mitochondrial fusion/fission, I first quantitated mitochondrial size at PrP^{PG14} AGG sites in axons of neurons expressing PrP^{PG14}-mCh for two to five days (**Figure 3.6A**). I found smaller mitochondria retained within PrP^{PG14} endoggresome-rich sites (**Figure 3.6B**), and mitochondrial fragments also moved away from the AGG site in the anterograde direction (**Figure 3.6A**). The overall size of mitochondria trapped in PrP^{PG14} axons decreased as the number of PrP^{PG14} endoggresomes increased from 12 hours to five days post-transfection of PrP^{PG14}-mCh (**Figure 3.6C**). These data suggest a link between accumulation of PrP^{PG14} endoggresomes in axons and the progressive imbalance of mitochondrial dynamics towards smaller mitochondria retained at the AGG sites.

In a previous study, and in **Chapter 2**, the S3EM ultrastructure of PrP^{PG14} axons showed mitochondria and endolysosomes trapped in the axonal swellings and often were in close contacts (Chassefeyre et al., 2021). Endolysosomes marked with Rab7 have been shown to regulate mitochondrial fission via direct

membrane contact with mitochondria, to promote fission at the contact sites (Wong et al., 2018). To investigate the mechanistic basis of enhanced mitochondrial fission within AGG sites, I first used high-resolution live imaging to test whether Rab7 strongly associated with mitochondria within PrP^{PG14} AGG sites. Neurons were co-transfected with three components: mito-mTagBFP2 and PrP^{WT}-mCh/PrP^{PG14}-mCh and $Rab7^{WT}$-EGFP/$Rab7^{Q67L}$-EGFP mutant—that cannot undergo GTP hydrolysis and cannot be released from endosomal membranes (Mukhopadhyay et al., 1997), which has been shown previously to inhibit Rab7-associated mitochondrial fission pathway effectively (Wong et al., 2019). Colocalization analysis showed that mito-mTagBFP2 highly colocalized with both $Rab7^{WT}$-EGFP and $Rab7^{Q67L}$-EGFP at PrP^{PG14} endoggresome-rich sites, compared to NON-AGG control sites and to control PrP^{WT}-mCh endoggresome-free axons at two days post-transfection (**Figure 3.6E**). High-resolution live imaging micro-movement analysis revealed mitochondrial fission occurred within AGG swelling sites in neurons overexpressing $Rab7^{WT}$-EGFP (**Figure 3.6F**). Importantly, fission did not occur as frequently in PrP^{PG14}-mCh AGG swelling sites of neurons overexpressing the constitutively active $Rab7^{Q67L}$-EGFP (**Figure 3.6F**). To quantitate these observations, I calculated a mitochondrial fission index as the frequency of fission normalized to mitochondrial lengths at a given timeframe. These data indicate that the frequency of mitochondria fission was higher in AGG sites of endoggresome-rich axons than in NON-AGG regions or in control PrP^{WT} axons (**Figure 3.6G**). Altogether, these observations indicate that PrP^{PG14} axonal swellings are hubs for organelle-organelle contact that mediate mitochondrial remodeling towards fission through Rab7 GTPase activity.

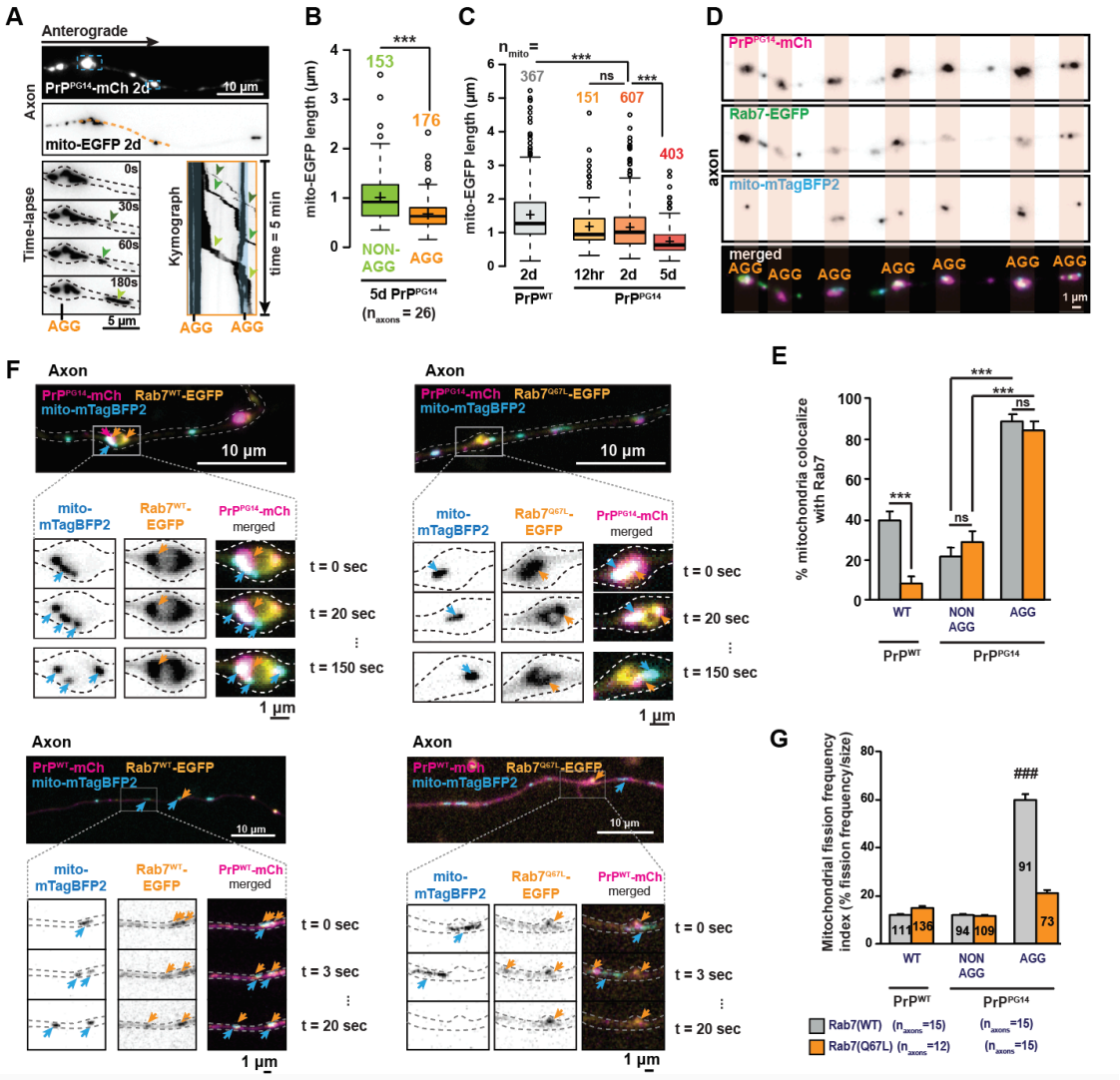


Figure 3.6 Rab7-mediated mitochondrial fission at PrPPG14 aggregate sites. (A) First-frame images of axons co-expressing PrP^{PG14}-mCh and mito-EGFP for 2d. The yellow dotted line indicates an imaging region of time-lapse (bottom left) and kymograph (right). **(B)** Quantitation of mito-EGFP length at AGG vs NON-AGG sites at 5 days post-PrP^{PG14}-mCh expression. **(C)** Quantitation of mito-EGFP length co-transfected with PrP^{WT}-mCh for 2 days or PrP^{PG14}-mCh for 12 hours, 2 days, and 5 days. **(D)** Axons co-expressing PrP^{PG14}-mCh, Rab7-EGFP, and mito-mTagBFP2. Highlights indicate AGG sites. **(E)** Quantitation of percent mito-mTagBFP2 colocalize with $Rab7^{WT/Q67L}$-EGFP at WT, NON-AGG, or AGG sites. **(F)** First-frame images of axons co-expressing PrP^{PG14}-mCh (top left and top right) or PrP^{WT}-mCh (bottom left and bottom right), $Rab7^{WT}$-EGFP (top left and bottom left) or $Rab7^{Q67L}$-EGFP (top left and bottom left), and mito-mTagBFP2 and representative frames from time-lapse videos at WT or AGG sites (insets). **(G)** Quantitation of mitochondrial fission frequency index (% of fission frequency/ mitochondrial length). Box plots were shown with Tukey definition; (+) indicates the mean. All bar graphs are shown as mean ± SEM. ***p<0.001, **p<0.01, *p<0.05, ns = not significant; (B), (C) Kruskal-Wallis test. (E) Tukey's multiple comparison test.

3.3.7 Dysfunctional mitochondria are retained at PrP^{PG14} aggregate sites

Mitochondrial dysfunction occurs in the early and late stages of neurodegeneration, which was previously observed in PrDs (Wang et al., 2019, Foliaki et al., 2023, Wood et al., 2022). Mitochondrial membrane potential ($\Delta\Psi m$) is a metric of mitochondrial and neuronal health, and increased or decreased membrane potential has been associated with impairments to mitochondrial quality control in familial and infectious PrDs (Wood et al., 2022, Kim et al., 2022). I hypothesized that the fragmented mitochondria that accumulate at PrP^{PG14} endoggresome-rich sites are also dysfunctional in their ability to retain $\Delta\Psi m$. To test this, I loaded neurons with tetramethylrhodamine, ethyl ester (TMRE), a cell permeant dye that labels healthy mitochondria with $\Delta\Psi m$ and is not sequestered within depolarized mitochondria (Brunet et al., 2021, Lin et al., 2017). I measured the TMRE intensities of mitochondria within individual PrP^{PG14} endoggresome AGG swellings and compared it to that at NON-AGG sites or that in PrP^{WT}-mCh control axon. Neurons co-transfected with PrP^{PG14}-mCh or PrP^{WT}-mCh and Rab7(WT)-EGFP, previously shown to potentiate mitochondrial fission at AGG sites (**Figure 3.6G**), showed a significant reduction in TMRE signal at the AGG sites (**Figure 3.7A, B**), and the percentage of mito-EGFP that could retain TMRE dropped significantly, compared to mito-EGFP in NON-AGG and WT control regions (**Figure 3.7C**). Thus, PrP^{PG14} endoggresome-mediated mitochondrial transport dysfunction and elevated fission are associated with compromised mitochondrial integrity within PrP^{PG14} axonal swelling micro-domains, which contribute to the axonal and neuronal pathologies.

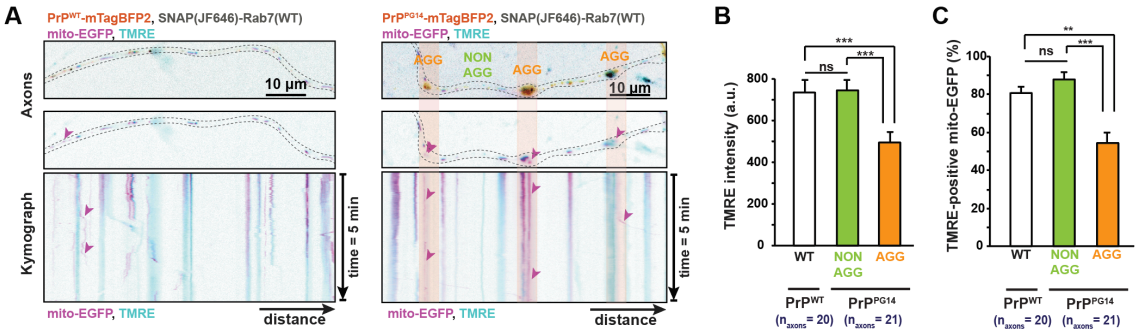


Figure 3.7 Dysfunctional mitochondria accumulates within PrP^{PG14} aggregate sites. (A) Representative inverted color first-frames of axons (top two panels) and kymographs (bottom panel) generated from time-lapse movies (5 minutes, 300 frames, 1 frame/sec) of PrP^{WT}- or PrP^{PG14}-mTagBFP2, co-transfected with SNAP(JF646)-Rab7 and mito-EGFP and treated with 25 nM of TMRE. Arrowheads point to TMRE-negative mito-EGFP. **(B)** TMRE intensities per mito-EGFP in WT, NON-AGG, or AGG regions. **(C)** Percent mito-EGFP that are TMRE-positive. All bar graphs are shown as mean ± SEM. ***p<0.001, **p<0.01, *p<0.05, ns = not significant, **(B), (C)** Tukey's multiple comparison test.

3.3.8 Correlative fluorescence and FIB-SEM of PrP^{PG14} aggregate sites revealed organelle-cytoskeletal remodeling *in situ*

The S3EM study of PrP^{PG14} axonal swellings (Chassefeyre et al., 2021) provided limited data to quantify the disruption of cytoskeleton and mitochondrial defects, to compare to those in the control axonal sites. In collaboration with the Advanced Imaging Center of the Howard Hughes Medical Institute (HHMI), Janelia Research Campus, we performed correlative SR-Airyscan and enhanced focused ion beam for scanning electron microscopy (FIBSEM) (Hoffman et al., 2020) on cultured primary hippocampal neurons grown on 3-mm Sapphire coverslips and co-transfected with (1) dsRed-Mito-7, (2) either PrP^{WT}-mEmerald (control) or PrP^{PG14}-mEmerald, and (3) either Rab7^{WT}-SNAP(JF646) or Rab7^{Q67L}-SNAP(JF646) (See Method Section **3.2.11** for detail). This sample preparation yielded a healthy primary culture and efficient co-transfection of all three components, and axons with endoggresomes could be identified by SR-

Airyscan imaging (**Figure 3.8A**). I performed the initial ultrastructural assessment of the transfected neuron from the aligned FIBSEM big-data overview and found that MT bundles/tracks, mitochondria, vesicular and endomembrane structures, and endoplasmic reticulum (ER) were easily identifiable in the 3D raw data (**Figure 3.8B**). I then mapped one of the regions with few prominent axonal swellings from a transfected neuron and found evidence of fragmented MT tracks that were not bundled together, and mitochondrial accumulation and membrane contacts with endoggresomes and with ER at the AGG sites, which were virtually absent from NON-AGG sites (**Figure 3.8A-B**), consistent with the findings in **Figure 3.3** and **Figure 3.6**. Thus, in addition to the Rab7 pathway that drives mitochondrial fission, the mitochondrial-ER contacts and recruitment of actin to the contact site (**Figure 3.3A-B**) to constrict mitochondrial tubule (Steffen and Koehler, 2018) could play a role during aberrant mitochondrial fission inside the PrP^{PG14} axonal swelling micro-domains. Actin and ER membrane contacts to mitochondria are important to maintain the metabolic flux in the oxidative phosphorylation (OXPHOS) system and mitochondrial morphology (Illescas et al., 2021, Abrisch et al., 2020). Here, I found that mitochondria that were in contact with endoggresomes or those that were caught during the fission process at the AGG sites showed disrupted cristae structures, compared to those mitochondria in NON-AGG sites and those in PrP^{WT} axons (**Figure 3.8C-D**), consistent with the finding in **Figure 3.7** that mitochondria retained at AGG sites become dysfunctional. Interestingly, overexpression of $Rab7^{Q67L}$-SNAP(JF646) with PrP^{PG14}-mEmerald did not rescue swollen mitochondrial morphology, even though fission was inhibited at the AGG sites (**Figure 3.6G**). The Encalada Lab and the Manor lab team at the Salk Institute are currently in a process of creating a 3D segmentation model of mitochondrial

morphology and mitochondrial contact networks at the AGG sites, in comparison to the control NON-AGG sites and in PrP^{WT} control axons, to determine the contribution of endosomal- versus ER-mediated fission. In conclusion, the ultrastructural data from the FIBSEM analyzed thus far were consistent with the hypothesis that organelle-cytoskeletal remodeling occurred locally at the endoggresome axonal swelling sites.

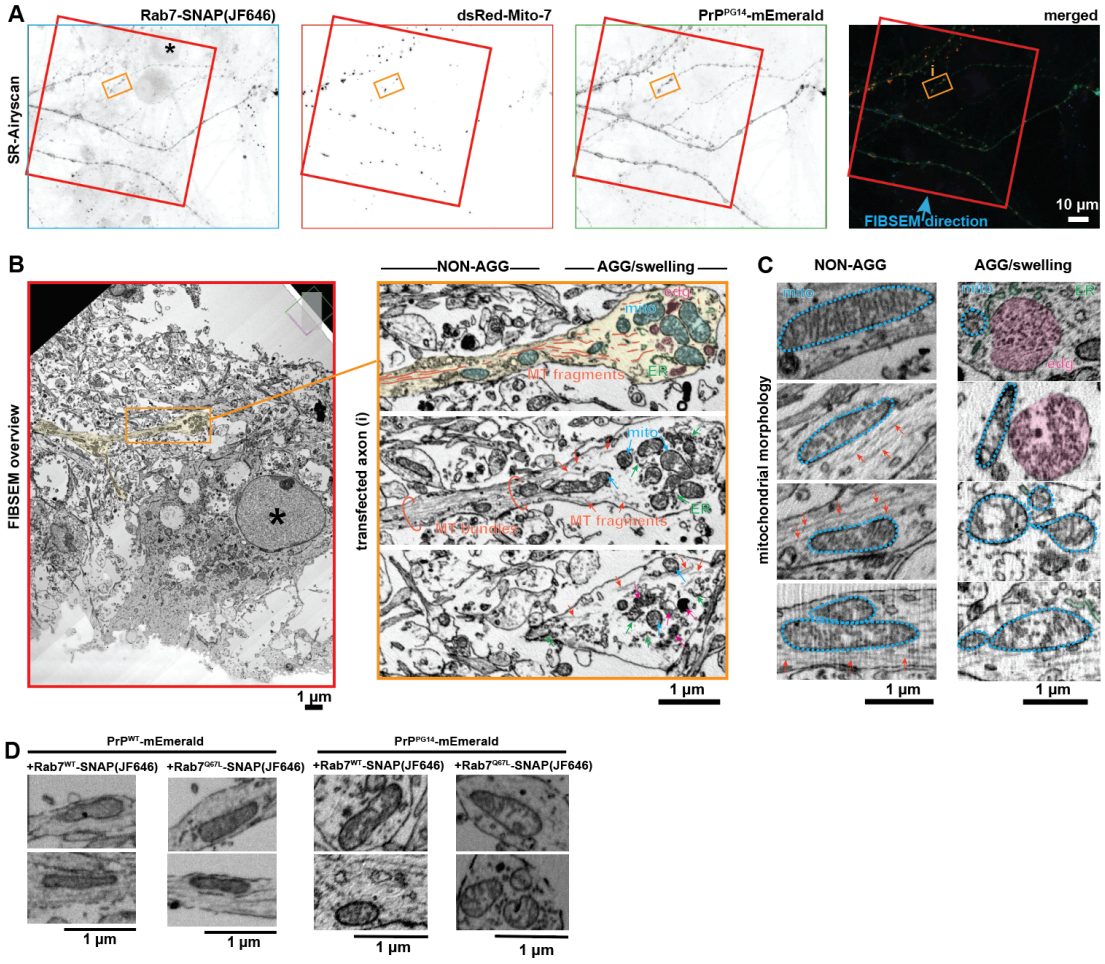


Figure 3.8 Correlative fluorescence and FIBSEM of cultured primary neurons. (A) SR-Airyscan images of neurons on the Sapphire coverslips, co-transfected with Rab7-SNAP(JF646), dsRed-Mito-7, PrP^{PG14}-mEmerald. Red squares show a region for FIB milling and SEM. **(B)** A representative slice from an aligned FIBSEM bigdata. The orange inset in (B) is the region (i) in (A). (Right) 3 representative slices of the FIBSEM dataset showing axonal NON-AGG and AGG/swelling regions, highlighting MT bundles versus fragments (orange), mito (blue), ER

(green), and endoggresomes (pink). **(C)** Examples of mitochondrial morphology taken from NON-AGG and AGG regions of the transfected neurons in (A). Orange arrows point to MT. Endoggresomes (pink) and ER (green) are identified. **(D)** Mitochondrial morphology from 4 FIBSEM datasets of neurons that co-transfected with dsRed-Mito-7, either PrP^{WT}-mEmerald (control) or PrP^{PG14}-mEmerald, and either $Rab7^{WT}$-SNAP(JF646) or $Rab7^{Q67L}$-SNAP(JF646). Data in (A) were collected by Adriaan Verhelle and Yin Wu. Data in (B)-(E) were collected by Jesse Aaron.

3.4 Conclusion and discussions

In this **Chapter 3**, I investigated the consequences of the formation of enlarged mutant PrP endoggresomes that distend the axon into swellings on axonal function. I modeled axonal PrP^{PG14} aggregation in a cultured primary hippocampal neuronal system over time, to unveil the mechanisms of localized cytoskeletal disruptions and organelle accumulations within local axonal hubs of PrP^{PG14} endoggresomes. Using high-and super-resolution light microscopy, with single-particle micro-movement analyses of cargoes, and correlative light and EM (CLEM) imaging, I proposed the working model for the mechanisms of local impairments that develop within axonal swellings, leading to cascades of defects ensue at very early stages after expression of PrP^{PG14}. These localized micro-phenotypes include anterograde transport jams due to altered architecture of MT tracks that kinesin-1 and kinesin-3 cargoes mobilize on, and the sequestration of mitochondria, endolysosomes, and molecular motors at swelling sites. Following this cascade of events, PrP^{PG14} axonal swelling sites are hubs for organelle-organelle contacts—between mitochondria, ER, and active Rab7-positive endolysosomes—to promote mitochondrial remodeling towards enhanced fission that compromise mitochondrial functional integrity in axons. This is summarized in **Figure 3.9**.

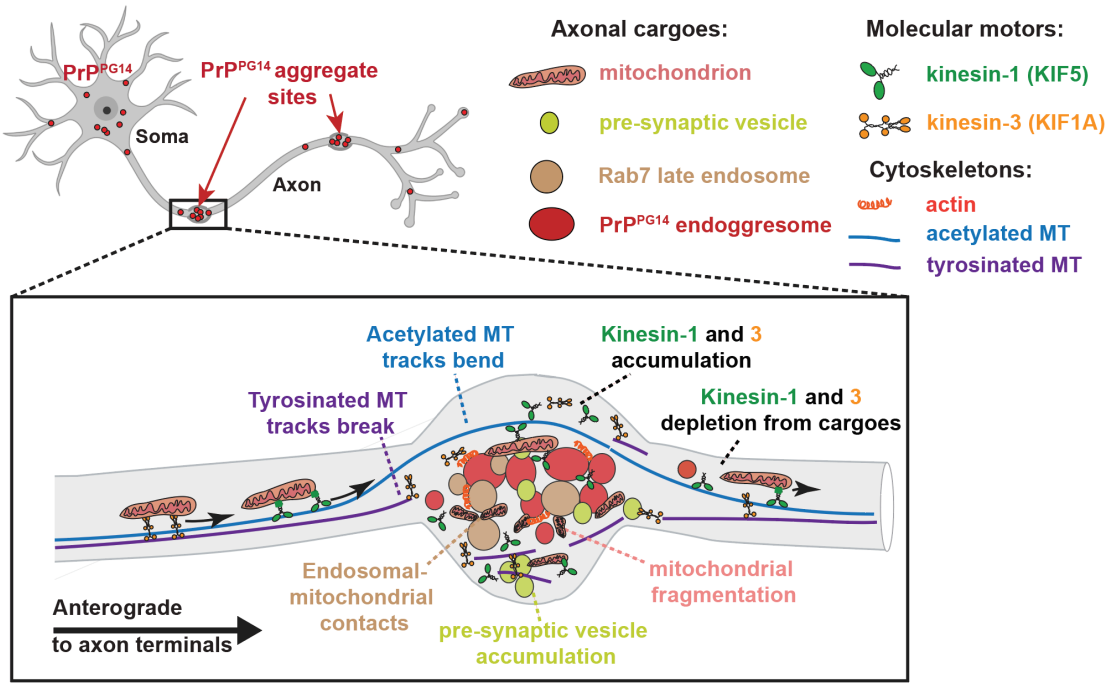


Figure 3.9 Working model of the mechanism of cytoskeletal-organelle remodeling by PrP^{PG14} endoggresomes. PrP^{PG14} endoggresomes are stalled at various sites along mammalian axons where they distend axons into swellings. At these sites, axonal transport of mitochondria and pre-synaptic vesicles occurs selectively in anterograde over retrograde direction. Selective transport impairment could be due to (1) kinesin-1 and -3 are sequestered at the swelling sites and deplete from mitochondria that mobilize through and (2) acetylated MT tracks bend and tyrosinated MT tracks break at these swelling sites. PrP^{PG14} endoggresomes also contain Rab7 and could bring more Rab7 endosomes into contacts with mitochondria at the swelling sites, leading to elevated mitochondrial fission and dysfunction.

Stable MT tracks in axons contain acetylation and detyrosination, two PTMs allow MTs to bend under mechanical stress (Xu et al., 2017b). Our observations are consistent with this notion, as stable, acetylated MTs curve while tyrosinated (unmodified) MTs break at PrP^{PG14} endoggresome-rich sites (**Figure 3.3**), suggesting that enlarged PrP^{PG14} endoggresomes exert mechanical stress from within axons. Our data further point to the breakage of tyrosinated MTs as an important initiating event that precedes transport disruption and

motor/organelle accumulations within localized axonal swelling regions. Tyrosinated MTs are used by kinesin-3 (KIF1), to carry mitochondria, pre-synaptic vesicles containing SYP and PrP towards the distal axons and pre-synapse (Sgro et al., 2013, Lo et al., 2011, Hall and Hedgecock, 1991). In contrast, kinesin-1 (KIF5) prefers to land and walk on stable acetylated MTs (Balabanian et al., 2017, Reed et al., 2006), and kinesin-1 is required for the uninterrupted movement of mitochondria, pre-synaptic vesicles, as well as of PrP^{C} and PrP^{mut} vesicles along axons (Encalada et al., 2011, Chassefeyre et al., 2021, Sgro et al., 2013, Lo et al., 2011, Hall and Hedgecock, 1991). Thus, kinesin-3-mediated transport process is expected to be directly affected by broken tyrosinated MTs, while bending acetylated MTs likely sustain the transport of kinesin-1 cargoes to a certain extent. As it is unclear how kinesin-1 and kinesin-3 coordinate activities when bound simultaneously to a cargo (Guardia et al., 2016, Campbell, 2018), it is possible that complex interactions between these motors and MT tracks dictate the final outcome of motility of mitochondria within and through these sites, and this regulated process is disrupted in the presence of endoggresomes.

MT defects might not be responsible for the very early transport defects first observed for the anterograde movement of PrP^{PG14} vesicles at 12 hours post-transfection, when presumably the MT cytoskeleton system is intact. A possibility is that the initial dynamic sorting of endolysosomes containing PrP^{PG14} into fused enlarged endoggresomes (Chassefeyre et al., 2021) could inhibit transport of Golgi-derived vesicles that travel towards the distal ends. As mitochondrial movement is unaffected at the 12-hour timepoint, mitochondrial motility impairments at 2 days post-PrP^{PG14} expression could be due to local traffic disruptions directly caused by endoggresomes within the AGG sites.

The observation that anterograde, but not retrograde transport of many neuronal cargoes, was impaired in endoggresome-rich axons was unexpected. Previous work predicted that disruptions to kinesin-mediated anterograde movement would impact dynein-mediated retrograde transport because these opposing motors often associate simultaneously to the same cargo to coordinate bidirectional transport activities (Encalada et al., 2011, Ally et al., 2009). Both kinesin-1 and dynein can associate to mitochondria simultaneously (Fenton et al., 2021), and it is possible that mitochondria moving in the retrograde direction by dynein (Pilling et al., 2006) utilize intact acetylated MTs tracks. Dynein was shown *in vitro* to initially associate to tyrosinated MT tracks but continue translocating on detyrosinated MT tracks (McKenney et al., 2016). Thus, it could be that at the AGG sites, dynein hops on broken tyrosinated MTs but continues movement with its cargo on detyrosinated, stable MTs. In addition, the differences in the susceptibility of anterograde versus retrograde transport to insults could stem from differences in the intrinsic properties of kinesin and dynein motor proteins. Previous studies using *in vitro* motility and biophysical assays indicated that a single dynein molecule could avoid physical obstacles by taking side-steps around MT bundles (Can et al., 2014, Ferro et al., 2019). A single kinesin-1 motor domain, unlike dynein, walks linearly on protofilament MT tracks and needs to work in teams for uninterrupted movement upon encountering physical obstacles (Ferro et al., 2019). Thus, in the normal crowded environment of axons, which are accentuated by the presence of enlarged endoggresomes and other retained organelles at the swelling sites, dynein-driven cargoes might be capable of navigating through dense cytoskeletal networks that remain intact at those sites, while the kinesin-1-mediated process fails. Notably,

in agreement with a previous study in an PrP^{Sc}-infected mouse, they found that dynein-mediated retrograde transport was not directly affected, but instead motor-cargo associations might be the target of infectious prions prior to clinical onset *in vivo* (Ermolayev et al., 2009). While it is unclear whether mechanisms of axonal impairment in infectious PrP^{Sc} models are similar to our familial PrD model in primary neurons, the data are consistent, as we showed here that motor-cargo associations were impaired on mitochondria and vesicular cargoes that encounter and mobilize through PrP^{PG14} aggregate sites, which requires kinesin cargo binding domain (**Figure 3.4**).

Ultrastructural studies of the brains of human patient diagnosed with PrDs revealed the accumulation of misfolded PrP within dystrophic neurites (Liberski et al., 2018, Godsave et al., 2008, Veith et al., 2009, Kovacs et al., 2012, Arnold et al., 1995, Sikorska et al., 2004). Complex membrane-bound structures were observed to co-exist within swollen neurites, including autophagic vacuoles, lysosomal electron-dense bodies, and enlarged endolysosomes, that were considered common features of PrD pathology (Liberski et al., 2018, Godsave et al., 2008, Veith et al., 2009). These axonopathy phenotypes had also been observed in cell lines infected with PrP^{Sc}, as well as in the brains of rodent models of familial and sporadic PrP^{Sc} diseases (Magalhaes et al., 2005, Liberski et al., 2018, Daude et al., 1997, Fioriti et al., 2005, Arnold et al., 1995, Veith et al., 2009). In addition to prionopathies, dystrophic axonal swellings is a common and early feature in the brains of patients with various other neurodegenerative diseases—including AD, PD, and HD (Stokin et al., 2005, Newell et al., 1999, Sapp et al., 1999, Zanusso et al., 2007). In AD, dystrophic axons also contained enlarged endosomes, and this is known amongst the earliest neuronal lesions identified thus far (Cataldo et al., 2004, Cataldo et al., 2000). These observations

highlight the importance of understanding the mechanisms of axonotoxicity as imparted by the presence of intra-axonal misfolded protein aggregates in these diseases.

In the familial PrD model presented in **Chapter 2** and **Chapter 3** of this thesis, axonal misfolded PrP aggregates cause neurodegeneration, and the reduction of axonal aggregate formation by modulating its biogenesis pathway rescues neuronal function and viability (Chassefeyre et al., 2021). To what extent the modulation of endolysosomal pathways contributes to the formation of aggregates in other neurodegenerative disorders is unknown. However, as misfolded proteins like tau, α-synuclein, APP and Huntingtin are associated in part with endolysosomes for sorting and trafficking quality control (Wu et al., 2013, Xie et al., 2022, Trajkovic et al., 2017), it merits further investigations whether the defects to the cytoskeleton and transport within axonal micro-domains that contain misfolded aggregates contribute to axonotoxicity in the rest of the proteinopathies. The subcellular lesions identified in this study provide new pathways that can be therapeutically targeted for their amelioration and for the rescue of axonal lesions that are the primary vulnerability targets in the proteinopathies (See **Chapter 5**: Future Directions).

3.5 References

Abramov, A. Y., Berezhnov, A. V., Fedotova, E. I., Zinchenko, V. P. & Dolgacheva, L. P. 2017. Interaction of misfolded proteins and mitochondria in neurodegenerative disorders. *Biochem Soc Trans,* 45**,** 1025-1033.

Abrisch, R. G., Gumbin, S. C., Wisniewski, B. T., Lackner, L. L. & Voeltz, G. K. 2020. Fission and fusion machineries converge at ER contact sites to regulate mitochondrial morphology. *J Cell Biol,* 219, e201911122.

Adalbert, R. & Coleman, M. P. 2013. Review: Axon pathology in age-related neurodegenerative disorders. *Neuropathol Appl Neurobiol,* 39**,** 90-108.

Alexiou, A., Nizami, B., Khan, F. I., Soursou, G., Vairaktarakis, C., Chatzichronis, S., Tsiamis, V., Manztavinos, V., Yarla, N. S. & Md Ashraf, G. 2018. Mitochondrial Dynamics and Proteins Related to Neurodegenerative Diseases. *Curr Protein Pept Sci,* 19**,** 850-857.

Ally, S., Larson, A. G., Barlan, K., Rice, S. E. & Gelfand, V. I. 2009. Opposite-polarity motors activate one another to trigger cargo transport in live cells. *J Cell Biol,* 187**,** 1071-82.

Arnold, J. E., Tipler, C., Laszlo, L., Hope, J., Landon, M. & Mayer, R. J. 1995. The abnormal isoform of the prion protein accumulates in late-endosome-like organelles in scrapie-infected mouse brain. *J Pathol,* 176**,** 403-11.

Atherton, J., Houdusse, A. & Moores, C. 2013. MAPping out distribution routes for kinesin couriers. *Biol Cell,* 105**,** 465-87.

Balabanian, L., Berger, C. L. & Hendricks, A. G. 2017. Acetylated Microtubules Are Preferentially Bundled Leading to Enhanced Kinesin-1 Motility. *Biophys J,* 113**,** 1551-1560.

Borchelt, D. R., Davis, J., Fischer, M., Lee, M. K., Slunt, H. H., Ratovitsky, T., Regard, J., Copeland, N. G., Jenkins, N. A., Sisodia, S. S. & Price, D. L. 1996. A vector for expressing foreign genes in the brains and hearts of transgenic mice. *Genet Anal,* 13**,** 159-63.

Brunet, M. A., Jacques, J. F., Nassari, S., Tyzack, G. E., Mcgoldrick, P., Zinman, L., Jean, S., Robertson, J., Patani, R. & Roucou, X. 2021. The FUS gene is dual-coding with both proteins contributing to FUS-mediated toxicity. *EMBO Rep,* 22**,** e50640.

Burgess, R. W. & Crish, S. D. 2018. Editorial: Axonopathy in Neurodegenerative Disease. *Front Neurosci,* 12**,** 769.

Cai, D., Mcewen, D. P., Martens, J. R., Meyhofer, E. & Verhey, K. J. 2009. Single molecule imaging reveals differences in microtubule track selection between Kinesin motors. *PLoS biology,* 7**,** e1000216.

Campbell, G. E. 2018. *Kinesin-1 and Kinesin-3 Coordinate the Transport of Synaptic Vesicle Precursors in Mammalian Axons.* Ph.D., The Scripps Research Institute.

Can, S., Dewitt, M. A. & Yildiz, A. 2014. Bidirectional helical motility of cytoplasmic dynein around microtubules. *eLife,* 3**,** e03205.

Cataldo, A. M., Petanceska, S., Terio, N. B., Peterhoff, C. M., Durham, R., Mercken, M., Mehta, P. D., Buxbaum, J., Haroutunian, V. & Nixon, R. A. 2004. Abeta localization in abnormal endosomes: association with earliest Abeta elevations in AD and Down syndrome. *Neurobiol Aging,* 25**,** 1263-72.

Cataldo, A. M., Peterhoff, C. M., Troncoso, J. C., Gomez-Isla, T., Hyman, B. T. & Nixon, R. A. 2000. Endocytic pathway abnormalities precede amyloid beta deposition in sporadic Alzheimer's disease and Down syndrome: differential effects of APOE genotype and presenilin mutations. *Am J Pathol,* 157**,** 277-86.

Chaiamarit, T., Verhelle, A., Chassefeyre, R., Shukla, N., Weiser Novak, S., Andrade, L. R., Manor, U. & Encalada, S. E. 2023. Mutant Prion Protein Endoggresomes are Hubs for Local Axonal Organelle-Cytoskeletal Remodeling. *bioRxiv***,** 2023.03.19.533383.

Chassefeyre, R., Chaiamarit, T., Verhelle, A., Novak, S. W., Andrade, L. R., Leitao, A. D. G., Manor, U. & Encalada, S. E. 2021. Endosomal sorting drives the formation of axonal prion protein endoggresomes. *Sci Adv,* 7**,** eabg3693.

Choi, H. S., Choi, Y. G., Shin, H. Y., Oh, J. M., Park, J. H., Kim, J. I., Carp, R. I., Choi, E. K. & Kim, Y. S. 2014. Dysfunction of mitochondrial dynamics in the brains of scrapie-infected mice. *Biochem Biophys Res Commun,* 448**,** 157-62.

Culley, S., Tosheva, K. L., Matos Pereira, P. & Henriques, R. 2018. SRRF: Universal live-cell super-resolution microscopy. *Int J Biochem Cell Biol,* 101, 74-79.

Daude, N., Lehmann, S. & Harris, D. A. 1997. Identification of intermediate steps in the conversion of a mutant prion protein to a scrapie-like form in cultured cells. *J Biol Chem,* 272, 11604-12.

Deckwerth, T. L. & Johnson, E. M., Jr. 1994. Neurites can remain viable after destruction of the neuronal soma by programmed cell death (apoptosis). *Dev Biol,* 165, 63-72.

Encalada, S. E., Szpankowski, L., Xia, C. H. & Goldstein, L. S. 2011. Stable kinesin and dynein assemblies drive the axonal transport of mammalian prion protein vesicles. *Cell,* 144, 551-65.

Ermolayev, V., Cathomen, T., Merk, J., Friedrich, M., Hartig, W., Harms, G. S., Klein, M. A. & Flechsig, E. 2009. Impaired axonal transport in motor neurons correlates with clinical prion disease. *PLoS Pathog,* 5, e1000558.

Fenton, A. R., Jongens, T. A. & Holzbaur, E. L. F. 2021. Mitochondrial adaptor TRAK2 activates and functionally links opposing kinesin and dynein motors. *Nat Commun,* 12, 4578.

Fernandes, M. C., Andrade, L. R., Andrews, N. W. & Mortara, R. A. 2011a. Trypanosoma cruzi trypomastigotes induce cytoskeleton modifications during HeLa cell invasion. *Mem Inst Oswaldo Cruz,* 106, 1014-6.

Fernandes, M. C., Cortez, M., Flannery, A. R., Tam, C., Mortara, R. A. & Andrews, N. W. 2011b. Trypanosoma cruzi subverts the sphingomyelinase-mediated plasma membrane repair pathway for cell invasion. *J Exp Med,* 208, 909-21.

Ferro, L. S., Can, S., Turner, M. A., Elshenawy, M. M. & Yildiz, A. 2019. Kinesin and dynein use distinct mechanisms to bypass obstacles. *eLife,* 8, e48629.

Fioriti, L., Dossena, S., Stewart, L. R., Stewart, R. S., Harris, D. A., Forloni, G. & Chiesa, R. 2005. Cytosolic prion protein (PrP) is not toxic in N2a cells and primary neurons expressing pathogenic PrP mutations. *J Biol Chem,* 280, 11320-8.

Foliaki, S. T., Smith, A., Schwarz, B., Bohrnsen, E., Bosio, C. M., Williams, K., Orru, C. D., Lachenauer, H., Groveman, B. R. & Haigh, C. L. 2023. Altered energy metabolism in Fatal Familial Insomnia cerebral organoids

is associated with astrogliosis and neuronal dysfunction. *PLoS Genet,* 19, e1010565.

Godsave, S. F., Wille, H., Kujala, P., Latawiec, D., Dearmond, S. J., Serban, A., Prusiner, S. B. & Peters, P. J. 2008. Cryo-immunogold electron microscopy for prions: toward identification of a conversion site. *J Neurosci,* 28, 12489-99.

Guardia, C. M., Farias, G. G., Jia, R., Pu, J. & Bonifacino, J. S. 2016. BORC Functions Upstream of Kinesins 1 and 3 to Coordinate Regional Movement of Lysosomes along Different Microtubule Tracks. *Cell Rep,* 17, 1950-1961.

Guedes-Dias, P., Nirschl, J. J., Abreu, N., Tokito, M. K., Janke, C., Magiera, M. M. & Holzbaur, E. L. F. 2019. Kinesin-3 Responds to Local Microtubule Dynamics to Target Synaptic Cargo Delivery to the Presynapse. *Curr Biol,* 29, 268-282 e8.

Gunawardena, S., Her, L. S., Brusch, R. G., Laymon, R. A., Niesman, I. R., Gordesky-Gold, B., Sintasath, L., Bonini, N. M. & Goldstein, L. S. 2003. Disruption of axonal transport by loss of huntingtin or expression of pathogenic polyQ proteins in Drosophila. *Neuron,* 40, 25-40.

Hall, D. H. & Hedgecock, E. M. 1991. Kinesin-related gene unc-104 is required for axonal transport of synaptic vesicles in C. elegans. *Cell,* 65, 837-47.

Harms, K. J., Tovar, K. R. & Craig, A. M. 2005. Synapse-specific regulation of AMPA receptor subunit composition by activity. *J Neurosci,* 25, 6379-88.

Hoffman, D. P., Shtengel, G., Xu, C. S., Campbell, K. R., Freeman, M., Wang, L., Milkie, D. E., Pasolli, H. A., Iyer, N., Bogovic, J. A., Stabley, D. R., Shirinifard, A., Pang, S., Peale, D., Schaefer, K., Pomp, W., Chang, C. L., Lippincott-Schwartz, J., Kirchhausen, T., Solecki, D. J., Betzig, E. & Hess, H. F. 2020. Correlative three-dimensional super-resolution and block-face electron microscopy of whole vitreously frozen cells. *Science,* 367, eaaz5357.

Hummel, J. J. A. & Hoogenraad, C. C. 2021. Specific KIF1A-adaptor interactions control selective cargo recognition. *J Cell Biol,* 220, e202105011.

Illescas, M., Penas, A., Arenas, J., Martin, M. A. & Ugalde, C. 2021. Regulation of Mitochondrial Function by the Actin Cytoskeleton. *Front Cell Dev Biol,* 9, 795838.

Jacobson, C., Schnapp, B. & Banker, G. A. 2006. A change in the selective translocation of the Kinesin-1 motor domain marks the initial specification of the axon. *Neuron,* 49, 797-804.

Janke, C. & Magiera, M. M. 2020. The tubulin code and its role in controlling microtubule properties and functions. *Nat Rev Mol Cell Biol,* 21, 307-326.

Jaqaman, K., Loerke, D., Mettlen, M., Kuwata, H., Grinstein, S., Schmid, S. L. & Danuser, G. 2008. Robust single-particle tracking in live-cell time-lapse sequences. *Nat Methods,* 5, 695-702.

Kevenaar, J. T. & Hoogenraad, C. C. 2015. The axonal cytoskeleton: from organization to function. *Front Mol Neurosci,* 8, 44.

Kim, M. J., Kim, H. J., Jang, B., Kim, H. J., Mostafa, M. N., Park, S. J., Kim, Y. S. & Choi, E. K. 2022. Impairment of Neuronal Mitochondrial Quality Control in Prion-Induced Neurodegeneration. *Cells,* 11, 2744.

Konishi, Y. & Setou, M. 2009. Tubulin tyrosination navigates the kinesin-1 motor domain to axons. *Nat Neurosci,* 12, 559-67.

Kovacs, G. G., Molnar, K., Keller, E., Botond, G., Budka, H. & Laszlo, L. 2012. Intraneuronal immunoreactivity for the prion protein distinguishes a subset of E200K genetic from sporadic Creutzfeldt-Jakob Disease. *J Neuropathol Exp Neurol,* 71, 223-32.

Kuijpers, M., Azarnia Tehran, D., Haucke, V. & Soykan, T. 2021. The axonal endolysosomal and autophagic systems. *J Neurochem,* 158, 589-602.

Kwon, S. E. & Chapman, E. R. 2011. Synaptophysin regulates the kinetics of synaptic vesicle endocytosis in central neurons. *Neuron,* 70, 847-54.

Lee, W. C., Yoshihara, M. & Littleton, J. T. 2004. Cytoplasmic aggregates trap polyglutamine-containing proteins and block axonal transport in a Drosophila model of Huntington's disease. *Proc Natl Acad Sci U S A,* 101, 3224-9.

Li, H., Li, S. H., Yu, Z. X., Shelbourne, P. & Li, X. J. 2001. Huntingtin aggregate-associated axonal degeneration is an early pathological event in Huntington's disease mice. *J Neurosci,* 21, 8473-81.

Liberski, P. P., Gajos, A. & Sikorska, B. 2018. Dystrophic neurites accumulating autophagic vacuoles show early stages of neuritic destruction. *Folia Neuropathol,* 56, 175-178.

Lim, J. & Yue, Z. 2015. Neuronal aggregates: formation, clearance, and spreading. *Dev Cell,* 32**,** 491-501.

Lin, M. Y., Cheng, X. T., Tammineni, P., Xie, Y., Zhou, B., Cai, Q. & Sheng, Z. H. 2017. Releasing Syntaphilin Removes Stressed Mitochondria from Axons Independent of Mitophagy under Pathophysiological Conditions. *Neuron,* 94**,** 595-610 e6.

Lo, K. Y., Kuzmin, A., Unger, S. M., Petersen, J. D. & Silverman, M. A. 2011. KIF1A is the primary anterograde motor protein required for the axonal transport of dense-core vesicles in cultured hippocampal neurons. *Neurosci Lett,* 491**,** 168-73.

Maday, S. & Holzbaur, E. L. F. 2014. Autophagosome biogenesis in primary neurons follows an ordered and spatially regulated pathway. *Dev. Cell,* 30**,** 71-85.

Maday, S., Twelvetrees, A. E., Moughamian, A. J. & Holzbaur, E. L. 2014. Axonal transport: cargo-specific mechanisms of motility and regulation. *Neuron,* 84**,** 292-309.

Magalhaes, A. C., Baron, G. S., Lee, K. S., Steele-Mortimer, O., Dorward, D., Prado, M. A. & Caughey, B. 2005. Uptake and neuritic transport of scrapie prion protein coincident with infection of neuronal cells. *J Neurosci,* 25**,** 5207-16.

Mckenney, R. J., Huynh, W., Vale, R. D. & Sirajuddin, M. 2016. Tyrosination of alpha-tubulin controls the initiation of processive dynein-dynactin motility. *EMBO J,* 35**,** 1175-85.

Medrano, A. Z., Barmada, S. J., Biasini, E. & Harris, D. A. 2008. GFP-tagged mutant prion protein forms intra-axonal aggregates in transgenic mice. *Neurobiol Dis,* 31**,** 20-32.

Mukhopadhyay, A., Barbieri, A. M., Funato, K., Roberts, R. & Stahl, P. D. 1997. Sequential actions of Rab5 and Rab7 regulate endocytosis in the Xenopus oocyte. *J Cell Biol,* 136**,** 1227-37.

Neumann, S., Chassefeyre, R., Campbell, G. E. & Encalada, S. E. 2017. KymoAnalyzer: a software tool for the quantitative analysis of intracellular transport in neurons. *Traffic,* 18**,** 71-88.

Newell, K. L., Boyer, P., Gomez-Tortosa, E., Hobbs, W., Hedley-Whyte, E. T., Vonsattel, J. P. & Hyman, B. T. 1999. Alpha-synuclein immunoreactivity is present in axonal swellings in neuroaxonal dystrophy and acute traumatic brain injury. *J Neuropathol Exp Neurol,* 58**,** 1263-8.

Norris, S. R., Soppina, V., Dizaji, A. S., Schimert, K. I., Sept, D., Cai, D., Sivaramakrishnan, S. & Verhey, K. J. 2014. A method for multiprotein assembly in cells reveals independent action of kinesins in complex. *J Cell Biol,* 207**,** 393-406.

Okada, Y., Yamazaki, H., Sekine-Aizawa, Y. & Hirokawa, N. 1995. The neuron-specific kinesin superfamily protein KIF1A is a unique monomeric motor for anterograde axonal transport of synaptic vesicle precursors. *Cell,* 81**,** 769-80.

Ovesny, M., Krizek, P., Borkovec, J., Svindrych, Z. & Hagen, G. M. 2014. ThunderSTORM: a comprehensive ImageJ plug-in for PALM and STORM data analysis and super-resolution imaging. *Bioinformatics,* 30**,** 2389-90.

Owen, F., Poulter, M., Collinge, J., Leach, M., Lofthouse, R., Crow, T. J. & Harding, A. E. 1992. A dementing illness associated with a novel insertion in the prion protein gene. *Brain Res Mol Brain Res,* 13**,** 155-7.

Pilling, A. D., Horiuchi, D., Lively, C. M. & Saxton, W. M. 2006. Kinesin-1 and Dynein are the primary motors for fast transport of mitochondria in Drosophila motor axons. *Mol Biol Cell,* 17**,** 2057-68.

Reed, N. A., Cai, D., Blasius, T. L., Jih, G. T., Meyhofer, E., Gaertig, J. & Verhey, K. J. 2006. Microtubule acetylation promotes kinesin-1 binding and transport. *Curr. Biol.,* 16**,** 2166-2172.

Sapp, E., Penney, J., Young, A., Aronin, N., Vonsattel, J. P. & Difiglia, M. 1999. Axonal transport of N-terminal huntingtin suggests early pathology of corticostriatal projections in Huntington disease. *J Neuropathol Exp Neurol,* 58**,** 165-73.

Schwarz, T. L. 2013. Mitochondrial trafficking in neurons. *Cold Spring Harb Perspect Biol,* 5, a011304.

Sgro, A. E., Bajjalieh, S. M. & Chiu, D. T. 2013. Single-axonal organelle analysis method reveals new protein-motor associations. *ACS Chem Neurosci,* 4**,** 277-84.

Sheng, Z. H. & Cai, Q. 2012. Mitochondrial transport in neurons: impact on synaptic homeostasis and neurodegeneration. *Nat Rev Neurosci,* 13**,** 77-93.

Shields, L. Y., Li, H., Nguyen, K., Kim, H., Doric, Z., Garcia, J. H., Gill, T. M., Haddad, D., Vossel, K., Calvert, M. & Nakamura, K. 2021. Mitochondrial fission is a critical modulator of mutant APP-induced neural toxicity. *J Biol Chem,* 296**,** 100469.

Sikorska, B., Liberski, P. P., Giraud, P., Kopp, N. & Brown, P. 2004. Autophagy is a part of ultrastructural synaptic pathology in Creutzfeldt-Jakob disease: a brain biopsy study. *Int J Biochem Cell Biol,* 36**,** 2563-73.

Song, Y. & Brady, S. T. 2015. Post-translational modifications of tubulin: pathways to functional diversity of microtubules. *Trends Cell Biol,* 25**,** 125-36.

Steffen, J. & Koehler, C. M. 2018. ER-mitochondria contacts: Actin dynamics at the ER control mitochondrial fission via calcium release. *J Cell Biol,* 217**,** 15-17.

Stokin, G. B., Lillo, C., Falzone, T. L., Brusch, R. G., Rockenstein, E., Mount, S. L., Raman, R., Davies, P., Masliah, E., Williams, D. S. & Goldstein, L. S. 2005. Axonopathy and transport deficits early in the pathogenesis of Alzheimer's disease. *Science,* 307**,** 1282-8.

Szpankowski, L., Encalada, S. E. & Goldstein, L. S. 2012. Subpixel colocalization reveals amyloid precursor protein-dependent kinesin-1 and dynein association with axonal vesicles. *Proc Natl Acad Sci U S A,* 109**,** 8582-7.

Tarsa, L. & Goda, Y. 2002. Synaptophysin regulates activity-dependent synapse formation in cultured hippocampal neurons. *Proc Natl Acad Sci U S A,* 99**,** 1012-6.

Tas, R. P., Chazeau, A., Cloin, B. M. C., Lambers, M. L. A., Hoogenraad, C. C. & Kapitein, L. C. 2017. Differentiation between Oppositely Oriented Microtubules Controls Polarized Neuronal Transport. *Neuron,* 96**,** 1264-1271 e5.

Tinevez, J. Y., Perry, N., Schindelin, J., Hoopes, G. M., Reynolds, G. D., Laplantine, E., Bednarek, S. Y., Shorte, S. L. & Eliceiri, K. W. 2017. TrackMate: An open and extensible platform for single-particle tracking. *Methods,* 115**,** 80-90.

Trajkovic, K., Jeong, H. & Krainc, D. 2017. Mutant Huntingtin Is Secreted via a Late Endosomal/Lysosomal Unconventional Secretory Pathway. *J Neurosci,* 37**,** 9000-9012.

Vande Velde, C., Mcdonald, K. K., Boukhedimi, Y., Mcalonis-Downes, M., Lobsiger, C. S., Bel Hadj, S., Zandona, A., Julien, J. P., Shah, S. B. & Cleveland, D. W. 2011. Misfolded SOD1 associated with motor neuron mitochondria alters mitochondrial shape and distribution prior to clinical onset. *PLoS One,* 6**,** e22031.

Veith, N. M., Plattner, H., Stuermer, C. A., Schulz-Schaeffer, W. J. & Burkle, A. 2009. Immunolocalisation of PrPSc in scrapie-infected N2a mouse neuroblastoma cells by light and electron microscopy. *Eur J Cell Biol,* 88**,** 45-63.

Wang, Y., Xu, E., Musich, P. R. & Lin, F. 2019. Mitochondrial dysfunction in neurodegenerative diseases and the potential countermeasure. *CNS Neurosci Ther,* 25**,** 816-824.

Wong, Y. C., Peng, W. & Krainc, D. 2019. Lysosomal Regulation of Inter-mitochondrial Contact Fate and Motility in Charcot-Marie-Tooth Type 2. *Dev Cell,* 50**,** 339-354 e4.

Wong, Y. C., Ysselstein, D. & Krainc, D. 2018. Mitochondria-lysosome contacts regulate mitochondrial fission via RAB7 GTP hydrolysis. *Nature,* 554**,** 382-386.

Wood, A. R., Foliaki, S. T., Groveman, B. R., Walters, R. O., Williams, K., Yuan, J., Zou, W. Q. & Haigh, C. L. 2022. Hereditary E200K mutation within the prion protein gene alters human iPSC derived cardiomyocyte function. *Sci Rep,* 12**,** 15788.

Wu, J. W., Herman, M., Liu, L., Simoes, S., Acker, C. M., Figueroa, H., Steinberg, J. I., Margittai, M., Kayed, R., Zurzolo, C., Di Paolo, G. & Duff, K. E. 2013. Small misfolded Tau species are internalized via bulk endocytosis and anterogradely and retrogradely transported in neurons. *J Biol Chem,* 288**,** 1856-70.

Xie, Y. X., Naseri, N. N., Fels, J., Kharel, P., Na, Y., Lane, D., Burre, J. & Sharma, M. 2022. Lysosomal exocytosis releases pathogenic alpha-synuclein species from neurons in synucleinopathy models. *Nat Commun,* 13**,** 4918.

Xu, C. S., Hayworth, K. J., Lu, Z., Grob, P., Hassan, A. M., Garcia-Cerdan, J. G., Niyogi, K. K., Nogales, E., Weinberg, R. J. & Hess, H. F. 2017a. Enhanced FIB-SEM systems for large-volume 3D imaging. *eLife,* 6**,** e25916.

Xu, Z., Schaedel, L., Portran, D., Aguilar, A., Gaillard, J., Marinkovich, M. P., Thery, M. & Nachury, M. V. 2017b. Microtubules acquire resistance from mechanical breakage through intralumenal acetylation. *Science,* 356**,** 328-332.

Yogev, S., Cooper, R., Fetter, R., Horowitz, M. & Shen, K. 2016. Microtubule Organization Determines Axonal Transport Dynamics. *Neuron,* 92**,** 449-460.

Youle, R. J. & Van Der Bliek, A. M. 2012. Mitochondrial fission, fusion, and stress. *Science,* 337**,** 1062-5.

Zanusso, G., Polo, A., Farinazzo, A., Nonno, R., Cardone, F., Di Bari, M., Ferrari, S., Principe, S., Gelati, M., Fasoli, E., Fiorini, M., Prelli, F., Frangione, B., Tridente, G., Bentivoglio, M., Giorgi, A., Schinina, M. E., Maras, B., Agrimi, U., Rizzuto, N., Pocchiari, M. & Monaco, S. 2007. Novel prion protein conformation and glycotype in Creutzfeldt-Jakob disease. *Arch Neurol,* 64**,** 595-9.

Zhong, G., He, J., Zhou, R., Lorenzo, D., Babcock, H. P., Bennett, V. & Zhuang, X. 2014. Developmental mechanism of the periodic membrane skeleton in axons. *eLife,* 3, e04581.

Zhu, T., Chen, J. L., Wang, Q., Shao, W. & Qi, B. 2018. Modulation of Mitochondrial Dynamics in Neurodegenerative Diseases: An Insight Into Prion Diseases. *Front Aging Neurosci,* 10**,** 336.

4

Mechanism and Function of mRNA transport to the axonal pre-synapse

Content

4.1 Introduction 175

4.2 Materials and Methods 177

4.2.1 *Drosophila* genetics 177

A. Maintenance temperature and crosses 177

B. *Gal4/Gal80^{ts}/UAS* gene expression control system 182

C. Transgenesis of the MS2 lines by CRISPR/Cas9 and MS2-MCP mating scheme for live imaging of endogenous mRNA 183

D. Tissue- and time-specific regulation of gene expression with Flippase (FLP) recognition target (FRT) site precise insertion to the genomic loci 186

4.2.2 *Drosophila* larval fillet preparation and spaced chemical stimulation 190

4.2.3 *Drosophila* larval brain primary culture 193

4.2.4 Immunofluorescence (IF) 195

4.2.5 RNA single-molecule fluorescence in situ hybridization (smFISH) 197

4.2.6 Image analysis for smFISH and IF at the NMJ 200

4.2.7 Live imaging of mRNA with MS2-MCP system with denoising 203

4.2.8 RNA single-molecule hybridization chain reaction (smHCR) 204

4.2.9 High-throughput larval locomotion assay and analysis 207

4.2.10 Generation of graphs, figures, and statistical analyses 209

4.3 Results 209

4.3.1 Absolute quantitation of mRNA copy number in the *Drosophila* larval motoneurons 209

4.3.2 Oscillatory bidirectional motion of mRNA in motoneuron axons 212

4.3.3 Reduction of Kinesin-1 and Cytoplasmic Dynein motor speed impairs axonal mRNA localization and synaptic plasticity 215

4.3.4 Kinesin-1 and Imp are putative axonal transport machinery for *rab11* mRNA and are required for synaptic plasticity. 220

4.3.5 Reduction of *rab11* mRNA copy number, not protein, correlates with NMJ development 223

4.3.6 A family of RabGTPase transcripts are localized to axon terminals and glial extensions at the NMJ and are important for function 225

4.4 Conclusion and discussion 229

4.5 References 234

4.1 Introduction

The extended architecture of neurons and glial cells in the central and peripheral nervous systems poses a major challenge for effective delivery and maintenance of proteins at the periphery. In neurons, messenger ribonucleic acid (mRNA) can be actively transported along microtubules (MTs) from the soma and to be stably kept locally in distal axons, dendrites, and at the synapses, where protein synthesis and degradation machineries are present for local translation (Das et al., 2019; Rangaraju et al., 2017). After transcription, mRNA can be alternatively spliced into different isoforms, some of which contain signals that recruit *cis*- and *trans*-acting factors to regulate its stability and transport, including hitchhiking on organelles (Bhat et al., 2022; Vargas et al., 2022). Recent studies propose that the mRNA localization for localized translation in the periphery of neurons and glia is a ubiquitous strategy of many protein families, including the transcripts of molecular motors and their adaptor proteins, and of small GTPases in the Rab and Arf/Arf-like(Arl) families (Rangaraju et al., 2017; Sun and Schuman, 2022; Gala et al., 2022; Titlow et al., 2022). The function of many Rab proteins to orchestrate vesicular and endosomal sorting at the synapse is well-established; however, our current understanding of *rab* mRNA transport and local translation at distal axonal sites is extremely limited.

The technological progress of quantitative RNA visualization tools allows scientists to detect single-molecule RNA species at high throughout, high sensitivity, and high precision (Shah et al., 2016; Yang et al., 2017; Lee et al., 2022). An RNA single-molecule *in situ* hybridization (smFISH) survey of 200 transcripts from *Drosophila* yellow fluorescent protein (YFP) protein-trap collections revealed that YFP-tagged proteins and mRNAs of *rab1*, *rab11,* and

Rab guanosine diphosphate (GDP) disassociation inhibitor (*gdi*) are present at the motoneuron terminal boutons at the neuromuscular junction (NMJ), possibly being actively transported to undergo localized translation (Titlow et al., 2022). Rab11 protein is a master regulator of endosome recycling at the neuronal pre-synapse and a modulator of synaptic function/dysfunction in Huntington's disease (HD) (Giorgini and Steinert, 2013; Kokotos et al., 2018). The presence of mRNAs of *rab11* and its chaperone *gdi* suggests the unexplored roles of localized protein synthesis to regulate membrane trafficking pathways at the pre-synaptic compartment. This experimental chapter aimed to explore the mechanism and function of mRNA transport in motoneurons towards their long-lived residence at the *Drosophila* larval NMJ, a well-established model to study synaptic development and plasticity to the molecular detail. Sensitive detection of endogenous *rab11* mRNA by smFISH showed that the transcripts are present in motoneuron terminal boutons, glial protrusions, and the post-synaptic densities in the muscle at the NMJ. High-resolution live imaging of *rab11* and *gdi* mRNAs by endogenous insertion of MS2 stem loop to bind MS2-capping protein fused to GFP (MCP-GFP) indicated that both transcripts show bidirectional, yet non-processive transport in cultured motoneuron axons. Proper localization of *rab11* and *gdi* mRNAs at the motoneuron axon terminal boutons requires kinesin-1 heavy chain (Khc), but not dynein heavy chain (Dhc), even though both *kinesin-1* and *dynein* mutant larvae display defects in synaptic plasticity and crawling behavior. To find out a putative RBP that mediates axonal entry of *rab11* mRNA to be transported to the axon termini, individual-nucleotide resolution UV crosslinking and immunoprecipitation (iCLIP) from *Drosophila* cells and the larval brains identified that a conserved RBP called insulin growth factor II

(IGF-II) mRNA binding protein (Imp) has a strong preference for the 3′ untranslated region (UTR) of *rab11* transcripts. Here, I discuss two transgenesis strategies that could be used to insert Flippase enzyme recognition target (FRT) sites within the Imp-binding regions of the *rab11* 3'UTR (or other Imp targets) to test whether the putative localization signal within the transcripts is necessary for mRNA localization and neuromuscular function, with tissue- and developmental stage- specificity. Thus far, I found that reducing Imp level or Khc protein activity or both specifically in motoneurons during the larval stages reduces the copy number of *rab11* mRNA at the NMJ pre-synaptic axon termini and resulted in defects of synaptic plasticity and larval locomotion. Knocking down of *rab11* by a validated RNAi in motoneurons during the larval stages also reduced *rab11* mRNA copy number at the NMJ pre-synapse. Finally, I found that transcripts of many *Rab* genes are localized at the motoneuron axon termini and glial extensions at the NMJ, many of which showed tissue-specific functional requirements upon RNAi knock-down by tissue-specific drivers, suggesting the generalized yet unexplored aspects of RNA-based regulation of membrane trafficking at the synapse.

4.2 Materials and Methods

4.2.1 *Drosophila* genetics

A. Maintenance temperature and crosses

The fly lines used in this study were kept in a standard cornmeal-agar food at 18˚C for long-term maintenance, 25˚C for most experiments, and 30˚C for temperature-sensitive experiments (such as those containing *tub-gal80*^{ts} and *khc*^{ts}). The fly stocks at 18˚C were tipped to a new food every 3-4 weeks. Flies at

25˚C were tipped to a new food every 1-2 weeks. Flies that were shifted to 30˚C were kept no more than 3 days and only the crawling late 3rd instar larvae were collected. Virgin female tubes were maintained at 18˚C and shifted to 25˚C during the day to maximize the number of pupal eclosion. The experiments done at room temperature in this study means 19-21˚C. The full list of all genotypes, the source, and genetic crosses are provided in Table 1.

Number	Abbreviation	Genotypes	Source/Publication
1	**Oregon-R (OrR)/ wildtype (WT)**	**Oregon-R**	**Davis Lab Stock**
2	Double balancers	$;\frac{Gla}{CyOGFP};\frac{pri}{TM6B^{tb}}$	Davis Lab Stock
3	khc^{27}	$;\frac{khc^{27}}{CyOGFP};\frac{pri}{TM6B^{tb}}$	Davis Lab Stock (Brendza et al., 2000)
4	khc^{23}	$;\frac{khc^{23}}{CyOGFP};$	Davis Lab Stock (Brendza et al., 1999)
5	$\boldsymbol{khc^{27}/khc^{23}}$	$;\frac{\boldsymbol{khc^{27}}}{\boldsymbol{khc^{23}}};$	$;\frac{\boldsymbol{khc^{27}}}{\boldsymbol{CyOGFP}};\frac{\boldsymbol{pri}}{\boldsymbol{TM6B^{tb}}}\times;\frac{\boldsymbol{khc^{23}}}{\boldsymbol{CyOGFP}};$
6	khc^{ts}	$w;\frac{khc^{1ts}}{CyOGFP};\frac{pri}{TM6B^{tb}}$	Davis Lab Stock (Saxton et al., 1991)
7	$\boldsymbol{khc^{ts}/khc^{23}}$	$;\frac{\boldsymbol{khc^{1ts}}}{\boldsymbol{khc^{23}}};$	$\boldsymbol{w};\frac{\boldsymbol{khc^{1ts}}}{\boldsymbol{CyOGFP}};\frac{\boldsymbol{pri}}{\boldsymbol{TM6B^{tb}}}\times;\frac{\boldsymbol{khc^{23}}}{\boldsymbol{CyOGFP}};$
8	khc^{8}	$;\frac{khc^{8}}{CyODGY};$	Davis Lab Stock (Brendza et al., 1999)
9	$\boldsymbol{khc^{ts}/khc^{8}}$	$;\frac{\boldsymbol{khc^{1ts}}}{\boldsymbol{khc^{8}}};$	$\boldsymbol{w};\frac{\boldsymbol{khc^{1ts}}}{\boldsymbol{CyOGFP}};\frac{\boldsymbol{pri}}{\boldsymbol{TM6B^{tb}}}\times;\frac{\boldsymbol{khc^{8}}}{\boldsymbol{CyODGY}};$
10	dhc^{8-1}	$;;\frac{dhc64C^{8-1}}{TM6B^{tb}}$	Davis Lab Stock (Melkov et al., 2016)
11	dhc^{6-6}	$;;\frac{dhc64C^{6-6}}{TM6B^{tb,D,Hu}}$	Davis Lab Stock (Gepner et al., 1996)
12	$\boldsymbol{dhc^{8-1}/dhc^{6-6}}$	$;;\frac{\boldsymbol{dhc64C^{8-1}}}{\boldsymbol{dhc64C^{6-6}}}$	$;;\frac{\boldsymbol{dhc64C^{8-1}}}{\boldsymbol{TM6B^{tb}}}\times;;\frac{\boldsymbol{dhc64C^{6-6}}}{\boldsymbol{TM6B^{tb},D,Hu}}$
13	$rab11MS2\times24^{+dsRed}$	$;;\frac{Rab11MS2x24^{+dsRed}}{"}$	This study by Francesca Robertson

14	*rab11MS2×24^{loxed}*	; $\frac{CyoGFP}{+}$; $\frac{Rab11MS2x24^{loxed}}{TM6B^{tb}}$	This study by Francesca Robertson
15	*UAS-mCD8mCh, MCPGFP, tubGal80^{ts}*	; $\frac{UAS-mCD8mCh,MCPGFP}{CyOGFP}$; $\frac{tubGal80^{ts}}{TM6B^{tb}}$	This study by Francesca Robertson
16	*rab11MS2×24^{loxed}, UAS-mCD8mCh, MCPGFP*	; $\frac{UAS-mCD8mCh,MCPGFP}{+}$; $\frac{Rab11MS2x24^{loxed}}{TM6B^{tb}}$	; $\frac{UAS-mCD8mCh,MCPGFP}{CyOGFP}$; $\frac{tubGal80^{ts}}{TM6B^{tb}}$ × ; $\frac{CyoGFP}{+}$; $\frac{Rab11MS2x24^{loxed}}{TM6B^{tb}}$
17	*gdi2MS2×24^{+dsRed}*	; $\frac{Gdi2MS2\times24^{+DsRed}}{"}$;	This study by Francesca Robertson
18	*gdi2MS2×24^{loxed}*	; $\frac{Gdi2MS2\times24^{loxed}}{CyOGFP}$; $\frac{pri}{TM6B^{tb}}$	This study by Francesca Robertson
19	*gdi2MS2×24^{loxed}, D42-Gal4*	; $\frac{Gdi2MS2\times24^{loxed}}{CyOGFP}$; $\frac{D42Gal4}{TM6B^{tb}}$	This study by Francesca Robertson
20	*OK371-Gal4, tub-gal80^{ts}*	; $\frac{OK371Gal4}{CyOGFP,"}$; $\frac{tubGal80^{ts}}{TM6B^{tb},"}$	This study, balanced from w^{1118}; P{GawB}VGlut^{OK371} (BDSC#26160)
21	*D42-Gal4, tub-gal80^{ts}*	; $\frac{tubGal80^{ts}}{CyOGFP,"}$; $\frac{D42Gal4}{TM6B^{tb},"}$	This study, balanced from w*; P{GawB}D42 (BDSC#8816)
22	***rab11MS2×24^{loxed}; OK371>MCP-GFP, mCD8-mCh; tub-Gal80^{ts}***	; $\frac{UAS-MCPGFP,mCD8mCh}{OK371Gal4}$; $\frac{Rab11MS2x24^{+dsRed}}{tubGal80^{ts}}$	; $\frac{OK371Gal4}{"}$; $\frac{tubGal80^{ts}}{"}$ × ; $\frac{UAS-MCPGFP,mCD8mCh}{+}$; $\frac{Rab11MS2x24^{+dsRed}}{TM6B^{tb}}$
23	***gdi2MS2×24^{loxed}; D42>MCP-GFP, mCD8-mCh; tub-Gal80^{ts}***	; $\frac{Gdi2MS2\times24^{loxed}}{UAS-mCD8mCh,MCPGFP}$; $\frac{D42Gal4}{tubGal80^{ts}}$	; $\frac{Gdi2MS2\times24^{loxed}}{CyOGFP}$; $\frac{D42Gal4}{TM6B^{tb}}$ × ; $\frac{UAS-mCD8mCh,MCPGFP}{CyOGFP,"}$; $\frac{tubGal80^{ts}}{TM6B^{tb},"}$

24	***rab11MS2×24^{loxed}; D42>MCP-GFP, mCD8-mCh; tub-Gal80^{ts}***	$;\frac{UAS-MCPGFP,mCD8mCh}{tubGal80^{ts}};\frac{Rab11MS2x24^{+dsRed}}{D42Gal4}$	$;\frac{tubGal80^{ts}}{"};\frac{D42Gal4}{"}\times;\frac{UAS-MCPGFP,mCD8mCh}{+};\frac{Rab11MS2x24^{+dsRed}}{TM6B^{tb}}$
25	*Imp* RNAi	$;\frac{tubgal80^{ts}}{CyOGFP,"};\frac{UAS-ImpRNAi}{TM6B^{tb},"}$	This study, derived from RRID: BDSC_34977 (Samuels et al., 2020)
26	*Rab11* RNAi	*UAS-Rab11* RNAi (KK) on II	VDRC: 108382
27	*Rab4* RNAi	*UAS-Rab4* RNAi (GD) on III	VDRC: 24672
28	*Rab5* RNAi	*UAS-Rab5* RNAi (KK) on II	VDRC: 103945
29	*Rab7* RNAi	*UAS-Rab7* RNAi (GD) on III	VDRC: 40337
30	*Rab8* RNAi	*UAS-Rab8* RNAi (GD) on II	VDRC: 28092
31	*Rab9* RNAi	*UAS-Rab9* RNAi (KK) on II	VDRC: 107192
32	*Rab35* RNAi	*UAS-Rab35* RNAi (KK) on II	VDRC: 101361
33	***Repo-Gal4, UAS-mCD8GFP***	$;\frac{UAS-mCD8GFP}{"};\frac{RepoGal4}{TM6B^{tb}}$	**Davis Lab Stock**
34	***Mdr65-Gal4, UAS-mCD8GFP***	$;;\frac{Mdr65Gal4,UAS-mCD8GFP}{TM6B^{tb},"}$	**Davis Lab Stock**
35	**Imp-GFSTF2**	**y[1] w[*] Mi{PT-GFSTF.2}Imp[MI05901-GFSTF.2]**	RRID:BDSC_60237

Table 1 *Drosophila* lines used in this study. The ones in bold are used for experiments.

B. *Gal4/Gal80^{ts}/UAS* gene expression control system

The *Gal4/UAS* system comprises of a transcription activator GAL4 from yeast and the enhancer called the upstream activation sequence (*UAS*) that GAL4 binds to activate transcription (Duffy, 2002). The presence of GAL4 by itself has little to no effect, and in *Drosophila*, >10,000 of '*Gal4* lines' were created to express GAL4 in specific tissues/cell types thereby driving tissue-specific transcription of *Drosophila* promotors linked to *UAS* (Fischer et al., 1988). *Gal80^{ts}* is a temperature-sensitive allele of GAL80 repressor that binds GAL4 and prevents the activation of a gene under *UAS* (Sean E. McGuire et al., 2004). In *Drosophila*, *gal80^{ts}* was cloned under tubulin promotor (*tub-gal80^{ts}*), and when combined with *Gal4* lines could control *Gal4* expression at any life stage, with optimal repression between 18-20°C and de-repression at 30°C (Sean E McGuire et al., 2004). A combination of *Gal4/Gal80^{ts}/UAS* in a single fly allows a spatial and temporal control over transgene expression.

In this study, I used two well-characterized motoneuron *Gal4* drivers, *OK371-Gal4* and *D42-Gal4* (Sanyal, 2009), crossed to *tub-gal80^{ts}* from the Bloomington *Drosophila* Stock Center. *OK371-Gal4* was reported to express earlier than *D42-Gal4* (Xia et al., 2012), but both labeled abundant types of motor neurons in the VNC and the NMJ of the 3rd instar larvae. These lines were kept balanced with appropriate 2nd or 3rd chromosome balancers, and the homozygotes were selected for crossing to *UAS* transgene (Table 1). For glial markers, I used *repo-Gal4* for a pan-glial driver line, and *Mdr65-Gal4* for sub-perineurial glial driver.

C. Transgenesis of the MS2 lines by CRISPR/Cas9 and MS2-MCP mating scheme for live imaging of endogenous mRNA

MS2 stem loops were introduced to the endogenous loci of *rab11* and *gdi* genes with CRISPR/Cas9 technology by Francesca Robertson following a published protocol (Hoppe and Ashe, 2021). In brief, the sequences of the genes (+1kb of flanking sequences) were downloaded on ensemble (https://www.ensembl.org/). CRISPOR (http://crispor.tefor.net/) tool was used to help design and evaluate guide RNA (gRNA). The gRNA sequences were selected based on the lowest number of off-targets. When 3-4nt off-targets mismatches were present, these mismatches should be within the 'seed' sequence, or on a different chromosome, and are not exonic. To make the guide construct (GC), pCFD5 cloning protocol was used to express multiple tRNA-flanked Cas9 gRNAs under the control of the RNA pol III promoter U6:3 (Fu et al., 2014; Port et al., 2014). To design the homology constructs (HC), 500-nt left and right homology arms (HA) (ordering from DNAstring: https://www.thermofisher.com/uk/en/home/life-science/cloning/gene-synthesis.html) were inserted into pDsRed_MS2v5x24 vector using In-Fusion (Takara Bio) (**Figure 4.1A**). The LHA was inserted at the SacI site in the pDsRed_MS2v5x24 vector. The RHA is inserted at the SpeI site in the pDsRed_MS2v5x24 (**Figure 4.1A**). The positive transformed bacterial colonies were sent to sequencing (SourceBioscience).

Then, a mix of 500 ng/µL of the HC and 250 ng/µL of the GC were sent to the Cambridge Fly Facility. For both *rab11* and *gdi*, the DNA mix was injected into the fly BL55821 (genotype y[1] M{GFP[E.3xP3]=vas-Cas9.RFP-}ZH-2A w[1118]) that expresses Cas9 protein in the ovary under control of vas

regulatory sequences. Insertion is marked with 3xP3-GFP. The original loxP-3xP3-RFP-loxP was removed from M{vas-Cas9} to generate M{vas-Cas9.RFP-}. The Cambridge Fly Facility sent back the transformed, balanced +dsRed stock, and we checked the flies first for the health and reproduction, and whether the flies could become homozygotes for the transgenes. We double checked if the insertion is in the right place by PCR the region outside of HA into the MS2 tags. Then, the flies were crossed to a Cre-expressing line y[1] w[67c23]; MKRS, P{ry[+t7.2]=hsFLP}86E/TM6B, P{w[+mC]=Crew}DH2, Tb[1] (BDSC#1501) to 'lox out' the +DsRed marker. The progeny lines *rab11*-MS2×24^{loxed} and *gdi2*-MS2×24^{loxed} were balanced for the experiments (Table 1) (**Figure 4.1B**).

To label mRNA carrying MS2 stem loops, the MS2 capping protein conjugated to GFP (MCP-GFP) was expressed under *UAS* control for tissue-specific *Gal4* expression control, and usually co-expressed with *UAS-mCD8-mCh* to label the whole cell. The version of MCP-GFP that we use contains a nuclear localization sequence (NLS) to sequester unbound MCP to the nucleus (Bauer et al., 2019), thus allowing RNA-bound MCP-GFP puncta to be observed with little background fluorescence. In our experience, this system needs to be combined with *tub-gal80*^{ts} to limit the MCP-GFP expression to a few days prior to imaging.

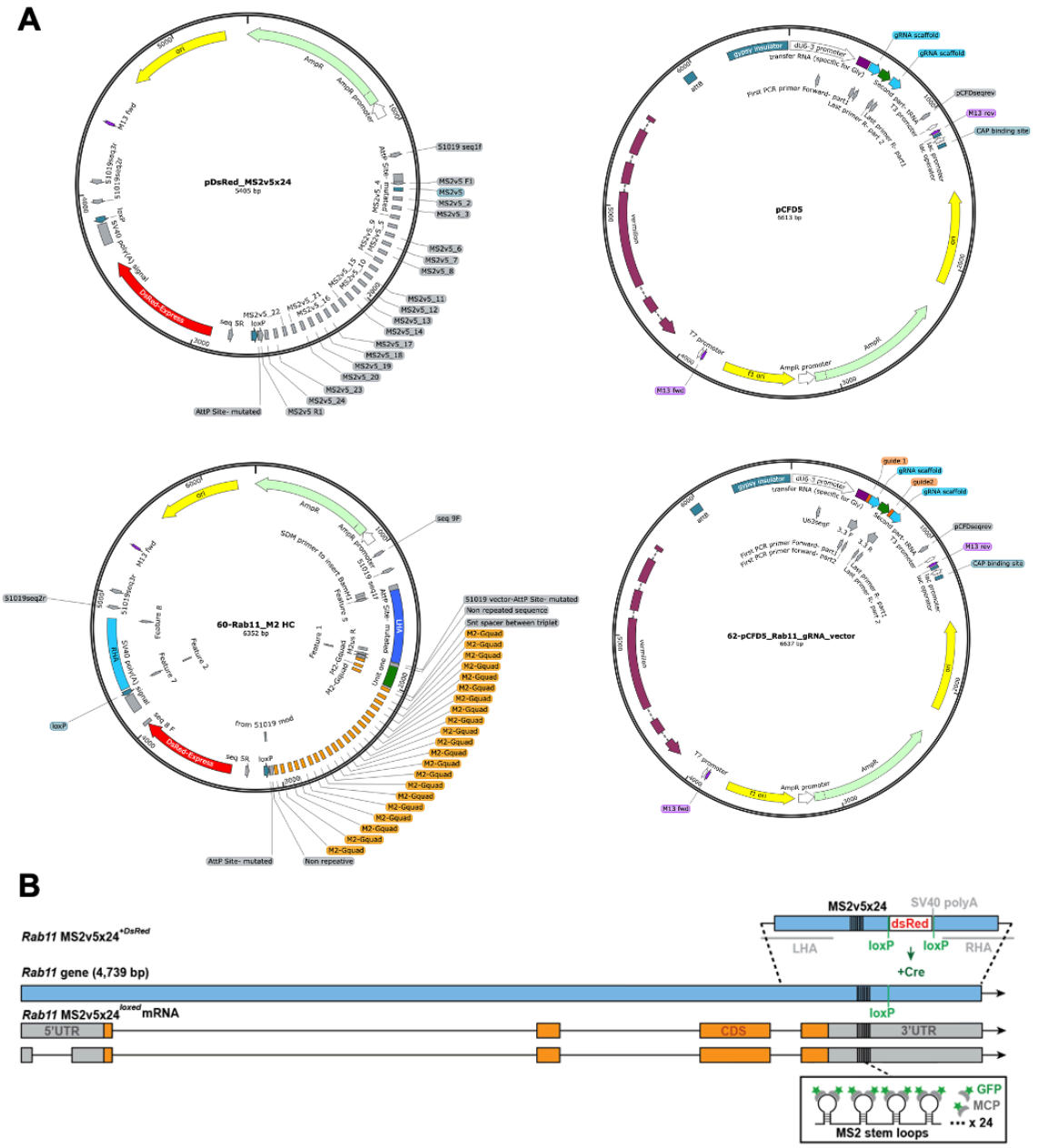


Figure 4.1 Transgenesis of *Rab11* MS2 lines for MS2-MCP imaging. **(A)** pDsRed_MS2v5x24 original vector for Homology Construct (HC) cloning (top left), Rab11 HC vector containing left homology arm (LHA) and right homology arm (RHA) (bottom left), pCFD5 original vector for Guide Construct (GC) cloning (top right), Rab11 GC construct (bottom right). **(B)** The successful homology-directed repair from CRISPR/Cas9 technology yielded a $Rab11MS2v5{\times}24^{+dsRed}$ fly. DsRed was first removed by Cre expression. $Rab11MS2v5{\times}24^{loxed}$ mRNA with 24×MS2 step loops in the 3'UTR can be occupied by 48 molecules of MS2-capping protein-GFP (MCP-GFP). UTR = untranslated region. CDS = coding sequence.

D. Tissue- and time-specific regulation of gene expression with Flippase (FLP) recognition target (FRT) site precise insertion to the genomic loci

(1) ΦC31 integrase-mediated attP × attB cassette exchange

Among many powerful *Drosophila* genetics resources, a recent development of nearly 3,000 gene/enhancer trap collections based on the transposon *Minos*-Mediated Integration Cassette (MiMIC) and CRISPR-Mediated Integration Cassette (CRIMIC) provides pre-existing landing sites in the *Drosophila* genome for a Recombinase-Mediated Cassette Exchange (RMCE) (Avellaneda and Schnorrer, 2022; Lee et al., 2018; Nagarkar-Jaiswal et al., 2015; Venken et al., 2011). This genetic tool allows a precise, unidirectional swap between a DNA cassette flanked by two attachment sites from bacteriophage (*attP* sites) in the genome of MiMIC/CRIMIC flies and any piece of DNA flanked by two attachment sites from bacteria (*attB* sites) that can be cloned and purified in the lab for co-injection with ΦC31 integrase for RMCE (Chalberg et al., 2006).

I aim to insert two parallel-oriented wildtype Flippase Recognition Target (FRT) sites ($^{5'}$GAAGTTCCTATTC*tctagaaa*G*t*ATAGGAACTTC$^{3'}$), a highly efficient conditional deletion than the Cre/Lox system (Park et al., 2011), in the 3'UTR of *rab11* gene to perform Flippase-mediated cleavage of the 3'UTR piece. To achieve this, I will use the TI{CRIMIC.TG4.1}*Rab11*$^{\text{CR60112-TG4.1}}$ (*rab11*-CRIMIC) line, which contains 2×*attP*-flanked cassette in the first intron (**Figure 4.2C**). The *rab11*-CRIMIC adults are viable and available to order from the Bloomington *Drosophila* Stock Center (BDSC #93953). Next, there is an existing *attB* gene trap plasmid with a splice acceptor (SA) right after *attB1* site (pBS-

KS-attB1-2-GT-SA) (**Figure 4.2A**) that is suitable for cloning *rab11* CDS (exon 2-4) and modified 3'UTR with FRT sites between two *attB* sites by Gibson Assembly (**Figure 4.2B**). The polyadenylation signal of *Drosophila* (Retelska et al., 2006) is inserted after the second FRT site and before attB2 site for a proper 3' end processing. The correct insertion of all components in this modified plasmid called pBS-KS-attB1-2-GT-SA-*Rab11*-2×FRT-3'UTR is to be confirmed by PCR before sending for microinjection into *rab11*-CRIMIC embryos along with ΦC31 integrase for RMCE (**Figure 4.2C**). Successful cassette exchange can be confirmed with PCR for a present of FRT sites at the 3'UTR and/or screened for a lack of GFP in the original CRIMIC cassette (**Figure 4.2C-D**). Mature mRNA of *rab11*Δ3'UTR-2×FRT should contain FRT sites at the 3'UTR, and the rest of the mRNA should be the same as unmodified *rab11* mRNA (**Figure 4.2E**), which can be confirmed by smFISH. The phenotype of homozygous or balanced *rab11*Δ3'UTR-2×FRT larvae should be thoroughly checked, including testing for normal *rab11* transcription, proper *rab11* mRNA localization and stability in neurons, and checked for NMJ morphology, as well as larval behaviors compared to a wildtype.

To cleave off the 3'UTR of *rab11* mRNA in a tissue- and time-specific manner, the homozygous *rab11*Δ3'UTR-2xFRT or balanced *rab11*Δ3'UTR-2xFRT/*TM6B*^{tb} flies will be mated to flies containing *D42-Gal4* or other motoneuron drivers, *UAS-Flippase*, and *tub-gal80*^{ts}. The flies containing all 4 components do not express the Flippase enzyme at 18°C due to Gal80^{ts} inhibition (**Figure 4.2F**) but do express the Flippase enzyme at 30°C in the absence of Gal80^{ts} protein, resulting in a cleavage of 3'UTR region flanked by the FRT sites (**Figure 4.2G-H**). This method presents a novel and precise mRNA manipulation, to determine whether a signal within the 3'UTR or other regions of a transcript

is necessary for post-transcriptional regulations (i.e., stability, transport, localization) and function, in a tissue-specific and developmental stage-specific manner.

The strength of this method is that there are already a few thousands of existing MiMIC/CRIMIC lines with precise location of the *attP* landing sites in the 5' or 3' UTRs or intronic regions. In addition, during cloning of *attB* plasmids, DNA pieces—such as FRT sites and poly(A) signal—can be assembled with different cDNAs easily to scale up the Gibson assembly to study several genes or make several deletions of the same gene. The downside of this method is that unexpected alternative splicing patterns could lead to the transcripts that do not contain FRT sites (**Figure 4.2D**).

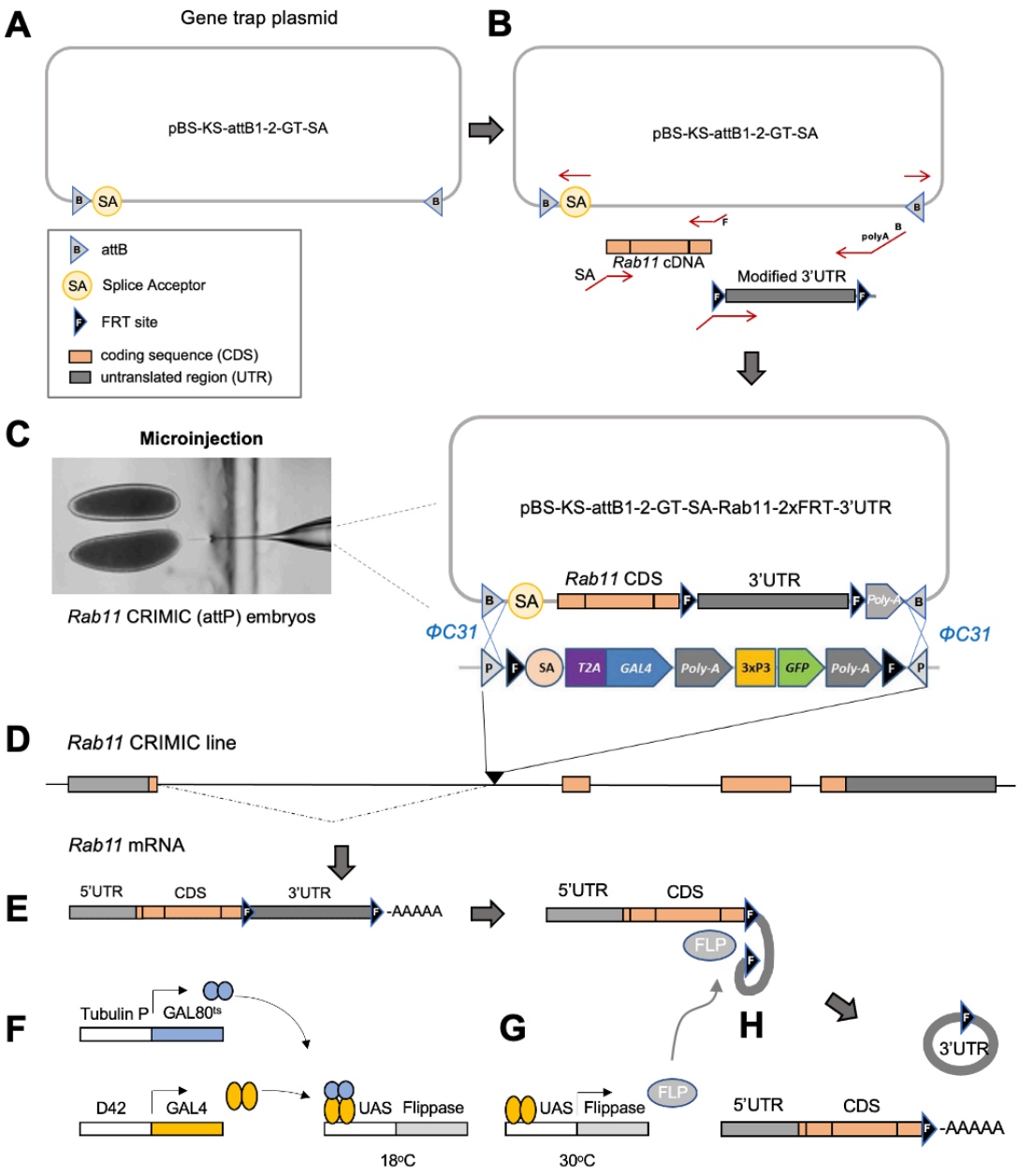


Figure 4.2 Transgenesis of Rab11Δ3'UTR-2xFRT and FLP mating scheme for tissue-specific knockdown in post-developmental stages. (A) A gene trap plasmid construct. (B) Gibson assembly of different DNA fragments. (C) Microinjection of the designed plasmid in the Rab11 CRIMIC embryos. (D) Rab11 CRIMIC landing site. (E) Mature mRNA of the transgenic fly. (F) Spatial and temporal control of Flippase expression with tubGAL80^{ts}. (G) At 30°C, Flippase binds FRT sites and cleaves off the 3'UTR of Rab11. (H) A truncated Rab11 lacking 3'UTR.

(2) CRISPR-mediated double stranded homology donor (dsDNA drop-in)

To overcome a possibility of aberrant splicing that could result in missing FRT sites in the transcripts (**Figure 4.2**), we collaborated with Oguz Kanca and Hugo Bellen to come up with an alternative strategy using the CRISPR/Cas9 genome editing to insert FRT sites directly to endogenous *rab11* 3'UTR regions. This method was shown to efficiently and precisely knock-in a DNA fragment containing FRT sites (Kanca et al., 2019). Using this strategy, the knock-in *rab11* 3'UTR flanked by 2 FRT sites is cloned to pHD-ScarlessDsRed donor vector, which allows for identification of successful integration, and then the dsRed cassette can be cleaved off by a single cross to PBac transposase (https://flycrispr.org/scarless-gene-editing/). The mature mRNA of desired transgenic flies will be similar to those made with the ΦC31 integrase-mediated attP × attB cassette exchange (**Figure 4.2E**) and the following Flippase-mediated excision in tissue- and stage-specific manner can be performed similarly (**Figure 4.2F-H**). Both the CRIMIC-based strategy (**Figure 4.2A-D**) and the CRISPR-knock in-based strategy presented here, followed by Flippase-mediated 3'UTR removal (**Figure 4.2F-H**), are to be performed during and following the completion of this thesis.

4.2.2 *Drosophila* larval fillet preparation and spaced chemical stimulation

The *Drosophila* larval fillet preparation was performed according to a published protocol (Parton et al., 2010). I collected the wandering 3rd instar larvae of similar size (from either the side of the tube or from the top of the food) and washed them thoroughly with tap water on a bed full of tissue papers. Then, I placed individual larvae dorsal side up on a custom-made clean Sylgard 184

silicone elastomer dish and used 0.1 mm diameter stainless steel Austerlitz insect pins, cut and bent to shape like number 7, to fix their head and tail one by one without over-stretching their body. I then filled the larvae inside the Sylgard dish with HL3, 0.3 mM Ca^{2+} buffer (Table 2), used the Vannas-Tübingen Spring Scissors, 0.1 mm diameter tip (Fine Science Tools) to make a small incision around mid-body on the dorsal side, and cut the cuticle in the upward motion towards the tail. The guts were removed by gentle pulling and cutting of tracheae. Then, I used the scissors to cut the cuticle towards the head (avoid cutting the brain). Four additional insect pins were used to fix the cuticle to four corners, without overstretching (**Figure 4.3A-B**). Larvae were washed a few times and kept in the HL3, 0.3 mM Ca^{2+} buffer no longer than 1-hour post-dissection and fixed to perform IF and/or smFISH. Successful fillet preparation yielded intact NMJs from A2-A6 on the left and right sides of the larval body, and the pre- and post-synaptic IF staining, with DAPI nuclear counter-stain and smFISH against endogenous transcripts can be visualized simultaneously in 3D (**Figure 4.4C**). Larvae with damaged NMJs were discarded.

I performed a spaced chemical stimulation with high potassium (KStim) assay to induce ghost bouton formation according to established protocols (Ataman et al., 2008; Piccioli and Littleton, 2014) (**Figure 4.3D-E**). For this assay, I pinned the dissected larvae shorter and more relaxed than usual to allow for muscle contraction during the stimulation. I prepared fresh KStim buffer ($HL3K^{+}$) or Mock buffer (HL3, 1mM Ca^{2+}) (Table 2) and submerged larvae in KStim or Mock (control) for 2 min intervals, 3 times, with 10 min intervals in Mock buffer in between and the final 30 minutes in Mock buffer before fixation (**Figure 4.3E**). I removed the guts and pinned four corners of the fillet 5-10 minutes prior to fixation. NMJs of OrR wildtype larvae that were fixed right

away (**Figure 4.3C**) or those in the Mock stimulation control did not form as many new boutons as the KStim condition (**Figure 4.4E-F**), meaning that the KStim paradigm in my hand is a sensitive readout of synaptic plasticity as a result of acute neuronal stimulation by high K^+.

The quantitation of the ghost bouton number was performed manually. The ghost bouton is defined as a HRP-positive, Dlg-negative, rounded neuronal process that often (but not always) connects to another mature bouton (Ataman et al., 2006) and has a size comparable to its neighboring mature boutons (**Figure 4.3C**). The size is included as a criteria to exclude HRP-positive pre-synaptic debris, which are destabilized newly-formed boutons that occur normally, and the pre-synaptic debris formation is enhanced upon neuronal activation (Fuentes-Medel et al., 2009).

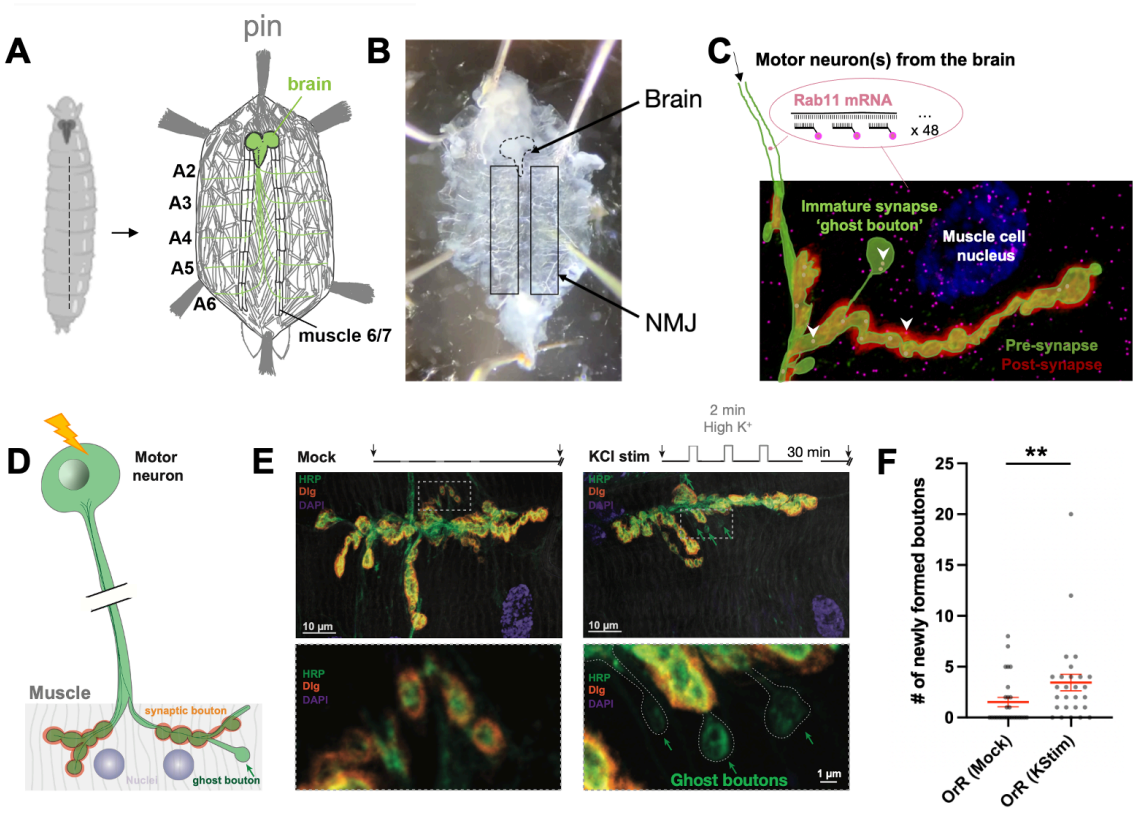


Figure 4.3 Drosophila larval fillet preparation, smFISH, IF, and KStim paradigm. **(A)** A schematic of fillet preparation, exposing the body wall muscle and motor neuron innervation. The stereotypical neuromuscular functions (NMJs) between the longitudinal muscles 6/7 form between abdominal segment A2-A6. **(B)** An image of actual larval fillet preparation taken from the dissection microscope. The locations of the brain and the NMJs are highlighted. **(C)** Larval NMJ is a model to study mRNA localization by smFISH, in the motoneuron axon termini (pre-synapse) (green – HRP staining), or the post-synapse (red – Dlg/Post-synaptic density staining). *Rab11* transcript detection by smFISH showed as diffraction limited spots at the pre- and post-synapse, in the muscle cell nucleus and cytoplasm (pink spots, arrowheads). **(D)** KStim paradigm to study activity-dependent synaptic plasticity at the NMJ. The degree of synaptic plasticity is quantified by the number of ghost bouton/newly formed boutons lacking the post-synaptic density (Dlg staining). **(E)** Representative images of Mock (control – no high K^+ intervals) and KStim (with 3× 2-min interval of high K^+, 10-min between the interval, and the last 30 min prior to fixation and staining). Arrows point to examples of the ghost boutons. **(F)** Quantitation of the number of ghost boutons in Mock vs. KStim of OrR wildtype larvae. The graph showed mean ± SEM with all datapoints, **p<0.01, Wilcoxon rank-sum test.

4.2.3 *Drosophila* larval brain primary culture

I followed the primary neuronal culture protocols of *Drosophila* larval brain from previous publications (Egger et al., 2013; Lu et al., 2015). I dissected the brains

from the clean wandering 3rd instar larvae in a freshly prepared supplemented Schneider's *Drosophila* medium (Sterile Lonza BioWhittaker Schneider's *Drosophila* Medium [catalog no. 04-351Q] + 10% heat-inactivated fetal bovine serum [HyClone FBS: SH30071.02] + 1% penicillin-streptomycin/pen-strep [Gibco]) on a Sylgard dish. I used the Vannas-Tübingen Spring Scissors to cut the larvae in half around the abdominal segment 3/4 and flipped the head part sideway. This procedure allowed the brain to float out from the cut point. I used the forceps to gently squeeze the brain out, then I cut the brain from its connecting tissue and pipetted individual brain into a microfuge tube containing the supplemented Schneider's medium.

After collecting 8-10 brains (for plating per one dish), I rinsed the dissected brains 3 times in 1× Rinaldini's solution (Table 2) containing 1% pen-strep and centrifuged for 5 minutes at 300g at room temperature each time before removing the supernatant. Then, I added 1 mL of sterile filtered Collagenase I (0.5 mg/mL) and incubated at room temperature for 1 hour to chemically dissociate cells inside the brain. I later optimized the chemical dissociation protocol for motoneuron culture (Lu et al., 2015) by using Liberase (Roche) containing Collagenase I+II and neuronal proteases at 2.5 mg/mL in 1× Rinaldini solution. Then, I spin down the brains for 5 minutes at 300g at room temperature, removed the supernatant, and resuspended the brains in the supplemented Schneider's medium. I spin down the brains for another 5 minutes at 300g at room temperature, removed the supernatant, put back ~100 μL of the supplemented Schneider's medium, and pipetted continuously for 2 minutes to physically dissociate the brains into single cells (avoid making bubbles). Lastly, I pipetted the concentrated solution of brain cells and pushed the solution through

a sterile 40 µm cell strainer (Starlab) that was in contact with 2 mL of the supplemented Schneider's medium on the poly-L-lysine-coated glass bottom dish, to allow individual neurons to spread out and land on the glass-bottom dish evenly as single cells.

The successful results of this protocol include the observation of neurite outgrowth within 2 hours *in vitro* (**Figure 4.4A**). Cultured neurons from the brain of 3rd instar larvae extend neurites extensively during day *in vitro* 1-2 (DIV1-2) and by DIV3-4 the axon is specified, which can be visualized by a translocation of neuronal cargoes such as mitochondria, and the presence of the dynamic growth cones and filopodia (**Figure 4.4B**).

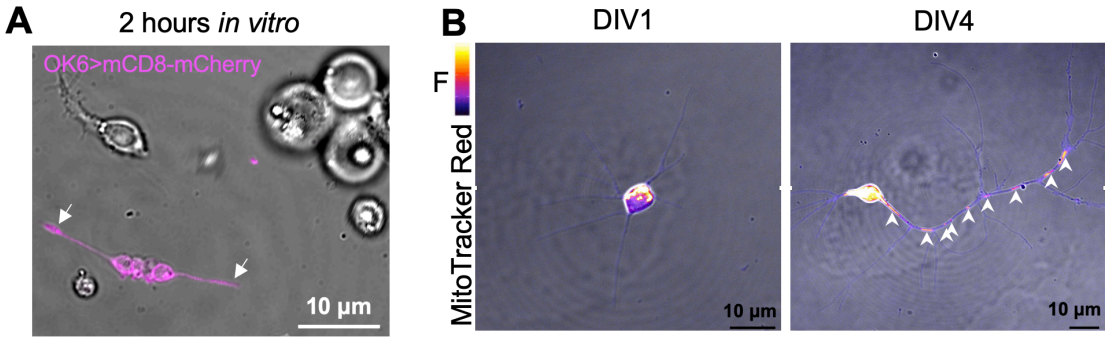


Figure 4.4 Growth and morphology or cultured neurons from the brain of *Drosophila* 3rd instar larvae. (A) Primary culture from the brain of motoneuron driver OK6>mCD8-mCh larvae, showing mCD8-mCh-positive neurons that extend neurites (arrows) by 2 hours *in vitro*. **(B)** MitoTracker Red signal in single primary neurons at DIV1 and DIV4. At DIV1, mitochondria do not localize to neurites, while at DIV4, mitochondria translocate to axons (arrowheads).

4.2.4 Immunofluorescence (IF)

The following primary antibodies were used: 1:100 mouse-anti Rab11 (BD Biosciences, AB_397984), 1:100 rabbit anti-KHC (Cytoskeleton, Inc. AKIN01), 1:100 mouse 4F3 anti-discs large (anti-Dlg) (DHSB, AB_528203). The following secondary antibodies/dyes were used: 1:200 Goat anti-mouse AlexaFluor647,

1:200 Donkey anti-mouse AlexaFluor647, 1:200 Donkey anti-mouse AlexaFluor594, 1:200 Donkey anti-rabbit AlexaFluor568, 1:500 ChromoTek GFP-Booster AlexaFluor488, 1:100 DyLight405 Goat anti-Horseradish Peroxidase (anti-HRP), 1:100 AlexaFluor488 Goat anti-HRP, and 1:500-1:1000 DAPI.

For IF protocol on the fillet preparation, I put 4% PFA in PBTX (1×PBS + 0.3% Triton X-100) on the Sylgard dish containing dissected larvae for 30 minutes at room temperature (RT) with gentle rocking. After a few washes in PBS, I removed the pins and put all larva in a microcentrifuge tube and incubate in PBTX at RT for 45 minutes. Fillet were then stained in a primary antibody solution at 4°C with gentle rocking overnight. In the next day, the larvae were washed four times in PBTX, 5 minutes each with gentle rocking at RT. The larvae then were incubated in PBTX with secondary antibodies and DAPI for 1 hour at RT with gentle rocking. Afterwards, the larvae were washed four times in PBTX, 5 minutes each with gentle rocking at RT. Finally, I transferred the larvae ventral side down to a glass slide with a double-sided tape platform, flooded the larvae with Vectashield or SlowFade mounting media for 30 minutes, and mounted the cut-open side with #1.5 coverslip. I sealed the coverslip onto the glass slide with a quick-dry nail polish.

For the IF protocol on the primary culture, I fixed neurons in 4% PFA, 4% sucrose in 1×PBS + 0.1% Triton X-100 on coverslips inside the 24-well plate for 25 minutes RT with gentle rocking. Following a few washes in 1×PBS + 0.1% Triton X-100, the coverslips were transferred to a clean parafilm bed in a custom-made humidified chamber and incubated in primary antibody solution at 4°C with gentle rocking overnight. In the next day, the coverslips were washed with

1×PBS four times and were incubated in a secondary antibody solution with DAPI counterstain for 1 hour. After four more washes in 1×PBS, the coverslips were mounted on the hard-set Vectashield or ProLong diamond antifade mounting media and sealed with nail polish. The samples were imaged immediately or within 1 week of mounting.

4.2.5 RNA single-molecule fluorescence in situ hybridization (smFISH)

First, smFISH probes were designed on the Stellaris probe designer online tool (https://www.biosearchtech.com/support/tools/design-software/stellaris-probe-designer), with the maximum number of probes set to 48, oligo lengths of 20nt, and minimum spacing of 3nt. The target sequence was downloaded from the flybase website (https://flybase.org/). All probes output sequences were saved for ordering as DNA plates from IDT (https://eu.idtdna.com/site/order/plate/index/dna/1798), with normalized yield of 200 μM DNA oligos in IDTE pH 8.0, 50 μL/well. All oligos (or ODD/EVEN numbered oligoes) on the plates were pooled into a single microfuge tube and were conjugated to red or far-red fluorescent dyes as described previously (Gaspar et al., 2017; Lee et al., 2022). In brief, the dyes such as Atto633, AlexaFluor647, Atto565, or Cy3 were conjugated to ddUTP with NHS chemistry, and stored at -20°C in nuclease-free water at 1 mM concentration. Then, 200 μM of pooled oligos were mixed with 1 nM of dye-ddUTP and TdT enzyme in 5× TdT buffer in nuclease-free water at 37°C for 12-16 hours. The Oligo clean & concentrator kit (Zymo) was used to normalize the conjugated probes to 25 μM in TE buffer (10 mM Tris pH 8, 0.1 mM EDTA). The optical density at 260 nm (OD260) of unlabeled and labeled probes were checked on the NanoDrop

Spectrophotometer against the OD at optimal emission wavelength of the dye for the final concentration of labeled probes and degree of labeling (DOL).

I followed the smFISH procedure on the fillet preparation according to previous published works from the Davis lab (Titlow et al., 2020; C.-P. Yang et al., 2017). Briefly, the dissected larvae were fixed in 4% PFA in DEPC-treated PBTX for 30 minutes with gentle rocking. Then, the larvae were washed 1-2 times in DEPC-treated PBS and transferred to an RNase-free microfuge tubes. I performed 3 rounds of permeabilization in the DEPC-treated PBTX for 15-20 minutes each. Larvae were washed and incubated in the Wash buffer (Table 2) at 37°C for 30 minutes. Then, 250 nM of smFISH probes in Hybe buffer (Table 2) were added to hybridize overnight at 37°C with gentle rocking. In the next day, Larvae were washed in the Wash buffer 3 times, at least 5 minutes each round, and then were incubated in the Wash buffer containing HRP-Dylight-405 or -488 and DAPI. Larvae were washed 3-4 more times in the Wash buffer, at least 5 minutes each round, washed 1-2 more times in the Wash buffer without formamide (2×SSC in nuclease-free water), and a last wash in nuclease-free water. Larvae were then transferred to a clean glass slide with the double-sided tape platform, placing the ventral side down and the dissected side up. Vectashield or Slowfade mounting media were added for at least 30 minutes before mounting with #1.5 glass coverslip. The samples were imaged immediately or within 1 week of mounting.

To perform smFISH on the primary culture, I fixed neurons in 4% PFA, 4% sucrose in 1×PBS + 0.1% Triton X-100 on coverslips inside the 24-well plate for 25 minutes RT with gentle rocking. Following a few washes in 1×PBS + 0.1%

Triton X-100 inside the 24-well plate, the coverslips (cell side up) were transferred to a clean, RNase-free parafilm bed in a custom-made humidified chamber and incubated in Wash buffer at RT with gentle rocking for 30 minutes. Then, 100 μL drop of 250 nM of smFISH probes in Hybe buffer (Table 2) were added to a clean, RNase-free parafilm bed, and the coverslips were flipped (cell side down) onto the Hybe buffer. I hybridized the coverslip overnight at 37°C with gentle rocking, making sure that the humidified chamber was tightly sealed with parafilm to avoid coverslip drying. On the next day, the coverslips were washed four times in the Wash buffer, at least 5 minutes in each wash, and were incubated in the Wash buffer containing a secondary antibody or DAPI for 1 hour at RT. After three more washes in the Wash buffer, one more wash in the Wash buffer without formamide, and one more wash in a nuclease-free water, the coverslips were mounted on the hard-set Vectashield or ProLong diamond antifade mounting media on a glass slide and sealed with nail polish. The samples were imaged immediately or within 1 week of mounting.

Solution	Composition
HL3, 0.3 mM Ca^{2+}	70 mM NaCl, 5 mM KCl, 20 mM $MgCl_2$, 10 mM $NaHCO_3$, 5 mM trehalose, 115 mM sucrose, 5 mM HEPES, 0.3 mM $CaCl_2$, pH 7.2-7.4
HL3, 1 mM Ca^{2+}	70 mM NaCl, 5 mM KCl, 20 mM $MgCl_2$, 10 mM $NaHCO_3$, 5 mM trehalose, 115 mM sucrose, 5 mM HEPES, 1 mM $CaCl_2$, pH 7.2-7.4
HL3 K^+	40 mM NaCl, 90 mM KCl, 20 mM $MgCl_2$, 10 mM $NaHCO_3$, 5 mM trehalose, 5 mM sucrose, 5 mM HEPES, 1.5 mM $CaCl_2$, pH 7.2-7.4
10X Rinaldini Solution	4 g NaCl, 100 mg KCl, 25 mg NaH_2PO_4, 500 mg $NaHCO_3$, 500 mg glucose in 50 mL H_2O (filter sterilized, stored at -20°C)
Wash buffer (smFISH)	2×SSC, 10% deionized formamide, in Ambion nuclease-free water
Hybe buffer (smFISH)	2×SSC, 10% deionized formamide, 10% dextran-sulfate, in Ambion nuclease-free water

Table 2 Custom-made solutions used in this study.

4.2.6 Image analysis for smFISH and IF at the NMJ

Raw images acquired from the Olympus spinning disk confocal were stored as .vsi files and then were batch-converted to .tif in Fiji (ImageJ) for image processing (**Figure 4.5A**). I wrote custom Fiji plugins to create 3D mask from HRP channel with 3D Hysteresis thresholding (https://mcib3d.frama.io/3d-suite-imagej/plugins/Segmentation/3D-Hysteresis-Segmentation/), that I determined empirically to perform best to threshold the HRP signal at the NMJ. The results were manually checked to delete HRP signal outside of the NMJ (mostly from the nerve) (**Figure 4.5B**). Then, the image calculation function was performed to mask smFISH signal within the 3D segmented HRP mask (**Figure 4.5C**). All codes are available on https://github.com/Tai-Ch/NMJ_3DSegmentation.

Then, the masked smFISH images were input to the Big-FISH python processing pipeline version 0.4.0 (https://github.com/fish-quant/big-fish), initially written in Jupyter notebook by Jeff Lee, a postdoc in the Davis lab, and I optimized this code for NMJ analysis. Briefly, in this pipeline, the raw smFISH images were masked first, prior to Big-FISH processing, and the threshold was chosen manually, based on image-by-image inspection of smFISH signal post-log filtering. Later, after finding out that the chosen threshold was consistent throughout various experiments, the Big-FISH version 0.6.2 was used for automated thresholding and batch analysis. The elbow curve method was used to determine the threshold (**Figure 4.5D**) (Imbert et al., 2022). In this updated pipeline, the raw images were first batch-processed in Big-FISH to get all coordinates at the sub-pixel resolution. Then, the coordinates were mapped onto

the 3D HRP mask of the NMJ later, and the number of single molecules mRNA within the mask were quantified. The number of *rab11* transcripts detected from manual and automated thresholding methods were comparable (**Figure 4.5E**).

To analyze the intensity of protein within the NMJ pre-synapse from IF experiments, the 3D thresholding and masking method were applied similarly. Then, z stack images containing the fluorescence from the antibodies within the NMJ pre-synapse were max project intensity to 2D image. The magic wand tool was used to select fluorescence signal in for all NMJ islands, and the mean intensity per image was recorded and quantified. The NMJ area was also recorded from the max project of the 3D mask using the magic wand tool.

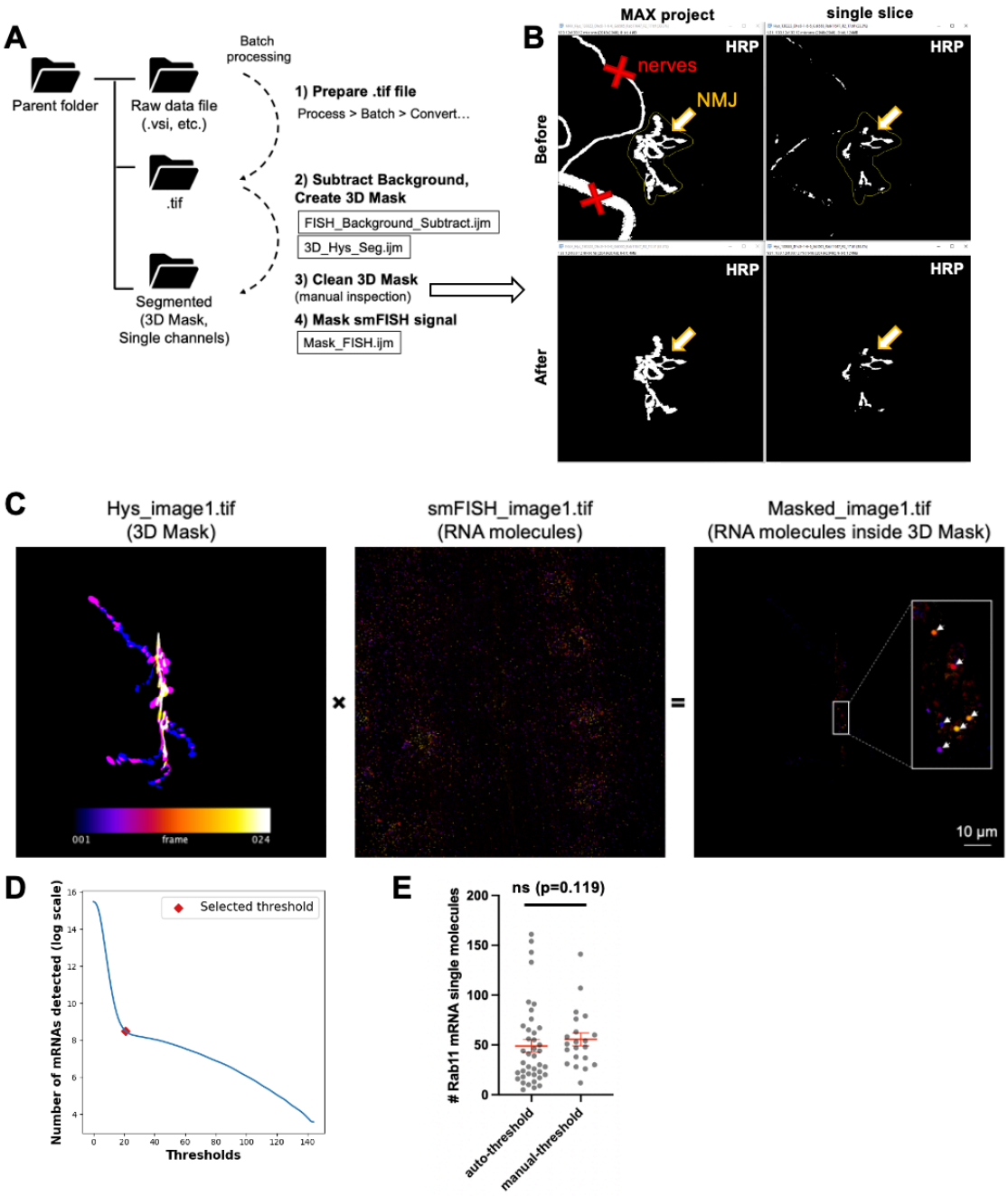


Figure 4.5 A semi-automated and automated pipeline of 3D segmentation of fluorescence signal inside the motoneuron terminal boutons. **(A)** Organization of data for batch processing. .ijm files are automated batch processing code for ImageJ Macros. **(B)** Manual inspection of HRP signal post-segmentation. Arrows point to NMJ. Crosses mark the nerves that are manually deleted. **(C)** An example of a 'clean' 3D mask and smFISH signal color-coded by frames/depth of field. Masked image (insets) shows single RNA molecules inside a 3D mask (arrows). **(D)** The elbow plot method to determine threshold for single-molecule smFISH signals. **(E)** The quantitation of *rab11* mRNA copy number in OrR in different biological replicates, using auto-threshold versus

manual threshold for single-molecule detection. Mean ± SEM (red lines) with all datapoints (grey dots). p=0.119, Wilcoxon rank-sum test.

4.2.7 Live imaging of mRNA with MS2-MCP system with denoising

To perform live imaging of MS2-mRNA bound to MCP-GFP, primary neurons from the 3rd instar *Drosophila* larval brains were cultured until DIV3-4. Neurons were incubated at 30°C for 2 days until the imaging time. The 561-nm laser was used to screen for mCherry expression in motor neurons by *D42-Gal4*>mCD8-mCh, and the z-stack of the whole cell was captured to ensure that high MCP-GFP expression was in the nucleus and some MCP-GFP foci were present in the cytoplasm of the soma and the neurites. Then, a single color, one single stack timelapse was acquired with 488-nm laser with the frame rate of 3.3 Hz (200 frames, 1 minute), with <30% laser power and 0.1 second exposure time to avoid photobleaching.

To minimize phototoxicity during axon imaging and to maximize temporal resolution, I decreased the laser power and exposure time about 5- to 10-fold. Then, raw videos were subjected to image restoration by patch-based denoising on ND-SAFIR program (https://team.inria.fr/serpico/software/nd-safir/), performed in a python pipeline by Danail Stoychev, according to a published method (Boulanger et al., 2010; Hailstone et al., 2020). The denoised videos were input to KymoAnalyzer software, an ImageJ Macros for semi-automated analysis (Neumann et al., 2017). In this analysis, tracks were drawn on kymographs manually, and segmental parameters such as velocities and run lengths were analyzed automatically.

4.2.8 RNA single-molecule hybridization chain reaction (smHCR)

The smHCR (v3.0) (Choi et al., 2018) is a variation of smFISH to detect individual RNA molecules, by using a smaller number of split-pair oligonucleotide probes targeting a region of a transcript that get amplified by the Alexa Fluor-conjugated propagating hairpins (**Figure 4.6A**). The advantages of smHCR over traditional smFISH protocol is that smHCR signal is brighter and performs better in the thick samples (Shah et al., 2016); furthermore, the requirement for less probe coverage allowed robust detection of short transcripts.

To design the smHCR probes, the following R workflow was used: https://github.com/jefflee1103/HCRv3_probe_design. To design the HCR probes against *Rab* GTPases transcripts, the coding sequence (CDS) of the gene was first used to generate at least 5 paired probes. When the probe number output was lower than 5, the blast strength was changed from 1 to 5, and if this change still yielded <5 outputs, the whole exon sequence of *Rab* was used instead. The range of 5-10 paired split probes conjugated to B1, B2, B3, or B4 initiators (Choi et al., 2014) were ordered from Sigma and to amplify with to HCR amplifiers conjugated with AF647, AF488, AF546, or AF594, respectively.

To perform HCR on the *Drosophila* 3rd instar larval fillet preparation, larvae were dissected in HL3, 0.3 mM Ca^{2+} buffer as described in the Method section 4.2.2. Then, I fixed the tissues in 4% PFA, in PBTX (with 0.3% Triton X-100) for 30 minutes at RT. After fixation, I removed the brain, the nerves, detached the larvae from the Sylgard dish, and transferred all larvae to distinct microfuge tubes for different probe combination. I rinsed larvae 3 times in PBTX, and left shaking at RT for 20 minutes twice. Then, to hybridize the primary

probes, I rinsed larvae in a freshly made 5×SSCT buffer (5×SSC + 0.1% Tween-20). Then, I put larvae in the freshly made hybridization solution (5×SSC + 30% formamide + 10% Dextran sulphate (w/v) + 0.1% Tween-20) for 40 minutes at 37°C. The larvae were incubated with 4 nM concentration of each oligo split probe in the hybridization solution overnight at 37°C. In the next day, I washed the larvae 4 times in the freshly made wash solution (5×SSC + 30% formamide + 0.1% Tween-20), 15 minutes each time at 37°C. Larvae were again washed in 5×SSCT buffer and kept in 5×SSCT buffer at RT while preparing the chain amplification solution. I made 1:10 dilution (300 nM) of the chain amplification solution in nuclease-free water as personal stock. Then, I heated these tubes to 95°C for 90 seconds and immediately transferred to RT, protected from light, and allowed to cool for 30 minutes (avoid shaking). I then pooled 6 nM of each probe (1:50 dilution) to the amplification solution (5×SSC + 10% Dextran sulphate (w/v) + 0.1% Tween-20) and incubated the samples for 10 hours at RT, with gentle shaking. I included in this amplification solution HRP-DyLight405/ AlexaFluor488 (1:100) and DAPI (1:500-1:1000) to label neurons and nuclei, respectively. After the amplification step is complete, I rinsed the larvae 3 times in the 5×SSCT buffer and left on the shaker at RT for another 30 minutes. I performed the final rinse in a nuclease free water and immediately mount the larvae on the raised platform glass slide-coverslip sandwich in the SlowFade diamond antifade mountant (Invitrogen). HCR samples were imaged within the week of sample preparation with the spinning disc confocal, 100×/1.45N.A. Objectives for the optimal single molecule detection.

By using the *Drosophila* lines with genetically labelled glial cells, for example Mdr65>CD8-GFP that expressed GFP to the cell surface of the sub-

perineurial glia at the larval NMJ, I could visualize 2 or more *Rab* transcripts in glia or neurons at the NMJ (**Figure 4.6B**).

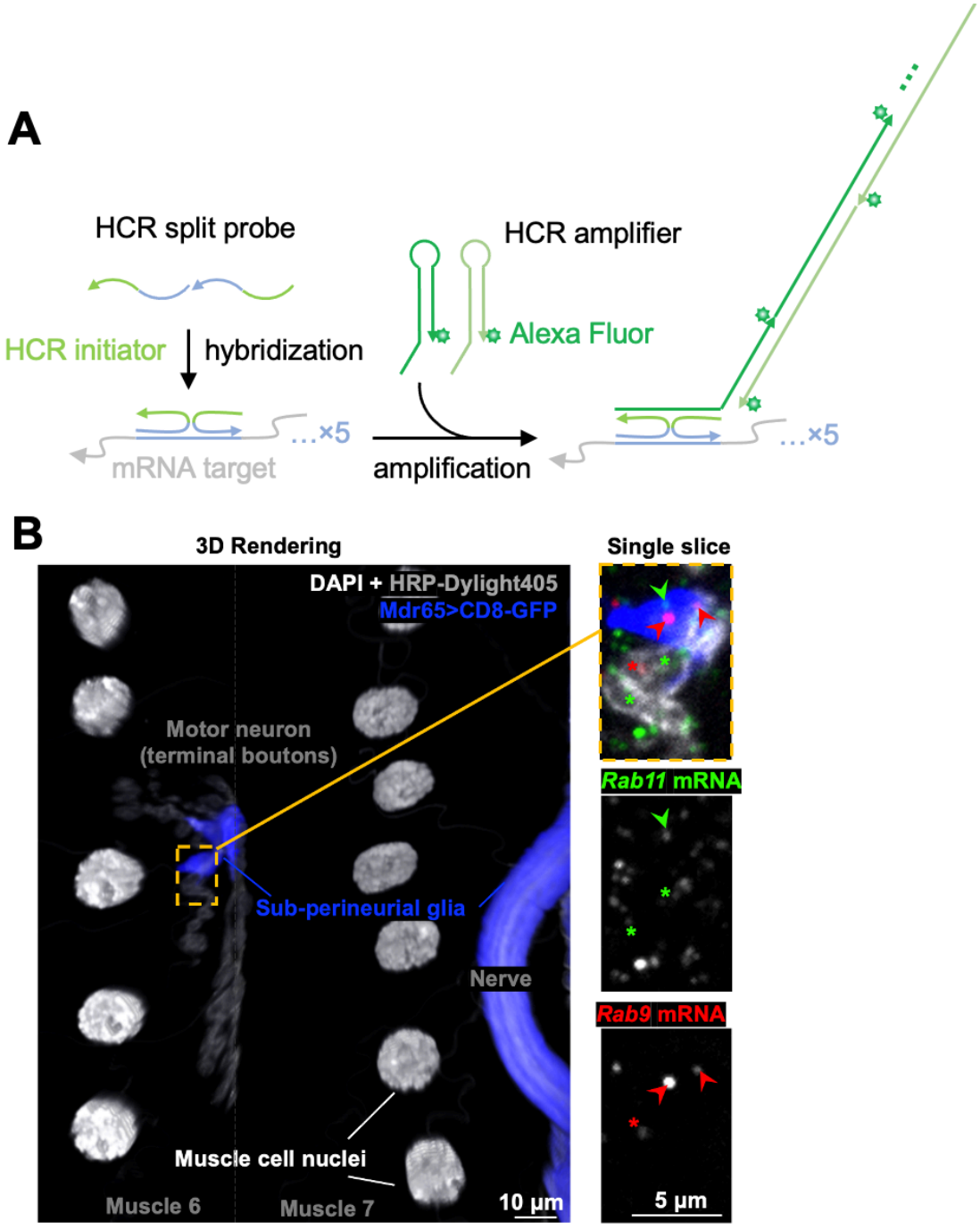


Figure 4.6 smHCR schematic and imaging. (A) Each HCR split probe contains HCR initiator sequence and complementary sequence to mRNA target. Amplification with HCR amplifier

results in polymerization of fluorescently-labeled oligos, allowing visualization of mRNA single molecules. (B) A representative 3D rendering of NMJ; muscle cell nuclei labeled with DAPI, neurons labeled with HRP-Dylight405. This Mdr65>CD8-GFP expresses GFP to the membrane of sub-perineurial glia along the nerve and at the NMJ. Insets show single-slice overlay of Rab11 (green) and Rab9 (red) mRNAs on the same sample. Arrowheads point to mRNA in glial extension; asterisks mark mRNA in motor neuron terminal boutons.

4.2.9 High-throughput larval locomotion assay and analysis

Larval crawling assay was performed by the following setup. Fly larvae raised in different temperatures were acclimated at room temperature (19-21°C) for at least 30 minutes inside humidified plates, protected from light. The 1% agar plates were taken out of the 4°C to the room temperature at least 1 hour prior to the experiments. The behavioral chamber was set with even light illumination from the bottom, with minimal external light and sound disruption, and the agar plate was put in the middle. The iPhone 11 Pro was set at a constant distance from the plates above and was set for 4K video acquisition mode at 30 frames per second (fps). Right before the video acquisition, 4-6 larvae were picked up gently with a paintbrush and put in the middle of the clean agar plate at the same time. The larvae were then put in the behavioral chamber, and I recorded larval crawling for 3 minutes. I then put larvae to a different plate and cleaned the agar plate well each time with 70% ethanol, 2-3 tap water washes, and dried with Kimwipes. The experiments proceeded with random order of larval genotypes.

The videos were then processed in the BioImageOperation (BIO) C++ program (https://github.com/folterj/BioImageOperation/), with background subtraction weight = 0.05, threshold of cluster = 0.1, cluster min area = 600 pixels, cluster max area = 2800 pixels, track max move = 20 pixels, min active = 3 pixels, and min inactive = 3 pixels. These parameters were empirically determined and worked to detect larvae of all genotypes in this study.

The .csv file outputs from BIO were processed in R with the code written by Jeff Lee (https://github.com/jefflee1103/Image-analysis/tree/main/crawling-assay_BIO), based on a published protocol (Torres-Méndez et al., 2022). Briefly, clusters that appeared in the first 5-second and were closest to the center of the videos were filtered as real larva signal. Larval trajectory straightness to evaluate the efficiency of directed walks was determined by using the R package 'trajr' (McLean and Skowron Volponi, 2018). Straightness indices ranged between 0 (being infinitely tortuous) and 1 (a perfectly straight line). Contour length of each larva at a given time was calculated from the total Euclidean distances between all contour points. The primary axis circumference (L) was calculated as $\pi \times$ the primary axis length, defined as being the largest Euclidean distances between pairwise contour points. A curvature ratio was computed per frame as the total contour length/primary axis circumference, and a ratio of 0.9 or above was taken as 'curved body' as previously (Torres-Méndez et al., 2022). This number was validated in my dataset to be sensitive for curved body detection. A summary of data was subjected to Shapiro-Wilk test for normality in R. Tukey's multiple comparison tests were used for normally distributed datasets (and plotted as box plots), and Dunn's multiple comparison tests were used for non-normal distribution (and plotted as violin plots).

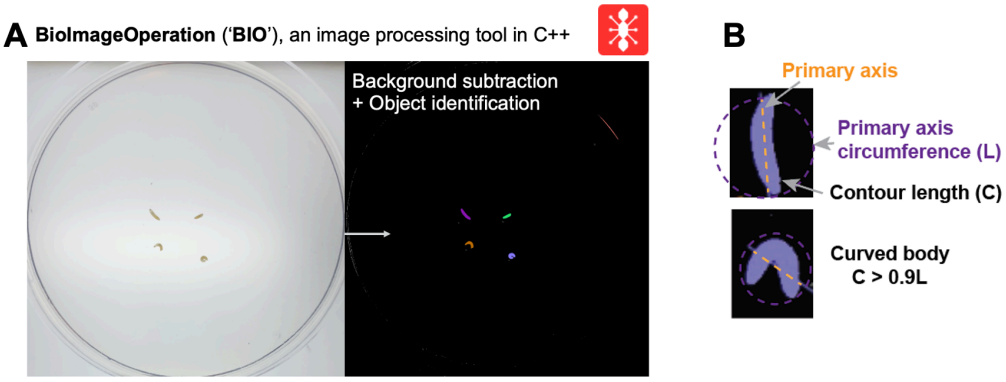


Figure 4.7 Larval crawling assay analysis. (A) A setup of *Drosophila* 3rd instar larvae in the middle of 1% agar 10-cm diameter plate with even illumination (left) and the automated background subtraction with individual larvae identification as 'clusters' with different colors (right). **(B)** The definition of curved body for the curvature ratio analysis.

4.2.10 Generation of graphs, figures, and statistical analyses

Graphs in this chapters were plotted and analyzed in either GraphPad Prism or RStudio. The image figures were prepared in ImageJ, and arranged/labeled in the Adobe Illustrators and Microsoft Powerpoint. For statistical analyses, the normality test was usually performed prior to statistical test selection. All smFISH and ghost bouton number datasets were assumed to be non-normal distribution. All data presented here were from at least 2 biological replicates, otherwise stated. The summary statistics, graphs, p values, and statistical tests were declared in the figure legends of each figure.

4.3 Results

4.3.1 Absolute quantitation of mRNA copy number in the *Drosophila* larval motoneurons

Previously, a survey of mRNA localization pattern throughout the nervous system of *Drosophila* by smFISH found 18 out of 200 (9%) of YFP-trapped genes where their YFP-tagged transcripts, including *yfp-rab11* and *yfp-gdi*, at the larval

NMJ pre-synaptic axon terminal boutons (Titlow et al., 2022). In this work, however, low copy number of single-molecule mRNA was detected, and the transcript detection method was indirect via the *yfp* sequence presented in some but not all transcript isoforms. Furthermore, it remains unclear whether these detected transcripts are highly enriched at the pre-synaptic sites, compared to the neuronal cell bodies. Here, I first validated the mRNA localization screen results with 36×*Rab11* exon probes, designed to detect all transcript isoforms (**Figure 4.8A**). To determine the detection efficiency of the custom-made smFISH probes at the *Drosophila* larval NMJ, I divided the exon probes to ODD- and EVEN-numbered probes and conjugated them to two dyes—ODD-Atto565/EVEN-AlexaFluor647 and EVEN-Atto565/ODD-AlexaFluor647 (**Figure 4.8B**)—performed smFISH and analyzed colocalization between ODD/EVEN switched pairs in 3D as previously (Lee et al., 2022). The analysis was done at the NMJs between the longitudinal body wall muscle 6 and muscle 7 of the abdominal segments A2-A6 on a fillet preparation with the brain intact (Parton et al., 2010) (**Figure 4.8G**). Traditionally, a standard smFISH is performed with 48× oligonucleotide probes, but the length of *Rab11* exons allows for only 36-probe coverage. Surprisingly, I found here that using only 18 split probes was sufficient to detect single-molecule *Rab11* mRNA at the NMJ, as shown by the fluorescence profile of consistent intensities (**Figure 4.8C, E**). The averaged percent overlaps between two *Rab11* split probes were 76.7% and 82.2% when the whole NMJ was analyzed and became 87.1% and 90.2% for transcripts inside motoneuron terminal boutons only, with some NMJs showing 98% detection efficiency (**Figure 4.8D-F**).

The extremely high detection sensitivity allowed near-absolute estimation of *rab11* mRNA copy number localized in the soma versus the axon termini of motoneurons. I performed smFISH with the validated *rab11* exon probes and imaged *rab11* transcripts at the ventral nerve cord (VNC) of the brain (where the motoneuron cell bodies are located) compared to those transcripts localized at the NMJ. The particle number per soma was averaged based on the number of a nuclear marker DAPI puncta in the VNC. The results suggested that *rab11* mRNA was 2 to 10 times more enriched at the axon termini/the pre-synaptic sites than the soma, with the copy number between 20 and 100 molecules per NMJ (**Figure 4.8H**). When the copy number was normalized by area of each neuronal compartment, *rab11* mRNA showed similar densities between the soma and the axon termini (**Figure 4.8H-I**), suggesting a mechanism that ensures the polarized but even distribution of mRNA within different neuronal compartments.

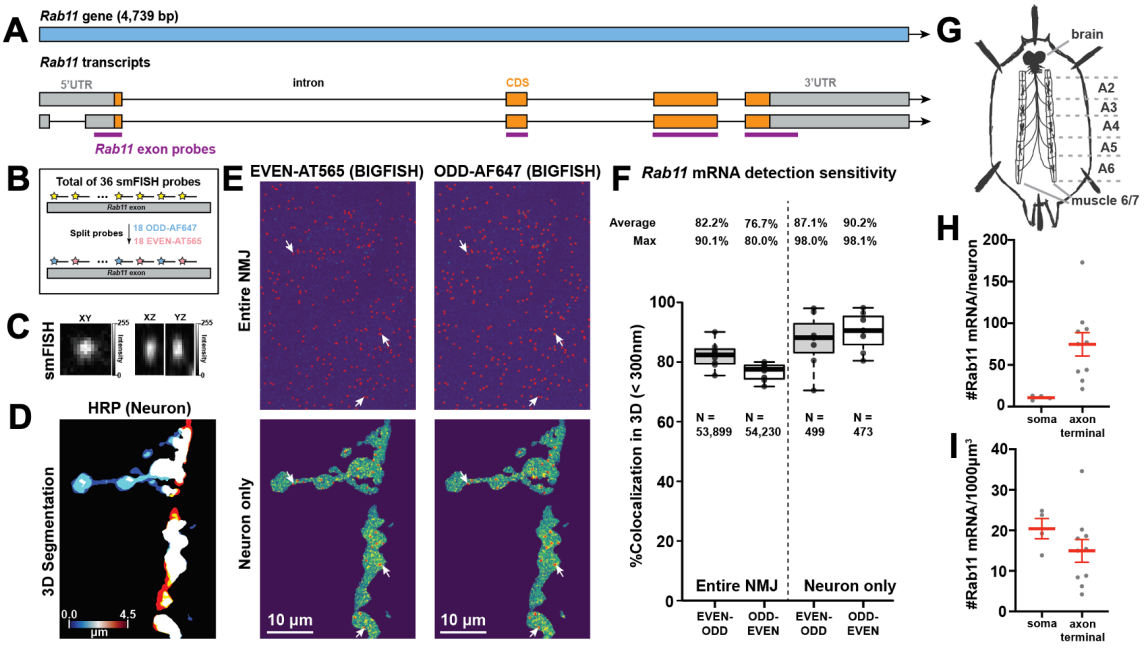


Figure 4.8 Sensitive detection of Rab11 transcripts at the NMJ pre-synapse. (A) A schematic of *Rab11* gene (top) and transcript variants (bottom). From left to right, grey box = 5'untranslated

region (UTR), orange box = protein coding sequence (CDS), line = intron, grey box = 3'UTR, violet lines indicate exon probe coverage. **(B)** Schematic of split probe strategy, AF647 = AlexaFluor647, AT565 = ATTO565. **(C)** Representative *Rab11* smFISH single molecule in xy and orthogonal view (xz and yz). **(D)** 3D segmentation of neurons, pseudo-color coded by z depth (left) and *Rab11* smFISH signal within the 3D volume (right). **(E)** BIGFISH single molecule detection (red dots) from smFISH images of entire NMJ. Arrows point to colocalization events. **(F)** % colocalization in 3D between *Rab11* ODD and EVEN probes by nearest neighbor analysis (<300 nm). Box plot with Tukey's definition, all data points shown, N indicates total number of Rab11 single molecules. **(G)** Schematic of *Drosophila* 3rd instar larva fillet preparation, exposing NMJ of the body wall muscles 6-7 from abdominal segments A2-A6. **(H)** Number of Rab11 mRNA copy number in the soma versus axon termini. **(I)** The densities of Rab11 mRNA in the soma versus axon termini. (H-I) Mean ± SEM (red lines) with all datapoints (grey dots).

4.3.2 Oscillatory bidirectional motion of mRNA in motoneuron axons

To investigate the transport and distribution of *rab11* mRNA by live imaging, MS2 stem loops were inserted at the 3'UTR of *rab11* gene by a CRISPR/Cas9-based approach by Francesca Robertson, a postdoc in the Davis lab (unpublished) (**Figure 4.9A**, **Method 2.2.1C**). A transient expression of the GFP-tagged MS2 capping protein (MCP-GFP) in larval motoneurons for 1 day showed single-molecule detection of *rab11* mRNA in the motoneuron soma inside the VNC of 3rd instar larval brain (**Figure 4.9B-C**). The high degree of overlap between MCP-GFP puncta and *rab11* exon smFISH confirmed that MCP-GFP puncta label true single mRNA molecules (**Figure 4.9C**). However, *rab11* MS2/MCP-GFP mRNA particles were not readily observed at the NMJ pre-synapse (**Figure 4.9C**). This could be because the binding of MCP-GFP to newly synthesized *rab11* MS2 transcripts may destabilize the mRNA, thus they could not reach the NMJ. Alternatively, the MS2 loop insertion in the 3'UTR of *rab11* transcripts might disrupt its binding to the trans-factors that are required for long-distance axonal transport.

I next tested whether *rab11* MS2 transcripts bound to MCP-GFP could at least in principle reach the periphery of the motor neuron axons if present in the axons while they are developing. I cultured larval motor neurons from the larval brains using a previously established protocol (Lu et al., 2015) up to the day *in vitro* 5 (DIV5) where axons became distinguishable from dendrites by their morphology, and neuronal cargoes such as mitochondria moved bidirectionally in axons (**Figure 4.4B**). High- resolution live imaging followed by a patch-based denoising algorithm (Carlton et al., 2010) allowed for direct visualization of *rab11* MS2/MCP-GFP particles that move bidirectionally in axons and dendrites (**Figure 4.9D**), suggesting that *rab11* MS2 mRNA bound to MCP-GFP can enter the axons at least when they are developing. I performed a motoneuron-specific labeling strategy for *rab11* and *gdi* MS2/MCP-GFP to quantitate the transport dynamics of axon-localized mRNA particles by a single-particle transport analysis (Neumann et al., 2017) (**Figure 4.9D, F**). I found that both *rab11* and *gdi* mRNA particles actively move in both the anterograde and the retrograde direction, with similar velocities and run lengths (**Figure 4.9D, F, G, H**), suggesting similar transport machineries might be at play. Altogether, these results revealed that the axonal transport of *rab11* mRNA and *gdi* mRNA at steady state in developing neurites is tightly regulated by a bidirectional transport mechanism that could contribute to distribution of mRNA in mature axons *in vivo*.

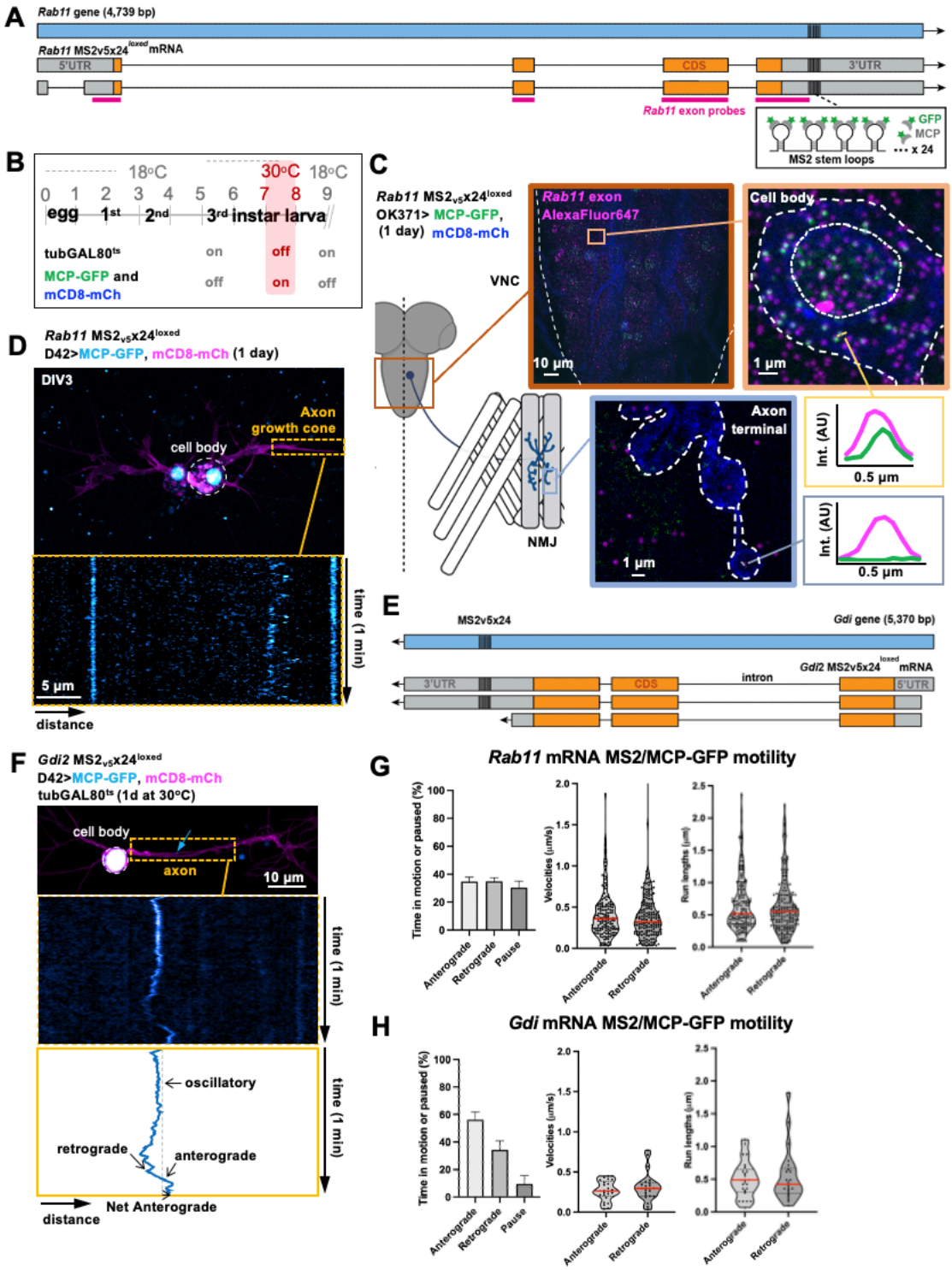


Figure 4.9 Live imaging of *Rab11* and *Gdi* mRNAs by MS2/MCP system. (A) a schematic of *Rab11* gene (top) and transcripts, containing 24×MS2 step loops in the 3'UTR. One MS2 loop can be occupied by two GFP-tagged MS2 coat protein (MCP-GFP) molecules (inset). Regions for

Rab11 exon smFISH probes are highlighted (magenta). **(B)** a timeline for conditional co-expression of MCP-GFP and mCD8-mCh in motoneurons at late 3rd instar larval stage. tubGAL80ts is turned off at 30°C for 1 day when OK371>MCP-GFP and mCD8-mCh or D42> MCP-GFP and mCD8-mCh is turned on. Larvae were put back at 18°C for 1 more day to allow for MCP-GFP-tagged mRNA distribution. **(C)** representative images of the VNC region of the brain and the NMJ from a fillet preparation of the indicated fly genotype (MCP-GFP shown in green, mCD8-mCh shown in blue), with smFISH against Rab11 exon (magenta). Line scan intensity profiles (insets) show MCP-GFP/Rab11 mRNA colocalization in the brain or lack of MCP-GFP at the axon termini. **(D)** Live imaging of cultured primary neurons from the brain of day 6-7 larvae, at day *in vitro* 3 (DIV3). Cell body of a single neuron is indicated with dotted circle. A time-lapse was taken at 3.3 Hz (3.3 frames/sec; 200 frames; 1 minute), and a kymograph from the axonal growth cone (yellow dotted box) was shown below. **(E)** a schematic of *Gdi* gene (top) and transcripts, containing 24×MS2 step loops in the 3'UTR of the long isoforms. **(F)** Live imaging of cultured primary neurons from the brain of day 6-7 larvae, at day *in vitro* 3 (DIV3). Cell body of a single neuron is indicated with dotted circle. A time-lapse was taken at 3.3 Hz (3.3 frames/sec; 200 frames; 1 minute), and a kymograph from the axon (yellow dotted box) was shown below. A track was traced and labelled as oscillatory, anterograde, and retrograde movement. **(G)** Quantitation of segmental transport parameters of *Rab11*-MS2/MCP-GFP mRNA particles from cultured neuron axons in (D). **(H)** Quantitation of segment parameters of *Gdi*-MS2/MCP-GFP mRNA particles from cultured neuron axons in (F). In (G)-(H), % time in motion/paused was shown as mean ± SEM; velocities and run lengths were shown as violin plots with median (red line) and all datapoints.

4.3.3 Reduction of Kinesin-1 and Cytoplasmic Dynein motor speed impairs axonal mRNA localization and synaptic plasticity

The molecular motors Kinesin-1 and/or Dynein carry mRNA along MT tracks bidirectionally, during long-distance active axonal transport (Das et al., 2019; Kanai et al., 2004; Zhang et al., 2001). It is unclear whether the disruption to either Kinesin-1 or Dynein function negatively impacts mRNA delivery to the NMJ pre-synapse. *Rab11* and *gdi* transcripts move bidirectionally along motoneuron axons with the speed and run lengths similar to other kinesin-1 and dynein cargoes (**Figure 4.9G-H**) (Maday et al., 2014), prompting us to hypothesize that Kinesin-1 and Dynein are required for transport and localization of these transcripts to/at the motoneuron axon termini.

First, I made the *kinesin-1* and *dynein* mutant flies carrying one copy of the null allele and another copy of 'slow' motor allele (i.e. having 2-fold reduction in ATP turnover rate), as trans-heterozygotes as described previously (Titlow et al., 2022). Our lab previously found that khc^{27}/khc^{23} was shown to lower abundant mRNA *shaggy* (*sgg*) copy number at the NMJ pre-synapse (Titlow et al., 2022), and $dhc^{8\text{-}1}/dhc^{6\text{-}10}$ was shown to reduce the speed of dynein-dependent transport of *gurken* mRNA along the MT in the *Drosophila* oocytes (MacDougall et al., 2003). To first test the phenotypes of null/hypomorphic motor mutants by larval crawling analysis, I put mutant and OrR control larvae on 1% agar plate and analyzed body curvature and trajectories of individual larvae over 3 minutes (Torres-Méndez et al., 2022) (**Method 4.2.9**). Compared to a wildtype crawling behaviors, khc^{27}/khc^{23} larvae failed to reach the edge of the agar plates (**Figure 4.10A**), and displayed a reduction in average crawling speed (**Figure 4.10B**), with an increase percent time spent in a "curved body" position (**Figure 4.10C**)— a characteristic of *kinesin-1* associated motoneuron disease phenotypes described previously as 'tail-flipping' (Hurd and Saxton, 1996). Compared to wild type OrR controls, $dhc^{8\text{-}1}/dhc^{6\text{-}6}$ mutant larvae showed movement in tortuous paths (**Figure 4.10A**), but the speed and body shape of the mutants were comparable to the controls (**Figure 4.10B-C**). Next, to test the ability of *kinesin-1* and *dynein* mutant larvae to form new boutons upon spaced chemical stimulation, larvae of all genotypes were subjected to KStim paradigm for 45 minutes prior to fixation, co-immunostained with HRP (for neuron/pre-synapse) and Dlg (muscle/post-synapse), and the number of boutons lacking Dlg (called ghost boutons/newly formed boutons) were quantified (**Method 4.2.2**). I found that both khc^{27}/khc^{23} and $dhc^{8\text{-}1}/dhc^{6\text{-}6}$ larvae were not able to form as many new boutons as the OrR

wildtype control larvae (**Figure 4.10D**). Thus, a slowdown of cargo delivery to the synapse via Kinesin-1 and Dynein motor speed disruption negatively impacts the larval synaptic plasticity and neuromuscular function.

Kinesin-1 is required during embryonic to neurite development and axon regeneration (Konjikusic et al., 2021; Lu et al., 2015). Cultured motoneurons from khc^{27}/khc^{23} larval brains showed shorter neurites and delayed axon specification (Lu et al., 2015), prompting us to speculate that RNA mislocalization in khc^{27}/khc^{23} neurons could be indirect due to developmental defects. To disrupt axonal transport post-specification of axons, I surveyed trans-heterozygotes of a temperature-sensitive null kinesin-1 mutant (khc^{ts})—where its kinesin-1 functions normally at 18-25°C but becomes inactive at 30°C—and combined this with a hypomorphic mutant. khc^{ts}/khc^{8} larvae showed mild body-curved phenotype upon being shifted to a restrictive temperature (30°C), in comparison to khc^{ts}/khc^{23} larvae that replicate similar phenotype as a constitutive kinesin-1 mutant khc^{27}/khc^{23} (**Figure 4.10E**). Thus, I chose to analyze *rab11* and *gdi* mRNA copy number at the NMJ pre-synaptic boutons of OrR control, khc^{ts}/khc^{23} and $dhc^{8\text{-}1}/dhc^{6\text{-}6}$. As expected, the number of *rab11* mRNA single molecules at the motoneuron termini were significantly lower in khc^{27}/khc^{23} compared to OrR control (**Figure 4.10F**). Unexpectedly, the number of *rab11* and *gdi* transcripts at the motoneuron termini were significantly higher in khc^{ts}/khc^{23} larvae that were raised for 2 days at 30°C to disrupt kinesin-1 function (**Figure 4.10G-H**). However, this could be due to the temperature-specific effects independent of the mutant. Raising larvae at 30°C increased bouton number and branches at the NMJ (Sigrist et al., 2003). I plan to repeat this experiment by shifting OrR and dynein mutants to 30°C at the same time as khc^{ts}/khc^{23} and repeated the experiments and the analysis again to make sure that the

temperature is a control variable. Importantly, the number of *rab11* and *gdi* mRNA single molecules in the NMJ pre-synapse of $dhc^{8\text{-}1}/dhc^{6\text{-}6}$ was not different from those of a wildtype control, raised at the same temperature, suggesting that despite a requirement of dynein for synaptic plasticity, dynein is not likely required in the delivery and proper localization of *rab11* and *gdi* mRNA at the axon termini.

In conclusion, my current findings suggested that both Kinesin-1 and Dynein are required for the larval neuromuscular function and synaptic plasticity. However, only Kinesin-1, not Dynein, is implicated in the delivery of *rab11* and *gdi* transcripts to the axon termini, that could manifest during the development or during post-developmental stages via axonal transport.

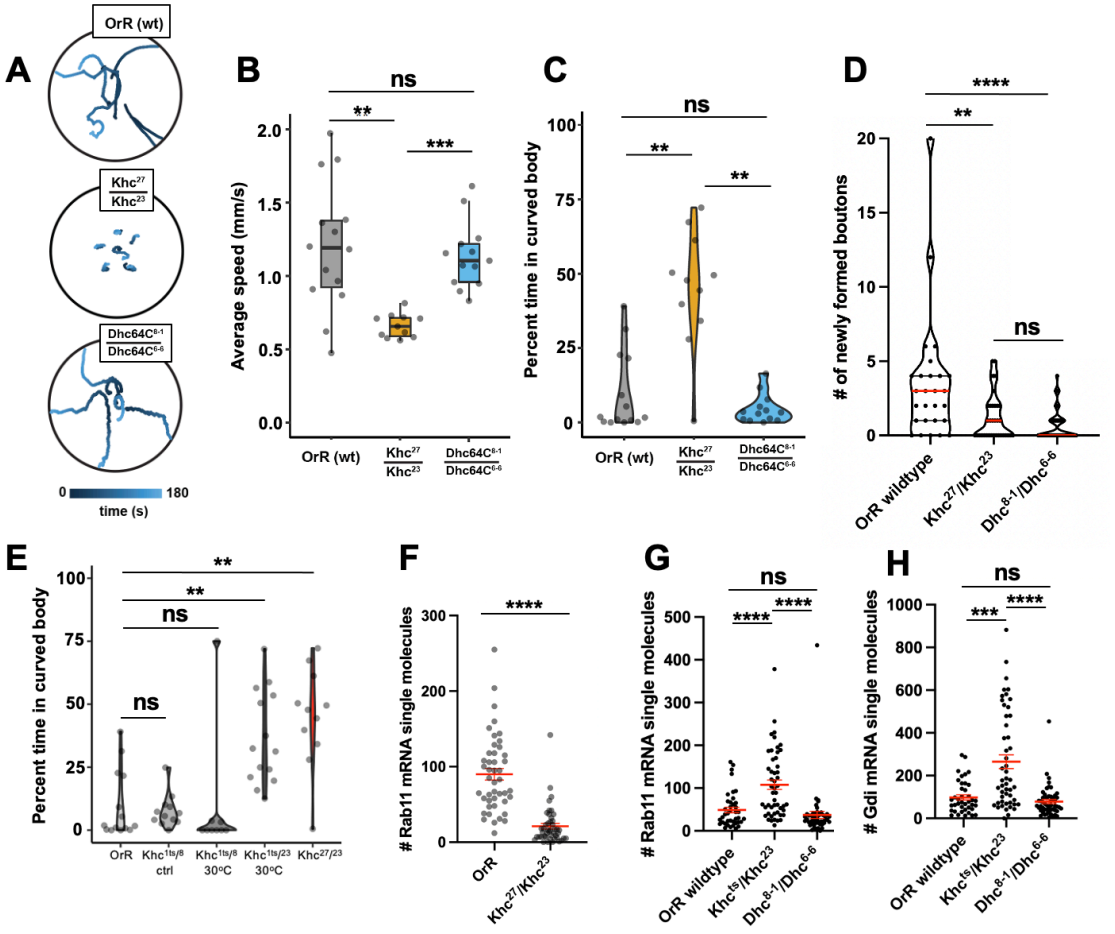


Figure 4.10 Kinesin-1 and dynein mutant larvae show defects in locomotion, synaptic plasticity, and mRNA localization. **(A)** representative tracks of wildtype (wt; OrR), kinesin-1 mutant (Khc^{27}/Khc^{23}), or dynein mutant ($Dhc64C^{8-1}/Dhc64C^{6-6}$; in short Dhc^{8-1}/Dhc^{6-6}) larval crawling in 3 minutes. **(B)** Average speed of larval crawling in wt, kinesin-1 and dynein mutants. Box plot with Tukey's definition. **(C)** Percent time larvae spent in curved body. Violin plots. **(D)** Number of newly formed boutons from KStim experiments. **(E)** Percent time larvae of conditional and constitutive kinesin mutants spent in curved body. Violin plots. **(F)** Number of *Rab11* mRNA single molecules at the motoneuron terminal boutons of OrR vs. constitutive kinesin-1 mutant larvae. **(G)** Number of *Rab11* mRNA single molecules at the motoneuron terminal boutons of OrR vs. conditional kinesin-1 mutant vs. dynein mutant larvae. **(H)** Number of *Gdi* mRNA single molecules at the motoneuron terminal boutons of OrR vs. conditional kinesin-1 mutant vs. dynein mutant larvae. ****$p<0.0001$, ***$p<0.001$, **$p<0.01$, *$p<0.05$, ns = not significant. (B), (C), (D), (G), (H) Dunn's multiple comparison tests. (E) Dunnett's multiple comparison tests. (F) Wilcoxon rank-sum test.

4.3.4 Kinesin-1 and Imp are putative axonal transport machinery for *rab11* mRNA and are required for synaptic plasticity.

It is unknown how *rab11* mRNA is recruited by Kinesin-1 for axonal transport in the *Drosophila* motoneurons. Axonal transport of Imp was previously studied in the *Drosophila* adult mushroom body γ neuron, and live imaging showed that Imp moved bidirectionally in axons where it carried *chickadee* mRNA that encoded profilin, a regulator of actin dynamics in flies (Medioni et al., 2014). In addition, individual-nucleotide resolution crosslinking and immunoprecipitation (iCLIP) experiment in *Drosophila* cells identified multiple transcripts of small GTPases that bind Imp: these include *rab11*, *rac1*, *cdc42*, *gdi*, and *arf79f* (Hansen et al., 2015). Jeff Lee from our research group performed another Imp iCLIP experiment from the *Drosophila* 2^{nd}-3^{rd} instar larval brains and found cumulative count of the iCLIP reads restricted within the 3'UTR of *rab11* (**Figure 4.11A**), consistent with the literature that Imp preferentially binds the 3'UTR of the target transcripts (Hansen et al., 2015). Here, I hypothesized that Imp and kinesin-1 are required for *rab11* mRNA transport and delivery to the larval NMJ pre-synapse.

First, a GFP-tagged Imp (Imp-GFP) from a new generation protein-trap transgenic fly with GFP inserted in all Imp isoforms (Davie et al., 2018) displayed oscillatory motion in DIV3-4 cultured neuron axons, with the particle speed within the range of kinesin-1-mediated process (**Figure 4.11B**), suggesting that Imp-GFP particles translocate and undergo active transport in larval motoneuron axons, similar to the adult fly mushroom body γ neurons (Medioni et al., 2014). Furthermore, immunofluorescence against endogenous kinesin-1 heavy

chain (Khc) showed colocalization with Imp-GFP in the proximal axons (**Figure 4.11C**). smFISH against *rab11* and *gdi* transcripts in the same samples revealed triple colocalization events between Imp-GFP, *rab11* mRNA, and *gdi* mRNA (**Figure 4.11D**). These results suggest that Khc/Imp/*rab11* and *gdi* mRNAs enter motoneuron axons as a complex.

Next, to test whether Imp is required for *in vivo* delivery of *rab11* mRNA to the NMJ pre-synapse, I knocked down Imp conditionally in motoneurons at the larval stages using the *gal4/UAS* in combination with *tub-gal80^{ts}* (**Figure 4.11E**). Raising larvae at 30°C for 2 days before the dissection and fixation for experiments was sufficient to reduce Imp level in the soma, compared to the same genotype at 18°C control and to OrR wildtype (**Figure 4.11F**). Conditional knockdown of Imp during the larval stages resulted in a reduced number of *rab11* mRNA molecules in motoneuron axon termini and their bouton area at the NMJ (**Figure 4.11G, H**), suggesting that Imp is required for mRNA localization in axons and for NMJ development in the larval stages.

Finally, to test whether conditional knock-down of Imp and dysfunction of Khc together negatively impact on synaptic plasticity, the number of newly formed boutons were quantified in mutant combinations. Larvae carrying one copy of the temperature-sensitive *khc* null mutant (*khc^{ts}*/+) showed no significant decline in the ability to form new boutons compared to OrR wild type larvae. In contrast, a conditional knockdown of Imp in motoneurons (*D42>Imp* RNAi) alone and double mutants *D42>Imp* RNAi combining with *khc^{ts}*/+ showed severe plasticity defects (**Figure 4.11I**). These results strongly suggest that both Khc and Imp are required to carry *rab11* mRNA to the motoneuron pre-synaptic termini and are important for larval NMJ synaptic plasticity *in vivo*.

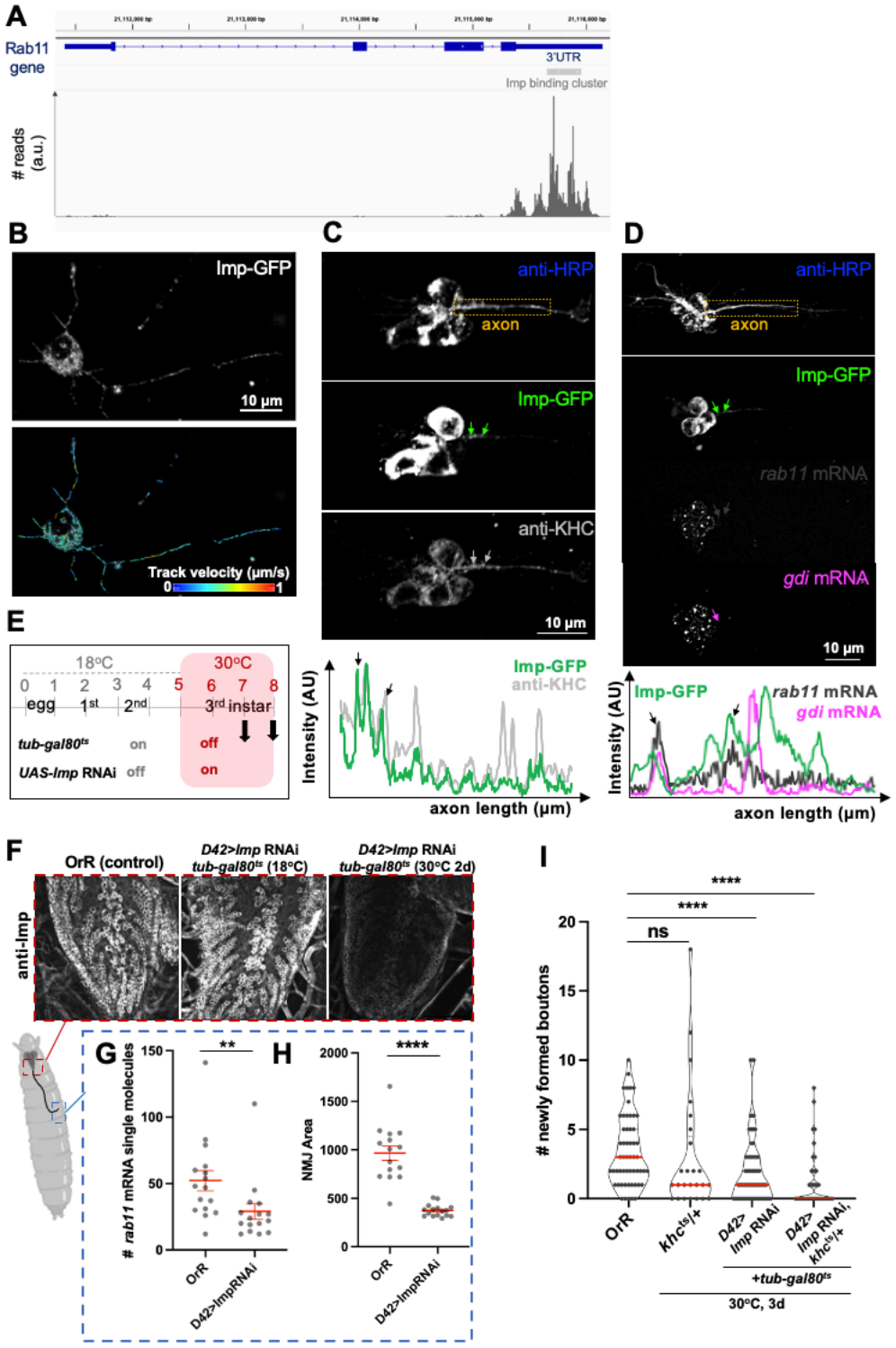


Figure 4.11 Imp is a putative RBP for Rab11 mRNA localization in axons and is required for synaptic plasticity. (A) *Rab11* gene and the number of Imp iCLIP reads showing Imp binding

clusters at the 3'UTR. **(B)** First-frame image of live imaging of Imp-GFSTF2 in DIV3 cultured primary neurons (top) and detected single-particle color-coded track velocities overlay (bottom) from 1-minute video. **(C)** IF images of Imp-GFSTF2 in DIV3 cultured primary neurons, co-immunostained with antibodies against HRP and KHC. Fluorescence intensity plot profile was taken from the highlighted axon region (yellow box). Arrows point to colocalization events. **(D)** smFISH images of Imp-GFSTF2 in DIV3 cultured primary neurons, against *Rab11* and *Gdi* exons, immunostained with antibody against HRP. Fluorescence intensity plot profile was taken from the highlighted axon region (yellow box). Arrows point to colocalization events. **(E)** Timeline for Imp RNAi knockdown with tubGAL80^{ts}. **(F)** (top) IF images of anti-Imp antibody in the VNC from OrR (wt-control), D42>Imp RNAi (control), and D42>Imp RNAi for 2 days. **(G)** Number of *Rab11* mRNA at the NMJ pre-synapse of OrR versus D42>Imp RNAi for 2 days. **(H)** Area of the NMJ pre-synapse of OrR versus D42>Imp RNAi for 3 days. **(I)** Quantitation of the number of newly formed boutons in OrR, Khc^{ts}/+ (30°C for 3d), D42>Imp RNAi, with tubGAL80^{ts} (30°C for 3d), and Khc^{ts}/+, D42>Imp RNAi, with tubGAL80^{ts} (30°C for 3d). ****p<0.0001, ***p<0.001, **p<0.01, *p<0.05, ns = not significant. (H-I) Mean ± SEM; Wilcoxon rank-sum tests. (J) Violin plots with median and all datapoints; Dunnett's multiple comparison tests.

4.3.5 Reduction of *rab11* mRNA copy number, not protein, correlates with NMJ development

Next, I aimed to test the functional role of *rab11* mRNA and Rab11 protein in the NMJ, pre-synaptically. I detected *rab11* mRNA in both immature and mature NMJ boutons (**Figure 4.3C**), suggesting that localized translation of *rab11* mRNA might have a role in synaptic development and plasticity. First, immunofluorescence against Rab11 protein after K^+-stimulation showed high level of protein expression in newly formed boutons. However, there was no significant difference in protein level of Imp at the pre-synapses of existing and new boutons in KStim compared with Mock control conditions (**Figure 4.12A, B**). I conclude that acute neuronal stimulation did not change Rab11 protein level significantly. The emerging Rab11 proteins in newly formed boutons could come from protein transport from neighboring mature boutons or axons. Alternatively, new Rab11 protein could originate from *de novo* protein synthesis of mRNA in the newly formed boutons. Distinguishing between these possibilities will require

additional specific experiments. For example, the use of a technique to directly visualize translationally active *rab11* mRNA molecules, such as a FISH-based assay to detect ribosome interactions with mRNA (FLARIM) (Burke et al., 2017; Richer et al., 2021), could help determine the precise contribution of *de novo* protein synthesis in newly formed synaptic boutons.

It was important to test how a reduction in *rab11* expression in motoneurons affects *rab11* mRNA copy number, Rab11 protein level, NMJ morphology, and function. I performed conditional knockdown with a validated *rab11* RNAi in motoneurons at larval stages by combining *OK371-Gal4* with *tub-gal80^{ts}*, shifting the larvae to restrictive temperature of 30°C for 3 days, and performed smFISH-IF on the larval fillet preparation. Conditional *rab11* knockdown in motoneurons resulted in reduced NMJ area that correlated with reduced *rab11* mRNA copy number, while the protein level did not change significantly, compared those in OrR wildtype (**Figure 4.12C-E**). These data highlighted that lowered *rab11* gene expression resulted in *rab11* mRNA mis-localization that correlated with impaired NMJ development, while Rab11 protein level remained unchanged at the NMJ pre-synaptic axon termini. The production of Rab11 proteins might be happening in a different timeframe or in a different sub-cellular position than observed here. The results thus far on the discordance between mRNA, protein, and function of *rab11* implied a complex post-transcriptional regulation at the NMJ pre-synapse that required further investigation.

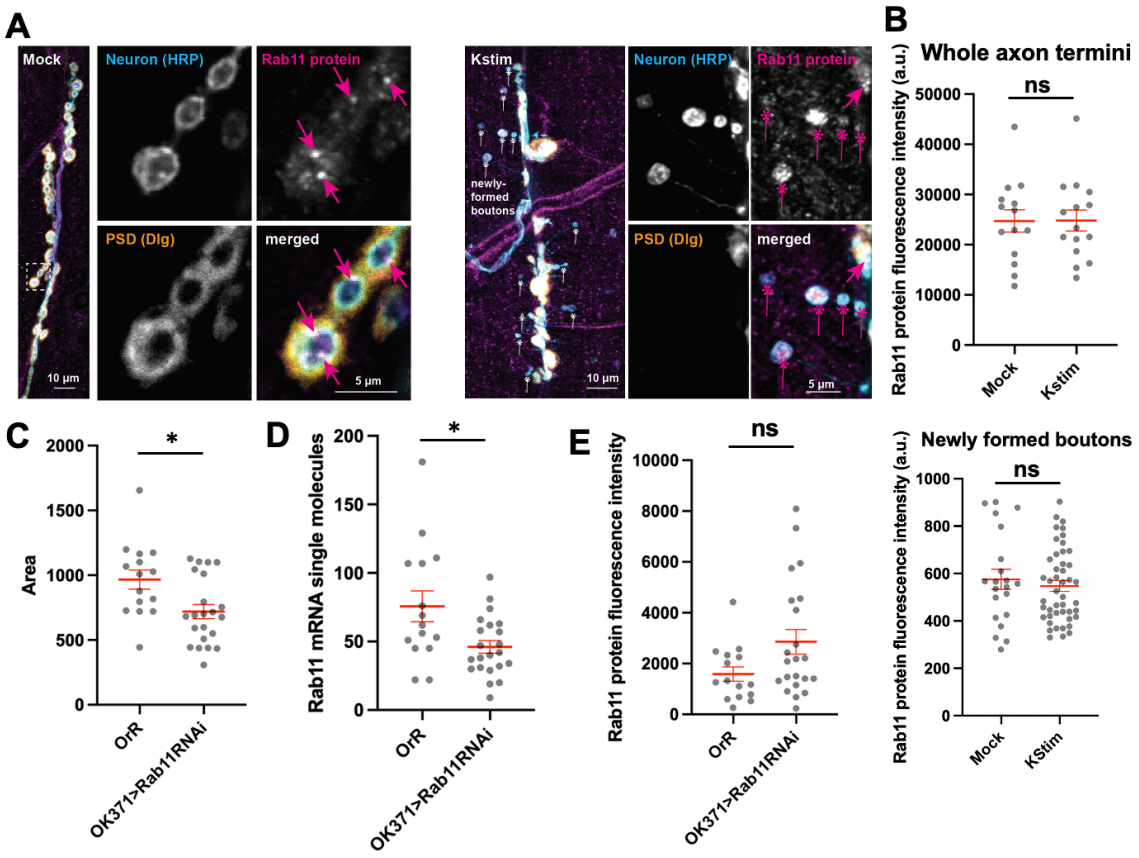


Figure 4.12 *Rab11* mRNA and protein level in *Rab11* knockdown and chemically stimulated NMJ. (A) Representative images of Mock (left) or Kstim (right) of NMJ co-stained with HRP (neuron), Dlg/PSD (post-synaptic density), and Rab11 protein. Arrows point to Rab11 protein in mature boutons. Asterisks highlight Rab11 protein in newly formed boutons. **(B)** Quantitation of Rab11 protein intensity in the whole axon termini at the NMJ (top graph) or only within newly formed boutons (bottom graph) in Mock vs. KStim larvae. **(C)** Area of the motor neuron axon termini in OrR control vs. OK371>Rab11 RNAi. (D) The number of Rab11 mRNA single molecules within the motor neuron axon termini in OrR control vs. OK371>Rab11 RNAi. (E) Rab11 protein intensity within the motor neuron axon termini in OrR control vs. OK371>Rab11 RNAi. All OK371>RNAi lines contained tubGAL80^{ts} and were shifted to 30°C for 3d at the larval stages. All graphs show mean ± SEM. *p<0.05, ns = not significant. Kruskal-Wallis tests.

4.3.6 A family of RabGTPase transcripts are localized to axon terminals and glial extensions at the NMJ and are important for function

The discovery of *rab11* and *gdi* mRNA localization at the axon termini of *Drosophila* larval motoneurons raised a possibility that mRNA localization is a common mechanism relevant for other small GTPases and their chaperones. A

meta-analysis of synaptic transcriptome/translatome predicted that 12 of 15 *Drosophila* Rab protein family which have mammalian orthologs—i.e., Rab1, Rab2, Rab4, Rab5, Rab6, Rab7, Rab9, Rab10, Rab11, Rab14, Rab18, and Rab35—localize their mRNAs to glial cytoplasmic extensions at the synapse (Gala et al., 2022). Furthermore, 6 of 11 of *Drosophila* Arf/Arf-like(Arl) family—i.e., Arf79F/Arf1, Arf102f/Arf4, Arf51F/Arf6, Arl4, Arl8, and Sar1—are also on the list of predicted localized transcripts, raising the possibility that mRNA localization to the periphery of polarized cells in the nervous system is ubiquitous or very common in the small GTPase protein families. However, whether these transcripts are actually present at the *Drosophila* larval NMJ has not been investigated in detail.

One of the major challenges to survey mRNA localization of the entire small GTPases was that exons of many *Rab* genes are relatively small and difficult to be detected quantitatively by smFISH, which requires 24-48 oligonucleotide probes. To overcome this difficulty, I utilized a single-molecule hybridization chain reaction (smHCR) approach (Shah et al., 2016), where only a minimum of 5-10 oligonucleotide probes are required to hybridize to exons or protein coding regions. Another advantage of smHCR over smFISH is that smHCR allows multiplexing of 3-6 dyes per sample, and it uses a common dye-conjugated oligo amplifiers that recognize common initiator sequences (Shah et al., 2016). This allowed me to save time and budget in the survey of mRNA localization of many genes at once. Using this method, thus far, I found that mRNAs of *rab1*, *rab4*, *rab5*, *rab7*, *rab9*, *rab11*, *rab14*, and *rab18* were present at the neuronal axon termini and glial extensions at the NMJ (**Figure 4.13G**), confirming that many *rab* transcripts were localized at the cell periphery as

predicted. It was difficult to quantitatively compare the absolute number and enrichment of certain transcripts in axon termini or glial extensions versus the cell bodies, due to the limited spatial and axial resolution of the spinning disc confocal. To distinguish the localization of individual smHCR spots when the two cell types were closely intertwined, a complementary super-resolution technique such as 3D-structured illumination microscopy (3D-SIM) is required to determine the relative enrichment of multiple *rab* GTPases transcripts in distal sites of neurons versus glia.

To test whether some of the highly localized transcripts are functionally important in neurons and glia, I performed conditional knockdown of *UAS-RNAi* lines against recycling endosomes-associated *rab* GTPases in motoneurons or glia at the larval stages and monitored their crawling behaviors. I found that knocking down recycling endosome regulators *rab8* and *rab9* in addition to *rab11* specifically in motoneurons negatively impacted larval crawling (**Figure 4.13A-C**). In addition, knocking down recycling endosome regulators *rab4* and *rab35* in glia showed severed larval crawling defects (**Figure 4.13D-F**). These results confirmed the importance of localized mRNA of many *rab* GTPases of similar pathway. Also, different types of *rab* mRNAs are required for recycling endosome function and neuromuscular function in neurons versus in glia. These preliminary results suggest exciting new avenues for future studies to investigate the unexplored aspect of mRNA localization mechanism and function of localized translation of membrane trafficking regulators in neuronal and glial extensions at the synapse, during development and plasticity, with relevance to pathophysiology in neurological diseases (See **Chapter 5**, Future Directions).

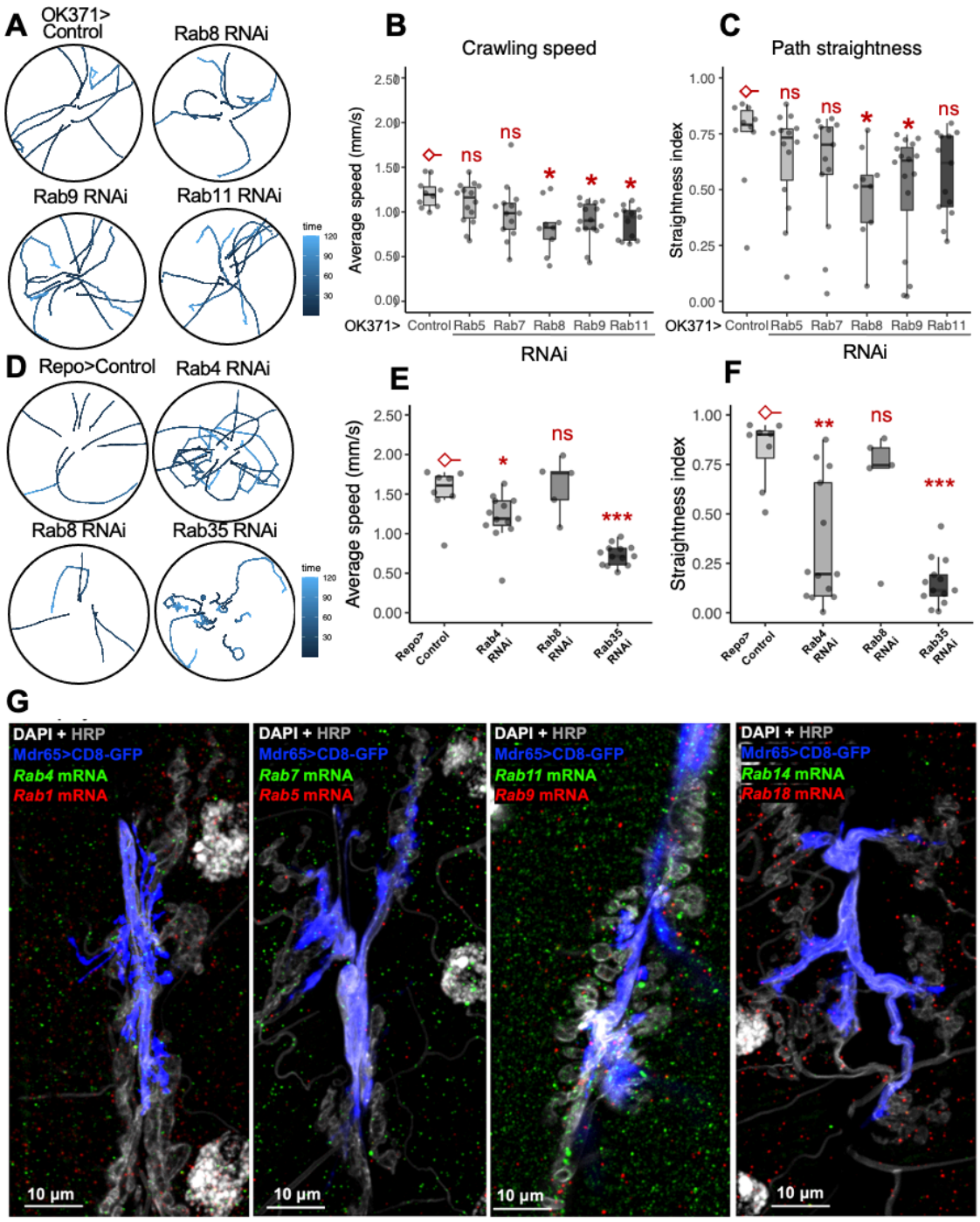


Figure 4.13 Functional requirements of multiple Rab species and the mRNA localization in the axon termini and glial extension at the NMJ. **(A,D)** Larval crawling tracks (2 minutes) from the center as a starting point. **(B,E)** Quantitation of crawling speed. **(C,F)** Path straightness index. (A-C) *Rab* RNAi in motoneurons (*OK371-Gal4*). (D-F) *Rab* RNAi in glia (*Repo-Gal4*). **(G)** smHCR analysis of 2 genes/samples of Mdr65>CD8-GFP larvae (labeled sub-perineurial glia at

the NMJ), co-stained with DAPI (nuclei marker), and HRP (neuronal marker). All images shown here are maximum intensity projection.

4.4 Conclusion and discussion

In this chapter, I performed high-resolution quantitative imaging studies of mRNA localization and determined its physiological roles at the distal axonal synapses of the *Drosophila* larval NMJ. I focused primarily on dissecting the mRNA transport mechanisms of *rab11*—a recycling endosome regulator—and found that Kinesin-1 and Imp are required for the delivery of *rab11* mRNA to localize at the pre-synaptic motoneuron axon termini, possibly to localize Rab11 protein synthesis. Furthermore, I found that Kinesin-1, Imp, and several mRNAs that are carried into axons by these transport machinery components are required for NMJ development and for synaptic plasticity. Finally, I found the transcripts of many endosomal GTPases and their chaperone *gdi* at neuronal tips and in glial extensions at the NMJ. I propose here that localization of mRNAs for activity-dependent translation required for synaptic plasticity is related to membrane trafficking regulation that we still know very little about, mechanistically and functionally, and in terms of its relevance in diseases.

The novelty of this study lies within the unorthodox view of membrane trafficking regulation by localized translation of *rab* GTPase transcripts. The canonical thinking about membrane trafficking regulation in highly polarized cells such as neurons is that different Rab proteins—such as Rab5 for early endosomes, Rab7 for late endosomes, and Rab11 for recycling endosomes—are spatially distributed to where they are needed to function, and that most regulatory steps are via the cycle of membrane association/disassociation control (Kiral et al., 2018; Winckler et al., 2018). Newly synthesized, prenylated Rabs are chaperoned by GDI protein and kept in the cytosol, before these Rabs associate

with the correct membrane and are activated by GEF to trigger downstream transport, sorting, or fusion of vesicles (Soldati et al., 1993; Wu et al., 2007). The discovery that local production of soluble RabGTPases distally could potentially change our understanding of how different Rab proteins are compartmentalized and integrated into pathways in a highly polarized cell. Future studies need to address the relative contribution of newly synthesized Rab proteins versus the recycled Rab proteins that were extracted from the membrane by GDI.

The abundant detection of mRNA at the NMJ pre-synapse is unexpected. Among all *rab* GTPses in *Drosophila*, *rab11* is the highest-expressed gene from the S2 cultured cells (Gillingham et al., 2014). However, in a highly polarized cell such as in the motoneuron, it is unclear how *rab11* mRNA is distributed from the cell body towards the distal synapse. Here, I performed sensitive mRNA detection by smFISH to count the number and density of *rab11* mRNA molecules in the cell bodies versus the NMJ synapse (**Figure 4.8**). This observation suggest that there must be an active mechanism to ensure the distribution of mRNA to the distal axonal sites. The genome-wide measurement of RNA synthesis and decay rates in the larval brain via metabolic labeling suggests that *rab11* mRNA's half-life is 210 minutes (Thompson et al., 2022). This RNA stability estimate alone might not be sufficient to rationalize the long-lived residence of 20-100 *rab11* mRNA copies at the axon termini with little turnover over a day (**Figure 4.8-4.9**). It is thus possible that a sub-population of *rab11* mRNA that exits the brain to enter axons to be delivered to the NMJ has higher stability due to the production of transcript isoforms that contain *cis*-regulatory elements to recruit axon-specific RBPs that protect mRNA from a degradation mechanism (Burow et al., 2015). These *cis*- and *trans*-acting factors to localize *rab11* mRNA in axons are not

completely well-understood. In this study, I determined the *trans*-factors and found that kinesin-1 heavy chain (Khc) and a conserved RBP called Imp constitute the axonal transport machinery for *rab11* mRNA axonal entry in motoneurons. Imp was previously studied to preferentially binds the 3'UTR of its target transcripts (Hansen et al., 2015), and this was confirmed in this study by iCLIP from the *Drosophila* larval brain that Imp binds strongest to the 280-nt cluster in the *rab11* 3'UTR (**Figure 4.11A**), which could be a potential *cis*-element that I am seeking. I designed a sophisticated genetic strategy to test whether tissue- and time-specific deletion of the putative *cis*-regulatory elements in the mRNA *in vivo* impairs axonal transport and localization of mRNA of interests (**Figure 4.2**), which could have functional consequences on the NMJ function (*work in progress*). The pipeline presented here would be beneficial for studying the sub-cellular mechanisms of post-transcriptional regulation, especially axonal transport, of many localized mRNAs that we still know very little about.

Localization of mRNA at the distal location away from its synthesis site occurs throughout a lifetime of an organism, from the development of embryos to during synaptic remodeling in adults (Medioni et al., 2012). Disruption of mRNA localization prior to axonal specification could negatively impact mRNA localization at a later stage due to the impaired infrastructure of axonal transport components. Kinesin-1, for example, is required to slide MT fragments into neurites, prior to the formation of stable MT tracks for axonal transport (Lu et al., 2015). In addition, Imp plays a crucial role during neuroblast (neural stem cell) growth and division prior to neuron specification (Samuels et al., 2020), but Imp also plays another role to transport mRNA of actin regulators in adult fly neurons (Medioni et al., 2014). Hence, this study utilized the temperature-sensitive conditional mutants to disrupt kinesin-1 and Imp function specifically

during the late larval stage, when axons already innervated the muscles to form the NMJ but still undergo active remodeling— a process called synaptic plasticity (Menon et al., 2013). The distinction between developmental defects versus plasticity defects as a result of molecular motor and/or RBP disruption require sophisticated genetic tool that was made possible in the *Drosophila* model.

It is still unclear when mRNA is actively transported to the axon termini, and whether this process is constitutive or is responsive to certain stimuli. Axonal transport of several pre-synaptic cargoes are responsive to neuronal activity, and their transport becomes processive until they reach the destination distally in axons (Birdsall et al., 2022; Sheng and Cai, 2012). It is unclear whether mRNA transport in axons is regulated similarly by the neuronal activity. The primary culture from the larval brain that regenerates axons over a few days *in vitro* showed mRNA motility alongside the developing axons, and thus I speculate that *in vivo*, a population of long-lived mRNAs could co-migrate along with the axonal growth to find muscle and form the NMJ. Surprisingly, *rab11* mRNA particles in developing axons exhibit oscillatory movement, with little net anterograde or retrograde displacement (**Figure 4.9**), and it is unclear what, if any at all, triggers a switch from oscillatory to a directional processive movement of mRNA in axons. A combination of *in vitro* primary culture and *in vivo* NMJ models to study mRNA transport in real time as axons develop, mature, and exhibit physiological activity, with the mathematical modeling that integrates RNA stability data with RNA transport dynamics, could provide unprecedented insights into the post-transcriptional regulation of enriched mRNA at the cell periphery.

Apart from the motoneuron axons that innervate the muscle at the NMJ, glial cells, including the sub-perineurial glia and perineurial glia, form blood-nerve barriers and some extend its cytoplasmic processes into the NMJ synapses (Brink et al., 2012). The tripartite (three-part) synapse between a neuron (pre-synapse), a muscle cell (post-synapse), and a glia is common among invertebrate and vertebrate NMJs (Danjo et al., 2011; Feng and Ko, 2008). Transcripts that localize to the tip of axons also localize to the tip of glial protrusions, but the glial-specific function of these transcripts, especially membrane-trafficking related ones, at the synapse is unexplored. Imp is expressed and localized to PNS glial extensions at the same larval stage as in neurons (Dalia Gala, per comm.), and MT network and molecular motors likely play a role in active transport of many mRNA to the glial extensions. In this study, I performed RNAi knockdown of *rab* GTPases genes related to the recycling endosome pathway in motoneuron versus glia and found that *rab8* and *rab35* are required in glia for neuromuscular function. The initial survey of larval crawling defects from neuron- vs glia-specific *rab* RNAi done in this experimental chapter presented a quick and easy way to pick interesting *rab* GTPases to follow up and study in addition to *rab11*. It is also important to determine whether RNAi knockdown of the same *rab* GTPases in motoneuron versus in glia results in differential defects of NMJ development, synaptic plasticity, and crawling behaviors. The successful completion of this systematic study will be a valuable resource for the *Drosophila* and membrane trafficking research communities. Altogether, the results thus far highlight unexplored complexity of membrane trafficking at axon termini and glia at the distal synapses, by localized translation of Rab GTPase network with potential relevance to pathophysiology and neurological diseases.

4.5 References

Ataman, B., Ashley, J., Gorczyca, D., Gorczyca, M., Mathew, D., Wichmann, C., Sigrist, S.J., Budnik, V., 2006. Nuclear trafficking of Drosophila Frizzled-2 during synapse development requires the PDZ protein dGRIP. Proceedings of the National Academy of Sciences 103, 7841–7846. https://doi.org/10.1073/pnas.0600387103

Ataman, B., Ashley, J., Gorczyca, M., Ramachandran, P., Fouquet, W., Sigrist, S.J., Budnik, V., 2008. Rapid Activity-Dependent Modifications in Synaptic Structure and Function Require Bidirectional Wnt Signaling. Neuron 57, 705–718. https://doi.org/10.1016/j.neuron.2008.01.026

Avellaneda, J., Schnorrer, F., 2022. Tagging Drosophila Proteins with Genetically Encoded Fluorophores, in: Dahmann, C. (Ed.), Drosophila: Methods and Protocols, Methods in Molecular Biology. Springer US, New York, NY, pp. 251–268. https://doi.org/10.1007/978-1-0716-2541-5_12

Bauer, K.E., Segura, I., Gaspar, I., Scheuss, V., Illig, C., Ammer, G., Hutten, S., Basyuk, E., Fernández-Moya, S.M., Ehses, J., Bertrand, E., Kiebler, M.A., 2019. Live cell imaging reveals 3′-UTR dependent mRNA sorting to synapses. Nat Commun 10, 3178. https://doi.org/10.1038/s41467-019-11123-x

Bhat, V.D., Jayaraj, J., Babu, K., 2022. RNA and neuronal function: the importance of post-transcriptional regulation. Oxford Open Neuroscience 1, kvac011. https://doi.org/10.1093/oons/kvac011

Birdsall, V., Kirwan, K., Zhu, M., Imoto, Y., Wilson, S.M., Watanabe, S., Waites, C.L., 2022. Axonal transport of Hrs is activity dependent and facilitates synaptic vesicle protein degradation. Life Science Alliance 5. https://doi.org/10.26508/lsa.202000745

Boulanger, J., Kervrann, C., Bouthemy, P., Elbau, P., Sibarita, J.-B., Salamero, J., 2010. Patch-based nonlocal functional for denoising fluorescence microscopy image sequences. IEEE Trans Med Imaging 29, 442–454. https://doi.org/10.1109/TMI.2009.2033991

Brendza, K.M., Rose, D.J., Gilbert, S.P., Saxton, W.M., 1999. Lethal Kinesin Mutations Reveal Amino Acids Important for ATPase Activation and Structural Coupling*. Journal of Biological Chemistry 274, 31506–31514. https://doi.org/10.1074/jbc.274.44.31506

Brendza, R.P., Sheehan, K.B., Turner, F.R., Saxton, W.M., 2000. Clonal tests of conventional kinesin function during cell proliferation and differentiation. Mol Biol Cell 11, 1329–1343. https://doi.org/10.1091/mbc.11.4.1329

Brink, D.L., Gilbert, M., Xie, X., Petley-Ragan, L., Auld, V.J., 2012. Glial Processes at the Drosophila Larval Neuromuscular Junction Match Synaptic Growth. PLOS ONE 7, e37876. https://doi.org/10.1371/journal.pone.0037876

Burke, K.S., Antilla, K.A., Tirrell, D.A., 2017. A Fluorescence in Situ Hybridization Method To Quantify mRNA Translation by Visualizing Ribosome–mRNA Interactions in Single Cells. ACS Cent Sci 3, 425–433. https://doi.org/10.1021/acscentsci.7b00048

Burow, D.A., Umeh-Garcia, M.C., True, M.B., Bakhaj, C.D., Ardell, D.H., Cleary, M.D., 2015. Dynamic regulation of mRNA decay during neural development. Neural Dev 10, 11. https://doi.org/10.1186/s13064-015-0038-6

Carlton, P.M., Boulanger, J., Kervrann, C., Sibarita, J.-B., Salamero, J., Gordon-Messer, S., Bressan, D., Haber, J.E., Haase, S., Shao, L., Winoto, L., Matsuda, A., Kner, P., Uzawa, S., Gustafsson, M., Kam, Z., Agard, D.A., Sedat, J.W., 2010. Fast live simultaneous multiwavelength four-dimensional optical microscopy. Proceedings of the National Academy of Sciences 107, 16016–16022. https://doi.org/10.1073/pnas.1004037107

Chalberg, T.W., Portlock, J.L., Olivares, E.C., Thyagarajan, B., Kirby, P.J., Hillman, R.T., Hoelters, J., Calos, M.P., 2006. Integration specificity of phage phiC31 integrase in the human genome. J Mol Biol 357, 28–48. https://doi.org/10.1016/j.jmb.2005.11.098

Choi, H.M.T., Beck, V.A., Pierce, N.A., 2014. Next-generation in situ hybridization chain reaction: higher gain, lower cost, greater durability. ACS Nano 8, 4284–4294. https://doi.org/10.1021/nn405717p

Choi, H.M.T., Schwarzkopf, M., Fornace, M.E., Acharya, A., Artavanis, G., Stegmaier, J., Cunha, A., Pierce, N.A., 2018. Third-generation in situ hybridization chain reaction: multiplexed, quantitative, sensitive, versatile, robust. Development 145, dev165753. https://doi.org/10.1242/dev.165753

Danjo, R., Kawasaki, F., Ordway, R.W., 2011. A Tripartite Synapse Model in Drosophila. PLoS One 6, e17131. https://doi.org/10.1371/journal.pone.0017131

Das, S., Singer, R.H., Yoon, Y.J., 2019. The travels of mRNAs in neurons: Do they know where they are going? Curr Opin Neurobiol 57, 110–116. https://doi.org/10.1016/j.conb.2019.01.016

Davie, K., Janssens, J., Koldere, D., De Waegeneer, M., Pech, U., Kreft, Ł., Aibar, S., Makhzami, S., Christiaens, V., Bravo González-Blas, C., Poovathingal, S., Hulselmans, G., Spanier, K.I., Moerman, T., Vanspauwen, B., Geurs, S., Voet, T., Lammertyn, J., Thienpont, B., Liu, S., Konstantinides, N., Fiers, M., Verstreken, P., Aerts, S., 2018. A Single-Cell Transcriptome Atlas of the Aging Drosophila Brain. Cell 174, 982-998.e20. https://doi.org/10.1016/j.cell.2018.05.057

Duffy, J.B., 2002. GAL4 system in Drosophila: a fly geneticist's Swiss army knife. Genesis 34, 1–15. https://doi.org/10.1002/gene.10150

Egger, B., van Giesen, L., Moraru, M., Sprecher, S.G., 2013. In vitro imaging of primary neural cell culture from Drosophila. Nat Protoc 8, 958–965. https://doi.org/10.1038/nprot.2013.052

Feng, Z., Ko, C.-P., 2008. The role of glial cells in the formation and maintenance of the neuromuscular junction. Ann N Y Acad Sci 1132, 19–28. https://doi.org/10.1196/annals.1405.016

Fischer, J.A., Giniger, E., Maniatis, T., Ptashne, M., 1988. GAL4 activates transcription in Drosophila. Nature 332, 853–856. https://doi.org/10.1038/332853a0

Fu, Y., Sander, J.D., Reyon, D., Cascio, V.M., Joung, J.K., 2014. Improving CRISPR-Cas nuclease specificity using truncated guide RNAs. Nat Biotechnol 32, 279–284. https://doi.org/10.1038/nbt.2808

Fuentes-Medel, Y., Logan, M.A., Ashley, J., Ataman, B., Budnik, V., Freeman, M.R., 2009. Glia and Muscle Sculpt Neuromuscular Arbors by Engulfing Destabilized Synaptic Boutons and Shed Presynaptic Debris. PLOS Biology 7, e1000184. https://doi.org/10.1371/journal.pbio.1000184

Gala, D.S., Lee, J.Y., Kiourlappou, M., Titlow, J.S., Teodoro, R.O., Davis, I., 2022. Mammalian glial protrusion transcriptomes predict localization of Drosophila glial transcripts required for synaptic plasticity. https://doi.org/10.1101/2022.11.30.518536

Gaspar, I., Wippich, F., Ephrussi, A., 2017. Enzymatic production of single-molecule FISH and RNA capture probes. RNA 23, 1582–1591. https://doi.org/10.1261/rna.061184.117

Gepner, J., Li, M., Ludmann, S., Kortas, C., Boylan, K., Iyadurai, S.J.P., McGrail, M., Hays, T.S., 1996. Cytoplasmic Dynein Function Is Essential in Drosophila melanogaster. Genetics 142, 865–878. https://doi.org/10.1093/genetics/142.3.865

Gillingham, A.K., Sinka, R., Torres, I.L., Lilley, K.S., Munro, S., 2014. Toward a Comprehensive Map of the Effectors of Rab GTPases. Developmental Cell 31, 358–373. https://doi.org/10.1016/j.devcel.2014.10.007

Giorgini, F., Steinert, J.R., 2013. Rab11 as a modulator of synaptic transmission. Commun Integr Biol 6, e26807. https://doi.org/10.4161/cib.26807

Hailstone, M., Waithe, D., Samuels, T.J., Yang, L., Costello, I., Arava, Y., Robertson, E., Parton, R.M., Davis, I., 2020. CytoCensus, mapping cell identity and division in tissues and organs using machine learning. eLife 9, e51085. https://doi.org/10.7554/eLife.51085

Hansen, H.T., Rasmussen, S.H., Adolph, S.K., Plass, M., Krogh, A., Sanford, J., Nielsen, F.C., Christiansen, J., 2015. Drosophila Imp iCLIP identifies an RNA assemblage coordinating F-actin formation. Genome Biology 16, 123. https://doi.org/10.1186/s13059-015-0687-0

Hoppe, C., Ashe, H.L., 2021. CRISPR-Cas9 strategies to insert MS2 stem-loops into endogenous loci in Drosophila embryos. STAR Protocols 2, 100380. https://doi.org/10.1016/j.xpro.2021.100380

Hurd, D.D., Saxton, W.M., 1996. Kinesin mutations cause motor neuron disease phenotypes by disrupting fast axonal transport in Drosophila. Genetics 144, 1075–1085. https://doi.org/10.1093/genetics/144.3.1075

Imbert, A., Ouyang, W., Safieddine, A., Coleno, E., Zimmer, C., Bertrand, E., Walter, T., Mueller, F., 2022. FISH-quant v2: a scalable and modular tool for smFISH image analysis. RNA 28, 786–795. https://doi.org/10.1261/rna.079073.121

Kanai, Y., Dohmae, N., Hirokawa, N., 2004. Kinesin transports RNA: isolation and characterization of an RNA-transporting granule. Neuron 43, 513–525. https://doi.org/10.1016/j.neuron.2004.07.022

Kanca, O., Zirin, J., Garcia-Marques, J., Knight, S.M., Yang-Zhou, D., Amador, G., Chung, H., Zuo, Z., Ma, L., He, Y., Lin, W.-W., Fang, Y., Ge, M.,

Yamamoto, S., Schulze, K.L., Hu, Y., Spradling, A.C., Mohr, S.E., Perrimon, N., Bellen, H.J., 2019. An efficient CRISPR-based strategy to insert small and large fragments of DNA using short homology arms. eLife 8, e51539. https://doi.org/10.7554/eLife.51539

Kiral, F.R., Kohrs, F.E., Jin, E.J., Hiesinger, P.R., 2018. Rab GTPases and Membrane Trafficking in Neurodegeneration. Curr Biol 28, R471–R486. https://doi.org/10.1016/j.cub.2018.02.010

Kokotos, A.C., Peltier, J., Davenport, E.C., Trost, M., Cousin, M.A., 2018. Activity-dependent bulk endocytosis proteome reveals a key presynaptic role for the monomeric GTPase Rab11. Proceedings of the National Academy of Sciences 115, E10177–E10186. https://doi.org/10.1073/pnas.1809189115

Konjikusic, M.J., Gray, R.S., Wallingford, J.B., 2021. The developmental biology of kinesins. Developmental Biology 469, 26–36. https://doi.org/10.1016/j.ydbio.2020.09.009

Lee, J.Y., Wing, P.A., Gala, D.S., Noerenberg, M., Järvelin, A.I., Titlow, J., Zhuang, X., Palmalux, N., Iselin, L., Thompson, M.K., Parton, R.M., Prange-Barczynska, M., Wainman, A., Salguero, F.J., Bishop, T., Agranoff, D., James, W., Castello, A., McKeating, J.A., Davis, I., 2022. Absolute quantitation of individual SARS-CoV-2 RNA molecules provides a new paradigm for infection dynamics and variant differences. eLife 11, e74153. https://doi.org/10.7554/eLife.74153

Lee, P.-T., Zirin, J., Kanca, O., Lin, W.-W., Schulze, K.L., Li-Kroeger, D., Tao, R., Devereaux, C., Hu, Y., Chung, V., Fang, Y., He, Y., Pan, H., Ge, M., Zuo, Z., Housden, B.E., Mohr, S.E., Yamamoto, S., Levis, R.W., Spradling, A.C., Perrimon, N., Bellen, H.J., 2018. A gene-specific T2A-GAL4 library for Drosophila. eLife 7, e35574. https://doi.org/10.7554/eLife.35574

Lu, W., Lakonishok, M., Gelfand, V.I., 2015. Kinesin-1–powered microtubule sliding initiates axonal regeneration in Drosophila cultured neurons. Mol Biol Cell 26, 1296–1307. https://doi.org/10.1091/mbc.E14-10-1423

MacDougall, N., Clark, A., MacDougall, E., Davis, I., 2003. Drosophila gurken (TGFα) mRNA Localizes as Particles that Move within the Oocyte in Two

Dynein-Dependent Steps. Developmental Cell 4, 307–319. https://doi.org/10.1016/S1534-5807(03)00058-3

Maday, S., Twelvetrees, A.E., Moughamian, A.J., Holzbaur, E.L.F., 2014. Axonal transport: Cargo-specific mechanisms of motility and regulation. Neuron 84, 292–309. https://doi.org/10.1016/j.neuron.2014.10.019

McGuire, Sean E., Mao, Z., Davis, R.L., 2004. Spatiotemporal gene expression targeting with the TARGET and gene-switch systems in Drosophila. Sci STKE 2004, pl6. https://doi.org/10.1126/stke.2202004pl6

McGuire, Sean E, Roman, G., Davis, R.L., 2004. Gene expression systems in Drosophila: a synthesis of time and space. Trends in Genetics 20, 384–391. https://doi.org/10.1016/j.tig.2004.06.012

McLean, D.J., Skowron Volponi, M.A., 2018. trajr: An R package for characterisation of animal trajectories. Ethology 124, 440–448. https://doi.org/10.1111/eth.12739

Medioni, C., Mowry, K., Besse, F., 2012. Principles and roles of mRNA localization in animal development. Development 139, 3263–3276. https://doi.org/10.1242/dev.078626

Medioni, C., Ramialison, M., Ephrussi, A., Besse, F., 2014. Imp Promotes Axonal Remodeling by Regulating profilin mRNA during Brain Development. Current Biology 24, 793–800. https://doi.org/10.1016/j.cub.2014.02.038

Melkov, A., Baskar, R., Alcalay, Y., Abdu, U., 2016. A new mode of mitochondrial transport and polarized sorting regulated by Dynein, Milton and Miro. Development 143, 4203–4213. https://doi.org/10.1242/dev.138289

Menon, K.P., Carrillo, R.A., Zinn, K., 2013. Development and plasticity of the Drosophila larval neuromuscular junction. Wiley Interdiscip Rev Dev Biol 2, 647–670. https://doi.org/10.1002/wdev.108

Nagarkar-Jaiswal, S., Lee, P.-T., Campbell, M.E., Chen, K., Anguiano-Zarate, S., Cantu Gutierrez, M., Busby, T., Lin, W.-W., He, Y., Schulze, K.L., Booth, B.W., Evans-Holm, M., Venken, K.J., Levis, R.W., Spradling, A.C., Hoskins, R.A., Bellen, H.J., 2015. A library of MiMICs allows tagging of genes and reversible, spatial and temporal knockdown of proteins in Drosophila. eLife 4, e05338. https://doi.org/10.7554/eLife.05338

Neumann, S., Chassefeyre, R., Campbell, G.E., Encalada, S.E., 2017. KymoAnalyzer: a software tool for the quantitative analysis of

intracellular transport in neurons. Traffic 18, 71–88. https://doi.org/10.1111/tra.12456

Park, Y.-N., Masison, D., Eisenberg, E., Greene, L.E., 2011. Application of the FLP/FRT system for conditional gene deletion in yeast Saccharomyces cerevisiae. Yeast 28, 673–681. https://doi.org/10.1002/yea.1895

Parton, R.M., Vallés, A.M., Dobbie, I.M., Davis, I., 2010. Drosophila larval fillet preparation and imaging of neurons. Cold Spring Harb Protoc 2010, pdb.prot5405. https://doi.org/10.1101/pdb.prot5405

Piccioli, Z.D., Littleton, J.T., 2014. Retrograde BMP Signaling Modulates Rapid Activity-Dependent Synaptic Growth via Presynaptic LIM Kinase Regulation of Cofilin. J. Neurosci. 34, 4371–4381. https://doi.org/10.1523/JNEUROSCI.4943-13.2014

Port, F., Chen, H.-M., Lee, T., Bullock, S.L., 2014. Optimized CRISPR/Cas tools for efficient germline and somatic genome engineering in Drosophila. Proceedings of the National Academy of Sciences 111, E2967–E2976. https://doi.org/10.1073/pnas.1405500111

Rangaraju, V., tom Dieck, S., Schuman, E.M., 2017. Local translation in neuronal compartments: how local is local? EMBO Rep 18, 693–711. https://doi.org/10.15252/embr.201744045

Retelska, D., Iseli, C., Bucher, P., Jongeneel, C.V., Naef, F., 2006. Similarities and differences of polyadenylation signals in human and fly. BMC Genomics 7, 176. https://doi.org/10.1186/1471-2164-7-176

Richer, P., Speese, S.D., Logan, M.A., 2021. FLARIM v2.0, an improved method to quantify transcript-ribosome interactions in vivo in the adult Drosophila brain. https://doi.org/10.1101/2021.08.13.456301

Samuels, T.J., Järvelin, A.I., Ish-Horowicz, D., Davis, I., 2020. Imp/IGF2BP levels modulate individual neural stem cell growth and division through myc mRNA stability. eLife 9, e51529. https://doi.org/10.7554/eLife.51529

Sanyal, S., 2009. Genomic mapping and expression patterns of C380, OK6 and D42 enhancer trap lines in the larval nervous system of Drosophila. Gene Expr Patterns 9, 371–380. https://doi.org/10.1016/j.gep.2009.01.002

Saxton, W.M., Hicks, J., Goldstein, L.S.B., Raff, E.C., 1991. Kinesin heavy chain is essential for viability and neuromuscular functions in Drosophila, but

mutants show no defects in mitosis. Cell 64, 1093–1102. https://doi.org/10.1016/0092-8674(91)90264-Y

Shah, S., Lubeck, E., Schwarzkopf, M., He, T.-F., Greenbaum, A., Sohn, C.H., Lignell, A., Choi, H.M.T., Gradinaru, V., Pierce, N.A., Cai, L., 2016. Single-molecule RNA detection at depth by hybridization chain reaction and tissue hydrogel embedding and clearing. Development 143, 2862–2867. https://doi.org/10.1242/dev.138560

Sheng, Z.-H., Cai, Q., 2012. Mitochondrial transport in neurons: impact on synaptic homeostasis and neurodegeneration. Nat Rev Neurosci 13, 77–93. https://doi.org/10.1038/nrn3156

Sigrist, S.J., Reiff, D.F., Thiel, P.R., Steinert, J.R., Schuster, C.M., 2003. Experience-dependent strengthening of Drosophila neuromuscular junctions. J Neurosci 23, 6546–6556. https://doi.org/10.1523/JNEUROSCI.23-16-06546.2003

Soldati, T., Riederer, M.A., Pfeffer, S.R., 1993. Rab GDI: a solubilizing and recycling factor for rab9 protein. Mol Biol Cell 4, 425–434. https://doi.org/10.1091/mbc.4.4.425

Sun, C., Schuman, E.M., 2022. Logistics of neuronal protein turnover: Numbers and mechanisms. Molecular and Cellular Neuroscience 123, 103793. https://doi.org/10.1016/j.mcn.2022.103793

Thompson, M.K., Ceccarelli, A., Ish-Horowicz, D., Davis, I., 2023. Dynamically regulated transcription factors are encoded by highly unstable mRNAs in the *Drosophila* larval brain. RNA 29, 1020-2032. https://doi.org/10.1261/rna.079552.122

Titlow, J., Robertson, F., Järvelin, A., Ish-Horowicz, D., Smith, C., Gratton, E., Davis, I., 2020. Syncrip/hnRNP Q is required for activity-induced Msp300/Nesprin-1 expression and new synapse formation. Journal of Cell Biology 219, e201903135. https://doi.org/10.1083/jcb.201903135

Titlow, J.S., Kiourlappou, M., Palanca, A., Lee, J.Y., Gala, D.S., Ennis, D., Yu, J.J.S., Young, F.L., Pinto, D.M.S., Garforth, S., Francis, H.S., Strivens, F., Mulvey, H., Dallman-Porter, A., Thornton, S., Arman, D., Järvelin, A.I., Thompson, M.K., Kounatidis, I., Parton, R.M., Taylor, S., Davis, I., 2022. Systematic analysis of YFP gene traps reveals common discordance between mRNA and protein across the nervous system. J Cell Biol 222, e202205129. https://doi.org/10.1101/2022.03.21.485142

Torres-Méndez, A., Pop, S., Bonnal, S., Almudi, I., Avola, A., Roberts, R.J.V., Paolantoni, C., Alcaina-Caro, A., Martín-Anduaga, A., Haussmann, I.U., Morin, V., Casares, F., Soller, M., Kadener, S., Roignant, J.-Y., Prieto-Godino, L., Irimia, M., 2022. Parallel evolution of a splicing program controlling neuronal excitability in flies and mammals. Science Advances 8, eabk0445. https://doi.org/10.1126/sciadv.abk0445

Vargas, J.N.S., Sleigh, J.N., Schiavo, G., 2022. Coupling axonal mRNA transport and local translation to organelle maintenance and function. Current Opinion in Cell Biology 74, 97–103. https://doi.org/10.1016/j.ceb.2022.01.008

Venken, K.J.T., Schulze, K.L., Haelterman, N.A., Pan, H., He, Y., Evans-Holm, M., Carlson, J.W., Levis, R.W., Spradling, A.C., Hoskins, R.A., Bellen, H.J., 2011. MiMIC: a highly versatile transposon insertion resource for engineering Drosophila melanogaster genes. Nat Methods 8, 737–743.

Winckler, B., Faundez, V., Maday, S., Cai, Q., Almeida, C.G., Zhang, H., 2018. The Endolysosomal System and Proteostasis: From Development to Degeneration. J. Neurosci. 38, 9364–9374. https://doi.org/10.1523/JNEUROSCI.1665-18.2018

Wu, Y.-W., Tan, K.-T., Waldmann, H., Goody, R.S., Alexandrov, K., 2007. Interaction analysis of prenylated Rab GTPase with Rab escort protein and GDP dissociation inhibitor explains the need for both regulators. Proc Natl Acad Sci U S A 104, 12294–12299. https://doi.org/10.1073/pnas.0701817104

Xia, R., Liu, Y., Yang, L., Gal, J., Zhu, H., Jia, J., 2012. Motor neuron apoptosis and neuromuscular junction perturbation are prominent features in a Drosophila model of Fus-mediated ALS. Molecular Neurodegeneration 7, 10. https://doi.org/10.1186/1750-1326-7-10

Yang, C.-P., Samuels, T.J., Huang, Y., Yang, L., Ish-Horowicz, D., Davis, I., Lee, T., 2017. Imp and Syp RNA-binding proteins govern decommissioning of Drosophila neural stem cells. Development 144, 3454–3464. https://doi.org/10.1242/dev.149500

Yang, L., Titlow, J., Ennis, D., Smith, C., Mitchell, J., Young, F.L., Waddell, S., Ish-Horowicz, D., Davis, I., 2017. Single molecule fluorescence in situ hybridisation for quantitating post-transcriptional regulation in Drosophila

brains. Methods 126, 166–176.
https://doi.org/10.1016/j.ymeth.2017.06.025

Zhang, H.L., Eom, T., Oleynikov, Y., Shenoy, S.M., Liebelt, D.A., Dictenberg, J.B., Singer, R.H., Bassell, G.J., 2001. Neurotrophin-Induced Transport of a β-Actin mRNP Complex Increases β-Actin Levels and Stimulates Growth Cone Motility. Neuron 31, 261–275.
https://doi.org/10.1016/S0896-6273(01)00357-9

5

Conclusions and Future Directions

Content

5.1 Conclusions

The published research article (Chassefeyre et al., 2021) and the peer-reviewed protocol (Chaiamarit et al., 2023b) presented in **Chapter 2** of my thesis contain several novel findings. First, I, along with the co-authors, identified a new organelle called 'endoggresome.' Endoggresome (endosomal aggresome) is a new type of mutant PrP aggregate structure, distinguishable from the previously identified aggresome, insoluble protein deposit (IPOD), and juxta nuclear quality control compartment (JUNQ) because of three reasons: (1) Endoggresomes are neurotoxic, not neuroprotective; (2) endoggresomes are membrane-bound, not cytosolic; and (3) endoggresome form within axons, not in the perinuclear region of the cell body (Chassefeyre et al., 2021; Kristiansen et al., 2005; Takalo et al., 2013). Another novel finding is the very first characterization of a pathway that forms neurotoxic endoggresomes in axons. We named this pathway, axonal rapid endosomal sorting and transport-dependent aggregation (ARESTA). ARESTA sounds like the word 'arrested' that implies the nature of endoggresomes 'being stuck in axons' due to the growing in size, in combination with limited lysosomal degradative capacity in axons and impaired retrograde transport to bring

endoggresomes for somatic degradation (Chassefeyre et al., 2021). Modulation of the ARESTA components reduced axonal endoggresome formation and circumvented neuronal dysfunction; thus, ARESTA is an anti-aggregation pathway amenable to therapeutic intervention in the prionopathies (Chassefeyre et al., 2021). Notably, the trafficking itinerary of misfolded mutant PrP via ARESTA in axons shares some similarities to the RESET clearance pathway in non-neuronal cells (Satpute-Krishnan et al., 2014; Zavodszky and Hegde, 2019) and in the soma of neurons (Chassefeyre et al., 2021), where bouts of exo- and endo-cytosis are crucial for endolysosomal targeting. The dual, opposing roles of secretory-endolysosomal trafficking pathways to clear misfolded PrP in the soma, and to form neurotoxic PrP endoggresomes in the axon, shed light on the fundamental question about why the neuronal axon is vulnerable to protein misfolding diseases (PMDs). To investigate whether other misfolded proteins that cause neurodegenerative pathologies also traffic via ARESTA—which possibly include the amyloid precursor protein (APP) and tau implicated in the Alzheimer's disease (AD)—we presented an optimized protocol in cultured primary neuron as a model to use drugs and fluorescent dyes to modulate and monitor trafficking of misfolded proteins through the secretory-endolysosomal pathways in real-time in *bona fide* axons (Chaiamarit et al., 2023b). This step-by-step protocol should facilitate follow-up studies to test whether ARESTA is a generalized mechanism in the proteinopathies.

In **Chapter 3**, I addressed the following question: how do endoggresomes impair axonal function locally where they are formed? The events that occur early in disease, as neurotoxic aggregates first appear inside axons, are rarely scrutinized in real-time with sub-cellular mechanistic details. In this study, I found that, at the axonal swelling sites where endoggresomes formed and resided,

the MT cytoskeleton bent/broke selectively dependent on the post-translational modification (PTM) status, and neuronal cargoes—such as synaptic vesicle precursors and mitochondria—that translocated on these MT tracks towards the synapse were pre-maturely stalled (Chaiamarit et al., 2023a). As a result, mitochondria and Rab7-containing late endosomes (LEs) came into close contacts at the endoggresome hotspots, leading to Rab7-mediated mitochondrial fission and mitochondrial dysfunction at the axonal swelling hubs (Chaiamarit et al., 2023a). **Chapter 3** also contains the first-ever ultrastructure of endoggresome-containing axonal swellings with MT track disruptions and organelle accumulations, resolved by correlative super-resolution fluorescence and enhanced focus ion beam scanning electron microscopy (eFIB-SEM). Similar type of work was performed in the Parkinson's disease (PD) model and similar observations were found of the interaction between mitochondria and endolysosomes, leading to mitochondrial and synaptic dysfunctions (Mahul-Mellier et al., 2020). The axonal swellings observed in early-stage AD model also contained disrupted cytoskeleton, molecular motors, and traffic jams of vesicles (Stokin et al., 2005). These previous observations, along with my new findings, strongly suggest that disruption of organelle-cytoskeletal interactions, especially to mitochondrial dynamics and vesicular transport towards the synapse, are common pathological features among many neurodegenerative diseases. The continuing use of correlative microscopy in combination with high spatial- and temporal-resolution live imaging in cultured primary neurons could potentially unveil subcellular mechanisms in various neurological diseases.

Rab GTPase network is central to the vesicle transport, sorting, and maturation in healthy axons and directly participates in the initiation and

progression of prionopathies as discussed in **Chapter 2–Chapter 3**. Yet, the *de novo* synthesis of Rab GTPases at the distal axonal location has not been studied. In **Chapter 4**, I investigate the axonal transport and putative function of mRNAs that encode the regulators of recycling endosome (RE) trafficking, *rab11* and its chaperone *gdi*, at the distal synapses. The local protein synthesis at the pre- and post-synaptic sites is proposed drive activity-dependent synaptic plasticity and memory mechanisms (Donlin-Asp et al., 2021; Fernandez-Moya et al., 2014; Sasaki, 2020), but what types of mRNAs get transported, to be kept locally in the periphery, and to be translated into functioning proteins in response to neuronal stimuli are not completely understood. To this end, I employed sophisticated *Drosophila* genetic tools to tag endogenous mRNA for high-resolution live imaging *in vivo* and *in cellulo* of single axons, and presented a systematic way to dissect the *cis*-regulatory signals in mRNA and *trans*-acting factors that are necessary and/or sufficient for mRNA to travel along axons to the pre-synapse, in cell-type specific and developmental stage-specific manners. In this Chapter, I found that several axonal transport components—including kinesin-1, dynein, and a conserved RNA-binding protein Imp that binds many types of *rab* mRNAs including *rab11*—were required for synaptogenesis at the *Drosophila* larval neuromuscular junction (NMJ). The high-resolution, sensitive detection of endogenous transcripts by RNA single-molecule fluorescence *in situ* hybridization (smFISH) and the automated analysis pipeline to count mRNA single molecules *in vivo* presented a powerful tool to analyze a reduction in mRNA copy number within a single synaptic compartment. Disruption of kinesin-1 motor function and/or a reduction in Imp protein level specifically in the larval motoneurons resulted in reduced number of localized *rab11* mRNA at the NMJ, suggesting that kinesin-1 and Imp are required for mRNA localization

to the axon periphery and are putative axonal tags for the long-lived *rab11* mRNA population. Apart from *rab11* mRNA, which encodes the major recycling endosome regulator in metazoans, I detected a myriad of *rab* GTPases transcripts by single-molecule hybridization chain reaction (smHCR). I performed neuron- and glia-specific RNAi-screen of *Drosophila* recycling endosome-associated transcripts and found that *rab8* and *rab9* were required in motoneurons while *rab4* and *rab35* were required in glia for unimpaired larval crawling behaviors. The differential requirements for different *rab* GTPases in neurons and glia that meet their cytoplasmic ends at the NMJ synapse are novel findings. Altogether, this thesis Chapter presents an unorthodox view of 'RNA-centric' membrane trafficking regulation in the periphery, via the localized translation of long-lived mRNA population of *rab* GTPases and adds important missing steps in the working model of trafficking regulation during synaptic development and plasticity.

These findings from three experimental chapters of my thesis open up avenues for the future research directions, towards translational research areas to better understand membrane trafficking regulations in disease.

5.2 Future Directions

5.2.1 Investigating the maturation and cell-to-cell spread of mutant PrP endoggresomes

A. The multivesicular bodies (MVBs) and exosome secretion of mutant PrP

In **Chapter 2**, I presented the pathway that formed mutant PrP endoggresomes at the initial stages. I observed the morphology and transport dynamics PrP^{PG14}

vesicles and aggregates from 12 hours to 10 days post-transfection and found that PrP^{PG14} underwent dynamic sorting and maturation post-endocytosis/post-homotypic fusion during ARESTA.

The first evidence of endosomal maturation came from the S3EM, that showed a PrP^{PG14} signal within the membrane-bound structures resembling the MVBs with intra-luminal vesicles (ILVs) (Chassefeyre et al., 2021). At the same cross section, budding vesicles with similar diameter size as the ILVs were observed, suggesting that these extracellular vesicles could represent exosomes that might contain misfolded mutant PrP. PrP^{C} was previously shown to be secreted in exosomes, and this could be a route for cell-to-cell transfer of PrP^{Sc} (Fevrier et al., 2004; Hartmann et al., 2017). PrP^{mut}/PrP^{Sc}-containing exosomes could cross the blood brain barriers and could be taken up by glial cells, initiating the neuroinflammatory cascades and neurodegeneration at the tissue level (Pascual et al., 2019). Other misfolded proteins including α-synuclein and Aβ were also found in exosomes (Gupta and Pulliam, 2014). Thus, understanding the factors that steer the trafficking itinerary of misfolded mutant PrP towards the MVB-exosomal pathway instead of endolysosomal targeting for clearance is a crucial next step to understand tissue-level disease progression.

The two outstanding questions that merit further investigations are:

(1) Does modulation of ARESTA components (such as reducing kinesin-1 and ARL8b function) decrease MVB formation and exosome secretion?

(2) Does misfolded mutant PrP, especially PrP^{PG14}, that forms in endoggresomes in one cell induce misfolding and aggregation of PrP^{WT} in neighboring cells?

Question **(1)** can be addressed with existing tools, presented in **Chapter 2**. However, a better marker of MVB is needed to distinguish EEs and LEs that are

endolysosomes, from LEs that are MVBs by fluorescence microscopy, since Rab7, Rab11, and Rab35 that are present on the MVBs are also present in many other endosomal identities. A new technology for exosome fluorescence labeling via click chemistry could be helpful to observe co-migration of fluorescently-labeled PrP^{PG14} in ILVs and as exosomes by live imaging (Song et al., 2020). To address question **(2)**, a tool such as conjugating photoactivatable (PA) or photoconvertible (PC) fluorescent proteins to mutant PrP would be helpful to follow the activated fluorescence signal that originates in one neuron and transfers to the neighboring neurons or glia. Alternatively, co-culturing neurons and glia (of the same or different genotypes) in microfluidic chambers where only neuronal axons are allowed to cross the middle microgrooves (Liu et al., 2008) could be a great strategy to test if cell-to-cell spread of PA/PC-PrP^{PG14} occur primarily from distal axonal sites.

B. The membraneless aggregates and the liquid-liquid phase separation (LLPS) and phase transition of mutant PrP

In addition to the membrane-bound endoggresomes of mutant PrP, I also observed 'membraneless' PrP aggregates by several methods. Membrane-extraction SEM, with taxol and phalloidin addition to stabilize MT and actin while removing all membrane-bound structures, showed detergent-resistant droplet-like structures surrounded by actin (Chaiamarit et al., 2023a). This led us to hypothesize that misfolded mutant PrP becomes the droplet-like structures via the liquid-liquid phase separation (LLPS). LLPS was shown to occur to the intrinsically disordered proteins (IDPs) or proteins that contain the intrinsically disordered region (IDRs) or the 'prion-like' domains (Sprunger and Jackrel,

2021). The mouse PrP contains the IDR in its N-terminus, which includes the octapeptide repeats (OR) whose expansions are commonly associated with familial PrDs, such as PrP^{PG14} (Chiesa et al., 2000; Polido et al., 2021). In addition, PrP^{C} can naturally undergo α- and β-cleavages in the cell, both of which produce N-terminal fragments containing the IDR (Liang and Kong, 2012). The N-terminal sequence of PrP^{C}, especially the OR and the sequences immediately following the OR, was shown to be necessary and sufficient for LLPS *in vitro* (Kamps et al., 2021), but whether the full-length and N-terminal fragments of PrP^{C}/PrP^{WT} and PrP^{PG14} undergo LLPS *in cellulo* and undergo phase-transition into solid/gel-like droplets in axons remain uninvestigated.

Based on these observations, the two outstanding questions are:

(1) Do mutant PrP aggregates formed by LLPS become neurotoxic?

(2) What are the components in the membraneless mutant PrP aggregates that either maintain its aggregation status, or that could be targeted for degradation?

The first step is to clone the truncated N-terminal PrP^{WT} and PrP^{PG14} constructs, known to undergo LLPS *in vitro*, and characterize their axonal aggregation with similar methods presented in Chapters 2-3. Then, the aims are to test by live imaging if these truncated PrP^{WT} and PrP^{PG14} constructs form membraneless droplets similarly to the full-length PrP constructs, or form droplets to a much greater extent in axons. Neuronal function and viability can be tested for the constructs which have the greater propensity to undergo LLPS in neuronal cells.

It remains difficult to do experiments on question **(1)** above with endogenous or full-length PrP, without knowing how to shift the formation of membrane-bound endoggresomes to get more membraneless aggregates and to

test the impacts of increased membraneless aggregates on neuronal viability. The first step towards understanding how this process works is to identify the complete maturation process of mutant PrP aggregates inside axons, by following the aggregation process in real-time at high-resolution. The cultured primary neurons expressing PrP^{PG14} presented here has the potential to provide further insights into aggregate maturation beyond the membrane-bound stages of PrP trafficking.

Question **(2)** is an important question for the development of therapeutic intervention for the prionopathies. Phase-separated granules of protein-RNA assemblage can become a convenient target of autophagy, a process that has different functions at various life stages, from the disassembly of P granules during the embryonic development to release back the cytoplasmic contents, to the quality control mechanism to degrade misfolded protein such as FUS, which is implicated in the familial ALS (Wang and Zhang, 2019). What factors determine the initiation of autophagy for phase-separated granules of misfolded protein including the mutant PrP remain unknown. The RNAs were shown to be involved in the fate switch of P granules from autophagic degradation to aggregation in *Caenorhabditis elegans* (Zheng et al., 2023). Once misfolded PrP become cytosolic, it is predicted to become a magnet for many other proteins and RNAs due to the nature of its IDR. It is a priority to systematically determine the molecular composition of axonal misfolded mutant PrP aggregates by mass spectrometry-based approaches, to identify the presence/absence of QC proteins or other proteins that might give us a hint towards understanding heterogeneous identities of PrP aggregates in axons and finding potential therapeutic targets.

5.2.2 Targeting the subcellular pathways for the reversal of misfolded mutant PrP-induced pathologies

A. Knock-down of specific ARESTA components

Kinesin-1 (KIF5) is a major component of the ARESTA pathway that gets recruited onto PrP^{mut} vesicles by ARL8b via SKIP and KLC1 adaptor subunit of KIF5 (Chassefeyre et al., 2021). In primary cultured neurons from *Kif5c* $^{-/-}$ mice, endoggresome formation is reduced due to decreased flux of PrP^{mut} vesicles that enter axons, and more importantly, neuronal viability is rescued in *Kif5c* $^{-/-}$ neurons, compared to WT control neurons, that expressed PrP^{mut} (Chassefeyre et al., 2021). Thus, kinesin-1 is required for the initial stage of toxic mutant PrP endoggresome formation.

After the endoggresomes are formed along the length of the axon at the swelling sites, kinesin-1 accumulates significantly at these swelling sites and depletes from cargoes such as mitochondria and vesicles, that encounter and mobilize through the aggregate sites (Chaiamarit et al., 2023a). It is likely that during the progression of prionopathies, the disruption of kinesin-1 pathway becomes the secondary consequence of misfolded aggregates rather than the primary cause of neurodegeneration (Goldstein, 2012). Thus, a reduction of kinesin-1 in neurons is not likely a practical therapeutic intervention because mitochondria and other kinesin-1 cargoes will be disrupted in addition to the reduction of endoggresome formation.

A better strategy, conceptually, would be to divert kinesin-1 on mutant PrP endoggresomes to other important neuronal cargoes. Mitochondria, for examples, utilize Miro and Milton as kinesin-1 adaptors, and it is tempting to test if overexpression of Miro and/or Milton alone could rescue mitochondrial

transport defects in PrP^{mut} axons and help those mitochondria that are stuck to move away from the aggregate sites. Alternatively, knocking down SKIP, a specific adaptor of KIF5/KLC1 to PrP^{mut} vesicles, could be a strategy to reduce endoggresome formation and revert the pathologies (Chassefeyre et al., 2021). As shown previously, reduction of ARL8b and HOPS function at the protein level decreased endoggresome formation in axons, and this was sufficient to rescued neuronal viability in culture (Chassefeyre et al., 2021). Whether reduced SKIP, ARL8b or HOPS could also reverse mitochondrial and cytoskeletal pathological defects in addition to endoggresome formation merits further investigations.

Ultimately, the modulation of ARESTA in endoggresome formation and the functional consequences in reversing prionopathies should be tested *in vivo* in the mouse model, with the readily optimized AAV technology for PrP^{PG14} delivery (Chassefeyre et al., 2021). It is practical to test whether induced-PrP^{PG14} expression in the hippocampus, the cerebellum, or other PrD-affected regions of the brain of ARL8b knockout/mutant mice produce similar pathologies and behavioral defects, compared to the WT mice, or rescue them. Successful completion of this *in vivo* characterization would give much weight to the proposed ARESTA biogenesis pathway of misfolded mutant PrP.

B. Restoring the balance of mitochondrial fission-fusion

Mis-regulation of mitochondrial fission/fusion dynamics is implicated in synaptic plasticity defects as well as in neurodegeneration (Bertholet et al., 2016). Mitochondrial fission is elevated at the axonal swelling sites containing PrP^{PG14} endoggresomes (Chaiamarit et al., 2023a). The aberrant mitochondrial fission is partly due to increased Rab7 LE contacts with retained mitochondria in the

axonal swellings, and the overexpression of dominant-negative Rab7^{Q67L} reduces mitochondrial fission frequency in axons to a certain extent (Chaiamarit et al., 2023a). Other parallel pathways exist to regulate the balance of mitochondrial fission and fusion dynamics, such as via actin nucleation (Manor et al., 2015) and ER-mitochondrial contacts (Abrisch et al., 2020). ER tubules were observed in contacts with mitochondria in PrP^{PG14} axonal swellings, but whether the axonal ER alone is capable of triggering mitochondrial fission in the normal and pathological conditions is unclear. One could test if a knockdown/mutant of ER-associated fission protein inverted formin 2 (INF2) rescues mitochondrial fission phenotypes in PrP^{PG14} axonal swellings similar to overexpression of Rab7^{Q67L}. Mitofusin 1 (Mfn1), on the other hand, is present at the mitochondrial outer membrane and localizes to ER-mitochondrial interface, to mark the site of mitochondrial fusion (Abrisch et al., 2020). Would overexpression of Mfn1 be sufficient to decrease mitochondrial fission, increase mitochondrial fusion, and restore mitochondrial function in PrP^{PG14} axons? These are some ideas that could be tested in primary neuronal culture easily. In conclusion, there are multiple mitochondrial dynamics regulators that could be surveyed for potential rescue to pathogenic fission and dysfunction of mitochondria to rescue axonal health in the prionopathies.

C. Upregulation of Autophagy

Upregulation of autophagy is a normal QC process when the cell is under stress, infection, or overwhelmed proteostasis (He and Klionsky, 2009). Defective autophagy could be partly at play during the accumulation of PrP^{PG14} endoggresomes. Recently, a collaborative study with the Encalada lab at Scripps Research tested a mammalian target of rapamycin (mTOR) inhibitor-

independent autophagy activator compound called 'CCT020312' and found that this compound dose-dependently reduced endoggresome densities and rescued axonal transport defects, after endoggresomes prominently accumulated in axons (Yoon et al., 2022). In addition, this autophagy activator 'CCT020312' cleared cytosolic aggregated tau proteins and restored lysosomal function in familial AD patient-derived neurons (Yoon et al., 2022). The follow-up studies are needed to test if clearance of misfolded PrP and tau aggregates in axons by autophagy upregulation could rescue other pathological events, such as disrupted MT tracks and mitochondrial defects, that occur post-aggregate formation.

5.2.3 Investigating the localized translation of *Rab* GTPases in *Drosophila* models of neurodegenerative diseases

The transcripts of many *rab* GTPases are present at the axon termini and glial extensions at the *Drosophila* larval NMJ synapse, as presented at the end of **Chapter 4**. I synthesized data from several findings on mRNA and protein localization of *Drosophila* Rab GTPases in different neuronal compartments and glia and intersected the list with known Imp targets as a Venn diagram (**Figure 5.1**) (Chan et al., 2011; Dunst et al., 2015; Gala et al., 2022; Kiral et al., 2018; Zhang et al., 2007). The transcripts that I confirm to localize at the fly larval NMJ in this thesis are highlighted in bold, and the *rab* genes associated with various neurological diseases are given different symbols (**Figure 5.1**). This diagram informs us that Rab5, Rab7, and Rab11 are culprits in many neurodegenerative diseases—including in ALS, AD, HD, and PrDs—and RNA mis-localization might play a role in the disease pathogenesis. In particular, Rab5 and Rab11 have proteins and their transcripts enriched at the distal

axons/synapses, and the mechanisms of transport and localization *rab5* mRNA to motoneuron axon termini could be investigated similar to the experiments on *rab11* mRNA in **Chapter 4**. Whether localized translation of *rab5* and *rab11* plays a role in synaptic development, plasticity, and in the initiation/progression of neurodegenerative pathologies remain to be tested.

Rab35 is an interesting gene to follow up. I found that knocking down *rab35* with a validated RNAi in the larval-stage motoneurons is lethal (data not shown), but *rab35* RNAi with a pan-glial driver, *repo-Gal4*, showed strong crawling defects (**Figure 4.13D-F**). Rab35 controls endosome recycling and exosome secretion in dividing and post-mitotic cells (Kouranti et al., 2006), and Rab35 works together with Rab11 to control cell differentiation, axonal and dendritic growth, and synaptic plasticity (Rozés-Salvador et al., 2020). My glial-specific knockdown data suggest that Rab35 might have a function in glia to maintain proper neuromuscular development and behavior.

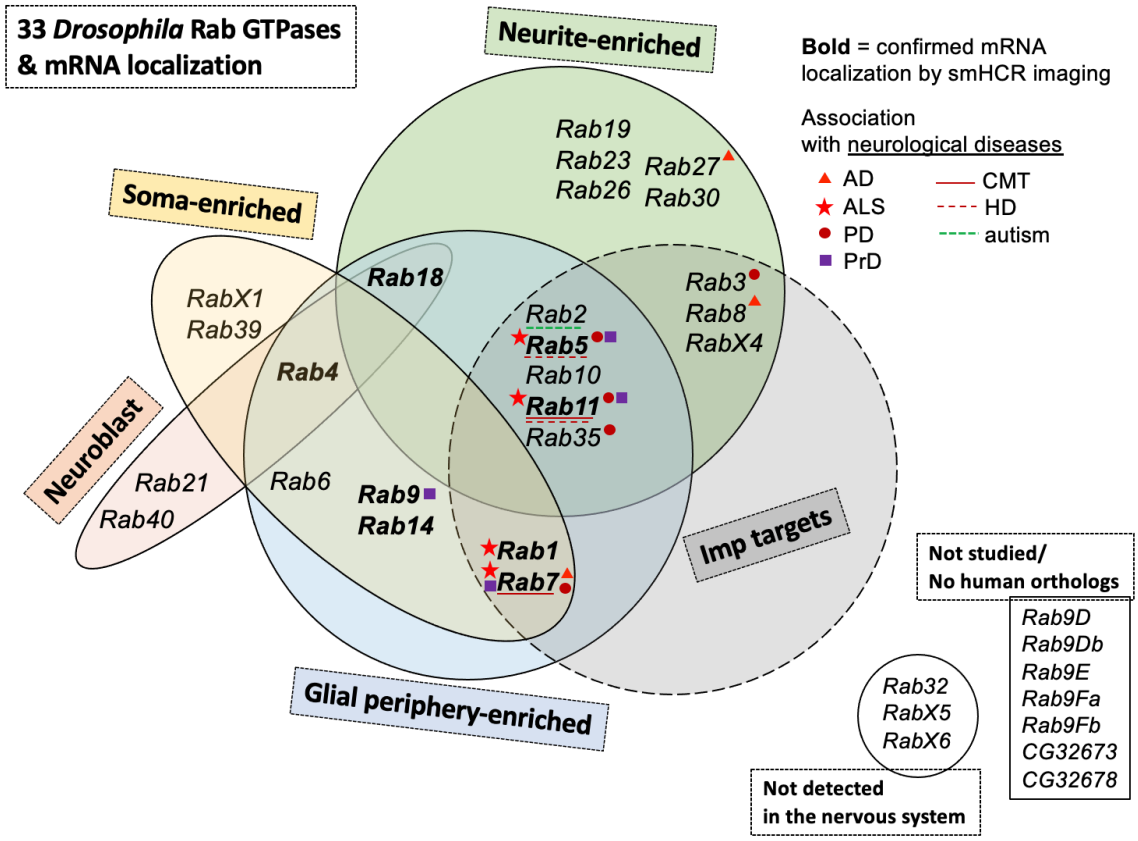


Figure 5.1 Diagram of *rab* mRNA localization in neurons/neuronal precursors and glia of *Drosophila*. Genes in bold were confirmed to localize at the cell periphery by smHCR in this thesis. Genes with previously known association to neurological diseases are highlighted with different symbols, such as Alzheimer's disease (AD), amyotrophic lateral sclerosis (ALS), Parkinson's disease (PD), prion disease (PrD), Charcot-Marie-Tooth (CMT) disease, Huntington's disease (HD), and autism (via SFARI gene database: https://www.sfari.org/).

The RNA localization data are preliminary findings that allow for follow-up studies with FISH-based methods to detect their stability and translation efficiency (Richer et al., 2021; Samuels et al., 2020). I propose the following two research questions. **(1)** Do localized transcripts in neuronal and glial extensions at the NMJ synapse undergo active translation? A fluorescence assay to detect ribosome interactions with mRNA (FLARIM) works by designing overlapping oligonucleotide probes of ribosomal RNA (rRNA) and mRNA target, with HCR

technology to amplify the fluorescence signal specifically when the ribosome and mRNA target are in close proximity (Burke et al., 2017). The Davis lab is currently optimizing and testing FLARIM method on several localized transcripts for their translational activity. Using FLARIM as a tool will give a quantitative measure of the number of actively translating mRNAs, which could be tested in combination with RNAi knockdown of putative post-transcriptional regulators that control translation.

(2) Is mRNA localization affected in the *Drosophila* model of protein misfolded diseases? A few, successful *Drosophila* models of ALS-associated mutations of TAR DNA-binding protein 43 (TDP-43), fused in sarcoma (FUS) and C9orf72 exist, which exhibit axonal protein aggregation, axonal transport defects, and behavioral phenotypes (Baldwin et al., 2016). Again, the FISH-based method is ideal to test whether many *rab* mRNAs become mis-localized in these disease models. I present, in this thesis, an optimized FISH-based method for the absolute quantitation of mRNA number, as well as genetic tools to disrupt *cis*- and *trans*-acting factors controlling axonal RNA localization. The future use of these tools on fly disease models, and complementary mammalian systems, will support the notion of 'RNA-centric' roles of Rab GTPases in neurological diseases.

5.3 References

Abrisch, R.G., Gumbin, S.C., Wisniewski, B.T., Lackner, L.L., Voeltz, G.K., 2020. Fission and fusion machineries converge at ER contact sites to regulate mitochondrial morphology. Journal of Cell Biology 219, e201911122. https://doi.org/10.1083/jcb.201911122

Baldwin, K.R., Godena, V.K., Hewitt, V.L., Whitworth, A.J., 2016. Axonal transport defects are a common phenotype in Drosophila models of ALS. Hum Mol Genet 25, 2378–2392. https://doi.org/10.1093/hmg/ddw105

Bertholet, A.M., Delerue, T., Millet, A.M., Moulis, M.F., David, C., Daloyau, M., Arnauné-Pelloquin, L., Davezac, N., Mils, V., Miquel, M.C., Rojo, M., Belenguer, P., 2016. Mitochondrial fusion/fission dynamics in neurodegeneration and neuronal plasticity. Neurobiol Dis 90, 3–19. https://doi.org/10.1016/j.nbd.2015.10.011

Burke, K.S., Antilla, K.A., Tirrell, D.A., 2017. A Fluorescence in Situ Hybridization Method To Quantify mRNA Translation by Visualizing Ribosome–mRNA Interactions in Single Cells. ACS Cent Sci 3, 425–433. https://doi.org/10.1021/acscentsci.7b00048

Chaiamarit, T., Verhelle, A., Chassefeyre, R., Shukla, N., Novak, S.W., Andrade, L.R., Manor, U., Encalada, S.E., 2023a. Mutant Prion Protein Endoggresomes are Hubs for Local Axonal Organelle-Cytoskeletal Remodeling. https://doi.org/10.1101/2023.03.19.533383

Chaiamarit, T., Wu, Y., Verhelle, A., Encalada, S., 2023b. Fluorescence Assays for Real-Time Tracking of Cell Surface Protein Internalization and Endosomal Sorting in Axons of Primary Mouse Hippocampal Neurons. BIO-PROTOCOL 13. https://doi.org/10.21769/BioProtoc.4651

Chan, C.-C., Scoggin, S., Wang, D., Cherry, S., Dembo, T., Greenberg, B., Jin, E.J., Kuey, C., Lopez, A., Mehta, S.Q., Perkins, T.J., Brankatschk, M., Rothenfluh, A., Buszczak, M., Hiesinger, P.R., 2011. Systematic discovery of Rab GTPases with synaptic functions in Drosophila. Curr Biol 21, 1704–1715. https://doi.org/10.1016/j.cub.2011.08.058

Chassefeyre, R., Chaiamarit, T., Verhelle, A., Novak, S.W., Andrade, L.R., Leitao, A.D.G., Manor, U., Encalada, S.E., 2021. Endosomal sorting drives the formation of axonal prion protein endoggresomes. Sci Adv 7, eabg3693.

Chiesa, R., Drisaldi, B., Quaglio, E., Migheli, A., Piccardo, P., Ghetti, B., Harris, D.A., 2000. Accumulation of protease-resistant prion protein (PrP) and apoptosis of cerebellar granule cells in transgenic mice expressing a PrP insertional mutation. Proc Natl Acad Sci U S A 97, 5574–9.

Donlin-Asp, P.G., Polisseni, C., Klimek, R., Heckel, A., Schuman, E.M., 2021. Differential regulation of local mRNA dynamics and translation following

long-term potentiation and depression. Proc Natl Acad Sci U S A 118, e2017578118. https://doi.org/10.1073/pnas.2017578118

Dunst, S., Kazimiers, T., von Zadow, F., Jambor, H., Sagner, A., Brankatschk, B., Mahmoud, A., Spannl, S., Tomancak, P., Eaton, S., Brankatschk, M., 2015. Endogenously Tagged Rab Proteins: A Resource to Study Membrane Trafficking in Drosophila. Developmental Cell 33, 351–365. https://doi.org/10.1016/j.devcel.2015.03.022

Fernandez-Moya, S.M., Bauer, K.E., Kiebler, M.A., 2014. Meet the players: local translation at the synapse. Front Mol Neurosci 7, 84. https://doi.org/10.3389/fnmol.2014.00084

Fevrier, B., Vilette, D., Archer, F., Loew, D., Faigle, W., Vidal, M., Laude, H., Raposo, G., 2004. Cells release prions in association with exosomes. Proceedings of the National Academy of Sciences 101, 9683–9688. https://doi.org/10.1073/pnas.0308413101

Gala, D.S., Lee, J.Y., Kiourlappou, M., Titlow, J.S., Teodoro, R.O., Davis, I., 2022. Mammalian glial protrusion transcriptomes predict localization of Drosophila glial transcripts required for synaptic plasticity. https://doi.org/10.1101/2022.11.30.518536

Goldstein, L.S., 2012. Axonal transport and neurodegenerative disease: can we see the elephant? Prog Neurobiol 99, 186–90.

Gupta, A., Pulliam, L., 2014. Exosomes as mediators of neuroinflammation. Journal of Neuroinflammation 11, 68. https://doi.org/10.1186/1742-2094-11-68

Hartmann, A., Muth, C., Dabrowski, O., Krasemann, S., Glatzel, M., 2017. Exosomes and the Prion Protein: More than One Truth. Front Neurosci 11, 194. https://doi.org/10.3389/fnins.2017.00194

He, C., Klionsky, D.J., 2009. Regulation Mechanisms and Signaling Pathways of Autophagy. Annu Rev Genet 43, 67–93. https://doi.org/10.1146/annurev-genet-102808-114910

Kamps, J., Lin, Y.-H., Oliva, R., Bader, V., Winter, R., Winklhofer, K.F., Tatzelt, J., 2021. The N-terminal domain of the prion protein is required and sufficient for liquid–liquid phase separation: A crucial role of the Aβ-binding domain. Journal of Biological Chemistry 297, 100860. https://doi.org/10.1016/j.jbc.2021.100860

Kiral, F.R., Kohrs, F.E., Jin, E.J., Hiesinger, P.R., 2018. Rab GTPases and Membrane Trafficking in Neurodegeneration. Curr Biol 28, R471–R486. https://doi.org/10.1016/j.cub.2018.02.010

Kouranti, I., Sachse, M., Arouche, N., Goud, B., Echard, A., 2006. Rab35 regulates an endocytic recycling pathway essential for the terminal steps of cytokinesis. Curr Biol 16, 1719–1725. https://doi.org/10.1016/j.cub.2006.07.020

Kristiansen, M., Messenger, M.J., Klohn, P.C., Brandner, S., Wadsworth, J.D., Collinge, J., Tabrizi, S.J., 2005. Disease-related prion protein forms aggresomes in neuronal cells leading to caspase activation and apoptosis. J Biol Chem 280, 38851–61.

Liang, J., Kong, Q., 2012. α-Cleavage of cellular prion protein. Prion 6, 453–460. https://doi.org/10.4161/pri.22511

Liu, W.W., Goodhouse, J., Jeon, N.L., Enquist, L.W., 2008. A Microfluidic Chamber for Analysis of Neuron-to-Cell Spread and Axonal Transport of an Alpha-Herpesvirus. PLOS ONE 3, e2382. https://doi.org/10.1371/journal.pone.0002382

Mahul-Mellier, A.-L., Burtscher, J., Maharjan, N., Weerens, L., Croisier, M., Kuttler, F., Leleu, M., Knott, G.W., Lashuel, H.A., 2020. The process of Lewy body formation, rather than simply α-synuclein fibrillization, is one of the major drivers of neurodegeneration. Proceedings of the National Academy of Sciences 117, 4971–4982. https://doi.org/10.1073/pnas.1913904117

Manor, U., Bartholomew, S., Golani, G., Christenson, E., Kozlov, M., Higgs, H., Spudich, J., Lippincott-Schwartz, J., 2015. A mitochondria-anchored isoform of the actin-nucleating spire protein regulates mitochondrial division. eLife 4, e08828. https://doi.org/10.7554/eLife.08828

Pascual, M., Ibáñez, F., Guerri, C., 2019. Exosomes as mediators of neuron-glia communication in neuroinflammation. Neural Regen Res 15, 796–801. https://doi.org/10.4103/1673-5374.268893

Polido, S.A., Kamps, J., Tatzelt, J., 2021. Biological Functions of the Intrinsically Disordered N-Terminal Domain of the Prion Protein: A Possible Role of Liquid–Liquid Phase Separation. Biomolecules 11, 1201. https://doi.org/10.3390/biom11081201

Richer, P., Speese, S.D., Logan, M.A., 2021. FLARIM v2.0, an improved method to quantify transcript-ribosome interactions in vivo in the adult Drosophila brain. https://doi.org/10.1101/2021.08.13.456301

Rozés-Salvador, V., González-Billault, C., Conde, C., 2020. The Recycling Endosome in Nerve Cell Development: One Rab to Rule Them All? Frontiers in Cell and Developmental Biology 8, 603794.

Samuels, T.J., Järvelin, A.I., Ish-Horowicz, D., Davis, I., 2020. Imp/IGF2BP levels modulate individual neural stem cell growth and division through myc mRNA stability. eLife 9, e51529. https://doi.org/10.7554/eLife.51529

Sasaki, Y., 2020. Local Translation in Growth Cones and Presynapses, Two Axonal Compartments for Local Neuronal Functions. Biomolecules 10, 668. https://doi.org/10.3390/biom10050668

Satpute-Krishnan, P., Ajinkya, M., Bhat, S., Itakura, E., Hegde, R.S., Lippincott-Schwartz, J., 2014. ER stress-induced clearance of misfolded GPI-anchored proteins via the secretory pathway. Cell 158, 522–33.

Song, S., Shim, M.K., Lim, S., Moon, Y., Yang, S., Kim, J., Hong, Y., Yoon, H.Y., Kim, I.-S., Hwang, K.Y., Kim, K., 2020. In Situ One-Step Fluorescence Labeling Strategy of Exosomes via Bioorthogonal Click Chemistry for Real-Time Exosome Tracking In Vitro and In Vivo. Bioconjugate Chem. 31, 1562–1574. https://doi.org/10.1021/acs.bioconjchem.0c00216

Sprunger, M.L., Jackrel, M.E., 2021. Prion-Like Proteins in Phase Separation and Their Link to Disease. Biomolecules 11, 1014. https://doi.org/10.3390/biom11071014

Stokin, G.B., Lillo, C., Falzone, T.L., Brusch, R.G., Rockenstein, E., Mount, S.L., Raman, R., Davies, P., Masliah, E., Williams, D.S., Goldstein, L.S., 2005. Axonopathy and transport deficits early in the pathogenesis of Alzheimer's disease. Science 307, 1282–8.

Takalo, M., Salminen, A., Soininen, H., Hiltunen, M., Haapasalo, A., 2013. Protein aggregation and degradation mechanisms in neurodegenerative diseases. Am J Neurodegener Dis 2, 1–14.

Wang, Z., Zhang, H., 2019. Phase Separation, Transition, and Autophagic Degradation of Proteins in Development and Pathogenesis. Trends in Cell Biology 29, 417–427. https://doi.org/10.1016/j.tcb.2019.01.008

Yoon, L., Botham, R.C., Verhelle, A., Sanz-Martinez, P., Xu, J., Cole, C.M., Tan, E.P., Chou, C.C., Cuoco, C.A., Massey, L.A., Labra, S., Elia, L.P., Ta, A., Ardejani, M.S., Lee, K., Kline, G.M., Xiao, Q., Cano-Franco, S., Lyang, N.J., Hou, W.C., Yu, A., Fox, S., Ko, Y., Wulkop-Gil, C., Ibrahim, L.H., Jiang, S., Meneses, A., Nelson, L.T., Peng, H., Lipton, S.A., Bollong, M.J., Hansen, M., Morimoto, R.I., Petrassi, H.M., Wiseman, R.L., Powers, E.T., Finkbeiner, S., Garza, D., Finley, D., Prado, M.A., Dikic, I., Frydman, J., Johnson, K.A., Silva, M.C., Haggarty, S.J., Stolz, A., Encalada, S.E., Kelly, J.W., 2022. mTOR inhibitor-independent Autophagy Activator Ameliorates Tauopathy and Prionopathy Neurodegeneration Phenotypes. https://doi.org/10.1101/2022.09.29.509997

Zavodszky, E., Hegde, R.S., 2019. Misfolded GPI-anchored proteins are escorted through the secretory pathway by ER-derived factors. eLife 8, e46740.

Zhang, J., Schulze, K.L., Hiesinger, P.R., Suyama, K., Wang, S., Fish, M., Acar, M., Hoskins, R.A., Bellen, H.J., Scott, M.P., 2007. Thirty-one flavors of Drosophila rab proteins. Genetics 176, 1307–1322. https://doi.org/10.1534/genetics.106.066761

Zheng, H., Peng, K., Gou, X., Ju, C., Zhang, H., 2023. RNA recruitment switches the fate of protein condensates from autophagic degradation to accumulation. Journal of Cell Biology 222, e202210104. https://doi.org/10.1083/jcb.202210104

Appendix

A. Curriculum Vitae (CV)

Curriculum Vitae

TAI CHAIAMARIT

Department of Biochemistry
University of Oxford
Oxford, UK OX1 3QU

Work: +44 (0)1865 613271
Mobile: +44 (0)7310 576395
Email: tai.chaiamarit@lincoln.ox.ac.uk

CAREER GOAL

Dedicated and motivated final-year PhD/DPhil candidate in Biology/Biochemistry with background in neurobiology and research experience in studying the mechanisms of axonal transport impairments and neurodegeneration. Seeking a faculty position to leverage expertise in neurobiology, cell biology, microscopy, and experience with various animal/cellular models to further investigate the roles of membrane trafficking regulation in neuronal development, synaptic plasticity, and how such processes fail in neurodevelopmental and neurodegenerative diseases.

EDUCATION

The Scripps Research Institute — La Jolla, CA
Department of Biochemistry, University of Oxford — Oxford, UK
Joint PhD/DPhil in Biology and Biochemistry — **Expected June 2023**

University of Wisconsin-Madison, College of Letters and Science — Madison, WI
B.S. Biology (with Neurobiology) — **May 2017** — **GPA: 3.898**

PUBLICATIONS

Chaiamarit T, Wu Y, Verhelle A, Encalada SE. 2023. **Fluorescence Assays for Real-Time Tracking of Cell Surface Protein Internalization and Endosomal Sorting in Axons of Primary Mouse Hippocampal Neurons**. *Bio-protocol*, *13*(7), e4651. https://doi.org/10.21769/BioProtoc.4651

Chaiamarit T, Verhelle A, Chassefeyre R, Shukla N, Novak SW, Andrade LR, Manor U, Encalada SE. 2023. **Mutant Prion Protein Endoggresomes are Hubs for Local Axonal Organelle-Cytoskeletal Remodeling**. *bioRxiv*, 2023.03.19.533383. https://doi.org/10.1101/2023.03.19.533383

Chassefeyre R*, **Chaiamarit T***, Verhelle A*, Novak SW, Andrade LR, Leitao ADG, Manor U, Encalada SE. 2021. **Endosomal Sorting Drives the Formation of Mutant Prion Protein Endoggresomes**. *Science Advances* 7(52); DOI: 10.1126/sciadv.abg3693. ***Co-authors**

Nieto-Torres JL, Shanahan SL, Chassefeyre R, **Chaiamarit T**, Zaretski S, Landeras-Bueno S, Verhelle A, Encalada SE, Hansen M. 2021. **LC3 Phosphorylation Regulates FYCO1 Binding and Directional Transport of Autophagosomes**. *Current Biology* S0960-9822(21)00750-8. https://doi.org/10.1016/j.cub.2021.05.052.

Pisithkul T, Schroeder JW, Trujillo EA, Yeesin P, Stevenson DM, **Chaiamarit T**, Coon JJ, Wang JD, Amador-Noguez D. 2019. **Metabolic Remodeling During Biofilm Development of *Bacillus Subtilis***. *mBio* 10:e00623-19. https://doi.org/10.1128/mBio.00623-19.

AWARDS AND SCHOLARSHIPS

- Thai Government Scholarship from the Development and Promotion of Science and Technology Talents Project (DPST) to study biology-related fields up to a Doctoral degree (May 2012 - present)
- Skaggs-Oxford Scholarship to pursue a joint PhD/DPhil in Biology/Biochemistry in the USA and the UK (August 2017 - present)
- Dorris Neuroscience Travel Awards to give an oral presentation at the 2019 ASCB|EMBO Meeting in Washington, DC, USA (May 2019)
- Best Poster Presentation Prize, 3rd Place, at the 3rd La Jolla Aging Meeting, The Salk Institute for Biological Studies, La Jolla, CA, USA (March 2019)
- Comprehensive Honors (Honors in Liberal Arts and Honors in Major), the highest honor offered by College of Letters and Science, University of Wisconsin-Madison (May 2017)
- Phi Beta Kappa, Alpha Chapter of Wisconsin (May 2017)
- Honors Senior Thesis Summer Research Grant on "Metabolic Remodeling during biofilm development of *Bacillus subtilis*" (May 2016)

RESEARCH EXPERIENCES AND SKILLS

Ilan Davis' Lab: Graduate Student (October 2019 – present)

- **Research Project.** (1) Investigating axonal localization mechanism of membrane trafficking-related transcripts and their roles in *Drosophila* neuromuscular function
  (2) Developing a correlative light and electron microscopy (CLEM) pipeline to detect and map single mRNAs and mRNA transport machinery in *Drosophila* cells and tissues
- **Approaches and Skills.** Single-molecule fluorescence *in situ* hybridization (smFISH), smFISH probe design and synthesis, *Drosophila* genetics and husbandry, *Drosophila* larval dissection, K^+ stimulation to induce neuromuscular junction synaptic plasticity, *Drosophila* primary neuronal culture, *Drosophila* macrophage culture, immunofluorescence, spinning disc confocal microscopy, image analysis in ImageJ, Python, statistical analysis in R.

Sandra Encalada's Lab: Graduate student (August 2017 – October 2019)

- **Research Project.** (1) The biogenesis pathway of mutant prion aggregates in mouse primary neurons and the consequences of the prion aggregate formation on axonal transport of pre-synaptic vesicles and mitochondria, as well as molecular motors and microtubule dysfunctions.
  (2) Leading a collaborative project with Janelia Research Campus to reconstruct the 3D architecture of dystrophic axonal swellings containing mutant prion aggregates by correlative fluorescence and FIB-SEM, using machine learning-driven analysis of organelle-cytoskeletal remodeling.
- **Approaches and Skills.** Primary mouse hippocampal culture, plasmid preparation, molecular cloning, transfection and lentiviral transduction, microfluidic culture, immunofluorescence, Western blot, TIRF microscopy, Airyscan confocal microscopy, SEM, image analysis in MATLAB.

Gabriel Lander's Lab: Rotation graduate student (November 2017 – February 2018)

- **Research Project.** Molecular analysis of hexameric structure and assembly defects of disease-causing mutations in a human mitochondrial AAA+ protease AFG3L2.

- **Approaches and Skills.** Negative stain EM, Homology modeling, single-particle cryo-EM preparation and analysis pipeline, protein purification.

Daniel Amador-Noguez's Lab: Undergraduate research assistant (August 2015 – May 2017)

- **Research Project.** Remodeling of metabolic pathways during biofilm development of a Gram-positive bacterium *Bacillus subtilis*. (Senior Honor thesis)
- **Approaches and Skills**. HPLC/MS-based metabolomics

Peter Lipton's Lab: Undergraduate research assistant (January 2016 – May 2017)

- Developed a behavioral paradigm to study spatial pattern completion, a theory of hippocampal memory formation, in rat.

CONFERENCES AND PRACTICAL WORKSHOPS

- **Oral Presentation** (selected) titled **"Mutant Prion Aggregates Remodel Organelle-Cytoskeletal Interactions in Axons"** and **Poster Presentation** at the BSDB|BSCB Joint Spring Meeting, University of Warwick, UK (3rd – 6th April 2022)
- **Oral Presentation** (selected) titled **"Neuronal Traffic Jams: Mammalian Prion Aggregates-mediated Axonal Impairments"** and **Poster Presentation** at the ASCB|EMBO Meeting, Washington DC (7th – 11th December 2019)
- **Oral Presentation** at the Scripps Research Graduate Student Symposium, The Alexandria at Torrey Pines, La Jolla, CA, USA (22nd – 23rd November 2019)
- **Poster Presentation** at the 3rd La Jolla Aging Meeting, La Jolla, CA, USA (29th March 2019)
- **Poster Presentation** at the Scripps Research Graduate Student Symposium, UCLA Conference Center, Los Angeles, CA, USA (14th – 16th October 2018)
- **Optical Microscopy & Imaging in the Biomedical Sciences (OMIBS)**, Marine Biological Laboratory (MBL), Wood Holes, MA, USA (20th – 30th August 2018)
- **Super Resolution Microscopy Workshop**, The Salk Institute of Biological Studies, La Jolla, CA, USA (7th – 10th May 2018)

TEACHING, MENTORING, VOLUNTEER WORK AND LEADERSHIP

• Mentoring Laetitia Dewavrin, an undergraduate Part II (MSc) student (University of Oxford) on a day-to-day basis	October 2022 – May 2023
• Actively participated in recruitment of prospective PhD students (Scripps Research)	2017 – 2019
• Teaching Assistant, Neurobiology of Disease class (Scripps Research)	Spring 2018
• Science Saturday Volunteer (Scripps Research): Lab tour and demos for local middle and high school students in San Diego area	2017 – 2018
• Discussion Leader of Introductory Biochemistry (UW-Madison): Leading a discussion section, tutoring the problem sets, answering student questions	2015 – 2016
• Tutor with Greater University Tutoring Service (UW-Madison): - General Physics - Introductory Biochemistry and Neurobiology	Spring 2015– Fall 2016

- Honors Students Organization (UW-Madison): Organizing academic and social events for students in the L&S Honors Program
  - Secretary 2016 – 2017
  - Volunteer Chair 2015 – 2016
  - Co-academic Chair 2014 – 2015

- President of Thai Student Association (UW-Madison): Leading, organizing, and joining cultural events on campus 2015 – 2016

B. Chassefeyre R*, **Chaiamarit T*,** Verhelle A*, Novak SW, Andrade LR, Leitao ADG, Manor U, Encalada SE**. 2021. Endosomal Sorting Drives the Formation of Mutant Prion Protein Endoggresomes.** *Science Advances* 7(52):eabg3693. https://www.science.org/doi/10.1126/sciadv.abg3693 ***Co-authors**

CELLULAR NEUROSCIENCE

Endosomal sorting drives the formation of axonal prion protein endoggresomes

Romain Chassefeyre[1,2,3]†‡, Tai Chaiamarit[1,2,3]†, Adriaan Verhelle[1,2,3]†, Sammy Weiser Novak[4], Leonardo R. Andrade[4], André D. G. Leitão[1,2,3], Uri Manor[4], Sandra E. Encalada[1,2,3]*

Copyright © 2021 The Authors, some rights reserved; exclusive licensee American Association for the Advancement of Science. No claim to original U.S. Government Works. Distributed under a Creative Commons Attribution License 4.0 (CC BY).

The pathogenic aggregation of misfolded prion protein (PrP) in axons underlies prion disease pathologies. The molecular mechanisms driving axonal misfolded PrP aggregate formation leading to neurotoxicity are unknown. We found that the small endolysosomal guanosine triphosphatase (GTPase) Arl8b recruits kinesin-1 and Vps41 (HOPS) onto endosomes carrying misfolded mutant PrP to promote their axonal entry and homotypic fusion toward aggregation inside enlarged endomembranes that we call endoggresomes. This axonal rapid endosomal sorting and transport-dependent aggregation (ARESTA) mechanism forms pathologic PrP endoggresomes that impair calcium dynamics and reduce neuronal viability. Inhibiting ARESTA diminishes endoggresome formation, rescues calcium influx, and prevents neuronal death. Our results identify ARESTA as a key pathway for the regulation of endoggresome formation and a new actionable antiaggregation target to ameliorate neuronal dysfunction in the prionopathies.

INTRODUCTION

The progressive accumulation of misfolded proteins as intraneuronal pathologic aggregates is a feature of neurodegenerative disorders (*1*). Axons are particularly vulnerable to the formation of aggregates, which are often observed at dystrophic swelling sites, and can contain wild-type (WT) or mutant misfolded proteins that lose solubility and become cytotoxic to the neuron and to neighboring cells via spreading (*1*–*3*). The molecular mechanisms and pathways that drive the formation of misfolded protein aggregates versus their clearance in axons remain undefined.

To regulate sorting, signaling, and metabolic function, axons rely on active microtubule-based transport machinery that enables the distribution of vesicles and organelles to distal axonal domains via kinesin-dependent anterograde movement (*4*), and the retrograde movement of axonal cargos toward the soma by cytoplasmic dynein, for efficient lysosomal-based degradation (*5*). Axonal homeostasis also depends on an interconverting endolysosomal trafficking system that spreads over long distances. The regulation of intraneuronal endolysosomal sorting is, in part, orchestrated by Arl8b, an Arf-like (Arl) family of small guanosine triphosphatase (GTPase) that recruits kinesin, and the multiunit homotypic fusion and protein sorting (HOPS) complex onto late endosomes (LEs) to drive their motility to the cell periphery and toward homotypic fusion with other LEs (*6*, *7*). Axonal transport and endolysosomal trafficking allow the sorting of neuronal cargos between subcellular vesicular compartments in axons. Whether and how misfolded and aggregation-prone proteins co-opt axonal endolysosomal trafficking systems to form aggregates in axons are unknown.

Mutations in prion protein (PrP) *PRNP* gene associated with inherited human prion disease (*8*) can result in the intraneuronal deposition of insoluble PrP aggregates, including within dystrophic axons in brains of patients with prion disease, as well as in familial rodent models of the disease (*9*–*11*). The mechanisms of misfolded PrP aggregate formation and deposition within neurons, as well as their connection to neurotoxicity, remain debated. Mutant and infectious PrP have been observed to accumulate in the cytosol as aggresomes (*12*–*14*). However, misfolded PrP also largely accumulates inside endocytic membrane compartments in cultured cells and in neurons in human brains of patients with prion disease (*13*, *15*–*19*), pointing toward a possible role of endolysosomal pathways in PrP aggregation. Endolysosomal membrane sorting and trafficking are central to PrP physiology and pathology, as both $PrP^{C/WT}$ (cellular/WT) and misfolded mutant PrP are glycosylphosphatidylinositol (GPI)–anchored proteins that transit to the cell surface from the endoplasmic reticulum (ER) via the Golgi in the lumen of membrane compartments, from where they are endocytosed back for recycling in endosomes, or that transit to lysosomes for degradation (*17*, *20*–*22*). PrP also resides in recycling endosomes or in multivesicular bodies (MVBs), locations critical for PrP conversion to misfolded conformations (*15*, *16*) and for its packaging for extracellular release in exosomes during cell-to-cell spread (*23*). How mutant PrP sorts between endolysosomal compartments in axons is unclear, but identification of the subcellular itinerary where mutant PrP aggregates form, transit, and become neurotoxic in axons is critical for understanding the basis of axonotoxicity in the prionopathies and may have implications for understanding the axonal etiology of other neurodegenerative disorders. Here, by systematically analyzing the neuronal trafficking itineraries of misfolded mutant PrP that causes familial prion disease in humans, we identified endosomal pathways that impose markedly different fates on mutant PrP: One pathway drives mutant PrP for degradation in the soma, while a second Arl8b/kinesin-1/HOPS axis propels mutant PrP into the axon for sorting, fusion, and aggregation inside endolysosomal structures that we term endoggresomes. Axonal endoggresomes impair calcium dynamics and reduce neuronal viability, but reducing the function of Arl8b/kinesin-1/HOPS components inhibits endoggresome formation in axons and circumvents neuronal toxicity and neuronal death. Our findings identify the endolysosomal trafficking

[1]Department of Molecular Medicine, The Scripps Research Institute, La Jolla, CA 92037, USA. [2]Dorris Neuroscience Center, The Scripps Research Institute, La Jolla, CA 92037, USA. [3]Neurodegeneration New Medicines Center, The Scripps Research Institute, La Jolla, CA 92037, USA. [4]Waitt Advanced Biophotonics Center, Salk Institute for Biological Studies, La Jolla, CA 92037, USA.
*Corresponding author. Email: encalada@scripps.edu
†These authors contributed equally to this work.
‡Present address: Evotec, 31036 Toulouse, France.

Downloaded from https://www.science.org at University of Oxford on April 20, 2023

system as a key player in the discriminating itinerary of misfolded mutant PrP within neurons toward degradation versus aggregation and point to the Arl8b/kinesin-1/HOPS pathway as an antiaggregation target amenable to therapeutic intervention that can modulate neuronal dysfunction in the prionopathies.

RESULTS

Mutant PrP is transported by kinesin-1 in vesicles and forms aggregates in axons

To characterize mutant PrP aggregate formation in axons, we established an in cellulo system in primary murine hippocampal neurons transiently expressing fluorescently tagged or untagged fusions of a PrP mutant harboring a nine octapeptide insertion called PrP^{PG14} (fig. S1A). This mutant was previously associated with dementia and ataxia in humans and with neurological illness in mouse disease models (*24*, *25*). Expression of PrP was under the Mouse PrP (MoPrP) promoter (*26*) and contained the endogenous PrP secretory signal sequence (SS) and GPI anchor sequence to ensure proper translocation to the ER and delivery to the plasma membrane, respectively. Live imaging showed prominent PrP^{PG14} axonal aggregate inclusions 1 day after the expression of PrP^{PG14}-mCh (mCherry), PrP^{PG14}-EGFP (enhanced green fluorescent protein), or untagged PrP^{PG14}, and these increased over time compared to small vesicles observed in axons of PrP^{WT}-mCh–expressing neurons (Fig. 1A and fig. S1B). These observations are consistent with previous studies showing intra-axonal aggregates in a PrP^{PG14}-EGFP transgenic mouse model (*11*). Correlative fluorescence and scanning electron microscopy revealed localization of PrP^{PG14}-mCh inclusions to axonal dystrophic swellings averaging 1.57 ± 0.13 μm in length and 0.54 ± 0.05 μm in width (means ± SEM) (Fig. 1B). PrP^{PG14}-EGFP inclusions formed in differentiated Neuro2a (N2a) cells (fig. S1C), where PrP^{PG14}-mCh exhibited limited resistance to proteinase K (PK) (fig. S1D), as shown previously (*27*), suggesting that this mutant partly and constitutively misfolded upon transient expression. Prominent intra-axonal inclusions were also generated in axons of neurons expressing $PrP^{D177N(M128)}$-mCh (Fig. 1C), a point mutation (D178N/M129 in humans) that causes prion fatal familial insomnia (*28*), indicating that axonal aggregates are a generalized feature of at least some familial PrP mutations and not unique to PrP^{PG14}.

In addition to large aggregates, high-resolution live imaging revealed the presence of small PrP^{PG14}-EGFP vesicles that underwent active bidirectional transport in axons (Fig. 1D and movie S1). Single-particle image analysis (*29*) revealed that, 2 days after expression, most motile PrP^{PG14}-mCh or PrP^{PG14}-EGFP vesicles moved in the anterograde direction toward the synapse, as observed for PrP^{WT}-mCh vesicles (Fig. 1, D and E; fig. S2, A and B; and movie S2) [transport parameters are defined in (*29*)] and as previously characterized for yellow fluorescent protein (YFP)–PrP^{C} vesicles (*30*). In contrast, PrP^{PG14}-mCh aggregates remained largely stationary or moved with net velocities that were 20 to 50 times slower (0.05 to 0.1 μm/s) than those of vesicles (0.5 to 4 μm/s) (vesicles versus aggregates are defined in Materials and Methods; Fig. 1, D and E, and fig. S2B). Depletion of kinesin-1C (KIF5C), an anterograde motor that we previously identified as required for the movement of YFP-PrP^{C} vesicles in axons (*30*), resulted in an overall impairment of anterograde movement of PrP^{PG14}-mCh or PrP^{PG14}-EGFP vesicles toward the axonal termini. Defects included significant reductions in the densities and flux (number of vesicles per time) of anterograde-moving vesicles and an increased number of stalled vesicles (Fig. 1, F to H). Vesicles that continued to move spent less time moving toward the synapse, moved slower, and paused for longer periods during an anterograde run (Fig. 2I and fig. S2, B to D). These observations indicate that misfolded PrP^{PG14} is actively transported in vesicles by kinesin-1 in axons, where it also forms largely immobile aggregates at dystrophic swelling sites.

Vesicular and aggregated mutant PrP reside in endolysosomes in axons

To identify the axonal membrane compartments containing misfolded PrP^{PG14}, we imaged axons expressing PrP^{PG14}-mCh and various endolysosomal markers. Live imaging and quantitative analysis revealed substantial colocalization and cotransport of PrP^{PG14}-mCh vesicles and aggregates with EGFP-labeled Rab5, Rab11, Rab7, and LAMP1, markers for early endosomes, recycling endosomes, LEs, and endolysosomes, respectively (Fig. 2A and fig. S3A). Extensive colocalization was confirmed for PrP^{PG14}-mCh vesicles and aggregates in axons fixed and stained with antibodies recognizing endogenous endosomal proteins including early endosomes (EEA1), LEs (Rab7), and endolysosomes [LAMP1 (lysosomal associated membrane protein 1)] (fig. S3B). Time-lapse live imaging also revealed extensive cotransport of PrP^{PG14}-mCh vesicles with a fluorescently labeled fusion carrying only the SS of neuropeptide Y (NPY; referred to as SS-EGFP) (Fig. 2A), shown previously to exit the Golgi and traverse through the secretory pathway before cellular secretion (*31*), indicating that PrP^{PG14} particles are Golgi-derived. To directly test that Golgi-derived PrP^{PG14} vesicles entered to the axon in endolysosomes from the soma, we performed live imaging of a photoactivatable (PA) PrP^{PG14}-PAmCh fusion following irradiation of the soma with a 405-nm laser in neurons also expressing EGFP-Rab7 (Fig. 2B). We observed the rapid transition and cotransport of PrP^{PG14}-PAmCh vesicles with EGFP-Rab7–positive LEs from the soma into the axon, where they also colocalized with large PrP^{PG14}-PAmCh aggregates after 1 hour (Fig. 2B). These data demonstrate the direct soma-to-axon entry of PrP^{PG14}-PAmCh vesicles and suggest that PrP^{PG14}/Rab7 (LE)–positive vesicles contribute to the buildup of large aggregates in axons.

We next sought to determine whether misfolded PrP^{PG14} aggregates resided in endosomes. We first tested whether PrP^{PG14} cofractionated biochemically with Rab7 from detergent-free sucrose-floated membrane fractions (fig. S3C). We observed PrP in floated vesicle fractions of N2a cells transfected with either PrP^{WT}-mCh or PrP^{PG14}-mCh using antibodies against PrP or mCh (fig. S2, C and D). Floated fractions were positive for Rab7, confirming the biochemical isolation of LEs (fig. S2, C and D). To ascertain that floated membrane fractions contained misfolded and aggregated PrP^{PG14}, we subjected these fractions to PK digestion and to an insolubility assay using nondenaturing detergents, two assays used to test for misfolded PrP conformations, including of PrP^{PG14} (*18*, *25*). Western blots showed that PrP^{PG14}-mCh isolated in floated membrane fractions was partially resistant to PK digestion and more detergent insoluble compared to PrP^{WT}-mCh (fig. S2, E and F), indicating that vesicular PrP^{PG14} in primary neurons acquires major biochemical properties characteristic of conformationally misfolded and aggregated PrP (*11*, *27*).

To further determine whether PrP^{PG14} aggregates localized within endosomal membrane compartments, we performed correlative light and single or volumetric three-dimensional (3D) reconstructions

Downloaded from https://www.science.org at University of Oxford on April 20, 2023

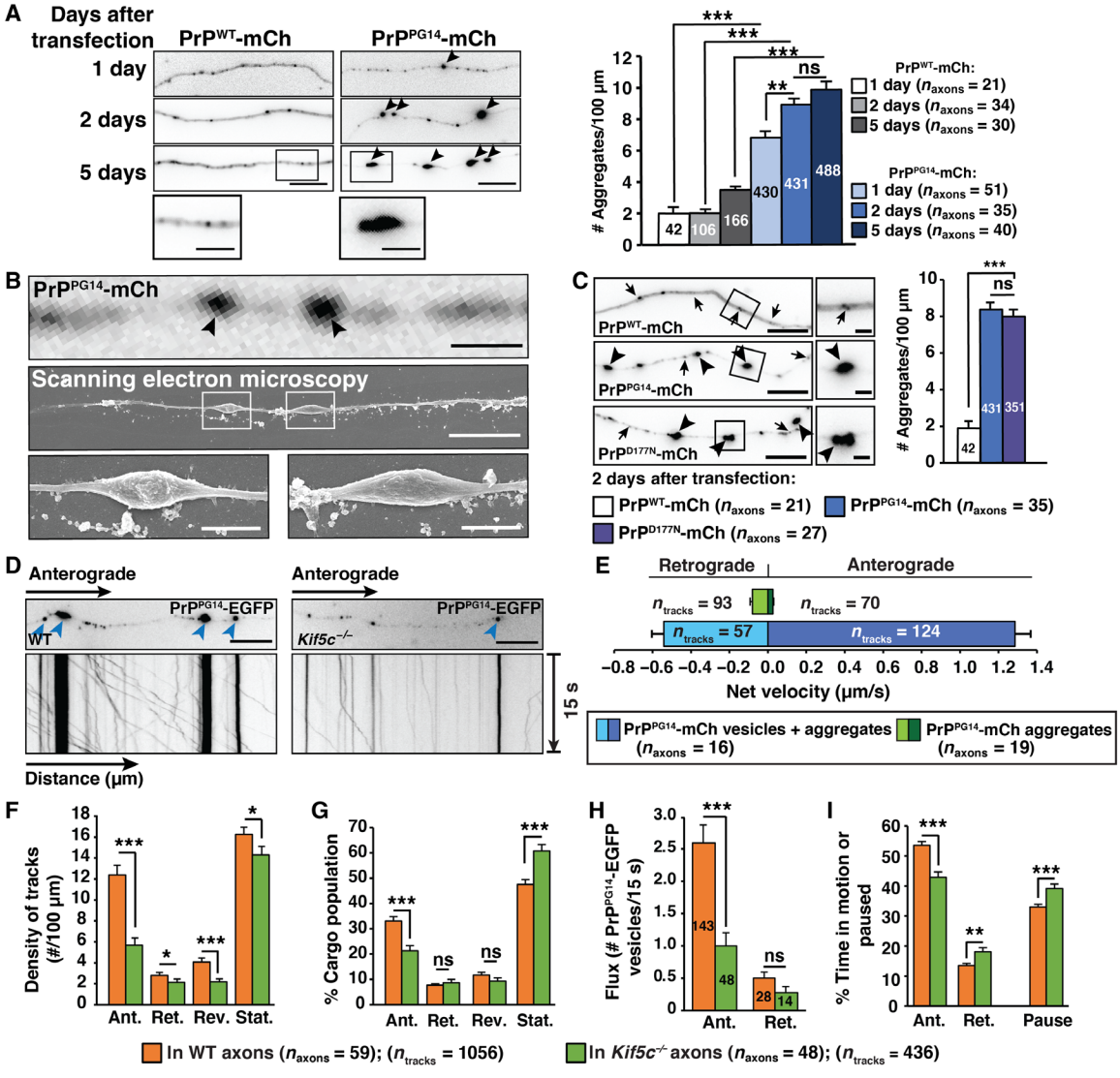


Fig. 1. PrP^{PG14} forms intra-axonal aggregates. (**A**) Representative images of axons expressing PrP^{WT}-mCh and PrP^{PG14}-mCh (left). Arrowheads indicate aggregates in all images. Scale bars, 10 µm. Insets show enlargements. Scale bars, 5 µm. Aggregate densities (right). (**B**) Correlative light-electron microscopy images of swellings 2 days after PrP^{PG14}-mCh transfection. Swelling number = 20. Scale bars, 10 µm. Insets show enlargements. Scale bars, 2 µm. (**C**) Images of axons expressing indicated proteins 2 days after transfection (left). Arrows indicate vesicles. Scale bars, 10 µm. Insets show enlargements. Scale bars, 2 µm. Aggregate densities (right). (**D**) First frames and kymographs of PrP^{PG14}-EGFP vesicle and aggregate transport in WT and *Kif5c*$^{-/-}$ axons. Scale bars, 10 mm. (**E**) Net velocities of PrP^{PG14}-mCh vesicles and aggregates. (**F**) Densities, (**G**) population breakdown, (**H**) flux, and (**I**) percent time in motion/paused of PrP^{PG14}-EGFP vesicles in WT and *Kif5c*$^{-/-}$ axons. Numbers of vesicles are inside the bars (H). Ant., anterograde; Ret., retrograde; Rev., reversals; Stat., stationary. (A, C, and E) Bars represent means ± SEM. Numbers of aggregates/tracks are inside the bars. $^{**}P < 0.01$ and $^{***}P < 0.001$; ns, not significant; Student's *t* test, Šidák correction. (F to I) Bars represent means ± SEM. $^{*}P < 0.05$, $^{**}P < 0.01$, and $^{***}P < 0.001$; Student's *t* test. #, number

using serial sectioning scanning electron microscopy (S3EM) of aggregate versus nonaggregate regions. This approach allows the precise mapping of PrP^{PG14}-mCh signal to structures in the S3EM images. Compared to nonaggregate regions, cross sections that mapped to PrP^{PG14}-mCh–positive aggregate sites revealed large electron-dense structures that resided within membrane compartments resembling endosomes, measuring an average length of 1286.9 ± 195.7 nm (mean ± SEM; $n = 7$) (Fig. 2C). Collectively, these data indicate that PrP^{PG14} is actively transported into the axon in Golgi-derived endolysosomal compartments that contribute to the formation of aggregates inside endomembrane structures that we term endoggresomes. The presence of endoggresomes suggests mechanisms that actively promote mutant PrP aggregate formation in axons and/or of those that impair their clearance.

Transient access of misfolded PrP^{PG14} to the axonal cell surface contributes to endoggresome formation

PrP is a secreted protein that transits to the cell surface (*20*). To determine whether PrP^{PG14} expressed in cultured neurons traveled along axons and accessed the plasma membrane along the axon en route to aggregation, we transfected neurons with PrP^{PG14}-mCh or PrP^{WT}-mCh fusion constructs containing a bungarotoxin binding

Downloaded from https://www.science.org at University of Oxford on April 20, 2023

sequence (BBS; referred to as PrP^{PG14}-mCh-BBS or PrP^{WT}-mCh-BBS; fig. S4A). The media of these neurons was treated with Alexa Fluor 647-labeled bungarotoxin (BTX) [BTX-a647 (*32*)] for 10 min at 4°C to inhibit active endocytosis, and neurons were fixed without permeabilization before imaging (fig. S4B). BTX-a647 signal was colocalized with a subset of PrP^{PG14}-mCh-BBS-positive puncta along axons (Fig. 3A), indicating that the latter accessed the axonal plasma membrane. BTX-a647 labeling was specific, as a647 signal was not observed in neurons expressing PrP^{WT}-mCh or PrP^{PG14}-mCh without the BBS sequence (fig. S4C). To determine whether PrP^{PG14}

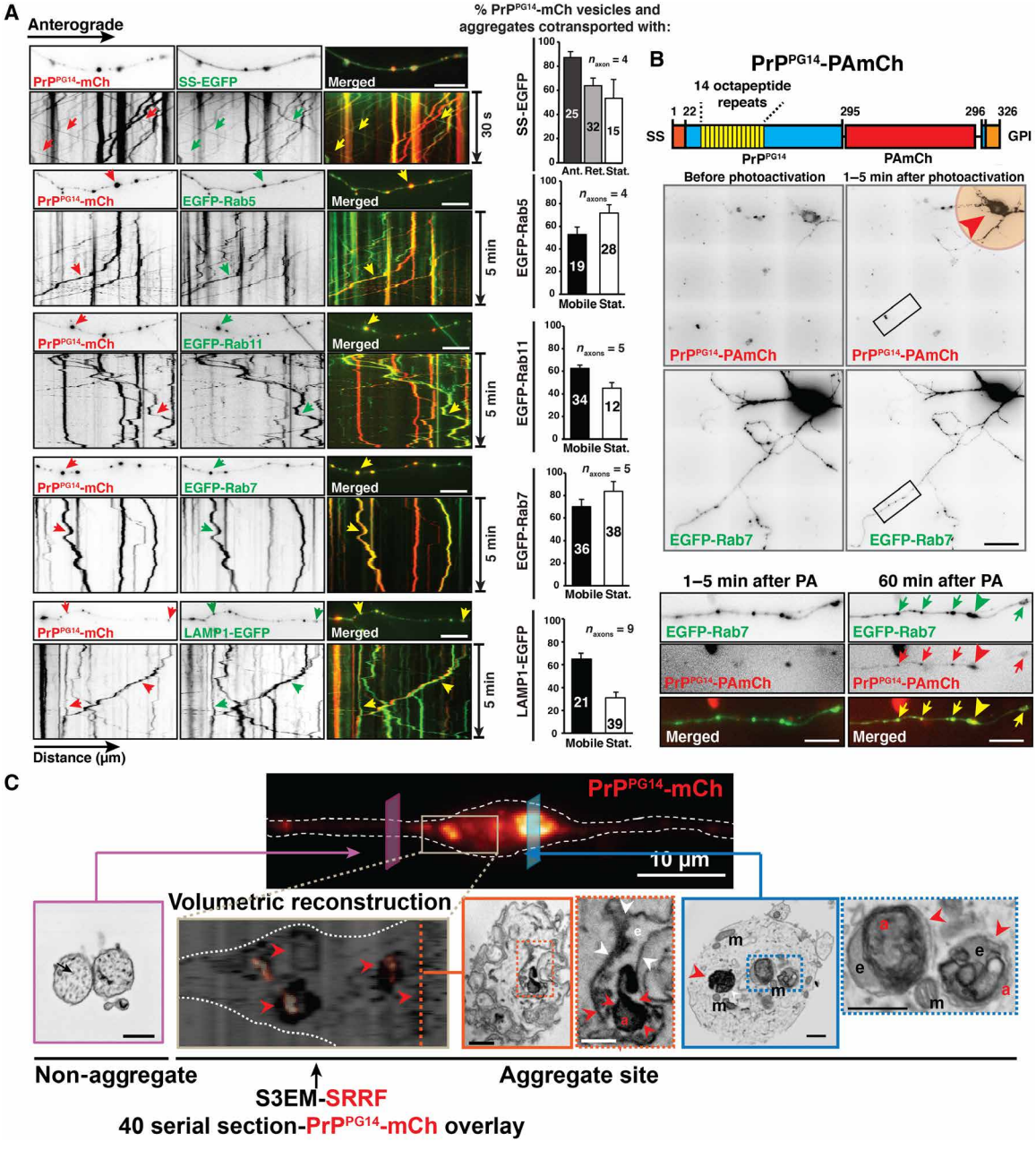


Fig. 2. Golgi-derived PrP^{PG14} resides in axonal endolysosomes. (**A**) First-frame images and kymographs of time-lapse movies of axons coexpressing PrP^{PG14}-mCh and various compartment markers (left): SS-EGFP, EGFP-Rab5, EGFP-Rab11, EGFP-Rab7, or LAMP1-EGFP. Arrows point to cotransport. Quantitation of cotransport (right). Bars represent means ± SEM. Vesicle or aggregate numbers are shown inside the bars. Scale bars, 10 μm. (**B**) Schematic of PrP^{PG14}-PAmCh construct (top). GPI, GPI anchor. Representative images of a hippocampal neuron cotransfected with PrP^{PG14}-PAmCh and EGFP-Rab7 before and after photoactivation (pink circle, arrowhead) of the cell body with a 405-nm laser (middle). Scale bar, 50 μm. Enlargements of inset in middle panels (bottom). Scale bar, 10 μm. Arrows indicate colocalization. Arrowheads points to endoggresomes. Number of neurons = 3. (**C**) Correlative fluorescence (top) and S3EM representative cross sections (bottom). Volumetric 3D reconstruction through the axonal PrP^{PG14}-mCh aggregate site is shown with superresolution radial fluctuation (SRRF) fluorescence overlay. Red arrowheads point to PrP^{PG14}-mCh-positive aggregates (a). White arrowheads point to endosomes (e). m, mitochondria; nonagg, nonaggregate. Scale bar (top panel of correlative image), 10 mm. Other scale bars, 500 nm.

Downloaded from https://www.science.org at University of Oxford on April 20, 2023

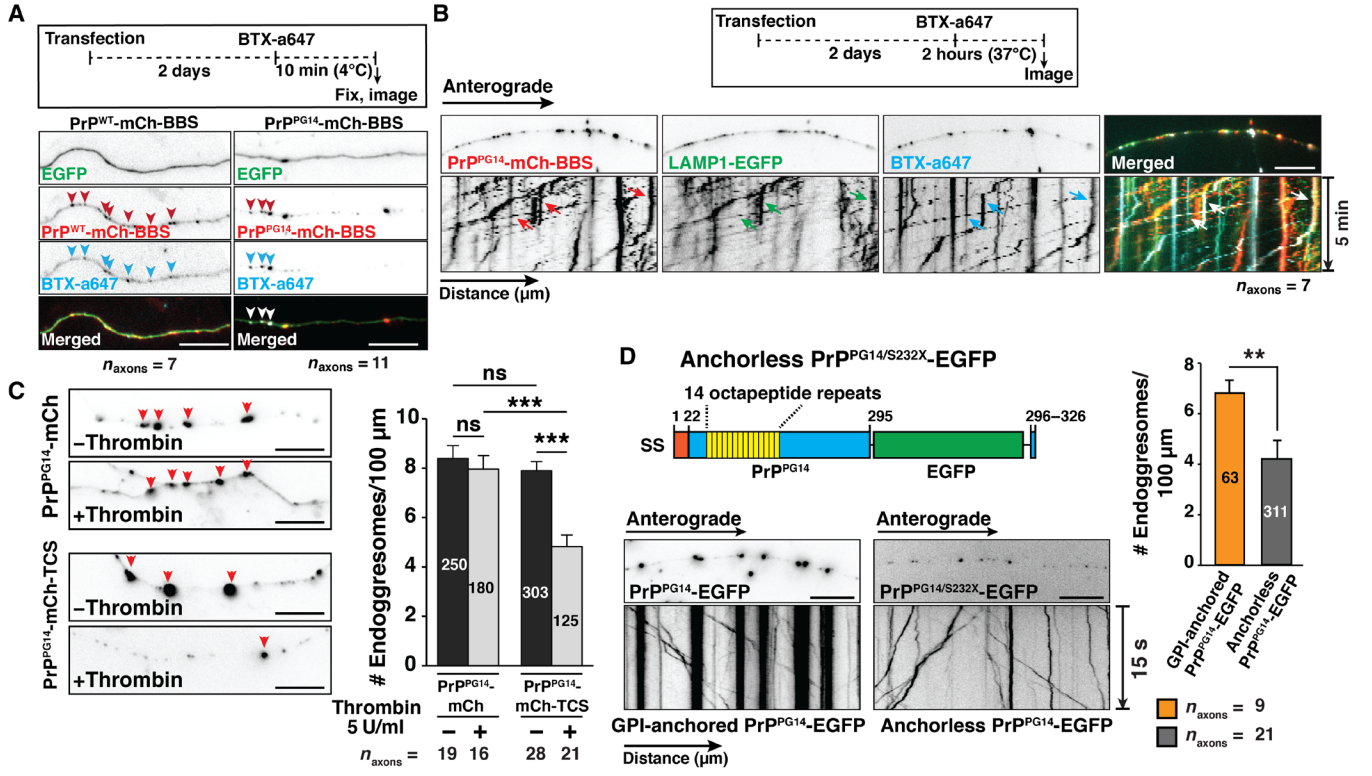


Fig. 3. Endoggresome formation requires the rapid transit of mutant PrP to the axonal cell surface. (**A**) Outline of 10-min BBS internalization assay (top). Representative images of axons expressing EGFP and PrP^{WT}-mCh-BBS or PrP^{PG14}-mCh-BBS and labeled with BTX-a647 (bottom). Arrowheads point to colocalization. Scale bars, 10 µm. (**B**) Outline of 2-hour BBS internalization assay (top). Representative first frames of time-lapse movies and kymographs of axons expressing PrP^{PG14}-mCh-BBS and LAMP1-EGFP, and labeled with BTX-a647. Arrows point to cotransport. Scale bar, 10 µm. (**C**) Representative images of axons expressing PrP^{PG14}-mCh or PrP^{PG14}-mCh-TCS, with or without thrombin treatment (left). Arrowheads point to endoggresomes. Scale bars, 10 µm. Quantitation of endoggresome densities (right). Numbers of endoggresomes are shown inside the bars. Bars represent means ± SEM. ***$P < 0.001$; Student's *t* test, Tukey's correction. (**D**) Schematic diagram of anchorless $PrP^{PG14/S232X}$-EGFP construct (top left). Representative images and kymographs of hippocampal axons expressing PrP^{PG14}-EGFP or $PrP^{PG14/S232X}$-EGFP (bottom left). Scale bars, 10 µm. Quantitation of endoggresome densities (right). Numbers of endoggresomes are shown inside the bars. Bars represent means ± SEM. **$P < 0.01$; Student's *t* test.

was sorted into LEs following internalization, neurons coexpressing PrP^{PG14}-mCh-BBS and LAMP1-EGFP were treated with BTX-a647 for 2 hours at 37°C before live imaging or fixation and permeabilization (fig. S4B). We observed extensive colocalization and cotransport between intra-axonal PrP^{PG14}-mCh-BBS, LAMP1-EGFP, and BTX-a647 signal (Fig. 3B), indicating that PrP^{PG14}-mCh-BBS was sorted into LEs after endocytosis. BTX-a647 punctate signal was observed along the length of axons, revealing that PrP^{PG14} undergoes dynamic bouts of exocytosis and endocytosis throughout the axonal surface. The addition of the BBS sequence did not alter endoggresome densities in axons (fig. S4D). Inhibition of endocytosis with dynasore, a dynamin GTPase inhibitor, resulted in a significant, albeit partial decrease in internalization of BTX-a647-labeled PrP^{PG14}-mCh particles (fig. S4E), suggesting that PrP^{PG14}-mCh is partly internalized by clathrin-dependent pathways.

To determine whether targeting of PrP^{PG14}-mCh to the cell surface was required to form intra-axonal aggregates, we quantified endoggresome densities in axons of neurons expressing PrP^{PG14}-mCh tagged or not with a thrombin cleavage sequence (TCS; referred as PrP^{PG14}-mCh-TCS) and treated or not with thrombin protease (5 U/ml) for 48 hours (fig. S4F). Thrombin treatment resulted in significantly reduced densities of PrP^{PG14}-mCh-TCS endoggresomes compared to untagged PrP^{PG14}-mCh (Fig. 3C), indicating that access to the plasma membrane contributes substantially to the formation of endoggresomes in axons. We further tested this cell surface requirement by expressing an anchorless PrP^{PG14} double mutant ($PrP^{PG14/S232X}$-EGFP) that is unable to associate with membranes (*21*). While small $PrP^{PG14/S232X}$-EGFP vesicles were actively transported in axons, the density of endoggresomes was largely and significantly reduced (Fig. 3D), suggesting that, upon secretion, $PrP^{PG14/S232X}$-EGFP is released in the absence of the GPI anchor and thus cannot endocytose and contribute to aggregation. These data show that the transient transit of PrP^{PG14} to the cell surface and subsequent rapid endocytosis all along the length of axons contribute to the sorting of Golgi-derived PrP^{PG14} into endosomes to form endoggresomes in LEs.

An Arl8b/kinesin-1/HOPS pathway drives PrP^{PG14} endoggresome formation in axons

Two observations led us to hypothesize that direct Golgi-to-LE and/or LE homotypic fusion (*33*–*35*) also contributed to endoggresome biogenesis in axons. First, axonal PrP^{PG14} particles were endocytosed from the cell surface into single endosomes (Fig. 3B), but, over a period of 2 to 5 days, PrP^{PG14} was observed in enlarged LEs (Figs. 1, A and B, and 2C), suggesting fusion of endosomes after endocytosis. Second, preventing PrP^{PG14} internalization along axons

Downloaded from https://www.science.org at University of Oxford on April 20, 2023

reduced but did not abolish the number of PrP^{PG14} endoggresomes (Fig. 3C), suggesting the presence of parallel endoggresome-forming pathways. As Arl8b orchestrates endolysosomal trafficking and fusion (*6*), we first evaluated whether it associated with PrP^{PG14} endosomal vesicles to direct their homotypic fusion in axons toward endoggresome formation. Live imaging showed that most PrP^{PG14}-mCh vesicles co-migrated with $Arl8b^{WT}$-GFP (80%) or with active GTP-bound $Arl8b^{Q75L}$-GFP and LAMP1-mTagBFP2 particles, but not with soluble dominant-negative guanosine diphosphate (GDP)–bound $Arl8b^{T34N}$-GFP (Fig. 4A and fig. S5A). Two days after co-expression, we observed $Arl8b^{WT}$-mCh and PrP^{PG14}-mTagBFP2 vesicle colocalization in the soma, and these vesicles co-transported with SS (from NPY)–EGFP into the axon (fig. S5, B and C), suggesting that Arl8b loaded onto post-Golgi PrP^{PG14} vesicles and entered the axon as a complex. Endogenous Arl8b, as recognized with an anti-Arl8b antibody, also colocalized with PrP^{PG14} vesicles in axons (fig. S9C). To evaluate the role of Arl8b on endoggresome formation, we expressed inactive untagged GDP-bound $Arl8b^{T34N}$, or Arl8b function was reduced using previously validated short hairpin RNAs (shRNAs) (fig. S5D) (*36*). Endoggresome densities were significantly decreased in axons of neurons treated with Arl8b shRNAs and in those expressing GDP-bound inactive $Arl8b^{T34N}$, while overexpression of untagged

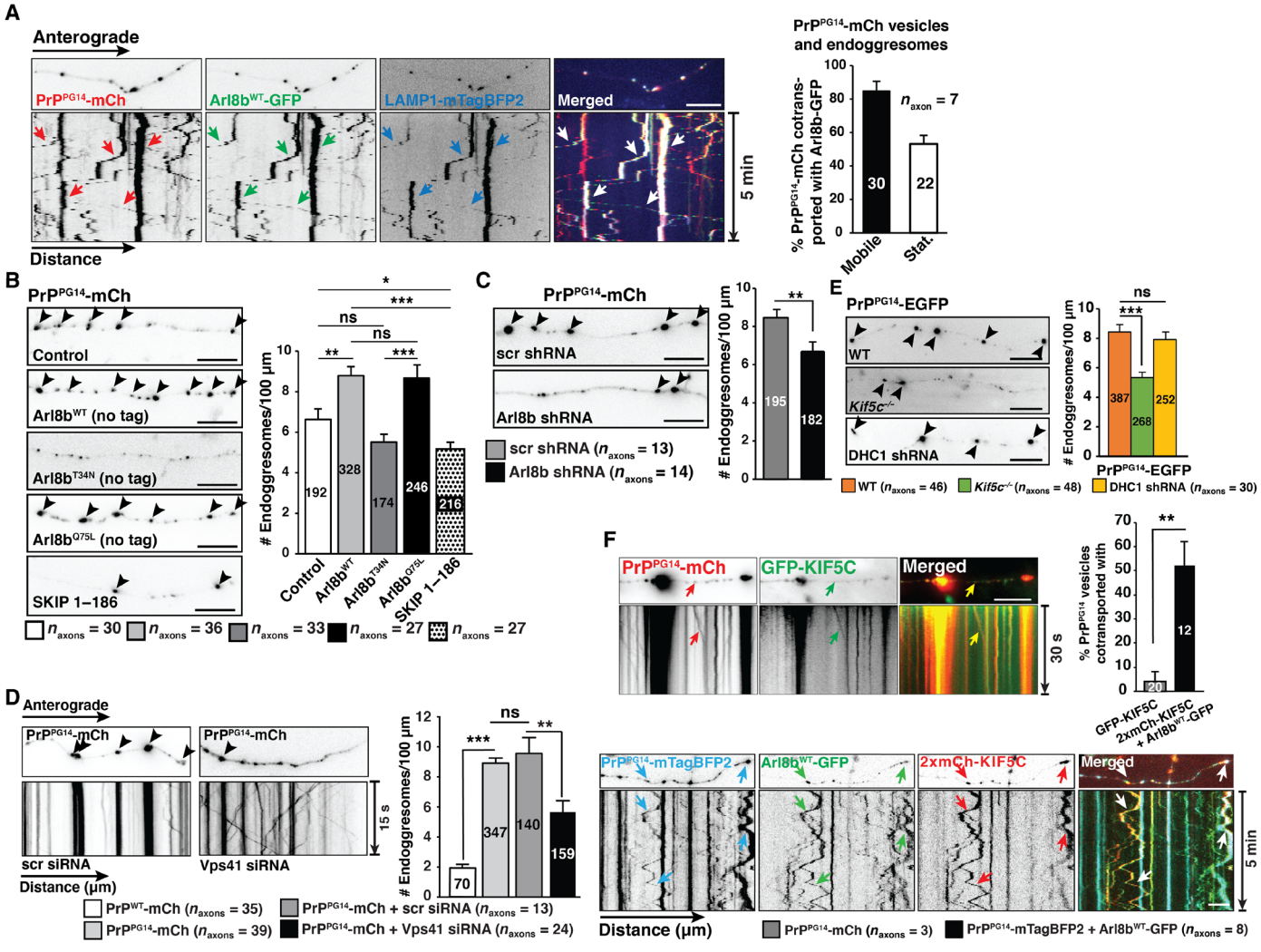


Fig. 4. The axonal rapid endosomal sorting and transport-dependent aggregation pathway drives mutant PrP endoggresome formation. (**A**) First frames of time-lapse movies and kymographs of axons expressing the indicated markers (left). Arrows indicate cotransport. PrP^{PG14}-mCh and $Arl8b^{WT}$-GFP percentage contransport (right). Vesicle/endoggresome numbers are inside the bars. Bars represent means ± SEM. (**B**) Images of PrP^{PG14}-mCh axons coexpressing the indicated markers. Control, empty vector. Arrowheads indicate endoggresomes. Endoggresome densities (right). Endoggresome numbers are inside the bars. (**C**) Images of axons from neurons expressing PrP^{PG14}-mCh treated with scrambled (scr) or Arl8b shRNAs (left). Arrowheads indicate endoggresomes. Endoggresome densities (right). Endoggresome numbers are inside the bars. (**D**) First frames of time-lapse movies and kymographs of axons coexpressing PrP^{PG14}-mCh and scr or Vps41 siRNAs (left). Arrowheads indicate endoggresomes. Endoggresome densities (right). Endoggresome numbers are inside the bars. (**E**) Images of PrP^{PG14}-EGFP endoggresomes in WT, *Kif5c*$^{-/-}$, and DHC1 shRNA axons (left). Arrowheads indicate endoggresomes. Endoggresome densities (right). Endoggresome numbers are inside the bars. (**F**) First frames of time-lapse movies and kymographs of axons expressing PrP^{PG14}-mCh and GFP-KIF5C (top left), as well as PrP^{PG14}-mTagBFP2, $Arl8b^{WT}$-GFP, and 2xmCh-KIF5C (bottom). Arrows indicate cotransport. Percentage of cotransport (top right). Vesicle numbers are inside the bars. (B to D) Bars represent means ± SEM. *$P < 0.05$, **$P < 0.01$, and ***$P < 0.001$; Student's *t* test, Šidák correction. (E and F) Bars represent means ± SEM. ***$P < 0.001$; **$P < 0.01$; Student's *t* test. Scale bars, 10 µm.

Downloaded from https://www.science.org at University of Oxford on April 20, 2023

Arl8b^{WT} or GTP-active Arl8b^{Q75L} increased endoggresome densities in axons (Fig. 4, B and C).

We next evaluated the mechanistic basis of Arl8b-mediated endoggresome formation. We first tested whether Arl8b recruited its effectors SifA and kinesin-interacting protein (SKIP), KIF5C, and Vps41 to PrP^{PG14} vesicles (*7*). Live imaging showed extensive cotransport between vesicles carrying PrP^{PG14}-mTagBFP2, Arl8b^{WT}-mCh, and EGFP-hSKIP; PrP^{PG14}-mCh and EGFP-hSKIP; Arl8b^{WT}-mCh and EGFP-hSKIP; and PrP^{PG14}-mCh and EGFP-Vps41 (fig. S5E). To next determine the role of Arl8b effectors in the trafficking, fusion, and aggregation of PrP^{PG14} in axons, we reduced the function of Vps41 using small interfering RNAs (siRNAs) (fig. S5, F and G), and the function of SKIP was inhibited using a peptide comprising amino acids 1 to 186 (SKIP 1–186) previously shown to be required to bridge interactions between Arl8b and kinesin-1 (*37*). We observed significantly decreased endoggresome densities following reduction and inhibition of Vps41 and SKIP (Fig. 4, B and D). Furthermore, reducing Vps41 resulted in small and less stationary PrP^{PG14}-mCh vesicles in the soma and axons (Fig. 4D and fig. S5, G and H), suggesting decreased vesicle fusion, and showing restored vesicular motility. To determine the role of kinesin-1 in endoggresome formation, we quantitated endoggresome densities in axons of kinesin-1C knockout (KO) (*Kif5c*$^{-/-}$) mice, kinesin light chain 1 (KLC1) KO (*Klc1*$^{-/-}$) mice, and conditional kinesin-1B KO (*Kif5b*$^{pflox/pflox}$) mice (*38*). The latter two kinesin-1 subunits were previously implicated in the anterograde transport of YFP-PrP^{C} vesicles (*30*). Endoggresome densities were significantly decreased 2 days after PrP^{PG14}-mCh transfection, in axons from *Kif5c*$^{-/-}$, *Klc1*$^{-/-}$, and *Kif5b*$^{pflox/pflox}$ neurons—the latter in a cre-adenovirus multiplicity of infection (MOI) dose-dependent manner—compared to WT hippocampal axons (Fig. 4E and fig. S6, A to C). Decreased endoggresome densities were sustained for at least 10 days in *Kif5c*$^{-/-}$ axons (fig. S6D). Overexpression of EGFP-KIF5C in *Kif5c*$^{-/-}$ neurons transfected with PrP^{PG14}-mCh restored higher axonal endoggresome densities, demonstrating that decreased densities were due to the specific removal of KIF5C (fig. S6E). Notably, aggregate densities in axons of *Kif5c*$^{-/-}$ neurons expressing PrP$^{D177N(M128)}$-mCh were also significantly lower (fig. S6F), indicating a generalized requirement of kinesin-1 for generating intra-axonal endoggresomes of various mutant PrPs. To test whether endoggresome formation in axons was the result of generalized transport impairments, the function of the main neuronal retrograde motor cytoplasmic dynein heavy chain 1 (DHC1) was reduced using previously validated shRNAs (*30*). Despite impairing PrP^{PG14}-mCh vesicle transport, and thus identifying DHC1 as a retrograde motor for these vesicles (fig. S6G), reducing DHC1 did not alter PrP^{PG14}-EGFP endoggresome densities (Fig. 4E).

To determine whether Arl8b drives endoggresome formation via recruitment of kinesin-1 to PrP^{PG14} vesicles, we performed live imaging of vesicle transport of neurons coexpressing PrP^{PG14}-mTagBFP2 and 2xmCh-KIF5C in the presence or absence of Arl8b^{WT} overexpression. Overexpression of Arl8b^{WT}-GFP significantly increased the percentage of PrP^{PG14}-mTagBFP2 vesicles that cotransported with 2xmCh-KIF5C (Fig. 4F), suggesting recruitment of 2xmCh-KIF5C by Arl8b. Moreover, flux and densities of PrP^{PG14}-mCh vesicles were significantly enhanced in axons upon Arl8b^{WT} overexpression (fig. S6H). Recruitment of KIF5C by Arl8b depended on Arl8b GTPase activity (fig. S6I). Together, these data indicate that GTP-active Arl8b^{WT} loads onto Golgi-derived PrP^{PG14} vesicles, recruits SKIP, kinesin-1, and Vps41, and acts as a key driver of the anterograde movement and fusion of PrP^{PG14} vesicles in the axon, promoting endoggresome formation. Thus, we term this process Axonal Rapid Endosomal Sorting and Transport-dependent Aggregation (ARESTA).

Direct and indirect ARESTA converge on Arl8b to form axonal endoggresomes

As endoggresome formation occurs by first accessing the axonal cell surface (Fig. 3) or by direct transport and fusion (Fig. 4), we investigated whether these pathways act independently or in concert via Arl8b, by overexpressing Arl8b^{WT} to promote endoggresome formation while inhibiting the uptake of cell surface PrP^{PG14}. Live imaging of neurons expressing PrP^{PG14}-mCh-TCS and simultaneously transfected with Arl8b^{WT}-GFP revealed the same increased endoggresome densities in axons treated or not with thrombin (fig. S6J). These observations revealed that Arl8b^{WT} overexpression alone was sufficient to promote endoggresome formation, bypassing the contribution of endocytosed PrP^{PG14}, and suggest that aggregation via direct fusion and via internalization act in parallel.

We next evaluated whether Arl8b associated with PrP^{PG14} vesicles endocytosed from the cell surface to drive endoggresome formation. Live imaging of axons expressing PrP^{PG14}-mCh-BBS and Arl8b^{WT}-GFP and treated in the media with BTX-a647 resulted in extensive cotransport between these three vesicle populations (fig. S6K). Thus, Arl8b loads onto PrP^{PG14} vesicles that are endocytosed from the cell surface along the axon, as well as to post-Golgi vesicles (fig. S5, A and E), to mediate PrP^{PG14} endosome fusion. These "indirect" and "direct" ARESTA pathways act in parallel and converge on Arl8b, a key regulator of mutant PrP endoggresome formation.

Misfolded PrP is degraded in the soma but persists in axons because of impaired retrograde transport and diminished lysosomal degradation capacity

The axon has limited local degradation capacity, with an increasing gradient of acidification of endosomal organelles from distal to proximal axonal regions (*39*, *40*). Thus, most cargos require active retrograde transport for degradation upon fusion with lysosomes enriched in the soma (*5*, *41*, *42*). To determine how PrP^{PG14} endoggresomes persist in axons, we tested for local axonal degradation impairments and/or failure of PrP^{PG14} vesicles to undergo retrograde transport. Several observations suggested local axonal deficits in lysosomal maturation and clearance. First, axonal endoggresomes increased over time compared to PrP^{WT}-mCh–positive puncta (Fig. 1A), suggesting impaired in situ degradation. Second, treatment of PrP^{PG14}-mCh neurons with bafilomycin A1 (BafA1), an inhibitor of a lysosomal V–adenosine triphosphatase (ATPase) proton pump that acidifies vesicles (*43*), did not increase endoggresome densities compared to dimethyl sulfoxide (DMSO)–treated controls (fig. S7A), suggesting the absence of actively degradative endolysosomal compartments. As a positive control, PrP^{WT}-mCh neurons treated with BafA1 showed a significant increase in endoggresome densities compared to DMSO controls, indicating inhibition of acidification (fig. S7A). Consistent with these observations, LysoTracker signal was not readily observed in PrP^{PG14}-mCh axons (Fig. 5A and fig. S7B). Third, BTX-a647 treatment and wash-off of neurons expressing PrP^{WT}-mCh-BBS resulted in reduced BTX-a647 axonal fluorescence intensity after 24 hours, compared to the steady BTX-a647 axonal fluorescence levels in neurons expressing PrP^{PG14}-mCh-BBS (Fig. 5B and fig. S7C), suggesting that a day after treatment, endocytosed PrP^{PG14}-mCh-BBS

Downloaded from https://www.science.org at University of Oxford on April 20, 2023

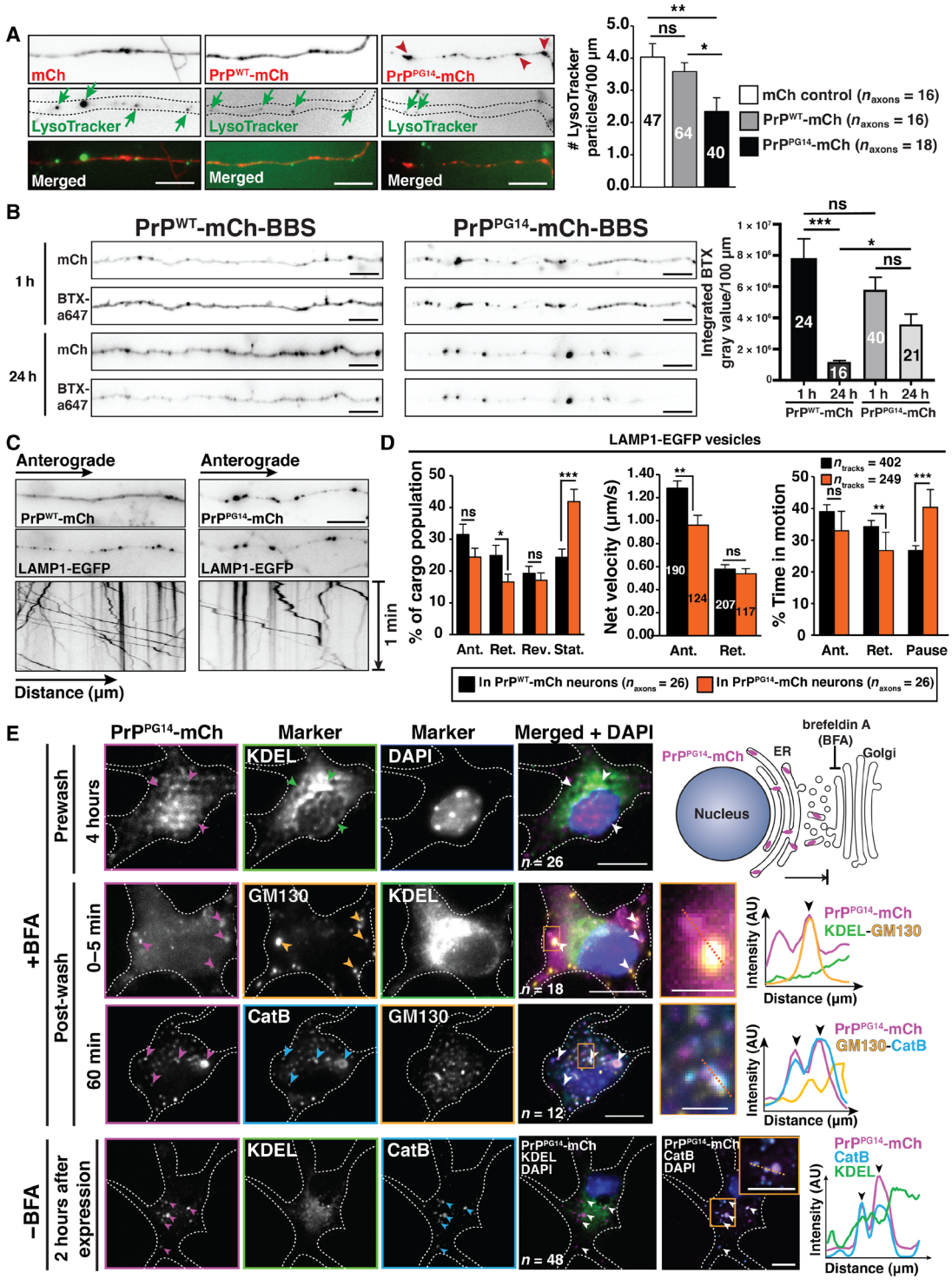


Fig. 5. Endoggresomes are maintained in axons because of impaired retrograde transport and lysosomal degradation. (**A**) Images of LysoTracker-positive vesicles in mCh, PrP^{WT}-mCh, or PrP^{PG14}-mCh-expressing axons (left). Arrows indicate vesicles, and arrowheads indicate endoggresomes. Scale bars, 10 µm. LysoTracker vesicle densities (right). Vesicle numbers are inside the bars. (**B**) Images of BTX-a647–labeled axons 1 and 24 hours after labeling (left). Scale bars, 10 µm. BTX signal intensity (right). Axon numbers are inside the bars. PrP^{WT}-mCh-BBS: four and three replicates for 1 and 24 hours, respectively; and PrP^{PG14}-mCh-BBS: three and two replicates for 1 and 24 hours, respectively. (**C**) Images of PrP^{WT}-mCh or PrP^{PG14}-mCh axons (top), and LAMP1-EGFP first frames of a time-lapse movie (middle) and kymographs (bottom). Scale bar, 10 µm. (**D**) LAMP1-EGFP vesicles: Population percentage (left), net velocities (middle), and percent time in motion/paused (right). Track numbers are inside the bars. (**E**) Images of soma of neurons expressing PrP^{PG14}-mCh and stained with antibodies against the indicated markers. Arrowheads indicate colocalization. Schematic of the BFA assay (top right). Line scans are intensity profiles of regions indicated by dotted lines inside insets. Scale bars (main panels), 10 µm. Scale bars (insets), 250 nm. (A, B, and D) Bars represent means ± SEM. *P < 0.05, **P < 0.01, and ***P < 0.001; Student's t test, Tukey's correction. DAPI, 4′,6-diamidino-2-phenylindole; AU, arbitrary units.

Downloaded from https://www.science.org at University of Oxford on April 20, 2023

molecules were not significantly degraded in lysosomes compared to PrP^{WT}-mCh-BBS–internalized molecules.

To determine whether retrograde PrP^{PG14} vesicle transport was impaired, live imaging and quantitative analysis showed that, in addition to the largely stationary or slow-moving PrP^{PG14}-mCh larger endoggresomes (Fig. 1E and fig. S2B), PrP^{PG14}-EGFP vesicles also moved slower and with less processivity in anterograde and retrograde directions compared to PrP^{WT}-EGFP vesicles (fig. S7D). To further test whether overall retrograde transport was impaired in PrP^{PG14}-mCh neurons, LAMP1-EGFP vesicle transport was imaged live. In PrP^{PG14}-mCh axons, the proportion of stationary LAMP1-EGFP vesicles was significantly increased and fewer vesicles moved in the retrograde direction (Fig. 5, C and D). LAMP1-EGFP vesicles also spent more time paused and less time moving toward the soma in PrP^{PG14}-mCh versus PrP^{WT}-mCh axons (Fig. 5D). Thus, PrP^{PG14} vesicles and endoggresomes, as well as LAMP1-positive LEs, are not properly transported toward the soma, nor are they actively degraded in axonal lysosomes, contributing to their sustained presence in axons.

As lysosomes are enriched in the soma (*5*), we evaluated whether PrP^{PG14}-mCh was actively degraded in the soma by systematically analyzing the trafficking itinerary of misfolded PrP^{PG14} immediately upon neuronal expression. Live imaging of neurons expressing PrP^{PG14}-mCh and treated with brefeldin A (BFA), an inhibitor of the secretory pathway (*44*), showed ER retention of PrP^{PG14}-mCh for at least 6 hours (Fig. 5E and fig. S8A). Untreated or post–BFA wash neurons showed rapid, efficient, and successive translocation within minutes, and by 2 hours of expression, of PrP^{PG14}-mCh from the ER to the Golgi and to compartments positive for cathepsin B (CatB), an acidic hydrolase required for lysosomal substrate degradation (Fig. 5E and fig. S8A). Neurons expressing PrP^{PG14}-mCh-BBS and treated with BTX-a647 in the media showed colocalization of these vesicles with LAMP1-EGFP (fig. S8B), indicating internalization into LEs. This labeling was specific, as neurons transfected with PrP^{PG14} fusion constructs without the BBS tag did not reveal any BTX-a647 signal (fig. S8C). Furthermore, PrP^{PG14}-mTagBFP2 vesicles colocalized with LysoTracker and Magic Red in the soma (fig. S8D), a fluorogenic substrate that activates upon cleavage by active CatB (*45*). Live imaging showed the active disappearance of PrP^{PG14}-mCh puncta that colocalized with LAMP1-EGFP, suggesting active degradation in the soma via the cell surface (fig. S8E and movie S3). To further test whether PrP^{PG14} underwent lysosomal degradation in the soma, we treated neurons expressing PrP^{WT}-mCh or PrP^{PG14}-mCh and exposed to LysoTracker Green with either BafA1 or DMSO. Quantitative imaging showed a significant increase in fluorescence intensity in the soma of PrP^{WT}-mCh– and PrP^{PG14}-mCh–expressing neurons treated with BafA1, compared to those treated with DMSO (fig. S8F), indicating that PrP undergoes somatic lysosomal-based degradation. Because this clearance pathway resembles a previously characterized rapid ER stress–induced export (RESET) pathway in non-neuronal cells (*21*), we evaluated whether PrP^{PG14} expression turned on ER stress in neurons. Coexpression of PrP^{PG14}-EGFP and an ER stress transcriptional reporter (ERSE-mCh) (*46*) resulted in significantly increased signal compared to that observed in neurons expressing either soluble EGFP or PrP^{WT}-EGFP (fig. S8G), indicating constitutive ER stress activation. Thus, while secreted misfolded PrP is actively cleared in somatic lysosomes by a process similar to RESET, PrP^{PG14} vesicles and endoggresomes are neither effectively transported toward the soma nor actively degraded in the axon, contributing to their sustained axonal presence.

Arl8b is a key determinant of PrP^{PG14} axonal entry

Because Arl8b is an endolysosomal GTPase, to determine whether Arl8b tags PrP^{PG14} endolysosomes destined for axonal entry versus PrP^{PG14} vesicles shuttled to lysosomes in the soma for degradation, we followed the ER-to-LE itinerary of PrP^{PG14}-mTagBFP2 (or PrP^{PG14}-mCh) and Arl8b in the soma and proximal axons of neurons treated or not with BFA. Live imaging showed that, while PrP^{PG14}-mTagBFP2 (or PrP^{PG14}-mCh) translocated from the ER to the Golgi and to LAMP1-mTagBFP2–positive endolysosomes immediately after BFA wash, as observed earlier (Fig. 5E), colocalization between PrP^{PG14}-mTagBFP2 (or PrP^{PG14}-mCh) and Arl8b puncta was not observed during the ER-to-LE itinerary, but only 2 hours after transfection (fig. S9A). This time period was after PrP^{PG14} was observed to transit to lysosomes (Fig. 5E). To determine whether Arl8b associated with PrP^{PG14} vesicles as they internalized to LEs from the somatic cell surface, neurons were cotransfected with PrP^{PG14}-mCh-BBS and LAMP1-mTagBFP2, treated in the medium with BTX-a647, and fixed and stained with an antibody against endogenous Arl8b. Imaging of the soma revealed the colocalization of PrP^{PG14}-mCh-BBS and LAMP1-mTagBFP2 vesicles that were also positive for BTX-a647 signal but that were negative for Arl8b (fig. S9B). Instead, colocalization of Arl8b with PrP^{PG14}-mCh-BBS, BTX-a647 signal, and LAMP1-mTagBFP2 vesicles occurred in the proximal axon (fig. S9, B and C), consistent with our earlier observations in more distal axonal regions (fig. S6K), indicating that Arl8b does not recognize PrP^{PG14} vesicles that are internalized from the somatic cell surface. Thus, Arl8 is absent from endocytosed PrP^{PG14} vesicles undergoing lysosomal-based degradation in the soma, but uniquely loads onto post-Golgi PrP^{PG14} vesicles that enter the axon, suggesting that Arl8b is a key regulator of PrP^{PG14} axonal entry.

PrP^{PG14} neurons display ARESTA-dependent impaired calcium intake dynamics and decreased neuronal viability

To probe whether axonal PrP^{PG14} endoggresomes lead to neuronal dysfunction, we tested whether the intrinsic capacity of cultured hippocampal neurons expressing PrP^{PG14}-mCh to intake calcium upon KCl-induced depolarization was compromised, as shown previously for cerebellar granule cultured neurons (*47*). Neurons transduced with PrP^{WT}-mCh or PrP^{PG14}-mCh adeno-associated virus (AAV-DJ) displayed high transduction efficiencies of 96 ± 2% and 97 ± 2% (means ± SEM), respectively, and endoggresome densities comparable to those observed in transfected axons (fig. S10). Single-cell calcium imaging of AAV-DJ-PrP^{PG14}-mCh–transduced neurons preloaded with the calcium-sensitive dye Fluo-4 AM (acetoxymethyl esters) resulted in a defective calcium influx in response to KCl-induced depolarization compared to AAV-DJ-PrP^{WT}-mCh–transduced neurons (Fig. 6, A and B). Reducing endoggresome formation via depletion of ARESTA component kinesin-1 (Fig. 4E) in neurons transduced with AAV-DJ-PrP^{PG14}-mCh resulted in calcium influx dynamics comparable to those of neurons transduced with AAV-DJ-PrP^{WT}-mCh (Fig. 6, A and B). Calcium intake was not altered in control *Kif5c*$^{-/-}$ neurons transduced with AAV-DJ-PrP^{WT}-mCh (Fig. 6, C and D).

To further determine the effect of PrP^{PG14} endoggresomes, the cell viability of WT versus *Kif5c*$^{-/-}$ neurons or versus neurons with reduced Vps41 and Arl8b function expressing PrP^{PG14}-mCh versus

Downloaded from https://www.science.org at University of Oxford on April 20, 2023

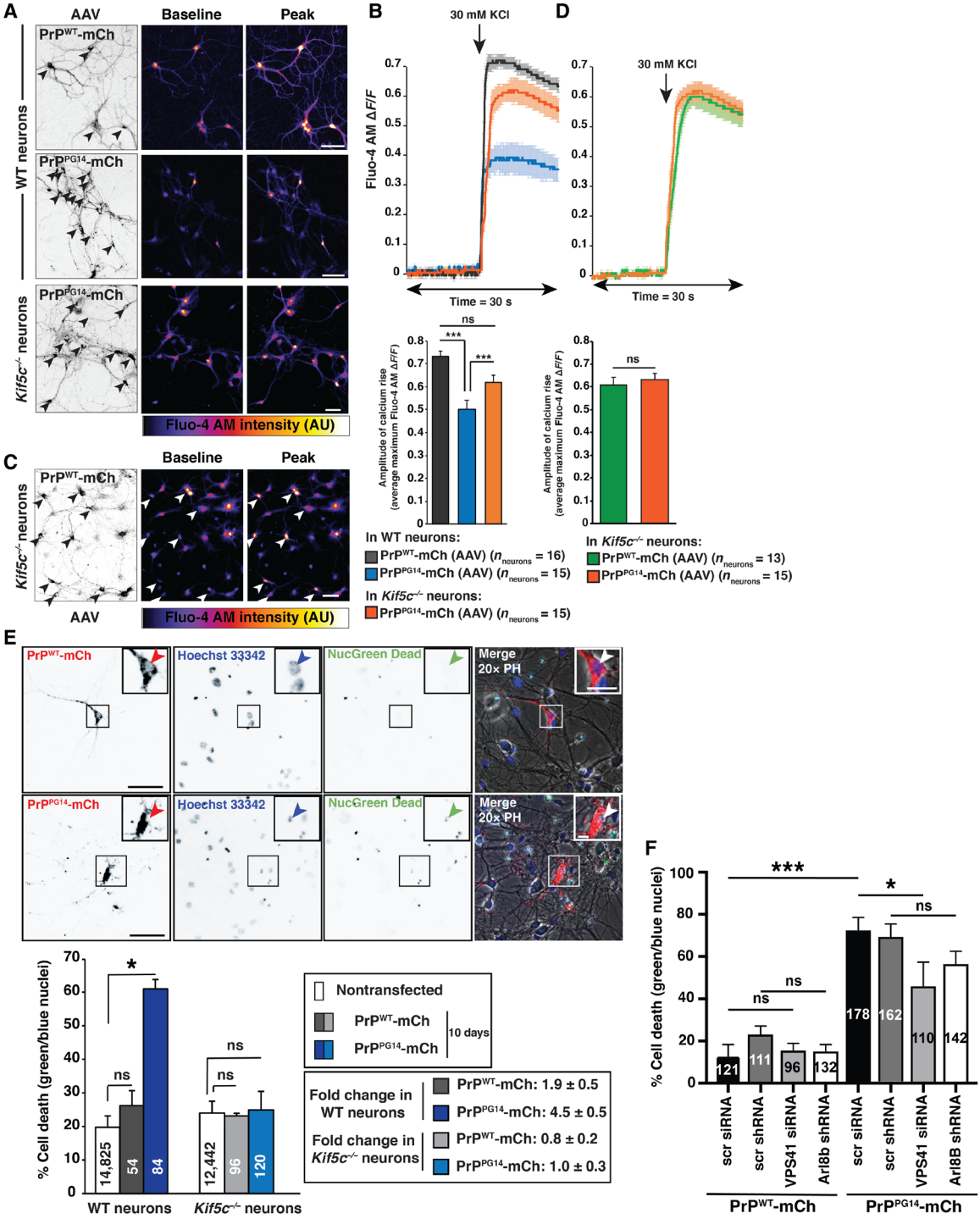


Fig. 6. ARESTA-dependent impaired calcium intake dynamics and decreased neuronal viability of PrP^{PG14} neurons. (**A** and **C**) Images of PrP^{WT}-mCh or PrP^{PG14}-mCh AAV-transduced WT or *Kif5c*$^{-/-}$ neurons (left). Arrowheads indicate the soma. Baseline and peak Fluo-4 AM intensities before (Baseline; middle) and after KCl treatment (Peak; right). Scale bars, 50 μm. (**B** and **D**) KCl-induced depolarization response curve from normalized Fluo-4 AM intensities from (A) and (C) (top). Arrows indicate the KCl treatment time. Average maximum amplitude of calcium rise (bottom). Bars represent means ± SEM. ***$P < 0.001$; Student's *t* test, Tukey's correction. (**E**) Images of neurons expressing PrP^{WT}-mCh or PrP^{PG14}-mCh and stained with Hoechst 33342 and NucGreen Dead (top). Arrowheads indicate nuclei. Insets are enlargements. Scale bars (main figures), 100 μm. Scale bars (insets), 20 μm. Percentage of cell death (bottom left). Cell numbers are inside the bars. Fold changes between indicated conditions (bottom right). Bars represent means ± SEM. *$P < 0.05$; Kruskal-Wallis test. PH, phase contrast. (**F**) Percentage cell death of neurons transduced with AAV8-PrP^{WT}-mCh or AAV8-PrP^{PG14}-mCh and treated with indicated siRNAs/shRNAs. $N = 21$ to 26 individual wells (96-well plate) analyzed per condition from three independent replicates. Cell numbers are inside the bars. Bars represent means ± SEM. *$P < 0.05$ and ***$P < 0.001$; Kruskal-Wallis test.

Downloaded from https://www.science.org at University of Oxford on April 20, 2023

PrP^{WT}-mCh was quantified. At 10 days after PrP^{PG14}-mCh transfection, when endoggresomes were prominent in WT axons (fig. S6D), expression of PrP^{PG14}-mCh resulted in a ~4.5-fold increase in neuronal death compared to nontransfected neurons or those expressing PrP^{WT}-mCh (Fig. 6E). Notably, neuronal death 10 days after transfection was not significantly different in *Kif5c*$^{-/-}$ neurons expressing PrP^{PG14}-mCh compared to those expressing PrP^{WT}-mCh or not transfected, suggesting that reduced endoggresome formation in KIF5C-depleted axons prevented neuronal death. Moreover, neuronal death was decreased when neurons were treated with shRNAs against Arl8b and with siRNAs against Vps41 (Fig. 6F). These data indicate that endoggresomes are neurotoxic and decrease neuronal viability, and inhibiting their formation by reducing the function of ARESTA pathway components abrogates these defects.

DISCUSSION

The accumulation of misfolded proteins inside axons is a prominent feature of neurodegenerative pathologies, including of prion diseases (*13*, *48*–*51*). By modeling the formation of intra-axonal mutant PrP aggregates involved in human prion disease (*24*), we uncovered endolysosomal pathways in mammalian neurons that sort post-Golgi mutant PrP vesicles into two divergent itineraries: one for immediate lysosomal degradation in the soma in a process resembling RESET (*21*, *22*), and the other toward the axon by an Arl8b/kinesin-1/HOPS ARESTA axis that ensures their axonal entry, fusion, and aggregation inside endolysosomes that we call endoggresomes (fig. S11). The opposing nature of these pathways appears to stem in large part from the highly polarized neuronal architecture, with an established highly degradative somatic compartment where mutant PrP is actively cleared versus an axonal compartment where ARESTA actively drives endoggresome formation and where limited lysosomal degradation sustains them. These distinct itineraries account for the enhanced vulnerability of axons versus the soma in generating aggregates and highlight the importance of investigating aggregate-driven mechanisms in neuronal systems. We posit that this soma versus axon compartmentalization also explains the differential susceptibility of neurons versus non-neuronal cells to the formation of aggregates and to aggregate-driven proteotoxicity that is characteristic of neurodegenerative disorders.

The discovery that mutant PrP undergoes degradation in the soma versus aggregation in the axon was unexpected because, in non-neuronal cells, essentially all misfolded PrP particles were shown to degrade via RESET, indicating that this pathway represents a bona fide and effective quality control and clearance mechanism for misfolded PrP (*22*). While the precise ratio of PrP^{PG14} particles undergoing immediate somatic degradation versus ARESTA-dependent aggregation in our neuronal system is unknown, our data show that expression of mutant PrP in neurons activates ER stress, followed by its delivery into lysosomes in the soma, suggesting that RESET-like degradative mechanisms are also at play in neurons. How the population of post-Golgi mutant PrP vesicles is selected for immediate degradation in the neuronal soma is unclear. A possible mechanism was shown for an artificial PrP mutant in non-neuronal cells, which triggers ER stress activation and traffics to the cell surface in a complex with ER chaperones and cargo receptors, and these associations appear to be critical tags for this itinerary toward degradation (*22*). Our observations showing that expression of mutant PrP robustly activates neuronal ER stress make this a plausible initial event that regulates the degradation via RESET, but this requires further investigation. Our data also show that a second population of post-Golgi mutant PrP vesicles skip somatic degradation but are instead funneled into the axon for aggregation by a regulated ARESTA process that depends on Arl8b recognition. Sorting of post-Golgi mutant PrP vesicles into the axon occurs by recruitment of kinesin-1/Vps41 (HOPS) by Arl8b, for association with ~80% of PrP^{PG14} vesicles. Arl8b is absent from RESET- and degradation-bound PrP^{PG14} vesicles, indicating that this complex could represent an axonal tag. Direct Golgi-to-axon cargo transport within the secretory pathway has been reported for other endosomal vesicles, including those carrying tropomyosin-related kinase B (TrkB) receptors (*52*). Moreover, Vps41 is known to be involved in direct Golgi-to-LE sorting (*53*), so this role appears conserved during interactions with mutant PrP vesicles. How Arl8b recognizes mutant PrP vesicles at the Golgi merits further investigation, but the mechanism could involve known Arl8b endosomal sorting regulators. A BORC [biogenesis of lysosome-related organelles complex (BLOC)-one related complex]-Arl8b complex that couples Arl8b to LEs has been shown to drive LE distribution uniquely toward the periphery of axons and not to dendrites (*45*, *54*), making it a candidate regulator of axonal entry of mutant PrP vesicles that merits further investigation. It is also plausible that other endolysosomal pathways could contribute to formation of aggregates inside axons, as the role of GTPases in the accumulation of mutant PrP is recognized in the literature. For example, genetic modulation of endosomal Rab11 results in the accumulation in the secretory pathway of mutant $PrP^{D177N/M128}$ associated with fatal familial insomnia (FFI), a prion disease (*55*). In addition, overexpression of Rab9 inhibits PrP^{Sc} accumulation in neuronal cell lines, pointing to a role of LEs in prion conversion (*56*), and inhibition of MVB inhibition of MVB maturation via reduction of Rab7 activity resulted in the significant reduction of PrP^{Sc} levels, suggesting that MVBs could be sites of PrP^{Sc} conversion (*15*).

The identification of endoggresomes highlights the distinct nature of these structures from previously characterized intracellular cytosolic aggregate assemblies, including aggresomes, insoluble protein deposits (IPODs), and juxtanuclear quality control compartments (JUNQs) (*14*, *57*). In comparison to these structures, our data show that endoggresomes form inside membranes instead of the cytosol, depend on kinesin-based anterograde transport instead of dynein-based retrograde movement for their formation, form distally in axons and remain at distal sites away from perinuclear domains, are not clearly targeted for degradation, and impart toxicity rather than being cytoprotective. The presence of endoggresomes inside endomembrane structures raises the possibility that further dynamic sorting events may occur during their lifetime. It will be important in future studies to explore the possible maturation and dynamics of endoggresomes as they reside inside axons for longer periods of time, including subcellular events occurring within and around these pathophysiological hubs that could delineate local impairments to axonal function.

The presence of membrane-bound endoggresomes as neurotoxic structures in axons is consistent with previous observations showing intralysosomal accumulations of PrP^{PG14} in dystrophic swollen neurites in hippocampal and cerebellar granule cell layer neurons in transgenic mice (*58*). The generality of endoggresomes and ARESTA within the prionopathies and to other neurodegenerative pathologies requires further investigation. However, our analyses indicate that,

Downloaded from https://www.science.org at University of Oxford on April 20, 2023

at least in the case of $PrP^{D177N/M128}$, the formation of intra-axonal aggregates also depends on kinesin-1C function, indicating that endolysosomal pathways might be a common aggregation mechanism of familial PrP mutations. Ultrastructural studies of human patient brains have shown the accumulation of other PrP mutants within dystrophic neurites inside endolysosomes (*13*, *48*–*51*, *59*), as well as in PrP^{Sc}-infected cell lines, and in brains of rodent models of familial and sporadic human PrP^{Sc} disease, suggesting that ARESTA may be a generalized mechanism that accounts for decades-long observations of endolysosomal assemblies in dystrophic neurites in prion brains, including those caused by aggregation of misfolded WT PrP (*19*, *48*, *50*, *59*–*61*). Despite the presence within endolysosomes, mutant PrP has also been reported to form aggresomes in the cytosol of neurons, where they were targeted for clearance by ER-associated degradation (ERAD) (*12*), although whether these represent toxic structures is debated (*61*). However, extensive characterization of the trafficking and turnover of many misfolded GPI-anchored PrP mutants showed that they are normally poor ERAD substrates, are not dependent on proteasomal degradation, and exit the ER for degradation in lysosomes (*62*). Thus, it is possible that RESET-like degradation in the soma and endoggresome formation in axons are favored itineraries by misfolded PrP as primary pathways, but a shift toward aggresome formation may occur when and if RESET and eventually ERAD are overwhelmed or compromised following extensive and sustained ER stress. Once formed in axons, endoggresomes persist because of poor local axonal clearance and impaired retrograde transport toward the soma that would promote its degradation. Consistent with our observations, defects in lysosomal maturation and degradation, as well as in retrograde axonal transport, have been documented in neuronal cell lines persistently infected with prions (*63*), as well as in prion-infected mouse models of disease (*64*).

The generality of endoggresomes and ARESTA to other neurodegenerative pathologies is a tantalizing possibility given the reliance of tau, the amyloid precursor protein (APP)/amyloid beta (Aβ), α-synuclein, and huntingtin on endosomal pathways for their processing and spread (*65*–*67*); thus, this prospect merits further investigation. Notably, enlarged endosomes represent a common endosomal "traffic jam" phenotype in Alzheimer's disease (AD) and are considered among the earliest neuronal lesions identified thus far (*68*–*71*). Genome-wide association studies (GWAS), whole exome and genome sequencing data, and multiple human genetics analyses have identified endolysosomal genes as risk hubs associated with early pathophysiological changes in AD (*72*, *73*). It will be key to determine whether the ubiquitous enlarged endosomes observed in early-stage neurodegenerative pathologies and associated with cellular toxicity could be regulated by the ARESTA pathway. As genetic modulation of ARESTA components resulted in changes in endoggresome densities with measurable consequences to the function and viability of neurons, the identification of the Arl8b/kinesin-1/HOPS axis provides an antiaggregation target that can modulate neuronal dysfunction and delineate the differential vulnerability of axons to aggregate-induced pathologies.

MATERIALS AND METHODS

Mouse lines

Our mouse protocols were reviewed and approved by the Institutional Animal Care and Use Committee (IACUC) at The Scripps Research Institute (Scripps Research), and all colonies were maintained following the guidelines recommended by the Department of Animal Resources at Scripps Research. C57BL/6 WT mice were obtained from Charles River Laboratories. Kinesin-1C–null ($Kif5c^{-/-}$) and KLC1-null ($Klc1^{-/-}$) mice were generated as described previously (*30*). $Kif5c^{-/-}$ mice were maintained as homozygotes and were backcrossed in the C57BL/6 background for at least six generations. $Klc1^{-/-}$ mice were bred as heterozygotes to generate homozygous pups. The conditional homozygous kinesin-1B floxed mouse ($Kif5b^{pflox/pflox}$) was generated as described previously (*38*).

Primary neuronal cultures

Primary hippocampal neuronal cultures were prepared as described previously (*30*). Briefly, hippocampi were dissected from P0 to P2 mouse neonates in cold Hanks' balanced salt solution (HBSS) (Gibco) supplemented with 0.08% D-glucose (Sigma-Aldrich), 0.17% Hepes, and 1% penicillin-streptomycin (Pen-Strep) (Gibco); filter-sterilized; and adjusted to pH 7.3. Dissected hippocampi were washed twice with cold HBSS (Gibco) and individually incubated at 37°C for 15 to 20 min in a sterile solution of 45 U of papain (Worthington), 0.01% deoxyribonuclease (DNase) (Sigma-Aldrich), 1 mg of DL-cysteine (Sigma-Aldrich), 1 mg of bovine serum albumin (BSA) (Sigma-Aldrich), and 25 mg of D-glucose (Sigma-Aldrich) in phosphate-buffered saline (PBS) (Gibco). Hippocampi were washed twice with Dulbecco's modified Eagle's medium (DMEM) (Gibco) supplemented with 10% fetal bovine serum (FBS) (Gibco) (preheated to 37°C) and disrupted by 10 to 12 cycles of aspiration through a micropipette tip. Dissociated neurons were then resuspended in warm DMEM (Gibco) documented with 10% FBS (Gibco) and plated in 24-well plates containing 12-mm glass coverslips pretreated with poly-L-lysine (50 μg/ml) (Sigma-Aldrich) in borate buffer [1.24 g of boric acid (Thermo Fisher Scientific) and 1.90 g of borax (Sigma-Aldrich) in 500 ml of cell culture–grade water, adjusted to pH 8.5, and filter-sterilized]. After 1 hour, the medium was replaced with Neurobasal-A medium (Gibco), supplemented with 2% B-27 (Gibco) and 0.25% GlutaMAX (Gibco). Primary neurons were maintained in an incubator at 37°C and in a 5.5% CO_2 atmosphere.

For quantitative live imaging of axonal transport, hippocampal neurons were plated in microfluidic chambers or in regular 24-well glass coverslips as described previously (*30*). For calcium imaging, hippocampal neurons were plated directly onto #1.5 glass-bottom dishes (MatTek) precoated with poly-L-lysine (50 μg/ml) (Sigma-Aldrich) in borate buffer.

Cell culture

N2a cells (American Type Culture Collection) were grown in DMEM (Gibco), supplemented with 10% FBS (Gibco) and 1% Pen-Strep (Gibco) in an incubator at 37°C and in a 5.5% CO_2 atmosphere. Cells were passaged twice a week to low confluency using 0.05% trypsin-EDTA (Gibco).

Design of DNA constructs

The MoPrP.Xho PrP^{WT}-EGFP and MoPrP.Xho PrP^{PG14}-EGFP constructs were a gift from D. Harris (Boston University) (*11*). All other constructs were generated using the In-Fusion HD Cloning Plus Kit (Clontech) for the final cloning of DNA fragments into the recipient vector. All polymerase chain reaction (PCR) amplifications were performed using the Phusion High-Fidelity DNA Polymerase (New England Biolabs). For the construction of MoPrP.Xho PrP^{WT}-mCh and MoPrP.Xho PrP^{PG14}-mCh constructs, EGFP was replaced

Downloaded from https://www.science.org at University of Oxford on April 20, 2023

with mCh using assembly PCR. Briefly, three individual PCRs were performed to amplify the (1) N terminus of PrP^{WT} or PrP^{PG14}, (2) C terminus of PrP, and (3) mCh including 20– and 22–base pair overlaps to the 3′ of (1) and 5′ of (2), respectively.

(i) The N terminus of PrP was amplified using the following primers: P1 N terminus (forward): 5′-CTAGTGGTACCTCGAGATGGCGAACCTTGGCTAC-3′ and P2 N terminus (reverse): 5′-CATGGTGGCGACCGGTGGATCC-3′.

(ii) The C terminus of PrP was amplified using the following primers: P3 C terminus (forward): 5′-TCCGGACTCAGATCTCGAGCTCAAG-3′ and P4 C terminus (reverse): 5′-AGCAGGAAGGCTCGAGTCATCCCACGATCAGGAA-3′.

(iii) mCh was amplified using the following primers: P5 mCh (forward): 5′-ATCCACCGGTCGCCACCATGGTGAGCAAGGGCGAGGA-3′ and P6 mCh (reverse): 5′-GCTCGAGATCTGAGTCCGGACTTGTACAGCTCGTCCATGCCG-3′.

PCR products (1 to 3) were gel-purified and subsequently stitched together (1 ng each) using a PCR performed without primers. After 20 cycles, PCR was interrupted; primers P1 (forward) and P4 (reverse) (0.5 μM each) were added to specifically amplify the complete product. The reaction was supplemented with 100 μM dNTPs (deoxynucleotide triphosphates) and 0.5 mM $MgCl_2$ and ran for 30 more cycles. Generation of MoPrP.Xho PrP^{WT}-mTagBFP2 and MoPrP.Xho PrP^{PG14}-mTagBFP2 constructs was done using the same assembly PCR strategy.

P5 mTagBFP2 (forward): 5′-ATCCACCGGTCGCCACCATGGTGTCTAAGGGCGAAGA-3′, and P6 mTagBFP2 (reverse): 5′-GCTCGAGATCTGAGTCCGGAATTAAGCTTGTGCCCCAGTT-3′.

Generation of the untagged MoPrP.Xho PrP^{WT} and MoPrP.Xho PrP^{PG14} was done using the same assembly PCR strategy.

(1) The N terminus of PrP was amplified using the following primers: P1 N terminus (forward): 5′-CTAGTGGTACCTCGAGATGGCGAACCTTGGCTAC-3′ and P2 N terminus (reverse): 5′-CATGGTGGCGACCGGTGGATCC-3′.

(2) The C terminus of PrP was amplified using the following primers: P3 C terminus (forward): 5′-CCGGTCGCCACCATGTCCGGACTCAGATCTCGAGCTCAAG-3′ and P4 C terminus (reverse): 5′-AGCAGGAAGGCTCGAGTCATCCCACGATCAGGAA-3′.

Generation of MoPrP.Xho PrP^{WT}-PAmCh and MoPrP.Xho PrP^{PG14}-PAmCh was done using the same assembly PCR strategy from PAmCh1-C1 (a gift from V. Verkhusha, Albert Einstein College of Medicine, New York) (*74*), which contains the following mutations: E26V/A58T/K69N/L84F/N99K/S148L/I165V/Q167P/L169V/I203R.

P5 PAmCh (forward): 5′-ATCCACCGGTCGCCACCATGGTGAGCAAGGGCGAGGA-3′ and P6 PAmCh (reverse): 5′-GCTCGAGATCTGAGTCCGGACTTGTACAGCTCGTCCATGCCG-3′.

To generate BBS-tagged constructs, MoPrP.Xho PrP^{WT}-mCh-BBS and MoPrP.Xho PrP^{PG14}-mCh-BBS, a 13–amino acid BBS tag (WRYYESSLEPYPD) was inserted at the Bsp EI site in the linker between mCh and C-terminal PrP sequence downstream of mCh. The following oligos were used to amplify the BBS sequence:

BBS (forward): 5′-CCGGATGGAGATACTACGAGAGCTCCCTGGAGCCCTACCCTGACT-3′ and BBS (reverse): 5′-TACCTCTATGATGCTCTCGAGGGACCTCGGGATGGGACTGAGGCC-3′.

The PCR products were annealed and cloned in PrP^{WT}-mCh in a pcDNA3.1 plasmid and PrP^{PG14}-mCh in a pcDNA3.1 plasmid. PrP^{WT}-mCh-BBS and PrP^{PG14}-mCh-BBS sequences were amplified by PCR and subcloned into the MoPrP.Xho vector. A similar strategy was used to generate the TCS-tagged constructs MoPrP.Xho PrP^{WT}-mCh-TCS and MoPrP.Xho PrP^{PG14}-mCh-TCS. The following oligos were used to amplify the six–amino acid TCS tag (LVPRGS) and to insert it at the Bsp EI site downstream of mCh:

TCS (forward): 5′-GCTGTACAAGTCCGGACTGGTGCCGCGCGGCAGCTCCGGACTCAGATCTC-3′ and TCS (reverse): 5′-GAGATCTGAGTCCGGAGCTGCCGCGCGGCACCAGTCCGGACTTGTACAGC-3′.

To generate the LAMP1-EGFP construct, red fluorescent protein (RFP) was replaced with EGFP in the plasmid LAMP1-RFP (a gift from E. Holzbaur, University of Pennsylvania). To generate SS-EGFP derived from NPY, the first 84 nucleotides corresponding to the SS of NPY were amplified from mouse brain complementary DNA (cDNA) and cloned between Bgl II and Bam HI sites in the pEGFP-N3 vector. To design EGFP-Rab5, EGFP-Rab7, and EGFP-Rab11a, the corresponding sequences were amplified from mouse brain cDNA and cloned between Xho I and Bam HI sites in the pEGFP-C1 vector (a gift from H. Lashuel, Swiss Federal Institute of Technology):

Rab5 (forward): 5′-TCTCGAGCTCAAGCTTTAATGGCTAATCGAGGAGCAACA-3′ and Rab5 (reverse): 5′-TAGATCCGGTGGATCCTCAGTTACTACAACACTGGCTTCTGG-3′, Rab7 (forward): 5′-TCTCGAGCTCAAGCTTATGACCTCTAGGAAGAAAGTGTTG-3′ and Rab7 (reverse): 5′-TAGATCCGGTGGATCCTCAACAACTGCAGCTTTCTG-3′, and Rab11a (forward): 5′-TCTCGAGCTCAAGCTTATGGGAACACGCGACGACGTA-3′ and Rab11a (reverse): 5′-TAGATCCGGTGGATCCGATGTTCTGACAGCACTGCACCTTT-3′.

T34N and Q75L mutations were introduced in pDEST47-$Arl8b^{WT}$-GFP plasmid (Addgene, #67404) using the QuikChange II XL Site-Directed Mutagenesis Kit (Agilent). To generate untagged Arl8b constructs, the Arl8b coding sequence was cloned in the pBI-CMV3 bidirectional promoter vector (Clontech). The KLC1-TAP plasmid was a gift from L. S. B. Goldstein (University of California San Diego). 2xmCh-KIF5C was designed by subcloning 2xmCh from KIF5C(1–560)-2xmChEF(C) (Addgene, #61664) in pCDNA3.1. Then, a full-length KIF5C sequence was amplified from pGFP-KIF5C (a gift from M. Peckham, University of Leeds) and cloned downstream of 2xmCh. To generate the SKIP 1 to 186 construct, the sequence of the first 186 amino acids was cloned in pcDNA3.1 at the Hind III and Bam HI site.

SKIP 1 to 186 (forward): 5′-CTAGCGTTTAAACTTAAGCTTATGGAGCCGGGGGAGGTGAAG-3′ and SKIP 1 to 186 (reverse): 5′-CCACACTGGACTAGTGGATCCGACCGAGCTGGGAAGGCGGTC-3′.

Transfections

Hippocampal neurons were transiently transfected using Lipofectamine 2000 (Thermo Fisher Scientific), following the manufacturer's instructions. DNA and Lipofectamine were diluted in nonsupplemented Neurobasal-A medium (Gibco). For most experiments, neurons grown on 12-mm coverslips in 24-well plates were transfected using 2 μl of Lipofectamine and 0.4 or 0.8 μg of DNA per well. Otherwise, neurons were grown in microfluidic chambers and transfected using 1.2 μl of Lipofectamine and 0.5 μg of DNA per chamber. Medium was changed 1 hour after transfection.

N2a cells were transiently transfected using Lipofectamine 2000 (Thermo Fisher Scientific) following the manufacturer's instructions.

Downloaded from https://www.science.org at University of Oxford on April 20, 2023

DNA and Lipofectamine were diluted in DMEM (Gibco). Experiments were performed in six-well plates, using 8 μl of Lipofectamine and 2 μg of DNA per well.

Adenovirus and AAV transductions

Cre-recombinase adenovirus transduction (Ad5CMVCre; University of Iowa) was performed as described previously (*30*). Briefly, hippocampal neurons isolated from kinesin-1B conditional KO mice ($KifB^{pflox/pflox}$) were treated at 6 days in vitro (DIV) with 0, 100, or 400 MOI of adenovirus, corresponding to 0, 5×10^6, or 2×10^7 plaque-forming units (PFUs), respectively. Neurons were incubated for 2 hours with the virus and then washed twice with Neurobasal-A medium (Gibco) containing 2% B-27 (Gibco) and 0.25% GlutaMAX (Gibco). Neurons were transfected with fluorescently labeled PrP constructs at 9 DIV and imaged at 11 DIV.

PrP^{WT}-mCh and PrP^{PG14}-mCh were cloned into the pAAV-hSyn-MCS backbone between the Bam HI and Eco RI sites (a gift from T. Golde, University of Florida).

Forward: 5′-CCGCGAGCTCGGATCCATGGCGAACCTTGGCTACTG-3′ and reverse: 5′-CTTCCTGATCGTGGGATGAGAATTCCTCGAGCAGC-3′.

AAV was made using the AAV-DJ Helper Free Packaging System (Cell Biolabs) using published protocols (*75*). Hippocampal neurons growing in 24-well plates were treated overnight with 4 μl of the viral stock at 7 DIV and imaged at 12 DIV.

Knockdown using shRNAs and siRNAs

To knockdown Arl8b from neurons, the following 21-mer shRNA previously validated inserts were cloned separately in the pLKO.3G vector (Addgene, plasmid #14748): scrambled shRNA (CCTAAGGTTAAGTCGCCCTCG), Arl8b shRNA #1 (CCTCTCGAAATGAACTGCATA), and Arl8b shRNA #3 (CGAGGAGTCAATGCAATTGTT). Validation of shRNA constructs for the reduction of Arl8b was done by transfecting mouse N2a cells at 40% confluency with pLKO3.G-Arl8b shRNAs #1 and #2 either separately or together using Lipofectamine 2000 (Invitrogen). Dynein was knocked down by transfection of neurons with a previously validated DHC1 shRNA lentiviral construct (GTGATGCCATACGAGAGAA). A scrambled shRNA construct was used as control (GCACACGTATCGACGTATC) (*30*). Transfection rates were >80% and were ascertained by counts of GFP fluorescence on cell bodies. shRNAs were expressed for 48 or 72 hours before harvesting, lysed in radioimmunoprecipitation assay (RIPA) buffer, and evaluated by Western blot using rabbit anti-Arl8b (ProteinTech) and anti–α-tubulin as a loading control (Sigma-Aldrich). N2a cells were harvested at the same time points for reverse transcription PCR generation using an iScript cDNA Synthesis kit (Bio-Rad), and quantitative PCR (qPCR) was performed using the FastStart Universal SYBR Green Mastermix (Roche) to test for reduced Arl8b mRNA levels.

To knock down VPS41 from neurons, we used the ON-TARGETplus SMART pool siRNA from Dharmacon. VPS41 siRNA #1: CCAAAGGAACAUUAAACGA, VPS41 siRNA #2: GUUUGUACUGGCGGGAAA, VPS41 siRNA #3: GGAGAAGAAUUUCACGAGA, and VPS41 siRNA #4: UGACAUAAGUCUUCGCCCA. Nontargeting siRNA #1: UGGUUUACAUGUCGACUAA was used as a control.

Live imaging microscopy

Live imaging of soma and axons of hippocampal neurons was done on 9- to 15-DIV neurons, 2 days after transfection, except otherwise indicated. In some experiments, fluorescently labeled PrP constructs were cotransfected with soluble EGFP or mCh constructs to visualize the neuronal morphology and facilitate the determination of axonal polarity. Coverslips (12 mm) were transferred and flipped onto 35-mm glass-bottom dishes (MatTek) containing 2 ml of Neurobasal-A medium (Gibco), containing 2% B-27 (Gibco) and 0.25% GlutaMAX (Gibco) medium. Neurons were imaged using a Nikon Ti-E Perfect Focus inverted microscope equipped with a total internal reflection fluorescence microscopy (TIRFM) setup, with an Andor iXon + DU897 EM camera, and a 100×/1.49 numerical aperture (NA) oil objective. Solid-state 405-, 488-, and 561-nm lasers were used for detecting mTagBFP2, GFP, and mCh, respectively. Lasers were positioned at varying angles for pseudo-TIRFM (pTIRFM) acquisition. Transfection rates were ~1%, which enabled imaging of individual neurons.

Time-lapse movies of fast vesicular transport in axons were 15 s long and collected at a frame rate of 10 frames/s (10 Hz). Movies of aggregate/endoggresome transport were 5 min (300 s) long and collected at a frame rate of 1 frame/s (1 Hz). Movies of LAMP1-EGFP vesicular transport were 1 min long and collected at a frame rate of 5 frames/s (5 Hz). For all images and movies acquired, the exposure time was set to 100 ms. Pixel size was 0.16 μm. Plates with cultured neurons were maintained at 37°C and 5.5% CO_2 throughout the total imaging period. All axonal transport movies were taken in a central region of the axon, at least 150 μm away from both the soma and the axon tip.

For GFP/mCh axonal cotransport analyses, images were acquired using a Nikon near-simultaneous two-color LAMBDA 10-3 optical filter switch imaging setup. Exposure times were 75 ms, and 488/561-nm images were collected with a 50-ms delay. For live imaging of axonal transport, high-resolution imaging of vesicle cotransport was done using a high frame rate: 30 s long and at 5 frames/s (5 Hz). Low–frame rate cotransport movies were obtained for analyses of endoggresome transport: 5 min (300 s) long and collected at 1 frame/s (1 Hz). Time-lapse imaging was performed during 5 min at a frame rate of 5 frames/s.

Fixation and immunofluorescence

Neurons were fixed with 4% paraformaldehyde (PFA; Electron Microscopy Services) containing 4% sucrose (Sigma-Aldrich) for 30 min at 37°C. Cells were washed once in 50 mM glycine in PBS and three more times in PBS. If applicable, cells were permeabilized by incubating the coverslips in 0.1% Triton X-100 (Sigma-Aldrich) in PBS for 8 to 10 min followed by three washes with PBS. Coverslips were incubated in blocking solution [10% immunoglobulin G (IgG)–free BSA and 5% donkey serum or goat serum in PBS; Jackson ImmunoResearch] for 30 min at room temperature (RT), followed by incubation with primary antibodies in blocking solution for 1 hour at RT or overnight at 4°C. After three washes in PBS, neurons were incubated with secondary antibodies in blocking solution for 1 hour at RT or overnight at 4°C. If applicable, neurons were counterstained with 300 nM 4′,6-diamidino-2-phenylindole (DAPI) (Thermo Fisher Scientific) for 5 min. After three washes in PBS, coverslips were washed once in H_2O and mounted in ProLong Diamond antifade reagent (Thermo Fisher Scientific).

The following antibodies were used for immunofluorescence: mouse anti-KDEL (1:100; Santa Cruz Biotechnology), rabbit anti-GM130 (1:100; Abcam), goat anti-mouse CatB (1:40; R&D Systems), rabbit polyclonal IgG anti-mCh (1:100; Gentex), recombinant Fab

Downloaded from https://www.science.org at University of Oxford on April 20, 2023

anti-PrP (1:200; clone HuM-D13) (*76*), rabbit anti-Arl8b (1:200; ProteinTech), and mouse anti-Vps41 (1:100; clone D-12, Santa Cruz Biotechnology). The following antibodies were used for Western blot: rabbit anti-Arl8b (1:200; ProteinTech) and mouse anti–α-tubulin (1:500; Sigma-Aldrich).

Correlative fluorescence and scanning electron microscopy

Hippocampal neurons were plated in microfluidic chambers and cotransfected at 8 DIV with PrP^{PG14}-mCh and soluble EGFP. Two days after transfection, the positions of transfected neurons inside the microfluidic chamber were mapped using live fluorescence microscopy with a Nikon S Plan Fluor ELWD 20×/0.45 [infinity]/0-2 objective. Neurons were fixed in ice-cold 2.5% glutaraldehyde in 0.1 M Na cacodylate buffer (pH 7.3), and 1% trehalose was added before the removal of chamber to expose cells for washing with buffer. Neurons were fixed in 1% osmium tetroxide, washed thoroughly with distilled water, and dehydrated in a graded ethanol series. Samples were immersed in 100% hexamethyldisilazane (HMDS) for 3 min and allowed to dry before mounting on a stub with carbon tape. Samples were sputter-coated with iridium at 10 μA to a thickness of approximately 5 nm [Electron Microscopy Science (EMS) model 150T S]. The coverslips were then examined on a Hitachi S4300 scanning electron microscope (Hitachi High Technologies America Inc., Pleasanton, CA) at 5 kV with settings adjusted according to needs.

Correlative fluorescence and S3EM

Hippocampal neurons were plated on 35-mm gridded #1.5 glass-bottom dish (Cellvis) pretreated with poly-L-lysine (50 μg/ml) (Sigma-Aldrich) in borate buffer and transfected at 8 DIV with PrP^{PG14}-mCh using Lipofectamine 2000 (Thermo Fisher Scientific). Two days after transfection, neurons were first imaged using live fluorescence and phase-contrast microscopy with a Nikon S Plan Fluor ELWD 20×/0.45 [infinity]/0-2 objective to map the location of transfected neurons on the grid. PrP^{PG14}-mCh endoggresome sites were imaged using superresolution radial fluctuation (SRRF) microscopy settings (*77*) (20 frames/s, 100 frames) with a pTIRFM setup, with an Andor iXon + DU897 EM camera, and a 100×/1.49 NA oil objective. Samples were fixed on the gridded culture dish while live imaging by carefully mixing an equal volume of 2× EM fixative (5% glutaraldehyde and 4% PFA in 0.1 M cacodylate buffer with 3 mM $CaCl_2$) warmed to 37°C with 2 ml of Neurobasal-A medium (Gibco), containing 2% B-27 (Gibco) and 0.25% GlutaMAX (Gibco). Samples were immediately removed from the microscope, fixative medium solution was discarded, and cells were left in fresh ice-cold 1× fixative for 90 min and rinsed three times with ice-cold 0.1 M cacodylate buffer with 3 mM $CaCl_2$. Coverslips were post-fixed and stained with 1.5% reduced osmium for 35 min, rinsed five times with MilliQ water, and stained again with 1% aqueous uranyl acetate for 1 hour at RT before serial dehydration with graded solutions of ice-cold ethanol in water. Samples were then fully dehydrated in two 10-min rinses of anhydrous ethanol at RT before infiltration with Durcupan resin. After 3:1, 1:1, and 1:3 ethanol-resin 2-hour infiltration steps, the samples were infiltrated with pure resin for 2 hours before another change of fresh pure resin and left overnight at RT. A final change of fresh resin was performed, and infiltrated samples were polymerized for 48 hours at 65°C. Coverslips were dissolved by immersion in concentrated hydrofluoric acid. Correlative light-electron microscopy was achieved using laser-branded fiducials in a thinly embedded sample, as previously described (*78*). Briefly, regions of interest (ROIs) that included SRRF-imaged PrP^{PG14}-mCh axon segments were identified by their grid positions and dark osmium staining. ROIs were marked using the cutting laser of a Zeiss PALM laser cutting microscope to provide orientation and fiducial guides for further trimming and ultramicrotomy. ROIs were carefully identified under a dissecting microscope and excised from the coverslip using a jeweler saw and a scalpel, with careful thought given to the future block-face orientation. The small (1 mm by 2 mm by 2mm) sample block was glued to a blank resin block such that the ROIs were orthogonal to the cutting plane and approximately 100 μm from the cutting surface. Laser marks on the block face helped to identify the location of the ROI using the ultramicrotome optics. The block was carefully trimmed using a 90° diamond trimming knife (Diatome). About 200 serial sections were collected in total over four chips.

The chips were mounted on aluminum stubs using double-sided carbon sticky tape and loaded into a Zeiss Sigma VP scanning electron microscope. Chip mapping and the imaging of serial sections were facilitated by SmartSEM (Zeiss) and Atlas 5 (Fibics) software packages. Maps of all of the serial sections on the silicon chips were collected at 500 nm per pixel. Laser marks could be identified in the resin boundary at low magnification, demarcating the ROI in each section. The ROI of the axon segment containing the PrP^{PG14}-mCh endoggresomes was identified and captured across 40 serial-section scanning electron micrographs. ROIs were imaged at 2 nm per pixel using an electron backscatter detector (Gatan). In high-vacuum mode, a 3-keV beam in high-current mode with a 30-μm aperture at a working distance of 9 mm was found to produce signal from which we could resolve membrane and organelle (e.g., microtubule) ultrastructure. Sections were aligned using Photoshop (Adobe) and elastic alignment functions embedded in Fiji [National Institutes of Health (NIH)]. A central orthogonal projection (i.e., *x-z*) of the S3EM data was used to correlate the SRRF-processed data and produce overlay. Sections were sampled from throughout the aggregate and nonaggregate sites with reference to the correlated volume.

Hippocampal neuron live assays with drug treatments and fluorescent dyes

To retain PrP^{PG14} in the ER, BFA (BioLegend) was applied at 5 μg/ml at the same time as PrP^{WT}-mCh or PrP^{PG14}-mCh transfections and incubated for 2 to 6 hours. Neurons were washed two to three times with Neurobasal-A medium (Gibco) before fixation.

For characterization of PrP^{PG14} at the cell surface of the soma or axons, neurons grown in 24-well plates were transfected with a PrP^{PG14}-mCh-BBS construct for 1 hour. Neurons were treated with BTX-a647 (Molecular Probes) by applying it to the medium and as described previously (*32*). Briefly, we pretreated neurons for 1 hour with 100 μM tubocurarine hydrochloride (Sigma-Aldrich) to eliminate nonspecific binding to other receptors (*32*). Neurons were then incubated with BTX-a647 (7 μg/ml) in the medium, during indicated times and at indicated temperatures. To inhibit clathrin-mediated endocytosis, 80 μM dynasore (Sigma-Aldrich) was added 30 min before BTX-a647 treatment and kept during the labeling. DMSO was used as a control. Internalized PrP^{PG14} particles were defined as PrP^{PG14}-mCh-BBS particles that were both positively labeled with BTX-a647 and actively transporting within axons. Quantification of internalization in the presence or absence of dynasore was performed by measuring the proportion of BTX-a647–positive particles that were actively transporting.

Downloaded from https://www.science.org at University of Oxford on April 20, 2023

To characterize PrP axonal degradation in axons, neurons transfected with PrP^{WT}-mCh-BBS or PrP^{PG14}-mCh-BBS were incubated with BTX-a647 for 10 min, followed by a wash-off. Axons where imaged at 1 and 24 hours after BTX-a647 treatment. PrP axonal degradation was determined by drawing ROIs around the axons and by image analysis following integration of the total gray value.

PrP surface expression pattern in axons was analyzed by incubating neurons with BTX-a647 during 10 min at 4°C before fixation. LysoTracker Green (Molecular Probes) was incubated at 50 nM, 1 to 2 hours before live imaging. Magic Red from the Cathepsin B Assay (ImmunoChemistry Technologies) was incubated for 1 to 2 hours before live imaging. DMSO stock (260×) of Magic Red dye was diluted in sterile diH_2O, and 10 µl was applied onto neurons in each well containing 250 µl of Neurobasal-A medium (Gibco). BafA1 (Sigma-Aldrich) was incubated at 10 nM during 6 hours. Longer incubation times affected neuronal survival. DMSO was used as a control.

For the characterization of PrP^{PG14} lysosomal degradation in the soma, hippocampal neurons were transfected with PrP^{PG14}-mCh or PrP^{WT}-mCh. One day after transfection, neurons were treated with 10 nM BafA1 for 6 hours and 50 nM LysoTracker Green for 1 hour before live imaging of the soma. PrP accumulation was determined by drawing ROIs around the soma and integration of the total gray value.

For characterization of PrP^{PG14} cleavage at the cell surface, hippocampal neurons were transfected with PrP^{PG14}-mCh-TCS or PrP^{PG14}-mCh. Neurons were incubated with or without thrombin protease (5 U/ml) (Sigma-Aldrich) 2 hours after transfection. This treatment was maintained for 48 hours. We did not observe any effect of thrombin treatment (5 U/ml) on neuronal survival.

For characterization of (in)dependence between direct and indirect ARESTA, hippocampal neurons were transfected with PrP^{PG14}-mCh-TCS and $Arl8b^{WT}$-GFP. Neurons were incubated with or without thrombin protease (5 U/ml) (Sigma-Aldrich) 24 hours after transfection. This treatment was maintained for 24 hours. We did not observe any effect of thrombin treatment (5 U/ml) on neuronal survival.

Photoactivation of PrP^{PG14}-PAmCh

Neurons were cotransfected with EGFP-Rab7 and PrP^{PG14}-PAmCh. Two days after transfection, PrP^{PG14}-PAmCh was photoactivated using a 405-nm laser burst pointed at the cell body (40% laser power, 3-s exposure), and neurons were imaged using live fluorescence microscopy. The fate of single photoactivated particles and their delivery into axons was followed for 60 min by taking 5 × 5 stitching images every 5 min.

PK resistance assay

N2a cells were transfected with PrP^{WT}-mCh or PrP^{PG14}-mCh (pcDNA3.1 vector) and lysed 48 hours after transfection in PBS containing 0.5% NP-40 (Sigma-Aldrich), 0.5% sodium deoxycholate (Sigma-Aldrich), 0.2% sarkosyl (Sigma-Aldrich), and 0.5% Triton X-100. Proteins in 500 µg of lysate were digested using PK (0, 0.05, 0.1, 0.5, 1, or 5 µg/ml; Thermo Fisher Scientific) for 30 min at 37°C. The reaction was blocked by adding freshly prepared phenylmethylsulfonyl fluoride (PMSF) (0.8 mg/ml) (TCA; Sigma-Aldrich). The equivalent of 20 µg of each sample was analyzed by immunoblotting using an anti-PrP–specific antibody (D13) (a gift from D. Burton, Scripps Research). Samples corresponding to 1 and 5 µg/ml of PK were also precipitated using trichloroacetic acid (TCA; Sigma-Aldrich) to concentrate the proteins. The equivalent of 120 µg of each sample was analyzed by immunoblotting.

The PK assay of the sucrose gradient–floated fraction was done on 20 µg of an 8/35% sucrose-floated vesicle fraction that was digested using PK (0, 0.5, 1, 2, or 5 µg/ml) for 30 min at 37°C. The digestion reaction was blocked by addition of freshly prepared PMSF (0.8 mg/ml) (Sigma-Aldrich). The sample was analyzed by immunoblotting with Fab anti-PrP (1:200; clone Hum-D13).

Detergent insolubility assay

A detergent insolubility assay was used following previously established protocols (*60*). Briefly, N2a cells were transfected with PrP^{WT}-mCh or PrP^{PG14}-mCh constructs using Lipofectamine 2000 (Thermo Fisher Scientific). Two days after transfection, membrane-bound vesicles were isolated in a sucrose gradient vesicle floatation assay. Vesicles in the 8/35% sucrose fraction were lysed in a buffer containing 150 mM NaCl, 50 mM tris-HCl (pH 7.5), 0.5% Triton X-100, and 0.5% sodium deoxycholate, supplemented with protease inhibitors [pepstatin and leupeptin (1 mg/ml), 0.5 mM phenylmethylsulfonyl fluoride, and 2 mM EDTA). Lysates were centrifuged for 5 min at 16,000*g* to remove cellular debris, followed by ultracentrifugation at 265,000*g* for 40 min to pellet detergent-insoluble protein. Fifteen micrograms of both pellet and supernatant fraction was analyzed by immunoblotting using Fab anti-PrP (1:200; clone Hum-D13).

SDS-PAGE and immunoblotting

Neuronal lysates were resuspended in Laemmli buffer and resolved by SDS–polyacrylamide gel electrophoresis (SDS-PAGE) in 8 to 12% polyacrylamide gels. Proteins were electrotransferred onto polyvinylidene difluoride (PVDF) membranes. Membranes were blocked for 30 min at RT in tris-buffered saline (TBS) containing 0.1% Tween 20 and 5% dry milk. They were incubated overnight at 4°C with primary antibodies diluted in TBS-Tween-milk. After six washes in TBS-Tween, the membranes were further incubated for 1 hour at RT with fluorescent secondary antibodies (LI-COR) diluted in TBS-Tween-milk. After six more washes in TBS-Tween, the membranes were imaged using LI-COR Odyssey imaging system using recommended antibodies.

Sucrose gradient vesicle flotations

N2a cells grown in 150 mm by 20 mm dishes were transfected with PrP^{WT}-mCh or PrP^{PG14}-mCh constructs using Lipofectamine 2000 (Thermo Fisher Scientific). Cells were washed twice with PBS (Gibco) and harvested from each 150-mm dish using 10 ml of PBS. Cells were harvested and resuspended in 0.5 ml of a solution composed of 8% (w/v) sucrose (Sigma-Aldrich) in distilled water, 3 mM imidazole (Sigma-Aldrich), and 1× cOmplete Protease Inhibitor (Millipore-Sigma). Resuspended cells were homogenized using a 25-gauge syringe needle attached to a 1-ml syringe (Sigma-Aldrich); samples were homogenized by 20 passages. A 100-µl fraction of the resulting homogenate was collected (fraction 1), and the remainder was centrifuged at 3000*g* using a Sorvall RT7 Plus benchtop centrifuge (Thermo Fisher Scientific). The supernatant was collected, and the pellet was again resuspended in a minimal volume of 8% sucrose solution and centrifuged as above. The two rounds of supernatant fractions were pooled to constitute the post-nuclear supernatant (PNS) (fraction 2). The PNS in 8% (w/v) sucrose was mixed with a

Downloaded from https://www.science.org at University of Oxford on April 20, 2023

solution of 70% (w/v) sucrose in distilled water, 3 mM imidazole, and 1× cOmplete Protease Inhibitor to constitute a ~40% sucrose solution containing the PNS.

The PNS was bottom-loaded on a sucrose step gradient consisting of 35 and 8% sucrose. After centrifugation at 41,500 rpm for 2 hours at 4°C, on an Optima LE-90K SW50.1 rotor (Beckman Coulter), fractions were collected, including the 8/35% (8/35) sucrose fraction–containing membrane-bound floated vesicles. Protein concentration of fractions were measured using a Pierce BCA protein assay kit (Thermo Fisher Scientific), run on SDS-PAGE, and analyzed by Western blot using Fab anti-PrP (1:200; clone Hum-D13), anti-mCh polyclonal antibody raised in rabbit (1:1000) (Genetex), or anti-Rab7 monoclonal antibody raised in rabbit (1:1000; clone D95F2 XP, Cell Signaling Technology).

Calcium imaging

Hippocampal cultures from WT (C57BL6) or *Kif5c*$^{-/-}$ mice were plated directly on #1.5 glass-bottom dishes (MatTek), at a density of 8 to 15 neurons/420 μm^2 of field of view. Cultures were loaded with 2 μM Fluo-4 AM (Thermo Fisher Scientific) in Neurobasal-A medium supplemented with B-27 without phenol red for 30 min at 37°C in a 5.5% CO_2 atmosphere, as recommended by an Invitrogen protocol. Cultures were washed three times and incubated for another 30 min in the B-27–supplemented Neurobasal-A without phenol red before imaging to allow complete de-esterification of intracellular AM esters. Before and during imaging, a calcium imaging buffer [140 mM NaCl, 5 mM KCl, 2 mM $CaCl_2$, 0.8 mM $MgCl_2$, 10 mM glucose, and 10 mM Hepes (pH 7.4)] was applied. Neurons were imaged using a Nikon S Plan Fluor ELWD 20×/0.45 [infinity]/0-2 objective in a temperature-controlled enclosure set to 37°C. Epifluorescence excitation was provided by a metal halide–doped mercury arc lamp (Nikon Intensilight). High temporal-resolution images (5 frames/s) were taken for 1 min with an electron multiplying charge coupled device camera (EM-CCD; Andor iXon3 897). Fluo-4 AM fluorescence were collected using Chroma filters (ET-GFP [ET470/40x T495lpxr, ET525/50m]). Depolarization was induced by applying KCl to a final concentration of 30 mM at the 30-s time point during acquisition. Still images of PrP^{WT}-mCh or PrP^{PG14}-mCh of the same region were collected using ET-DsRed [ET545/30x, T570lp, ET620/60m] Chroma filter.

Cell death assay and imaging

ReadyProbes Cell Viability Imaging Kit (Blue/Green) (Thermo Fisher Scientific) was used to quantify cell death. Briefly, two drops of NucBlue Live reagent (Hoechst 33342) and two drops of NucGreen Dead reagent were added onto 10- to 14-DIV hippocampal neurons grown on the coverslips containing 1 ml of Neurobasal-A medium (Gibco), supplemented with 2% B-27 (Gibco) and 0.25% GlutaMAX (Gibco). Neurons were incubated at 37°C for 30 min before fixation with 4% PFA (Electron Microscopy Services) containing 4% sucrose (Sigma-Aldrich) for 30 min at 37°C. Cells were washed once in 50 mM glycine in PBS and three more times in PBS before mounting in ProLong Diamond antifade reagent (Thermo Fisher Scientific). Fixed neurons were imaged using a Nikon S Plan Fluor ELWD 20×/0.45 [infinity]/0-2 objective. Epifluorescence excitation was provided by a metal halide–doped mercury arc lamp (Nikon Intensilight). Blue and green nuclei staining were collected using UV-2E/C [AT350/50x, T400lp, ET460/50m] and ET-GFP [ET470/40x, T495lpxr, ET525/50m] Chroma filters, respectively. PrP^{WT}-mCh or PrP^{PG14}-mCh fluorescence were collected using the ET-DsRed [ET545/30x, T570lp, ET620/60m] Chroma filter.

Quantification and statistical analysis

Neuronal soma image analysis

All images of neuronal soma were processed in ImageJ (NIH). Rolling-ball background fluorescence correction was applied to all images. 3D deconvolution was applied using synthetic Gaussian point spread function (PSF) and Richardson-Lucy algorithms in DeconvolutionLab2 (*79*). All images and line scan fluorescence intensity graphs were displayed as maximum intensity projection.

Analysis of axonal transport dynamics from time-lapse movies

Axonal transport analysis was performed using the custom-made and previously validated KymoAnalyzer ImageJ package of macros (*29*). KymoAnalyzer is freely available for download from our laboratory website (www.encalada.scripps.edu/kymoanalyzer), and a detailed description of the software and the definition of all parameters calculated are available in the website and in our publication (*29*). Briefly, kymographs were generated from time-lapse movies. Particle trajectories were manually assigned from the kymograph images. Track and segment-related parameters were automatically calculated by KymoAnalyzer.

Colocalization and cotransport quantifications

We determined colocalization by merging line scan intensity profiles of different channels in the same graph and quantifying the average number of peaks that overlapped between different channels. For cotransport analyses, individual and merged color kymographs were generated, and quantification of the average number of tracks that overlapped between each pair of vesicular cargos was analyzed. Vesicle tracks were sorted in anterograde, retrograde, and stationary populations, or as indicated for individually analyzed parameters. Endoggresome tracks were sorted in mobile and stationary populations or as indicated for individually analyzed parameters.

Definition of PrP^{PG14} vesicles versus aggregates/endoggresomes

We defined PrP^{PG14} endoggresomes/aggregates by (i) their biochemical profile, a definition that we used in biochemical assays, or by (ii) their fluorescence intensity profile in imaging assays, when PrP^{PG14} was tagged with a fluorescence protein (PrP^{PG14}-mCh or PrP^{PG14}-EGFP), or untagged, as recognized with antibodies against PrP, a definition that we used for axonal transport and axonal density analyses. First, biochemically, PrP^{PG14} endoggresomes were defined as done previously (*11*), as PrP^{PG14} protein that is recognized on an SDS-PAGE gel compared to PrP$^{C/WT}$ by their (i) detergent insolubility and (ii) limited PK digestion at PK concentrations below 1 to 2 μg/ml compared to PrP^{WT} (*25*, *27*, *80*). Second, in fluorescence imaging assays for axonal transport analyses, fluorescently tagged (mCh or EGFP) PrP^{PG14} endoggresomes/aggregates were recognized as those PrP^{PG14} particles whose transport was slow (<0.5 μm/s) in movies taken at 1 Hz for 5 min. At this temporal resolution, PrP^{PG14}-mCh or PrP^{PG14}-EGFP vesicles were too faint and moved too fast (0.5 to 4 μm/s) to be tracked accurately. Instead, PrP^{PG14}-mCh– or PrP^{PG14}-EGFP–tagged vesicles were identified as those PrP^{PG14} particles actively moving at speeds that resembled those of PrP^{WT}-mCh or PrP^{WT}-EGFP vesicles (between 0.5 and 3.0 μm/s) when imaged at 10 Hz (imaged for 15 s). To quantify densities of PrP^{PG14} endoggresomes/aggregates in fixed axons, still images were taken of axons or neurons transfected with fluorescently labeled

Downloaded from https://www.science.org at University of Oxford on April 20, 2023

PrP^{PG14} constructs (mCh or EGFP) or transfected with untagged PrP^{PG14} and stained by antibodies against PrP. Quantification of the maximal gray intensities of five small PrP^{PG14} vesicle puncta was done for each image analyzed, after subtracting the fluorescence background using the Brightness and Contrast tool of ImageJ. PrP^{PG14} endoggresome/aggregates were defined as particles that displayed maximal gray fluorescence intensities 1.5 times above that of the average maximal gray fluorescence intensities of five PrP^{PG14} vesicles in the same axon. The particles still present in the image after thresholding were considered as endoggresomes. Axon length was measured using the polyline tool of ImageJ. Endoggresome density was expressed as the average number of aggregates per 100 μm of the axon length.

Calculation of densities of LysoTracker-positive particles

For LysoTracker-positive vesicle densities, we measured the axon length using the polyline tool of ImageJ and quantified all the particles labeled by LysoTracker Green along this line. Densities were plotted per 100 μm of the axon length.

ERSE-mCh and Vps41 fluorescence quantification

Neurons were cotransfected with the pEGFP-C1, MoPrP.Xho PrP^{WT}-EGFP or MoPrP.Xho PrP^{PG14}-EGFP, and the transcriptional ER stress reporter ERSE-mCh (a gift from L. Plate, Vanderbilt University) (*46*). Increases in the activity of ER stress pathways activate ERSE, and soluble mCh is synthesized. Total fluorescence intensities (gray values; arbitrary unit) of ERSE-mCh and Vps41 were quantified using ImageJ, using circular ROIs of 30 μm in diameter centered around the soma. The polyline tool was used to draw ROIs spanning the entire axonal length.

Calcium imaging analysis

ROIs were marked around the soma of neurons expressing PrP^{WT}-mCh or PrP^{PG14}-mCh, and we measured the average fluorescence for each ROI at a given time point. The average Fluo-4 AM fluorescence over time was collected using an ImageJ Time Series Analyzer V3 plugin and normalized to $\Delta F/F$ by subtracting the fluorescence intensity of each time point (F) to an average fluorescence before addition of KCl (F_0) and divided by F. Rolling-ball background fluorescence correction was applied to all images before fluorescence intensity analysis.

Cell death quantitation

All image processing was done in ImageJ. The total number of NucBlue Live–positive nuclei (blue channel) was determined as follows: Background fluorescence was corrected on each image by applying a Gaussian blur filter with a radius of 12 to a duplicate of each image and subtracting this filtered image from the original. An automatic threshold was applied to the resulting images using the Li algorithm followed by a watershed filter, both in ImageJ. Total nuclei were counted using a minimum size threshold of 15 and circularity of 0.10. The total amount of NucGreen Dead–positive nuclei (green channel) were determined using the same method, now using a Gaussian blur filter with a radius of 10, thresholding using the Yen algorithm available in ImageJ, and nuclei determination using a minimum size threshold of 15 and circularity of 0.10.

Generation of graphs and figures

Graphs of average values were generated using Microsoft Excel. Cumulative frequency graphs were generated using the CDF function in MATLAB (MathWorks). Box plots were generated using BoxPlotR, an application in the shiny package from RStudio (http://shiny.chemgrid.org/boxplotr/). Figures were drawn in Adobe Illustrator.

Statistical analyses

All the transport parameters measured in this study were first tested for normality using the MATLAB Lilliefors test. For parameters following a normal distribution, we performed Student's t test. For non-normal parameters, we performed a permutation t test (rndttest function in MATLAB). For all parameters, differences in medians were also checked using the Wilcoxon rank sum test (rnk function in MATLAB). The nonparametric Kolmogorov-Smirnov test was used to evaluate the equality of two sample distributions (in cumulative distribution functions). Most of the parameters are presented as means ± SEM. Multiple comparison corrections were used where appropriate. Details about each parameter, including definition of center, value and definition of n, statistical test used, and P values, can be found in specific figures and/or in the figure legends.

SUPPLEMENTARY MATERIALS

Supplementary material for this article is available at https://science.org/doi/10.1126/sciadv.abg3693

REFERENCES AND NOTES

1. S. J. Lee, H. S. Lim, E. Masliah, H. J. Lee, Protein aggregate spreading in neurodegenerative diseases: Problems and perspectives. *Neurosci. Res.* **70**, 339–348 (2011).
2. J. Vaquer-Alicea, M. I. Diamond, Propagation of protein aggregation in neurodegenerative diseases. *Annu. Rev. Biochem.* **88**, 785–810 (2019).
3. G. B. Stokin, C. Lillo, T. L. Falzone, R. G. Brusch, E. Rockenstein, S. L. Mount, R. Raman, P. Davies, E. Masliah, D. S. Williams, L. S. B. Goldstein, Axonopathy and transport deficits early in the pathogenesis of Alzheimer's disease. *Science* **307**, 1282–1288 (2005).
4. S. Maday, A. E. Twelvetrees, A. J. Moughamian, E. L. F. Holzbaur, Axonal transport: Cargo-specific mechanisms of motility and regulation. *Neuron* **84**, 292–309 (2014).
5. Q. Cai, L. Lu, J. H. Tian, Y. B. Zhu, H. Qiao, Z. H. Sheng, Snapin-regulated late endosomal transport is critical for efficient autophagy-lysosomal function in neurons. *Neuron* **68**, 73–86 (2010).
6. I. Hofmann, S. Munro, An N-terminally acetylated Arf-like GTPase is localised to lysosomes and affects their motility. *J. Cell Sci.* **119**, 1494–1503 (2006).
7. D. Khatter, V. B. Raina, D. Dwivedi, A. Sindhwani, S. Bahl, M. Sharma, The small GTPase Arl8b regulates assembly of the mammalian HOPS complex on lysosomes. *J. Cell Sci.* **128**, 1746–1761 (2015).
8. S. B. Prusiner, Biology and genetics of prions causing neurodegeneration. *Annu. Rev. Genet.* **47**, 601–623 (2013).
9. Y. Gu, S. Verghese, S. Bose, M. Mohan, N. Singh, Mutant prion protein D202N associated with familial prion disease is retained in the endoplasmic reticulum and forms 'curly' intracellular aggregates. *J. Mol. Neurosci.* **32**, 90–96 (2007).
10. R. Nixon, R. Camicioli, K. Jamison, L. Cervenakova, J. A. Mastrianni, The PRNP-V180I mutation is associated with abnormally glycosylated PrPCJD and Intracellular PrP accumulations, in *Proceedings of the XIVth International Congress of Neuropathology Scientific Programme. Brain Pathology*, Zurich, Switzerland (2000), vol. 10, p. 670.
11. A. Z. Medrano, S. J. Barmada, E. Biasini, D. A. Harris, GFP-tagged mutant prion protein forms intra-axonal aggregates in transgenic mice. *Neurobiol. Dis.* **31**, 20–32 (2008).
12. J. Ma, S. Lindquist, Wild-type PrP and a mutant associated with prion disease are subject to retrograde transport and proteasome degradation. *Proc. Natl. Acad. Sci. U.S.A.* **98**, 14955–14960 (2001).
13. G. G. Kovacs, K. Molnar, E. Keller, G. Botond, H. Budka, L. Laszlo, Intraneuronal immunoreactivity for the prion protein distinguishes a subset of E200K genetic from sporadic Creutzfeldt-Jakob Disease. *J. Neuropathol. Exp. Neurol.* **71**, 223–232 (2012).
14. M. Kristiansen, M. J. Messenger, P.-C. Klöhn, S. Brandner, J. D. F. Wadsworth, J. Collinge, S. J. Tabrizi, Disease-related prion protein forms aggresomes in neuronal cells leading to caspase activation and apoptosis. *J. Biol. Chem.* **280**, 38851–38861 (2005).
15. Y. I. Yim, B. C. Park, R. Yadavalli, X. Zhao, E. Eisenberg, L. E. Greene, The multivesicular body is the major internal site of prion conversion. *J. Cell Sci.* **128**, 1434–1443 (2015).
16. Z. Marijanovic, A. Caputo, V. Campana, C. Zurzolo, Identification of an intracellular site of prion conversion. *PLOS Pathog.* **5**, e1000426 (2009).
17. D. R. Borchelt, A. Taraboulos, S. B. Prusiner, Evidence for synthesis of scrapie prion proteins in the endocytic pathway. *J. Biol. Chem.* **267**, 16188–16199 (1992).
18. B. Caughey, G. J. Raymond, D. Ernst, R. E. Race, N-terminal truncation of the scrapie-associated form of PrP by lysosomal protease(s): Implications regarding the site of conversion of PrP to the protease-resistant state. *J. Virol.* **65**, 6597–6603 (1991).

Downloaded from https://www.science.org at University of Oxford on April 20, 2023

19. A. C. Magalhaes, G. S. Baron, K. S. Lee, O. Steele-Mortimer, D. Dorward, M. A. Prado, B. Caughey, Uptake and neuritic transport of scrapie prion protein coincident with infection of neuronal cells. *J. Neurosci.* **25**, 5207–5216 (2005).
20. R. S. Hegde, N. S. Rane, Prion protein trafficking and the development of neurodegeneration. *Trends Neurosci.* **26**, 337–339 (2003).
21. P. Satpute-Krishnan, M. Ajinkya, S. Bhat, E. Itakura, R. S. Hegde, J. Lippincott-Schwartz, ER stress-induced clearance of misfolded GPI-anchored proteins via the secretory pathway. *Cell* **158**, 522–533 (2014).
22. E. Zavodszky, R. S. Hegde, Misfolded GPI-anchored proteins are escorted through the secretory pathway by ER-derived factors. *eLife* **8**, e46740 (2019).
23. A. Fehlinger, H. Wolf, A. Hossinger, Y. Duernberger, C. Pleschka, K. Riemschoss, S. Liu, R. Bester, L. Paulsen, S. A. Priola, M. H. Groschup, H. M. Schatzl, I. M. Vorberg, Prion strains depend on different endocytic routes for productive infection. *Sci. Rep.* **7**, 6923 (2017).
24. F. Owen, M. Poulter, J. Collinge, M. Leach, R. Lofthouse, T. J. Crow, A. E. Harding, A dementing illness associated with a novel insertion in the prion protein gene. *Brain Res. Mol. Brain Res.* **13**, 155–157 (1992).
25. R. Chiesa, P. Piccardo, B. Ghetti, D. A. Harris, Neurological illness in transgenic mice expressing a prion protein with an insertional mutation. *Neuron* **21**, 1339–1351 (1998).
26. D. R. Borchelt, J. Davis, M. Fischer, M. K. Lee, H. H. Slunt, T. Ratovitsky, J. Regard, N. G. Copeland, N. A. Jenkins, S. S. Sisodia, D. L. Price, A vector for expressing foreign genes in the brains and hearts of transgenic mice. *Genet. Anal.* **13**, 159–163 (1996).
27. R. Chiesa, B. Drisaldi, E. Quaglio, A. Migheli, P. Piccardo, B. Ghetti, D. A. Harris, Accumulation of protease-resistant prion protein (PrP) and apoptosis of cerebellar granule cells in transgenic mice expressing a PrP insertional mutation. *Proc. Natl. Acad. Sci. U.S.A.* **97**, 5574–5579 (2000).
28. R. Medori, H. J. Tritschler, A. LeBlanc, F. Villare, V. Manetto, H. Y. Chen, R. Xue, S. Leal, P. Montagna, P. Cortelli, P. Tinuper, P. Avoni, M. Mochi, A. Baruzzi, J. J. Hauw, J. Ott, E. Lugaresi, L. Autilio-Gambetti, P. Gambetti, Fatal familial insomnia, a prion disease with a mutation at codon 178 of the prion protein gene. *N. Engl. J. Med.* **326**, 444–449 (1992).
29. S. Neumann, R. Chassefeyre, G. E. Campbell, S. E. Encalada, KymoAnalyzer: A software tool for the quantitative analysis of intracellular transport in neurons. *Traffic* **18**, 71–88 (2017).
30. S. E. Encalada, L. Szpankowski, C.-h. Xia, L. S. B. Goldstein, Stable kinesin and dynein assemblies drive the axonal transport of mammalian prion protein vesicles. *Cell* **144**, 551–565 (2011).
31. R. El Meskini, L. Jin, R. Marx, A. Bruzzaniti, J. Lee, R. Emeson, R. Mains, A signal sequence is sufficient for green fluorescent protein to be routed to regulated secretory granules. *Endocrinology* **142**, 864–873 (2001).
32. Y. Sekine-Aizawa, R. L. Huganir, Imaging of receptor trafficking by using alpha-bungarotoxin-binding-site-tagged receptors. *Proc. Natl. Acad. Sci. U.S.A.* **101**, 17114–17119 (2004).
33. J. P. Luzio, V. Poupon, M. R. Lindsay, B. M. Mullock, R. C. Piper, P. R. Pryor, Membrane dynamics and the biogenesis of lysosomes. *Mol. Membr. Biol.* **20**, 141–154 (2003).
34. P. Arvan, X. Zhao, J. Ramos-Castaneda, A. Chang, Secretory pathway quality control operating in Golgi, plasmalemmal, and endosomal systems. *Traffic* **3**, 771–780 (2002).
35. A. Couve, C. Hetz, RESETing ER proteostasis: Selective stress pathway hidden in the secretory route. *EMBO J.* **33**, 2444–2446 (2014).
36. S. Garg, M. Sharma, C. Ung, A. Tuli, D. C. Barral, D. L. Hava, N. Veerapen, G. S. Besra, N. Hacohen, M. B. Brenner, Lysosomal trafficking, antigen presentation, and microbial killing are controlled by the Arf-like GTPase Arl8b. *Immunity* **35**, 182–193 (2011).
37. M. Ishida, N. Ohbayashi, M. Fukuda, Rab1A regulates anterograde melanosome transport by recruiting kinesin-1 to melanosomes through interaction with SKIP. *Sci. Rep.* **5**, 8238 (2015).
38. J. Cui, Z. Wang, Q. Cheng, R. Lin, X. M. Zhang, P. S. Leung, N. G. Copeland, N. A. Jenkins, K. M. Yao, J. D. Huang, Targeted inactivation of kinesin-1 in pancreatic β-cells in vivo leads to insulin secretory deficiency. *Diabetes* **60**, 320–330 (2011).
39. C. C. Overly, P. J. Hollenbeck, Dynamic organization of endocytic pathways in axons of cultured sympathetic neurons. *J. Neurosci.* **16**, 6056–6064 (1996).
40. P. P. Y. Lie, D. S. Yang, P. Stavrides, C. N. Goulbourne, P. Zheng, P. S. Mohan, A. M. Cataldo, R. A. Nixon, Post-Golgi carriers, not lysosomes, confer lysosomal properties to pre-degradative organelles in normal and dystrophic axons. *Cell Rep.* **35**, 109034 (2021).
41. C. C. Overly, K. D. Lee, E. Berthiaume, P. J. Hollenbeck, Quantitative measurement of intraorganelle pH in the endosomal-lysosomal pathway in neurons by using ratiometric imaging with pyranine. *Proc. Natl. Acad. Sci. U.S.A.* **92**, 3156–3160 (1995).
42. R. G. Parton, K. Simons, C. G. Dotti, Axonal and dendritic endocytic pathways in cultured neurons. *J. Cell Biol.* **119**, 123–137 (1992).
43. S. Pamarthy, A. Kulshrestha, G. K. Katara, K. D. Beaman, The curious case of vacuolar ATPase: Regulation of signaling pathways. *Mol. Cancer* **17**, 41 (2018).
44. R. D. Klausner, J. G. Donaldson, J. Lippincott-Schwartz, Brefeldin A: Insights into the control of membrane traffic and organelle structure. *J. Cell Biol.* **116**, 1071–1080 (1992).
45. G. G. Farias, C. M. Guardia, R. De Pace, D. J. Britt, J. S. Bonifacino, BORC/kinesin-1 ensemble drives polarized transport of lysosomes into the axon. *Proc. Natl. Acad. Sci. U.S.A.* **114**, E2955–E2964 (2017).
46. L. Plate, C. B. Cooley, J. J. Chen, R. J. Paxman, C. M. Gallagher, F. Madoux, J. C. Genereux, W. Dobbs, D. Garza, T. P. Spicer, L. Scampavia, S. J. Brown, H. Rosen, E. T. Powers, P. Walter, P. Hodder, R. L. Wiseman, J. W. Kelly, Small molecule proteostasis regulators that reprogram the ER to reduce extracellular protein aggregation. *eLife* **5**, e15550 (2016).
47. A. Senatore, S. Colleoni, C. Verderio, E. Restelli, R. Morini, S. B. Condliffe, I. Bertani, S. Mantovani, M. Canovi, E. Micotti, G. Forloni, A. C. Dolphin, M. Matteoli, M. Gobbi, R. Chiesa, Mutant PrP suppresses glutamatergic neurotransmission in cerebellar granule neurons by impairing membrane delivery of VGCC α2δ-1 subunit. *Neuron* **74**, 300–313 (2012).
48. P. P. Liberski, A. Gajos, B. Sikorska, Dystrophic neurites accumulating autophagic vacuoles show early stages of neuritic destruction. *Folia Neuropathol.* **56**, 175–178 (2018).
49. S. F. Godsave, H. Wille, P. Kujala, D. Latawiec, S. J. DeArmond, A. Serban, S. B. Prusiner, P. J. Peters, Cryo-immunogold electron microscopy for prions: Toward identification of a conversion site. *J. Neurosci.* **28**, 12489–12499 (2008).
50. J. E. Arnold, C. Tipler, L. Laszlo, J. Hope, M. Landon, R. J. Mayer, The abnormal isoform of the prion protein accumulates in late-endosome-like organelles in scrapie-infected mouse brain. *J. Pathol.* **176**, 403–411 (1995).
51. B. Sikorska, P. P. Liberski, P. Giraud, N. Kopp, P. Brown, Autophagy is a part of ultrastructural synaptic pathology in Creutzfeldt-Jakob disease: A brain biopsy study. *Int. J. Biochem. Cell Biol.* **36**, 2563–2573 (2004).
52. E. E. Zahavi, J. J. A. Hummel, Y. Han, C. Bar, R. Stucchi, M. Altelaar, C. C. Hoogenraad, Combined kinesin-1 and kinesin-3 activity drives axonal trafficking of TrkB receptors in Rab6 carriers. *Dev. Cell* **56**, 1552–1554 (2021).
53. M. S. Pols, E. van Meel, V. Oorschot, C. ten Brink, M. Fukuda, M. G. Swetha, S. Mayor, J. Klumperman, hVps41 and VAMP7 function in direct TGN to late endosome transport of lysosomal membrane proteins. *Nat. Commun.* **4**, 1361 (2013).
54. J. Pu, C. Schindler, R. Jia, M. Jarnik, P. Backlund, J. S. Bonifacino, BORC, a multisubunit complex that regulates lysosome positioning. *Dev. Cell* **33**, 176–188 (2015).
55. T. Massignan, E. Biasini, E. Lauranzano, P. Veglianese, M. Pignataro, L. Fioriti, D. A. Harris, M. Salmona, R. Chiesa, V. Bonetto, Mutant prion protein expression is associated with an alteration of the Rab GDP dissociation inhibitor alpha (GDI)/Rab11 pathway. *Mol. Cell. Proteomics* **9**, 611–622 (2010).
56. S. Gilch, C. Bach, G. Lutzny, I. Vorberg, H. M. Schatzl, Inhibition of cholesterol recycling impairs cellular PrP(Sc) propagation. *Cell. Mol. Life Sci.* **66**, 3979–3991 (2009).
57. M. Takalo, A. Salminen, H. Soininen, M. Hiltunen, A. Haapasalo, Protein aggregation and degradation mechanisms in neurodegenerative diseases. *Am. J. Neurodegener. Dis.* **2**, 1–14 (2013).
58. M. Jeffrey, C. Goodsir, G. McGovern, S. J. Barmada, A. Z. Medrano, D. A. Harris, Prion protein with an insertional mutation accumulates on axonal and dendritic plasmalemma and is associated with distinctive ultrastructural changes. *Am. J. Pathol.* **175**, 1208–1217 (2009).
59. N. M. Veith, H. Plattner, C. A. O. Stuermer, W. J. Schulz-Schaeffer, A. Bürkle, Immunolocalisation of PrPSc in scrapie-infected N2a mouse neuroblastoma cells by light and electron microscopy. *Eur. J. Cell Biol.* **88**, 45–63 (2009).
60. N. Daude, S. Lehmann, D. A. Harris, Identification of intermediate steps in the conversion of a mutant prion protein to a scrapie-like form in cultured cells. *J. Biol. Chem.* **272**, 11604–11612 (1997).
61. L. Fioriti, S. Dossena, L. R. Stewart, R. S. Stewart, D. A. Harris, G. Forloni, R. Chiesa, Cytosolic prion protein (PrP) is not toxic in N2a cells and primary neurons expressing pathogenic PrP mutations. *J. Biol. Chem.* **280**, 11320–11328 (2005).
62. A. Ashok, R. S. Hegde, Selective processing and metabolism of disease-causing mutant prion proteins. *PLOS Pathog.* **5**, e1000479 (2009).
63. S. Y. Shim, S. Karri, S. Law, H. M. Schatzl, S. Gilch, Prion infection impairs lysosomal degradation capacity by interfering with rab7 membrane attachment in neuronal cells. *Sci. Rep.* **6**, 21658 (2016).
64. V. Ermolayev, T. Cathomen, J. Merk, M. Friedrich, W. Hartig, G. S. Harms, M. A. Klein, E. Flechsig, Impaired axonal transport in motor neurons correlates with clinical prion disease. *PLOS Pathog.* **5**, e1000558 (2009).
65. J. Velier, M. Kim, C. Schwarz, T. W. Kim, E. Sapp, K. Chase, N. Aronin, M. DiFiglia, Wild-type and mutant huntingtins function in vesicle trafficking in the secretory and endocytic pathways. *Exp. Neurol.* **152**, 34–40 (1998).
66. J. R. T. van Weering, W. Scheper, Endolysosome and autolysosome dysfunction in Alzheimer's disease: Where intracellular and extracellular meet. *CNS Drugs* **33**, 639–648 (2019).
67. D. J. Vidyadhara, J. E. Lee, S. S. Chandra, Role of the endolysosomal system in Parkinson's disease. *J. Neurochem.* **150**, 487–506 (2019).
68. A. M. Cataldo, S. Petanceska, N. B. Terio, C. M. Peterhoff, R. Durham, M. Mercken, P. D. Mehta, J. Buxbaum, V. Haroutunian, R. A. Nixon, Abeta localization in abnormal

Downloaded from https://www.science.org at University of Oxford on April 20, 2023

endosomes: Association with earliest Abeta elevations in AD and Down syndrome. *Neurobiol. Aging* **25**, 1263–1272 (2004).
69. A. M. Cataldo, C. M. Peterhoff, J. C. Troncoso, T. Gomez-Isla, B. T. Hyman, R. A. Nixon, Endocytic pathway abnormalities precede amyloid beta deposition in sporadic Alzheimer's disease and Down syndrome: Differential effects of APOE genotype and presenilin mutations. *Am. J. Pathol.* **157**, 277–286 (2000).
70. A. Knupp, S. Mishra, R. Martinez, J. E. Braggin, M. Szabo, C. Kinoshita, D. W. Hailey, S. A. Small, S. Jayadev, J. E. Young, Depletion of the AD risk gene SORL1 selectively impairs neuronal endosomal traffic independent of amyloidogenic APP processing. *Cell Rep.* **31**, 107719 (2020).
71. S. A. Small, G. A. Petsko, Endosomal recycling reconciles the Alzheimer's disease paradox. *Sci. Transl. Med.* **12**, eabb1717 (2020).
72. M. Giri, M. Zhang, Y. Lu, Genes associated with Alzheimer's disease: An overview and current status. *Clin. Interv. Aging* **11**, 665–681 (2016).
73. C. M. Karch, A. M. Goate, Alzheimer's disease risk genes and mechanisms of disease pathogenesis. *Biol. Psychiatry* **77**, 43–51 (2015).
74. F. V. Subach, G. H. Patterson, S. Manley, J. M. Gillette, J. Lippincott-Schwartz, V. V. Verkhusha, Photoactivatable mCherry for high-resolution two-color fluorescence microscopy. *Nat. Methods* **6**, 153–159 (2009).
75. C. McClure, K. L. H. Cole, P. Wulff, M. Klugmann, A. J. Murray, Production and titering of recombinant adeno-associated viral vectors. *J. Vis. Exp.* **57**, e3348 (2011).
76. R. A. Williamson, D. Peretz, C. Pinilla, H. Ball, R. B. Bastidas, R. Rozenshteyn, R. A. Houghten, S. B. Prusiner, D. R. Burton, Mapping the prion protein using recombinant antibodies. *J. Virol.* **72**, 9413–9418 (1998).
77. N. Gustafsson, S. Culley, G. Ashdown, D. M. Owen, P. M. Pereira, R. Henriques, Fast live-cell conventional fluorophore nanoscopy with ImageJ through super-resolution radial fluctuations. *Nat. Commun.* **7**, 12471 (2016).
78. A. Burel, M.-T. Lavault, C. Chevalier, H. Gnaegi, S. Prigent, A. Mucciolo, S. Dutertre, B. M. Humbel, T. Guillaudeux, I. Kolotuev, A targeted 3D EM and correlative microscopy method using SEM array tomography. *Development* **145**, dev160879 (2018).
79. D. Sage, L. Donati, F. Soulez, D. Fortun, G. Schmit, A. Seitz, R. Guiet, C. Vonesch, M. Unser, DeconvolutionLab2: An open-source software for deconvolution microscopy. *Methods* **115**, 28–41 (2017).
80. E. Biasini, A. Z. Medrano, S. Thellung, R. Chiesa, D. A. Harris, Multiple biochemical similarities between infectious and non-infectious aggregates of a prion protein carrying an octapeptide insertion. *J. Neurochem.* **104**, 1293–1308 (2008).

Acknowledgments: We thank M. Wood at the Scripps Research EM core for performing the scanning electron microscopy experiments; D. Harris (Boston University), E. Holzbaur (University of Pennsylvania), M. Peckham (University of Leeds), L. Plate (Vanderbilt University), L. S. B. Goldstein (University of California San Diego), V. Verkhusha (Albert Einstein College of Medicine), as well as A. Williamson and D. Burton (Scripps Research) for sharing reagents; and S. Ackerman, G. Campbell, S. Ferro-Novick, M. Hansen, J. Kelly, J. Lebeau, G. Lippi, K. Madhivanan, M. Petrascheck, L. Wiseman, F. Zampa, and all members of the Encalada Laboratory for valuable discussions and comments. **Funding:** This work was supported by NIH/NIA R01AG049483 grant (to S.E.E.), the Glenn Foundation for Medical Research Award for Research in Biological Mechanisms of Aging (to S.E.E.), New Scholar in Aging Award from the Lawrence Ellison Foundation (to S.E.E.), Baxter Family Foundation Award (to S.E.E.), the George E. Hewitt Foundation for Medical Research Postdoctoral Fellowship (to R.C. and A.D.G.L.), Thai Government Scholarship from the Development and Promotion of Science and Technology Talents (DPST) (to T.C.), Larry L. Hillblom Foundation Inc. (to U.M. and S.W.N.), Chan-Zuckerberg Initiative (to U.M.), Waitt Foundation Core Grant application NCI CCSG (CA014195) (to U.M., S.W.N., and L.R.A.), NSF NeuroNex Award no. 2014862 (to U.M. and S.W.N. and NIH/NIDCD R21 award DC018237 (to U.M. and L.R.A.). **Author contributions:** Conceptualization: R.C. and S.E.E. Methodology: R.C., T.C., A.V., S.W.N., L.R.A., U.M., and S.E.E. Investigation: R.C., T.C., A.V., S.W.N., L.R.A., and A.D.G.L. Validation: T.C., A.V., S.W.N., and L.R.A. Supervision: S.E.E. and U.M. Formal analysis: R.C., T.C., A.V., S.W.N., L.R.A., U.M., and S.E.E. Writing (original draft): R.C. and S.E.E. Writing (review and editing): S.E.E., T.C., and A.V. **Competing interests:** The authors declare that they have no competing interests. **Data and materials availability:** All data needed to evaluate the conclusions in the paper are present in the paper and/or the Supplementary Materials.

Submitted 30 December 2020
Accepted 5 November 2021
Published 22 December 2021
10.1126/sciadv.abg3693

Downloaded from https://www.science.org at University of Oxford on April 20, 2023

ScienceAdvances

Endosomal sorting drives the formation of axonal prion protein endoggresomes

Romain Chassefeyre, Tai Chaiamarit, Adriaan Verhelle, Sammy Weiser Novak, Leonardo R. Andrade, Andr D. G. Leito, Uri Manor, and Sandra E. Encalada

Sci. Adv., **7** (52), eabg3693.
DOI: 10.1126/sciadv.abg3693

View the article online
https://www.science.org/doi/10.1126/sciadv.abg3693
Permissions
https://www.science.org/help/reprints-and-permissions

Downloaded from https://www.science.org at University of Oxford on April 20, 2023

Use of this article is subject to the Terms of service

Science Advances (ISSN) is published by the American Association for the Advancement of Science. 1200 New York Avenue NW, Washington, DC 20005. The title *Science Advances* is a registered trademark of AAAS.
Copyright © 2021 The Authors, some rights reserved; exclusive licensee American Association for the Advancement of Science. No claim to original U.S. Government Works. Distributed under a Creative Commons Attribution License 4.0 (CC BY).

Science Advances
AAAS

Supplementary Materials for

Endosomal sorting drives the formation of axonal prion protein endoggresomes

Romain Chassefeyre, Tai Chaiamarit, Adriaan Verhelle, Sammy Weiser Novak, Leonardo R. Andrade, André D. G. Leitão, Uri Manor, Sandra E. Encalada*

*Corresponding author. Email: encalada@scripps.edu

Published 22 December 2021, *Sci. Adv.* **7**, eabg3693 (2021)
DOI: 10.1126/sciadv.abg3693

The PDF file includes:

Figs. S1 to S11
Legends for movies S1 to S3

Other Supplementary Material for this manuscript includes the following:

Movies S1 to S3

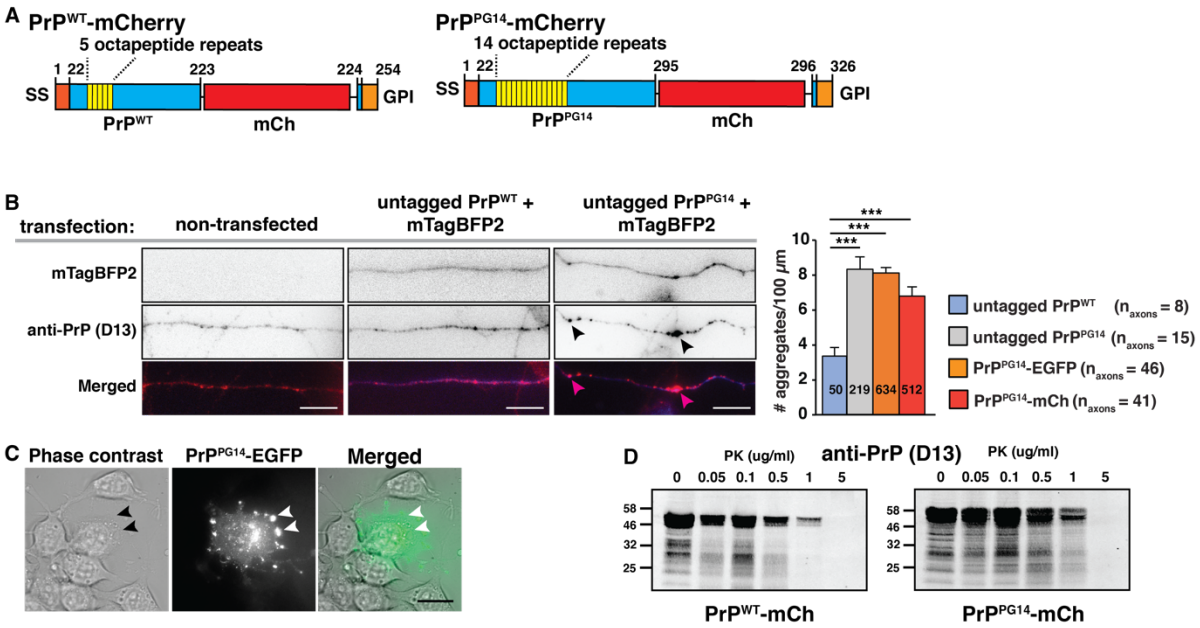


Fig. S1. Misfolded PrP^{PG14} forms aggregates inside axons. (A) Schematic of PrP^{WT}-mCh and PrP^{PG14}-mCh constructs. SS: signal sequence, GPI: GPI anchor. **(B)** Images of non-transfected axons and those co-expressing untagged PrP^{WT} or PrP^{PG14} with soluble mTagBFP2 (left) and aggregate quantification (right). Arrowheads point to aggregates. Scale bar = 10 µm. Bars represent means ± SEM. ***p<0.001, Kruskal- Wallis test. Aggregate numbers are shown inside bars. **(C)** Phase contrast and fluorescence images of a differentiated neuroblastoma (Neuro2a) cell expressing PrP^{PG14}-EGFP. Scale bar = 20 µm. **(D)** Representative Western blots showing of partial Proteinase K (PK) resistance by PrP^{PG14} aggregates from N2a cell lysates. Number of independent biological replicates = 3.

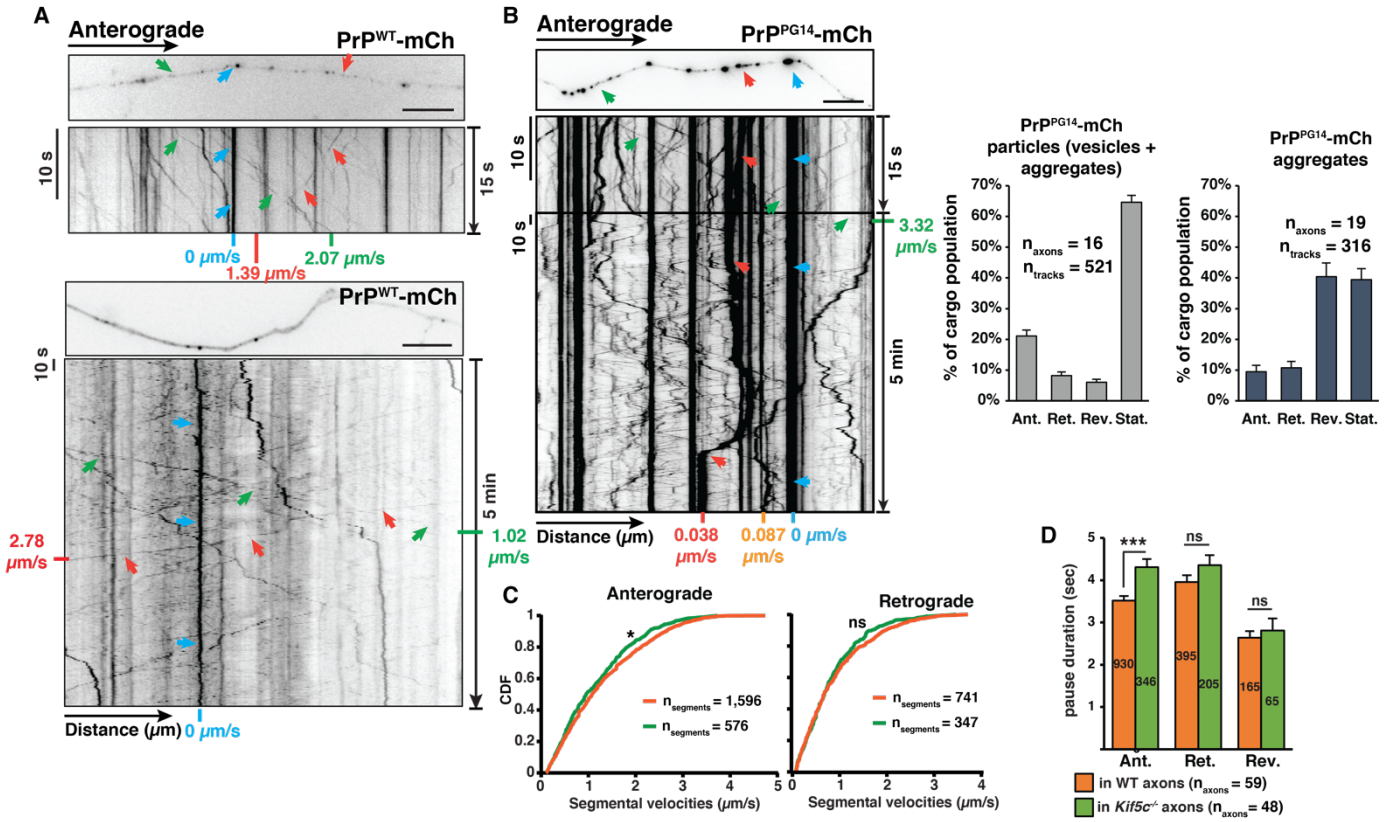


Fig. S2. PrP^{PG14} vesicles are transported in axons by kinesin-1. (**A**) First frames (top panels of each set) of time-lapse movies of axons expressing PrP^{WT}-mCh and corresponding kymographs (bottom panels of each set) at two time-scales. Arrows point to vesicles moving in the anterograde (green) or retrograde (red) directions, or that are stationary (blue). Scale bars = 10 μm. (**B**) First frame of time-lapse movie of an axon expressing PrP^{PG14}-mCh (top), and corresponding kymographs (middle-bottom) at two time-scales (left). Arrows point to vesicles or aggregates moving in the anterograde (green) or retrograde (red) directions, or that are stationary (blue). Scale bar = 10 μm. Population breakdown of PrP^{PG14}-mCh vesicles and aggregates (right). Bars represent means ± SEM. Ant. = anterograde, Ret. = retrograde, Rev. = reversals, Stat. = stationary. (**C**) Cumulative distribution frequency (CDF) of anterograde and retrograde

segmental PrP^{PG14}-EGFP vesicle velocities. *$p<0.05$, Kolmogorov-Smirnov test. (**D**) Pause duration of anterograde, retrograde and reversing PrP^{PG14}-EGFP vesicles. Numbers of vesicles are shown inside bars. Bars represent means ± SEM. ***$p<0.001$, ns = not significant, Student's t-test. Ant. = anterograde, Ret. = retrograde, Rev. = reversals.

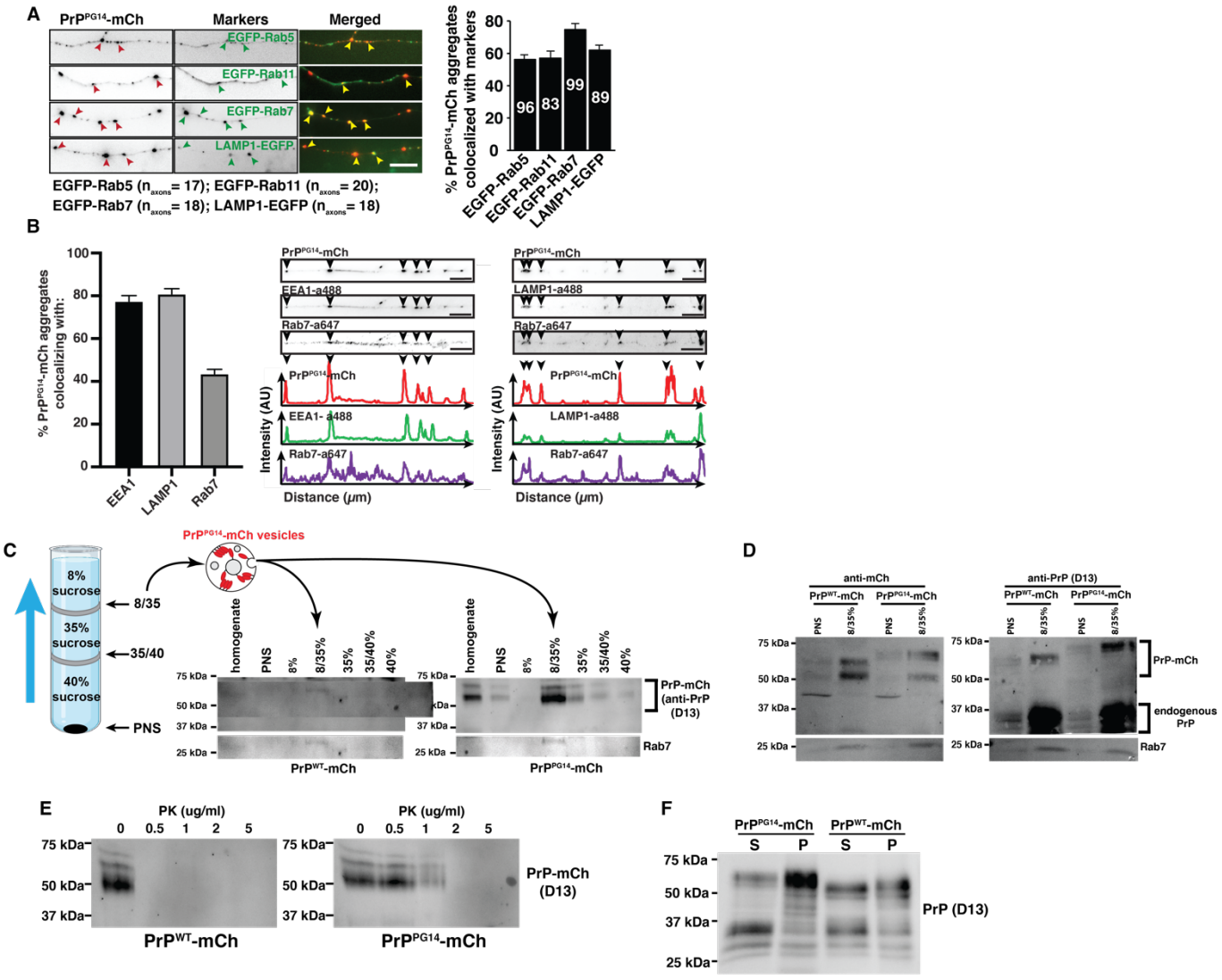


Fig. S3. Misfolded PrP^{PG14} resides in endolysosomal compartments. (**A**) Representative images of axons 2 days post-co-transfection with PrP^{PG14}-mCh and markers for EGFP-labeled Rab5, Rab11, Rab7, and LAMP1 (left). Arrowheads point to colocalizing aggregates. Scale bar = 10 μm. Quantitation of aggregate densities (right). Numbers of aggregates shown inside bars. Bars represent means ± SEM. (**B**) Quantitation of PrP^{PG14}-mCh aggregate colocalization with endogenous EEA1 (early endosomes), LAMP1 (endolysosomes) and Rab7 (LEs) (left). Representative immunofluorescence images of axons expressing PrP^{PG14}-mCh and stained with

antibodies to recognize endogenous EEA1 and Rab7 or LAMP1 and Rab7 (top right panels). Corresponding line scan plots for each channel (bottom right). Arrowheads indicate colocalization events. Scale bars = 10 μm. (**C**) Schematic diagram of a membrane flotation experiment (left) showing the 8/35 fraction ran on the Western blots in (C; right) and (D), and used as starting material for the Proteinase K (PK) and detergent insolubility assays in (E) and (F), respectively. Post-nuclear supernatant (PNS) from N2a cells homogenates were collected without detergent to prevent breaking of membranes and bottom loaded on a discrete sucrose gradient. Representative Western blots probed with an antibody against PrP (D13) show PrP^{PG14}-mCh signal (endogenous PrP shown in D), and against Rab7. Number of independent biological replicates = 3. (**D**) Representative Western blots showing PNS and 8/35 fractions from flotations of N2a cells transfected with PrP^{WT}- or PrP^{PG14}-mCh and probed with indicated antibodies. Number of independent replicates = 6. (**E**) Representative Western blots of PK-treated 8/35 membrane fractions of PrP^{WT} and PrP^{PG14} obtained from N2a cells as indicated in (**C**). Number of independent biological replicates = 3. (F) Representative Western blot of 8/35 membrane detergent soluble versus insoluble fractions obtained from PrP^{WT}-mCh and PrP^{PG14}-mCh expressing N2a cells as indicated in (**C**). Number of independent biological replicates = 2.

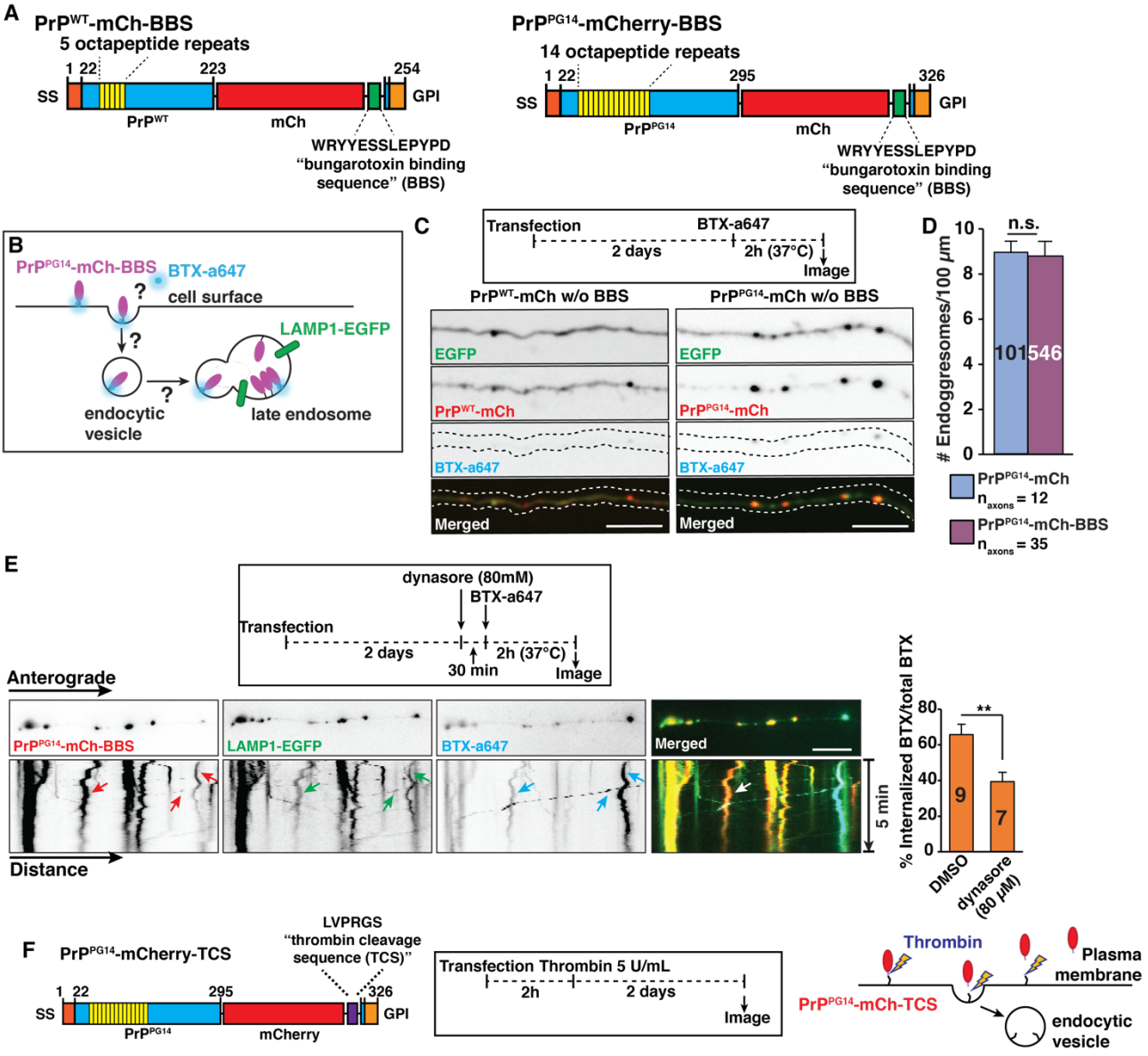


Fig. S4. PrP^{PG14} transiently traffics to the cell surface before intra-axonal aggregation. (**A**) Schematic of PrP^{WT}-mCh-BBS and PrP^{PG14}-mCh-BBS constructs. SS: signal sequence; GPI: GPI anchor. (**B**) Schematic of PrP^{PG14}-mCh-BBS internalization assay. (**C**) Experimental timeline of BTX-a647 labeling assay (top), and representative images of neurons expressing PrP^{WT}-mCh or PrP^{PG14}-mCh without BBS sequence, after treatment with BTX-a647 (bottom). Scale bars = 10 μm. (**D**) Quantitation of endoggresome densities from PrP^{PG14}-mCh and PrP^{PG14}-mCh-BBS-

expressing neurons treated with BTX-a647. Endoggresome numbers are shown inside bars. Bars represent means ± SEM. ns = not significant; Student's t-test. (**E**) Outline of Dynasore endocytosis assay (top). Representative first-frame images of time-lapse movie and kymographs of axons of neurons co-expressing PrP^{PG14}-mCherry-BBS, LAMP1-EGFP and treated with BTX-a647 (bottom left). Arrows point to cotransport. Scale bar = 10 μm. Quantitation of normalized percent internalized BTX-a647 signal (bottom right). Numbers of axons shown inside bars. Bars represent means ± SEM. **p<0.01, Student's t-test. (**F**) Schematic of PrP^{PG14}-mCh-TCS construct (left). SS: signal sequence; GPI: GPI anchor. Outline (middle) and schematic (right) of thrombin assay.

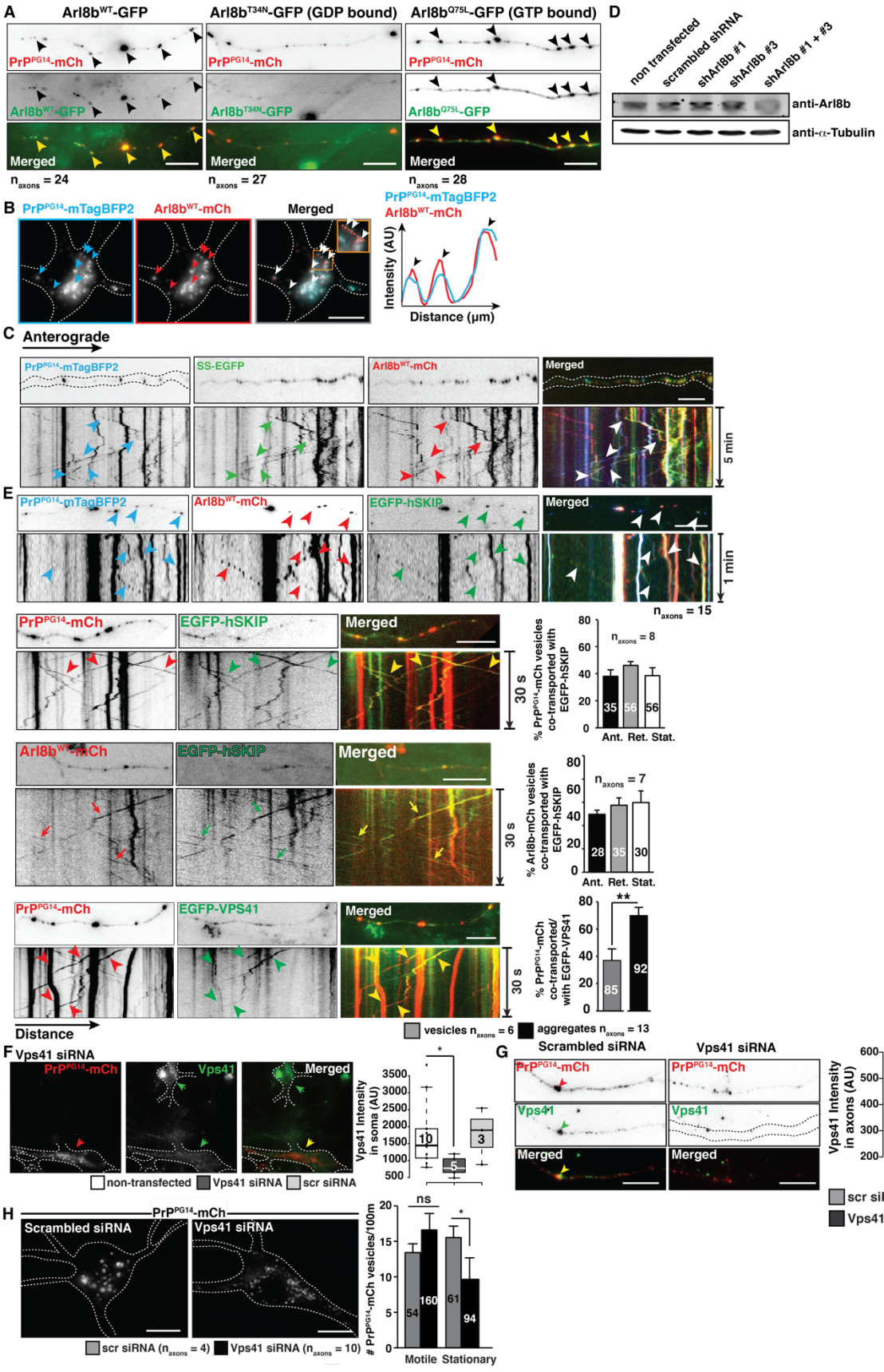

A
Arl8b^WT-GFP
Arl8b^T34N-GFP (GDP bound)
Arl8b^Q75L-GFP (GTP bound)
PrP^PG14-mCh
Arl8b^WT-GFP
Arl8b^T34N-GFP
Arl8b^Q75L-GFP
Merged
n_axons = 24
n_axons = 27
n_axons = 28
D
non transfected
scrambled shRNA
shArl8b #1
shArl8b #3
shArl8b #1 + #3
anti-Arl8b
anti-α-Tubulin
B
PrP^PG14-mTagBFP2
Arl8b^WT-mCh
Merged
Intensity (AU)
Distance (μm)
C
Anterograde
SS-EGFP
5 min
E
EGFP-hSKIP
1 min
n_axons = 15
30 s
% PrP^PG14-mCh vesicles co-transported with EGFP-hSKIP
n_axons = 8
35
56
56
Ant. Ret. Stat.
% Arl8b-mCh vesicles co-transported with EGFP-hSKIP
n_axons = 7
28
35
30
EGFP-VPS41
% PrP^PG14-mCh co-transported/ with EGFP-VPS41
**
85
92
Distance
vesicles n_axons = 6
aggregates n_axons = 13
F
Vps41 siRNA
Vps41
Vps41 Intensity in soma (AU)
10
5
3
non-transfected
Vps41 siRNA
scr siRNA
G
Scrambled siRNA
Vps41 siRNA
Vps41 Intensity in axons (AU)
9
15
H
Scrambled siRNA
Vps41 siRNA
scr siRNA (n_axons = 4)
Vps41 siRNA (n_axons = 10)
PrP^PG14-mCh vesicles/100m
ns
54
160
61
94
Motile Stationary

Fig. S5. Arl8b effectors are recruited to PrP^{PG14} vesicles to promote fusion and aggregation. (**A**) Representative images of neurons co-expressing PrP^{PG14}-mCh and $Arl8b^{WT}$-GFP, $Arl8b^{T34N}$-GFP, or $Arl8b^{Q75L}$-GFP (left panels), and line scan intensity profiles of region indicated by dotted orange line inside inset (right). Arrowheads point to colocalization. Scale bar = 10 μm. (**B**) Representative images of hippocampal soma co-expressing PrP^{PG14}-mTagBFP and $Arl8b^{WT}$-mCh. Arrowheads point to colocalization. Scale bar = 10 μm. (**C**) Representative first-frame images of time-lapse movies, and corresponding kymographs of axons from neurons co-expressing PrP^{PG14}-mTagBFP2, SS-EGFP (from NPY), and $Arl8b^{WT}$-mCh. Arrowheads point to cotransport. Number of axons = 4. Scale bar = 10 μm. (**D**) Representative Western blot of N2a cell lysates treated with indicated shRNAs. Replicates = 3. (**E**) Representative first-frame images of time-lapse movies, and corresponding kymographs of axons from neurons co-expressing indicated constructs (left panels). Arrowheads point to cotransport. Numbers of axons for PrP^{PG14}-mTagBFP2, $Arl8b^{WT}$-mCh and EGFP-hSKIP = 15. Scale bars = 10 μm. Quantitation of cotransport/colocalization (right). Bars represent means ± SEM. Numbers of vesicles or endoggresomes are shown inside bars. (**F**) Immunofluorescence images of the soma of neurons expressing PrP^{PG14}-mCh, transfected with Vps41 siRNA, and stained with antibodies against Vps41 (left panels). Arrows point to two neurons either transfected or untransfected with Vps41 shRNA. Scale bar = 10 μm. Quantitation of Vps41 signal intensity (right). Boxes show lower (Q1) and upper (Q3) quartile and median. Whiskers mark the 9 to 91 percentile range. Datapoints outside of this range are represented by individual dots. Numbers of neurons are shown inside boxplots. (**G**) Representative axons from neurons co-transfected with PrP^{PG14}-mCh and Vps41 siRNA, stained with antibodies against Vps41 (left panels). Arrowheads point to endoggresomes. Scale bars = 10 μm. Quantitation of Vps41 signal intensity (right). Box shows

lower (Q1) and upper (Q3) quartile and median. Whiskers mark the 9 to 91 percentile range. Datapoints outside of this range are represented by individual dots. Numbers of neurons are shown inside boxplots. (**H**) Representative images of soma of neurons co-transfected with PrP^{PG14}-mCh and shRNA scrambled or Vps41 siRNA (left panels). Scale bars = 10 μm. Quantitation of motile and stationary axonal PrP^{PG14}-mCh vesicle densities in neurons co-transfected with scrambled or Vps41 shRNAs (right). Numbers of vesicles are shown inside bars.

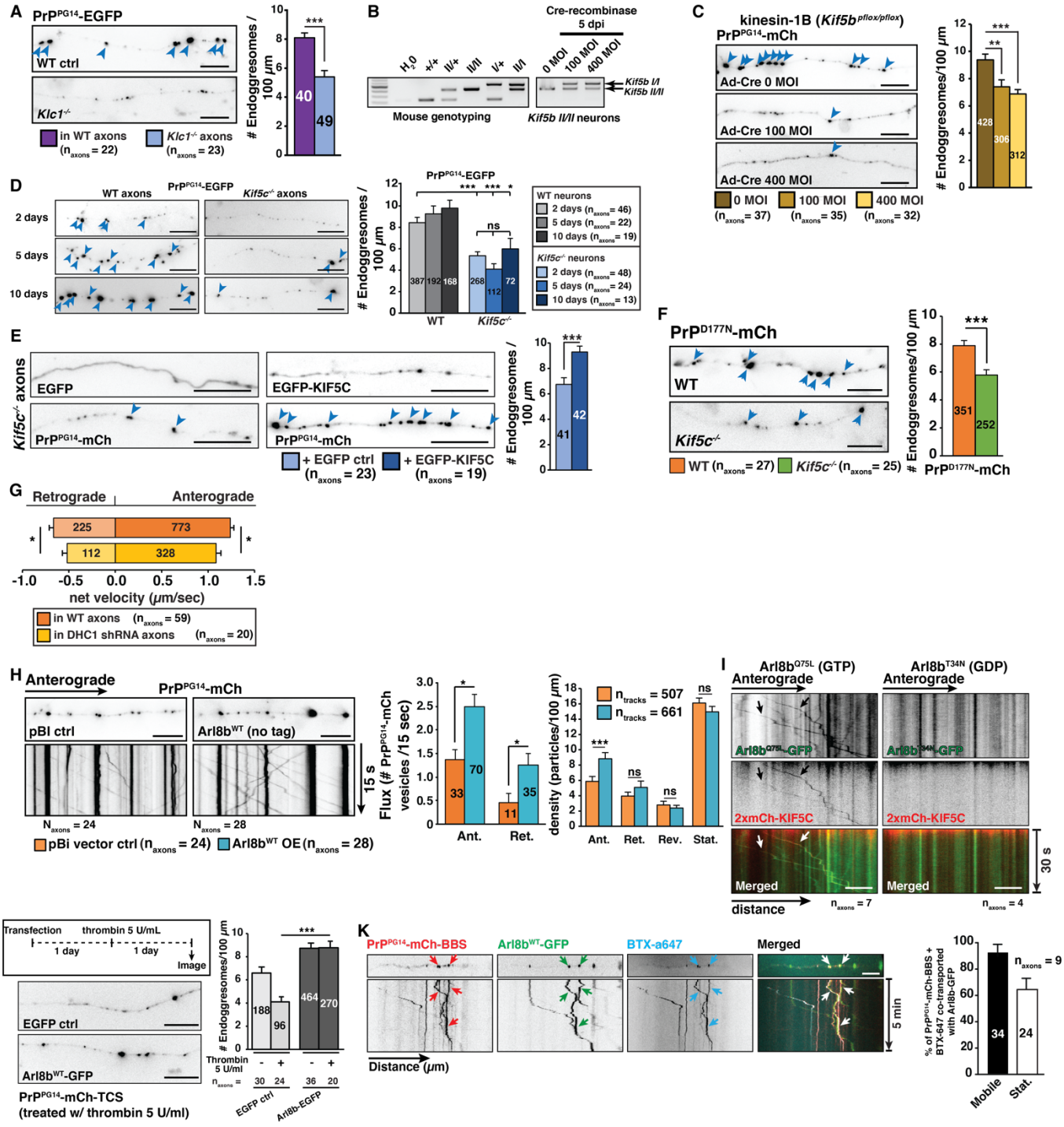


Fig. S6. ARESTA drives endoggresome formation in axons. (**A**) Images of WT and *Klc1*$^{-/-}$ axons expressing PrP^{PG14}-EGFP (left). Arrowheads point to endoggresomes. Scale bar = 10 µm. Quantitation of endoggresome densities (right). Bars represent means ± SEM. Numbers of

endoggresomes are shown inside bars. ***p<0.001, Student's t-test and Kruskal- Wallis test. (**B**) DNA gel of genotyping bands from Kinesin-1B neuron extracts treated with increasing amounts of cre-recombinase adenovirus (AVV-cre) at 5 days post-infection (dpi). Excision of *Kif5B* II occurs following cre-treatment to convert to a kinesin-1B I/+ product. MOI = Multiplicity of infection. (**C**) Images of *Kif5B* conditional knockout axons expressing PrP^{PG14}-mCh and treated with indicated AAV-cre units (left). Arrowheads point to endoggresomes. Scale bar = 10 μm. Quantitation of endoggresome densities (right). Bars represent means ± SEM. Numbers of endoggresomes are shown inside bars. **p<0.01, ***p<0.001, Student's t-test and Kruskal-Wallis test. (**D**) Images of axons from WT and *Kif5c*$^{-/-}$ neurons expressing PrP^{PG14}-EGFP at various time points post-transfection (left). Arrowheads point to endoggresomes. Scale bars = 10 μm. Quantitation of endoggresome densities (right). (**E**) Images of *Kif5c*$^{-/-}$ axons co-expressing soluble EGFP or EGFP-KIF5C and PrP^{PG14}-mCh (left). Scale bar = 10 μm. Quantitation of endoggresome densities (right). Bars represent means ± SEM. Numbers of endoggresomes are shown inside bars. ***p<0.001, Student's t-test and Kruskal- Wallis test. (**F**) Representative images of PrP^{D177N}-mCh aggregates in WT and *Kif5C*$^{-/-}$ axons (left). Arrowheads point to endoggresomes. Scale bar = 10 μm. Quantitation of aggregate densities (right). Bars represent means ± SEM. Numbers of endoggresomes are shown inside bars. ***p<0.001, Student's t-test and Kruskal- Wallis test. (**G**) Average net axonal velocities of PrP^{PG14}-EGFP vesicles in WT and DHC1 shRNA neurons. Numbers of tracks are shown inside bars. Bars represent means ± SEM. *p<0.05, Kruskal- Wallis test. (**H**) Representative first-frame images of time-lapse movies, and corresponding kymographs of axons from neurons expressing PrP^{PG14}-mCh and transfected with empty control pBi vector or untagged $Arl8b^{WT}$ (left panels). Scale bars = 10 μm. Quantitation of PrP^{PG14}-EGFP vesicle (middle). Quantitation of vesicle densities (right). Numbers of vesicles are

shown inside bars. Ant. = anterograde; Ret. = retrograde; Rev. = reversal; Stat. = stationary. Bars represent means ± SEM. *p<0.05, ***p<0.001, ns = not significant, Kruskal- Wallis test. (**I**) Representative kymographs of axons co-expressing Arl8b^{Q75L}-GFP or Arl8b^{T34N}-GDP and 2xmCh-KIF5C. Arrows indicate cotransport. Scale bars = 10 μm. (**J**) Outline of thrombin assay (top left), and representative images of axons of neurons co-expressing PrP^{PG14}-mCh-TCS and soluble EGFP or Arl8b^{WT}-GFP (bottom left). Scale bar = 10 μm. Quantitation of endoggresome densities (right). Number of endoggresomes are shown inside bars. Bars represent means ± SEM. ***p<0.001, Kruskal- Wallis test. (**K**) Representative first frames of time-lapse movie, and kymographs of axons expressing PrP^{PG14}-mCh-BBS, Arl8b^{WT}-GFP, and labeled with BTX-a647 (left panels). Arrows point to cotransport. Scale bar = 10 μm. Quantitation of cotransport (right). Numbers of vesicles are shown inside bars. Bars represent means ± SEM.

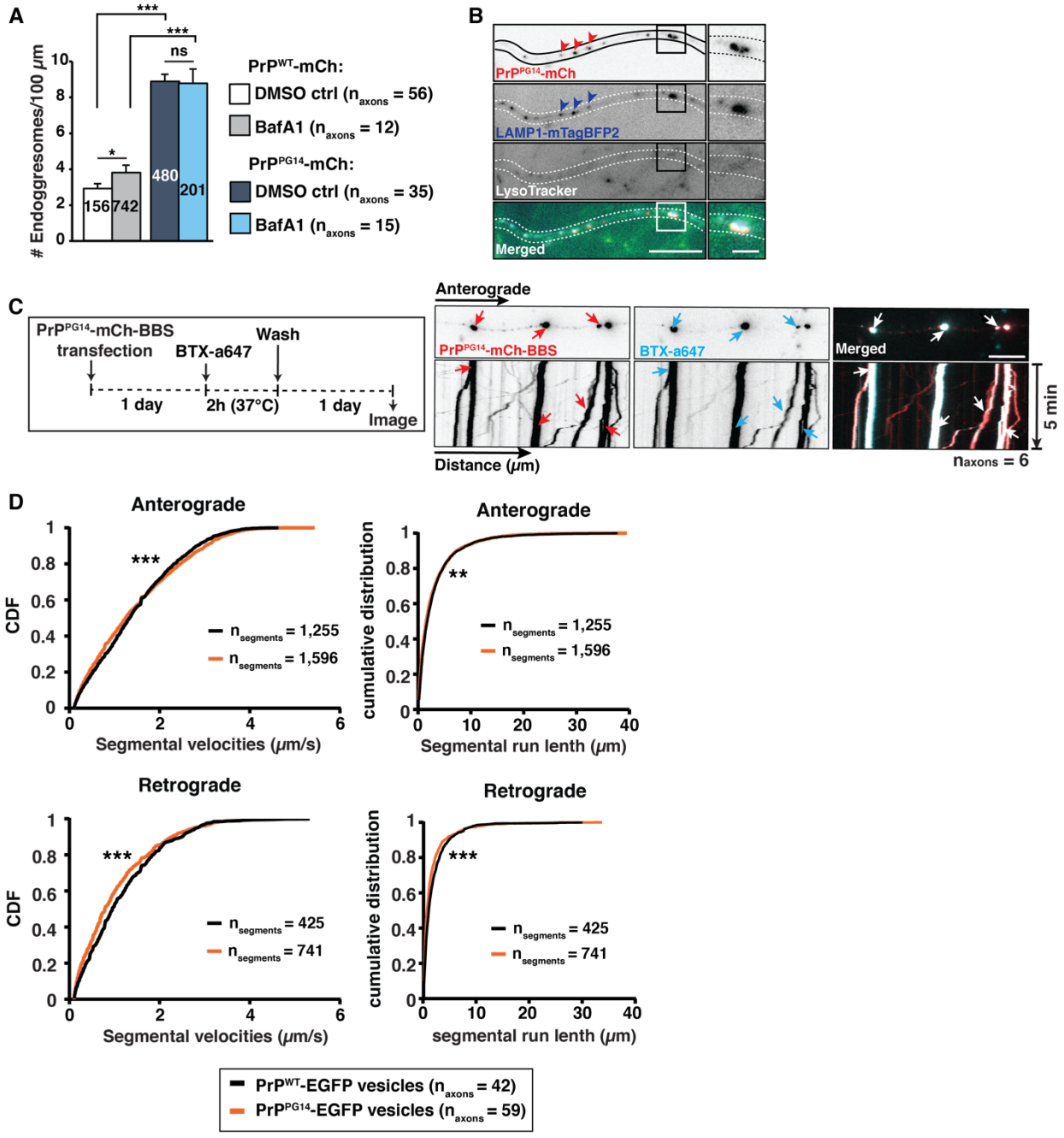


Fig. S7. Lysosomal degradation and retrograde transport deficits in PrP^{PG14}-expressing axons. (**A**) Quantitation of axonal PrP^{PG14}-mCh endoggresome densities in neurons treated with BafA1. Numbers of endoggresomes are shown inside bars. Bars represent means ± SEM**.** ***p<0.001, Kruskal- Wallis test. (**B**) Representative images of axons of neurons co-expressing

PrP^{PG14}-mCh and LAMP1-mTagBFP2 and treated with LysoTracker (left panels). Arrowheads point to colocalization. Scale bar = 10 μm. Enlargements of boxed regions (right panels). Scale bar = 2.5 μm. Number of axons = 21. (**C**) Outline of BTX assay (left). Representative first frames of time-lapse movie, and kymographs of BTX-a647-labeled PrP^{PG14}-mCh-BBS axons (right). Arrows point to cotransport. Scale bar = 10 μm. (**D**) Cumulative distribution frequencies (CDFs) of anterograde (top) and retrograde (bottom) segmental velocities and segmental run length of PrP^{WT}- and PrP^{PG14}-EGFP vesicles. **p<0.01, ***p<0.001, Kolmogorov-Smirnov test.

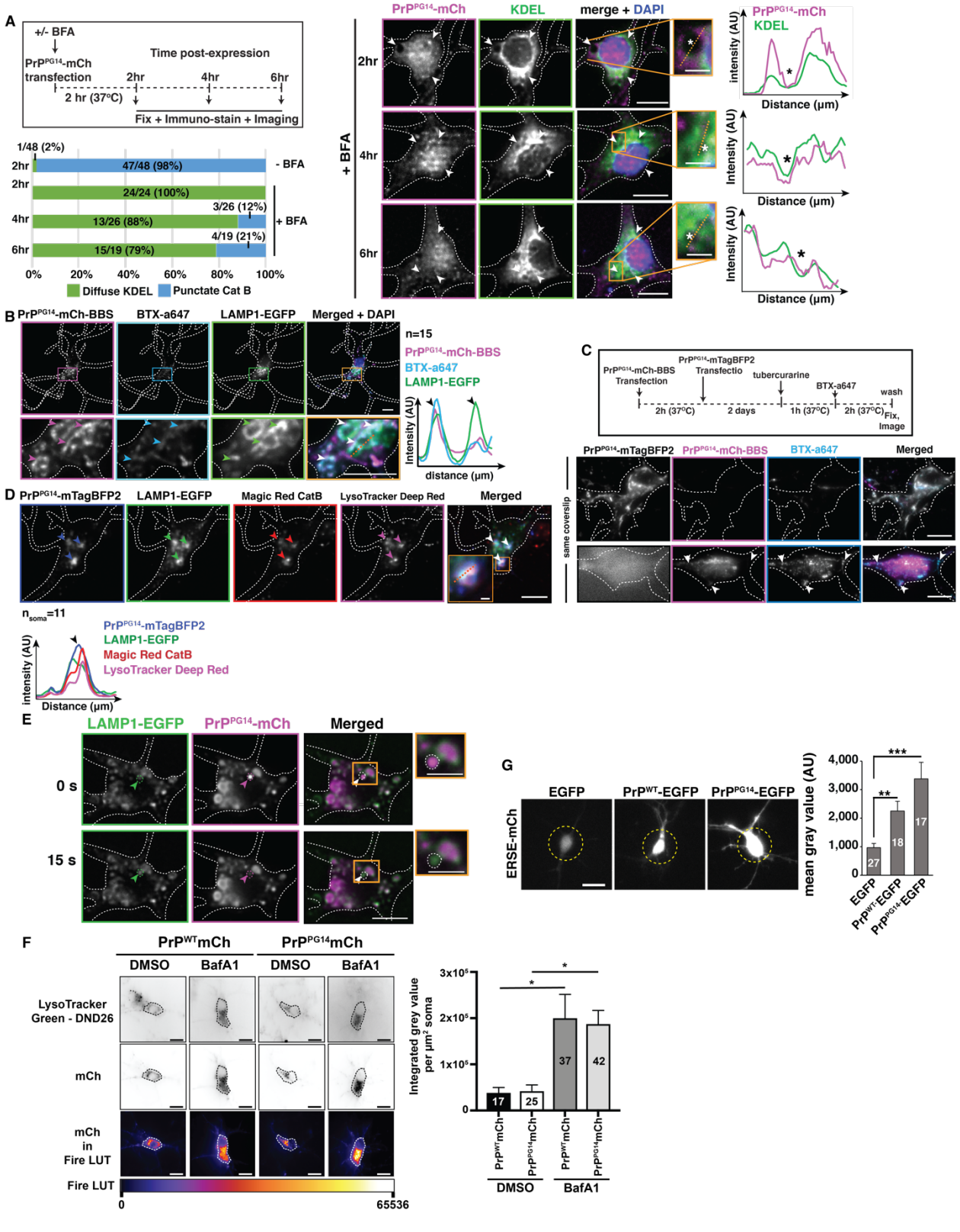

A
+/- BFA
PrP^PG14-mCh transfection
2 hr (37°C)
Time post-expression
2hr
4hr
6hr
Fix + Immuno-stain + Imaging
1/48 (2%)
47/48 (98%)
- BFA
24/24 (100%)
3/26 (12%)
13/26 (88%)
4/19 (21%)
15/19 (79%)
+ BFA
0%
20%
40%
60%
80%
100%
Diffuse KDEL
Punctate Cat B
PrP^PG14-mCh
KDEL
merge + DAPI
+ BFA
intensity (AU)
Distance (µm)
B PrP^PG14-mCh-BBS
BTX-a647
LAMP1-EGFP
Merged + DAPI
n=15
distance (µm)
C
PrP^PG14-mCh-BBS Transfection
PrP^PG14-mTagBFP2 Transfectio
tubercurarine
BTX-a647
wash
2h (37°C)
2 days
1h (37°C)
2h (37°C)
Fix, Image
PrP^PG14-mTagBFP2
PrP^PG14-mCh-BBS
BTX-a647
Merged
same coverslip
D PrP^PG14-mTagBFP2
LAMP1-EGFP
Magic Red CatB
LysoTracker Deep Red
Merged
n_soma=11
PrP^PG14-mTagBFP2
LAMP1-EGFP
Magic Red CatB
LysoTracker Deep Red
intensity (AU)
Distance (µm)
E
LAMP1-EGFP
PrP^PG14-mCh
Merged
0 s
15 s
G
EGFP
PrP^WT-EGFP
PrP^PG14-EGFP
ERSE-mCh
mean gray value (AU)
4,000
3,000
2,000
1,000
0
***
**
27
18
17
EGFP
PrP^WT-EGFP
PrP^PG14-EGFP
F
PrP^WTmCh
PrP^PG14mCh
DMSO
BafA1
DMSO
BafA1
LysoTracker Green - DND26
mCh
mCh in Fire LUT
Fire LUT
0
65536
Integrated grey value per µm² soma
3x10^5
2x10^5
1x10^5
0
*
*
17
25
37
42
PrP^WTmCh
PrP^PG14mCh
PrP^WTmCh
PrP^PG14mCh
DMSO
BafA1

Fig. S8. Somatic lysosomal clearance of neuronal PrP^{PG14}. (**A**) Outline of BFA assay (top left), and quantification of PrP^{PG14}-mCh colocalization with KDEL or CatB (bottom left). Numbers inside/above bars are total number and percentage of observed neurons. Representative images of soma of neurons expressing PrP^{PG14}-mTagBFP2 and stained with antibodies against ER (KDEL) or with DAPI nuclear marker at indicated time points in the presence of BFA. Arrowheads and asterisks in insets point to colocalization or non-colocalization events, respectively, also shown in enlarged insets and line scan intensity profiles of dotted lines (right). Scale bars = 10 μm. Scale bars of insets = 250 nm. (**B**) Representative images of a neuronal soma co-transfected with PrP^{PG14}-mCh-BBS and LAMP1-EGFP, and labeled with BTX-a647 (top left panels), and enlargement of insets (bottom left panels). Scale bars = 10 μm. Line scan intensity profiles of dotted lines (right). (**C**) Outline of BBS internalization assay (top). Representative images of two neurons taken from the same coverslip, sequentially transfected with PrP^{PG14}-mCh-BBS and PrP^{PG14}-mTagBFP2 constructs. Scale bars = 10 μm. (**D**) Representative images of the soma of a neuron co-transfected with PrP^{PG14}-mTagBFP2 and LAMP1-EGFP, and treated with Magic Red and LysoTracker Deep Red (top panels). Arrowheads and asterisk point to colocalization or non-colocalization events, respectively. Scale bar of main panels and of inset = 10 μm and 1 μm, respectively. Enlarged insets and line scan intensity profiles (bottom). (**E**) Images of a neuron co-expressing LAMP1-EGFP and PrP^{PG14}-mCh at two time points. Scale bar = 10 μm. Arrowheads point to a PrP^{PG14}-mCh disappearing vesicle (enlarged in inset). Scale bars in insets = 5 μm. (**F**) Representative black/white inverted fluorescence images of the soma of DMSO or BafA1- and LysoTracker Green-treated PrP^{WT}-mCh and PrP^{PG14}-mCh neurons (left panels). BafA1 treatment was for 12 hrs. Fire Look-up table (LUT) is shown on the bottom panels. Scale bar = 20 μm. Number of independent biological

replicates = 3. Quantitation of integrated grey values of soma data on left panels (right). Calculation of intensities was done on regions of interest (ROIs) drawn around soma on the mCh channel, and grey values are represented as integrated/cumulative grey value per μm^2 of soma. Numbers of soma are indicated inside bars. Bars represent means ± SEM**.** *$p<0.05$, Student's t-test. (**G**) Representative images (left panels) and quantitation of intensity levels (right) in neurons co-transfected with ERSE-mCh and EGFP (control), PrP^{WT}-EGFP, or PrP^{PG14}-EGFP. Dotted lines indicate 30 μm diameter circles used to measure total gray intensity values. Scale bar = 20 μm. Bars represent means ± SEM**.** **$p<0.01$, ***$p<0.001$, Student's t-test. Numbers of neurons are shown inside bars.

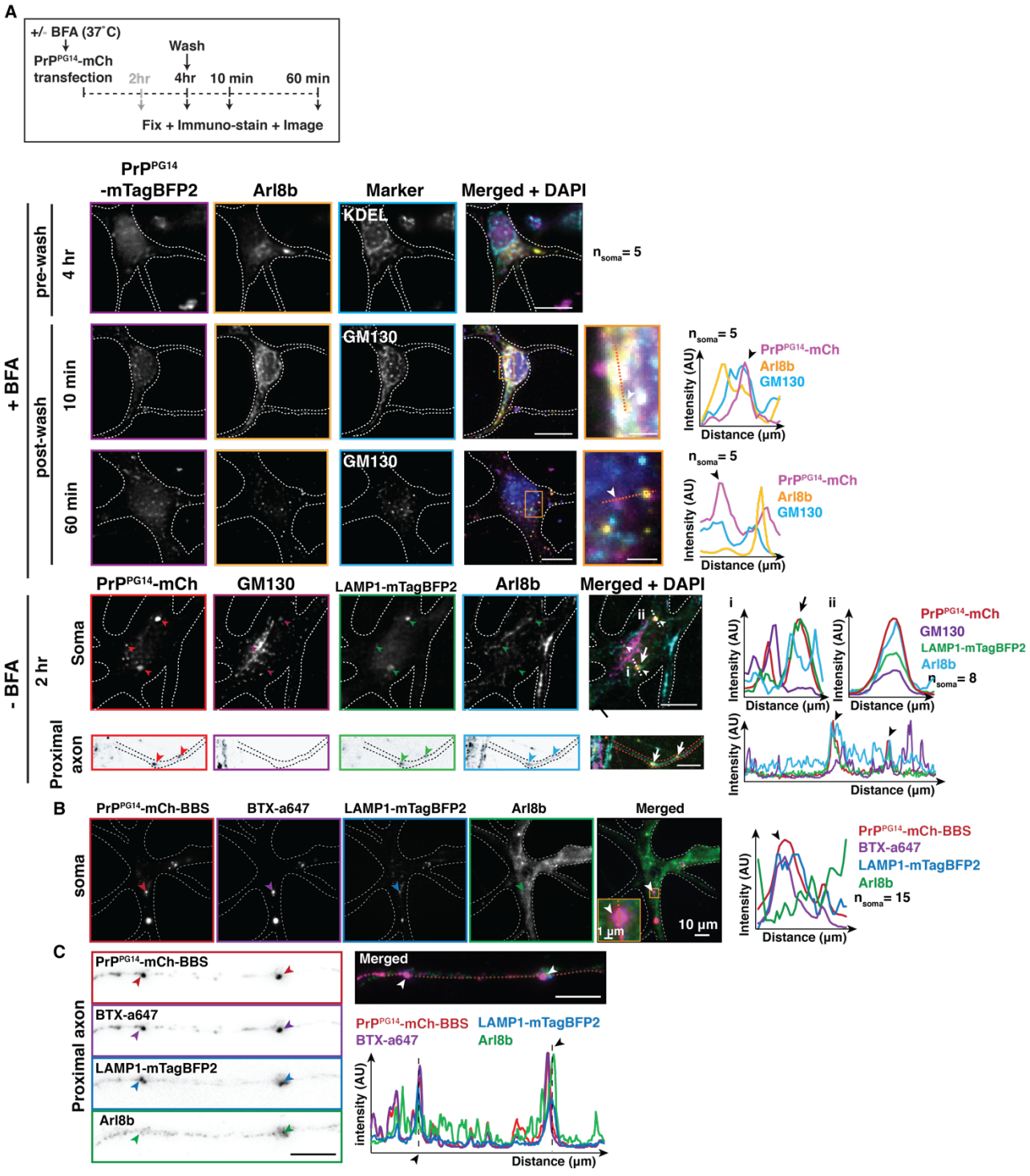


Fig. S9. Arl8b is a key determinant of PrP^{PG14} axonal entry. (**A**) Outline of BFA assay (top). Representative images of soma and proximal axons of different neurons expressing PrP^{PG14}-mTagBFP2 or PrP^{PG14}-mCh + LAMP1-mTagBFP2 and stained with antibodies against Arl8b,

ER (KDEL), Golgi (GM130), or with DAPI nuclear marker at indicated time points and conditions, with or without BFA treatment (bottom panels). Graphs to the right are of line scans of dotted lines inside insets. Arrowheads point to colocalization events, also shown in enlarged insets and in line scan intensity profiles. Scale bars in main panels = 10 μm. Scale bars in insets = 500 nm. (**B**) Representative images of PrP^{PG14}-mCh-BBS internalization in the soma (left panels) of neurons co-transfected with PrP^{PG14}-mCh-BBS and LAMP1-mTagBFP2, labeled with BTX-a647, and stained with an antibody against Arl8b. Arrowheads point to colocalization events, also shown in enlarged insets and in line scan intensity profile (right). Scale bars in main panel = 10 μm. Scale bars in inset = 1 μm. (**C**) Representative images of PrP^{PG14}-mCh-BBS internalization in axons (left and top right panels) of neurons co-transfected with PrP^{PG14}-mCh-BBS and LAMP1-mTagBFP2, labeled with BTX-a647, and stained with an antibody against Arl8b. Arrowheads point to colocalizing endoggresomes. Line scan intensity profile (right). Scale bar = 10 μm.

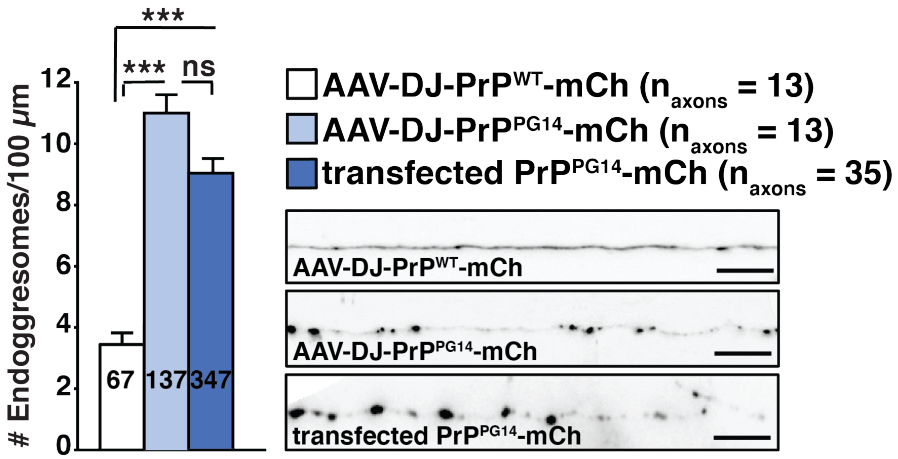


Fig. S10. Expression of AAV-DJ-PrP^{PG14}-mCh results in the formation of endoggresomes. Quantitation of endoggresome densities (left) and representative images (right) of axons from neurons transduced with AAV-DJ-PrP^{PG14}-mCh. Numbers of endoggresomes are shown inside bars. Scale bar = 10 µm.

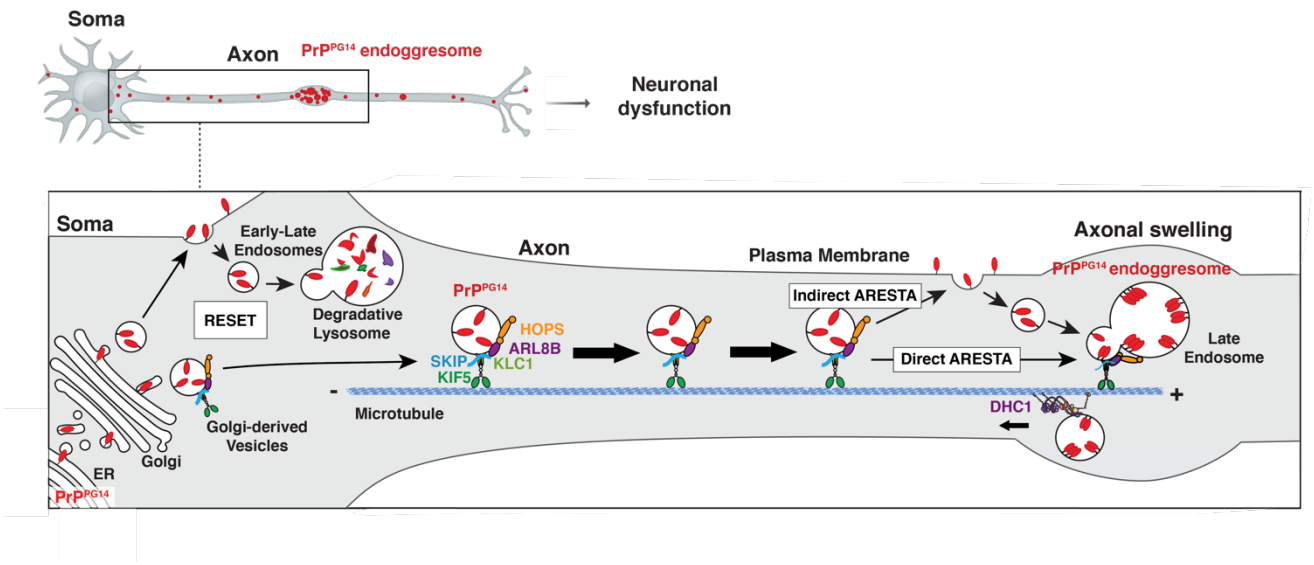


Fig. S11. Neuronal endolysosomal trafficking pathways that clear misfolded PrP in the soma and promote endoggresome formation in axons. Model showing endosomal pathways governing mutant PrP degradation versus aggregation in neurons. RESET acts in the soma to degrade PrP^{PG14} via the cell surface. Arl8b/kinesin-1/SKIP/HOPS earmarks PrP^{PG14} vesicles as endosomes and drives their axonal entry and toward ARESTA-dependent aggregation. Aggregation occurs following indirect targeting of PrP^{PG14} to late endosomes via the axonal cell surface, via its direct homotypic fusion, or both. Dynein-mediated retrograde transport and axonal degradative capacity are impaired in axons thus promoting the maintenance of endoggresomes in axons.

Movie S1.

Axonal transport of PrP^{PG14}-mCh vesicles and aggregates. Inverted contrast movie showing axonal transport of PrP^{PG14}-mCh vesicles and aggregates in an axon of a cultured hippocampal neuron.

Movie S2.

Axonal transport of PrP^{WT}-mCh vesicles. Inverted contrast movie showing axonal transport of PrP^{WT}-mCh vesicles in an axon of a cultured hippocampal neuron.

Movie S3.

Degradation of PrP^{PG14}-mCh in lysosomes in the soma. Movie of a neuron co-expressing LAMP1-EGFP (green) and PrP^{PG14}-mCh (red) showing PrP^{PG14}-mCh puncta disappearing.

C. Chaiamarit T, Wu Y, Verhelle A, Encalada SE. **2023. Fluorescence Assays for Real-Time Tracking of Cell Surface Protein Internalization and Endosomal Sorting in Axons of Primary Mouse Hippocampal Neurons.** *Bio-protocol*, *13*(7), e4651. https://doi.org/10.21769/BioProtoc.4651

bio-protocol

Open Access

Published: Apr 05, 2023

Fluorescence Assays for Real-Time Tracking of Cell Surface Protein Internalization and Endosomal Sorting in Axons of Primary Mouse Hippocampal Neurons

Tai Chaiamarit[1, 2, 3], Yin Wu[1, 2, 3], Adriaan Verhelle[1, 2, 3], and Sandra E. Encalada[1, 2, 3, *]

[1]Department of Molecular Medicine, The Scripps Research Institute, La Jolla, CA 92037, USA
[2]Dorris Neuroscience Center, The Scripps Research Institute, La Jolla, CA 92037, USA
[3]Neurodegeneration New Medicines Center, The Scripps Research Institute, La Jolla, CA 92037, USA
*For correspondence: encalada@scripps.edu

Abstract

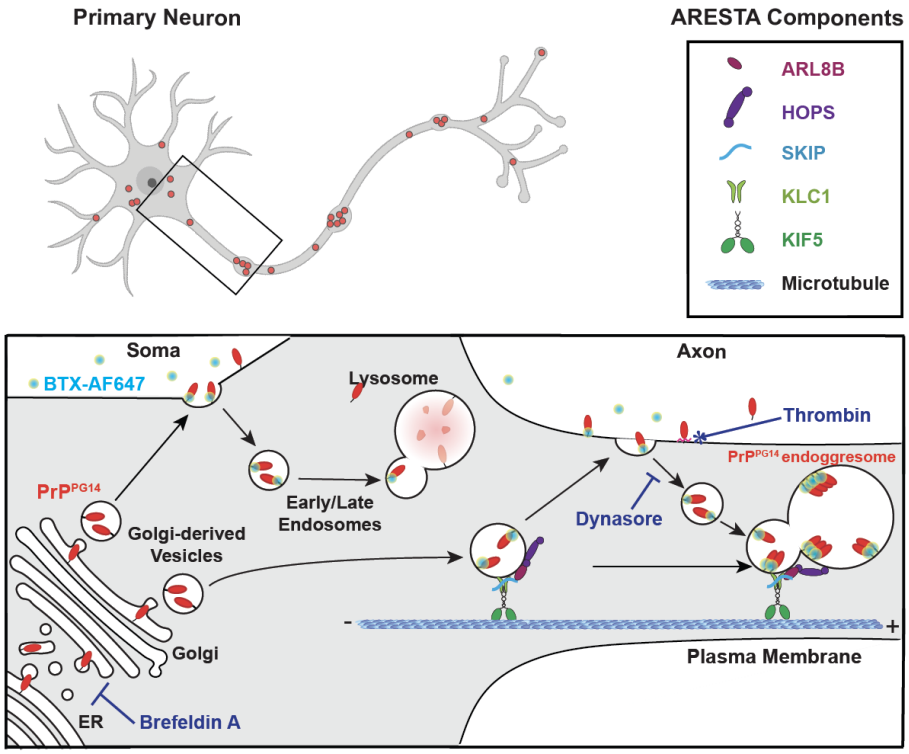
The trafficking and sorting of proteins through the secretory-endolysosomal system is critical for the proper functioning of neurons. Defects in steps of these pathways are associated with neuronal toxicity in various neurodegenerative disorders. The prion protein (PrP) is a glycosylphosphatidylinositol (GPI)-anchored protein that follows the secretory pathway before reaching the cell surface. Following endocytosis from the cell surface, PrP sorts into endosomes and lysosomes for further recycling and degradation, respectively. A few detailed protocols using drug treatments and fluorescent dyes have previously allowed the tracking of PrP trafficking routes in real time in non-neuronal cells. Here, we present a protocol optimized for primary neurons that aims to monitor and/or manipulate the trafficking and sorting of PrP particles at several steps during their secretory-endolysosomal itineraries, including (a) ER export, (b) endocytosis, (c) lysosomal degradation, and (d) accumulation in axonal endolysosomes. These primary neuron live assays allow for the robust quantitation of accumulation and/or degradation of PrP or of other membrane-associated proteins that transition from the ER to the Golgi via the cell surface.

Keywords: Primary neurons, Axonal transport, PrP, Trafficking, Endosomes, Endocytosis, ARESTA, Endoggresomes

This protocol was validated in: Sci Adv (2020), DOI: 10.1126/sciadv.abg3693

Copyright: © 2023 The Authors; exclusive licensee Bio-protocol LLC.
This is an open access article under the CC BY-NC license (https://creativecommons.org/licenses/by-nc/4.0/).

Graphical abstract



Background

Both wild-type (PrP^{WT}) and mutant prion proteins (PrP^{mut}) exit the ER and Golgi and follow secretory and endolysosomal trafficking pathways en route to somatodendritic and axonal cell surfaces, where PrP attaches via its glycosylphosphatidylinositol (GPI) anchor prior to internalization (Satpute-Krishnan et al., 2014; Zavodszky and Hegde, 2019; Chassefeyre et al., 2021). From the cell surface, PrP^{WT} is endocytosed and sorted into endosomes or lysosomes for recycling or degradation, respectively, while PrP^{mut} accumulates inside non-acidic/non-degradative enlarged endolysosomes where it can form aggregates called endoggresomes (Chassefeyre et al., 2021). PrP^{mut} endoggresome formation in axons occurs via an **a**xonal **r**apid **e**ndosomal **s**orting and **t**ransport-dependent **a**ggregation (ARESTA) pathway (Chassefeyre et al., 2021). In ARESTA, vesicles containing luminal PrP^{mut} exit from the Golgi after association with a protein complex composed of the small endolysosomal guanosine triphosphatase (GTPase) ARL8b. ARL8b recruits its effectors SifA and kinesin-interacting protein (SKIP), the kinesin-1 (KIF5C) molecular motor and associated kinesin light chain 1 (KLC1) subunit, and the vacuolar protein sorting 41 (VPS41), a member of the multiunit homotypic fusion and protein sorting (HOPS) complex (Hofmann and Munro, 2006; Khatter et al., 2015), which associate to endosomes carrying PrP^{mut} and promote their entry into the axon and their homotypic fusion to form endoggresomes (**Graphical abstract**). For aggregation to occur in axons, endosomes carrying PrP^{mut} homotypically fuse within axons after direct trafficking from the Golgi, or after undergoing rapid bouts of exocytosis and endocytosis throughout the axonal surface prior to fusion via the HOPS fusion complex. The rapid and very transient residence at the cell surface of PrP^{mut} compared to PrP^{WT} is key for the formation of endoggresomes vs. their degradation in axons. To understand the biology of misfolded PrP^{mut} endoggresome formation vs. the normal trafficking of PrP^{WT}, it is therefore critical to follow the transit of PrP particles throughout these subcellular itineraries.

Previous studies using drug treatments and fluorescent assays could monitor the trafficking routes of misfolded PrP in non-neuronal cells grown in culture (Satpute-Krishnan et al., 2014; Zavodszky and Hegde, 2019). However, as

neurons are primary targets in prion diseases, it is important to follow the subcellular sorting of misfolded PrP in neurons, including in highly polarized compartments such as axons, which are primarily affected in disease. Here, we present live assays to image and quantitate the formation of PrP^{mut} endoggresomes along their subcellular transit inside vesicles at the single-particle level using standard fluorescence microscopy, in either the soma or in axons of primary neurons, in the presence or absence of compounds that can modulate ER export and internalization capacity. These assays also monitor PrP^{mut} accumulation in endolysosomal compartments. These approaches allowed the identification of trafficking and sorting pathways of PrP^{mut} endoggresome biogenesis and would allow the monitoring of the trafficking of various other membrane proteins, including of the amyloid precursor protein (APP) or amyloid beta peptides implicated in the pathophysiology of Alzheimer's disease, using cultured primary neurons as a model system.

Materials and Reagents

1. 60 × 15 mm Nunc™ Cell Culture/Petri Dishes (Thermo Fisher, catalog number: 150288)
2. 150 × 21 mm Nunc™ Cell Culture/Petri Dishes (Thermo Fisher, catalog number: 168381)
3. 15 mL Falcon tube (Thermo Fisher, catalog number: 12565268)
4. #1.5 thickness 12 mm coverslip (Neuvitro, catalog number: NC0319857)
   Note: Wash 3× acetone, 3× ethanol, and rinse 3× with sterile water; store in sterile water.
5. Cell culture plate, size 24-wells, sterile, flat bottom, tissue-culture treated (Sigma, catalog number: SIAL0524)
6. Syringe filter Millex-GP, 33 mm, PES, 0.22 µm, gamma-sterile, hydrophilic, FDA, CE, 50 pc/PAK (Millipore, catalog number: MPSLGPM33RS)
7. Eppendorf® Safe-Lock microcentrifuge tubes, 1.5 mL (Sigma, catalog number: T9661)
8. 45 units of papain (Worthington, catalog number: PAPL LS003119)
9. Hanks' Balanced Salt Solution (HBSS), calcium, magnesium (Gibco, catalog number: 24020-117), store at 4 °C
10. Lipofectamine™ 2000 transfection reagent (Invitrogen, catalog number: 11668030), store at 4 °C
11. Brefeldin A solution (1,000×) (BioLegend, catalog number: 420601), 5 mg/mL, store at 4 °C
12. Bungarotoxin (BTX), Alexa Fluor® 647 (AF647) conjugate (Thermo Fisher, catalog number: B35450)
    Resuspend in H_2O at a concentration of 1 mg/mL
    Add sodium azide (Sigma, catalog number: 199931) at 2 mM
    Store small aliquots at -20 °C. Avoid freezing and thawing. Protect from light
13. Tubocurarine hydrochloride pentahydrate (Sigma, catalog number: T2379-100MG)
    Resuspend in H_2O at 10 mM stock concentration
    Store aliquots at 4 °C
14. Dynasore hydrate (Sigma, catalog number: D7693-5MG)
    Resuspend in DMSO to make 80 mM stock solution, store at -20 °C.
15. LysoTracker™ Green DND-26 (Invitrogen, catalog number: L7526), 1 mM, store at -20 °C
16. Magic Red Cathepsin-B Assay kit (ImmunoChemistry Technologies, catalog number: 937), store at 4 °C
    Resuspend in 200 µL DMSO to the vial to make 250× stock, store at 4 °C.
    Before each use, dilute the 250× DMSO stock in sterile H_2O at 1:10 to make 25× sub-stock. Use immediately.
17. Thrombin from rat plasma (Sigma, catalog number: T5772-100UN), lyophilized powder
    Resuspend in 1 mL to make a stock of 100 U/ml (20×), store at -20 °C.
18. Dimethyl sulfoxide (DMSO) (Sigma, catalog number: D4540), ≥99.5% (GC), suitable for cell culture
19. Phosphate-buffered saline (PBS), pH 7.2 (Gibco, catalog number: 20012027), suitable for cell culture
20. Water, cell culture grade (Corning, catalog number: 15363651)
21. Borate buffer (5 mL) (see Recipes)
    Boric acid (Fisher, catalog number: A73-500)
    Borax (Sigma, catalog number: B-9876)
22. 1 mL of 0.05% DNaseI (see Recipes)
    DNaseI (Boehringer, catalog number: 10104159001, 100 mg from bovine pancreas, grade II)
    $MgSO_4$ (Fisher, catalog number: BP213-1)
    HBSS (Gibco, catalog number: 24020-117) (without Pen-Strep)

23. Poly-L-lysine stock solution (see Recipes)
    5 mg bottle of Poly-L-lysine hydrobromide, molecular weight = 300,000, lyophilized powder, gamma-irradiated, BioXtra, suitable for cell culture (Sigma, catalog number: P5899-5MG)
24. Dissection media (see Recipes)
    HBSS (Gibco, catalog number: 24020117)
    D-glucose (Sigma, catalog number: G6152-100g or G5767-500g)
    HEPES (Sigma, catalog number: H4034-100g or H-7523-50g)
    Pen-Strep (Gibco, catalog number: 15140148 for 20 mL)
25. Brain digestion enzyme (Mixture A) (see Recipes)
    PBS (Gibco, catalog number: 21600069, or DPBS, catalog number: 14190-144)
    DL-cysteine HCl (Sigma, catalog number: C9768)
    BSA (Sigma, catalog number: A7906-100G)
    D-glucose (Sigma, catalog number: G6152)
26. Plating media (see Recipes)
    DMEM High Glucose (1×) with phenol red + L-Glut w/o Sod. Pyr. (Gibco, catalog number: 11965092)
    FBS (Gibco, catalog number: 26050-070)
27. Growth media (see Recipes)
    Neurobasal A (NBA) medium with phenol red (Gibco, catalog number: 10888022)
    B-27 Supplement (50×) (Gibco, catalog number: 17504044)
    GlutaMAX-I 100× (Gibco, catalog number: 35050061)

Equipment

1. Surgical scissors (sharp/blunt) 4–6” (Fine Science Tools, catalog number: 14028-10)
2. Dumont forceps Super Fine #7 (Fine Science Tools, catalog number: 11271-30)
3. For brain dissections: stereo microscope equipped with dual top and bottom illumination, and with 6× and 12× magnification eyepieces/objectives.
4. 5 mL Nunc™ serological pipettes (Thermo Scientific, catalog number: 170355N)
5. 10 mL Nunc™ serological pipettes (Thermo Scientific, catalog number: 170356N)
6. 25 mL Nunc™ serological pipettes (Thermo Scientific, catalog number: 170357N)
7. Nikon Ti-E Perfect Focus inverted fluorescence microscope, with a total internal reflection fluorescence (TIRF) setup, equipped with 100×/1.49NA objectives and Andor iXon + DU897 EM Camera
8. CO_2 incubator for live imaging on the microscope
9. 35 mm Dish | No. 1.5 Coverslip | 14 mm glass diameter | uncoated (MatTek, catalog number: P35G-1.5-14-C)
10. Biosafety cabinet Class II
11. SciSpin MINI microfuge BLUE, with rotor for 8 × 1.5/2.2 mL, (7,000 rpm/2,680 × *g*) (SciQuip, catalog numbers: SS-6050 and SS-6058)

Software

1. ImageJ (Fiji) software (free download from https://imagej.net/software/fiji/)
2. Microsoft Excel

Procedure

A. Hippocampal neuron plating preparation

Note: Steps 1–5 should be performed under sterile conditions in a tissue culture room and in a class II biosafety hood, equipped with a vacuum flask system and an aspirator hood.

1. Dilute poly-L-lysine stock solution to a working solution of 50 µg/mL. Add an appropriate amount of working solution to coat glass coverslips placed inside wells of a 24-well plate (~500 µL/well) or a 35 mm MatTek glass-bottom dish (~1 mL/well) and incubate at 37 °C for at least 2 h or overnight, a range that in our experience coats the coverslip surface for the proper adherence of hippocampal neurons.
2. Wash coverslips three times in sterile, cell culture grade water.
3. Fill each well of a 24-well plate containing single coverslips with 500 µL of Plating media (DMEM + 10% FBS) (half the final volume) and incubate at 37 °C and 5.0% CO_2 until plating (see **Notes #4** below).
4. Thaw Mixture A and DNase I. Mix 5 mL of Mixture A + 45 units of papain powder in a 15 mL Falcon tube and incubate in a 37 °C water bath for 15 min until papain dissolves completely. Then, add 1 mL of 0.05% DNase I, filter-sterilize the mixture through a 0.22 µm filter, and keep the solution in a 15 mL Falcon tube at room temperature for up to 2 h.
5. Pre-warm ~25 mL of the Plating media (DMEM + 10% FBS) at 37 °C and 5.0% CO_2 in a 150 mm dish.

B. Mouse hippocampal neuron isolation and plating [adapted from Kaech and Banker (2006)]

Note: Steps 1–8 can be done on a standard laboratory bench. Steps 9–16 should be done in a class II biosafety hood, equipped with a vacuum flask system and an aspirator hood. Steps 4–8 should be done quickly, ideally in under 30 min to avoid deterioration of tissue.

1. Collect mouse neonates at P0 (Day 0) and up to P2 (Day 2). Keep the pups in contact with a bag of warm water or with a preheated heating pad.
2. Clean the dissection tools with water and soap, followed by a wash with 70% ethanol.
3. Dish A and B: Put ~8 mL of Dissection media into two 60 mm dishes and in a 15 mL Falcon tube inside an ice bucket (Figure 1).
4. Decapitate the pups with surgical scissors into Dish A, containing the Dissection media. Shake gently to clean off the blood (Figure 1A).
5. Peel off the skin and the skull using two Dumont forceps. Isolate the brain into Dish B (Figure 1B).
6. Split the brain along the midline with Dumont forceps. Remove the cerebellum on the posterior side and discard. Position the medial side of the hemisphere facing up. Remove the midbrain (ventral part) by inserting the Dumont forceps ~45° and flipping. Peel off meninges (membrane covering cortex) and blood vessels (Figure 1C).
7. Ensure the hippocampus (seahorse/banana shaped) is visible and intact. To isolate hippocampus, stabilize the hemisphere by spearing the base of the brain and by cutting along the top edges of the hippocampus using Dumont forceps (Figure 1C).

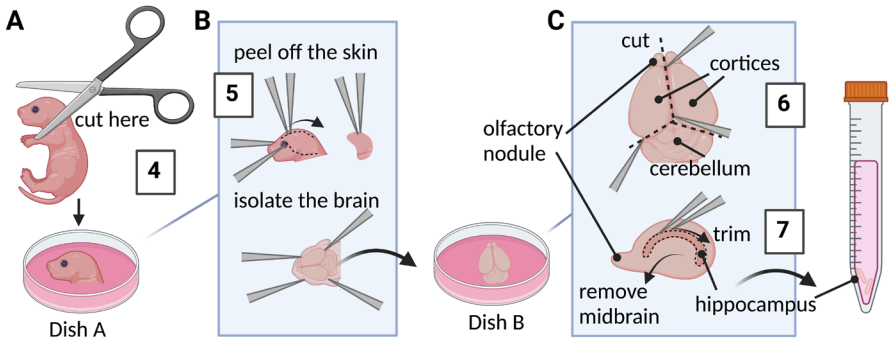


Figure 1. Isolation of hippocampi from mouse P0–P2 neonates for primary hippocampal cultures. (A) Decapitate; **(B)** Remove the brain; **(C)** Harvest the hippocampus (outlined by dotted lines in bottom figure). Numbers 4–7 correspond to steps in **Procedure B**. (adapted from https://www.thermofisher.com/us/en/home/references/protocols/neurobiology/neurobiology-protocols/isolation-of-mouse-primary-neurons.html).

8. Using a 10 mL serological pipette, gently transfer both hippocampi into a 15 mL Falcon tube containing Dissection media. Repeat the steps to harvest more hippocampi, if needed.
   Note: Work inside a biosafety hood for the rest of the protocol.
9. Aspirate the Dissection media and wash the hippocampi twice in ~8 mL of cold HBSS (without antibiotics).
   Note: Be careful not to aspirate hippocampi.
10. Aspirate HBSS. Add ~1 mL of the Brain Digestion Enzyme (5 mL of Mixture A + 45 units of papain + 1 mL of 0.05% DNaseI) per two hippocampi. Incubate for 15 min at 37 °C. Invert the tube gently by hand a couple of times every 2–5 min, so that dead cells on the outer layers detach during this step.
    Note: It is critical for viability of plated neurons that temperature is 37 °C and not higher.
11. Aspirate the Brain Digestion Enzyme slowly and gently. Wash twice with ~6 mL of Plating media (DMEM + 10% FBS), pre-warmed at 37 °C.
12. Aspirate the Plating media and add back ~1.2 mL of Plating media per two hippocampi. Use a P1000 micropipette to pipette up and down 7–10 times to dissociate the hippocampi (avoid making bubbles). Let the debris sink for 3–5 min.
13. Pipette ~1 mL of the top part of the supernatant containing dissociated cells into a new 15 mL Falcon tube and add 5 mL of the Plating media for a total volume of 6 mL.
14. *Plating cells in 24-well plates:* pipette ~500 µL of the cells into each well of a 24-well plate containing 500 µL of pre-warmed Plating media. Mix each well carefully. The cell density plated for experiments in this protocol is two hippocampi in 12 wells of a 24-well plate, which corresponds to ~ 70,000–125,000 cells per well.
15. Incubate the cells at 37 °C and 5.0% CO_2 (see **Notes #4** below), for 1–5 h to allow attachment of the cells to the coverslips.
16. Gently aspirate the Plating media one well at a time using a P1000 micropipette and replace immediately with 1 mL of Growth media (NBA + B-27 + GlutaMAX) per well. This media should be pre-warmed in the incubator at 37 °C and 5.0% CO_2 (see **Notes #4** below). Incubate cells at 37 °C and 5.0% CO_2 (see **Notes #4** below).
    Note: Do not let coverslips dry during media change.
17. Check the plate under the microscope for density, growth, and health of neurons every day. At Days in vitro (DIV) 2, neurites with growth cones should be visible in healthy neurons (**Figure 2A**). At DIV 4–5, axons (orange arrows) and dendrites (green arrows) are identifiable by morphology (**Figure 2B**). From this stage forward, neurons are ready for transfection and imaging. By DIV 9–10, axons and dendrites continue to grow and fasciculate extensively (**Figure 2C**). Researchers might find it difficult to discern a single axon without transfection of axonal fluorescent proteins.

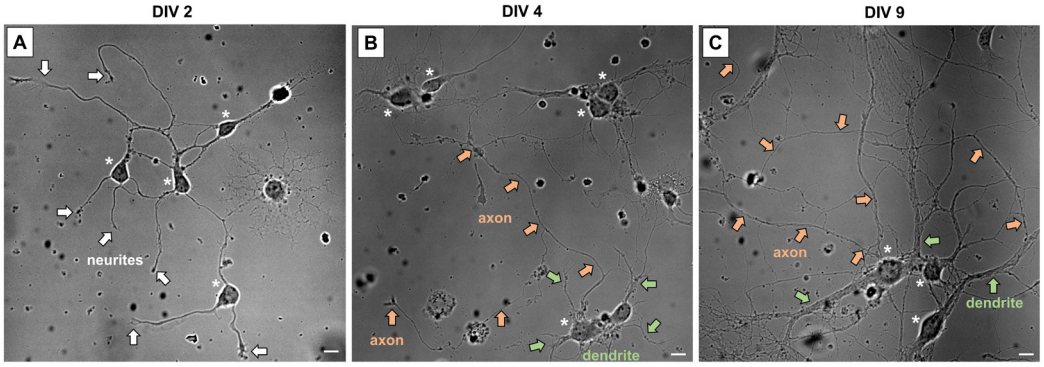


Figure 2. Growth of cultured primary hippocampal neurons at (A) day in vitro (DIV) 2, (B) DIV 4, (C) DIV 9. Neurons were plated at 1:12 dilution, i.e., two hippocampi were plated in 12 wells in a 24-well plate, yielding 75,000–125,000 cells/coverslip. Images were taken with a Nikon Plan Fluor 40×/1.3NA oil objective using Differential Interference Contrast (DIC) optics. Asterisks = soma; arrows point at axons (orange arrows) or dendrites (green arrows). Scale bar = 10 µm.

C. Transfection of cultured mouse hippocampal neurons

Note: This protocol is modified from one suggested for the use of Lipofectamine 2000 (Invitrogen™; https://www.thermofisher.com/us/en/home/references/protocols/cell-culture/transfection-protocol/lipofectamine-2000.html). This protocol is for the transfection of one coverslip in a 24-well plate of neurons at DIV 5–8; adjust accordingly for the number of coverslips required. These steps should be done under a sterile biosafety hood in a tissue culture room.

1. Prepare two 1.5 mL Eppendorf tubes.
   a. In tube 1, add 50 µL (volume adjusted) of Growth media + 400–800 ng of endotoxin-free purified plasmids that will be transfected. For PrP-mCherry (mCh) plasmids, we added 800 ng. Mix by flicking the tip of the Eppendorf tube and incubate for 5 min.
   b. In tube 2, add 48 µL of Growth media + 2 µL of Lipofectamine 2000. Mix by flicking the tip of the Eppendorf tube and incubate for 5 min.
2. Spin tube 1 and tube 2 quickly (~5 s) in a MINI microfuge.
3. After 5 min of incubation, combine the diluted DNA (tube 1) with the diluted Lipofectamine 2000 (tube 2) by dropwise pipetting. Mix by flicking the tip of the Eppendorf tube and incubate the mixture at room temperature for 30 min.
4. Transfer 500 µL of the media from each well of the 24-well plate, where neurons have been plated for 5–8 days (DIV 5–8), into empty wells of a 24-well plate and add 500 µL of new Growth media to these wells to make a total of 1mL. This will be the media to add back to each well of neurons after transfection to allow the transfer of neurotrophic factors secreted in each well pre-transfection.
5. Add 100 µL of plasmid-Lipofectamine 2000 mix to each well of the 24-well plate where the neurons are plated. Incubate at 37°C and 5.0% CO_2 for 2 h (see **Notes #4** below).
6. After 2 h, replace all the media from each well containing the neurons with the Growth media prepared in step 4. Protein expression from the plasmid transfection depends on the plasmid, protein being expressed, and concentration being transfected, but could occur as early as 45 min to 1 h after transfection.

   Notes:
   a. Incubation in Lipofectamine 2000 for longer than 3–4 h will result in toxicity.
   b. This protocol usually yields 1%–5% transfection efficiency, which is useful to observe fluorescent protein expression in single neurons and in single axons.

D. Brefeldin A (BFA) treatment

Note: Parts D–K will demonstrate the experimental procedures for PrP^{PG14}-mCh expressing neurons. The same procedures apply to PrP^{WT}-mCh (control) or any other membrane protein of interest.

1. Retention of PrP^{PG14}-mCh in the ER
   a. Prepare the transfection mixture (Lipofectamine 2000 + plasmids) as in **Procedure C**. In the 100 µL mixture, add 0.5 µL of 1,000× BFA solution (1:200 dilution).
   b. Apply the transfection mixture with BFA to neurons. The final concentration of BFA per well is 5 µg/mL (1×).
   c. Incubate for 1 h at 37 °C and 5.0% CO_2 (see **Notes** #4 below) and replace the media with 5 µg/mL BFA for another 1–5 h (**Figure 3A**).
   Note: Longer incubation time results in higher protein expression but more leakage from ER into other compartments.
   d. Image the PrP^{PG14}-mCh expression pattern in the soma and axons using live imaging. Use the same media with BFA during live imaging.
   Note: Neurons can be immunostained with organelle-specific antibodies to confirm protein localization in the cellular compartments at a given time (see examples in Chassefeyre et al., 2021).
2. Releasing PrP^{PG14}-mCh from the ER
   a. Repeat steps 1a–1c from **Procedure D**.
   b. After 2–6 h of 5 µg/mL BFA treatment, replace the media with new Growth media pre-warmed at 37 °C and 5.0% CO_2 (see **Notes #4** below; **Figure 3B**).
   c. Using a live imaging microscope, image the PrP^{PG14}-mCh expression pattern one or two days post-transfection in the soma and in axons every 10–30 min. The signal of PrP^{PG14}-mCh should appear as big, round punctate aggregates along the length of axons, and as large punctate aggregates in the soma. To confirm that PrP^{PG14}-mCh transits into lysosomes in the soma as observed previously (Chassefeyre et al., 2021), follow steps in **Procedure H**.

Note: Neurons can be immunostained with organelle-specific antibodies to confirm protein localization in the cellular compartments at a given time (see examples in Chassefeyre et al., 2021).

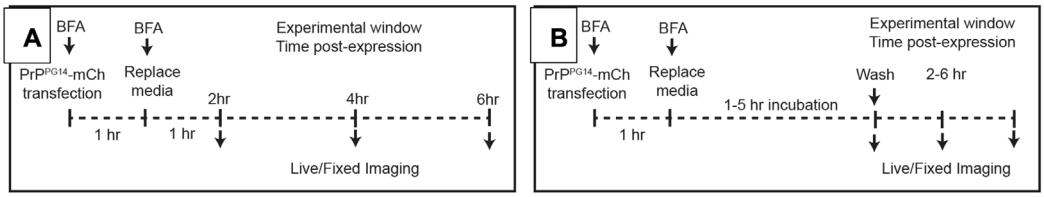


Figure 3. Timeline of Brefeldin A (BFA) treatment of hippocampal neurons. (A) Hold PrP^{PG14}-mCh in the ER. (B) Release PrP^{PG14}-mCh from the ER.

E. Imaging BTX-AF647-labeled surface PrP and its subsequent internalization (Figure 4)

1. Cloning of Bungarotoxin binding sequence (BBS) into PrP was fully described in Chessefeyre et al. (2021). In brief, a 13 amino-acid BBS tag (WRYYESSLEPYPD) was inserted at the BspEI site in the linker between mCh and the C-terminal of the PrP sequence downstream of mCh, which was shown to not alter PrP trafficking or endoggresome formation. Endotoxin-free purification of PrP^{PG14}-mCh-BBS in MoPrP.Xho vector is recommended for transfection of primary neurons.
2. Transfect neurons at DIV 5-8 with PrP^{WT}-mCh-BBS or PrP^{PG14}-mCh-BBS following the Lipofectamine 2000 protocol outlined in **Procedure C**.
3. Two days post-transfection, treat neurons with 150 µM tubocurarine chloride diluted in Growth media and incubate for 2 h at 37 °C and 5.0% CO_2 (see **Notes #4** below; Figure 4B).

Note: BTX can bind to acetylcholine (ACh) receptors on the surface of neurons. Tubocurarine blocks ACh receptors and thus reduces BTX-AF647 binding and background fluorescence signal.

4. Replace the Growth media containing tubocurarine with Growth media containing 7 µg/mL of BTX-AF647 and incubate neurons at 37 °C and 5.0% CO_2 (see **Notes #4** below) for 1 h.
5. Wash with Growth media and image the live BTX-AF647 signal immediately or one day later.

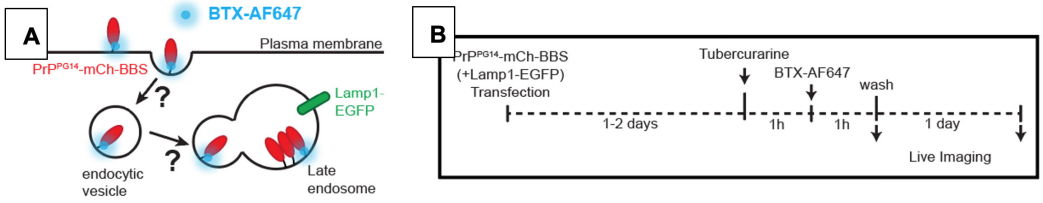


Figure 4. (A) Schematic and (B) timeline of BTX-AF647 treatment of hippocampal cultured neurons. Schematic for the live imaging of endocytosis of PrP^{PG14}-mCh-BBS into endocytic vesicles and/or the accumulation of PrP^{PG14}-mCh-BBS in endoggresomes one day after transfection.

F. Dynasore treatment to inhibit clathrin-mediated endocytosis of PrP^{PG14}-mCh from the neuronal cell surface

1. Follow **Procedure E** steps 1 and 2 to transfect DIV 5–8 neurons with PrP^{PG14}-mCh-BBS. One or two days post-transfection, add 0.5 µL of 80 nM Dynasore DMSO stock to 500 µL Growth media, mix well, and apply to neurons. Incubate for 30 min at 37 °C and 5.0% CO_2 (see **Notes #4** below) (Figure 5A).
2. Replace the media with Growth media + 150 µM Tubocurarine + 80 µM Dynasore and incubate for 1 h at 37 °C and 5.0% CO_2 (see **Notes #4** below) (Figure 5B).
3. Replace the media with Growth media + 7 µg/mL BTX-AF647 + 80 µM Dynasore and incubate for 1 h at 37 °C and 5.0% CO_2 (see **Notes #4** below) (Figure 5B).
4. Replace the media with Growth media and image neurons starting immediately and then at desired timepoints up to a day later, to image $PrP^{WT/PG14}$-mCh-BBS internalization and/or aggregation in endoggresomes and the requirement of clathrin-mediated endocytosis in these events (Figure 5B).

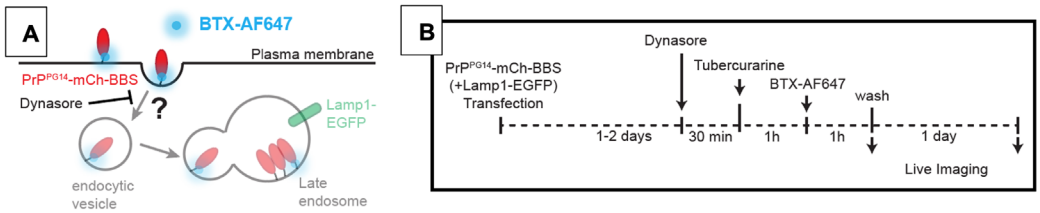


Figure 5. (A) Schematic and (B) timeline of BTX-AF647 treatment of cultured hippocampal neurons with Dynasore. Monitoring the inhibition of clathrin-mediated endocytosis on PrP^{PG14}-mCh-BBS internalization and/or on the formation of endoggresomes within one day after PrP^{PG14}-mCh-BBS expression.

G. Thrombin treatment to cleave off PrP at the cell surface

1. Cloning of Thrombin cleavage sequence (TCS)-tagged construct MoPrP.Xho PrP^{PG14}-mCh-TCS was described in Chassefeyre et al. (2021). Briefly, the TCS tag (LVPRGS) was inserted at the BspEI site downstream of mCh and was shown not to alter PrP trafficking or PrP^{PG14}-mCh endoggresome formation.

Endotoxin-free purification of PrP^{PG14}-mCh-BBS in MoPrP.Xho vector is recommended for transfection of primary neurons (Figure 6A).

2. Transfect neurons at DIV 5–8 with PrP^{PG14}-mCh-BBS following the Lipofectamine 2000 protocol outlined in **Procedure C** (Figure 6B).
3. After 2 h of incubation in Growth media + Lipofectamine 2000 transfection mix at 37 °C, 5.0% CO_2 (see **Notes #4** below), replace media with Growth media + 5 units/mL of Thrombin protease. Incubate neurons at 37 °C, 5.0% CO_2 (see **Notes #4** below) up to 2 days prior to live imaging of PrP^{PG14}-mCh endoggresome formation (Figure 6B).

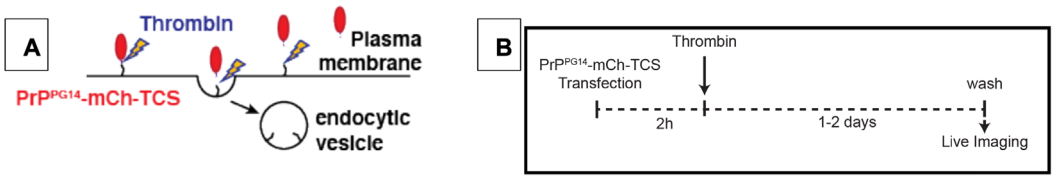


Figure 6. (A) Schematic and (B) timeline of Thrombin treatment of cultured hippocampal neurons. Cleavage of PrP^{PG14}-mCh at the TCS site and its release from the cell surface.

H. LysoTracker™ assay to probe for acidic endolysosomes

1. Grow and transfect neurons with PrP^{PG14}-mCh as described in **Procedure C** (Figure 7A).
2. Prepare 50 nM of LysoTracker™ Green (or other desired LysoTracker with different fluorescent dyes) in Growth media. Incubate DIV 5–8 neurons in LysoTracker for 2 h at 37 °C and 5.0% CO_2 (see **Notes #4** below). Wash 2–3 times in Growth media and incubate for 30 min at 37 °C and 5.0% CO_2 (see **Notes #4** below) prior to live imaging. Do not wait longer than 30 min as LysoTracker™ signal might grow fainter with time (Figure 7B).
3. Live image LysoTracker™ Green signal using a microscope equipped with a 488 nm laser (Figure 7B).
   Notes:
   a. *LysoTracker™ Green: optimal excitation wavelength is around 504 nm and optimal emission around 511 nm.*
   b. *LysoTracker™ fluorescence signal could be weak (Chassefeyre et al., 2021). Image LysoTracker™-treated neurons following the recommendations of vendors, which in our protocols is within 30 min to 1 h post-treatment of cells with LysoTracker™. This will circumvent the photobleaching that can occur after longer periods of LysoTracker™ treatment. Imaging using decreased laser power aids in avoiding photobleaching during image acquisition, as well as imaging using other microscopes, e.g., a lattice light sheet microscope. Ideally, this assay should be combined with other lysosomal protein markers (such as LAMP1) or Magic Red® (see **Procedure Part I**).*

I. Magic Red® Cathepsin B assay to probe the activity of Cathepsin B enzyme in degradative lysosomes (Figure 7)

1. Grow and transfect neurons with PrP^{PG14}-mCh as described in **Procedure C**.
2. Dilute 250× DMSO stock of Magic Red® in sterile H_2O. Apply 10 µL into each well of a 24-well plate with plated DIV 5–8 neurons, containing 250 µL of Growth media. Incubate for 2 h at 37 °C and 5.0% CO_2 (see **Notes #4** below) (Figure 7B).
3. Wash wells containing Magic Red® 2–3 times with Growth media. Incubate for 30 min at 37 °C and 5.0% CO_2 (see **Notes #4** below) prior to live imaging (Figure 7B).
4. Live image Magic Red® signal using a fluorescence microscope equipped with a 561 nm laser (Figure 7B).
   Notes:
   a. *Magic Red® has an excitation wavelength of 592 nm and an optimal emission of 628 nm.*
   b. *LysoTracker™ Green and DeepRed Magic Red® can be combined in the same experiment to cross-*

validate the observation that degradative and acidic endolysosomal organelles are present in the soma and in axons.

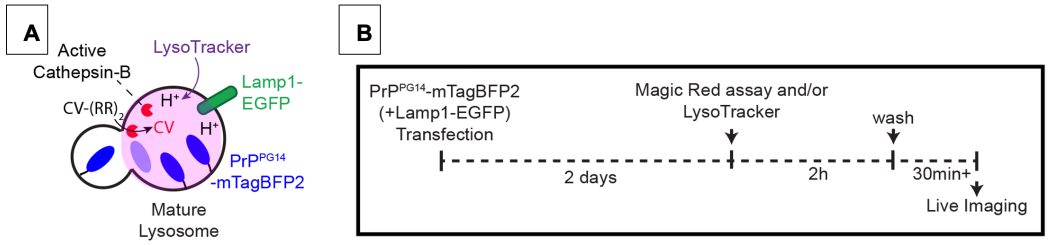


Figure 7. (A) Schematic and (B) timeline of LysoTracker™ or Magic Red® Cathepsin B Assays. Probing for PrP^{PG14}-mTagBFP2 in degradative endolysosomes.

J. Image acquisition and axon identification

1. Pre-warm the incubation chamber on the microscope until the temperature reaches a steady 37 °C. Prepare ahead of time the CO_2 chamber.
2. Live imaging of primary neurons grown on #1.5 glass coverslips in 24-well plates is done on 35 mm MatTek dishes. Add a mixture of ~500 µL of new Growth media and ~500 µL of old Growth media from the culture well to each 35 mm MatTek dish and keep dish at 37 °C and 5.0% CO_2 (see **Notes #4** below) prior to placing the coverslip inside (step 3).
3. Using Dumont tweezers with an angled fine tip, pick up the coverslip from the edge. Using care not to drop the coverslip, flip it with the cells side down onto the bottom of the MatTek dish, inside the glass bottom area.
4. Mount the MatTek dish on the microscope stage within a 37 °C and 5.0% CO_2 environment. Let the cells stabilize to that environment for 10–15 min prior to imaging.
5. Using 60× or 100× objectives with high NA, localize the transfected cells using widefield or fluorescence illumination. Distinguish dendrites vs. axons based on neuronal morphology (Encalada et al., 2011). Find the isolated axon region and acquire images.
   Note: Unless otherwise indicated, the axon region imaged is of a mid-axon region, defined as a location at least ~200 µm away from the soma and from the axon termini.

Data analysis

A. Quantitation of PrP^{PG14}-mCh endoggresome densities in axons using ImageJ

1. Subtract the background fluorescence from each of the raw images acquired: in ImageJ go to Process – Subtract background, adjust rolling ball radius using 'preview' (try rolling ball radius default = 50).
2. Draw an ROI using the segmented line tool as an outline on top of the axon (**Figure 8**). Adjust the line width to cover the axon width, which will depend on the width of the axon being analyzed (example below, line width = 1).

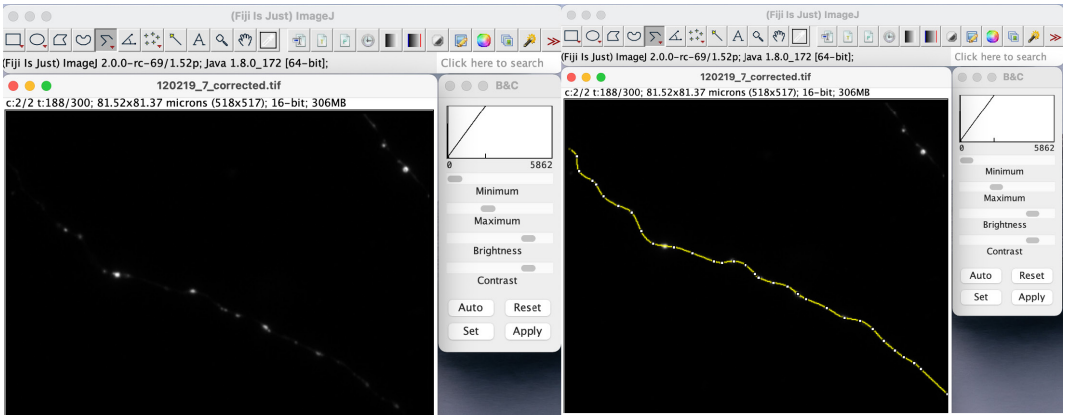


Figure 8. Subtraction of background fluorescence from images of axons of neurons expressing PrP^{PG14}-mCh. Screenshot showing the windows in ImageJ with representative images of an axon of a cultured hippocampal mouse neuron expressing PrP^{PG14}-mCh after background subtraction (left), and the window of the same axon image with the segmented line ROI drawn to outline the axon (right). Use brightness and contrast (B&C) tool to help visualize the axon contour.

To identify PrP^{PG14}-mCh endoggresomes:

3. In ImageJ, go to Analyze – plot profile. Following manual inspection of hundreds of images (Chassefeyre et al., 2021), we defined endoggresomes within axons, as PrP^{PG14}-mCh fluorescence puncta having an intensity of at least five times the intensity of small PrP^{PG14}-mCh vesicles (**Figure 9**; see **Notes #5**).

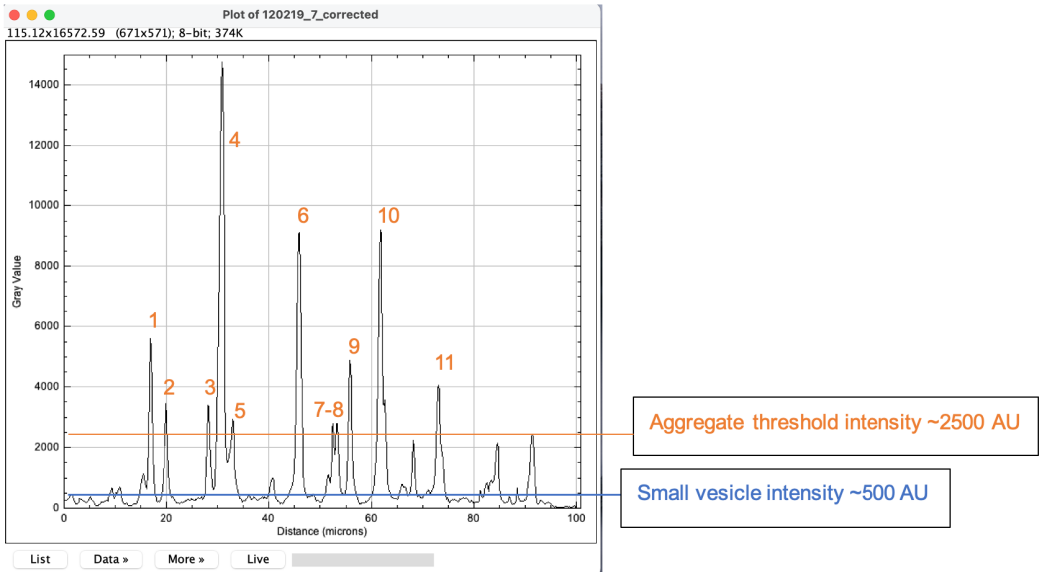


Figure 9. Plot profile of PrP^{PG14}-mCh fluorescent puncta in the axon from Figure 8. A plot profile of fluorescence intensities of the axon in Figure 8, obtained from the drawing of the segmented line ROI feature in ImageJ. The y-axis indicates the fluorescence intensity (gray values) in arbitrary units (AUs) from PrP^{PG14}-mCh point sources along the axon. Following visual examination of fluorescence intensity averages, a threshold was set at AUs = 500 to designate the smallest peaks representing signals from PrP^{PG14}-mCh vesicles. A threshold was then set at five times the vesicle intensity of 500 AUs, to designate these as PrP^{PG14}-mCh endoggresomes. Densities of PrP^{PG14}-mCh endoggresomes are then calculated by manual counts of the peaks. The definitions of thresholds are further described in detail in Chassefeyre et al. (2021).

4. Calculate PrP^{PG14}-mCh endoggresome densities for each axon image, as the number of peaks above threshold intensity (**Figure 9**) per length of axon. The length of the analyzed axon fragment is equal to the length of the segmented line (see step 2). Divide the number by length × 100 to get aggregate density/100 µm. Analyze only one axon region per neuron; this will be N_{axons}.
5. Statistical analysis: If the dataset is normally distributed, display means ± SEM and perform Student's t-test or ANOVA/multiple comparison tests as appropriate. If the dataset is not normally distributed, display boxplot, violin plot, or all data points and use non-parametric tests, such as Wilcoxon Rank Sum test or an appropriate multiple comparison test.

B. Co-transport analysis in axons using ImageJ

This protocol is for the analysis of co-transport of a non-PrP cargo (in this case of Lamp1-EGFP endolysosomes), and of PrP^{PG14}-mCh vesicles or endoggresomes moving (or not) along axons of culture mouse hippocampal neurons.

1. Co-transfect neurons with desired plasmids following the steps in **Procedure C**. In this case, neurons were co-transfected with PrP^{PG14}-mCh (400 ng) and Lamp1-EGFP (400 ng). Collect images for both PrP^{PG14}-mCh and Lamp1-EGFP channels, as indicated in **Procedure J**.
2. Open an image in ImageJ using split channels. Subtract background fluorescence from each raw image as indicated in step A above (**Figure 8, left**).
3. Draw ROI with segmented line tool onto the axon of the first channel as indicated in step A above (**Figure 8, right**). Adjust the line width to cover the axon width, which will depend on the width of the axon being analyzed (example below, line width = 1).
4. In ImageJ, go to Image – Stacks – Reslice [/]…This step will draw a kymograph showing the trajectories of Lamp-1-EGFP particles (x-axis) over time (y-axis) (**Figure 10**).

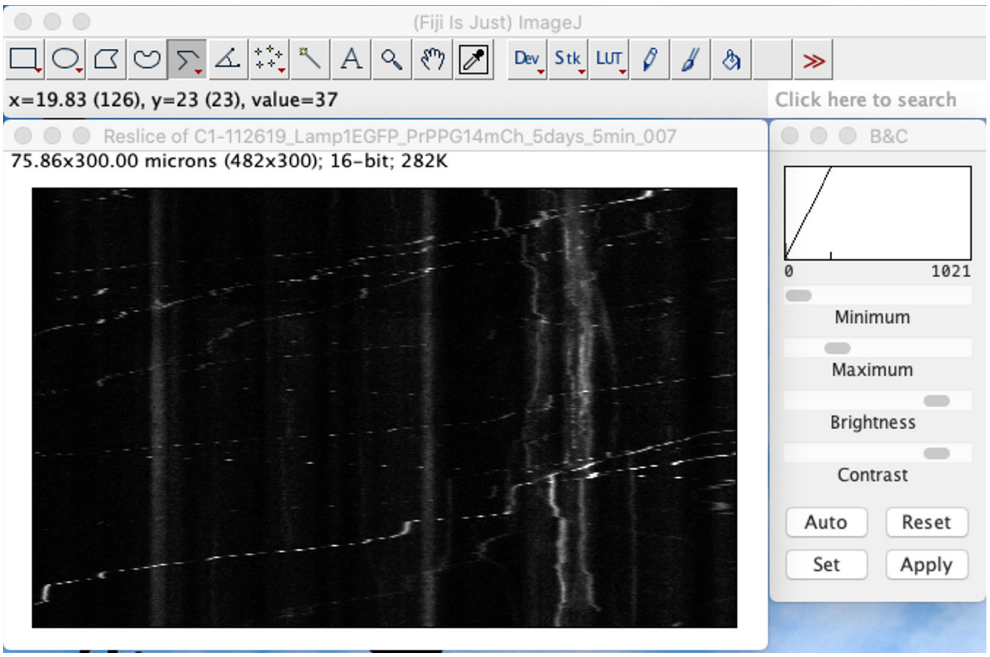


Figure 10. Transport of Lamp1-EGFP vesicles in axons of cultured hippocampal neurons. Screenshot of ImageJ showing a representative image of a kymograph of an axon showing the trajectories of Lamp1-EGFP moving or stationary vesicles. Movies were 5 min long and collected at a frame rate of 1 frame/s (1 Hz) using a Nikon TIRF microscope. For all images and movies acquired, the exposure time was set to 100 ms (Chassefeyre et al., 2021).

5. Transfer the ROI drawn from the Lamp1-EGFP image to the PrP^{PG14}-mCh image using command-E or using ROI manager in ImageJ.
6. In ImageJ, go to Image – Stacks – Reslice [/]… This step will draw a kymograph showing the trajectories of PrP^{PG14}-mCh particles (x-axis) over time (y-axis) (**Figure 11**).

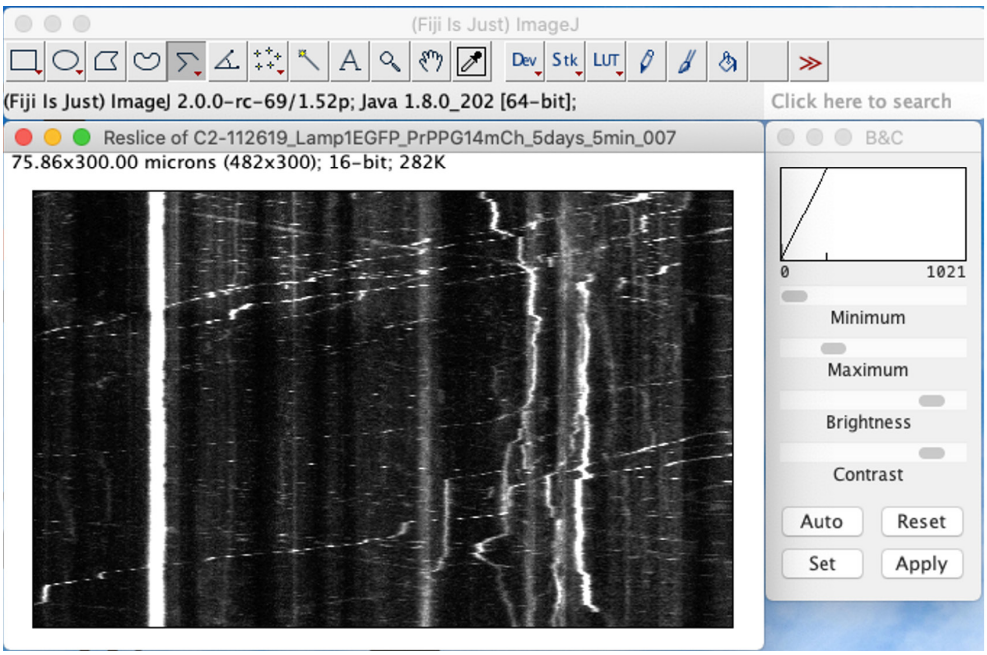


Figure 11. Transport of PrP^{PG14}-mCh vesicles in axons of cultured hippocampal neurons. Screenshot of ImageJ showing a representative image of a kymograph of an axon showing trajectories of PrP^{PG14}-mCh moving or stationary vesicles. Movies were 5 min long and collected at a frame rate of 1 frame/s (1 Hz) using a Nikon TIRF microscope. For all images and movies acquired, the exposure time was set to 100 ms (Chassefeyre et al., 2021).

7. Draw lines on kymographs to annotate all identifiable tracks on both channels (**Figure 12, left and middle panels**). Use brightness and contrast (B&C) tool to help visualize dim tracks.
   Note: The designation of trajectories/tracks, including of those that are dim in fluorescence, is determined empirically by the user. Contrast settings can be adjusted to visualize all tracks, if necessary, but it is advised to use consistency in the designation of all tracks including dim ones.
8. Copy and paste tracks onto the same image to visualize overlapping tracks (**Figure 12, right panel**).

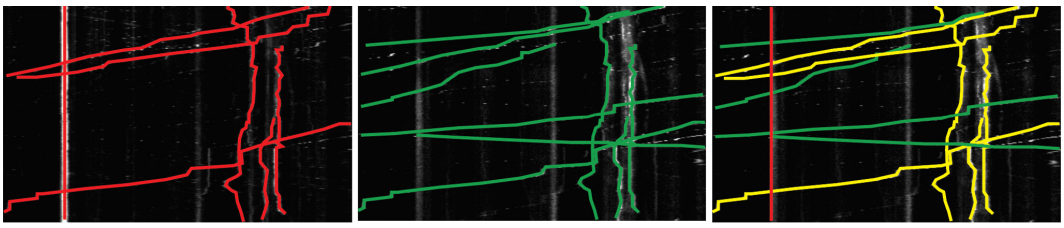


Figure 12. Analysis of kymographs of PrP^{PG14}-mCh vesicle movement. Representative kymograph images of PrP^{PG14}-mCh (left panel, red), and Lamp1-EGFP (middle panel, green) vesicle tracks/trajectories. Combined (right panel, yellow) tracks/trajectories indicate co-transport events.

9. Count percentage of co-transport trajectories per kymograph by calculating number of co-transport tracks divided by number of all tracks (of PrP^{PG14}-mCh) × 100. This indicates the degree of PrP^{PG14}-mCh

vesicles/endoggresomes co-transport with a Lamp1-EGFP vesicle. Record the numbers in Microsoft Excel. Analyze only one kymograph per axon of a neuron.

10. Perform statistical analysis. If the dataset is normally distributed, display means ± SEM and perform Student's t-test or ANOVA/multiple comparison tests as appropriate. If the dataset is not normally distributed, display boxplot, violin plot, or all data points and use non-parametric tests, such as Wilcoxon Rank Sum test or appropriate multiple comparison tests.

Notes

1. Collect the dataset for three biological replicates, i.e., primary hippocampal neurons plated from three different mice of the same genetic background, plated independently at different time points.
2. Co-transport analysis requires an appropriate temporal resolution of cargo movement. For example, to image the transport of PrP^{WT}-mCh or PrP^{PG14}-mCh vesicles, a suitable acquisition rate is 10 frames/s for 15 s. In contrast, to image the movement of PrP^{PG14}-mCh endoggresomes, which are largely stationary or move very slowly, use 1 frame/s for 5 min. Consult previous literature on different dynamics of organelles or membrane-bound compartments to get the best time-lapse video quality for quantitative analysis.
3. Imaging in the cell body requires deconvolution for widefield imaging or a confocal module. In axons, widefield or pseudo-TIRF is sufficient for quantitative imaging, due to little out-of-focus light in thin axonal regions.
4. For our experiments, incubators for culturing hippocampal mouse neurons were set at 5.5% CO_2 to ascertain that small observed fluctuations in CO_2 levels from the house lines did not result in CO_2 levels dropping below 5.0%, which is the standard level used for hippocampal neuronal culturing (Kaech and Banker, 2006). It is known that mouse hippocampal neurons can grow in >5% CO_2 (Geissler et al., 2013). During imaging in the TIRF microscope, CO_2 was supplied by a tank that provided continuous stable delivery of 5.0% CO_2 directly to the microscope incubation/imaging chamber.
5. The threshold of gray value for small vesicles and endoggresomes is determined empirically and independently for every image/individual axon.

Recipes

1. Borate buffer (5 mL)

1.24 g boric acid
1.90 g borax
Dissolve in 400 mL of ddH_2O, pH 8.5, filter-sterilize, and store at 4 °C.

2. 1 mL of 0.05% DNaseI

50 mg of DNaseI
0.5 mL of 1.2 M $MgSO_4$
100 mL of HBSS (without pen-strep)

3. Poly-L-lysine stock solution

Reagent	Final concentration	Amount
Poly-L-lysine (1 mg/mL)	0.05 mg/mL	0.5 mL
Borate buffer (pH 8.5)	n/a	9.5 mL
Total	n/a	10 mL

4. **Dissection media**

Adjust pH to 7.3, filter-sterilize, and store at 4 °C.

Reagent	Final concentration	Amount
HBSS	n/a	500 mL
D-glucose	n/a	0.4 g
HEPES	n/a	0.834 g
Pen-Strep	n/a	5 mL
Total	n/a	505 mL, pH 7.3, filter-sterilize

Brain digestion enzyme (Mixture A)

Filter-sterilize and store aliquots at -20 °C.

Reagent	Final concentration	Amount
PBS	n/a	4 mL
DL-cysteine HCl	n/a	1 mg
BSA	n/a	1 mg
D-glucose	n/a	25 mg
Total	n/a	5 mL

5. **Plating media**

500 mL of DMEM High Glucose (1×) with phenol red + L-Glut w/o Sod. Pyr.
50 mL of FBS
Store at 4 °C and pre-warm to 37 °C before plating.

Reagent	Final concentration	Amount
DMEM	n/a	28 mL/brain
Total	n/a	28 mL

6. **Growth media**

Store at 4 °C and pre-warm to 37 °C before plating

Reagent	Final concentration	Amount
NBA	n/a	48.875 mL
GlutaMAX	n/a	0.125 mL
B27	n/a	1 mL
Total	n/a	50 mL

Acknowledgments

We thank Romain Chassefeyre and co-authors of the original research paper (Chassefeyre et al., 2021) for performing experiments. This work was supported by NIH/NIA R01AG049483 and R01AG076745 grants; by the Glenn Foundation for Medical Research Award for Research in Biological Mechanisms of Aging; by a New Scholar in Aging Award from the Lawrence Ellison Foundation; and by a Baxter Family Foundation award to S.E.E. T.C. was supported by a Thai Government Scholarship from the Development and Promotion of Science and Technology Talents Project (DPST). A.V. and Y.W were supported by a Dorris Neuroscience Center Fellowship.

Competing interests

The authors declare no competing interests.

Ethics

Our mouse protocols were reviewed and approved by Institutional Animal Care and Use Committee (IACUC) at The Scripps Research Institute (Scripps Research) and all colonies were maintained following the guidelines recommended by the Department of Animal Resources (DAR) at Scripps Research.

References

Chassefeyre, R., Chaiamarit, T., Verhelle, A., Novak, S. W., Andrade, L. R., Leitao, A. D. G., Manor, U. and Encalada, S. E. (2021). Endosomal sorting drives the formation of axonal prion protein endoggresomes. *Sci Adv* 7(52): eabg3693.

Encalada, S. E., Szpankowski, L., Xia, C. H. and Goldstein, L. S. (2011). Stable kinesin and dynein assemblies drive the axonal transport of mammalian prion protein vesicles. *Cell* 144(4): 551-565.

Geissler, M., Gottschling, C., Aguado, A., Rauch, U., Wetzel, C. H., Hatt, H. and Faissner, A. (2013). Primary hippocampal neurons, which lack four crucial extracellular matrix molecules, display abnormalities of synaptic structure and function and severe deficits in perineuronal net formation. *J Neurosci* 33(18): 7742-7755.

Hofmann, I. and Munro, S. (2006). An N-terminally acetylated Arf-like GTPase is localised to lysosomes and affects their motility. *J Cell Sci* 119(Pt 8): 1494-1503.

Kaech, S. and Banker, G. (2006). Culturing hippocampal neurons. *Nat Protoc* 1(5): 2406-2415.

Khatter, D., Raina, V. B., Dwivedi, D., Sindhwani, A., Bahl, S. and Sharma, M. (2015). The small GTPase Arl8b regulates assembly of the mammalian HOPS complex on lysosomes. *J Cell Sci* 128(9): 1746-1761.

Satpute-Krishnan, P., Ajinkya, M., Bhat, S., Itakura, E., Hegde, R. S. and Lippincott-Schwartz, J. (2014). ER stress-induced clearance of misfolded GPI-anchored proteins via the secretory pathway. *Cell* 158(3): 522-533.

Zavodszky, E. and Hegde, R. S. (2019). Misfolded GPI-anchored proteins are escorted through the secretory pathway by ER-derived factors. *Elife* 8: e46740.

D. Chaiamarit T, Verhelle A, Chassefeyre R, Shukla N, Novak SW, Andrade LR, Manor U, Encalada SE. **2023. Mutant Prion Protein Endoggresomes are Hubs for Local Axonal Organelle-Cytoskeletal Remodeling.** *bioRxiv*, 2023.03.19.533383. https://doi.org/10.1101/2023.03.19.533383

bioRxiv preprint doi: https://doi.org/10.1101/2023.03.19.533383; this version posted March 21, 2023. The copyright holder for this preprint (which was not certified by peer review) is the author/funder. All rights reserved. No reuse allowed without permission.

Mutant Prion Protein Endoggresomes are Hubs for Local Axonal Organelle-Cytoskeletal Remodeling

Tai Chaiamarit[1-3], Adriaan Verhelle[1-3], Romain Chassefeyre[1-3, §], Nandini Shukla[1-3], Sammy Weiser Novak[4], Leonardo R. Andrade[4], Uri Manor[4], & Sandra E. Encalada[1-3, *]

[1]Department of Molecular Medicine, The Scripps Research Institute, La Jolla, CA, 92037 USA.

[2]Dorris Neuroscience Center, The Scripps Research Institute, La Jolla, CA, 92037 USA.

[3]Neurodegeneration New Medicines Center, The Scripps Research Institute, La Jolla, 92037 CA, USA

[4]Waitt Advanced Biophotonics Center, The Salk Institute for Biological Studies, La Jolla, 92037 CA, USA

[§]Present address: Evotec, 31036 Toulouse, France.

[*]Correspondence and requests for materials should be addressed to Sandra Encalada (encalada@scripps.edu).

bioRxiv preprint doi: https://doi.org/10.1101/2023.03.19.533383; this version posted March 21, 2023. The copyright holder for this preprint (which was not certified by peer review) is the author/funder. All rights reserved. No reuse allowed without permission.

Abstract

Dystrophic axons comprising misfolded mutant prion protein (PrP) aggregates are a characteristic pathological feature in the prionopathies. These aggregates form inside endolysosomes -called endoggresomes-, within swellings that line up the length of axons of degenerating neurons. The pathways impaired by endoggresomes that result in failed axonal and consequently neuronal health, remain undefined. Here, we dissect the local subcellular impairments that occur within individual mutant PrP endoggresome swelling sites in axons. Quantitative high-resolution light and electron microscopy revealed the selective impairment of the acetylated vs tyrosinated microtubule cytoskeleton, while micro-domain image analysis of live organelle dynamics within swelling sites revealed deficits uniquely to the MT-based active transport system that translocates mitochondria and endosomes toward the synapse. Cytoskeletal and defective transport results in the retention of mitochondria, endosomes, and molecular motors at swelling sites, enhancing mitochondria-Rab7 late endosome contacts that induce mitochondrial fission via the activity of Rab7, and render mitochondria dysfunctional. Our findings point to mutant Pr Pendoggresome swelling sites as selective hubs of cytoskeletal deficits and organelle retention that drive the remodeling of organelles along axons. We propose that the dysfunction imparted locally within these axonal micro-domains spreads throughout the axon over time, leading to axonal dysfunction in prionopathies.

bioRxiv preprint doi: https://doi.org/10.1101/2023.03.19.533383; this version posted March 21, 2023. The copyright holder for this preprint (which was not certified by peer review) is the author/funder. All rights reserved. No reuse allowed without permission.

INTRODUCTION

Compelling evidence indicates that axonal pathologies contribute to neurodegeneration in Alzheimer's disease (AD), Parkinson's disease (PD), Huntington's disease (HD), amyotrophic lateral sclerosis (ALS), and prion diseases[1-4]. Specifically, accumulations of misfolded and aggregate-prone proteins along axons are often observed at swelling sites, and these have been linked to neuronal dysfunction via poisoning of axonal transport[5,6], by trapping of organelles, proteins, and cytoskeletal elements, or by damage to mitochondrial dynamics and health[7-9]. Importantly, axonal deficits precede clinical manifestations and occur before neuronal cell body loss, strongly implicating axonal dysfunction as one of the earliest pathological events in neurodegeneration[3,10,11]. However, the subcellular mechanisms leading to axonal damage in the proteinopathies remain largely undefined.

Sporadic, infectious, and familial prion diseases (PrDs) are progressive and fatal neurodegenerative disorders commonly associated with neuronal loss, spongiform change, astrogliosis, and microglial activation[12]. Brain pathological lesions occur following conversion of the glycosylphosphatidylinositol (GPI)–anchored cellular/wild-type prion protein (PrP^{C}/PrP^{WT}) into an aggregate-prone misfolded PrP conformation (PrP^{Sc}-scrapie)[13-15]. PrDs are characterized by the deposition of misfolded PrP aggregates throughout the central nervous system (CNS), including within dystrophic swellings in axons[16], where human disease-associated mutant PrP has been shown to actively form neurotoxic aggregates within enlarged endolysosomes called endoggresomes[17]. In addition to PrP aggregates, axonal swellings also contain trapped mitochondria and enlarged membrane-bound endosomes[18], and these are commonly observed in axons of cultured primary neurons expressing disease-associated mutant PrP, in the brains of rodents infected with scrapie or that harbor PrP mutations, and in post-mortem brains of patients

bioRxiv preprint doi: https://doi.org/10.1101/2023.03.19.533383; this version posted March 21, 2023. The copyright holder for this preprint (which was not certified by peer review) is the author/funder. All rights reserved. No reuse allowed without permission.

with human prion disease[9,17-21]. The buildup of endosomes and organelles in axons suggest a breakdown of the axonal cytoskeletal and trafficking systems, but how the genesis of these putative pathological lesions relate to the presence of misfolded protein aggregates at localized regions in axons, remains unexplored.

Within the axon, tightly regulated endolysosomal trafficking and cytoskeletal-based transport systems ensure the faithful distribution of membrane-bound endolysosomal proteins and organelles over long distances[17,22]. The coordinated activities of the molecular motors kinesin and dynein drive the anterograde (toward synapse), and retrograde (toward cell body) movement, respectively, of pre-synaptic vesicles, mitochondria, and of endosomes along microtubule (MT) tracks that line up along the length of axons[23]. Regulation of axonal transport is achieved in part by MT post-translational modifications (PTMs) to tubulin, including acetylation and tyrosination/detyrosination, which impart MT track mechanical stability and also serve as signals for the recruitment of MT associated proteins (MAPs), molecular motors, and other regulatory signaling molecules[24-26]. An intact transport system is critical for the proper translocation and distribution of endosomes and mitochondria along axons, including to distal synapses where their close interactions regulate energy production and calcium/metabolite buffering[27]. Tight coordination of motor activity also drives mitochondrial fusion and fission dynamics, key events that ensure the maintenance of functional axonal mitochondria, especially during cellular stress[28]. Impairments in mitochondrial fusion/fission dynamics has been proposed to contribute to the pathophysiology of PrDs[29,30], yet it is unclear whether misfolded protein aggregation including of PrP, directly drives organelle-endosome accumulations and mitochondrial dysfunction in axons.

bioRxiv preprint doi: https://doi.org/10.1101/2023.03.19.533383; this version posted March 21, 2023. The copyright holder for this preprint (which was not certified by peer review) is the author/funder. All rights reserved. No reuse allowed without permission.

In an effort to understand the mechanisms of axonotoxicity in the familial prionopathies, here, we dissect the subcellular changes that occur within local axonal swelling sites that contain enlarged misfolded PrP endoggresomes in a neuronal model of familial prion disease. We show that a disease-associated PrP mutation harboring a 14-octapeptide repeat insertion (PrP^{PG14})[31] forms enlarged endoggresomes at axonal swelling sites that induce dysfunction to cytoskeletal MT stability uniquely within these localized domains. A cascade of selective poisoning of motor-dependent transport of mitochondria, pre-synaptic vesicles and other endosomes ensues, uniquely affecting their movement toward the synapse. Axonal swellings enriched with enlarged PrP endoggresome also actively trap molecular motors, mitochondria, and endosomes, enhancing endosome-mitochondrial contacts that directly drive local endosome-mediated mitochondrial fission. These observations suggest that axonal swelling sites containing misfolded PrP endoggresomes serve as axonotoxicity hubs that unleash cascades of selective cytoskeletal and motor destabilization, trigger disruptions in organelle movement, and are magnets for endosome-organelle assemblages that promote mitochondrial remodeling towards fission resulting in failed mitochondrial health. Importantly, the disruption of cytoskeletal and endosomal pathways within local axonal domains occur at early stages following initial expression of PrP mutations. Thus, the cascade of localized eddies of impairments that occur within swelling/aggregate sites in axons explain how axons are uniquely vulnerable to the formation of aggregates and how these aggregates trigger axonal demise. Moreover, these studies uncover local cytoskeletal and organelle-organelle dysfunction pathways as potential early targets of intervention for the development of therapies aimed at reversing these local axonal deficits in the PrDs.

bioRxiv preprint doi: https://doi.org/10.1101/2023.03.19.533383; this version posted March 21, 2023. The copyright holder for this preprint (which was not certified by peer review) is the author/funder. All rights reserved. No reuse allowed without permission.

RESULTS

Axonal transport is differentially impaired in axons with PrP^{PG14} endoggresomes

Our previous work showed that expression of PrP^{PG14}-mCherry (mCh) or -EGFP in hippocampal murine neurons resulted in the formation of large misfolded PrP^{PG14} aggregates inside endolysosomes—called endoggresomes—at localized swelling sites along axons[17] (**Supplementary Fig. 1a)**. PrP^{PG14}-EGFP endoggresomes were observed in axons 12 hours post-transfection, and endoggresome densities increased over 2 days of expression, while axons expressing PrP^{WT}- EGFP contained primarily small vesicles that were highly motile (**Supplementary Fig. 1b**). Densities of PrP^{PG14}-EGFP and PrP^{PG14}-mCh endoggresomes were comparable 2 days post-expression[17]. To investigate whether expression of PrP^{PG14}-mCh resulted in impaired axonal function, we characterized the axonal transport of three cargoes that actively mobilize in mammalian axons and that are required for proper axonal function—mitochondria, pre-synaptic vesicles, and PrP vesicles[32-34]. Single particle transport of these cargoes was imaged at high spatial and temporal resolution in axons of neurons co-transfected with PrP^{PG14}-mCh or PrP^{WT}-mCh and either mito-EGFP (containing the mitochondrial targeting sequence of Cytochrome c Oxidase subunit VIII fused to EGFP) or SYP-YFP (Synaptophysin fused to YFP; **Methods**). Time-lapse videos were analyzed using a custom-made single particle tracking analysis software to generate trajectory datasets[35]. At two days post-transfection, the densities of motile mito-EGFP particles were significantly reduced in PrP^{PG14}-mCh axons compared to PrP^{WT}-mCh controls (**Fig. 1a,b**), suggesting defective mitochondrial translocation into the axon. To further test whether the mitochondrial bidirectional movement was impaired, analysis of segmental trajectories 2 days post-expression revealed that mito-EGFP spent less time moving in the anterograde direction and more time pausing in PrP^{PG14}-mCh endoggresome-rich axons

bioRxiv preprint doi: https://doi.org/10.1101/2023.03.19.533383; this version posted March 21, 2023. The copyright holder for this preprint (which was not certified by peer review) is the author/funder. All rights reserved. No reuse allowed without permission.

compared to PrP^{WT}-mCh aggregate-free axons (**Fig. 1c**). These mito-EGFP particles also undertook shorter anterograde run lengths (**Fig. 1d**) and had reduced anterograde instantaneous velocities (**Fig. 1e**). Notably, retrograde transport dynamics of mito-EGFP particles remained unchanged in PrP^{PG14}-mCh endoggresome-rich axons compared to PrP^{WT}-mCh axons (**Fig. 1c-e**). These data show differential deficits in the movement of mitochondria uniquely towards the synapse. Notably, despite gradual accumulation of PrP^{PG14}-mCh endoggresomes 12 hours after initial PrP^{PG14}-mCh expression (**Supplementary Fig. 1b**), mito-EGFP transport was largely unaltered at this time point and thus was comparable to that in PrP^{WT}-mCh control axons (**Fig. 1a-c**), with an exception in the run lengths (**Fig. 1d**). These data indicate that mitochondrial transport impairment lags behind but progresses with time alongside PrP^{PG14} aggregation.

Mitochondria utilize kinesin-1 (KIF5 or kinesin heavy chain [KHC]) to translocate anterogradely to the axonal terminus[27]. However, reduction of a neuronally-enriched kinesin-3 (KIF1A) using a validated shRNA resulted in significant impairments to mitochondrial segmental run lengths and velocities as compared to those in D11 scrambled shRNA controls (**Supplementary Fig. 2a-c**), indicating that KIF1A is also an important driver of mitochondria movement in axons of hippocampal neurons. As the overall anterograde transport of mito-EGFP was defective upon expression of PrP^{PG14}-mCh (**Figure 1a-e**), this raises the possibility that both kinesin-1- and kinesin-3-driven transport dynamics are impaired in PrP^{PG14}-mCh-expressing axons.

We next analyzed the movement of another KIFA cargo, pre-synaptic vesicles carrying SYP-YFP, an integral membrane protein that is trafficked to the pre-synapse and is important for vesicle fusion, synaptic vesicle endocytosis, and recycling[36,37]. Transport dynamics of SYP-YFP vesicles 2 days post-transfection were analyzed using time-lapse quantitative fluorescence

bioRxiv preprint doi: https://doi.org/10.1101/2023.03.19.533383; this version posted March 21, 2023. The copyright holder for this preprint (which was not certified by peer review) is the author/funder. All rights reserved. No reuse allowed without permission.

microscopy at high spatial and temporal resolution (**Fig. 1f; Methods**). In comparison to axons expression PrP^{WT}-mCh, the percent time that SYP-YFP vesicles spent in anterograde motion in PrP^{PG14}-mCh axons was significantly decreased, while the time spent paused was increased (**Fig. 1g**). SYP-YFP vesicles also had significantly shorter segmental run lengths in PrP^{PG14}-mCh axons compared to PrP^{WT}-mCh control axons (**Fig. 1h**). As with mitochondrial transport, retrograde transport of SYP-YFP vesicles was also unaffected in the endoggresome-rich PrP^{PG14}-mCh axons (**Fig. 1g-h**), but a significantly higher proportion of SYP-YFP vesicles remain stationary in PrP^{PG14}-mCh axons, compared to PrP^{WT}-mCh axons (**Fig. 1i**), suggesting the overall retention of SYP-YFP transport towards the distal synapse.

In addition to forming PrP^{PG14} endoggresomes, axons of neurons expressing PrP^{PG14}-mCh contain motile Golgi-derived PrP^{PG14}-mCh vesicles that fuse in axons during active transport toward the synapse to form PrP^{PG14} endoggresomes (**Fig. 1j**; see **Methods** for definition of PrP^{PG14} vesicles versus endoggresomes)[17]. Quantitative single particle tracking analysis showed that 2 days post-expression, the percent anterograde-moving PrP^{PG14}-mCh vesicles in axons significantly decreased, while the percent of retrograde and stationary populations increased (**Fig. 1j,k**). These differences were amplified 5 days post-expression. At the 5-day time point, the time that PrP^{PG14}-mCh vesicles spent in motion in the anterograde direction was also significantly decreased, while more time was spent by PrP^{PG14}-mCh vesicles moving in the retrograde direction or paused (**Fig. 1l,m**). Altogether, starting at 12 hours post-transfection of PrP^{PG14}-mCh, gradual increases in transport deficits of PrP^{PG14}-mCh vesicles were observed, while mito-EGFP and SYP-YFP vesicle transport was impaired at 2 days post-transfection (**Fig. 1a-h**). These observations show that early transport defects exhibited by PrP^{PG14}-mCh vesicles concur with growing PrP^{PG14}-mCh endoggresome densities in axons at that time point

bioRxiv preprint doi: https://doi.org/10.1101/2023.03.19.533383; this version posted March 21, 2023. The copyright holder for this preprint (which was not certified by peer review) is the author/funder. All rights reserved. No reuse allowed without permission.

(**Supplementary Fig. 1b**), suggesting that the movement of PrP^{PG14}-mCh vesicles that are being removed from the motile vesicle pool to fuse and form enlarged endoggresomes[17], is progressively affected at very early stages. Moreover, the differential impairments uniquely to the anterograde transport of mitochondria and pre-synaptic suggest that anterograde transport is more susceptible to the presence of PrP^{PG14} aggregates in axons, and these observations raise the possibility of differential impairments to the anterograde transport machinery.

bioRxiv preprint doi: https://doi.org/10.1101/2023.03.19.533383; this version posted March 21, 2023. The copyright holder for this preprint (which was not certified by peer review) is the author/funder. All rights reserved. No reuse allowed without permission.

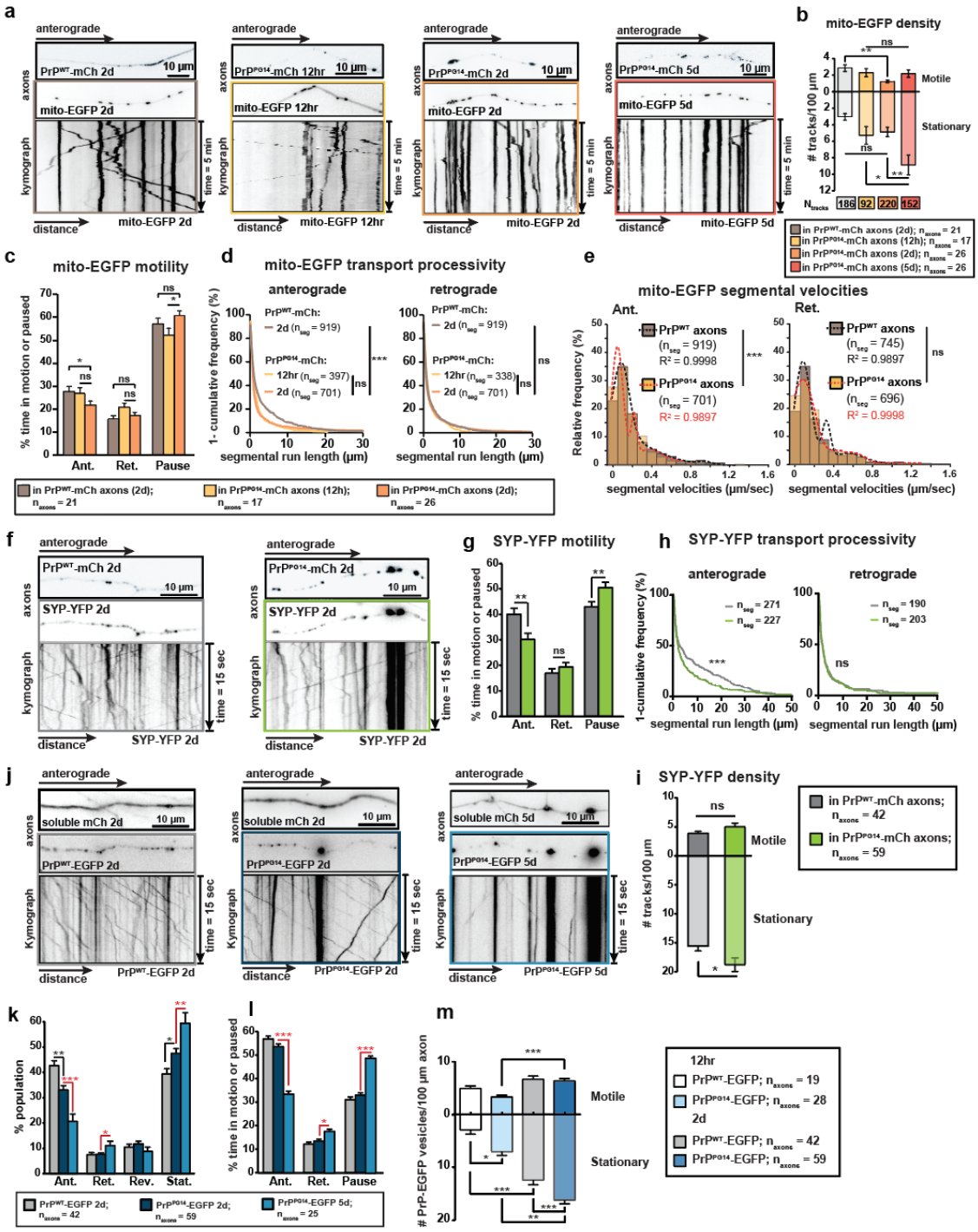


Fig. 1: Axonal transport is progressively impaired in PrP^{PG14}-mCh axons. a First-frame images of axons co-transfected with mito-EGFP and PrP^{WT}-mCh or PrP^{PG14}-mCh for 12 hours or 2 days (top two panels) and corresponding kymographs (bottom panel) generated from time-lapse movies (5 minutes, 300 frames, 1 frame/sec). **b** Densities of motile (top y-axis) or stationary (bottom y-axis) mito-EGFP. **c** Percent time mito-EGFP spends in anterograde (Ant.) or retrograde (Ret.) motion or paused. **d** Segmental run lengths of mito-EGFP plotted as 1-cumulative frequency (%). **e** Segmental velocities of mito-EGFP plotted as relative frequency

bioRxiv preprint doi: https://doi.org/10.1101/2023.03.19.533383; this version posted March 21, 2023. The copyright holder for this preprint (which was not certified by peer review) is the author/funder. All rights reserved. No reuse allowed without permission.

histogram (%) and fitted with multi-peaks Gaussian functions. R^2 values indicate the degree of Gaussian fits. **f** First-frame images of axons co-transfected with SYP-YFP and PrP^{WT}-mCh or PrP^{PG14}-mCh for 2 days (top two panels) and corresponding kymographs (bottom panel) generated from time-lapse movies (15 seconds, 150 frames, 10 frame/sec). **g** Percent time SYP-YFP spends in anterograde (Ant.), or retrograde (Ret.) motion, or paused. **h** Segmental run lengths of SYP-YFP plotted as 1-cumulative frequency (%). **i** Densities of motile (top y-axis) or stationary (bottom y-axis) SYP-YFP. **j** First-frame images of axons co-transfected with soluble mCh and PrP^{WT}-EGFP or PrP^{PG14}-EGFP for 2 or 5 days (top two panels) and corresponding kymographs (bottom panel) generated from time-lapse movies (15 seconds, 150 frames, 10 frame/sec). **k** Percent population with anterograde (Ant.), retrograde (Ret.), reversal (Rev.), or stationary (Stat.) tracks. **l** Percent time PrP^{WT}-EGFP or PrP^{PG14}-EGFP spend in anterograde (Ant.), or retrograde (Ret.) motion, or paused. **m** PrP^{WT}-EGFP or PrP^{PG14}-EGFP densities of motile (top y-axis) or stationary (bottom y-axis) vesicles. All bar graphs are shown as mean ± SEM. ***$p<0.001$, **$p<0.01$, *$p<0.05$, ns = not significant. **b**, **c, k, l, m** Student's t-test with Tukey's multiple comparison tests; **g, i** Student's t-test; **d**, **e**, and **h** Kolmogorov-Smirnov (K-S) test.

Local traffic jams at axonal PrP^{PG14} aggregate sites revealed by micro-movement analysis

As transport of mitochondria was impaired resulting in increased number of stalled mitochondria in axons of neurons expressing PrP^{PG14} (**Fig. 1a-c**), we next asked whether PrP^{PG14} endoggresomes directly hindered the movement of mitochondria and retained these organelles within these local swelling sites. We used single-particle tracking to image and quantitate the behavior of individual mitochondria within micro-domain regions at PrP^{PG14} endoggresome/aggregates sites (herein referred as 'PrP^{PG14} aggregate sites or AGG) vs non-aggregate regions (NON-AGG) (**Fig. 2a**). AGG and NON-AGG regions within the same axon were defined within 10-µm wide analysis windows (**Fig. 2a, d**). At each window, we quantified percentages of mito-EGFP that (1) passed through AGG sites without interruptions, (2) paused/slowed down at the AGG sites, and (3) stalled at the AGG sites, compared to those in control NON-AGG sites of axons of PrP^{PG14}-mCh-expressing neurons in the anterograde versus retrograde directions (**Fig. 2a-c**). Our data indicate that while ~50% of the mito-EGFP population stalled along axons (**Fig. 2c**), from those that retained motility, a significantly lesser

bioRxiv preprint doi: https://doi.org/10.1101/2023.03.19.533383; this version posted March 21, 2023. The copyright holder for this preprint (which was not certified by peer review) is the author/funder. All rights reserved. No reuse allowed without permission.

proportion moved through AGG sites without interruption compared to NON-AGG sites (**Fig. 2b**). Moreover, a significantly greater proportion of moving mitochondria paused at- or slowed down as they moved in the anterograde direction through AGG vs NON-AGG sites (**Fig. 2b**). These data suggest that PrP^{PG14} AGG sites are magnets for mitochondria, to promote the arrest or the slowing down of anterograde-moving mitochondria. To further characterize the degree of mitochondrial arrest at PrP^{PG14} AGG sites, mitochondrial micro-movement dynamics were quantified within 10 µm-wide windows surrounding individual AGG or NON-AGG sites (**Fig. 2d**). We measured the mean displacement of individual mito-EGFP from their centroid position over a x min period of live imaging, within 10 µm AGG vs NON-AGG windows (**Fig. 2d**). Compared to NON-AGG regions, single particle tracking revealed that mito-EGFP displacement was largely within the 10 µm window (<10 µm), thus mitochondria did not move as far (**Fig. 2e**). Analysis of segmental velocities within the 10 µm windows revealed that mito-EGFP at AGG sites moved significantly slower (<0.1 µm/s) compared to mitochondria at NON-AGG sites (**Fig. 2f**). Altogether, these data suggest that the mitochondrial motility impairments represent local 'traffic jams' at PrP^{PG14} endoggresome AGG sites and suggest that the global deficits in axonal transport of mitochondrial along axons result from micro-transport disruptions that start at AGG sites where PrP^{PG14} endoggresomes themselves are stalled, thus implicating PrP^{PG14} endoggresomes directly in the initiation of these local transport deficits.

bioRxiv preprint doi: https://doi.org/10.1101/2023.03.19.533383; this version posted March 21, 2023. The copyright holder for this preprint (which was not certified by peer review) is the author/funder. All rights reserved. No reuse allowed without permission.

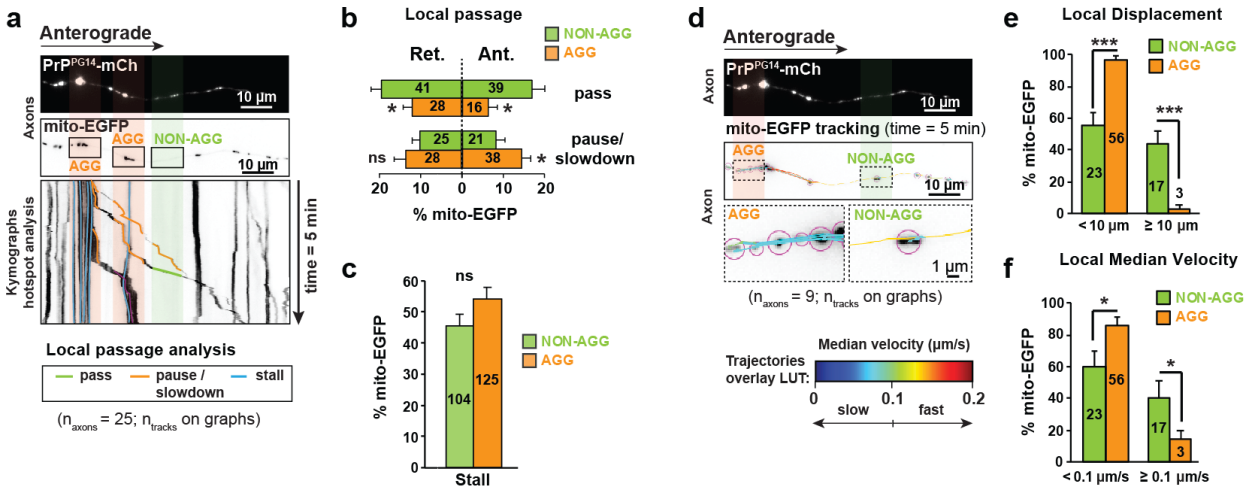


Fig. 2: Local axonal transport disruption of mito-EGFP micro-movements within PrP^{PG14}-mCh aggregate sites. a First-frame images of an axon co-transfected with PrP^{PG14}-mCh (top) and mito-EGFP (middle) and corresponding kymograph from a time-lapse movie (5 minutes, 300 frames, 1 frame/sec) of mito-EGFP transport with color-coded track assignment overlay (green = pass, orange = pause/slowdown, or blue = stall) at AGG and NON-AGG sites. **b** Percent number of mito-EGFP that pass or pause/slowdown in anterograde (Ant.; right x-axis) vs retrograde (Ret.; left x-axis) directions at AGG vs NON-AGG sites. **c** Percent number of mito-EGFP that are stalled at AGG vs NON-AGG sites. **d** First-frame images of an axon co-transfected with PrP^{PG14}-mCh (top) and mito-EGFP (bottom) from time-lapse movies (5 minutes, 300 frames, 1 frame/sec). Dotted rectangles outline 10 µm-wide PrP^{PG14} aggregate sites (AGG) or non-aggregate control sites (NON-AGG). Rainbow LUT pseudo color-coded overlays indicate median velocities ranges of tracks at AGG and NON-AGG regions (insets). **e** Percent number of mito-EGFP trajectories at AGG vs NON-AGG sites with track displacements of < 10 µm or ≥ 10 µm during a 5-minute acquisition period. **f** Percent number of mito-EGFP at AGG vs NON-AGG sites with median velocity of < 0.1 µm/s or ≥ 0.1 µm/s during the 5-minute acquisition. All bar graphs are shown as mean ± SEM. ***p<0.001, **p<0.01, *p<0.05, ns = not significant. **b**, **c**, **e**, **f** Student's t-test. Number of tracks are shown inside bar graphs. All analyses were done on axons after 2 days of PrP^{PG14}-mCh transfection.

Local changes to the actin and MT cytoskeleton drive at PrP^{PG14} aggregate sites

The cylindrical shape of the axon is supported by a tightly organized and regularly spaced actin-spectrin lattice localized below the plasma membrane, and by a system of MTs that line up the length of the axon[38,39]. An intact actin and MT cytoskeletal organization is a key determinants of axonal transport dynamics[39,40]. To investigate the mechanism(s) of mitochondrial arrest and transport impairments at AGG sites (**Fig. 1**), we characterized the actin and MT cytoskeletal integrity at localized axonal PrP^{PG14} AGG swelling sites. The ultrastructure

bioRxiv preprint doi: https://doi.org/10.1101/2023.03.19.533383; this version posted March 21, 2023. The copyright holder for this preprint (which was not certified by peer review) is the author/funder. All rights reserved. No reuse allowed without permission.

of actin and MT tracks inside axons was visualized using correlative light and scanning electron microscopy (CLEM) of cultured neurons grown on gridded coverslips. These cells were transfected with PrP^{PG14}-mCh for 2 days, subjected to a membrane-extraction (ME) protocol to remove lipids including the plasma membrane, and imaged using SEM. In this approach, the position of individual PrP^{PG14}-mCh endoggresomes was mapped within axons using fluorescence imaging, followed by treatment of live neurons with ME detergent buffers to remove lipid membranes, but also containing taxol to stabilize MTs and phalloidin to stabilize actin (**Fig. 3a**)[41]. Scanning electron micrographs revealed ring-like accumulations of actin surrounding, or localized with PrP^{PG14}-mCh aggregates (**Fig. 3a, b; Supplementary Fig. 3a**). Similar actin ring-like structures were observed using direct stochastic optical reconstruction microscopy (dSTORM) imaging of Phalloidin-AF647 at PrP^{PG14}-mCh AGG swellings (**Fig. 3b**), suggesting the active recruitment of actin to PrP^{PG14}-mCh aggregate AGG sites.

Axonal swelling sites also contained bending MTs that followed the contour of swellings at PrP^{PG14}-mCh AGG sites, as well as broken MTs that curled up/broke at AGG sites, while NON-AGG neighboring regions had straight MT bundles (**Fig. 3a, Supplementary Fig. 3a, b**). These observations were confirmed using 3D super-resolution (SR)-Airyscan imaging of α-tubulin that showed curved MT tracks around at AGG sites in contrast to straight MTs observed at NON-AGG regions (**Fig. 3c, Supplementary Fig. 3b**). MT stabilization is imparted by post-translational modifications (PTMs) to tubulin[42]. α-tubulin acetylation is a common PTM that confers MT stability and protects MTs from breakage under mechanical stress[43]. Acetylated MTs are selectively preferred by kinesin-1 for motility[44-46]. On the other hand, tyrosinated (unmodified) MT tracks that are less stable and prone to breakage upon stress, and have existing tyrosine tails on tubulin often associated with kinesin-3, a motor reported to prefer tyrosinated

bioRxiv preprint doi: https://doi.org/10.1101/2023.03.19.533383; this version posted March 21, 2023. The copyright holder for this preprint (which was not certified by peer review) is the author/funder. All rights reserved. No reuse allowed without permission.

MTs for motility usually though interactions with other MAPs[47-49]. Our observations of bending and breaking MTs prompted us to ask whether MT tracks with different PTMs were selectively impaired within PrP^{PG14} endoggresome AGG sites. PrP^{PG14}-mCh axons were immunostained with validated tubulin antibodies that recognize acetylated vs tyrosinated MTs. 3D SR-Airyscan, and a highly inclined and laminated optical sheet (HILO) with super-resolution radial fluctuation (SRRF) processing[50] revealed that most acetylated MT tracks bent or remained undisrupted while tyrosinated MT tracks broke at AGG sites, compared to NON-AGG sites (**Fig. 3d-f, Supplementary Fig. 3c**). These results are consistent with previous reports showing mechanically stable and breakage-resistance acetylated MT tracks[43]. Overall, these results show that actin and MTs are remodeled at the axonal swelling sites containing PrP^{PG14} endoggresomes. Furthermore, MT tracks with different PTMs are differentially impaired at the AGG sites. Because kinesin-1 and kinesin-3 recognize MT tracks with distinct PTMs, differential disruption of MTs at AGG sties could impinge on axonal transport dynamics of cargoes that depend on kinesin-1 and kinesin-3 for motility in axons.

bioRxiv preprint doi: https://doi.org/10.1101/2023.03.19.533383; this version posted March 21, 2023. The copyright holder for this preprint (which was not certified by peer review) is the author/funder. All rights reserved. No reuse allowed without permission.

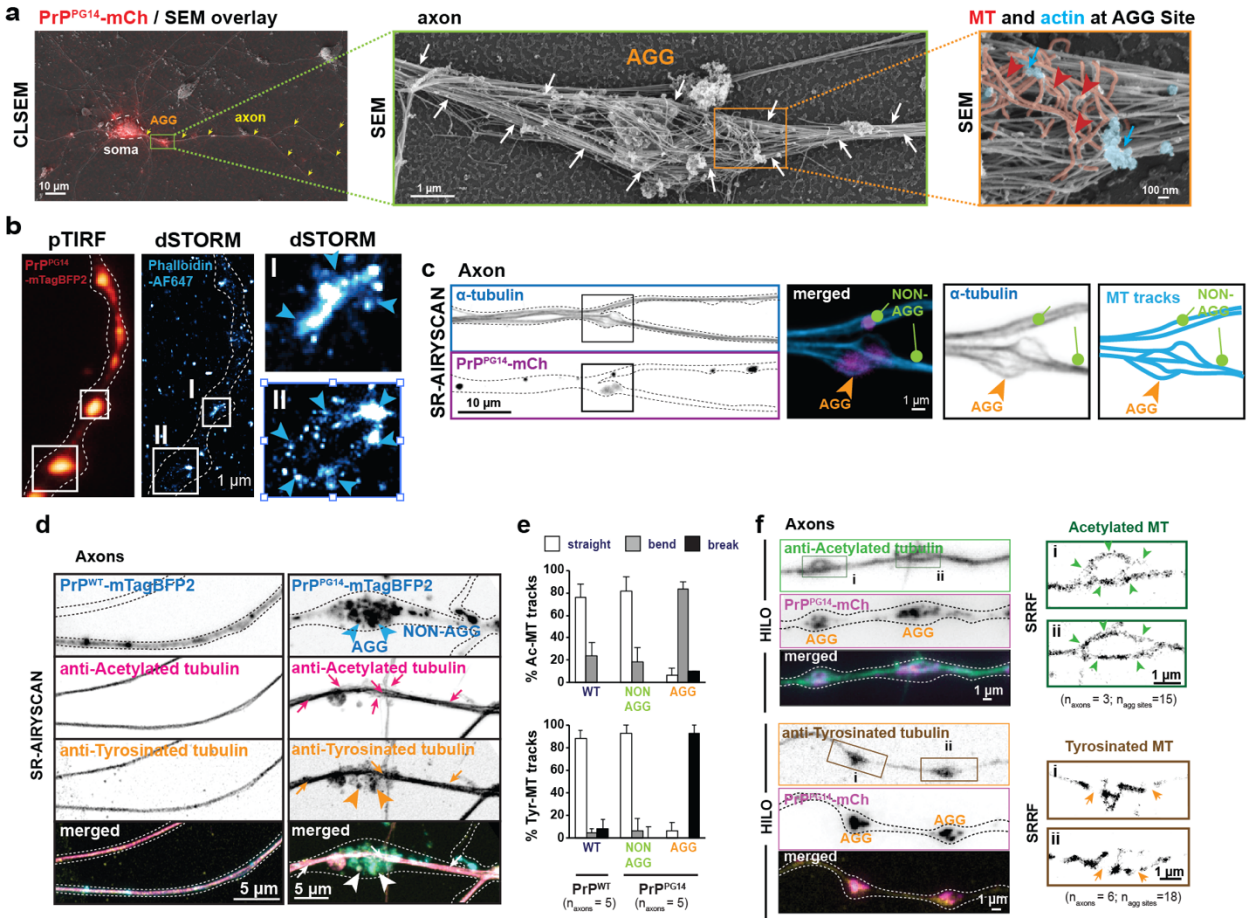


Fig. 3: Actin accumulation and selective impairment to MT track PTMs at PrP^{PG14} aggregate sites. a Membrane-extracted (ME) correlative light and scanning electron microscopy (CLSEM) image of a neuron transfected with PrP^{PG14}-mCh (red). Arrowheads indicate axons. Green Inset shown on middle panel. White arrows point to MT tracks. Orange inset shown on right panel. Blue arrows point to actin. Red arrowheads point to disrupted MT tracks. **b** Images of an axon from a neuron transfected with PrP^{PG14}-mTagBFP2 (red) imaged using highly-inclined and laminated optical sheet (HILO) microscopy, stained with Phalloidin-AF647 and imaged with direct STORM (dSTORM). Insets I-II of axonal swellings shown on the right. Arrowheads point to actin accumulation around the axonal swellings. **c** Super-resolution (SR) Airyscan confocal microscopy maximum projection images of PrP^{PG14}-mCh, immunostained with alpha tubulin antibody. Round Arrows indicate MT tracks at NON-AGG sites; Arrowheads indicate MT at AGG site. **d** SR-Airyscan images of PrP^{WT}- or PrP^{PG14}-mTagBFP2 axons, co-immunostained with acetylated (Ac) and tyrosinated (Tyr) tubulin antibodies. Arrows indicate intact/straight tracks; Arrowheads indicate broken MT. **e** Percent Ac- or Tyr-MT track architecture (straight, bend, or break) at WT (in PrP^{WT}-mTagBFP2 axons) and NON-AGG or AGG sites (in PrP^{PG14}-mTagBFP2 axons). **e** HILO microscopy images of PrP^{PG14}-mCh axons immunostained against either acetylated and tyrosinated tubulin, and corresponding Super-resolution radial fluctuation (SRRF)-processed images at the AGG sites (i-ii; insets). Insets: Arrowheads point to MT tracks bending; Arrows point to MT tracks breaking. See also figure S3.

bioRxiv preprint doi: https://doi.org/10.1101/2023.03.19.533383; this version posted March 21, 2023. The copyright holder for this preprint (which was not certified by peer review) is the author/funder. All rights reserved. No reuse allowed without permission.

Selective retention of kinesin-1 and kinesin-3 at PrP^{PG14} aggregate sites

The observed local and selective disruption of mitochondrial transport (**Fig. 2**), as well as the impaired MTs stability within PrP^{PG14} endoggresomes AGG sites (**Fig.3**), suggest defective interactions between molecular motors and cargoes at those sites. We first tested whether kinesin-1 (KHC - KIF5) and its associated adaptor subunit kinesin light chain 1 (KLC1), and kinesin-3 (KIF1A), two neuronally-enriched anterograde motors that bind to cargoes via adaptors and become activated in order to drive processive transport[51], were aberrantly retained within AGG sites. We used immunofluorescence and validated antibodies to quantitate fluorescence intensity distributions of endogenous KHC, KLC1, and KIF1A at the AGG sites, as a measure of the relative amount of KHC and KIF1A motors present at those sites (**Fig. 4a**). These intensity frequency distributions were compared to (1) those at control NON-AGG sites in axons of PrP^{PG14}-mCh-expressing neurons, and to (2) sites in axons of control PrP^{WT}-mCh-expressing neurons ('WT sites') (**Fig. 4a**). As shown previously, KHC, KLC1, and KIF1A staining in axons of neurons expressing PrP^{WT}-mCh was punctate[34,52], indicating that these proteins were localized to vesicular structures (**Fig. 4a**). However, intensities of KHC, KLC1, and KIF1A motors were higher at AGG sites, indicating the accumulation of motors within AGG swellings containing PrP^{PG14}-mCh endoggresomes (**Fig. 4a**). Quantitation of fluorescence intensity distributions confirmed these observations: comparison of fluorescence intensity distribution graphs between AGG and NON-AGG sites showed significantly wider and right-skewed distributions toward higher intensities for KHC, KLC1, and KIF1A at AGG sites compared to WT sites (**Fig. 4b**). Notably, the KLC1 intensity distribution graph at NON-AGG sites was significantly lower compared to those at WT sites, suggesting that KLC1 was depleted from cargo moving through NON-AGG areas.

bioRxiv preprint doi: https://doi.org/10.1101/2023.03.19.533383; this version posted March 21, 2023. The copyright holder for this preprint (which was not certified by peer review) is the author/funder. All rights reserved. No reuse allowed without permission.

Next, to test whether motor-cargo association was disrupted as a result of motor sequestration at the AGG sites, we analyzed kinesin-1 and kinesin-3 motor composition on individual mitochondria that mobilized through PrP^{PG14} endoggresome AGG sites, and compared this to the composition of motors associated with mitochondria in PrP^{WT} aggregate-free control axons. We used a sub-pixel localization algorithm[34,53] to detect and compare the degree of colocalization between KHC and KIF1A motor subunits on mitochondria labeled with mito-EGFP) (**Fig. 4c**). In this analysis, diffraction-limited puncta representing 'motor clusters' were analyzed containing one or more kinesin molecules. Our data show that mito-EGFP that had moved through at least one PrP^{PG14} endoggresome AGG site contained significantly less KHC and KIF1A motor clusters, compared to mito-EGFP in PrP^{WT} control axons (**Fig. 4d**). As mitochondria analyzed here had moved through at least than one AGG site, these observations suggest that kinesin-1 and kinesin-3 are depleted away from mitochondria as they passage through PrP^{PG14} AGG swellings, resulting in kinesin-1 and kinesin-3 accumulation at these sites.

bioRxiv preprint doi: https://doi.org/10.1101/2023.03.19.533383; this version posted March 21, 2023. The copyright holder for this preprint (which was not certified by peer review) is the author/funder. All rights reserved. No reuse allowed without permission.

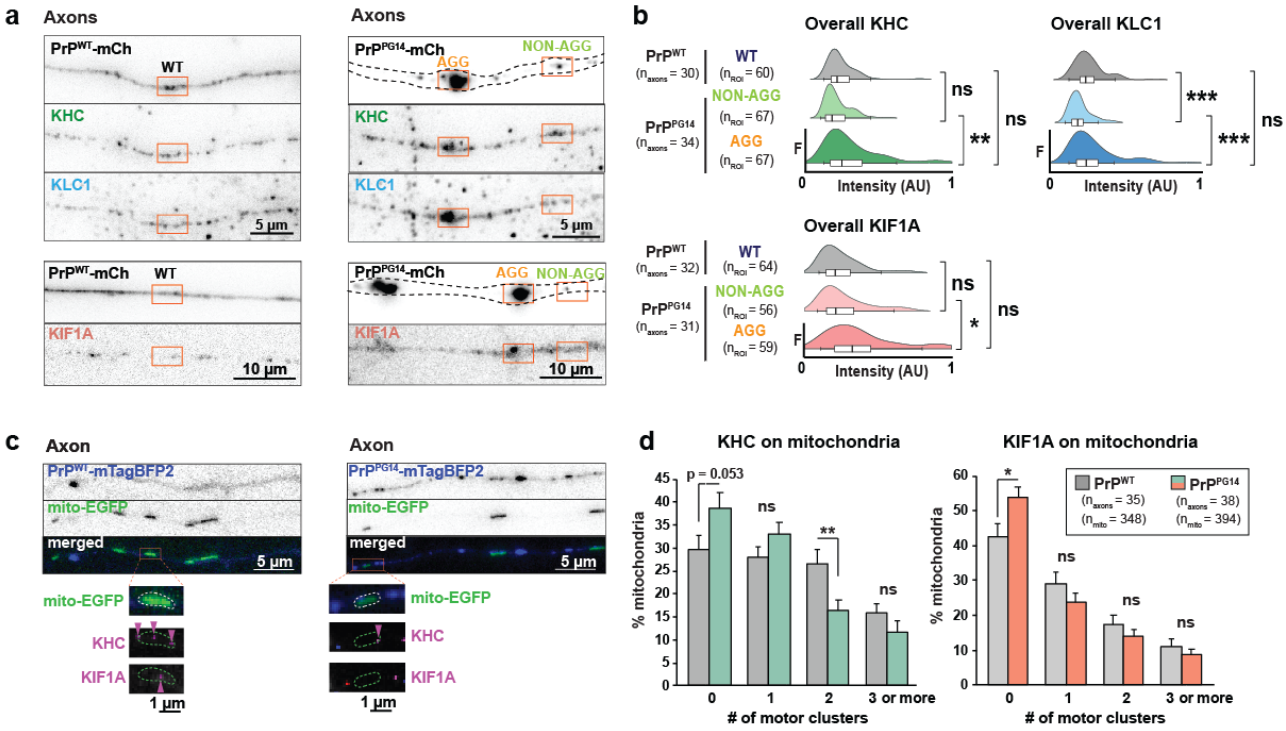


Fig. 4: Kinesin-1 and kinesin-3 accumulation at PrP^{PG14} aggregate sites and depletion from mitochondria. a Images of axons expressing PrP^{WT}-mCh or PrP^{PG14}-mCh, immunostained with KHC and KLC1 or with KIF1A antibodies. Orange boxes show AGG, NON-AGG, and WT ROIs. **b** Normalized intensity distribution frequencies (F) of KHC, KLC1, and KIF1A signal at AGG, NON-AGG, and WT sites plotted as box plots with kernel density estimates from histogram. **c** Representative inverted images of axons expressing PrP^{WT}-mTagBFP2 or PrP^{PG14}-mTagBFP2 and mito-EGFP, and immunostained with KHC and KIF1A antibodies. Insets (below) shown as overlay of sub-pixel localization detection (magenta spots; arrowheads). **d** Quantitation of percent mitochondria (mean ± SEM) colocalizing with 0, 1, 2, and ≥ 3 KHC or KIF1A motor clusters. ***p<0.001, **p<0.01, *p<0.05, ns = not significant; **b** Kruskal-Wallis test, **d** Student's t-test.

Retention of kinesin-1 at PrP^{PG14} aggregate sites requires its cargo-binding domain

As the cargo-binding KLC1 subunit of kinesin-1 was depleted from mitochondrial cargo that passed through PrP^{PG14} endoggresome AGG sites (**Fig. 4b**), to determine the mechanistic basis of motor sequestration at PrP^{PG14} AGG sites, we tested whether a well characterized truncated kinesin-1 (KIF5C[1-560]) consisting of the motor, neck linker, neck coil, and first stalk

bioRxiv preprint doi: https://doi.org/10.1101/2023.03.19.533383; this version posted March 21, 2023. The copyright holder for this preprint (which was not certified by peer review) is the author/funder. All rights reserved. No reuse allowed without permission.

domains, but that lacks the cargo binding domain and thus cannot associate with cargoes[54], was retained at PrP^{PG14} AGG sites. Neurons were co-transfected with PrP^{PG14}-mTagBFP2 (mTag blue fluorescence protein 2) and full-length (FL) KIF5C-2xmCh plus its adaptor subunit KLC1-TAP, or with a KIF5C(1-560)-2xmCh plus KLC1-TAP (**Fig. 5**). We found that KLC1-TAP overexpression was sufficient to recruit the FL KIF5C-2xmCh to PrP^{PG14} endoggresomes (**Fig. 5a**). These data are consistent with immunofluorescence image analysis of endogenous KIF5 (KHC) and KLC1 showing accumulation of these motors at PrP^{PG14} endoggresome AGG sites (**Fig. 4a,b**). In contrast, truncated KIF5C(1-560)-2xmCh did not accumulate at PrP^{PG14} AGG sites throughout axons, despite KLC1 overexpression (**Fig. 5b**). Instead, KIF5C(1-560)-2xmCh efficiently moved passed all AGG sites through the axon to accumulate at axonal termini **(Fig. 5c**) in a similar manner as previous observed in healthy cultured neurons[54]. Uninterrupted movement of KIF5C(1-560) is consistent with our observation that kinesin-1 prefers acetylated MTs, and these remained mostly intact and curved at the AGG sites (**Fig. 3d-f**), thus providing the tracks for KIF5C(1-560) transport toward the axon terminus. Next, although the movement of KIF5C(1-560) was not blocked, we tested whether motility dynamics of KIF5C(1-560) were impaired as it moved through PrP^{PG14} AGG sites before reaching the axon terminals. Fluorescence recovery after photobleaching (FRAP) analysis of KIF5C(1-560)-mCitrine (mCit) at the distal tips of axons of neurons expressing PrP^{PG14}-mCh vs. PrP^{WT}-mCh using adeno associated viruses (AAVs) 5 days post-transduction, a time point previously shown to form prominent aggregates[17], showed no significant difference in the FRAP recovery of KIF5C(1-560)-mCit in PrP^{PG14} endoggresome-rich axons compared to control PrP^{WT} axons devoid of endoggresomes (**Fig. 5c**), further suggesting that PrP^{PG14} endoggresomes do not block the transport of KIF5C(1-560) to the axonal termini. These data show that the cargo-binding domain

bioRxiv preprint doi: https://doi.org/10.1101/2023.03.19.533383; this version posted March 21, 2023. The copyright holder for this preprint (which was not certified by peer review) is the author/funder. All rights reserved. No reuse allowed without permission.

of KIF5C is sufficient and required for retention of cargo-motor complexes at PrP^{PG14} AGG swelling sites in axons. These observations suggest that there is selectivity in this retention, as motors without cargo-binding domains, i.e., without cargo, including soluble motors are not retained within AGG sites, thus indicating that only intact cargo-motor complexes are sequestered at PrP^{PG14} AGG sites.

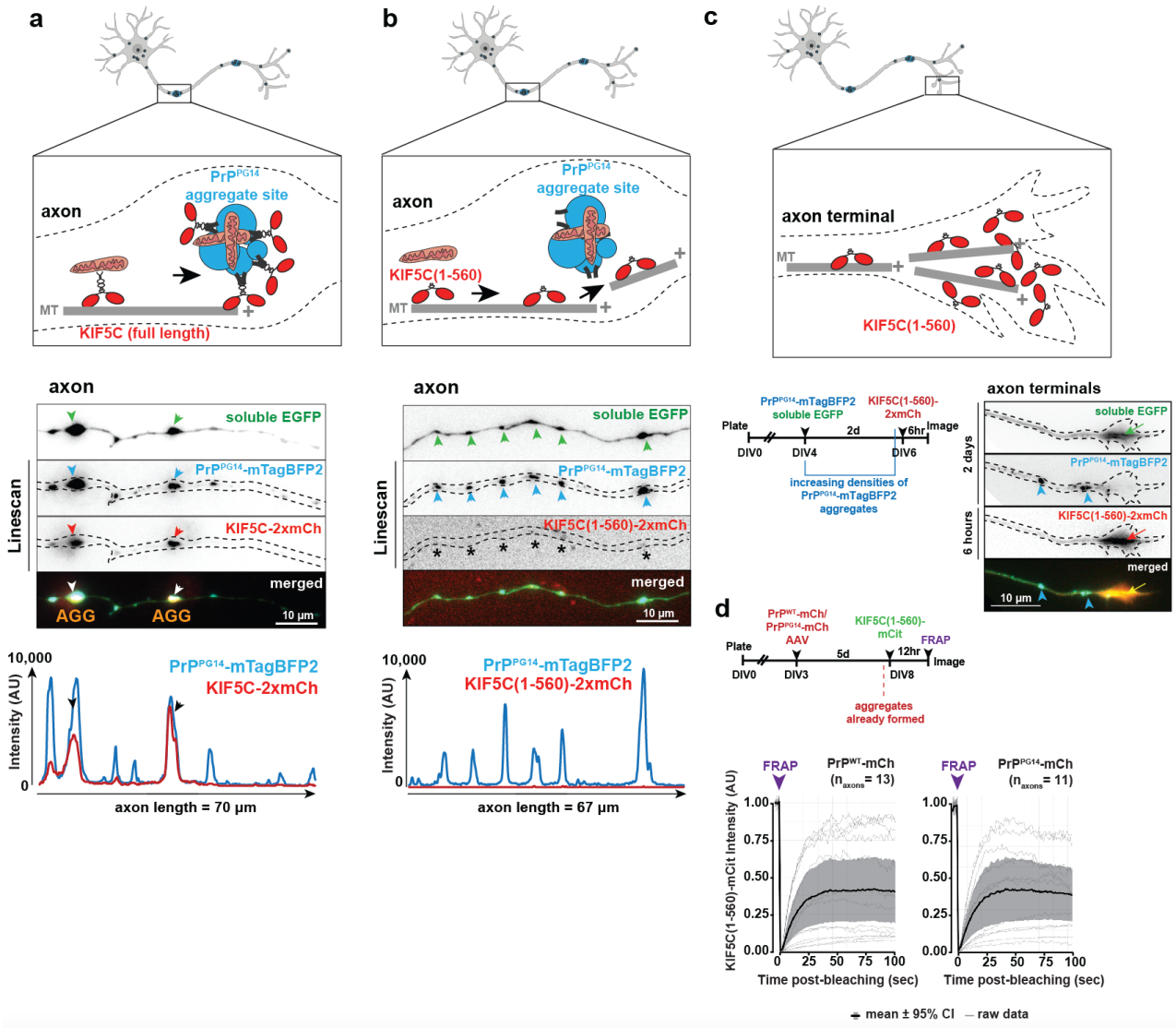


Fig. 5: Retention of kinesin-1 (KIF5C) at PrP^{PG14} AGG sites requires its cargo-binding domain. a Schematic (top) and representative inverted images of axons (middle) of neurons expressing soluble EGFP, PrP^{PG14}-mTagBFP2, and KIF5C-2xmCh for 2 days, and corresponding line scan intensity profiles (bottom) (n_{axons} = 9). **b** Schematic (top) and representative inverted

bioRxiv preprint doi: https://doi.org/10.1101/2023.03.19.533383; this version posted March 21, 2023. The copyright holder for this preprint (which was not certified by peer review) is the author/funder. All rights reserved. No reuse allowed without permission.

images of axons (middle) from neurons expressing soluble EGFP, PrP^{PG14}-mTagBFP2, and KIF5C(1-560)-2xmCh for 2 days, and corresponding line scan intensity profiles (bottom) (n_{axons} = 13). **c** Schematic (top), timeline of sequential transfection of EGFP and PrP^{PG14}-mTagBFP2 for 2 days and KIF5C(1-560)-2xmCh for 6 hours (bottom left), and images at the axon terminus (bottom right). Arrowheads point to endoggresomes. Arrows point to EGFP and KIF5C(1-560)-2xmCh accumulation at the axonal growth cone. **d** Timeline of FRAP assay (top) of axon terminals induced with PrP^{WT}- or PrP^{PG14}-mCh AAV for 5 days, sequentially transfected with KIF5C(1-560)-mCit for 12 hours prior to live imaging. (bottom) FRAP profile of KIF5C(1-560)-mCit.

Enhanced mitochondrial fission at PrP^{PG14} aggregate sites requires Rab7 GTPase activity

In addition to mitochondrial accumulation (**Fig. 2**), time-lapse live imaging using high-resolution microscopy revealed enhanced mitochondrial fission at PrP^{PG14} AGG sites (**Fig. 6a**, **Supplementary Video 1)**. To characterize mitochondrial fission, we first quantitated mitochondrial size at PrP^{PG14} AGG sites in axons of neurons expressing PrP^{PG14}-mCh for 5 days (**Fig. 6a**). We observed smaller mitochondria within PrP^{PG14} AGG sites (**Fig. 6b**), and while many smaller mitochondrial fragments were retained within AGG sites, some also moved outside of the AGG site in the anterograde direction (**Fig. 6a**). Moreover, the size of mitochondria trapped within PrP^{PG14} AGG sites decreased as the number of PrP^{PG14} endoggresomes increased from 12 hours to 5 days following initial expression of PrP^{PG14}-mCh (**Fig. 6c,d, Supplementary Fig. 1b**). These data suggest a link between the presence of PrP^{PG14} endoggresomes and the progressive imbalance of mitochondria fission dynamics at AGG sites.

Previous studies using ultrathin serial-sectioning SEM (S3EM) to visualize the ultrastructure of PrP^{PG14} axonal swellings showed mitochondria and endolysosomes trapped within PrP^{PG14} endoggresome AGG sites and making close contacts[17]. Endolysosomes marked with Rab7, a small GTPase that binds to endosomal membranes upon GTP hydrolysis[55], have been shown to regulate mitochondrial fission via direct contact with mitochondria, to promote fission at contact sites[56]. To investigate the mechanistic basis of enhanced mitochondrial fission

bioRxiv preprint doi: https://doi.org/10.1101/2023.03.19.533383; this version posted March 21, 2023. The copyright holder for this preprint (which was not certified by peer review) is the author/funder. All rights reserved. No reuse allowed without permission.

within AGG sites, we first used live high-resolution HILO imaging to test whether Rab7 associated with mitochondria within PrP^{PG14} endoggresome AGG sites. Neurons were co-transfected with mito-mTagBFP2 plus PrP^{WT}-mCh or PrP^{PG14}-mCh plus Rab7(WT)-EGFP or Rab7(Q67L)-EGFP. The latter is a constitutively active mutant that cannot undergo GTP hydrolysis and thus cannot be released from endosomal membranes[57], and that has been shown previously to inhibit mitochondrial fission[58]. Colocalization analysis showed that mito-mTagBFP2 highly colocalized with Rab7(WT/Q67L)-EGFP at AGG sites vs NON-AGG sites of PrP^{PG14}-mCh endoggresome-rich axons versus in control PrP^{WT}-mCh endoggresome-free axons at 2 days post-transfection (**Fig. 6e,f, Supplementary Fig. 4a**). HILO high-resolution imaging revealed mitochondrial (mito-mTagBFP2) fission occurred within PrP^{PG14}-mCh AGG swelling sites in neurons expressing Rab7(WT)-EGFP (**Fig. 6g**). Importantly, fission did not occur as frequently in PrP^{PG14}-mCh AGG swelling sites of neurons also expressing the constitutively active Rab7(Q67L)-EGFP (**Fig. 6h**). To quantitate these observations, we calculated a mitochondrial fission index as the frequency of fission normalized to mitochondrial lengths. These data indicate that the frequency of mitochondria fission at AGG sites was significantly higher than either fission in PrP^{WT} axons or in NON-AGG regions of axons of neurons expressing PrP^{PG14}-mCh (**Fig. 6i**). Mitochondria also underwent fission in axons of neurons co-expressing Rab7(WT)-EGFP but not in those overexpressing Rab7(Q67L)-EGFP (**Supplementary Fig. 4a, b**), consistent with an established role of Rab7 GTPase hydrolysis in mitochondrial fission in healthy cells[56]. Altogether, our observations indicate that PrP^{PG14} AGG swellings act as hubs for organelle-organelle contact hotspots that mediate mitochondrial remodeling via promoting its fission through Rab7 GTPase activity.

bioRxiv preprint doi: https://doi.org/10.1101/2023.03.19.533383; this version posted March 21, 2023. The copyright holder for this preprint (which was not certified by peer review) is the author/funder. All rights reserved. No reuse allowed without permission.

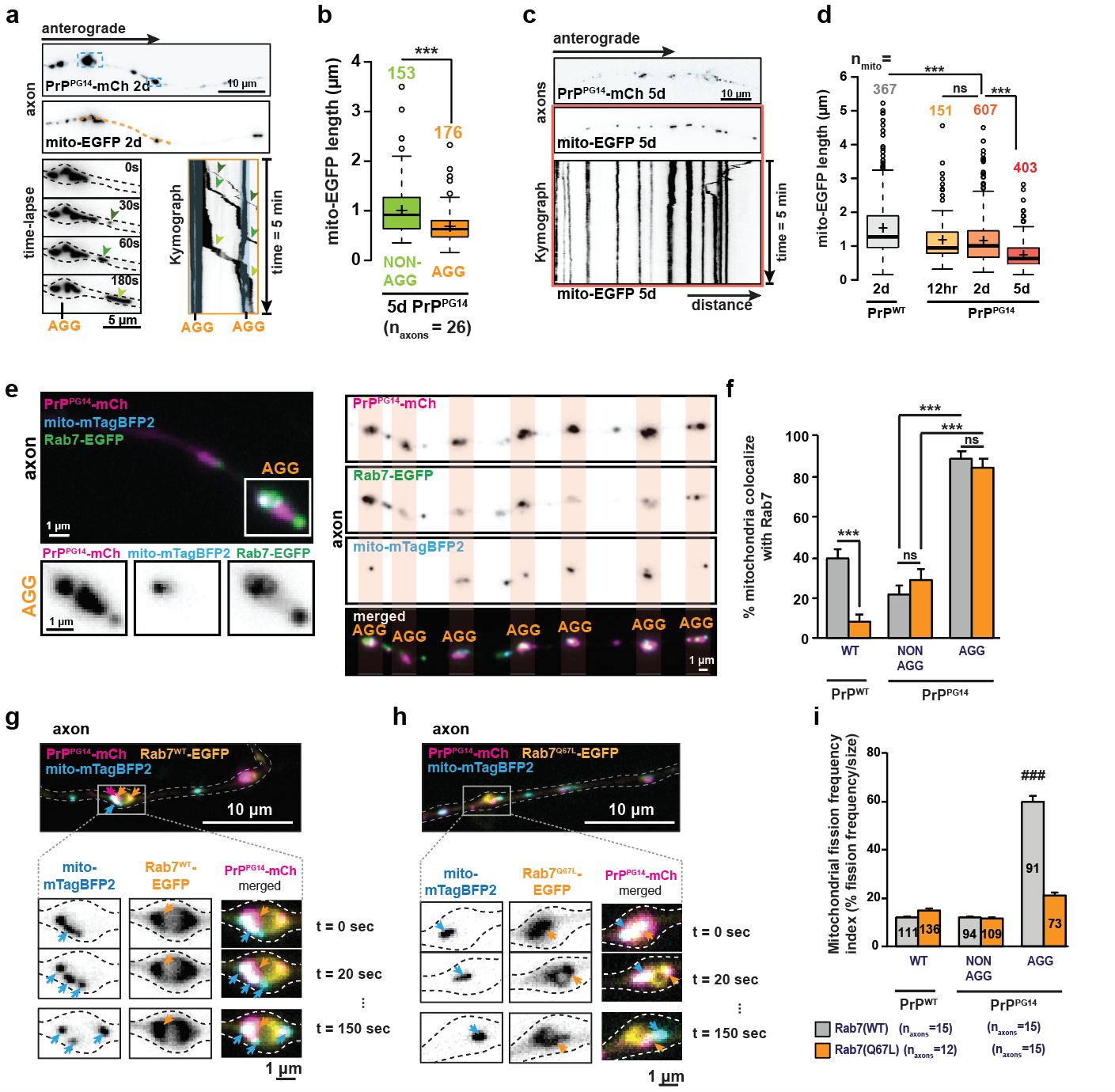


Fig. 6: Rab7-mediated mitochondrial fission at PrP^{PG14} aggregate sites. a First-frame images of axons co-expressing PrP^{PG14}-mCh and mito-EGFP for 2 d. The yellow dotted line indicates an imaging region of time-lapse (bottom left) and kymograph (right). **b** Quantitation of mito-EGFP length at AGG vs NON-AGG sites at 5 days post-PrP^{PG14}-mCh expression. **c** First-frame images of axons co-transfected with mito-EGFP and PrP^{PG14}-mCh for 5 days (top two panels) and corresponding kymographs (bottom panel) generated from time-lapse movies (5 minutes, 300 frames, 1 frame/sec). **d** Quantitation of mito-EGFP length co-transfected with PrP^{WT}-mCh for 2 days or PrP^{PG14}-mCh for 12 hours, 2 days, and 5 days. e Axons co-expressing PrP^{PG14}-mCh,

bioRxiv preprint doi: https://doi.org/10.1101/2023.03.19.533383; this version posted March 21, 2023. The copyright holder for this preprint (which was not certified by peer review) is the author/funder. All rights reserved. No reuse allowed without permission.

Rab7-EGFP, and mito-mTagBFP2. Insets and highlights indicate AGG sites. **f** Quantitation of percent mito-mTagBFP2 colocalize with Rab7(WT/Q67L)-EGFP at WT, NON-AGG, or AGG sites. **g** First-frame images of axons co-expressing PrP^{PG14}-mCh, $Rab7^{WT}$-EGFP, and mito-mTagBFP2 and representative frames from time-lapse videos at WT or AGG sites (insets). **h** First-frame images of axons co-expressing PrP^{PG14}-mCh, $Rab7^{Q67L}$-EGFP, and mito-mTagBFP2 and representative frames from time-lapse videos at WT or AGG sites (insets). **i** Quantitation of mitochondrial fission frequency index (% of fission frequency / mitochondrial length). Box plots were shown with Tukey definition; (+) indicates the mean. All bar graphs are shown as mean ± SEM. ***p<0.001, **p<0.01, *p<0.05, ns = not significant; **b, d** Kruskal-Wallis test. **f, i** Tukey's multiple comparison test. See also figure S4.

Dysfunctional mitochondria are retained at PrP^{PG14} aggregate sites

Mitochondrial dysfunction occurs at early and late stages of neurodegeneration, including in prion diseases[59-61]. Mitochondrial membrane potential ($\Delta\Psi m$) is central to neuronal health, and both increased and decreased membrane potential have been associated with impairments to neuronal mitochondrial quality control in familial and infectious prion disorders[61,62]. We hypothesized that the fragmented mitochondria that accumulate at PrP^{PG14} AGG sites become dysfunctional resulting in a defective ability to retain their membrane potential. To test this, we measured the membrane potential of mitochondria within individual PrP^{PG14} endoggresome AGG swellings and compared it to that at NON-AGG sites or to mitochondrial membrane potential in axons of neurons expressing PrP^{WT}-mCh controls. Neurons co-transfected with PrP^{PG14}-mCh or PrP^{WT}-mCh and Rab7(WT)-EGFP -which we showed potentiates mitochondrial fission at AGG sites (**Fig. 6g**)-, were loaded with TMRE (tetramethylrhodamine, ethyl ester), a cell permeant dye that accumulates and labels active mitochondria, and that is not sequestered within depolarized or inactive mitochondria[63,64]. Quantitation of TMRE intensity at mito-EGFP showed a significant reduced TMRE signal that mito-EGFP at the AGG sites had (**Fig. 7a, b**), and the percentage of mito-EGFP that could retain TMRE dropped significantly, compared to mito-EGFP in NON-AGG and WT control sites (**Fig. 7c**). Thus, PrP^{PG14} endoggresome-mediated

bioRxiv preprint doi: https://doi.org/10.1101/2023.03.19.533383; this version posted March 21, 2023. The copyright holder for this preprint (which was not certified by peer review) is the author/funder. All rights reserved. No reuse allowed without permission.

mitochondrial transport dysfunction and fragmentation are associated with compromised mitochondrial integrity within PrP^{PG14} axonal swellings.

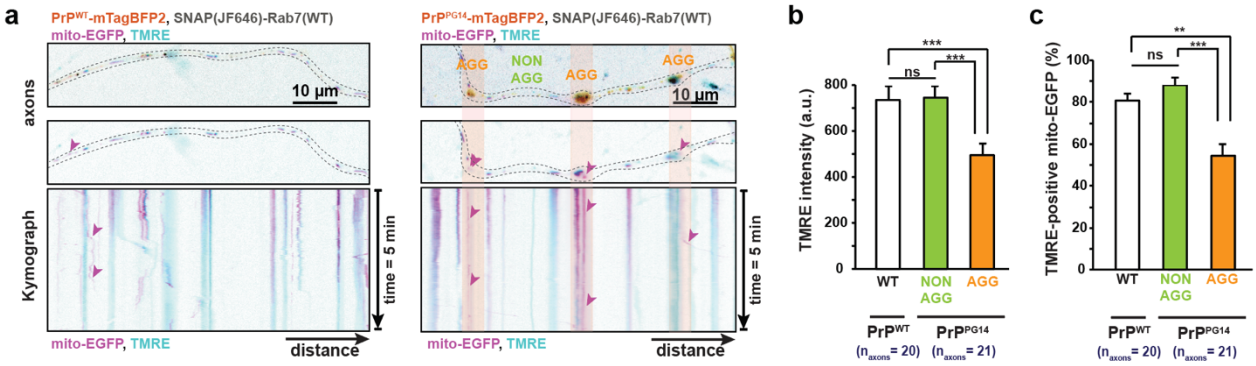


Fig. 7: Dysfunctional mitochondria accumulates within PrP^{PG14} aggregate sites. a Representative inverted color first frames of axons (top two panels) and kymographs (bottom panel) generated from time-lapse movies (5 minutes, 300 frames, 1 frame/sec) of PrP^{WT}- or PrP^{PG14}-mTagBFP2, co-transfected with SNAP(JF646)-Rab7 and mito-EGFP and treated with 25 nM of TMRE. Arrowheads point to TMRE-negative mito-EGFP. **b** TMRE intensities per mito-EGFP in WT, NON-AGG, or AGG regions. **c** Percent mito-EGFP that are TMRE-positive. All bar graphs are shown as mean ± SEM. ***p<0.001, **p<0.01, *p<0.05, ns = not significant; **b, c** Tukey's multiple comparison test.

DISCUSSION

Our previous work identified an endolysosomal pathway in mammalian axons call **a**xonal **r**apid **e**ndosomal **s**orting and **t**ransport-dependent **a**ggregation (ARESTA), as a principal driver of the initial stages of formation of enlarged misfolded mutant PrP aggregates inside endolysosomes (called endoggresomes) in axons, including of PrP^{PG14} [17]. ARESTA drives the formation of PrP^{PG14} endoggresomes via the homotypic sorting and fusion of endolysosomes containing PrP^{PG14}, as they traffic along axons[17]. Yet, how enlarged mutant PrP endoggresomes that distend the axon lead to axonal pathologies (axonopathies) and eventually to axonal degeneration, has remained unknown. In this study, we modeled axonal PrP^{PG14} aggregation in a cultured primary murine hippocampal neuronal system over time, to unveil the mechanisms of

bioRxiv preprint doi: https://doi.org/10.1101/2023.03.19.533383; this version posted March 21, 2023. The copyright holder for this preprint (which was not certified by peer review) is the author/funder. All rights reserved. No reuse allowed without permission.

localized cytoskeletal disruptions and organelle accumulations within local axonal swellings where PrP^{PG14} endoggresomes form. Using high-and super-resolution light microscopy, including single-particle micro-movement analyses of cargoes, and correlative light and EM imaging, we dissected the mechanisms of local impairments that develop at the subcellular and ultrastructural levels within aggregate swellings in axons. This detailed characterization revealed that PrP^{PG14} endoggresome swelling sites represent micro-hubs of toxicity along axons, where cascades of defects ensue at very early stages after expression of PrP^{PG14}. These localized micro-phenotypes include cytoskeletal remodeling, anterograde 'transport jams' due to altered architecture of MT tracks that kinesin-1 and kinesin-3 cargoes mobilize on, and the sequestration of mitochondria, endolysosomes, and molecular motors at swelling sites (**Fig. 8**). We propose that following this cascade of events, PrP^{PG14} axonal swelling sites become 'organelle-organelle contact hotspots' that drive the close contact between mitochondria and active Rab7-positive endolysosomes, to promote mitochondrial remodeling (via enhanced fission), and thus compromise mitochondrial functional integrity in axons (**Fig.8**).

bioRxiv preprint doi: https://doi.org/10.1101/2023.03.19.533383; this version posted March 21, 2023. The copyright holder for this preprint (which was not certified by peer review) is the author/funder. All rights reserved. No reuse allowed without permission.

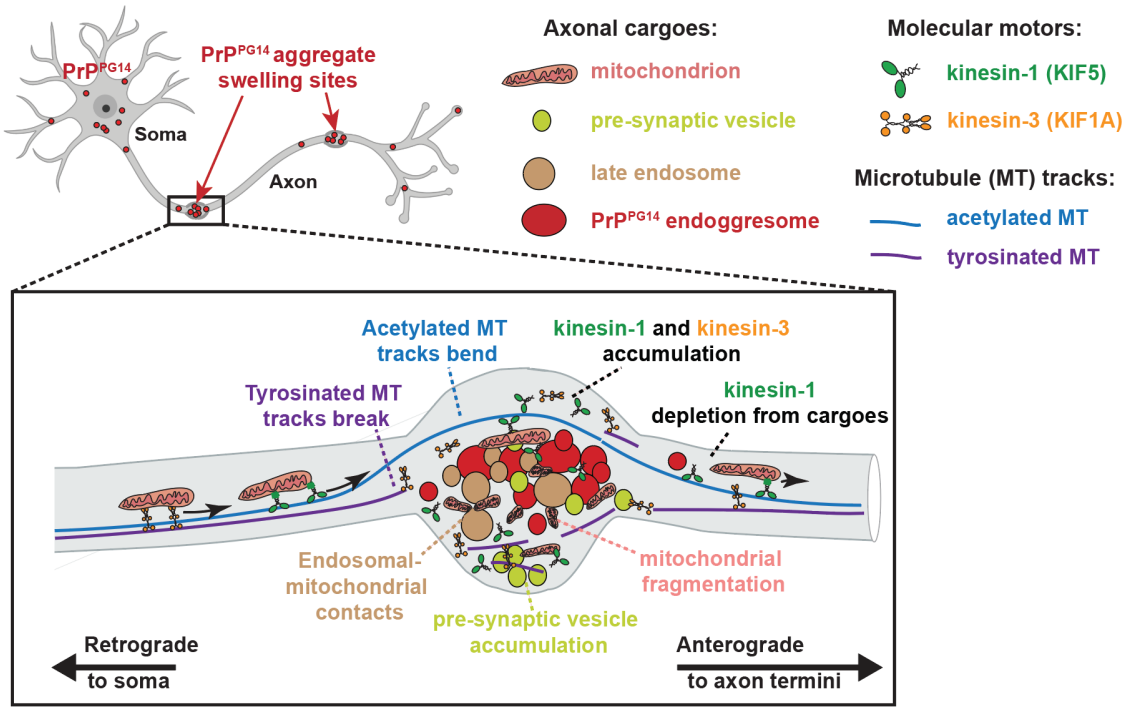


Fig. 8: Working model of the mechanism of cytoskeletal-organelle remodeling at PrP^{PG14} endoggresome swelling sites. PrP^{PG14} endoggresomes form at various sites along mammalian axons where they distend axons into swellings. At endoggresome sites (1) acetylated MT tracks bend and tyrosinated MT tracks break at these swelling sites, (2) kinesin-1 and -3 are sequestered and are depleted from mitochondria that mobilize through these sites, and (3) axonal transport of mitochondria, pre-synaptic and PrP^{PG14} vesicles is selectively impaired in the anterograde direction, and (4) PrP^{PG14} endoggresomes trap Rab7-endolysosomes and mitochondria, enhancing the close contact between these organelles, leading to elevated mitochondrial fission and dysfunction.

Previous studies showed that MT stabilization is conferred by regulation of acetylation vs tyrosination, two PTMs that elicit MTs to bend or break under mechanical stress[43]. Our data are consistent with these observations, as acetylated MTs curve while tyrosinated MTs break at PrP^{PG14} endoggresome swelling sites (**Fig. 3**), suggesting that enlarged PrP^{PG14} endoggresomes exert mechanical stress from within axons. Our data further suggest that breakage of tyrosinated MTs at swelling sites could be an important initiating event that precedes the cascade of downstream deficits, including transport defects and motor and organelle accumulations that are observed within localized swelling regions. Tyrosinated MTs are preferred by kinesin-3 (KIF1),

bioRxiv preprint doi: https://doi.org/10.1101/2023.03.19.533383; this version posted March 21, 2023. The copyright holder for this preprint (which was not certified by peer review) is the author/funder. All rights reserved. No reuse allowed without permission.

and this motor is used by mitochondria, pre-synaptic vesicles, and PrP vesicles (R. Chassefeyre, pers. comm.) to move toward the synapse[65-67]. On the other hand, kinesin-1 (KIF5) prefers bundled and stable acetylated MTs[46,68] and is also a motor for the movement of mitochondria, pre-synaptic vesicles, as well as of wild-type and mutant PrP vesicles[17,34] along axons[65-67]. Thus, kinesin-3 transport is expected to be directly affected by broken tyrosinated MTs, while bending acetylated MTs likely sustain the transport of kinesin-1 cargoes, including of mitochondria, through axonal swollen regions. As it is unclear how kinesin-1 and kinesin-3 coordinate activities when bound simultaneously to a cargo[47,69], it is possible that complex interactions between these motors and MT tracks dictate the final outcome of motility of mitochondria within and through these sites.

The global deficits observed primarily to the anterograde axonal transport of three different cargo—mitochondria, pre-synaptic and mutant PrP vesicles—point to disruptions to generalized motility pathways in axons of neurons expressing PrP^{PG14}, that are likely dictated at least in part, by the observed alterations to subsets of MTs with different PTMs. However, MT defects might not be responsible for the very early transport defects first observed for the anterograde movement of vesicles carrying PrP^{PG14} at 12 hours post-transfection, when only very few endoggresomes have formed (**Supplementary Fig. 1**), and when presumably the MT cytoskeleton is intact. These observations suggest that other even earlier deficits ensue in axons. A possibility is that the previously observed initial active and dynamic sorting of endolysosomes containing PrP^{PG14} into fused enlarged organelles[17] could inhibit transport of those endolysosomal vesicles during the process of forming larger endoggresomes. As mitochondrial movement is unaffected at the 12 hour earlier time point, our data suggest that mitochondrial motility impairments represent local traffic disruptions that result from micro-transport deficits

bioRxiv preprint doi: https://doi.org/10.1101/2023.03.19.533383; this version posted March 21, 2023. The copyright holder for this preprint (which was not certified by peer review) is the author/funder. All rights reserved. No reuse allowed without permission.

that start at AGG sites following the formation of PrP^{PG14} endoggresomes, thus implicating PrP^{PG14} endoggresomes directly in the initiation of these local transport deficits.

The observation that anterograde, but not retrograde transport of PrP^{PG14} vesicles, pre-synaptic vesicles, and mitochondria, was impaired in axons of neurons expressing PrP^{PG14}, was unexpected. Previous work showed that disruptions to kinesin-mediated anterograde movement of various cargoes in axons also impaired dynein-mediated retrograde transport because these opposing motors often associate simultaneously to the same cargo to coordinate activities[34,70]. Both kinesin-1 and dynein can associate to mitochondria simultaneously[71], thus a possibility is that mitochondria moving in the retrograde direction by dynein, the principal retrograde motor in axons[72], utilize intact acetylated MTs tracks. Previous *in vitro* studies showed that dynein associates to tyrosinated MTs tracks to initiate is movement, but that subsequently dynein can continue translocating on detyrosinated MTs[73]. Thus, it could be that dynein initiates movement on broken tyrosinated MTs in axons expressing PrP^{PG14}, but continues movement on acetylated (detyrosinated) MTs, and this possibility merits further exploration. Differences in anterograde versus retrograde transport impairments could also stem from differences in the intrinsic properties of kinesin and dynein proteins. Several studies using *in vitro* motility and biophysical assays showed that a single dynein molecule could take side-steps around MT tracks to avoid obstacles in dense cytoplasmic environments during cargo transport[74,75]. Kinesin-1, on the other hand, walks linearly on single protofilament tracks and works in teams to avoid obstacles[75]. Thus, in the normal crowded environment of axons, which are accentuated by the presence of enlarged PrP^{PG14} endoggresomes, dynein-driven cargoes might be capable of navigating through dense cytoskeletal networks while kinesin-1 molecules might not. Notably, a previous study in an PrP^{Sc}-infected mouse model suggested that the MT network and dynein-mediated retrograde

bioRxiv preprint doi: https://doi.org/10.1101/2023.03.19.533383; this version posted March 21, 2023. The copyright holder for this preprint (which was not certified by peer review) is the author/funder. All rights reserved. No reuse allowed without permission.

transport were not directly affected, but instead, they proposed that motor-cargo associations might be the target of infectious prions prior to clinical onset *in vivo*[76]. While it is unclear whether mechanisms of axonal impairment in infectious PrP^{Sc} models are similar to those in familial forms of prion disease, our data is consistent with this scenario, as we showed that motor-cargo associations were impaired and that kinesin-1 detachment and accumulation at PrP^{PG14} aggregate sites depend on the presence of the cargo binding domain of kinesin-1 (**Fig. 4**).

In prion diseases, ultrastructural studies of human patient brains with prion disease have revealed the accumulation of misfolded PrP within dystrophic neurites inside endolysosomes[18-21,77,78]. Other complex structures have been observed to co-exist with aggregates within swollen neurites, and are also considered common features of prion pathology, including autophagic vacuole-like membrane-bound organelles, lysosomal electron-dense bodies, enlarged endolysosomes, and membraneless electron-lucent areas of cytoplasm[18,20,77]. Some of these neuronal phenotypes have also been observed in cell lines infected with PrP^{Sc}, as well as in brains of rodent models of familial and sporadic human PrP^{Sc} disease [18,77-81]. The presence of dystrophic swellings in axons is also a common and early feature in brains of patients in various neurodegenerative pathologies including prion diseases, AD, PD, and HD[3,14,82,83]. In AD, dystrophic axons are also comprised of enlarged endosomes, and these lesions are considered amongst the earliest neuronal lesions identified thus far[84,85]. These observations highlight the importance of understanding the mechanisms of axonotoxicity as imparted by the presence of intra-axonal misfolded protein aggregates in these diseases.

In the familial PrDs, the formation of axonal misfolded PrP aggregates contributes to neurodegeneration, as reduction of axonal aggregates by modulating its biogenesis pathway rescues neuronal function[17]. To what extent modulation of endolysosomal pathways contributes

bioRxiv preprint doi: https://doi.org/10.1101/2023.03.19.533383; this version posted March 21, 2023. The copyright holder for this preprint (which was not certified by peer review) is the author/funder. All rights reserved. No reuse allowed without permission.

to the formation of aggregates in other neurodegenerative disorders is unknown. However, as misfolded proteins like tau, α-synuclein, APP and Huntingtin are associated at least in part with endolysosomes and undergo sorting and trafficking[86-88], it will be key to determine whether the defects to the cytoskeleton and micro-domain impairments observed in PrP^{PG14}-expressing neurons also participate in axonotoxicity in the rest of the proteinopathies. The subcellular lesions identified in this study provide new pathways that can be therapeutically targeted for their amelioration and for the rescue of axonal lesions that are the primary vulnerability targets in the proteinopathies.

METHODS

DNA constructs

PrP^{WT}-EGFP and PrP^{PG14}-EGFP in the MoPrP.Xho vector[89] were a gift from David A. Harris[16]. PrP^{WT}-mCh, PrP^{PG14}-mCh, PrP^{WT} -mTagBFP2, PrP^{PG14}-mTagBFP2 fusions were cloned by assembly PCR to replace EGFP as described previously[17]. Synaptophysin-YFP (SYP-YFP) in cEGFP vector was a gift from Ann Marie Craig[90]. Mito-EGFP in pcDNA3 vector was a gift from Christine Vande Velde[91]. Mito-mTagBFP2 was cloned by replacing EGFP in mito-EGFP with mTagBFP2 sequence in pcDNA3.1 from mTagBFP2-Lysosome-20 (Addgene #55308). KIF5C(1-560)-2xmCh-EF(C) (Addgene #61664) and KIF5C(1-560)-mCit (Addgene #61676) were a gift from Kristen Verhey[92]. 2xmCh-KIF5C in pcDNA3.1 was cloned by inserting in-frame KIF5C full length from EGFP-KIF5C (a gift from Anthony Brown) 2xmCh sequence from KIF5C(1-560)-2xmCh-EF(C) into pcDNA3.1 using InFusion Cloning kit (Takara). EGFP-Rab7A (Addgene #28047) and EGFP-Rab7A Q67L (Addgene #28049) were a gift from Qing Zhong. SNAP-Rab7A and SNAP-Rab7A Q67L were made by cloning Rab7A sequence from EGFP-Rab7A and EGFP-Rab7A Q67L plasmids into pSNAP-tag (m) Vector (Addgene #101135). Soluble BFP (mTagBFP2) in pcDNA3.1 was derived from mTagBFP2-Lysosome-20 (Addgene #55308). Soluble EGFP (pEGFP-C1 plasmid) was a gift from Hilal Lashuel. Soluble mCherry (pmCherry-N3 plasmid) was cloned from pmCherry-mito-7 (Addgene #55102).

Kif1a and *scrambled* shRNAs were part of a kinesin lentiviral mini-library, in a pLL3.7 GW lentiviral vector with Gateway entry modifications and a mCherry co-expression marker (unpublished data). The knockdown efficacy of *Kif1a* shRNA was evaluated by Western blot and qPCR from lysates of cultured hippocampal neurons transduced with lentivirus containing *Kif1a* shRNA-expressing plasmids (unpublished data).

Antibodies

The following primary antibodies were used for immunofluorescence (IF): mouse anti-KHC (clone H2; MAB1614; recognizes primarily KIF5C[34]) (1:100, EMD Millipore); goat anti-

bioRxiv preprint doi: https://doi.org/10.1101/2023.03.19.533383; this version posted March 21, 2023. The copyright holder for this preprint (which was not certified by peer review) is the author/funder. All rights reserved. No reuse allowed without permission.

KLC1 (V-17) (1:100, Santa Cruz Biotechnology); mouse anti-KIF1A (16/KIF1A) (1:100; BD Transduction Laboratory); mouse anti-alpha-tubulin (DM1A) (1:2000; Sigma-Aldrich); mouse anti-Acetylated tubulin (1:400; Sigma-Aldrich); rat anti-Tyrosinated tubulin [YL1/2] (1:1000; Abcam). The concentration of Goat anti-KLC1 (V-17) was validated previously for sub-pixel colocalization analysis[34]. The concentration of mouse anti-KHC and mouse anti-KIF1A were also validated for sub-pixel colocalization analysis (data not shown). All tubulin antibodies were validated previously to be suitable for IF for super-resolution imaging[48].

The following secondary antibodies were used for IF: Donkey anti-goat IgG (H+L) Alexa Fluor 488 (1:200; ThermoFisher; A-11055); Goat anti-mouse Atto647N (1:200 Sigma); Goat anti-rat Atto594 (1:200; Rockland Immuno); Alexa Fluor 647 Phalloidin in methanol (1:40; Invitrogen)

Cultured primary mouse hippocampal neurons

Primary mouse hippocampal neurons were prepared as described previously[17,34,93]. Briefly, hippocampi were dissected from 0 to 2-day-old mouse neonates, treated with Papain (Worthington) for 15 minutes, and dissociated by seven to ten cycles of aspiration through micropipette tips. Dissociated neurons were resuspended in Neurobasal-A medium containing 2% B-27 (Gibco) and 0.25% GlutaMAX supplements (Gibco). Neurons were plated in 24-well plates containing #1.5 1-mm round coverslips (Neurovitro) and were maintained at 37°C and in a 5% CO_2 atmosphere up to 12 DIV for imaging.

Transfection and live imaging of hippocampal neurons

Neurons were transfected at between 4-7 DIV. We used 2 µL of Lipofectamine 2000 (Invitrogen) and up to 1.6 µg total of DNA per well in 24 well plates. Transfection rates of cultured hippocampal neurons were ~5%, which enabled imaging of individual axons. Neurons were imaged using a Nikon Ti-E Perfect Focus inverted microscope equipped with a total internal reflection fluorescence (TIRF) setup, with an Andor iXon + DU897 EM Camera, and a 100X/1.49 NA oil objective. A 405-nm, 488-nm, 561-nm, and 640-nm laser lines were used to detect BFP, GFP, mCh, and JF646 fluorescence respectively, at an angle for optimal pseudo-TIRF/HILO acquisition. Movies of vesicular transport were 15 seconds long and collected at a frame rate of 10 frames/sec (10 Hz). Movies of mitochondrial transport were 5 minutes long and collected at a frame rate of 1 frame/sec (1 Hz). Cultured neurons were maintained at 37°C and 5% CO_2 throughout the total imaging period.

Quantitative analysis of cargo motility in whole axons

Analysis of cargo motility was performed by using *KymoAnalyzer*, an ImageJ macros package specifically designed to track the movement of particles in axons[35]. Briefly, kymographs (distance-time projections) were generated from time-lapse movies. Particle trajectories were manually assigned from the kymograph images. Track and segment-related parameters were

bioRxiv preprint doi: https://doi.org/10.1101/2023.03.19.533383; this version posted March 21, 2023. The copyright holder for this preprint (which was not certified by peer review) is the author/funder. All rights reserved. No reuse allowed without permission.

automatically calculated. Detailed definitions of all the transport parameters analyzed in this study were described previously[35].

Single-particle tracking (SPT) of mitochondria

SPT of mito-EGFP was done using *TrackMate*, a Fiji (ImageJ) plugin[94]. In brief, Laplacian of Gaussian (LoG) filter, median filter, and sub-pixel localization were applied to detect the blobs with diameter between 1-3 µm. Auto-thresholding was applied on the detected feature quality to restrict number of spots. The hyperstack displays contain tracks analyzed by LAP Tracker algorithm[95] with color codes based on parameters such as median velocity or displacement. Frame-to-frame linking maximum distance was set to 15 µm. Gap closing, segment splitting and merging were disabled to take into account all movement instances as independent.

Quantitative analysis of local cargo motility disruption

Local transport disruption analysis was performed manually. AGG sites are defined as a 10-µm window along axonal length containing particles that had fluorescence intensities above the average grey value of five traveling fluorescently labelled PrP^{PG14} cargos. NON-AGG sites are defined by a 10-µm window along axonal length that do not contain particles that had fluorescence intensities above the average grey value of five traveling fluorescently labelled PrP^{PG14} cargos. Particle trajectories were categorized into 3 groups. Pass tracks on kymographs are defined as diagonal tracks that cross AGG/NON-AGG sites without any change in slope. Pause/Slowdown tracks are defined as diagonal tracks that cross AGG/NON-AGG sites with any change in slope. Stall tracks are defined as stationary tracks with slope equal to 0 at AGG/NON-AGG sites.

Immunofluorescence and imaging of fixed neurons

Neurons were fixed with 4% PFA containing 4% sucrose during 30 minutes at 37°C. Neurons were washed 3 times in PBS before permeabilization in 0.1% TritonX-100 in PBS. After another 3 washes in PBS, neurons were incubated in a blocking solution containing 3% IgG-free bovine serum albumin, 5% Normal Goat/Donkey serum (Jackson ImmunoResearch) in PBS during 30 minutes at room temperature. Primary antibodies were incubated in blocking solution overnight at 4°C. After 3 washes in PBS, secondary antibodies were incubated in blocking solution during 1 hour at room temperature. Neurons on the coverslips were mounted onto glass slides using ProLong Diamond antifade reagent (Thermo Fischer) and imaged within 2-3 weeks post-fixation.

Quantitation of kinesin-1 and kinesin-3 fluorescence intensity

KHC was detected with a validated antibody that recognizes primarily KIF5C[34]. The analysis was done in Fiji (ImageJ). Briefly, normalized fluorescence intensity from AGG, NON-AGG, or WT sites was calculated from averaged gray values of antibody staining in those regions subtracted background fluorescence per image. Regions were selected by unbiased

bioRxiv preprint doi: https://doi.org/10.1101/2023.03.19.533383; this version posted March 21, 2023. The copyright holder for this preprint (which was not certified by peer review) is the author/funder. All rights reserved. No reuse allowed without permission.

method, by copying ROIs from PrP^{PG14}/PrP^{WT} channels to antibody channels, and the gray values were obtained in a batch analysis. The fluorescence intensity from the whole dataset then was plotted in the OriginLab software (https://www.originlab.com/).

Sub-pixel colocalization analysis

Single-particle detection with sub-pixel precision was performed as described previously[34,53]. In brief, all primary and secondary antibodies were validated for specificity and determined saturation curve. Tetraspeck beads were used to perform registration and to correct chromatic aberration between channels. Secondaries-only controls were included in every experiment. Raw fluorescence images were processed in MATLAB for single-particle detection. To determine motor colocalization on mitochondria in Fiji (ImageJ), ROIs were drawn around mito-EGFP signal and transferred to particle-detected images output from MATLAB, and number of motor clusters were counted manually.

FRAP

FRAP of KIF5C(1-560)-mCit was performed at the axon terminals. Briefly, A 405-nm laser was collimated and positioned in the middle of the field of view. Laser power and exposure time were determined empirically to ensure complete bleaching and avoid phototoxicity. For the acquisition, 5 images were collected before photobleaching (at 1 frame/sec; 1 Hz), immediately followed by a bleaching of 1-3 seconds, and 300 images were collected after photobleaching (at 1 frame/sec; 1 Hz). Before and after images were combined automatically in Nikon Elements software, and fluorescence intensity plots over time were analyzed in Fiji (ImageJ). Half-life ($t_{1/2}$) was calculated by fitting one-component exponential curve, using FRAP profiler ImageJ plugin (http://worms.zoology.wisc.edu/ImageJ/FRAP_Profiler_v2.java).

SRRF

SRRF processing was done using NanoJ-SRRF ImageJ plugin (https://github.com/HenriquesLab/NanoJ-SRRF). Briefly, 100 frames were collected at 50 frames/sec; 50 Hz. SRRF parameters were set as default (ring radius = 0.5; radiality magnification = 5; axes in ring = 6). Drift correction was applied.

STORM sample preparation and imaging

Hippocampal neurons were plated on MatTek glass bottom dishes (acid pre-washed according to N-STORM preparation protocol) and were transfected with PrP^{PG14}-mCh at DIV7. By 2 days post-transfection (DIV9), neurons were fixed in 3% PFA, 0.1% Glutaraldehyde (GA), 10% sucrose in PBS. Neurons were permeabilized in 0.1% Tx-100 for 8 minutes. Then, neurons were incubated in 0.5 µM of Phalloidin-AF647 overnight at 4ºC. Neurons were washed and kept in PBS at 4ºC to be imaged within 2 days post-staining.

STORM buffer was prepared according to STORM Protocol-Sample Preparation (Nikon, 2013), which included 50 mM TRIS, 10 mM NaCl pH 8, 0.5 mg/mL glucose oxidase, 40 µg/mL catalase, 10% glucose, and 100 mM β-mercaptoethanol (BME). STORM buffer was applied on the MatTek dish sample and sealed tightly before mounting on the microscope. More than

bioRxiv preprint doi: https://doi.org/10.1101/2023.03.19.533383; this version posted March 21, 2023. The copyright holder for this preprint (which was not certified by peer review) is the author/funder. All rights reserved. No reuse allowed without permission.

10,000 raw images were captured with Nikon N-STORM acquisition settings using 640-nm laser and 100X/1.49NA Objectives. STORM images were reconstructed using ThunderSTORM ImageJ plugin[96]. The display mode was based on an average shifted histogram approach, which provides similar results as conventional Gaussian rendering. All dSTORM images collected had sufficient blinking of AlexaFluor647 over 10,000 frames during acquisition.

Membrane-extraction SEM (ME-SEM) preparation and imaging

Neurons were plated on sterile MatTek dish containing gridded coverslip (https://www.mattek.com/store/p50g-2-14-fgrd-case/). Sterile custom-made PDMS molds were temporary attached on the dish to create smaller chamber with the same dimension (volume & surface area) as 24-well plate. Neurons were plated at the concentration of 2 hippocampi into 12 chambers (1:12) or lower and transfected with PrP^{PG14}-mCh at DIV7 following previously described protocol. Membrane extraction was performed 2 days post-transfection (DIV9). Live neurons were imaged with 20X/0.45NA objectives with phase contrast mode and 561-nm laser to find transfected neurons and its grid coordinates. Then, live neurons were treated with a membrane extraction solution containing 1% Triton X-100, 100 mM PIPES (pH 7.2), 4% sucrose, 1 mM $MgCl_2$, 10 μM taxol (Invitrogen) and 10 μM phalloidin (Sigma)[97]. After 20 minutes of gentle rocking, the neurons were washed three times with PBS with gentle pipetting during each wash to remove membrane debris from the sample. Neurons were then fixed with 2% glutaraldehyde, 4% paraformaldehyde [Electron Microscopy Sciences (EMS), Hatfield, PA, USA], 140 mM NaCl, 2 mM $CaCl_2$ and 1 mM $MgCl_2$ in 0.1 M HEPES (pH 7.2) for 30 minutes. Samples were transferred and post-fixed with 1% OsO4 (EMS) and 1% tannic acid (EMS) for 1 hour each, dehydrated with ethanol and critical point-dried from CO_2 (CPD 020 Balzers-Tec), and the coverslips were coated with a thin carbon layer (8 nm) (BAF 300, Balzers)[97] for imaging on Zeiss SIGMA Variable Pressure Field Emission Gun Scanning Electron Microscope.

Fluorescence images and SEM images were aligned manually on Adobe Illustrator.

Figure plotting and statistical analyses

Histograms were plotted in MATLAB (MathWorks), and Gaussian mode mixtures were generated using the Interactive Peak Fitter (ipf.m). Optimal fits were selected empirically based on optimal R^2 values. Box plots were plotted using the web-tool BoxPlotR (http://shiny.chemgrid.org/boxplotr/). Cumulative frequency distribution graphs were plotted using GraphPad Prism. Statistical analyses were performed using Microsoft Excel, GraphPad Prism, and MATLAB. Briefly, we first checked if the parameters were following a normal distribution using the Lilliefors test. For the parameters following a normal distribution (distribution of cargo populations, densities, etc.), we performed a Student's t-test or Tukey's multiple comparisons. Most of the other parameters that did not follow a normal distribution (velocities, run lengths, fluorescence intensity, etc.) were subjected to appropriate non-parametric tests. Differences between two medians were compared using the Wilcoxon rank-sum test, while pair-wise differences between three groups were compared with Kruskal-Wallis test. Differences between two population distribution were compared using Kolmogorov-Smirnov (K-S) test.

TMRE assay

bioRxiv preprint doi: https://doi.org/10.1101/2023.03.19.533383; this version posted March 21, 2023. The copyright holder for this preprint (which was not certified by peer review) is the author/funder. All rights reserved. No reuse allowed without permission.

Neurons for the TMRE assay were grown on the coverslip and transfected with 400 ng of SNAP-Rab7, 800 ng of PrP^{WT}-mTagBFP2 or PrP^{PG14}-mTagBFP2, and 200 ng of mito-EGFP. At 2 days post-transfection, neurons were treated with 25 nM TMRE (Invitrogen) in growth media for 20 minutes at 37°C as described previously[64]. Neurons were then washed 1 time in pre-warm PBS. Then, neurons were treated with 100 nM JF646-SNAP-tag ligands in growth media for 30 minutes at 37°C as described previously[98]. Neurons were washed 1 more time in warm PBS and put back in the growth media to perform live imaging immediately. 568-nm laser was used to detect TMRE signal, and 3-color simultaneous time-lapse imaging were collected at 0.5 frame/sec (0.5 Hz) on the OptoSplit III (Andor).

ACKNOWLEDGEMENTS

We thank Isabelle C. Romine for preliminary data collection; George Campbell for antibody validation and sub-pixel motor colocalization optimization; Tong Zhang for Airyscan microscopy training and data collection; Kathryn Spencer for STORM imaging training; Michael Petrascheck, Jeff Kelly, Kayal Madhivanan, David Soriano Castell, Andre Leitao, and current and past members of the Encalada lab for advice and constructive feedback. This work was supported, in part by NIH/NIA R01AG049483 and NIH/NIA R01AG076745-01 grants (to S.E.E.), the Glenn Foundation for Medical Research Award for Research in Biological Mechanisms of Aging (to S.E.E.), New Scholar in Aging Award from the Lawrence Ellison Foundation, Baxter Family Foundation award (to S.E.E.), T.C. was supported by a Royal Thai Government Scholarship from the Development and Promotion of Science and Technology Talents Project (DPST) and the Skaggs Graduate School of Chemical and Biological Sciences and Scripps Research, George E. Hewitt Foundation for Medical Research Postdoctoral Fellowship (to R.C.), Dorris Neuroscience Center Scholar Award (A.V.), Larry L. Hillblom Foundation Inc. (to U.M. and S.W.N.), Chan-Zuckerberg Initiative (to U.M.), Waitt Foundation Core Grant application NCI CCSG (CA014195) (to U.M., S.W.N., and L.R.A.), NSF NeuroNex Award no. 2014862 (to U.M. and S.W.N. and NIH/NIDCD R21 award DC018237 (to U.M. and L.R.A.).

Author Contributions

Conceptualization: T.C. and S.E.E. Methodology: T.C., A.V., R.C., N.S., S.W.N., L.R.A., U.M., and S.E.E. Investigation: T.C., A.V., R.C., N.S., S.W.N., L.R.A.Validation: T.C., A.V., S.W.N., and L.R.A. Supervision: S.E.E. and U.M. Formal analysis: T.C., A.V., R.C., N.S., S.W.N., U.M., and S.E.E. Writing (original draft): T.C and S.E.E. Writing (review and editing): S.E.E., T.C.

COMPETING INTERESTS

The authors declare no competing interests.

MATERIALS AND CORRESPONDANCE

Should be addressed to S.E.E. at encalada@scripps.edu

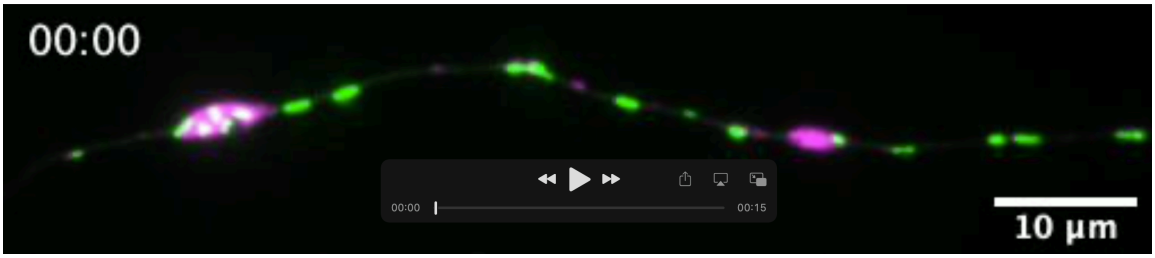
bioRxiv preprint doi: https://doi.org/10.1101/2023.03.19.533383; this version posted March 21, 2023. The copyright holder for this preprint (which was not certified by peer review) is the author/funder. All rights reserved. No reuse allowed without permission.

SUPPLEMENTAL INFORMATION

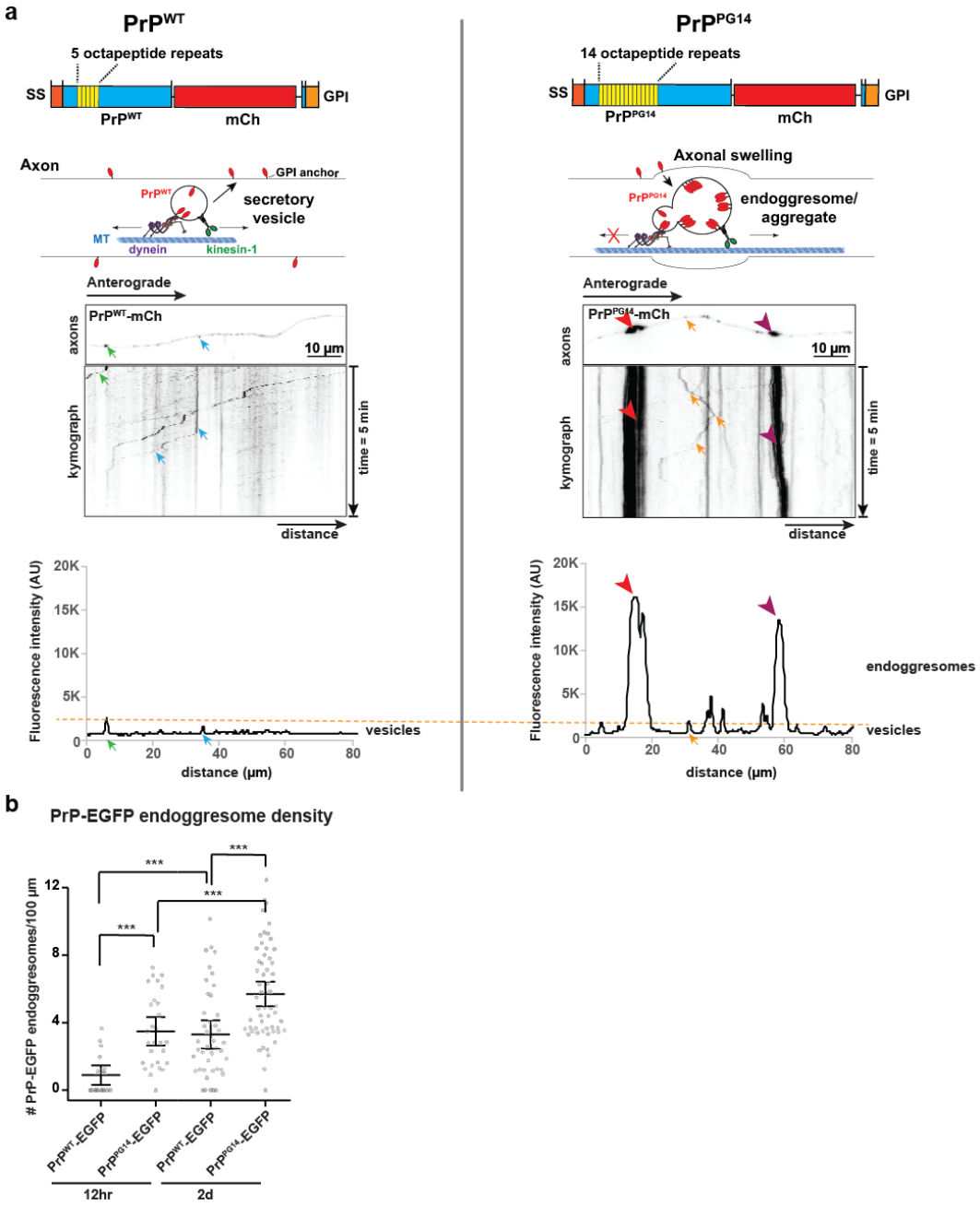
Mutant Prion Aggregates Induce Axonal Traffic Jams via Remodeling of Organelle-Cytoskeletal Interactions

Tai Chaiamarit, Adriaan Verhelle, Romain Chassefeyre, Nandini Shukla, Sammy Weiser Novak, Leonardo R. Andrade, Uri Manor, & Sandra E. Encalada

Supplementary Video 1. Mitochondrial transport disruption and mitochondrial fission at PrP^{PG14} aggregate sites. A 5-minute movie of an axon co-expressing PrP^{PG14}-mCh (magenta) and mito-EGFP (green) showing transport disruption (a swelling site on the right) and mitochondrial fragmentation (a swelling site on the left). Movement towards the right side of the video is anterograde direction. (Related to **Fig. 1 and Fig. 6**)

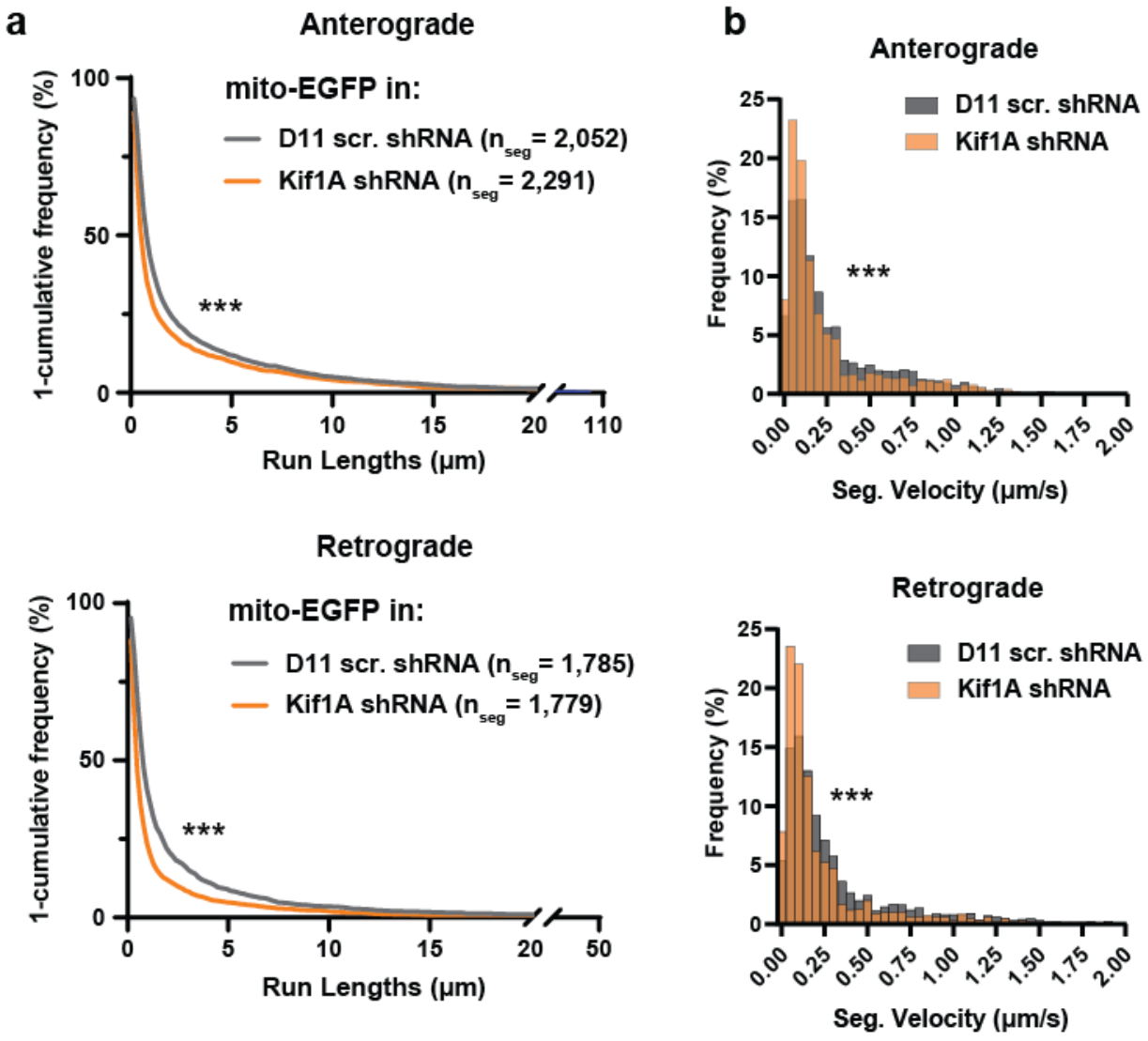


bioRxiv preprint doi: https://doi.org/10.1101/2023.03.19.533383; this version posted March 21, 2023. The copyright holder for this preprint (which was not certified by peer review) is the author/funder. All rights reserved. No reuse allowed without permission.



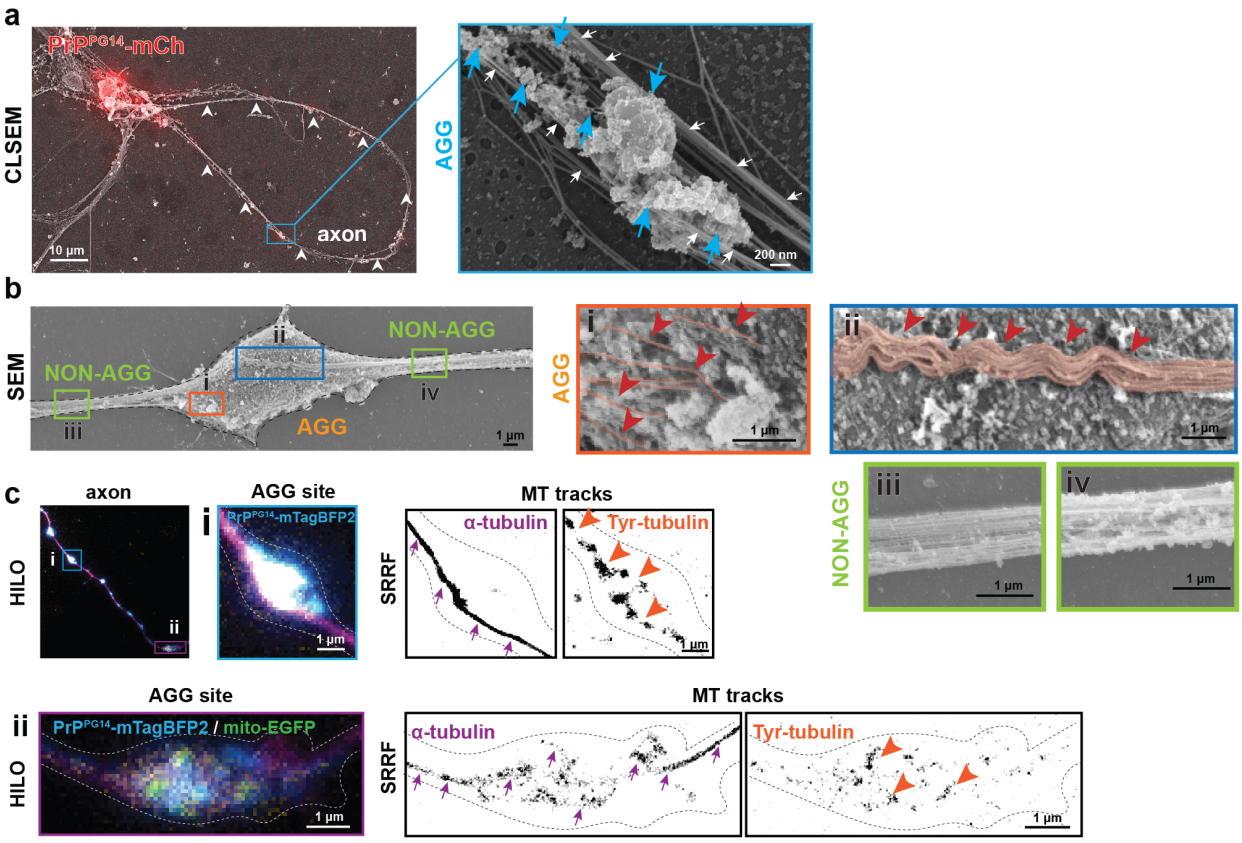
Supplementary Fig. S1: PrP^{PG14} forms aggregates inside axons. a Schematic of PrP^{WT}-mCh and PrP^{PG14}-mCh constructs (top panels; SS: signal sequence, GPI: GPI anchor), and representative images of axons first frame of a time-lapse movie showing PrP^{WT}-mCh and PrP^{PG14}-mCh vesicle transport in hippocampal axons of cultured neurons. Corresponding kymographs are shown below first movie frames. Fluorescence intensity profiles obtained from line scan plots (bottom panels), highlight key differences between PrP^{PG14}-mCh and PrP^{WT}-mCh control. Arrows point to vesicles. Arrowheads point to aggregates. **b** Quantitation of density of PrP-EGFP endoggresomes. The graph is shown as mean ± SEM with all datapoints. ***p<0.001, **p<0.01, *p<0.05, ns = not significant. Tukey's multiple comparison test.

bioRxiv preprint doi: https://doi.org/10.1101/2023.03.19.533383; this version posted March 21, 2023. The copyright holder for this preprint (which was not certified by peer review) is the author/funder. All rights reserved. No reuse allowed without permission.



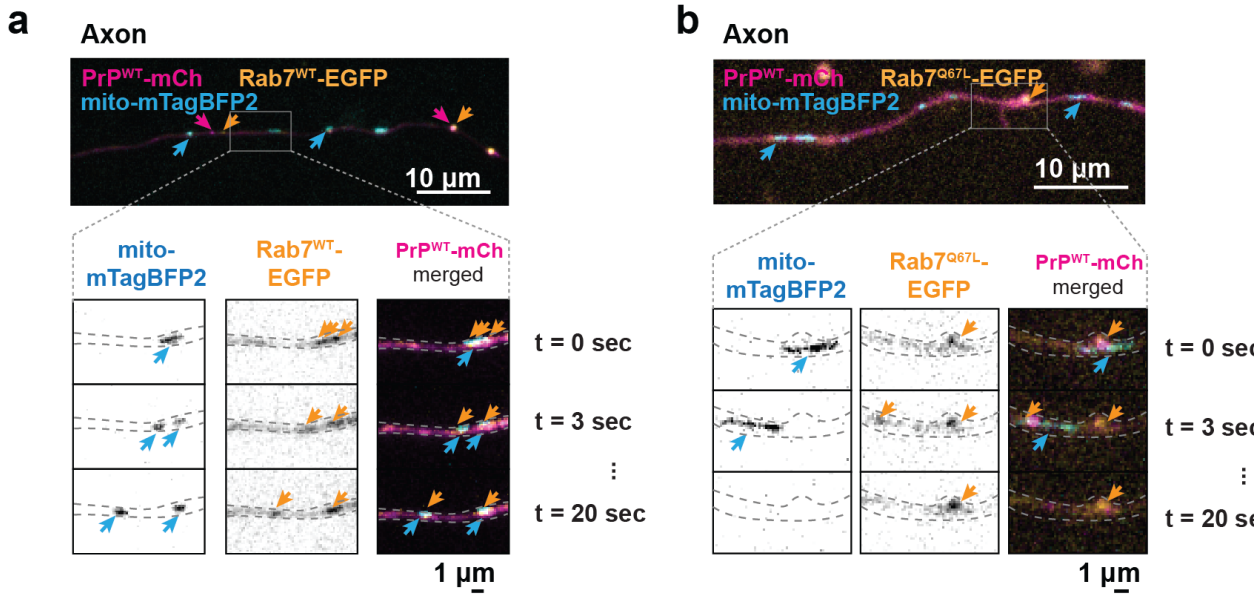
Supplementary Fig. S2: Mitochondrial transport in mammalian axons requires KIF1A. a Anterograde (top) and retrograde (bottom) segmental run lengths of mito-EGFP in D11 scrambled (scr.) shRNA vs Kif1A shRNA, plotted as 1-cumulative frequency (%). **b** Anterograde (top) and retrograde (bottom) segmental velocity of mito-EGFP in D11 scrambled (scr.) shRNA vs Kif1A shRNA plotted as relative frequency histogram. ***p<0.001, Kolmogorov-Smirnov (K-S) test.

bioRxiv preprint doi: https://doi.org/10.1101/2023.03.19.533383; this version posted March 21, 2023. The copyright holder for this preprint (which was not certified by peer review) is the author/funder. All rights reserved. No reuse allowed without permission.



Supplementary Fig. S3: Ultrastructure of the axonal cytoskeleton at PrP^{PG14} aggregate sites. a Membrane-extracted CLSEM image of a neuron transfected with PrP^{PG14}-mCh (red). White arrowheads indicate axons. Blue inset (right) shows an AGG site. White arrows point to MT tracks. Blue arrows point to actin surrounding PrP^{PG14} aggregates. **b** Membrane-extracted SEM image of an axonal region of a neuron transfected with PrP^{PG14}-mCh. Insets (i-ii) show AGG sites. Red arrowheads and pseudo-color highlights show broken (i) or bending (ii) MT tracks. Insets (iii-iv) show NON-AGG sites. **c** HILO image of an axon from a neuron co-transfected with PrP^{PG14}-mTagBFP2 and mito-EGFP, co-immunostained with alpha tubulin and antibodies against tyrosinated (Tyr) tubulin. Inset (i) shows AGG site and SRRF processed images of alpha tubulin and Tyr-tubulin channels. Inset (ii) shows a HILO image of PrP^{PG14}-mTagBFP2 and mito-EGFP at AGG site and SRRF processed images of alpha tubulin and Tyr-tubulin channels. Arrows point to straight/intact MT tracks. Arrowheads point to broken MT tracks.

bioRxiv preprint doi: https://doi.org/10.1101/2023.03.19.533383; this version posted March 21, 2023. The copyright holder for this preprint (which was not certified by peer review) is the author/funder. All rights reserved. No reuse allowed without permission.



Supplementary Fig. S4: Mitochondrial fission in PrP^{WT} axons. a First-frame images of axons co-expressing PrP^{WT}-mCh, $Rab7^{WT}$-EGFP, and mito-mTagBFP2 and representative frames from time-lapse videos at WT or AGG sites (insets). **b** First-frame images of axons co-expressing PrP^{WT}-mCh, $Rab7^{Q67L}$-EGFP, and mito-mTagBFP2 and representative frames from time-lapse videos at WT or AGG sites (insets). Arrows point to corresponding organelles in the first-frame images and time-lapse insets.

bioRxiv preprint doi: https://doi.org/10.1101/2023.03.19.533383; this version posted March 21, 2023. The copyright holder for this preprint (which was not certified by peer review) is the author/funder. All rights reserved. No reuse allowed without permission.

REFERENCES

1 Burgess, R. W. & Crish, S. D. Editorial: Axonopathy in Neurodegenerative Disease. *Front Neurosci* **12**, 769, doi:10.3389/fnins.2018.00769 (2018).

2 Lim, J. & Yue, Z. Neuronal aggregates: formation, clearance, and spreading. *Dev Cell* **32**, 491-501, doi:10.1016/j.devcel.2015.02.002 (2015).

3 Stokin, G. B. *et al.* Axonopathy and transport deficits early in the pathogenesis of Alzheimer's disease. *Science* **307**, 1282-1288, doi:10.1126/science.1105681 (2005).

4 Li, H., Li, S. H., Yu, Z. X., Shelbourne, P. & Li, X. J. Huntingtin aggregate-associated axonal degeneration is an early pathological event in Huntington's disease mice. *J Neurosci* **21**, 8473-8481 (2001).

5 Gunawardena, S. *et al.* Disruption of axonal transport by loss of huntingtin or expression of pathogenic polyQ proteins in Drosophila. *Neuron* **40**, 25-40, doi:10.1016/s0896-6273(03)00594-4 (2003).

6 Lee, W. C., Yoshihara, M. & Littleton, J. T. Cytoplasmic aggregates trap polyglutamine-containing proteins and block axonal transport in a Drosophila model of Huntington's disease. *Proc Natl Acad Sci U S A* **101**, 3224-3229, doi:10.1073/pnas.0400243101 (2004).

7 Alexiou, A. *et al.* Mitochondrial Dynamics and Proteins Related to Neurodegenerative Diseases. *Curr Protein Pept Sci* **19**, 850-857, doi:10.2174/1389203718666170810150151 (2018).

8 Abramov, A. Y., Berezhnov, A. V., Fedotova, E. I., Zinchenko, V. P. & Dolgacheva, L. P. Interaction of misfolded proteins and mitochondria in neurodegenerative disorders. *Biochem Soc Trans* **45**, 1025-1033, doi:10.1042/BST20170024 (2017).

9 Choi, H. S. *et al.* Dysfunction of mitochondrial dynamics in the brains of scrapie-infected mice. *Biochemical and biophysical research communications* **448**, 157-162, doi:10.1016/j.bbrc.2014.04.069 (2014).

10 Deckwerth, T. L. & Johnson, E. M., Jr. Neurites can remain viable after destruction of the neuronal soma by programmed cell death (apoptosis). *Dev Biol* **165**, 63-72, doi:10.1006/dbio.1994.1234 (1994).

11 Adalbert, R. & Coleman, M. P. Review: Axon pathology in age-related neurodegenerative disorders. *Neuropathol Appl Neurobiol* **39**, 90-108, doi:10.1111/j.1365-2990.2012.01308.x (2013).

12 Scheckel, C. & Aguzzi, A. Prions, prionoids and protein misfolding disorders. *Nat Rev Genet* **19**, 405-418, doi:10.1038/s41576-018-0011-4 (2018).

13 Prusiner, S. B. Prions. *Proc Natl Acad Sci U S A* **95**, 13363-13383, doi:10.1073/pnas.95.23.13363 (1998).

14 Zanusso, G. *et al.* Novel prion protein conformation and glycotype in Creutzfeldt-Jakob disease. *Arch Neurol* **64**, 595-599, doi:10.1001/archneur.64.4.595 (2007).

15 Soto, C. & Satani, N. The intricate mechanisms of neurodegeneration in prion diseases. *Trends Mol Med* **17**, 14-24, doi:10.1016/j.molmed.2010.09.001 (2011).

16 Medrano, A. Z., Barmada, S. J., Biasini, E. & Harris, D. A. GFP-tagged mutant prion protein forms intra-axonal aggregates in transgenic mice. *Neurobiol Dis* **31**, 20-32, doi:10.1016/j.nbd.2008.03.006 (2008).

17 Chassefeyre, R. *et al.* Endosomal sorting drives the formation of axonal prion protein endoggresomes. *Sci Adv* **7**, eabg3693, doi:10.1126/sciadv.abg3693 (2021).

bioRxiv preprint doi: https://doi.org/10.1101/2023.03.19.533383; this version posted March 21, 2023. The copyright holder for this preprint (which was not certified by peer review) is the author/funder. All rights reserved. No reuse allowed without permission.

18 Liberski, P. P., Gajos, A. & Sikorska, B. Dystrophic neurites accumulating autophagic vacuoles show early stages of neuritic destruction. *Folia Neuropathol* **56**, 175-178, doi:10.5114/fn.2018.78696 (2018).
19 Sikorska, B., Liberski, P. P., Giraud, P., Kopp, N. & Brown, P. Autophagy is a part of ultrastructural synaptic pathology in Creutzfeldt-Jakob disease: a brain biopsy study. *Int J Biochem Cell Biol* **36**, 2563-2573, doi:10.1016/j.biocel.2004.04.014 (2004).
20 Godsave, S. F. *et al.* Cryo-immunogold electron microscopy for prions: toward identification of a conversion site. *J Neurosci* **28**, 12489-12499, doi:10.1523/JNEUROSCI.4474-08.2008 (2008).
21 Kovacs, G. G. *et al.* Intraneuronal immunoreactivity for the prion protein distinguishes a subset of E200K genetic from sporadic Creutzfeldt-Jakob Disease. *J Neuropathol Exp Neurol* **71**, 223-232, doi:10.1097/NEN.0b013e318248aa70 (2012).
22 Kuijpers, M., Azarnia Tehran, D., Haucke, V. & Soykan, T. The axonal endolysosomal and autophagic systems. *J Neurochem* **158**, 589-602, doi:10.1111/jnc.15287 (2021).
23 Maday, S. & Holzbaur, E. L. F. Autophagosome biogenesis in primary neurons follows an ordered and spatially regulated pathway. *Dev. Cell* **30**, 71-85 (2014).
24 Song, Y. & Brady, S. T. Post-translational modifications of tubulin: pathways to functional diversity of microtubules. *Trends Cell Biol* **25**, 125-136, doi:10.1016/j.tcb.2014.10.004 (2015).
25 Janke, C. & Magiera, M. M. The tubulin code and its role in controlling microtubule properties and functions. *Nat Rev Mol Cell Biol* **21**, 307-326, doi:10.1038/s41580-020-0214-3 (2020).
26 Maday, S., Twelvetrees, A. E., Moughamian, A. J. & Holzbaur, E. L. Axonal transport: cargo-specific mechanisms of motility and regulation. *Neuron* **84**, 292-309, doi:10.1016/j.neuron.2014.10.019 (2014).
27 Schwarz, T. L. Mitochondrial trafficking in neurons. *Cold Spring Harb Perspect Biol* **5**, doi:10.1101/cshperspect.a011304 (2013).
28 Youle, R. J. & van der Bliek, A. M. Mitochondrial fission, fusion, and stress. *Science* **337**, 1062-1065, doi:10.1126/science.1219855 (2012).
29 Zhu, T., Chen, J. L., Wang, Q., Shao, W. & Qi, B. Modulation of Mitochondrial Dynamics in Neurodegenerative Diseases: An Insight Into Prion Diseases. *Front Aging Neurosci* **10**, 336, doi:10.3389/fnagi.2018.00336 (2018).
30 Shields, L. Y. *et al.* Mitochondrial fission is a critical modulator of mutant APP-induced neural toxicity. *J Biol Chem* **296**, 100469, doi:10.1016/j.jbc.2021.100469 (2021).
31 Owen, F. *et al.* A dementing illness associated with a novel insertion in the prion protein gene. *Brain Res Mol Brain Res* **13**, 155-157 (1992).
32 Tarsa, L. & Goda, Y. Synaptophysin regulates activity-dependent synapse formation in cultured hippocampal neurons. *Proc Natl Acad Sci U S A* **99**, 1012-1016, doi:10.1073/pnas.022575999 (2002).
33 Sheng, Z. H. & Cai, Q. Mitochondrial transport in neurons: impact on synaptic homeostasis and neurodegeneration. *Nat Rev Neurosci* **13**, 77-93, doi:10.1038/nrn3156 (2012).
34 Encalada, S. E., Szpankowski, L., Xia, C. H. & Goldstein, L. S. Stable kinesin and dynein assemblies drive the axonal transport of mammalian prion protein vesicles. *Cell* **144**, 551-565, doi:10.1016/j.cell.2011.01.021 (2011).

bioRxiv preprint doi: https://doi.org/10.1101/2023.03.19.533383; this version posted March 21, 2023. The copyright holder for this preprint (which was not certified by peer review) is the author/funder. All rights reserved. No reuse allowed without permission.

35 Neumann, S., Chassefeyre, R., Campbell, G. E. & Encalada, S. E. KymoAnalyzer: a software tool for the quantitative analysis of intracellular transport in neurons. *Traffic* **18**, 71-88, doi:10.1111/tra.12456 (2017).
36 Kwon, S. E. & Chapman, E. R. Synaptophysin regulates the kinetics of synaptic vesicle endocytosis in central neurons. *Neuron* **70**, 847-854, doi:10.1016/j.neuron.2011.04.001 (2011).
37 Okada, Y., Yamazaki, H., Sekine-Aizawa, Y. & Hirokawa, N. The neuron-specific kinesin superfamily protein KIF1A is a unique monomeric motor for anterograde axonal transport of synaptic vesicle precursors. *Cell* **81**, 769-780 (1995).
38 Zhong, G. *et al.* Developmental mechanism of the periodic membrane skeleton in axons. *Elife* **3**, doi:10.7554/eLife.04581 (2014).
39 Yogev, S., Cooper, R., Fetter, R., Horowitz, M. & Shen, K. Microtubule Organization Determines Axonal Transport Dynamics. *Neuron* **92**, 449-460, doi:10.1016/j.neuron.2016.09.036 (2016).
40 Kevenaar, J. T. & Hoogenraad, C. C. The axonal cytoskeleton: from organization to function. *Front Mol Neurosci* **8**, 44, doi:10.3389/fnmol.2015.00044 (2015).
41 Fernandes, M. C. *et al.* Trypanosoma cruzi subverts the sphingomyelinase-mediated plasma membrane repair pathway for cell invasion. *J Exp Med* **208**, 909-921, doi:10.1084/jem.20102518 (2011).
42 Atherton, J., Houdusse, A. & Moores, C. MAPping out distribution routes for kinesin couriers. *Biol Cell* **105**, 465-487, doi:10.1111/boc.201300012 (2013).
43 Xu, Z. *et al.* Microtubules acquire resistance from mechanical breakage through intralumenal acetylation. *Science* **356**, 328-332, doi:10.1126/science.aai8764 (2017).
44 Cai, D., McEwen, D. P., Martens, J. R., Meyhofer, E. & Verhey, K. J. Single molecule imaging reveals differences in microtubule track selection between Kinesin motors. *PLoS biology* **7**, e1000216 (2009).
45 Konishi, Y. & Setou, M. Tubulin tyrosination navigates the kinesin-1 motor domain to axons. *Nat Neurosci* **12**, 559-567, doi:10.1038/nn.2314 (2009).
46 Reed, N. A. *et al.* Microtubule acetylation promotes kinesin-1 binding and transport. *Curr. Biol.* **16**, 2166-2172 (2006).
47 Guardia, C. M., Farias, G. G., Jia, R., Pu, J. & Bonifacino, J. S. BORC Functions Upstream of Kinesins 1 and 3 to Coordinate Regional Movement of Lysosomes along Different Microtubule Tracks. *Cell Rep* **17**, 1950-1961, doi:10.1016/j.celrep.2016.10.062 (2016).
48 Tas, R. P. *et al.* Differentiation between Oppositely Oriented Microtubules Controls Polarized Neuronal Transport. *Neuron* **96**, 1264-1271 e1265, doi:10.1016/j.neuron.2017.11.018 (2017).
49 Guedes-Dias, P. *et al.* Kinesin-3 Responds to Local Microtubule Dynamics to Target Synaptic Cargo Delivery to the Presynapse. *Curr Biol* **29**, 268-282 e268, doi:10.1016/j.cub.2018.11.065 (2019).
50 Culley, S., Tosheva, K. L., Matos Pereira, P. & Henriques, R. SRRF: Universal live-cell super-resolution microscopy. *Int J Biochem Cell Biol* **101**, 74-79, doi:10.1016/j.biocel.2018.05.014 (2018).
51 Verhey, K. J. & Hammond, J. W. Traffic control: regulation of kinesin motors. *Nat Rev Mol Cell Biol* **10**, 765-777, doi:10.1038/nrm2782 (2009).
52 Hummel, J. J. A. & Hoogenraad, C. C. Specific KIF1A-adaptor interactions control selective cargo recognition. *J Cell Biol* **220**, doi:10.1083/jcb.202105011 (2021).

bioRxiv preprint doi: https://doi.org/10.1101/2023.03.19.533383; this version posted March 21, 2023. The copyright holder for this preprint (which was not certified by peer review) is the author/funder. All rights reserved. No reuse allowed without permission.

53 Szpankowski, L., Encalada, S. E. & Goldstein, L. S. Subpixel colocalization reveals amyloid precursor protein-dependent kinesin-1 and dynein association with axonal vesicles. *Proc Natl Acad Sci U S A* **109**, 8582-8587, doi:10.1073/pnas.1120510109 (2012).

54 Jacobson, C., Schnapp, B. & Banker, G. A. A change in the selective translocation of the Kinesin-1 motor domain marks the initial specification of the axon. *Neuron* **49**, 797-804, doi:10.1016/j.neuron.2006.02.005 (2006).

55 Kiral, F. R., Kohrs, F. E., Jin, E. J. & Hiesinger, P. R. Rab GTPases and Membrane Trafficking in Neurodegeneration. *Curr Biol* **28**, R471-R486, doi:10.1016/j.cub.2018.02.010 (2018).

56 Wong, Y. C., Ysselstein, D. & Krainc, D. Mitochondria-lysosome contacts regulate mitochondrial fission via RAB7 GTP hydrolysis. *Nature* **554**, 382-386, doi:10.1038/nature25486 (2018).

57 Mukhopadhyay, A., Barbieri, A. M., Funato, K., Roberts, R. & Stahl, P. D. Sequential actions of Rab5 and Rab7 regulate endocytosis in the Xenopus oocyte. *J Cell Biol* **136**, 1227-1237, doi:10.1083/jcb.136.6.1227 (1997).

58 Wong, Y. C., Peng, W. & Krainc, D. Lysosomal Regulation of Inter-mitochondrial Contact Fate and Motility in Charcot-Marie-Tooth Type 2. *Dev Cell* **50**, 339-354 e334, doi:10.1016/j.devcel.2019.05.033 (2019).

59 Wang, Y., Xu, E., Musich, P. R. & Lin, F. Mitochondrial dysfunction in neurodegenerative diseases and the potential countermeasure. *CNS Neurosci Ther* **25**, 816-824, doi:10.1111/cns.13116 (2019).

60 Foliaki, S. T. *et al.* Altered energy metabolism in Fatal Familial Insomnia cerebral organoids is associated with astrogliosis and neuronal dysfunction. *PLoS Genet* **19**, e1010565, doi:10.1371/journal.pgen.1010565 (2023).

61 Wood, A. R. *et al.* Hereditary E200K mutation within the prion protein gene alters human iPSC derived cardiomyocyte function. *Sci Rep* **12**, 15788, doi:10.1038/s41598-022-19631-5 (2022).

62 Kim, M. J. *et al.* Impairment of Neuronal Mitochondrial Quality Control in Prion-Induced Neurodegeneration. *Cells* **11**, doi:10.3390/cells11172744 (2022).

63 Brunet, M. A. *et al.* The FUS gene is dual-coding with both proteins contributing to FUS-mediated toxicity. *EMBO Rep* **22**, e50640, doi:10.15252/embr.202050640 (2021).

64 Lin, M. Y. *et al.* Releasing Syntaphilin Removes Stressed Mitochondria from Axons Independent of Mitophagy under Pathophysiological Conditions. *Neuron* **94**, 595-610 e596, doi:10.1016/j.neuron.2017.04.004 (2017).

65 Sgro, A. E., Bajjalieh, S. M. & Chiu, D. T. Single-axonal organelle analysis method reveals new protein-motor associations. *ACS Chem Neurosci* **4**, 277-284, doi:10.1021/cn300136y (2013).

66 Lo, K. Y., Kuzmin, A., Unger, S. M., Petersen, J. D. & Silverman, M. A. KIF1A is the primary anterograde motor protein required for the axonal transport of dense-core vesicles in cultured hippocampal neurons. *Neurosci Lett* **491**, 168-173, doi:10.1016/j.neulet.2011.01.018 (2011).

67 Hall, D. H. & Hedgecock, E. M. Kinesin-related gene unc-104 is required for axonal transport of synaptic vesicles in C. elegans. *Cell* **65**, 837-847, doi:10.1016/0092-8674(91)90391-b (1991).

bioRxiv preprint doi: https://doi.org/10.1101/2023.03.19.533383; this version posted March 21, 2023. The copyright holder for this preprint (which was not certified by peer review) is the author/funder. All rights reserved. No reuse allowed without permission.

68 Balabanian, L., Berger, C. L. & Hendricks, A. G. Acetylated Microtubules Are Preferentially Bundled Leading to Enhanced Kinesin-1 Motility. *Biophys J* **113**, 1551-1560, doi:10.1016/j.bpj.2017.08.009 (2017).

69 Campbell, G. E. *Kinesin-1 and Kinesin-3 Coordinate the Transport of Synaptic Vesicle Precursors in Mammalian Axons*, The Scripps Research Institute, (2018).

70 Ally, S., Larson, A. G., Barlan, K., Rice, S. E. & Gelfand, V. I. Opposite-polarity motors activate one another to trigger cargo transport in live cells. *J Cell Biol* **187**, 1071-1082, doi:10.1083/jcb.200908075 (2009).

71 Fenton, A. R., Jongens, T. A. & Holzbaur, E. L. F. Mitochondrial adaptor TRAK2 activates and functionally links opposing kinesin and dynein motors. *Nat Commun* **12**, 4578, doi:10.1038/s41467-021-24862-7 (2021).

72 Pilling, A. D., Horiuchi, D., Lively, C. M. & Saxton, W. M. Kinesin-1 and Dynein are the primary motors for fast transport of mitochondria in Drosophila motor axons. *Mol Biol Cell* **17**, 2057-2068, doi:10.1091/mbc.e05-06-0526 (2006).

73 McKenney, R. J., Huynh, W., Vale, R. D. & Sirajuddin, M. Tyrosination of alpha-tubulin controls the initiation of processive dynein-dynactin motility. *EMBO J* **35**, 1175-1185, doi:10.15252/embj.201593071 (2016).

74 Can, S., Dewitt, M. A. & Yildiz, A. Bidirectional helical motility of cytoplasmic dynein around microtubules. *Elife* **3**, e03205, doi:10.7554/eLife.03205 (2014).

75 Ferro, L. S., Can, S., Turner, M. A., ElShenawy, M. M. & Yildiz, A. Kinesin and dynein use distinct mechanisms to bypass obstacles. *Elife* **8**, doi:10.7554/eLife.48629 (2019).

76 Ermolayev, V. *et al.* Impaired axonal transport in motor neurons correlates with clinical prion disease. *PLoS Pathog* **5**, e1000558, doi:10.1371/journal.ppat.1000558 (2009).

77 Veith, N. M., Plattner, H., Stuermer, C. A., Schulz-Schaeffer, W. J. & Burkle, A. Immunolocalisation of PrPSc in scrapie-infected N2a mouse neuroblastoma cells by light and electron microscopy. *Eur J Cell Biol* **88**, 45-63, doi:10.1016/j.ejcb.2008.08.001 (2009).

78 Arnold, J. E. *et al.* The abnormal isoform of the prion protein accumulates in late-endosome-like organelles in scrapie-infected mouse brain. *J Pathol* **176**, 403-411, doi:10.1002/path.1711760412 (1995).

79 Magalhaes, A. C. *et al.* Uptake and neuritic transport of scrapie prion protein coincident with infection of neuronal cells. *J Neurosci* **25**, 5207-5216, doi:10.1523/JNEUROSCI.0653-05.2005 (2005).

80 Daude, N., Lehmann, S. & Harris, D. A. Identification of intermediate steps in the conversion of a mutant prion protein to a scrapie-like form in cultured cells. *J Biol Chem* **272**, 11604-11612 (1997).

81 Fioriti, L. *et al.* Cytosolic prion protein (PrP) is not toxic in N2a cells and primary neurons expressing pathogenic PrP mutations. *J Biol Chem* **280**, 11320-11328, doi:10.1074/jbc.M412441200 (2005).

82 Newell, K. L. *et al.* Alpha-synuclein immunoreactivity is present in axonal swellings in neuroaxonal dystrophy and acute traumatic brain injury. *J Neuropathol Exp Neurol* **58**, 1263-1268, doi:10.1097/00005072-199912000-00007 (1999).

83 Sapp, E. *et al.* Axonal transport of N-terminal huntingtin suggests early pathology of corticostriatal projections in Huntington disease. *J Neuropathol Exp Neurol* **58**, 165-173 (1999).

bioRxiv preprint doi: https://doi.org/10.1101/2023.03.19.533383; this version posted March 21, 2023. The copyright holder for this preprint (which was not certified by peer review) is the author/funder. All rights reserved. No reuse allowed without permission.

84 Cataldo, A. M. *et al.* Abeta localization in abnormal endosomes: association with earliest Abeta elevations in AD and Down syndrome. *Neurobiol Aging* **25**, 1263-1272, doi:10.1016/j.neurobiolaging.2004.02.027 (2004).
85 Cataldo, A. M. *et al.* Endocytic pathway abnormalities precede amyloid beta deposition in sporadic Alzheimer's disease and Down syndrome: differential effects of APOE genotype and presenilin mutations. *The American journal of pathology* **157**, 277-286 (2000).
86 Wu, J. W. *et al.* Small misfolded Tau species are internalized via bulk endocytosis and anterogradely and retrogradely transported in neurons. *J Biol Chem* **288**, 1856-1870, doi:10.1074/jbc.M112.394528 (2013).
87 Xie, Y. X. *et al.* Lysosomal exocytosis releases pathogenic alpha-synuclein species from neurons in synucleinopathy models. *Nat Commun* **13**, 4918, doi:10.1038/s41467-022-32625-1 (2022).
88 Trajkovic, K., Jeong, H. & Krainc, D. Mutant Huntingtin Is Secreted via a Late Endosomal/Lysosomal Unconventional Secretory Pathway. *J Neurosci* **37**, 9000-9012, doi:10.1523/JNEUROSCI.0118-17.2017 (2017).
89 Borchelt, D. R. *et al.* A vector for expressing foreign genes in the brains and hearts of transgenic mice. *Genetic analysis : biomolecular engineering* **13**, 159-163 (1996).
90 Harms, K. J., Tovar, K. R. & Craig, A. M. Synapse-specific regulation of AMPA receptor subunit composition by activity. *J Neurosci* **25**, 6379-6388, doi:10.1523/JNEUROSCI.0302-05.2005 (2005).
91 Vande Velde, C. *et al.* Misfolded SOD1 associated with motor neuron mitochondria alters mitochondrial shape and distribution prior to clinical onset. *PLoS One* **6**, e22031, doi:10.1371/journal.pone.0022031 (2011).
92 Norris, S. R. *et al.* A method for multiprotein assembly in cells reveals independent action of kinesins in complex. *J Cell Biol* **207**, 393-406, doi:10.1083/jcb.201407086 (2014).
93 Kaech, S. & Banker, G. Culturing hippocampal neurons. *Nat Protoc* **1**, 2406-2415, doi:10.1038/nprot.2006.356 (2006).
94 Tinevez, J. Y. *et al.* TrackMate: An open and extensible platform for single-particle tracking. *Methods* **115**, 80-90, doi:10.1016/j.ymeth.2016.09.016 (2017).
95 Jaqaman, K. *et al.* Robust single-particle tracking in live-cell time-lapse sequences. *Nat Methods* **5**, 695-702, doi:10.1038/nmeth.1237 (2008).
96 Ovesny, M., Krizek, P., Borkovec, J., Svindrych, Z. & Hagen, G. M. ThunderSTORM: a comprehensive ImageJ plug-in for PALM and STORM data analysis and super-resolution imaging. *Bioinformatics* **30**, 2389-2390, doi:10.1093/bioinformatics/btu202 (2014).
97 Fernandes, M. C., Andrade, L. R., Andrews, N. W. & Mortara, R. A. Trypanosoma cruzi trypomastigotes induce cytoskeleton modifications during HeLa cell invasion. *Mem Inst Oswaldo Cruz* **106**, 1014-1016 (2011).
98 Hoffman, D. P. *et al.* Correlative three-dimensional super-resolution and block-face electron microscopy of whole vitreously frozen cells. *Science* **367**, doi:10.1126/science.aaz5357 (2020).

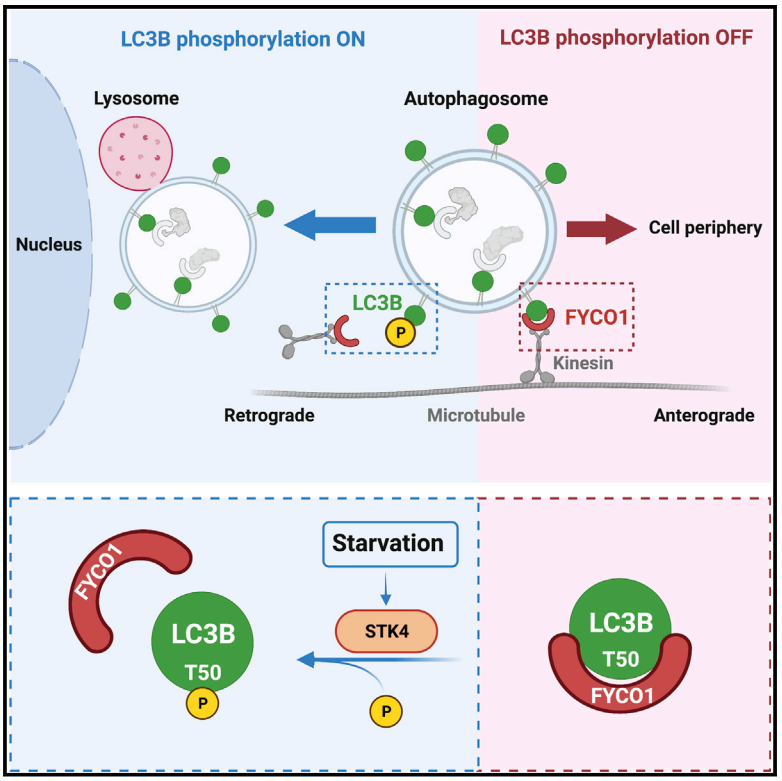
E. Nieto-Torres JL, Shanahan SL, Chassefeyre R, **Chaiamarit T,** Zaretski S, Landeras-Bueno S, Verhelle A, Encalada SE, Hansen M**. 2021. LC3 Phosphorylation Regulates FYCO1 Binding and Directional Transport of Autophagosomes.** *Current Biology* 31(15):3440-3449.e7. https://doi.org/10.1016/j.cub.2021.05.052

Report

Current Biology

LC3B phosphorylation regulates FYCO1 binding and directional transport of autophagosomes

Graphical abstract



Highlights

- STK4-mediated LC3B phosphorylation lowers LC3B binding to the transport protein FYCO1
- LC3B phosphorylation inhibition decreases retrograde transport of autophagosomes
- Block of LC3B phosphorylation also compromises autophagosome-lysosome association
- The STK4-LC3B-FYCO1 axis is a nutrient-sensitive, autophagy-regulatory pathway

Authors

Jose L. Nieto-Torres, Sean-Luc Shanahan, Romain Chassefeyre, ..., Adriaan Verhelle, Sandra E. Encalada, Malene Hansen

Correspondence

encalada@scripps.edu (S.E.E.), mhansen@sbpdiscovery.org (M.H.)

In brief

Nieto-Torres et al. describe that phosphorylation of the autophagy protein LC3B is critical for the retrograde transport of autophagosomes within cells. Block of LC3B phosphorylation leads to aberrant autophagosome transport and association with lysosomes. This pathway may be relevant for autophagy-related pathologies, such as neurodegeneration.

Nieto-Torres et al., 2021, Current Biology *31*, 3440–3449
August 9, 2021 © 2021 Elsevier Inc.
https://doi.org/10.1016/j.cub.2021.05.052

CellPress

CellPress

Current Biology

Report

LC3B phosphorylation regulates FYCO1 binding and directional transport of autophagosomes

Jose L. Nieto-Torres,[1,4] Sean-Luc Shanahan,[1,4,5] Romain Chassefeyre,[2,6] Tai Chaiamarit,[2,7] Sviatlana Zaretski,[1] Sara Landeras-Bueno,[3,8] Adriaan Verhelle,[2] Sandra E. Encalada,[2,*] and Malene Hansen[1,9,*]

[1]Program of Development, Aging and Regeneration, Sanford Burnham Prebys Medical Discovery Institute, La Jolla, CA 92037, USA
[2]Department of Molecular Medicine, Dorris Neuroscience Center, The Scripps Research Institute, La Jolla, CA 92037, USA
[3]Department of Immunology, The Scripps Research Institute, La Jolla, CA 92037, USA
[4]These authors contributed equally
[5]Present address: Massachusetts Institute of Technology, Cambridge, MA 02139, USA
[6]Present address: Evotec, Toulouse 31100, France
[7]Present address: University of Oxford, Oxford OX1 3QU, UK
[8]Present address: La Jolla Institute for Immunology, La Jolla, CA 92037, USA
[9]Lead contact
*Correspondence: encalada@scripps.edu (S.E.E.), mhansen@sbpdiscovery.org (M.H.)
https://doi.org/10.1016/j.cub.2021.05.052

SUMMARY

Macroautophagy (hereafter referred to as autophagy) is a conserved process that promotes cellular homeostasis through the degradation of cytosolic components, also known as cargo. During autophagy, cargo is sequestered into double-membrane vesicles called autophagosomes, which are predominantly transported in the retrograde direction to the perinuclear region to fuse with lysosomes, thus ensuring cargo degradation.[1] The mechanisms regulating directional autophagosomal transport remain unclear. The ATG8 family of proteins associates with autophagosome membranes[2] and plays key roles in autophagy, including the movement of autophagosomes. This is achieved via the association of ATG8 with adaptor proteins like FYCO1, involved in the anterograde transport of autophagosomes toward the cell periphery.[1,3–5] We previously reported that phosphorylation of LC3B/ATG8 on threonine 50 (LC3B-T50) by the Hippo kinase STK4/MST1 is required for autophagy through unknown mechanisms.[6] Here, we show that STK4-mediated phosphorylation of LC3B-T50 reduces the binding of FYCO1 to LC3B. In turn, impairment of LC3B-T50 phosphorylation decreases starvation-induced perinuclear positioning of autophagosomes as well as their colocalization with lysosomes. Moreover, a significantly higher number of LC3B-T50A-positive autophagosomes undergo aberrant anterograde movement to axonal tips in mammalian neurons and toward the periphery of mammalian cells. Our data support a role of a nutrient-sensitive STK4-LC3B-FYCO1 axis in the regulation of the directional transport of autophagosomes, a key step of the autophagy process, via the post-translational modification of LC3B.

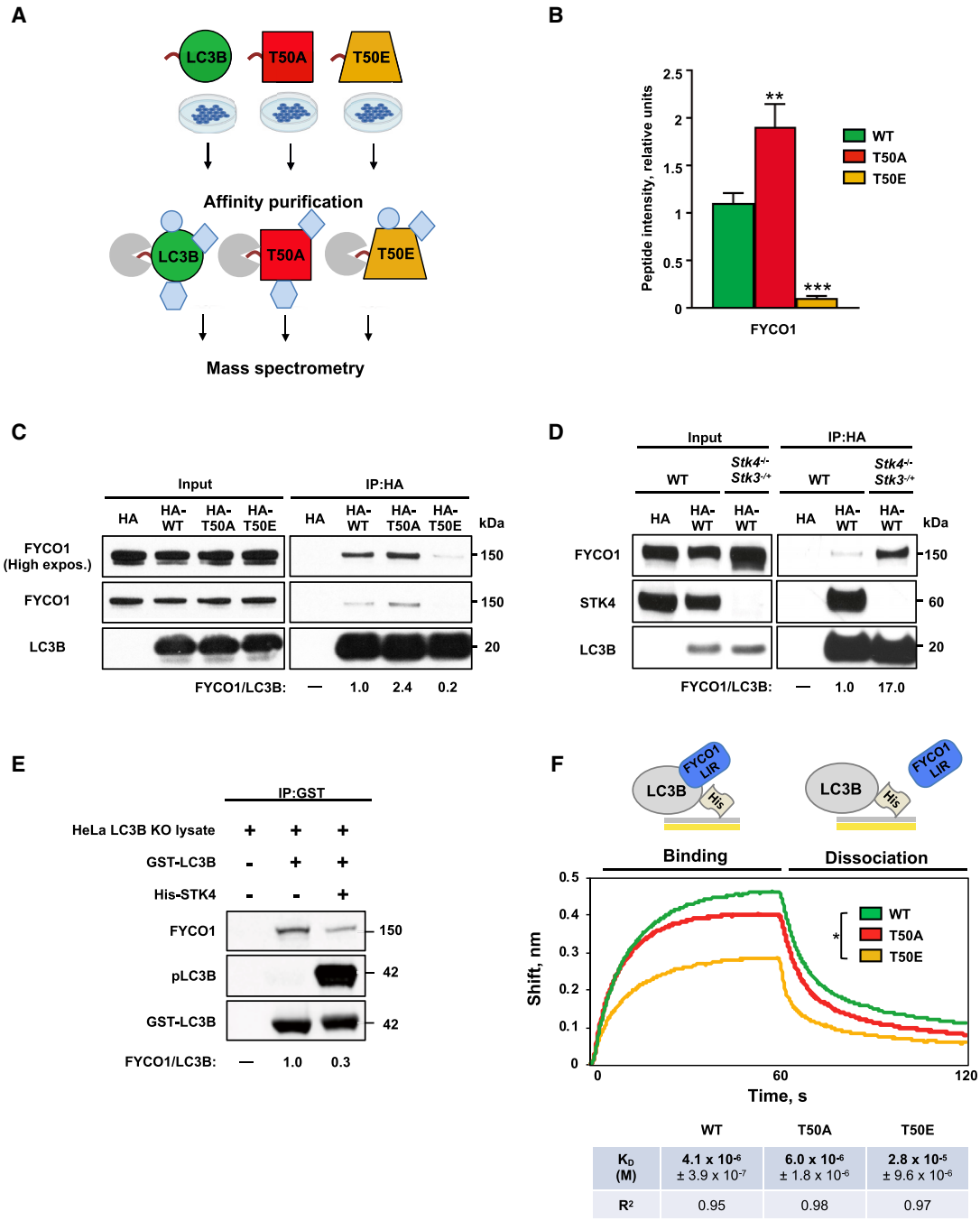
RESULTS

LC3B-T50 phosphorylation regulates the interaction between LC3B and FYCO1

We recently reported that phosphorylation of LC3B-T50 by STK4/MST1 is required for autophagy.[6] Specifically, depletion of *Stk4* or expression of a non-phosphorylatable LC3B-T50A mutant causes accumulation of autophagosomes throughout the cell and clustering of lysosomes around the nucleus, leading to a block in autophagy in mouse embryonic fibroblasts (MEFs) and in C2C12 mouse myoblasts.[6] We hypothesized that phosphorylation of LC3B might modulate its interaction with autophagy adaptor proteins that bind LC3B and other ATG8 proteins on the outer surface of autophagosomes. To test this, we identified LC3B binding partners via affinity purification of HA-tagged LC3B proteins followed by mass spectrometry from human 293T cells transiently expressing HA-tagged wild-type (WT) LC3B or the phospho-mutant forms LC3B-T50A (T50A, phospho-deficient) and LC3B-T50E (T50E, phospho-mimetic) (Figure 1A; Data S1). Of the LC3B interactors identified, FYCO1, a known autophagy adaptor protein,[3,4] showed the most HA-LC3B-T50 phosphorylation-sensitive binding; specifically, FYCO1 binding was ~2-fold higher to the HA-T50A mutant and ~5-fold lower to the HA-T50E mutant compared with binding to HA-LC3B-WT (Figure 1B; Data S1).

These results were validated in LC3B knockout (LC3B-KO) HeLa cells, which we generated using CRISPR-Cas9 technology and expressing HA-tagged-LC3B-WT, -T50A, or -T50E (Figure S1A). The HeLa LC3B-KO cell line background was used throughout the rest of the study unless otherwise indicated. Consistent with earlier reports in MEFs,[6] HA-T50A phospho-mutant showed similar phenotypes, displayed increased numbers of autophagosomes that

 © 2021 Elsevier Inc.



	WT	T50A	T50E
K_D (M)	4.1 x 10^{-6} ± 3.9 x 10^{-7}	6.0 x 10^{-6} ± 1.8 x 10^{-6}	2.8 x 10^{-5} ± 9.6 x 10^{-6}
R^2	0.95	0.98	0.97

Figure 1. LC3B phosphorylation modulates FYCO1-LC3B interactions

(A) Schematic of pull-down assays performed in HEK293T cells expressing HA-tagged WT (wild-type), T50A (phospho-deficient mutant), and T50E (phospho-mimetic mutant) LC3B proteins to identify LC3B phosphorylation-dependent interactors by mass spectrometry. See Data S1 for full dataset.

(B) Quantification of FYCO1 binding to HA-LC3B proteins determined by mass spectrometry. Mean ± SD of three technical replicates. **p < 0.0021, ***p < 0.0002, ****p < 0.0001 by one-way ANOVA. See also Data S1.

(C) Representative western blot of FYCO1 co-immunoprecipitated with HA-tagged LC3B proteins expressed in HeLa LC3B-KO cells (n = 3). See also Figures S2A, S2B, and S3G.

(D) Representative western blot of FYCO1 co-immunoprecipitated with HA-tagged LC3B proteins in *Stk4*$^{-/-}$;*Stk3*$^{-/+}$ and WT mouse embryonic fibroblasts (n = 3).

(E) Representative western blot of FYCO1 co-immunoprecipitated with non-phosphorylated or *in vitro*-phosphorylated GST-LC3B (n = 3). The GST-LC3B panel shows Coomassie staining in black pseudo color. See also Figures S2C and S2D.

(C–E) Values below blots are protein ratios in relative units.

(F) Biolayer interferometry assay of His-tagged LC3B proteins binding to a peptide containing FYCO1-LIR and adjacent amino acids.[4] Mean K_D ± SEM of three technical replicates and R^2 for binding curve fit are shown. *p < 0.05 by one-way ANOVA. See Data S1 for quantification of all western blots.

were insensitive to the autophagy inhibitor Bafilomycin A (Baf A), and exhibited LAMP1-positive vesicles that clustered in perinuclear regions (Figures S1B–S1D). Immunoprecipitation of HA-LC3B (Figure 1C) or mCherry (mCh)-FYCO1 (Figure S2A) followed by western blotting for the reciprocal protein confirmed the differential interaction of FYCO1 with HA-LC3B phospho-mutants. Likewise, FYCO1-HA-LC3B binding was increased in *Stk4*$^{-/-}$;*Stk3*$^{-/+}$ MEFs[6] (Figure 1D). Finally, *in vitro* phosphorylation of GST-LC3B on T50, verified with a phosphorylation-specific antibody,[6] reduced the GST-LC3B interaction with FYCO1 compared to non-phosphorylated GST-LC3B (Figure 1E). Notably, the LC3B phosphorylation-dependent binding profile of FYCO1 to LC3B (i.e., increased binding to HA-T50A, decreased binding to HA-T50E, as well as decreased binding to GST-pLC3B) was specific for FYCO1 since other known LC3B interactors KEAP1 and p62 bound to LC3B independently of T50 status (Figures S2B–S2D and S3G; Data S1), whereas NDP52 showed increased binding to HA-T50A and increased but variable binding to HA-T50E (Figures S2B and S3G). Collectively, these data indicate that STK4-mediated phosphorylation of LC3B decreases its interaction with FYCO1, suggesting a role for FYCO1 in STK4-LC3B-mediated autophagy regulation.

LC3B is known to directly interact with FYCO1 through an extended LC3-interacting region (LIR), which contains a core LIR and several adjacent amino acids.[3,4] Within the LC3B-FYCO1 binding interface, amino acid T50 of LC3B is located in close proximity to two aspartic acid residues preceding the core FYCO1 LIR (Figure S2E). We, therefore, speculated that LC3B-T50 phosphorylation may directly affect FYCO1-LC3B binding via disruption of the binding interface. To test this, we performed biolayer interferometry to measure the binding affinities between His-LC3B-WT or phospho-mutants (bacterially expressed and purified) and a FYCO1 33 amino-acid peptide (amino acids 1265–1298) spanning the LIR domain and its adjacent aspartic acids.[4] The binding affinity of His-LC3B-WT and the FYCO1 peptide was in the micromolar range (K_D ~4.1 × 10^{-6} M) (Figure 1F), similar to previous reports.[7] In contrast, the binding affinity between the FYCO1 peptide and phosphomimetic His-T50E was significantly lower (K_D ~2.8 × 10^{-5} M) than that of His-LC3B-WT (Figure 1F), suggesting that T50 phosphorylation may play a role in blocking the direct interaction between LC3B and the FYCO1-LIR region. Of note, His-T50A bound to the FYCO1 peptide with an affinity (K_D ~6.0 × 10^{-6} M) in the same micromolar range as His-LC3B-WT (Figure 1F). The similar binding affinities displayed by His-LC3B-WT and the His-T50A phospho-null mutant could stem from the lack of STK4-dependent phosphorylation of the bacteria-derived LC3B proteins used for the binding experiments, as STK4 is not expressed in bacteria.[8] Thus, the affinity binding data and the co-immunoprecipitation results suggest that phosphorylation of LC3B-T50 directly decreases the LC3B binding affinity for FYCO1, revealing that phosphorylation of LC3B regulates the interaction between LC3B and FYCO1 and decreases LC3B-FYCO1 binding affinity.

Subcellular localization of autophagosomes is regulated by LC3B-T50 phosphorylation in a FYCO1-dependent manner

As FYCO1 associates with LC3B on autophagosomes to regulate their transport,[3,4] we next asked whether LC3B-T50 phosphorylation status would affect FYCO1 localization to autophagosomes. LC3B is attached to autophagosomal membranes via lipidation of a C-terminal glycine.[9] Autophagosomes were defined as HA-LC3B-positive puncta, since lipidation-deficient versions (i.e., G120A) of WT and phospho-mutant LC3Bs cannot associate with autophagosome membranes[2] and, as expected, were diffusely localized (Figure S2F). The G120A versions of WT and phospho-mutant HA-LC3Bs maintained their differential binding to FYCO1 (Figure S2G), suggesting that LC3B lipidation and, by extension, autophagosomal membrane association may not be essential for LC3B phosphorylation to regulate LC3B-FYCO1 binding. Notably, the HA-LC3B colocalization with FYCO1 was much higher in HA-T50A, and lower in HA-T50E, as compared to those in HA-LC3B-WT-expressing cells (Figures 2A and 2B), indicating that LC3B-T50 phosphorylation decreases, whereas de-phosphorylation increases, the association of FYCO1 with autophagosomes, consistent with the LC3B-FYCO1 interaction and binding-affinity data (Figure 1). Unlike FYCO1, p62, KEAP1, and NDP52 showed only slightly increased colocalization to HA-T50A compared to HA-LC3B, and none of these three control LC3B interactors displayed decreased colocalization to HA-T50E as observed for FYCO1 (Figure S2H), further supporting the notion that LC3B phosphorylation may affect FYCO1 binding in a specific manner.

As FYCO1 regulates anterograde transport of autophagosomes,[3] we next asked whether the LC3B phosphorylation-dependent association with FYCO1 affected the subcellular positioning of autophagosomes. Immunofluorescence microscopy and imaging analysis revealed that the average distance between LC3B-positive puncta and the nucleus was significantly shorter in HA-T50E-expressing cells (~4.0 μm) than in cells expressing HA-LC3B-WT (~8.8 μm), whereas HA-T50A showed a longer average distance (~11.6 μm) (Figures 2C, 2D, and S3A). Notably, the dispersal of LC3B puncta to the cell periphery in HA-WT and HA-T50A-expressing cells was FYCO1 dependent, as small interfering RNA (siRNA)-mediated FYCO1 knockdown (Figure S2I) resulted in perinuclear accumulation of HA-LC3B puncta (Figures 2C, 2D, and S3A). These results show that the subcellular localization of LC3B puncta is regulated by LC3B phosphorylation in a FYCO1-dependent manner.

Starvation-induced perinuclear clustering of autophagosomes is regulated via an STK4-LC3B-FYCO1 axis

Starvation is a robust inducer of autophagy and is known to stimulate the perinuclear positioning of autophagosomes to promote fusion with lysosomes.[10] We investigated the effects of starvation on STK4-LC3B-FYCO1-mediated control of autophagosomal localization. Combined serum and amino-acid deprivation of HeLa cells resulted in an ~3-fold increase in the levels of phosphorylated (active) STK4 (STK4-pT183)[11] (Figure 3A), consistent with previous findings that the Hippo pathway is activated following serum deprivation.[12] In turn, siRNA-mediated depletion of STK4 (Figure S3B) prevented starvation-induced perinuclear clustering of LC3B-positive puncta in HA-LC3B-WT-expressing cells (Figures 3B, 3C, and S3C), suggesting that STK4-dependent phosphorylation of LC3B is required for starvation-induced perinuclear autophagosome positioning. Consistent with these results, starvation did not change the

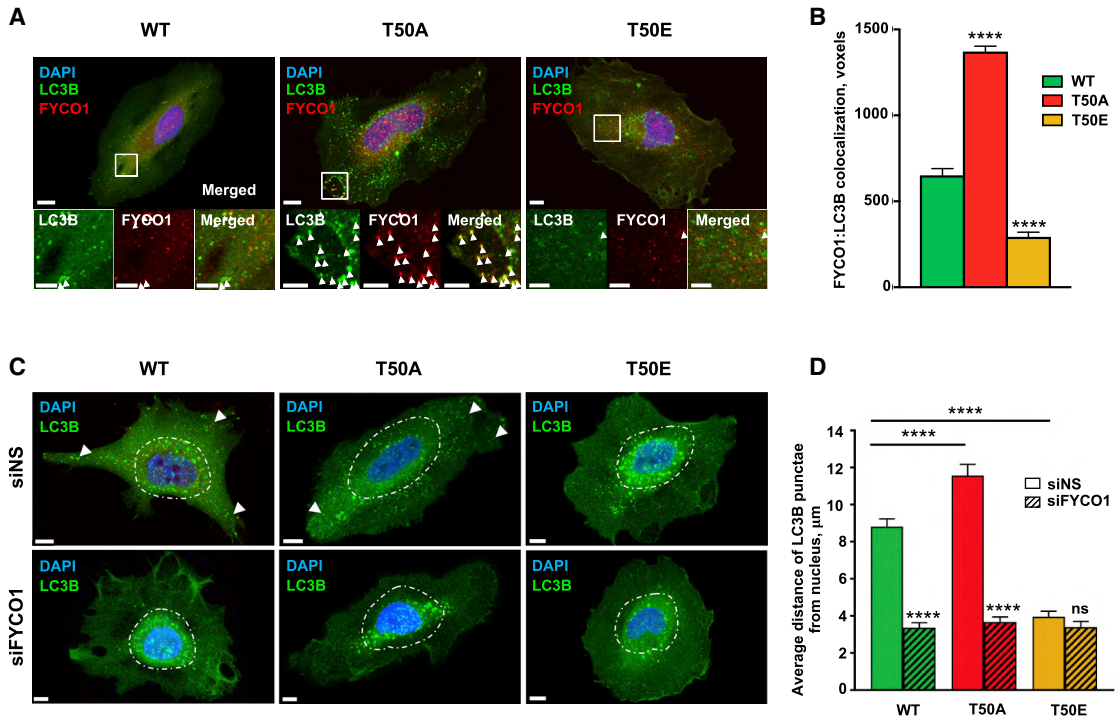


Figure 2. Subcellular localization of LC3B phospho-mutants is differentially regulated by FYCO1

(A) Representative immunofluorescence micrographs of HeLa-KO cells expressing HA-tagged LC3B-WT, T50A, or T50E co-stained for FYCO1. White arrowheads indicate LC3B:FYCO1 colocalization spots.

(B) Quantification of HA-LC3B:FYCO1 colocalized voxels (volumetric pixels). Mean ± SEM, ****$p < 0.0001$ by two-way ANOVA (n = 17–27 cells from three experiments). See also Figure S2H.

(C) Representative immunofluorescence micrographs of HA-tagged LC3B-WT, T50A, or T50E puncta in control (siNS) or siFYCO1-treated HeLa cells. The dashed line defines 10 μm from the outer nuclear edge. Scale bar, 10 μm. White arrowheads point to HA-LC3B-positive puncta in peripheral locations of the cell.

(D) Average distance between HA-LC3B-positive puncta and the nucleus. Mean ± SEM of n = 25–39 cells from three experiments. ****$p < 0.0001$ by two-way ANOVA. See also Figure S3A.

dispersed or perinuclear subcellular localization of LC3B-positive puncta in HA-T50A or HA-T50E cells, respectively (Figures 3D, 3E, and S3D). Thus, starvation induced STK4-mediated LC3B phosphorylation-dependent positioning of autophagosomes to the perinuclear region of mammalian cells. Because starvation-induced perinuclear positioning of autophagosomes promotes autophagosome-lysosome fusion,[13] we quantitated colocalization between HA-LC3B-WT or -LC3B phospho-mutants with either endolysosomal LAMP1 and lysosomal LAMP2 markers,[14] following starvation. Consistent with our previous observations in *Stk4*$^{-/-}$;*Stk3*$^{-/+}$ MEFs,[6] we observed that the starvation-induced increase in LAMP1/2 colocalization with HA-LC3B-WT was LC3B phosphorylation-dependent. Specifically, HA-T50A-LAMP1/2 colocalization was not induced by nutrient deprivation, whereas HA-T50E-LAMP1/2 colocalization was elevated compared to HA-WT in a starvation-independent manner (Figures 3F, 3G, and S3E). These results indicate that LC3B phosphorylation can promote the association of autophagosomes with lysosomes.

Finally, we hypothesized that the starvation-induced perinuclear vesicle-positioning originated from a decrease in LC3B-FYCO1 binding. To test this directly, we performed co-immunoprecipitation experiments and immunofluorescence microscopy of HeLa LC3B-KO cells expressing HA-LC3B-WT or phospho-mutants grown under normal or starvation conditions to determine the degree of LC3B-FYCO1 association. In HA-LC3B-WT-expressing cells, starvation caused an ~50% reduction in the levels of FYCO1 protein that co-immunoprecipitated with HA-LC3B (Figure 3H), as well as a >50% decrease in the percentage of HA-LC3B-positive puncta colocalizing with FYCO1 (Figure 3I). In contrast, starvation of cells expressing HA-T50A or HA-T50E only slightly reduced (~15%) the interaction between FYCO1 and either HA-LC3B phospho-mutant (Figure 3H) and had no significant effect on the colocalization of FYCO1 with HA-LC3B phospho-mutant-positive puncta (Figure 3I). Thus, starvation decreased the association between LC3B and FYCO1 in an LC3B-phosphorylation-dependent manner. In contrast, starvation strongly decreased both the binding and colocalization of KEAP1 and NDP52 to HA-LC3B-WT, HA-T50A, or HA-T50E (Figure S2H, S3F, and S3G), whereas the effect of starvation on the association of p62 to the LC3B phospho-mutants was relatively modest with p62 binding largely unaffected (Figures S3F and S3G) and a general small decrease in colocalization (Figure S2H; see figure legend for further discussion). Overall, our results indicate that nutrient deprivation regulates an STK4-LC3B-FYCO1 axis to control the subcellular positioning of autophagosomes in the perinuclear area of the cell, promoting the colocalization of autophagosomes with lysosomes.

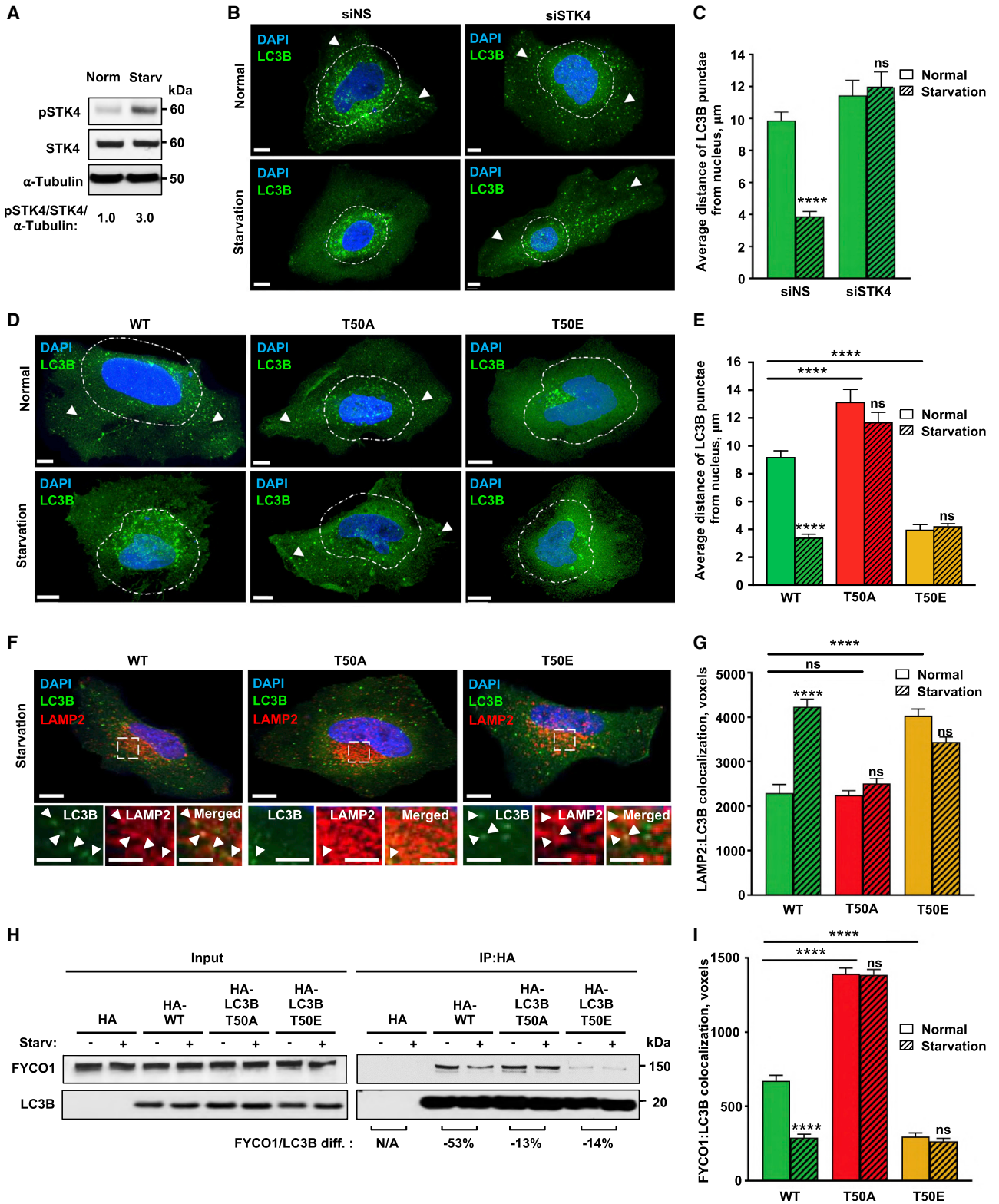


Figure 3. Starvation induces perinuclear localization of LC3B puncta in an LC3B phosphorylation- and FYCO1-dependent manner

(A) Representative western blot of total and phosphorylated STK4-T183 in HeLa LC3B-KO cells incubated in normal or starvation medium (n = 3). Values indicate pSTK4:STK4 protein ratio normalized to α-tubulin.

(B) Representative immunofluorescence micrographs of HA-LC3B puncta in HeLa LC3B-KO cells expressing control or STK4-targeting siRNA before or 1 h after incubation in starvation medium. Scale bar, 10 μm. White arrowheads point to HA-LC3B-positive puncta in peripheral locations of the cell.

(legend continued on next page)

LC3B phosphorylation regulates the directional transport of autophagosomes in mammalian cells and neurons

Previous work indicated that FYCO1 promotes the anterograde transport of autophagosomes and endosomes via its interaction with LC3B and the motor protein kinesin-1.[3,15] Because LC3B-T50 phosphorylation regulated both LC3B binding to FYCO1 (Figure 1), as well as autophagosome positioning (Figure 2), we next investigated whether LC3B-T50 phosphorylation plays a role in autophagosomal transport. By using super-resolution live-cell imaging in HeLa LC3B-KO cells, we found in two separate replicates that the majority of GFP-LC3B WT particles, representing autophagosomal vesicles, moved primarily in the retrograde direction toward the perinuclear region (Figures S4A and S4B; Video S1), consistent with previous reports.[16,17] In contrast, GFP-T50A particles were mainly transported in an anterograde direction toward the cell periphery (Figures S4A and S4B; Video S1). While the directional distribution of GFP-T50E particles was not significantly different from that of GFP-LC3B-WT (Figures S4A and S4B; Video S1), T50E particles displayed significant switches in directionality compared to GFP-LC3B WT or GFP-T50A particles, suggesting impaired coordination between anterograde and retrograde motors associated to those vesicles (Figure S4C; Video S1). These data suggest that phosphorylation of LC3B is important for directional retrograde transport of autophagosomes, and perinuclear positioning.

To further investigate the directionality of movement, we also evaluated the role of LC3B phosphorylation on autophagosome transport in axons of polarized cultured primary hippocampal neurons (Figure 4A). In axons, kinesin and dynein translocate cargoes in anterograde (toward the synapse) and retrograde (toward the soma) directions, respectively.[18] Previous studies showed that autophagosomes form in distal axonal regions and are transported retrogradely toward the soma, where they fuse with lysosomes to drive degradation.[18–20] Consistent with previous reports,[18,19] our single-particle live imaging and quantitative analysis[21] showed that the majority (~80%) of GFP-LC3B WT particles moved primarily in the retrograde direction (Figures 4B and 4C; Video S2), and these particles spent most (~60%) of time moving in this direction, i.e., toward the soma (Figure 4D). In contrast, quantitative analysis of the movement of GFP-T50A particles indicated an overall attenuation of retrograde transport parameters (i.e., mobile segments, time in motion, and density of particles; Figures 4B–4E; Video S2), with a corresponding increase in their anterograde movement dynamics: only ~60% of GFP-T50A particles moved in the retrograde direction, at the expense of a significant increase in the number of anterograde-moving GFP-T50A particles (~40%) (Figures 4B and 4C; Video S2), and their time spent moving toward the soma was significantly decreased to ~40%, while spending more time moving in the anterograde direction (Figure 4D; Video S2). Furthermore, GFP-T50A particles displayed significantly decreased retrograde flux (Figure 4F), a measure of retrograde traffic of GFP-T50A particles toward the soma, as calculated by the rate of movement as particles move through a randomly assigned gate at a single point in time (STAR Methods). Additional quantitative analysis showed that retrograde run lengths of GFP-T50A particles were significantly reduced, while anterograde run lengths were enhanced (Figure 4G; Video S2), consistent with overall impairments to the retrograde movement dynamics of GFP-T50A particles. Interestingly, the anterograde segmental velocities of GFP-T50A particles were also significantly increased, although our analysis did not reveal significant retrograde velocity changes (Figure S4D). Notably, more GFP-T50A particles were stationary compared to GFP-LC3B WT particles (Figure 4E), suggesting that, in addition to an overall change in retrograde movement and enhanced anterograde transport dynamics, LC3B phosphorylation is required for the proper activation of autophagosome motility.

To determine whether the aberrant enhanced anterograde transport of GFP-T50A particles was dependent on FYCO1, transport was quantitated in neurons where *Fyco1* function was downregulated using shRNAs. Live imaging revealed that compared to scrambled shRNA controls, the amount of time GFP-T50A particles spent moving in the anterograde direction was decreased to levels similar to that of GFP-LC3B WT particles (Figure 4H). Moreover, the density of anterograde moving as well as reversing GFP-T50A particles was significantly reduced in shRNA *Fyco1* axons, while that of GFP-LC3B WT particles remained unchanged (Figure S4F). These data indicate that LC3B phosphorylation is critical for the proper retrograde movement of autophagosomes and suggest that its absence attenuates retrograde movement and enhances anterograde transport in mammalian axons via interactions with FYCO1.

Finally, we analyzed the transport of GFP-T50E particles, which also displayed transport dynamics phenotypes, including a lower percentage of retrograde-moving particles, and significantly reduced retrograde run lengths compared to GFP-LC3B WT particles (Figures 4B, 4C, and 4G; Video S2). In addition, GFP-T50E

(C) Quantification of distance between LC3B puncta and the nucleus. Mean ± SEM of n = 18–23 cells from three experiments. ***p < 0.0002 by two-way ANOVA. See also Figure S3B.

(D and E) Representative immunofluorescence micrographs (D) and quantification of distance from the nucleus (E) of LC3B puncta in HeLa cells expressing the indicated HA-tagged LC3B proteins. Scale bar, 10 μm. White arrowheads point to HA-LC3B-positive puncta in peripheral locations of the cell. Mean ± SEM of n = 23–43 cells from three experiments. ****p < 0.0001 by two-way ANOVA. See also Figure S3D.

(F) Representative immunofluorescence micrographs of HeLa-KO cells expressing HA-tagged LC3B-WT, T50A, or T50E co-stained with antibodies against HA and LAMP2. Dotted insets are enlarged in bottom panels. Scale bars, 10 μm. White arrowheads point to HA-LC3B:LAMP1 colocalization events.

(G) HA-LC3B-LAMP2 colocalized voxels. Mean ± SEM of n = 30 cells from three experiments, *p < 0.0332, ***p < 0.0002, ****p < 0.0001 by two-way ANOVA. See also Figure S3E.

(H) Representative western blot of FYCO1 co-immunoprecipitated with HA-tagged LC3B proteins expressed in HeLa LC3B-KO cells before and 1 h after incubation in normal or starvation medium. Values under blots indicate percentage of decrease in HA-LC3B:FYCO1 protein ratio after starvation (n = 5). See also Figures S3F and S3G.

(I) HA-LC3B:FYCO1 colocalized voxels in HeLa LC3B-KO cells before or 1 h after incubation in starvation medium. Mean ± SEM of n = 18–30 cells from three experiments. ****p < 0.0001 by two-way ANOVA.

See also Figure S2H. See Data S1 for quantification of all western blots.

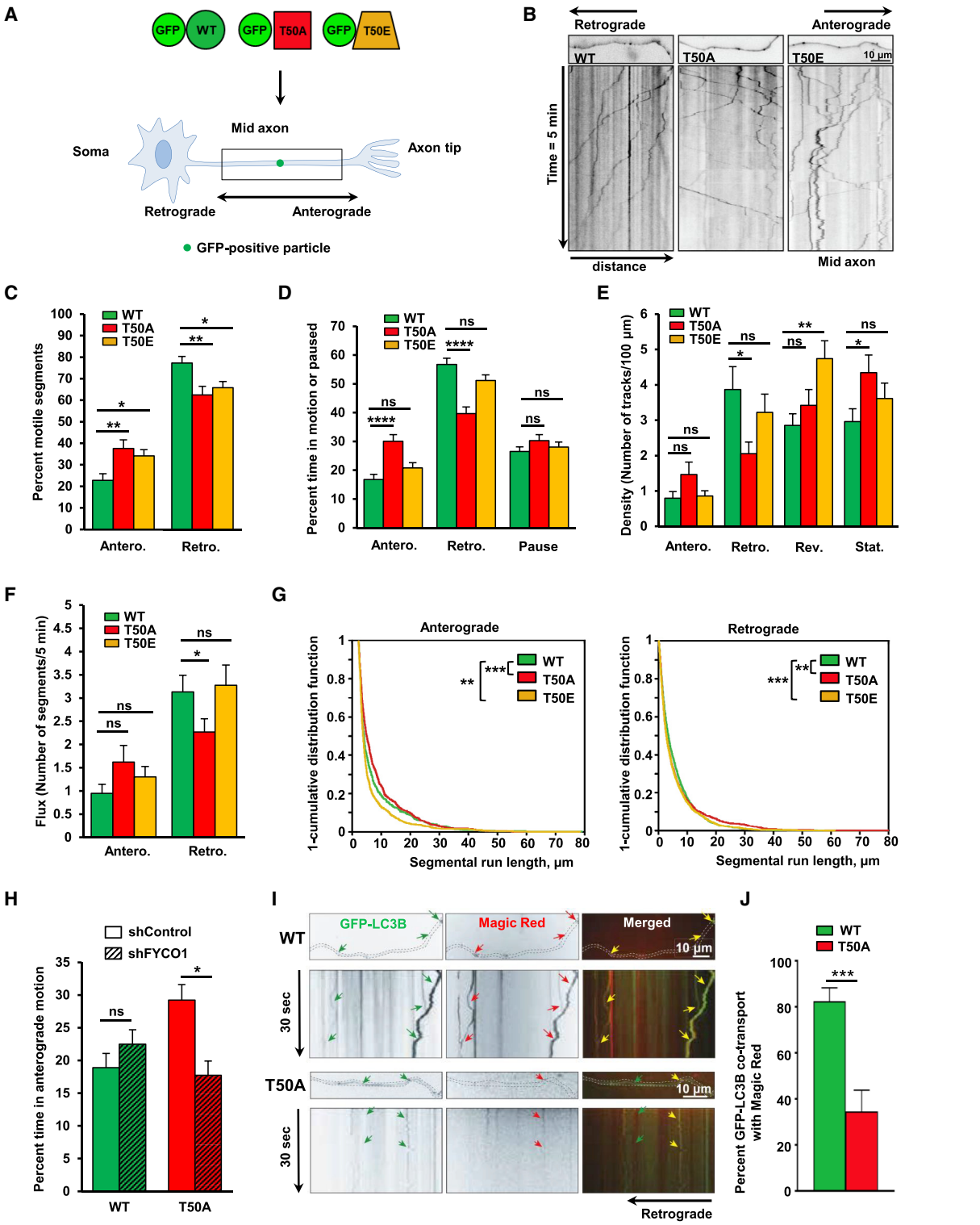


Figure 4. Directional transport of LC3B puncta is regulated by the LC3B phosphorylation

(A) Schematic illustration of experimental setup using primary mouse hippocampal neurons. Black box highlights the area of the cells imaged. Directional anterograde or retrograde movement of GFP-LC3B-positive particles is depicted.

(B) Representative images of primary mouse hippocampal neurons axons (first frame pictures) and kymographs of the indicated GFP-LC3B-positive particles (pseudo-black lines).

(legend continued on next page)

CellPress

particles showed significant impairments in anterograde run lengths and velocities (Figures 4G and S4D), and a significantly higher frequency of directionality switches (Figure S4G; Video S2), consistent with the increased numbers of switches observed in HeLa LC3B-KO cells (Figure S4C; Video S1). Overall, these data indicate that the state of LC3B phosphorylation and FYCO1 regulate the directional transport of autophagosomes in axons and that phosphorylation is required for the proper retrograde movement of autophagosomes in mammalian axons.

Because retrograde transport of autophagosomes is critical for association with degradative lysosomes *en route* to the soma, where lysosomes are enriched and where the bulk of degradation occurs,[22,23] we tested whether LC3B phosphorylation plays a role in the fusion of autophagosomes with lysosomes. To this end, we performed live imaging in the soma and axon of GFP-LC3B WT or T50A particles with Magic Red, a fluorogenic substrate that activates upon cleavage by the active Cathepsin B acidic hydrolase.[24] In axons, we observed that the majority (>80%) of GFP-LC3B WT particles co-migrated with Magic Red positive particles compared to T50A vesicles (~40%) (Figures 4I and 4J). Furthermore, immunofluorescence analysis in the soma revealed reduced colocalization between GFP-T50A vesicles and Cathepsin B compared to GFP-LC3B WT particles (Figures S4H–S4J). Altogether, these results are consistent with our observations in HeLa LC3B-KO cells (Figures 3F, 3G, and S3E), and in *Stk4*$^{-/-}$;*Stk3*$^{-/+}$ MEFs,[6] indicating that LC3B phosphorylation regulates autophagosome transport in mammalian axons to promote the association between autophagosome and degradative lysosomes.

DISCUSSION

In this study, we demonstrated that STK4-mediated phosphorylation of the autophagy protein LC3B is critical for regulating its interaction with the adaptor protein FYCO1 and for the regulation of directional autophagosomal transport and autophagosome-lysosome association in mammalian cells. We also showed that nutrient deprivation activates the STK4-LC3B-FYCO1 regulatory axis. These findings expand our fundamental understanding of the molecular regulation of autophagy with implications for numerous autophagy-dependent processes.[25]

STK4-mediated phosphorylation of LC3B at T50 reduced binding of FYCO1 to LC3B, consistent with a previous report,[26] as well as FYCO1 localization to autophagosomes.[3,4] This post-translational regulatory mechanism appeared specific for FYCO1, as the binding/association of KEAP1, p62, or NDP52 to LC3B was not affected in the same differential manner via LC3B phosphorylation. Compatible with the role of FYCO1 in anterograde transport of intracellular vesicles including autophagosomes,[3,4,15] we showed that lack of LC3B-T50 phosphorylation resulted in enhanced anterograde transport and aberrant positioning to the cell periphery of LC3B-positive autophagosomes in primary neurons as well as in HeLa LC3B-KO cells. Consequently, our data showed a decreased association of autophagosomes with lysosomes, which ultimately may explain the defects in autophagosome-lysosome fusion and the autophagy block observed in LC3B phosphorylation-deficient cells.[6] Based on these results, we speculate that in the absence of phosphorylation at T50, a switch occurs from a retrograde-moving LC3B complex to a LC3B-FYCO1-kinesin anterograde-moving one. Previous work has shown that retrograde autophagosome movement depends on the direct interaction between LC3B and JIP1, a scaffolding protein that recruits the dynein activator dynactin to these vesicles to drive their movement toward the soma of mammalian neurons.[5,27] Thus, we posit that dephosphorylation on T50 may mediate a shift from an LC3B-JIP1-dynein to an LC3B-FYCO1-kinesin complex to promote the anterograde movement of autophagosomes, impairing the retrograde movement and their fusion with lysosomes. In turn, STK4-mediated phosphorylation of LC3B could induce FYCO1 dissociation from mature autophagosomes to allow their retrograde JIP1-dependent transport to ensure lysosomal fusion and cargo degradation. This, as well as whether LC3B phosphorylation could similarly affect the binding of JIP1 or other retrograde transport-promoting adaptors remains to be investigated.

While our studies show that phosphorylation of LC3B was critical for driving the proper retrograde transport in LC3B T50A particles, T50E-positive particles revealed an unusually high frequency of directional switches in primary neurons and in HeLa LC3B-KO cells. T50E phospho-mutation has been suggested to affect LC3B conjugation to lipids,[26] which could indirectly affect

(C) Quantification of percentage of anterograde (Antero.) versus retrograde (Retro.) motile segments of GFP-LC3B-positive particles in primary hippocampal axons. A total of 6,921 motile segments were analyzed. Mean ± SEM of n = 33–38 cells from three experiments. *p < 0.05, **p < 0.01 by one-way ANOVA and Sidak's multiple comparison correction.

(D) Quantification of percentage of time in anterograde (Antero.) or retrograde (Retro.) motion or paused of GFP-LC3B-positive particles in primary hippocampal axons. A total of 824 GFP-LC3B-positive particles from 33–38 cells were analyzed. Mean ± SEM of n = 255–292 GFP-LC3B-positive particles from three experiments. ****p < 0.0001 by one-way ANOVA and Sidak's multiple comparison correction.

(E) Densities as numbers of tracks/100 μm of GFP-LC3B-positive particles in anterograde, retrograde, reversal (Rev.) motion, or stationary (Stat.) in primary hippocampal axons. Mean ± SEM of n = 33–38 cells from three experiments. *p < 0.05, **p < 0.01, by one-way ANOVA and Sidak's multiple comparison correction.

(F) Quantification of flux as numbers of anterograde versus retrograde tracks of GFP-LC3B-positive particles that pass a gate in 5 min in primary hippocampal axons. Mean ± SEM of n = 33–38 cells from three experiments. *p < 0.05, by one-way ANOVA and Sidak's multiple comparison correction.

(G) Cumulative distribution frequency graphs of anterograde and retrograde segmental run lengths of GFP-LC3B-positive particles in primary hippocampal axons. A total of 6,974 segments were analyzed from 33–38 cells from three experiments. *p < 0.05, **p < 0.01, ***p < 0.001 by Kolmogorov-Smirnov test adjusted with Bonferroni. Similar statistically significant comparisons were obtained when analyzing the data by rank-sum test (data not shown).

(H) Proportion of time spent in anterograde transport of GFP-LC3B-positive particles in mouse primary neurons with or without *Fyco1* knockdown. A total of 765 GFP-LC3B-positive particles from 28–33 cells were analyzed. Mean ± SEM of n = 142–229 GFP-LC3B-positive particles from three experiments. *p < 0.05 by non-parametric permutation Student's t test.

(I and J) Co-transport analysis of GFP-LC3B-positive particles and Magic Red in primary hippocampal axons. Mean ± SEM of n = 14–16 axons from three independent experiments. ***p < 0.001 by Student's t test.

For all the GFP-LC3B-positive particles transport-related experiments see also Videos S1 and S2 and Figure S4.

LC3B-mediated recruitment of transport proteins to autophagosomes and ultimately the transport of these vesicles. However, in our experimental system, the T50E phospho-mutant showed proficient lipidation (Figure S1E; see figure legend for further discussion), suggesting that the observed transport phenotypes may instead be caused by an altered regulation of the transport machinery. Additional experiments will be critical to explain the directional switches produced by LC3B-T50E, as well as to identify potential LC3B-T50 phosphatase(s) and other ATG8 family members involved in autophagosomal trafficking and recruitment of essential transport machinery.

We observed that starvation-induced perinuclear positioning of autophagosomes was dependent on STK4-mediated LC3B phosphorylation. We propose that the autophagosome repositioning process is initiated by starvation-induced activation of STK4, followed by LC3B phosphorylation, dissociation of FYCO1, and inhibition of anterograde transport and/or promotion of retrograde transport. In support of this model, anterograde transport of autophagosomes has been shown to decrease in HeLa cells during starvation.[28] We note that, while the regulatory consequences of the STK4-LC3B-FYCO1 axis are evident under nutrient starvation, this axis may operate both under nutrient-rich and nutrient-deprived conditions to ultimately facilitate the retrograde transport of autophagosomes and fusion with lysosomes, as well as preventing a premature retrograde transport of autophagosomes, as explained above. Nutrient deprivation may further boost this pathway to deal with the increased autophagosome population and support the increased autophagy flux triggered under these conditions. Activation of STK4 in low nutrient conditions may concomitantly reduce cell proliferation[29] and increase autophagy in an effort to re-establish homeostasis and restore nutrient availability. To this end, the nutrient-sensing complex mTORC2 has recently been identified as a direct inhibitor of STK4 activity,[30] and it will be appealing to investigate its potential role as an upstream regulator of the STK4-LC3B-FYCO1 axis. Indeed, it will be of interest to explore the role of this STK4-LC3B-FYCO1 regulatory axis in different biological processes, including in the decline in autophagy observed during aging and in many disease states,[10,31,32] where deregulation of autophagosome transport could be a crucial factor.

STAR★METHODS

Detailed methods are provided in the online version of this paper and include the following:

- KEY RESOURCES TABLE
- RESOURCE AVAILABILITY
  - Lead contact
  - Materials availability
  - Data and code availability
- EXPERIMENTAL MODEL AND SUBJECT DETAILS
  - Mammalian cell lines
  - Mouse primary hippocampal neurons
- METHOD DETAILS
  - Plasmids and oligonucleotides
  - Generation of HeLa LC3B knockout cells
  - Gene silencing, transient transfection, and cell treatment
  - Affinity purification
  - Mass spectrometry
  - Western blot
  - *In vitro* phosphorylation of LC3B and co-immunoprecipitation of FYCO1
  - Biolayer interferometry
  - Structural representation of the LC3B–FYCO1-LIR complex
  - Fluorescence and confocal microscopy
  - Live-cell imaging in HeLa cells
  - Live-cell imaging in primary mouse hippocampal neurons
- QUANTIFICATION AND STATISTICAL ANALYSIS
  - Vesicle number and positioning quantification in HeLa cells
  - Colocalization quantification
  - Particle tracking quantification in HeLa cells
  - Particle tracking quantification in primary mouse hippocampal neurons
  - Statistical analysis

SUPPLEMENTAL INFORMATION

Supplemental information can be found online at https://doi.org/10.1016/j.cub.2021.05.052.

ACKNOWLEDGMENTS

We thank Lee R. Lee for assistance with the affinity-purification experiments, Dr. Caroline Kumsta for help with data analysis and figure preparation, members of the Hansen and Encalada labs for helpful discussions and/or critical reading of the manuscript, Drs. Tony Hunter and Jill Meisenhelder (Salk Institute) for helpful discussions, Dr. Alex Rosa Campos (Sanford Burnham Prebys Proteomics Core) for support with the mass-spectrometry analysis, Leslie Boyd (Sanford Burnham Prebys Cell Imaging Core) and Salk Institute Biophotonics Core personnel for help with image acquisition and analysis, Dr. Erica Ollmann-Saphire (La Jolla Institute for Immunology) for help with the binding-affinity assays, and Dr. Dario Alessi (University of Dundee) for providing pBABE-mCherry-FYCO1 plasmid. Graphical abstract and part of Figure 1A were created using Biorender.com. We thank Nora Lyang (Hansen Lab) for help with graphical abstract design. J.N.T. was supported by a Fundacion Ramon Areces Postdoctoral Fellowship and a K99/R00 pathway to independence NIH grant (K99AG062774), R.C. was supported by the George E. Hewitt Foundation for Medical Research, and T.C. was supported by a Royal Thai Government Scholarship from the Development and Promotion of Science and Technology Talents Project (DPST). This work was funded by the following grants to S.E.E.: R01AG049483, The Glenn Foundation for Medical Research Glenn Award for Research in Biological Mechanisms of Aging, a New Scholar in Aging Award from the Lawrence Ellison Foundation, The Baxter Family Foundation, and to M.H.: R01 GM117466.

AUTHOR CONTRIBUTIONS

Conceptualization, J.N.T., S.-L.S., and M.H.; methodology, J.N.T., S.-L.S., R.C., T.C., S.Z., S.L.-B., A.V., S.E.E., and M.H.; validation, J.N.T., S.-L.S., R.C., T.C., S.Z., S.L.-B., A.V., S.E.E., and M.H.; investigation, J.N.T., S.-L.S., R.C., T.C., S.Z., S.L.-B. and A.V.; writing – original draft, J.N.T., S.-L.S., R.C., S.L.-B., S.E.E., and M.H.; writing – review & editing, J.N.T., S.-L.S., R.C., T.C., S.Z., S.L.-B., A.V., S.E.E., and M.H.; supervision, S.E.E. and M.H.; funding acquisition, J.N.T., R.C., T.C., S.E.E., and M.H.

DECLARATION OF INTERESTS

The authors declare no competing interests.

Received: January 31, 2020
Revised: January 7, 2021
Accepted: May 25, 2021
Published: June 18, 2021

REFERENCES

1. Søreng, K., Neufeld, T.P., and Simonsen, A. (2018). Membrane trafficking in autophagy. Int. Rev. Cell Mol. Biol. *336*, 1–92.
2. Slobodkin, M.R., and Elazar, Z. (2013). The Atg8 family: multifunctional ubiquitin-like key regulators of autophagy. Essays Biochem. *55*, 51–64.
3. Pankiv, S., Alemu, E.A., Brech, A., Bruun, J.A., Lamark, T., Overvatn, A., Bjørkøy, G., and Johansen, T. (2010). FYCO1 is a Rab7 effector that binds to LC3 and PI3P to mediate microtubule plus end-directed vesicle transport. J. Cell Biol. *188*, 253–269.
4. Olsvik, H.L., Lamark, T., Takagi, K., Larsen, K.B., Evjen, G., Øvervatn, A., Mizushima, T., and Johansen, T. (2015). FYCO1 contains a C-terminally extended, LC3A/B-preferring LC3-interacting region (LIR) motif required for efficient maturation of autophagosomes during basal autophagy. J. Biol. Chem. *290*, 29361–29374.
5. Fu, M.M., and Holzbaur, E.L. (2014). Integrated regulation of motor-driven organelle transport by scaffolding proteins. Trends Cell Biol. *24*, 564–574.
6. Wilkinson, D.S., Jariwala, J.S., Anderson, E., Mitra, K., Meisenhelder, J., Chang, J.T., Ideker, T., Hunter, T., Nizet, V., Dillin, A., and Hansen, M. (2015). Phosphorylation of LC3 by the Hippo kinases STK3/STK4 is essential for autophagy. Mol. Cell *57*, 55–68.
7. Cheng, X., Wang, Y., Gong, Y., Li, F., Guo, Y., Hu, S., Liu, J., and Pan, L. (2016). Structural basis of FYCO1 and MAP1LC3A interaction reveals a novel binding mode for Atg8-family proteins. Autophagy *12*, 1330–1339.
8. Halder, G., and Johnson, R.L. (2011). Hippo signaling: growth control and beyond. Development *138*, 9–22.
9. Tanida, I., Ueno, T., and Kominami, E. (2004). Human light chain 3/MAP1LC3B is cleaved at its carboxyl-terminal Met121 to expose Gly120 for lipidation and targeting to autophagosomal membranes. J. Biol. Chem. *279*, 47704–47710.
10. Bejarano, E., Murray, J.W., Wang, X., Pampliega, O., Yin, D., Patel, B., Yuste, A., Wolkoff, A.W., and Cuervo, A.M. (2018). Defective recruitment of motor proteins to autophagic compartments contributes to autophagic failure in aging. Aging Cell *17*, e12777.
11. Galan, J.A., and Avruch, J. (2016). MST1/MST2 protein kinases: regulation and physiologic roles. Biochemistry *55*, 5507–5519.
12. Plouffe, S.W., Meng, Z., Lin, K.C., Lin, B., Hong, A.W., Chun, J.V., and Guan, K.L. (2016). Characterization of Hippo pathway components by gene inactivation. Mol. Cell *64*, 993–1008.
13. Korolchuk, V.I., Saiki, S., Lichtenberg, M., Siddiqi, F.H., Roberts, E.A., Imarisio, S., Jahreiss, L., Sarkar, S., Futter, M., Menzies, F.M., et al. (2011). Lysosomal positioning coordinates cellular nutrient responses. Nat. Cell Biol. *13*, 453–460.
14. Saftig, P., and Klumperman, J. (2009). Lysosome biogenesis and lysosomal membrane proteins: trafficking meets function. Nat. Rev. Mol. Cell Biol. *10*, 623–635.
15. Raiborg, C., Wenzel, E.M., Pedersen, N.M., Olsvik, H., Schink, K.O., Schultz, S.W., Vietri, M., Nisi, V., Bucci, C., Brech, A., et al. (2015). Repeated ER-endosome contacts promote endosome translocation and neurite outgrowth. Nature *520*, 234–238.
16. Jahreiss, L., Menzies, F.M., and Rubinsztein, D.C. (2008). The itinerary of autophagosomes: from peripheral formation to kiss-and-run fusion with lysosomes. Traffic *9*, 574–587.
17. Kimura, S., Noda, T., and Yoshimori, T. (2008). Dynein-dependent movement of autophagosomes mediates efficient encounters with lysosomes. Cell Struct. Funct. *33*, 109–122.
18. Maday, S., Wallace, K.E., and Holzbaur, E.L.F. (2012). Autophagosomes initiate distally and mature during transport toward the cell soma in primary neurons. J. Cell Biol. *196*, 407–417.
19. Maday, S., and Holzbaur, E.L.F. (2014). Autophagosome biogenesis in primary neurons follows an ordered and spatially regulated pathway. Dev. Cell *30*, 71–85.
20. Dong, A., Kulkarni, V.V., and Maday, S. (2019). Methods for imaging autophagosome dynamics in primary neurons. Methods Mol. Biol. *1880*, 243–256.
21. Neumann, S., Chassefeyre, R., Campbell, G.E., and Encalada, S.E. (2017). KymoAnalyzer: a software tool for the quantitative analysis of intracellular transport in neurons. Traffic *18*, 71–88.
22. Cabukusta, B., and Neefjes, J. (2018). Mechanisms of lysosomal positioning and movement. Traffic *19*, 761–769.
23. Kulkarni, V.V., and Maday, S. (2018). Neuronal endosomes to lysosomes: a journey to the soma. J. Cell Biol. *217*, 2977–2979.
24. Boonacker, E., and Van Noorden, C.J.F. (2001). Enzyme cytochemical techniques for metabolic mapping in living cells, with special reference to proteolysis. J. Histochem. Cytochem. *49*, 1473–1486.
25. Levine, B., and Kroemer, G. (2019). Biological functions of autophagy genes: a disease perspective. Cell *176*, 11–42.
26. Shrestha, B.K., Skytte Rasmussen, M., Abudu, Y.P., Bruun, J.A., Larsen, K.B., Alemu, E.A., Sjøttem, E., Lamark, T., and Johansen, T. (2020). NIMA-related kinase 9-mediated phosphorylation of the microtubule-associated LC3B protein at Thr-50 suppresses selective autophagy of p62/sequestosome 1. J. Biol. Chem. *295*, 1240–1260.
27. Fu, M.M., Nirschl, J.J., and Holzbaur, E.L.F. (2014). LC3 binding to the scaffolding protein JIP1 regulates processive dynein-driven transport of autophagosomes. Dev. Cell *29*, 577–590.
28. Geeraert, C., Ratier, A., Pfisterer, S.G., Perdiz, D., Cantaloube, I., Rouault, A., Pattingre, S., Proikas-Cezanne, T., Codogno, P., and Poüs, C. (2010). Starvation-induced hyperacetylation of tubulin is required for the stimulation of autophagy by nutrient deprivation. J. Biol. Chem. *285*, 24184–24194.
29. Yu, F.X., and Guan, K.L. (2013). The Hippo pathway: regulators and regulations. Genes Dev. *27*, 355–371.
30. Sciarretta, S., Zhai, P., Maejima, Y., Del Re, D.P., Nagarajan, N., Yee, D., Liu, T., Magnuson, M.A., Volpe, M., Frati, G., et al. (2015). mTORC2 regulates cardiac response to stress by inhibiting MST1. Cell Rep. *11*, 125–136.
31. Hansen, M., Rubinsztein, D.C., and Walker, D.W. (2018). Autophagy as a promoter of longevity: insights from model organisms. Nat. Rev. Mol. Cell Biol. *19*, 579–593.
32. Tammineni, P., Ye, X., Feng, T., Aikal, D., and Cai, Q. (2017). Impaired retrograde transport of axonal autophagosomes contributes to autophagic stress in Alzheimer's disease neurons. eLife *6*, e21776.
33. Encalada, S.E., Szpankowski, L., Xia, C.H., and Goldstein, L.S.B. (2011). Stable kinesin and dynein assemblies drive the axonal transport of mammalian prion protein vesicles. Cell *144*, 551–565.
34. Bauer, D.E., Canver, M.C., and Orkin, S.H. (2015). Generation of genomic deletions in mammalian cell lines via CRISPR/Cas9. J. Vis. Exp. *95*, e52118.
35. Hutt, D.M., Loguercio, S., Campos, A.R., and Balch, W.E. (2018). A proteomic variant approach (ProVarA) for personalized medicine of inherited and somatic disease. J. Mol. Biol. *430* (18 Pt A), 2951–2973.
36. Sakurai, S., Tomita, T., Shimizu, T., and Ohto, U. (2017). The crystal structure of mouse LC3B in complex with the FYCO1 LIR reveals the importance of the flanking region of the LIR motif. Acta Crystallogr. F Struct. Biol. Commun. *73*, 130–137.
37. Coutu, D.L., Kokkaliaris, K.D., Kunz, L., and Schroeder, T. (2017). Three-dimensional map of nonhematopoietic bone and bone-marrow cells and molecules. Nat. Biotechnol. *35*, 1202–1210.

STAR★METHODS

KEY RESOURCES TABLE

REAGENT or RESOURCE	SOURCE	IDENTIFIER
Antibodies		
Rabbit polyclonal anti-FYCO1	Atlas Antibodies	HPA035526; RRID: AB_10672867
Rabbit monoclonal anti-LC3B (D11) XP	Cell Signaling Technologies (CST)	3868S; RRID: AB_2137707
Rabbit polyclonal anti-MST1	GeneTex	GTX109294; RRID: AB_1952076
Rabbit polyclonal anti-LAMP1	Abcam	ab24170; RRID: AB_775978
Rabbit polyclonal anti-p-MST1(Thr183)/ MST2(Thr180)	CST	3681S; RRID: AB_330269
Rabbit polyclonal anti pLC3B (Thr50)	21st Century Biochemicals	[6]
Mouse monoclonal anti-mCherry (1C51)	Novus Biologicals	NBP1-96752; RRID: AB_11034849
Mouse monoclonal anti-β-actin (C4)	Millipore Sigma	MAB1501; RRID: AB_2223041
Mouse monoclonal anti-HA (6E2)	CST	2367S; RRID: AB_10691311
Mouse monoclonal anti-α-tubulin (DM1A)	CST	3873P; RRID: AB_1904178
Rabbit polyclonal anti-LAMP2	Thermo Fisher	PA1-655; RRID: AB_2134625
Rabbit polyclonal anti-KEAP1	Proteintech	10503-2-AP; RRID: AB_2132625
Rabbit polyclonal anti-NDP52	GeneTex	GTX115378; RRID: AB_10620266
Mouse monoclonal anti-GFP	DHSB	DHSB-GFP-12A6; RRID: AB_2617417
Goat polyclonal anti-Mouse cathepsin B	R&D systems	AF965; RRID: AB_2086949
Goat anti-Rabbit HRP	CST	7074s; RRID: AB_2099233
Goat anti-Mouse HRP	CST	7076s; RRID: AB_330924
Goat anti-Rabbit Alexa Fluor 488	Thermo Fisher	A11034; RRID: AB_2576217
Goat anti-Rabbit Alexa Fluor 568	Thermo Fisher	A11011; RRID: AB_143157
Goat anti-Mouse Alexa Fluor 488	Thermo Fisher	A11001; RRID: AB_2534069
Goat anti-Mouse Alexa Fluor 568	Thermo Fisher	A11004; RRID: AB_2534072
Bacterial and virus strains		
DH5α competent *E. coli*	Thermo Fisher	18265017
One Shot Stbl3 *E. coli*	Thermo Fisher	C7373-03
Rosetta 2(DE3)pLysS *E. coli*	Millipore Sigma	71403
Chemicals, peptides, and recombinant proteins		
Dulbecco's Modified Eagle Medium (DMEM)	Corning	10-013-CV
Fetal bovine serum (FBS)	Thermo Fisher	26140049
DMEM (for primary neurons)	Thermo Fisher	11965
FBS (for primary neurons)	Thermo Fisher	10082147
Poly-L-lysine	Millipore Sigma	P5899
Neurobasal-A medium	Thermo Fisher	10888022
B-27	Thermo Fisher	17504044
GlutaMAX	Thermo Fisher	35050061
Earle's Balanced Salt Solution (EBSS): starvation medium	Thermo Fisher	24010043
Lipofectamine 2000	Thermo Fisher	11668019
Opti-MEM	Thermo Fisher	31985-070
Bafilomycin A1	Millipore Sigma	88899-55-2
DAPI	Millipore Sigma	D9542
RNAiMAX	Thermo Fisher	13778150
Saponin, from Quillaja pract.	Acros Organics	74499-23-3

(*Continued on next page*)

Continued

REAGENT or RESOURCE	SOURCE	IDENTIFIER
N3500 Nonidet-P40 substitute	US Biological	9036-19-5
Bovine serum albumin (BSA), protease free	Akron	AK1391-0100
cOmplete Protease Inhibitor Cocktail tablets	Millipore Sigma	11697498001
PhosSTOP	Millipore Sigma	4906845001
Pierce ECL Western Blotting Substrate	Thermo Fisher	32209
SuperSignal West Pico PLUS Chemiluminescent Substrate	Thermo Fisher	34577
SuperSignal West Femto Maximum Sensitivity Substrate	Thermo Fisher	34095
Prolong Gold Antifade Reagent	CST	9071
FYCO1 peptide (1265–1298 amino acids of the human protein)	Biomatik	N/A
GST-LC3B	Viva Bioscience	V32470-0500
His-STK4	Millipore Sigma	14-624
Magic Red Cathepsin B assay	Immunochemistry	937
Critical commercial assays		
Q5 Hot Start High-Fidelity 2X Master Mix	New England Biolabs	M0494S
Gibson Assembly Master Mix	New England Biolabs	E2611L
MycoScope PCR Mycoplasma Detection Kit	Genlantis	MY01100
Experimental models: Cell lines		
Human: HEK293T cells	ATCC	CRL-3216
Human: HeLa cells	ATCC	CCL-2
Human: HeLa cells lacking endogenous LC3B	This paper	N/A
Mouse: Immortalized MEFs	[6]	N/A
Mouse: Immortalized *Stk4*$^{-/-}$;*Stk3*$^{+/-}$ MEFs	[6]	N/A
Mouse: Primary hippocampal neurons	Encalada lab, see mice details below	N/A
Mouse: Neuro2a (N2A) neuroblastoma cells	ATCC	CCL-131
Experimental models: Organisms/strains		
C57BL/6	Charles River Laboratories	027
Oligonucleotides		
ON-TARGETplus Control Pool: Non-Targeting pool	Dharmacon	D-001810-10-05
ON-TARGETplus FYCO1 siRNA	Dharmacon	LQ-014350-01-0002
ON-TARGETplus SMARTpool: Human STK4	Dharmacon	L-004157-00-0005
See Table S1 for additional oligonucleotides	N/A	N/A
Recombinant DNA		
Plasmid: pHA-tag	This paper	N/A
Plasmid: pHA-LC3B	This paper	N/A
Plasmid: pHA-LC3B-T50A	This paper	N/A
Plasmid: pHA-LC3B-T50E	This paper	N/A
Plasmid: pHA-LC3B-G120A	This paper	N/A
Plasmid: pHA-LC3B-T50A-G120A	This paper	N/A
Plasmid: pHA-LC3B-T50E-G120A	This paper	N/A
Plasmid: pHA-STK4	This paper	N/A
Plasmid: pEGFP-LC3B	This paper	N/A
Plasmid: pEGFP-LC3B-T50A	[6]	N/A

(*Continued on next page*)

Continued

REAGENT or RESOURCE	SOURCE	IDENTIFIER
Plasmid: pEGFP-LC3B-T50E	[6]	N/A
Plasmid: pBABE-mCherry-FYCO1	Univ. of Dundee	DU45204
Plasmid: pSpCas9(bb)-2A-GFP	Addgene	48138
Plasmid: pSpCas9(bb)-2A-GFP-LC3B Human A	This paper	N/A
Plasmid: pSpCas9(bb)-2A-GFP-LC3B Human B1	This paper	N/A
Plasmid: pSpCas9(bb)-2A-GFP-LC3B Human B2	This paper	N/A
pLKO.1-puro non-targeting (scramble) shRNA Control	Millipore Sigma	SHC016-1EA
pLKO.1-puro FYCO1 shRNA 1	Millipore Sigma	TRCN0000184601
pLKO.1-puro FYCO1 shRNA 2	Millipore Sigma	TRCN0000183567
pLKO.1-puro FYCO1 shRNA 3	Millipore Sigma	TRCN0000179990
pLKO.1-puro FYCO1 shRNA 4	Millipore Sigma	TRCN0000178746
pLKO.1-puro FYCO1 shRNA 5	Millipore Sigma	TRCN0000183006
Software and algorithms		
SAINTq software	SourceForge	http://saint-apms.sourceforge.net/Main.html
In house R script (ver. 3.5.1, 64-bit)	SBP: Proteomics	https://www.r-project.org/
Octet software 10.0.1	FortéBio	https://www.sartorius.com/en/products/protein-analysis/octet-systems-software
PyMOL 2.3	Schrödinger	https://pymol.org/2/
Imaris 9.3.0	Bitplane	https://imaris.oxinst.com/
ImageJ	NIH	https://imagej.net/Fiji
KymoAnalyzer	Encalada Lab	https://www.encalada.scripps.edu/kymoanalyzer
Zen lite processing software	Zeiss	https://www.zeiss.com/microscopy/us/products/microscope-software/zen-lite.html
Prism 8	GraphPad	https://www.graphpad.com/scientific-software/prism/
Microsoft Office: Excel, PowerPoint, Word	Microsoft	https://www.microsoft.com/en-us/microsoft-365
RStudio	RStudio Inc	https://www.rstudio.com/
Image Lab	Thermo Fisher	https://www.bio-rad.com/en-us/product/image-lab-software?ID=KRE6P5E8Z
Other		
Pierce Anti-HA magnetic beads	Thermo Fisher	88836
Anti-RFP magnetic beads	MBL Life Science	M165-11
1-1/2 Micro glass coverslips – 12 mm diameter	Electron Microscopy Sciences	72230-01
Premium microscope slides (Superfrost)	Thermo Fisher	12-544-7
Spin-X centrifuge tube filter 0.45 μm cellulose acetate	Corning	8162
NuPAGE 4–12% Bis-Tris gels 1 mm × 10 wells	Thermo Fisher	NP0321BOX
Premium autoradiography film (5 × 7 in.)	Denville Scientific	E3012
Immobilon-P membrane, PVDF, 0.45 μm, 8.5 cm × 10 m roll	Millipore Sigma	IPVH85R

RESOURCE AVAILABILITY

Lead contact

Further information and requests for resources and reagents should be directed to and will be fulfilled by the Lead Contact, Malene Hansen (mhansen@sbpdiscovery.org).

Materials availability

Plasmids and cell lines generated in this study are available upon request to the Lead Contact.

Data and code availability

The published article includes all datasets generated in this study (See Data S1 for LC3B interactors proteomics data). The KymoAnalyzer software used to quantitively analyze the intracellular transport of vesicles in neurons is an open-source ImageJ-based package that can be downloaded from the Encalada lab website: https://www.encalada.scripps.edu/kymoanalyzer.

EXPERIMENTAL MODEL AND SUBJECT DETAILS

Mammalian cell lines

See Key resources table for details of all cells and reagents employed. HEK293T cells, HeLa cells (both human female origin), and N2A neuroblastoma cells (mouse male origin) were purchased from ATCC. Immortalized wild-type (WT) and STK4-deficient mouse embryonic fibroblasts (MEFs) were obtained as described.[6] Cell lines were cultured at 37°C in DMEM (Corning) supplemented with 10% fetal bovine serum (FBS, GIBCO), referred to as ''normal medium,'' and were routinely checked for mycoplasma using the MycoScope PCR detection kit according to the manufacturer's instructions (GenLantis).

Mouse primary hippocampal neurons

C57BL/6 wild-type mice used to isolate primary hippocampal neurons were originally obtained from Charles River Laboratories. Mice colonies were maintained according to the guidelines recommended by the Department of Animal Resources (DAR) at Scripps Research, which included free access to food and water, with a 12h light-dark cycle. All mouse protocols were reviewed and approved by Institutional Animal Care and Use Committee (IACUC) at The Scripps Research Institute (Scripps Research). Mouse hippocampal neurons were isolated from newborn mice and cultured as described.[33] Briefly, hippocampi were dissected from 1- or 2-day-old mice of either sex, treated with papain (Worthington) for 15 min, and disrupted by aspirating through a micropipette tip 7 to 10 times. Dissociated neurons were resuspended in normal medium and plated in 24-well plates containing 12-mm glass coverslips pretreated with 50 μg/ml poly-L-lysine (Sigma) in borate buffer at 37°C. The medium was exchanged for Neurobasal-A medium (GIBCO) containing 2% B-27 (GIBCO) and 0.25% GlutaMAX (GIBCO) 1 h after plating.

METHOD DETAILS

Plasmids and oligonucleotides

Plasmids encoding EGFP-tagged WT LC3B and phospho mutants (T50A and T50E) were obtained as described.[6] Plasmids encoding HA-tagged LC3B proteins were generated by replacing the EGFP sequence in the EGFP plasmids with an HA-tag followed by a Tobacco etch virus protease sequence recognition site and a Flag-Tag (Genewiz) using *Age*I and *Hind*III (New England Biolabs). Lipidation-deficient LC3B proteins were generated by mutagenic PCR using Q5 Hot Start High-Fidelity Master Mix (New England Biolabs) to introduce the GGG to GCT change that leads to a glycine to alanine (G120A) mutation. Bacterial expression plasmids encoding His-tagged WT, T50A, and T50E LC3B proteins were produced as described.[6] A plasmid encoding mCherry-tagged FYCO1 was generated by cloning the mCherry-FYCO1 gene from a pBABE-puro-mCherry-FYCO1 plasmid (Dr. Dario Alessi, University of Dundee) into the plasmid backbone of EGFP-LC3B (Addgene) by amplification of fragments using Q5 Hot Start High-Fidelity Master Mix and ligation using a Gibson Assembly Master Mix (New England Biolabs). pLKO.1-puro plasmids encoding scrambled shRNA and five FYCO1-targeted shRNAs were purchased from Sigma Aldrich. For details on oligonucleotides refer to Table S1.

Generation of HeLa LC3B knockout cells

LC3B gene knockout (KO) was performed using the CRISPR-CAS9 system according to a published protocol.[34] Briefly, HeLa cells were transfected with two plasmids encoding GFP-CAS9 (Addgene) and an sgRNA targeting the first or the fourth exon of the *LC3B* gene. After 24 h, GFP-positive cells were sorted by FACS and single cells were placed in 96-well plates. Clones were grown for 2–3 weeks and analyzed for gene deletion by PCR. Gene-edited clones were expanded in 24-well plates, and LC3B protein deficiency was confirmed by western blotting and immunofluorescence microscopy (See Figure S1) LC3B-KO cells were selected, expanded, and frozen before use in experiments.

Gene silencing, transient transfection, and cell treatment

Cells were reverse transfected with 10 nM of non-silencing control or specific gene-targeting siRNAs (siNS, siFYCO1, or siSTK4; Dharmacon) using Opti-MEM and lipofectamine RNAiMAX according to the supplier's recommendations (Life Technologies). After

48 h, cells were collected and used for experiments. Transient plasmid transfections were performed using Opti-MEM and Lipofectamine 2000 (Life Technologies), and cells were collected for experiments 24 h after transfection. For experiments with cells expressing siRNAs and plasmids, cells were transfected with siRNAs for 24 h and then transfected with the plasmid of interest for an additional 24 h before analysis.

For autophagy flux assays, cells were washed three times with normal medium, normal medium containing the late-autophagy blocking compound bafilomycin A_1 (BafA, Sigma) at 50 nM, or starvation medium (Earle's Balanced Salt Solution (Life Technologies) before incubation in the same media for the indicated times at 37°C.

Affinity purification

HeLa LC3B-KO cells, 293T cells, MEFs, or N2A cells were transiently transfected with plasmids (6.6 μg/10^6 cells) encoding HA-tag, HA-LC3B WT, HA-T50A or HA-T50E for 24 h, incubated with normal medium or starvation medium for 1 h, and then lysed with IP lysis buffer (0.5% NP-40, 150 mM NaCl, 50 mM Tris HCl, pH 7.5, protease inhibitors [cOmplete, Roche], and phosphatase inhibitors [PhosStop, Roche]). Cell lysates were clarified by serial centrifugation (600 × *g* for 3 min and 9300 × *g* for 10 min) and diluted 1.25-fold with lysis buffer. An aliquot of the lysate (5%) was reserved as input for western blotting and the remaining lysate was incubated with anti-HA magnetic beads (Pierce) overnight at 4°C. Beads were washed seven times with wash buffer (0.1% NP-40, 150 mM NaCl, 50 mM Tris HCl, pH 7.5) and three times with 50 mM Tris HCl, pH 7.5. Samples were then processed for mass spectrometry or western blot analysis as described below. For immunoprecipitation of mCherry-FYCO1, the same protocol was performed using anti-RFP magnetic beads (MBL Life Science).

Mass spectrometry

Mass spectrometry was performed at the Proteomics Core of Sanford Burnham Prebys Medical Discovery Institute. HA-tag (negative control), HA-LC3B WT, HA-T50A and HA-T50E proteins were immunoprecipitated (three experimental replicates: R1, R2 and R3) as described above and subjected to on-bead digestion as previously described.[35] The total peptide concentration was determined using a NanoDrop spectrophotometer (Thermo Fisher) and the samples were then analyzed by LC-MS/MS using a Proxeon EASY nanoLC system (Thermo Fisher Scientific) coupled to a Q-Exactive Plus mass spectrometer (Thermo Fisher Scientific). Peptides were separated using an analytical C18 Acclaim PepMap column (75 μm × 250 mm, 2 μm vesicles; Thermo Scientific) and a 180-min gradient at a flow rate of 300 μl/min: 1% to 5% B in 1 min, 5% to 20% B in 139 min, 20% to 35% B in 30 min, and 35% to 45% B in 10 min (A = formic acid 0.1%; B = 80% acetonitrile + 0.1% formic acid). Mass spectrometry settings were as described previously.[35] Mass spectra were analyzed with MaxQuant software version 1.5.5.1. Peptides were searched against the *Homo sapiens* Uniprot protein sequence database (downloaded July 2018) and GPM cRAP sequences (commonly known protein contaminants), as described.[35] Statistical analysis for the identified peptides was performed using an in-house R script (version 3.5.1) and SAINTq by the Proteomics Core of Sanford Burnham Prebys Medical Discovery. Identified LC3B protein interactors and corresponding intensity, as well as average normalized intensity ratios interactor/LC3B are shown in Data S1 (Excel sheets show raw (A) and normalized data (B), respectively). Benjamini-Hochberg correction with 10% false discovery rate, > 1.5 fold was applied to identify protein interactors binding either more or less to LC3B phospho mutants. NDP52 was not identified in this mass spectrometry analysis.

Western blot

Reserved input lysate (20 μg of total protein) or immunoprecipitated materials from affinity purifications were analyzed by standard western blotting protocols. Briefly, proteins were separated in Novex 4%–12% acrylamide Bis-Tris gels (NuPage) and transferred to PVDF membranes. Membranes were blocked in Tris-buffered saline containing 0.05% Tween-20 (TBST) and either 5% milk or 3% bovine serum albumin (BSA), according to the antibody manufacturer's recommendations, and then incubated for 2 h at room temperature with primary antibodies diluted in 1% milk or 3% BSA in TBST with gentle rocking. Blots were washed three times (total 30 min) and incubated with horseradish peroxidase (HRP)-conjugated anti-mouse or anti-rabbit secondary antibodies (Cell Signaling Technologies) for 1 h at room temperature with gentle rocking. Blots were washed again and developed with Pierce ECL Western Blotting substrate (Base, SuperSignal West Pico/Femto, depending on protein levels) and visualized using a Bio-Rad ChemiDoc Imaging System or with HyBlot CL autoradiography films (Denville). Quantification of band intensity was carried out using ImageJ (National Institutes of Health) software. Details of western blot quantification are shown in Data S1 sheet C.

In vitro phosphorylation of LC3B and co-immunoprecipitation of FYCO1

Aliquots of 3 μg of GST-LC3B (Viva Bioscience) were incubated alone or with 250 ng of His-STK4 (Millipore) in *in vitro* kinase reaction buffer (10 mM $MgCl_2$, 1 mM EGTA, 1 mM dithiothreitol, 0.5 μm ATP, 20 mM Tris, pH 7.5) for 1 h at 30°C. The *in vitro* kinase reaction mixtures were incubated with 350 μL clarified lysate of HeLa LC3B-KO cells (8 × 10^5 cell equivalents, prepared as described above) and glutathione-Sepharose beads (Bioworld) for 3 h at 4°C on a rotator. As a negative control, the same procedure was performed with a mock *in vitro* reaction buffer lacking GST-LC3B and His-STK4. Sepharose beads were washed seven times with wash buffer (0.1% NP-40, 150 mM NaCl, 50 mM Tris HCl, pH 7.5) and eluted by heating in Laemmli sample buffer at 95°C for 10 min. Samples were passed through a 0.45 μm cellulose acetate filter (Costar) and then subjected to western blot analysis.

Biolayer interferometry

Cultures (500 ml) of Rosetta 2(DE3) pLysS *E. coli* (Millipore) expressing human LC3B-WT, T50A, or T50E[6] were grown to an optical density of 0.4–0.6 at 600 nm, and recombinant protein expression was induced by addition of 0.5 mM isopropyl-β-D-thiogalactopyranoside (VWR) for 16–18 h at 25°C. Bacteria were harvested by centrifugation and lysed with a microfluidizer in 50 mM Tris-HCl (pH 8.0), 300 mM NaCl, 30 mM imidazole, and 2 mM β-mercaptoethanol (BME). The lysates were clarified by centrifugation, filtered, incubated with Ni-NTA beads for 1 h, and eluted in the same buffer containing 250 mM imidazole. The sample was then dialyzed overnight in Snakeskin dialysis tubing (3500 kDa pore size) in 50 mM Tris-HCl (pH 8.5), 100 mM NaCl, and 5 mM BME. The protein was concentrated using Amicon-3.5K filters and subjected to size exclusion chromatography on a Superdex 200 column (GE Healthcare). The concentration of eluted proteins was measured at 280 nm using a Nanodrop spectrophotometer and the proteins were verified by Coomassie Blue staining and western blotting. Purified His-LC3B-WT, T50A, or T50E proteins were diluted to 3 μg/ml in Dulbecco's phosphate-buffered saline (PBS; GIBCO) containing 0.1% BSA and 0.02% Tween-20 and immobilized on NTA capture sensors (FortéBio). Human FYCO1 peptide (amino acids 1265–1298, containing the LIR and adjacent residues)[4] was synthesized by Biomatik and reconstituted at 2 mg/ml in DMSO. The binding reaction was performed using two-fold serial dilutions of FYCO1 peptide (0.5–20 μM). The association and dissociation phases were analyzed for 60 s and the curves were inverted to fit them to a 1:1 model. Affinity constants were calculated from the kinetic constant after normalization for the buffer control. All binding measurements were performed on an Octet Red instrument (FortéBio) and the results were processed using Octet software 10.0.1 (FortéBio).

Structural representation of the LC3B–FYCO1-LIR complex

The crystal structure of a *Mus musculus* complex between LC3B and FYCO1-LIR peptide (PDB: 5WRD)[36] was represented in cartoon form using Pymol software. Distance measurements between T50 in LC3B and D1235 and D1236 adjacent to FYCO1-LIR (homologous to amino acids D1276 and 1277 in *Homo sapiens* FYCO1) were performed with Coot (Crystallographic Object-Oriented Toolkit) software and were found to be consistent with hydrogen bonding distances. The *Mus musculus* FYCO1-LC3B complex structure was chosen for representation because coverage of the FYCO1 peptide sequence was greater than in the human structure.

Fluorescence and confocal microscopy

Cells (2×10^5) were seeded in 24-well plates containing 12-mm glass coverslips, transiently transfected with the appropriate plasmids, and treated with normal or starvation medium as described above. After treatment, cells were fixed with 4% paraformaldehyde in PBS for 20 min and processed for fluorescence microscopy using standard protocols (https://www.cellsignal.com). Briefly, cells were incubated with primary antibodies against FYCO1 or autophagosomal and lysosomal proteins (see Key resources table) diluted in PBS containing 10% FBS and 0.2% saponin for 2 h at room temperature. Cells were then washed three times with PBS and incubated with Alexa Fluor 488- or 568-labeled secondary antibodies (Thermo Fisher) diluted at 1:1000 in PBS/10% FBS/0.2% saponin for 1 h at room temperature. Cells were washed three times in PBS, incubated with 4¢,6-diamidino-2-phenylindole (DAPI) to label nuclei, and mounted with Prolong Gold Antifade Reagent. Imaging was performed using a Zeiss LSM 710 NLO confocal microscope. For each condition, 15 to 20 images were acquired in randomly selected fields with a PlanApchromat 63X/1.4 DIC oil objective lens. An average of 10 to 15 stacks of 0.3 μm thickness were acquired.

Live-cell imaging in HeLa cells

HeLa LC3B-KO cells (2×10^5) were seeded in 35-mm glass-bottom dishes (MatTek) for 24 h and transfected with GFP-tagged LC3B expression plasmids as described above. The medium was then replaced and the cells were imaged 2 h later with a Zeiss LSM 880 Rear Port Laser Scanning Confocal and Airyscan FAST microscope equipped with a stage pre-heated to 37°C. Approximately 9 to 10 cells per condition were randomly selected for imaging using a PlanApchromat 63X/1.4 DIC oil objective lens with single photon lasers emitting at 488 nm. Each cell was imaged for 3 min (360 frames, 2 frames/s) and, on average, 8–10 slices were acquired through a total cell thickness of ~2.0–2.5 μm to ensure the complete punctum was captured for particle tracking in four dimensions.

Live-cell imaging in primary mouse hippocampal neurons

Hippocampal neurons were plated on 12-mm glass coverslips in 24-well plates, cultured for 8 to 10 days, and then transfected using 2 μL of Lipofectamine 2000 (Life Technologies) and 1.6 μg of DNA per well with the GFP-LC3B expression plasmids with or without scrambled shRNA or a mixture of five FYCO1-targeting shRNAs (Sigma Aldrich). The efficiency of shRNAs targeting *Fyco1* in mouse cells were verified in N2A neuroblastoma cells (data not shown), a proxy for primary neurons in which LC3B phospho mutants displayed autophagy phenotypes similar to other cell types (Figure S4E). At 48 h post-transfection, the mid-axon region of neurons was imaged using a Nikon Ti-E Perfect Focus inverted microscope equipped with a total internal reflection fluorescence (TIRF) setup, an Andor iXon + DU897 EM camera, and a 100X/1.49 NA oil objective. A 488 nm laser was used for detection of GFP. Lasers were positioned at an angle for pseudo-TIRF acquisition. Each neuron was imaged for 5 min (300 frames, 1 frame/s). Axons were distinguished from dendrites by morphology,[33] and the polarity of axons was determined by identification of soma and axonal termini for each movie.

QUANTIFICATION AND STATISTICAL ANALYSIS

Vesicle number and positioning quantification in HeLa cells

LC3B-positive autophagosomes were quantified using Imaris 9.3.0 (Bitplane, Zurich). Confocal images of individual cells were processed using the software "spots" feature with an estimated diameter of 0.5 μm and then corrected using the "different spot sizes:

region growing'' feature. Thresholds were set using the ''Quality'' feature and determined manually. The local contrast threshold for region-growing spots was then manually set and maintained. Puncta were counted manually in 2–3 cells per condition and compared with the Imaris software counts to verify the accuracy and precision of measurements. The ''surface'' feature was used to reconstruct the nucleus of each cell using DAPI staining. Following generation of spots and surface objects, distance transformation was performed between the outer nuclear surface and the LC3B-positive puncta. Distances for individual puncta were exported to Excel (Microsoft) and processed. The distance from the nucleus of each punctum were averaged for each cell and the collective average of all puncta from all cells were represented as a single data point. Additionally, all distances for each condition were pooled and represented as relative frequency distributions with a best-fit line (non-linear regression, Gaussian curve) for interpretation. The same procedures were performed for LAMP-1 (endolysosomal marker; estimated punctum diameter = 0.33 μm).

Colocalization quantification

Colocalization data for LC3B protein interactors and LC3B were processed using Imaris software. LC3B interactor- or LC3B-labeled channels were provided appropriate colocalization thresholds in the software ''coloc'' feature using the ''Polygon'' tool. The same channel thresholds were maintained for all cells, and the most intense fluorescent overlap was quantified by Imaris as voxels (i.e., overlap between volumetric pixels in either channel) as described.[37] The voxel value for each cell was averaged for each condition and used as a single data point for statistical analysis. Colocalization for GFP-LC3B and Cathepsin B in primary neuronal soma was done in Coloc 2 ImageJ plugin.

Particle tracking quantification in HeLa cells

Following raw image acquisition as described in the methods section, a maximum Z-projection of the movies taken from HeLa LC3B KO cells expressing GFP-LC3B proteins was generated using Zen Processing software. The movie files were further processed prior to particle tracking using Imaris image processing functions. The background subtraction function was set at 0.33 μm and a Gaussian-smoothing operation was used to remove the cytosolic GFP signal and to sharpen the visible puncta to improve particle tracking. GFP-positive puncta were marked using the spots feature of Imaris, with an estimated diameter of 0.5 μm for an individual punctum. An appropriate threshold was set to label all puncta visualized and was maintained for all movies analyzed. For particle tracking, the autoregressive motion algorithm was selected with 5–10 μm of maximum ''predicted distance'' and a maximum ''gap distance'' between 2 and 4 μm. Initial tracks were generated by Imaris and then manually curated and corrected to ensure each particle was assigned to the appropriate track for the duration of the movie. A reference frame was added over the nucleus and the general tracking statistics were exported to Excel for full processing. The final displacement relative to the reference frame labeled nucleus was subtracted from the initial displacement and each individual track was designated either ''anterograde'' or ''retrograde.'' The percentage of anterograde or retrograde particles was pooled for each cell and the mean was taken as a single data point for statistical analysis. To quantify directional switches in particle movement, the complete track and trajectories showed by every single particle were displayed and directional switches were arbitrarily determined and quantified by two independent people using visual inspection of individual tracks.

Particle tracking quantification in primary mouse hippocampal neurons

Axonal transport analysis was performed using KymoAnalyzer, a freely available ImageJ-based macro.[21] Briefly, kymographs were generated from time-lapse movies and particle trajectories were manually assigned from the kymograph images. Transport parameters, including direction, velocity, run length, time in motion, switches, and pauses, were automatically calculated by KymoAnalyzer. A detailed description of all the transport parameters used in this study can be found in Neumann et al.[21] Flux is measured by assigning a ''flux analysis gate'' in the middle of the kymographs to count the particles that cross the gate over the entire time span of the kymograph and calculate the rate of movement of particles through the assigned gate as a function of time. Co-transport experiments were done by near-simultaneous two-color imaging. Red-green images were collected with exposure time of 75 ms with a 50 ms delay between them using Nikon's proprietary LAMBDA 10-3 optical filter switch, for 30 s long and at 5 frames/sec (5 Hz) and 5 min (300 s) long at 1 frame/sec (1 Hz). Co-transport quantitation was done in ImageJ by creating individual and merged color kymographs to evaluate the degree of overlap between two channels.

Statistical analysis

Figure legends contain all information regarding statistical tests used, number of biological replicates, dispersion measures used, and specific p values. Statistical analysis and graph generation was conducted using Prism 8.0 software (GraphPad), unless otherwise noted. One-way and two-way ANOVA were performed to analyze single-grouped datasets (Figures 1B, 1F, 2B, S1D, S4B, and S4C) and double-grouped datasets (Figures 2D, 3C, 3E, 3G, 3I, S1C, and S3E), respectively. For all datasets, Tukey's comparison test with a single pooled variance and Geisser–Greenhouse correction was performed. P values are summarized using the GraphPad reporting method: 0.1234 (ns), 0.0332 (*), 0.0021 (**), 0.0002 (***), and < 0.0001 (****). Student's t test was used in Figures S2D and S4J 0.05 (*), and 0.01 (**). For the analysis of LC3B transport in primary hippocampal neurons, most axonal transport parameters did not follow a normal distribution. One-way ANOVA and Šidák's multiple comparison correction was used for Figures 4C–4F and S4G. For Figures 4H and S4F the non-parametric permutation t test (rndttest function of MATLAB [Mathworks] was used. For Figures 4G and S4D, parameter differences were analyzed using both the Rank Sum test (MATLAB [Mathworks]) and the Kolmogorov–Smirnov test (RStudio) adjusting p values for multiple comparisons using Bonferroni.

Current Biology, Volume *31*

Supplemental Information

LC3B phosphorylation regulates FYCO1 binding and directional transport of autophagosomes

Jose L. Nieto-Torres, Sean-Luc Shanahan, Romain Chassefeyre, Tai Chaiamarit, Sviatlana Zaretski, Sara Landeras-Bueno, Adriaan Verhelle, Sandra E. Encalada, and Malene Hansen

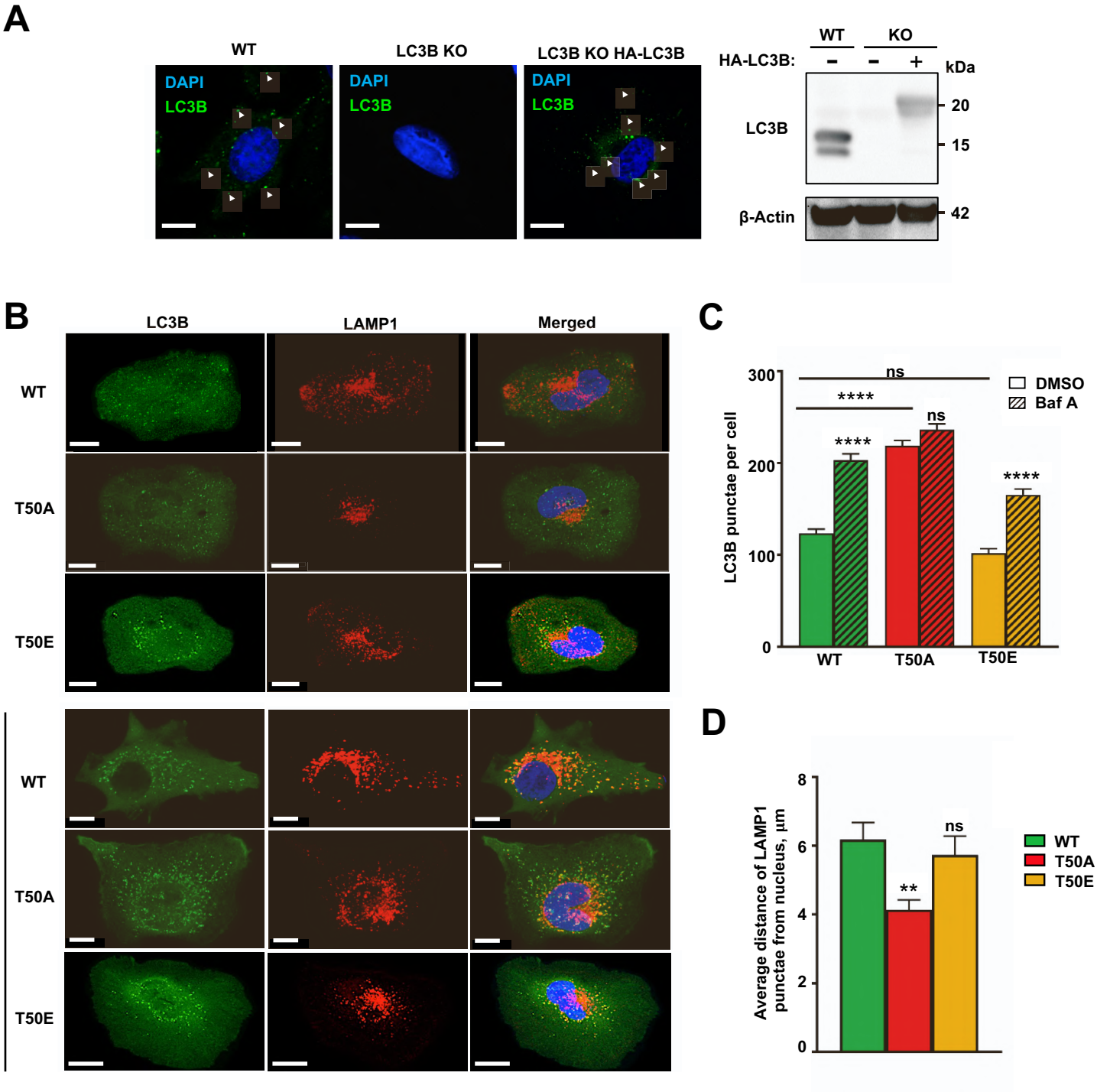

A
WT
LC3B KO
LC3B KO HA-LC3B
DAPI
LC3B
HA-LC3B:
WT
KO
kDa
20
15
42
LC3B
β-Actin
B
LC3B
LAMP1
Merged
WT
T50A
T50E
BafA
C
LC3B punctae per cell
300
200
100
0
ns
****
DMSO
Baf A
D
Average distance of LAMP1 punctae from nucleus, µm
8
6
4
2
0
**
WT
T50A
T50E
E
HA
Starvation
Baf A
kDa
LC3B
15
α-Tubulin
50
LC3B-II/LC3B-I:
1.0 1.2 0.9 1.1 1.3 1.1 1.8 1.8 1.8

Figure S1. Effects of LC3B phosphorylation on autophagy flux and lysosomal positioning in HeLa LC3B-KO cells. Related to STAR Methods. (**A**) Representative immunofluorescence micrographs of HeLa WT, LC3B-KO, or LC3B-KO transfected with HA-LC3B. Cells were stained with anti-HA antibody (green). Arrowheads indicate LC3B-positive puncta (potential autophagosomes). Right panel shows western blot of LC3B in the WT and LC3B-KO cells (n=3). (**B**) Representative immunofluorescence micrographs of LC3B-KO HeLa cells transiently expressing HA-LC3B-WT, HA-T50A, or HA-T50E and incubated in normal medium (upper panels) or medium containing 50 nM bafilomycin A1 (BafA; lower panels) for 6 h. Cells were stained with anti-HA (green) and anti-LAMP1 (red) antibodies. Nuclei were stained with DAPI (blue). (**C**) Quantification of HA-LC3B puncta in images shown in (B). Mean ± SEM of n=20 cells from three experiments. ****$p<0.00005$ by two-way ANOVA. (**D**) Quantification of the distance between lysosomes and the cell nucleus. Mean ± SEM of n=17–30 cells from three experiments. Such measurements were done from a sets of images including those shown in Figure S1C. ***$p<0.0005$ by two-way ANOVA. (**E**) Representative western blot of LC3B in the LC3B-KO cells transfected with HA-, HA-LC3B-WT, HA-T50A or HA-T50E (n=3). Cells were treated with full media, starvation media (EBSS) or starvation media with 250 nM Baf A for 2h. The normalized (via α-Tubulin) LC3B-II/LC3B-I intensity ratios are showed below the western blot as a readout for LC3B lipidation under the different conditions. The apparent discrepancies in our results with a recent report[S1] may stem from differences in protein tagging (HA in our case, vs. Myc) or cell line (HeLa LC3B-KO in our case vs. HEK293 LC3B-KO), and/or method of expression (transient in our case vs. stable). See **Data S1** for quantification of all western blots.

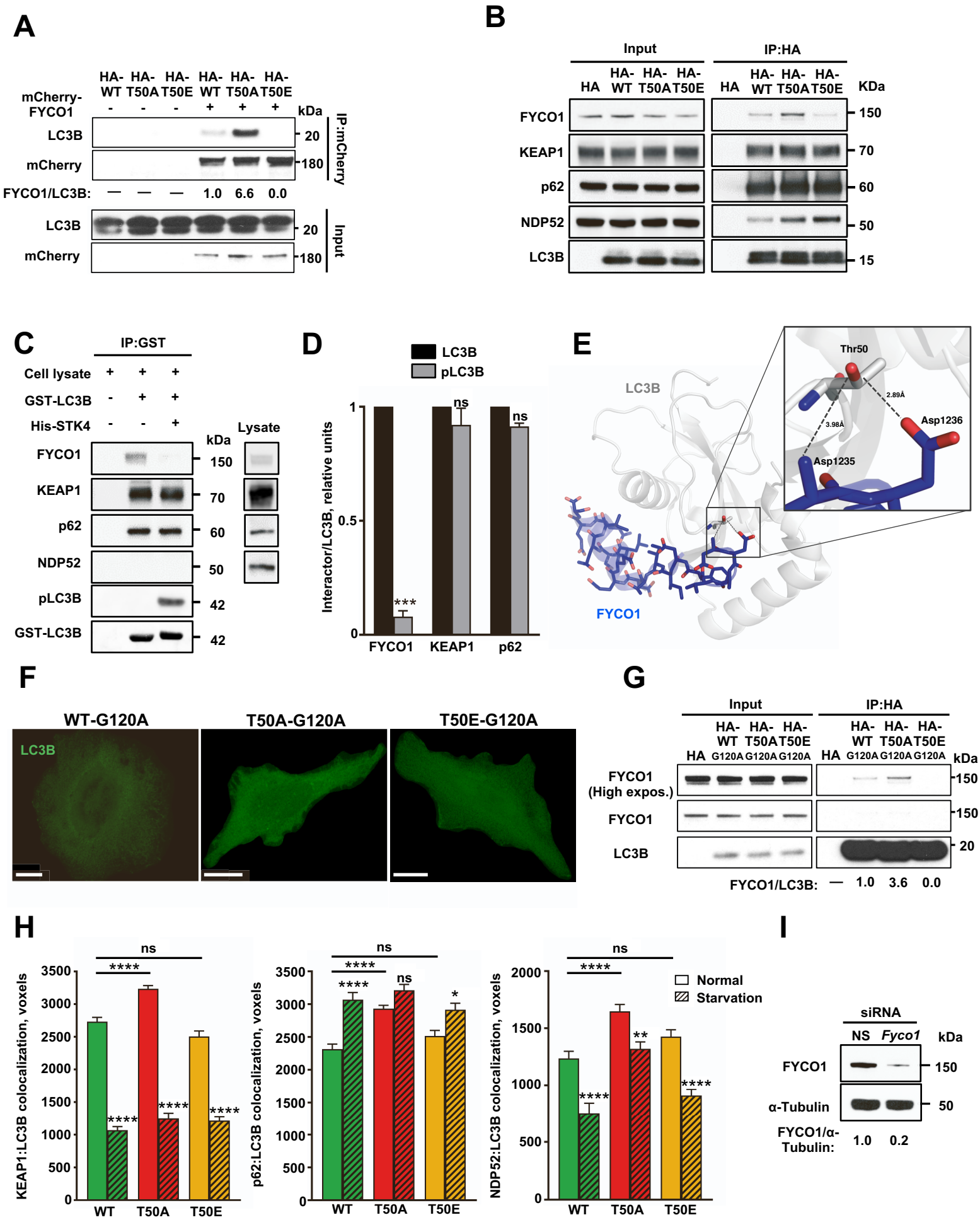

A
HA-WT
HA-T50A
HA-T50E
HA-WT
HA-T50A
HA-T50E
mCherry-FYCO1
kDa
IP:mCherry
LC3B
20
mCherry
180
FYCO1/LC3B:
1.0
6.6
0.0
Input
B
Input
IP:HA
HA
KDa
FYCO1
150
KEAP1
70
p62
60
NDP52
50
LC3B
15
C
IP:GST
Cell lysate
GST-LC3B
His-STK4
Lysate
FYCO1
KEAP1
p62
NDP52
pLC3B
42
GST-LC3B
D
LC3B
pLC3B
Interactor/LC3B, relative units
ns
***
FYCO1
KEAP1
p62
E
LC3B
Thr50
2.89Å
3.98Å
Asp1236
Asp1235
FYCO1
F
WT-G120A
T50A-G120A
T50E-G120A
LC3B
G
Input
IP:HA
HA-WT G120A
HA-T50A G120A
HA-T50E G120A
HA
kDa
FYCO1 (High expos.)
150
FYCO1
LC3B
20
FYCO1/LC3B:
1.0
3.6
0.0
H
KEAP1:LC3B colocalization, voxels
p62:LC3B colocalization, voxels
NDP52:LC3B colocalization, voxels
ns
****
*
**
Normal
Starvation
WT
T50A
T50E
I
siRNA
NS
Fyco1
kDa
FYCO1
150
α-Tubulin
50
FYCO1/α-Tubulin:
1.0
0.2

Figure S2. LC3B phosphorylation modulates FYCO1–LC3B interactions in an LC3B lipidation-independent manner. Related to Figures 1 and 2. (**A**) Representative western blot of LC3B co-immunoprecipitated with mCherry-FYCO1 in HeLa LC3B-KO cells expressing the indicated HA-tagged LC3B proteins. FYCO1/LC3B values indicate the ratio of proteins (n=2). (**B**) Representative western blot of LC3B-interacting proteins FYCO1, KEAP1, p62 and NDP52 co-immunoprecipitation with HA-tagged LC3B proteins expressed in HeLa LC3B-KO cells (n=3). See also **Figures 1C and S3G**. (**C**) Representative western blot of FYCO1, KEAP1, p62 and NDP52 co-immunoprecipitated with non-phosphorylated or *in vitro*-phosphorylated GST-LC3B (GST-LC3B panel shows Coomassie staining), and (**D**) quantification of three experimental co-immunoprecipitation replicates. Mean ± SD of three technical replicates, *p<0.05 Student's t-test. See also **Figure 1E**. While a recent report indicated that p62 binding to LC3B in HEK293 cells assessed by co-immunoprecipitation assays is decreased by T50E phospho-mutation[S1], our experimental approaches (see also **Figure S2H** for colocalization data and [S2]) indicate that T50 status does not significantly change LC3B binding to p62 in HeLa cells and MEFs. (**E**) Crystal structure of LC3B protein (gray) complexed with FYCO1-LIR (blue) (PDB 5WRD, *M. musculus*)[S3]. Potential hydrogen bonds (black dotted lines) between LC3B threonine 50 and two aspartic acid residues adjacent to the FYCO1-LIR are shown. (**F**) Representative immunofluorescence images of HeLa LC3B-KO cells expressing lipidation-deficient (G120A) HA-tagged LC3B proteins. Scale bar = 10 μm. Puncta counts: WT = 0.5 ± 0.3, T50A = 0.45 ± 0.2, T50E = 0.3 ± 0.2. n=20 cells from three experiments. (**G**) Representative western blot of FYCO1 co-immunoprecipitated with HA-tagged LC3B constructs (WT, T50A, T50E) containing the G120A mutation, which prevents lipidation, in HeLa LC3B-KO cells. The mutant proteins were expressed at levels similar to those of their lipidation-proficient counterparts. FYCO1/LC3B values indicate the ratio of proteins (n=3). (**H**) Colocalization between p62, KEAP1, and NDP52 with LC3B puncta "voxels" (volumetric pixels) in HeLa LC3B-KO cells expressing HA-tagged LC3B-WT, T50A, or T50E proteins before or 1 h after incubation in starvation medium. Mean ± SEM of n=20 cells from three experiments.

p<0.0021, ****p<0.0001 by two-way ANOVA. See also **Figure 2B. (**I**) Representative western blot of FYCO1 in HeLa cells expressing control non-silencing (NS) or FYCO1-targeting siRNAs. FYCO1/α-tubulin values indicate the ratio of proteins (n=3). See **Data S1** for quantification of all western blots.

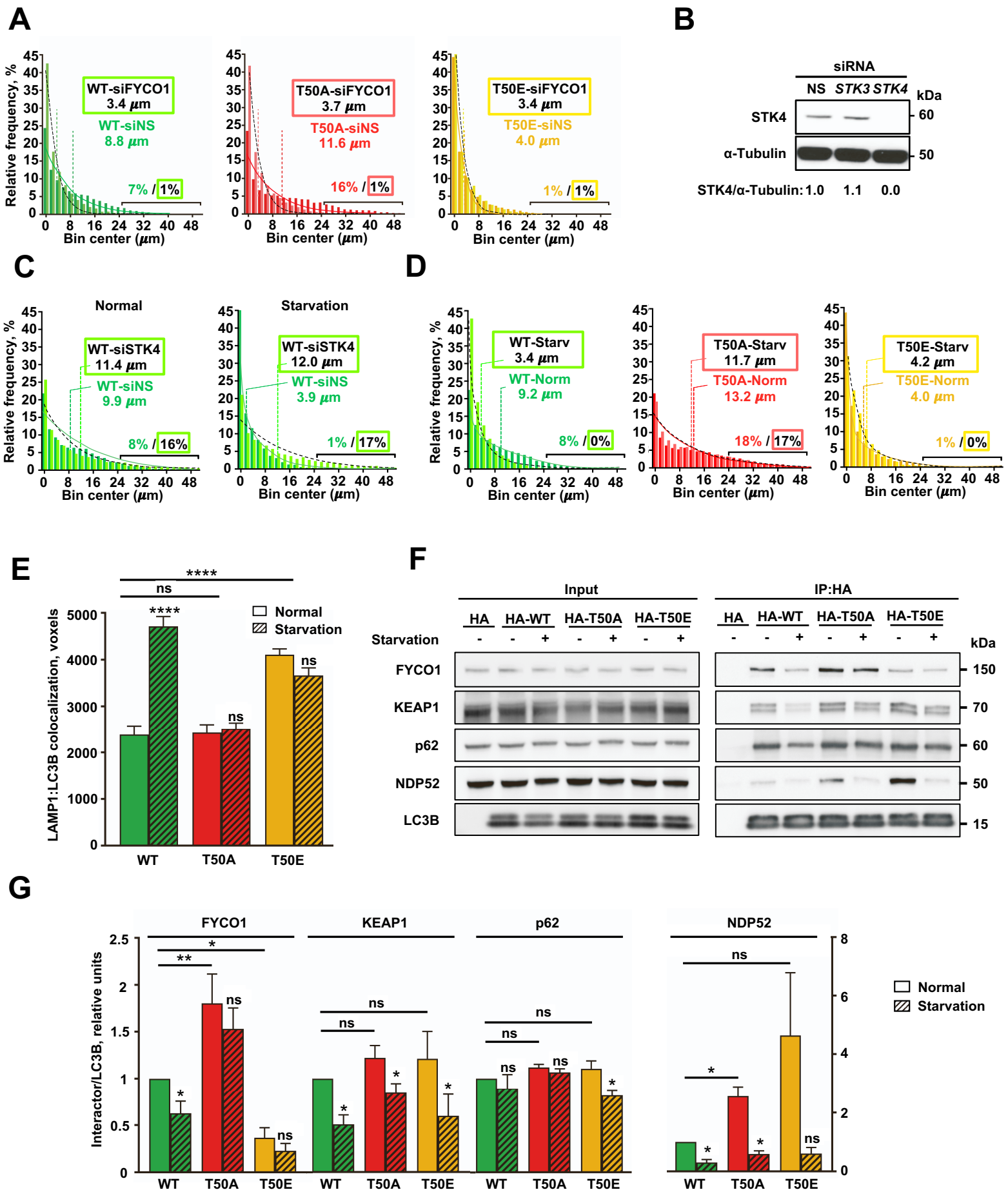

A
Relative frequency, %
WT-siFYCO1
3.4 μm
WT-siNS
8.8 μm
7% / 1%
T50A-siFYCO1
3.7 μm
T50A-siNS
11.6 μm
16% / 1%
T50E-siFYCO1
3.4 μm
T50E-siNS
4.0 μm
1% / 1%
Bin center (μm)
B
siRNA
NS
STK3
STK4
kDa
STK4
α-Tubulin
60
50
STK4/α-Tubulin: 1.0 1.1 0.0
C
Normal
Starvation
WT-siSTK4
11.4 μm
WT-siNS
9.9 μm
8% / 16%
WT-siSTK4
12.0 μm
WT-siNS
3.9 μm
1% / 17%
D
WT-Starv
3.4 μm
WT-Norm
9.2 μm
8% / 0%
T50A-Starv
11.7 μm
T50A-Norm
13.2 μm
18% / 17%
T50E-Starv
4.2 μm
T50E-Norm
4.0 μm
1% / 0%
E
LAMP1:LC3B colocalization, voxels
Normal
Starvation
****
ns
WT
T50A
T50E
F
Input
IP:HA
HA
HA-WT
HA-T50A
HA-T50E
Starvation
kDa
FYCO1
KEAP1
p62
NDP52
LC3B
150
70
60
50
15
G
FYCO1
KEAP1
p62
NDP52
Interactor/LC3B, relative units
Normal
Starvation
WT
T50A
T50E

Figure S3. **Effect of starvation and STK4 silencing on autophagosome positioning and FYCO1–LC3B colocalization. Related to Figures 2 and 3**. (**A**) Relative frequency distribution of the distance between autophagosomes and the nucleus in HeLa cells co-expressing HA-tagged LC3B proteins and control (siNS) or FYCO1-targeting siRNA. The mean distances are shown and a non-linear regression best-fit line was overlaid on each distribution. The percentage of HA-LC3B puncta located at distances greater than 25 μm from the nucleus is also shown. n=25–39 cells from three experiments. See also **Figures 2C and 2D**. (**B**) Representative western blot of STK4 levels in HeLa LC3B-KO cells treated with control non-silencing (NS), *Stk3*-targeting, or *Stk4*-targeting siRNAs. STK4/α-tubulin values indicate the ratio of proteins (n=3). (**C**) As for (A) except HeLa LC3B-KO cells were transfected with control or STK4-targeting siRNA. n=18–23 cells from three experiments. See also **Figure 3B**. (**D**) As for (A) except HeLa cells were incubated in normal or starvation medium. n=23–43 cells from three experiments. See also **Figures 3C and 3D**. **(E)** LC3B-LAMP1 colocalized voxels in HeLa cells expressing HA-tagged LC3B proteins. Mean ± SEM, ***p<0.0002 by two-way ANOVA. (n=30 cells from three experiments. See also **Figures 3F and G**. (**F**) Representative western blot of LC3B-interacting proteins FYCO1, p62 KEAP1, and NDP52 co-immunoprecipitated with HA-tagged LC3B proteins expressed in HeLa LC3B-KO cells before and 1 h after incubation in normal or starvation medium. (**G**) Co-immunoprecipitation quantification of three experimental replicates. Mean ± SD, *p<0.0332, **p<0.0021 by one-way ANOVA. See also **Figure 3H**. See **Data S1** for quantification of all western blots.

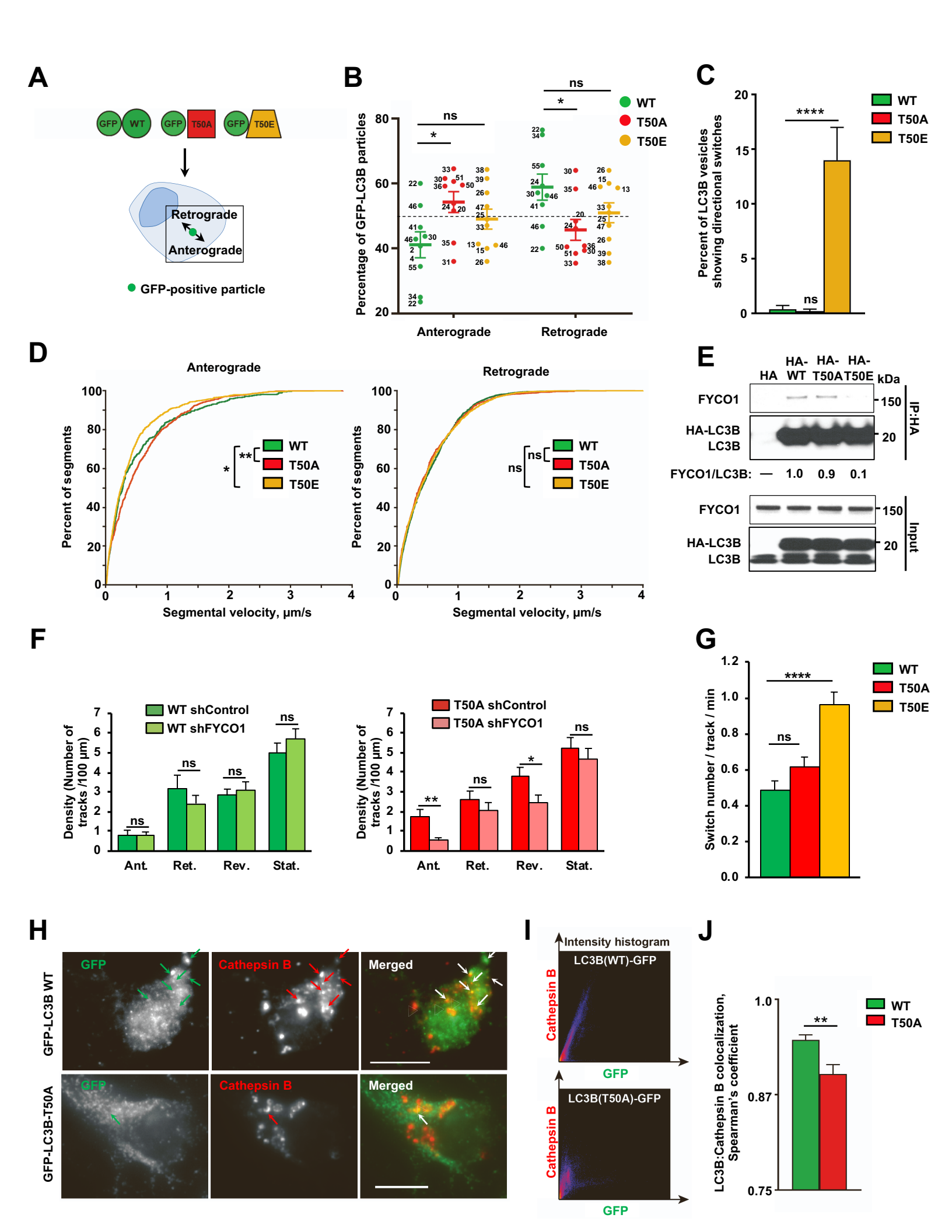

A
GFP
WT
GFP
T50A
GFP
T50E
Retrograde
Anterograde
GFP-positive particle
B
Percentage of GFP-LC3B particles
WT
T50A
T50E
ns
*
Anterograde
Retrograde
C
Percent of LC3B vesicles showing directional switches
****
ns
WT
T50A
T50E
D
Anterograde
Retrograde
Percent of segments
Segmental velocity, µm/s
**
*
ns
WT
T50A
T50E
E
HA
HA-WT
HA-T50A
HA-T50E
kDa
FYCO1
HA-LC3B
LC3B
IP:HA
FYCO1/LC3B: — 1.0 0.9 0.1
Input
150
20
F
WT shControl
WT shFYCO1
T50A shControl
T50A shFYCO1
Density (Number of tracks /100 µm)
Ant.
Ret.
Rev.
Stat.
ns
*
**
G
Switch number / track / min
****
ns
WT
T50A
T50E
H
GFP-LC3B WT
GFP-LC3B-T50A
GFP
Cathepsin B
Merged
I
Intensity histogram
LC3B(WT)-GFP
LC3B(T50A)-GFP
Cathepsin B
GFP
J
LC3B:Cathepsin B colocalization, Spearman's coefficient
**
WT
T50A

Figure S4. Effects of LC3B phosphorylation status on autophagy and autophagosome transport in mammalian cells. Related to Figure 4. (**A**) Schematic illustration of experimental setup for HeLa LC3B-KO cells. Black boxes highlight the area of the cells imaged. Directional anterograde or retrograde movement of LC3B-positive vesicles is depicted. (**B**) Percentage of anterograde or retrograde movement of GFP-LC3B-positive vesicles per cell determined by SR imaging. A total of 938 GFP-LC3B-positive vesicles were analyzed. Individual dots represent measurements obtained from individual cells, and number on the side indicates the number of vesicles/cell analyzed. Dotted horizontal line represents 50% value. Mean ± SEM of n=9–10 cells from two experiments. *p<0.0332 by one-way ANOVA. (**C**) Average percentage of GFP-LC3B-positive vesicles showing directional switches in HeLa LC3B-KO cells. A total of 938 GFP-LC3B-positive vesicles were analyzed. Mean ± SEM of n=9–10 cells from two experiments. ****p<0.0001 by one-way ANOVA. (**D**) Cumulative frequency graphs of anterograde and retrograde segmental velocities of GFP-LC3B-positive vesicles in mouse primary neurons. A total of 6974 segments were analyzed from 33–38 cells from three experiments. *p<0.05, **p<0.01 by Rank Sum test. (**E**) Representative western blot of FYCO1 co-immunoprecipitated with HA-tagged LC3B proteins in N2A cells. FYCO1/LC3B values indicate the ratio of proteins (n=3). (**F**) Densities of LC3B WT or T50A in anterograde (Antero.), retrograde (Retro.), reversal (Rev.) motion or stationary (Stat.) in primary hippocampal axons treated with FYCO1 silencing shRNA or scrambled shRNA control. Mean ± SEM of n=28–33 cells from three experiments. *p<0.05, **p<0.01 by non-parametric permutation t-test (**G**) Mean directional switches per particle per min of GFP-LC3B-positive vesicles in primary mouse neurons. Mean ± SEM of n=33–38 cells from three experiments. ****p<0.0001 by one-way ANOVA and Šidák's multiple comparison correction. (**H**) Immunofluorescence colocalization analysis of GFP-LC3B and Cathepsin B in neuronal somas. (**I**) Representative intensity colocalization histogram. (**J**) Quantitation of anti-GFP LC3B:anti-Cathepsin B Spearman’s coefficient. Mean ± SEM of n=13-14 cells from two experiments. **p<0.01, by Student’s t-test. For all the LC3B-positive vesicles transport-related

experiments see also **Videos S1 and S2 and Figure 4.** See **Data S1** for quantification of all western blots.

Name	Sequence (5'- 3')
pHA-LC3B FW	GCTACCGGTCGCCACCATGTAC
pHA-LC3B RS	CAGGGGGAGGTGTGGGAGG
mCherry-FYCO1 Insert FW	GCTAGCGCTACCGGTCGCCACCATGGTGAGCAAGGGCGAGGA
mCherry-FYCO1 Insert RS	GGTACCGTCGACTGCAGAATTCCTACAGGAAATCACTTCCATC
pmCherry-FYCO1 vector FW	GATGGAAGTGATTTCCTGTAGGAATTCTGCAGTCGACGGTACC
pmCherry-FYCO1 vector RS	CCCTTGCTCACCATGGTGGCGACCGGTA
LC3B G120A FW	CCCAGGAGACGTTCGCTATGAAATTGTCAGTG
LC3B G120A RS	CACTGACAATTTCATAGCGAACGTCTCCTGGG
sgRNA Human LC3B Exon1 FW	CACCGTCAAGCAGCGCCGCACCTT
sgRNA Human LC3B Exon1 RS	AAACAAGGTGCGGCGCTGCTTGAC
sgRNA Human LC3B Exon4 FW	CACCGTGCTTCCCAGTACTTGCAT
sgRNA Human LC3B Exon4 RS	AAACATGCAAGTACTGGGAAGCAC
Check del Human LC3B FW	CCACGCTGCGTGCCG
Check del Human LC3B RS	CCAATCAGTAGAGGGCCCAGATGC
Check del Human LC3B 2 FW	CCTGTTGGTGAACGGACACAGC
Check del Human LC3B 2 RS	CCCTGCGTTTGTGCCAACTG

Table S1. Oligonucleotides Used in This Study. Related to STAR Methods

SUPPLEMENTAL REFERENCES

S1. Shrestha, B.K., Rasmussen, M.S., Abudu, Y.P., Bruun, J.A., Larsen, K.B., Alemu, E.A., Sjøttem, E., Lamark, T., and Johansen, T. (2020). NIMA-related kinase 9 –mediated phosphorylation of the microtubule-associated LC3B protein at Thr-50 suppresses selective autophagy of p62/sequestosome 1. J. Biol. Chem. *295*, 1240–1260.

S2. Wilkinson, D.S., Jariwala, J.S., Anderson, E., Mitra, K., Meisenhelder, J., Chang, J.T., Ideker, T., Hunter, T., Nizet, V., Dillin, A., *et al.* (2015). Phosphorylation of LC3 by the Hippo Kinases STK3/STK4 Is Essential for Autophagy. Mol Cell *57*, 55–68.

S3. Sakurai, S., Tomita, T., Shimizu, T., and Ohto, U. (2017). The crystal structure of mouse LC3B in complex with the FYCO1 LIR reveals the importance of the flanking region of the LIR motif. Acta Crystallogr. Sect. Struct. Biol. Commun. *73*, 130–137.